RESEARCH PAPERS

This journal is printed on acid-free paper, which exceeds the ANSI Z39.48-1992 specification for permanence of paper and library materials. ⊗™
Ⓡ 85% recycled content, including 10% post-consumer fibers.

Thermal Protection of a Ground Layer With Phase Change Materials

X. Duan
Department of Mechanical and Manufacturing Engineering,
University of Manitoba,
75A Chancellors Circle,
Winnipeg, MB, R3T 5V6, Canada

G. F. Naterer[1]
Canada Research Chair Professor
Associate Dean
Faculty of Engineering and Applied Science,
University of Ontario Institute of Technology,
2000 Simcoe Street North,
Oshawa, ON, L1H 7K4, Canada

Conventional ground surface insulation can be used to protect power line foundations in permafrost regions from the adverse effects of seasonal freezing and thawing cycles. But previous studies have shown ineffective thermal protection against the receding permafrost with conventional insulation. In this paper, an alternative thermal protection method (phase change materials (PCMs)) is analyzed and studied experimentally. Seasonal ground temperature variations are estimated by an analytical conduction model, with a sinusoidal ground surface temperature variation. A compensation function is introduced to predict temperature variations in the foundation, when the ground surface reaches a certain temperature profile. Measured data are acquired from an experimental test cell to simulate the tower foundation. With thermal energy storage in the PCM layer, the surface temperature of the soil was modified, leading to changes in temperature in the foundation. Measured temperature data show that the PCM thermal barrier effectively reduces the temperature variation amplitude in the foundation, thereby alleviating the seasonal freezing and thawing cycles. Different thermal effects of the PCM thermal barrier were obtained under different air temperature conditions. These are analyzed via melting degree hours and freezing degree hours, compared with a critical number of degree hours. [DOI: 10.1115/1.3194764]

Keywords: phase change material, ground heat transfer, insulation, foundation, permafrost

1 Introduction

Thawing of permafrost beneath foundations in northern regions can cause severe damage to structures and facilities. There are two related types of problems: One is the seasonal thawing and freezing in the active layer, and the other is the degradation of permafrost (increase of the active layer). The freezing and thawing cycles may cause substantial heave, settlement, tilting, or other differential movements of a structure and may eventually cause failure of the foundation and damage to the structure. The problem becomes worse when combined with local permafrost degradation. Reference [1] provides a comprehensive overview of these problems and examples of thaw induced disruptions to engineered structures including pipelines, roads, power transmission lines, and electrical facilities. Reference [2] also reports a series of permafrost related foundation failure and structural deformation problems of pipelines, old buildings, and gas/water distribution systems at a Canadian site.

Several approaches can be used to protect the foundation of structures in permafrost. They can be categorized as thermal, structural, or geotechnical approaches. Since the fundamental problem is related to the temperature variation in the foundation, thermal approaches are more appropriate and more effective. Ground heat transfer with an insulation layer was analyzed by an interzone temperature profile estimation (ITPE) method for slab-on-grade floors [3]. A thermal barrier with adaptive heat transfer characteristics was developed for applications to zero gravity environments [4]. The most widely used thermal methods are ground cooling with air ventilation, and thermal barriers with insulation materials. The cooling method uses cold air, especially

during winter, to remove heat from the foundation so that the ground temperature is lowered, and the permafrost is preserved or recovered. Several air circulation-based devices, such as air convection piles [5], were studied for permafrost protection. The thermal insulation method increases the thermal resistance of the foundation, so as to reduce heat exchange between the atmosphere and the ground, thereby mitigating the freezing/thawing cycles, and possibly delaying the degradation of permafrost. Thermal insulation was used in the 1980s in Alaska for roadway and airfield engineering [6], and widely used in the arctic regions of Russia to prevent permafrost degradation and settlements [7]. Insulation sheets were also used to protect power transmission line foundations in northern regions of Canada [8]. In China, extensive studies were conducted in recent years for the thermal insulation protection of railway embankments in permafrost regions [9,10]. Different conventional insulation materials were applied, including styrofoam [8], expanded polystyrene (EPS), and polyurethane foam [9,10]. Recently, aerogel insulation blankets were also reported for thermal insulation during freezing processes [11].

The thermal insulation method has many advantages such as construction simplicity, low capital investment, and wide adaptability to different structures. But previous studies have shown significant disagreement in regards to overall thermal effectiveness of this method. Field observations of railway embankments with EPS insulation [9,10] showed that insulation can greatly reduce the range of annual ground temperatures and heat exchange. However, reducing the ground temperature range does not necessarily prevent freezing and thawing processes in the foundation. Daigle and Zhao [12] showed that the use of rigid polystyrene insulation actually promoted a fast frost penetration, due to the higher thermal diffusivity and lack of latent heat of the insulation board, as compared with ground material. Studies also found an increased temperature of shallow ground and deep permafrost under the insulation layers [9].

In view of the limitations of conventional insulation materials such as reduced effectiveness caused by moisture penetration, this

---
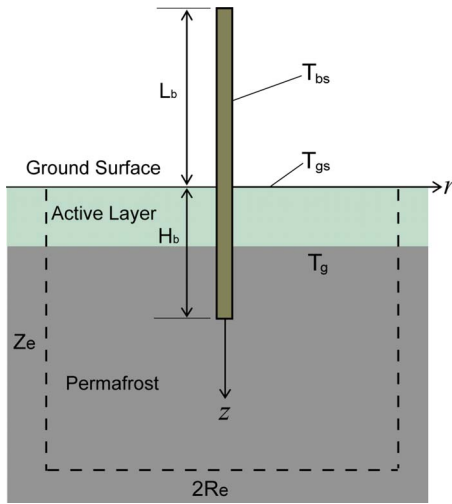
Fig. 1 Schematic of a simplified tower foundation—a metal rod buried in permafrost

Fig. 2 Daily averaged air and soil temperatures in Thompson, Manitoba, from the Canadian climate normals or averages data (1971–2000) [27]

study considers a thermal barrier made of phase change materials (PCMs) along the ground surface. The PCM layer absorbs and releases heat in summer and winter seasons, respectively, but remains at the phase change temperature for a significant period of time, thereby reducing the temperature amplitude at the ground surface. In this way, the problem of thawing and freezing cycles can be alleviated or even prevented. Phase change materials have been studied extensively in recent years. PCMs were used in thermal management of buildings for energy conservation and human comfort [13,14], as well as the design of electronic heat sinks [15,16]. Many other thermal management applications of PCMs were reported, including passive thermal management of batteries for electric vehicles [17] and thermal reservoirs for transient operation of fuel cells [18]. Naterer [19] described PCMs to prevent icing of bridges and reduce cracking of materials caused by repeated freezing and thawing. Such applications are similar to the present tower foundation protection problem, although no such studies have been previously reported for the present application.

Past studies have shown that PCMs are effective for passive thermal management. But there is little or no information available on how they perform for ground thermal protection. Thermal performance of PCM thermal barriers in altering the heat transfer processes in a tower foundation (see problem schematic in Fig. 1) will be studied in this paper, in order to design a thermal barrier for effective thermal protection. This paper analyzes heat transfer in the foundation with a PCM thermal barrier and conventional insulations, both analytically and experimentally. In particular, this study examines how a PCM thermal barrier alters the ground surface temperature variations. When a structure is built over permafrost, especially when metal footings are buried in the ground, heat conduction through the footing will lead to an additional thermal response in the local area surrounding the footing. This was confirmed previously by experimental and analytical studies [20–22]. In this study, thermal effects of the metal tower with different thermal barriers will also be investigated experimentally. This study provides both new analytical and experimental data that will be useful for the design of PCM thermal protections for structures in northern regions.

2 Formulation of Ground Heat Transfer

A model of heat conduction in a semi-infinite medium will be first used to analyze the seasonal temperature variations in the ground, without any structure. The ground is assumed to be homogenous with a constant thermal conductivity k_g and constant thermal diffusivity α_g, with a uniform initial temperature of T_i. This assumption of constant values for ground thermal conductiv-

ity and thermal diffusivity is often used in analytical ground heat transfer modeling [23,24]. The ground surface is assumed to have a time-varying temperature of $T_{gs}(t)$. Defining a temperature difference relative to the initial temperature, $\theta = T - T_i$. The initial temperature difference becomes zero, and the surface is kept at $\theta_{gs}(t) = T_{gs}(t) - T_i$. The transient temperature difference in the ground $\theta_g(z,t)$ can be expressed as [25,26]
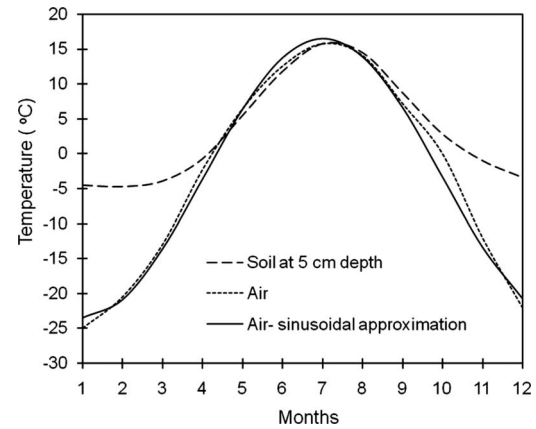
$$\theta_g = \frac{2}{\pi^{0.5}} \int_{z/2\sqrt{\alpha_g t}}^{\infty} \theta_{gs}\left(t - \frac{z^2}{4\alpha_g \beta^2}\right) e^{-\beta^2} d\beta \qquad (1)$$

where β is the integration variable. The solution in Eq. (1) is available from well-known classical solutions in heat transfer textbooks such as Refs. [25,26]. It involves the solution of the Fourier equation for a semi-infinite medium, initially at $\theta_{t=0} = 0$ with a boundary condition of $\theta_{z=0} = \theta_{gs}(t)$. The problem is solved with a continuous infinite plane doublet of strength $2\alpha_g \theta_{gs}(t)$ at the plane of $z=0$ to find the thermal response in an infinite medium.

The air and ground surface temperatures will be approximated by sinusoidal expressions. For example, Fig. 2 shows the temperatures of air and soil at a 5 cm depth in Thompson, Manitoba, Canada [27]. The air temperature can be approximated by

$$T_{air}(t) = 3.5 + 20 \sin\left(\frac{2\pi t}{12} - 2.1\right) \qquad (2)$$

where t is time in units of months. This temperature profile is similar to that of the ground surface temperature, except there is usually an insignificant temperature difference between the two. The ground surface temperature can be approximated by the following general sinusoidal expression:

$$\theta_{gs}(t) = \theta_{gsm} + A_{gs} \sin(w_{gs}t + \phi_{gs}) \qquad (3)$$

where θ_{gsm} is the average ground surface temperature, A_{gs} is the amplitude of the temperature variation, w_{gs} is the frequency of variation, and ϕ_{gs} is the phase lag. Substituting Eq. (3) into Eq. (1) leads to

$$\theta_g = \frac{2}{\pi^{0.5}} \int_{z/2\sqrt{\alpha_g t}}^{\infty} \left\{ \theta_{gsm} + A_{gs} \sin\left[w_{gs}\left(t - \frac{z^2}{4\alpha_g \beta^2}\right) + \phi_{gs} \right] \right\} e^{-\beta^2} d\beta \qquad (4)$$

If a long-term temperature response is needed, then the transient term can be neglected. This leads to the following approximate solution of the temperature difference [20]:
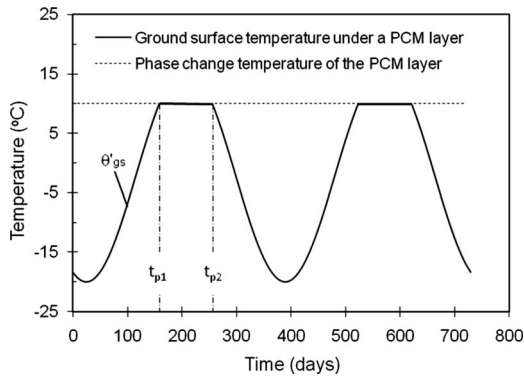
Fig. 3   Ground surface temperature with a PCM layer
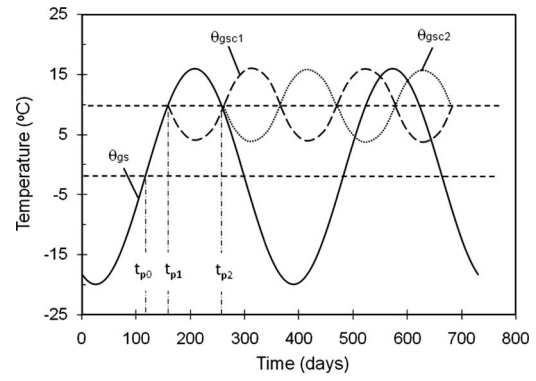
Fig. 4   Illustration of the compensation function method

$$\theta_g = \theta_{\text{gsm}}\,\text{erfc}\!\left(\frac{z}{2\sqrt{\alpha_g t}}\right) + A_{\text{gs}}e^{-z\sqrt{w_{\text{gs}}/2\alpha_g}}\sin\!\left(w_{\text{gs}}t - z\sqrt{\frac{w_{\text{gs}}}{2\alpha_g}} + \phi_{\text{gs}}\right)$$

$$(5)$$

Heat conduction in the ground will be altered when a PCM layer is placed along the ground surface. A PCM layer starts to melt downward when its top surface temperature $T_{s\text{PCM}}$ is greater than its phase change temperature $T_{f\text{PCM}}$. If the initial temperature of the PCM is the phase change temperature (Stefan problem), the melting distance can be calculated by the following equation [19]:

$$Z_{\text{PCM}}(t) = \sqrt{\frac{2k_{\text{PCM}}}{\rho_{\text{PCM}}L_{\text{PCM}}}(T_{s\text{PCM}} - T_{f\text{PCM}})t} \qquad (6)$$

where k_{PCM}, ρ_{PCM}, and L_{PCM} are the thermal conductivity, density, and latent heat of the phase change material, respectively. Therefore, the time needed for melting to a distance of H_{PCM} becomes

$$t_{\text{melt}} = \frac{H_{\text{PCM}}^2 \rho_{\text{PCM}} L_{\text{PCM}}}{2k_{\text{PCM}}(T_{s\text{PCM}} - T_{f\text{PCM}})} \qquad (7)$$

When the PCM layer of thickness H_{PCM} is placed over the ground surface, the melting time will be different than the time calculated by Eq. (7), depending on the thermal properties of the soil under the PCM layer. Moreover, if the initial temperature of the PCM layer is lower than its phase change temperature, the melting time will be longer than the calculated value. Nevertheless, Eq. (7) provides a useful estimation of the melting time for the design of the PCM layer.

The PCM layer can be designed with a particular phase change temperature, thickness, and thermal properties for a specific application. For example, it can be designed so that the melting time is longer than the warm period, during which the air temperature is higher than the phase change temperature of the PCM. In this way, the PCM layer will not be fully melted during the warm seasons, leading to a special ground surface temperature profile illustrated in Fig. 3. The original ground surface profile expressed in Eq. (3) is modified, and a nearly constant ground surface temperature portion (t_{p1} to t_{p2}) is introduced in the warm seasons, where t_{p1} and t_{p2} are the times when the original temperature profile reaches the phase change temperature of the PCM layer $T_{f\text{PCM}}$. In this example, $\theta_{\text{gsm}} = -2\,^\circ\text{C}$, $A_{\text{gs}} = 18\,^\circ\text{C}$, $w_{\text{gs}} = 2\pi/P_{\text{gs}}$ (where $P_{\text{gs}} = 365$ days), $\phi_{\text{gs}} = -2$, and the phase change temperature of the PCM layer is $T_{f\text{PCM}} = 10\,^\circ\text{C}$.

Transient heat conduction in the ground with this boundary condition can be solved by introducing a series of compensation functions and superposing them to the original ground surface temperature profile using Eq. (5). Figure 4 illustrates this method with the first two compensation functions for the first warm season. The cycle period of the compensation functions is twice the melting period, i.e., $2(t_{p2} - t_{p1})$. The amplitude of the compensation functions is the difference between the original peak ground

surface temperature and the phase change temperature of the PCM layer, i.e., $\theta_{\text{gsm}} + A_{\text{gs}} - T_{f\text{PCM}}$. The phase lag between the first compensation function and the original temperature profile is $t_{p2} - t_{p0}$, where t_{p0} is the time instant when the original temperature profile θ_{gs} reaches its average temperature, as shown in Fig. 4. The phase lag between the first and second compensation function is $t_{p2} - t_{p1}$. The two compensation functions can be expressed by

$$\theta_{\text{gsc1}} = (\theta_{\text{gsm}} + A_{\text{gs}} - T_{f\text{PCM}})\sin\!\left[\left(\frac{\pi}{t_{p2} - t_{p1}}\right)(t + \phi_{\text{gs}} - t_{p2} + t_{p0})\right]$$

$$(8)$$

$$\theta_{\text{gsc2}} = (\theta_{\text{gsm}} + A_{\text{gs}} - T_{f\text{PCM}})\sin\!\left[\left(\frac{\pi}{t_{p2} - t_{p1}}\right)(t + \phi_{\text{gs}} - t_{p2} + t_{p0}) - \pi\right]$$

$$(9)$$

Similar functions can be used for other warm seasons, except for different phase lags.

In Sec. 3, both conventional insulation materials and phase change materials will be studied experimentally, with respect to thermal protection of a simulated power transmission tower. Results of experimental measurements in a test cell will be presented for different thermal protection methods.

3   Experimental Setup and Measurement Procedure

Figure 5 shows a schematic of the experimental apparatus. A cubic container is made with 2.54 cm thick Plexiglas with an inner
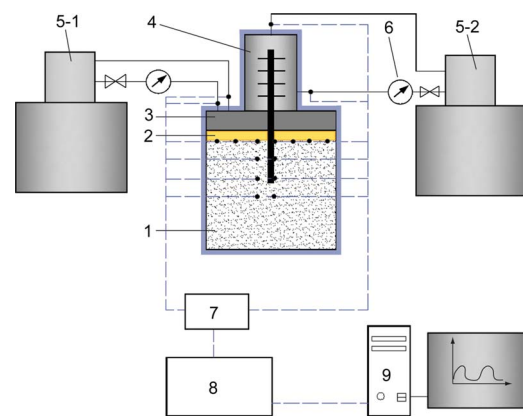
Fig. 5   Schematic of the experimental system. 1: Container, 2: Thermal barrier, 3: Plate heat exchanger, 4: Circular heat exchanger and metal rod, 5: Temperature controlled baths, 6: Flow sensors, 7: Thermocouple analog input modules, 8: USB chassis for cDAQ-9172, 9: Computer and data logger program, ●: Thermocouples.
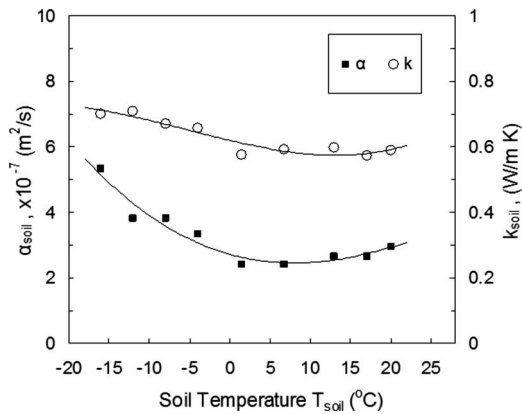
Fig. 6 Soil thermal conductivity and diffusivity at different temperatures ($\lambda_{soil}=16.5\%$)

volume of $200\times200\times200$ mm^3, filled with soil or another heat transfer medium. An additional layer of composite fabric was used for further insulation purposes. A multipass plate heat exchanger, with temperature controlled fluid circulating within it, was installed on the top of the container to simulate a varying air temperature over the ground surface. The bottom plate of the heat exchanger was fabricated with aluminum, while the cover was made of stainless steel. The inner surfaces of the heat exchanger were coated with a thin layer of epoxy for protection against corrosion. The plate heat exchanger was enclosed by the walls of the container and a Plexiglas cover, 20 mm thick. A circular heat exchanger was designed together with an aluminum rod to represent the tower footing. It can be inserted into the container through a hole located at the center of the cover. A temperature controlled fluid then circulates around the finned part of the rod inside the circular heat exchanger, to simulate the air temperature around the above-ground portion of the simulated metal structure (metal tower). The shell of this heat exchanger was made with acrylonitrile butadiene styrene (ABS) for insulation purposes. The 3 mm thick ABS shell was wrapped with another layer of composite fabric of 8 mm thickness to provide additional thermal insulation.

Two different heat transfer media were used in the experiments. A dry medium (flour) was initially used in the test cell for 1D heat conduction validation of the experimental setup. It has the following properties: density of $\rho_{flr}=780$ kg/m^3, thermal conductivity of $k_{flr}=0.24$ W/m K, and thermal diffusivity of $\alpha_{flr}=1.6\times10^{-7}$ m^2/s. The other medium is real soil obtained from a field site near a power transmission tower in Oshawa, Ontario, Canada. The soil was mixed thoroughly to reach a uniform structure before its properties were measured, i.e., density ρ_{soil}, moisture content λ_{soil}, thermal conductivity k_{soil}, and thermal diffusivity α_{soil}. The density of the soil was measured to be $\rho_{soil}=1174$ kg/m^3. The volumetric moisture content of the soil was measured by a soil moisture sensor (type EC-5 ECH2O, from Decagon Devices, Inc., Pullman, WA), $\lambda_{soil}=16.5\%$. A soil property sensor (type TP01, from Hukseflux Thermal Sensors, Delft, The Netherlands) was used to measure the thermal conductivity and diffusivity of the soil, which were found to be dependent on the soil temperature, as illustrated in Fig. 6. The PCM thermal barrier is placed between the top surface of the heat transfer media and the bottom of the flat plate heat exchanger, where good contact was realized by fastening the cover of the test cell. It is a phase change material pack, named RPCM cool pack, made from animal and vegetable sources. Two packs, one with a nominal thickness of 10 mm and another of 20 mm, were used in the experiments. The RPCM has a phase change temperature of 18°C, a density of 840 kg/m^3, a thermal conductivity of 0.55 W/m K, a specific heat of 2.1 kJ/kg K, and latent heat of 195 kJ/kg.

The circulating fluids for both the plate and circular heat exchangers were supplied by two heating and refrigerating baths (from NESLAB Instruments, Waltham, MA), ULT-80 and RTE 140, respectively. The ULT-80 bath can provide a temperature ranging from −80°C to +10°C, with a stability of $\pm0.03\,°C$. The RTE 140 can provide a temperature ranging from −40°C to +150°C, with a stability of $\pm0.05\,°C$. Two different fluids were used for different temperature ranges. When the lowest desired temperature is higher than 1°C, tap water was used in the baths. When the lowest temperature is below 1°C, a nonfreezing fluid is used, namely a 50/50 mixture (by volume) of filtered tap water and ethylene glycol. The flow rates of the circulating water were measured with flow sensors (type FTB603B, from Omega, Laval, QC).

A data acquisition system was used for the temperature measurements, including 15 T-type thermocouple (TC) probes (Omega) that were inserted horizontally into the enclosure at different locations through three sides of the Plexiglas walls, with five TCs on each side. The radial distance R between the TCs and the aluminum rod was the same for each side, but it varied for different sides. When thermal barriers were applied on the top surface, another five T-type thermocouples were distributed over the soil surface to measure its temperature variation. In addition, eight T-type thermocouples were installed at the inlets and outlets of the two heat exchangers to monitor the circulating fluid temperatures. The thermocouples were connected to six thermocouple analog input (TAI) modules NI 9211 (National Instruments, Austin, TX) with a differential connection mode. Each TAI module provided four channel inputs. The TAI modules were connected to a cDAQ-9172 (National Instrument) chassis, which is connected to the computer for data acquisition and analysis.

Efforts were made to minimize experimental errors and uncertainties as much as possible. T-type thermocouple wires were used to connect the inserted probes and the analog input modules. These wires were made as short as possible to reduce the uncertainty in the measured temperature, which was the dominant uncertainty in the study. An uncertainty analysis was conducted by the method of Kline and McClintock [28]. The results are summarized in Table 1. The uncertainty of the measured temperature includes the cold-junction compensation sensor accuracy, errors caused by the NI 9211 modules, as well as the accuracy of the thermocouple probe itself. Time was recorded by the VI logger, based on the CPU time for transient temperature measurements. The precision limit was assumed negligible. The bias limit arose from the inaccuracy of defining the starting time of the measurements, which lies in the range of 5 s.

4 Results and Discussion

4.1 One-Dimensional Transient Heat Conduction Validation. In order to validate the experimental system and analytical solutions, 1D heat conduction was first considered using a dry medium (flour) in the test cell, with an initial temperature $T_i=22.1\,°C$. Without any thermal barrier and circular heat ex-
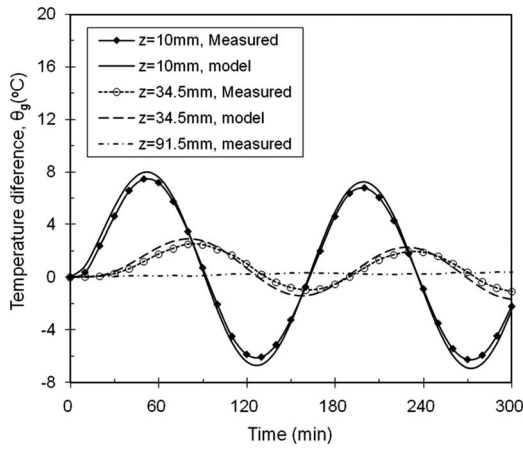
Fig. 7 Measured and analytical results for one-dimensional transient heat conduction

Fig. 8 Variations in simulated air temperature above the PCM layer ($T_{u\text{PCM}}$) and the soil surface temperature under the PCM layer ($T_{b\text{PCM}}$)

changer, a sinusoidal surface temperature in the following form was obtained by circulating temperature controlled fluid through the flat plate heat exchanger:

$$T_f = 22.1 + 16 \sin\left(\frac{2\pi t}{P} + \frac{2\pi}{3} - 2\right) \qquad (10)$$

where the cyclic period P is 146 min in this case. This leads to a top boundary temperature of

$$\theta_{gs}(t) = 16 \sin\left(\frac{2\pi t}{P} + \frac{2\pi}{3} - 2\right)$$

and the temperature difference in the test cell can be calculated by Eq. (5) and compared with the measured results, as shown in Fig. 7. Good agreement was obtained at both locations. The results show the decrease in temperature variation amplitude with depth in the ground. A nearly constant temperature at $z = 91.5$ mm also confirms that heat conduction only propagates to a fixed depth within the test cell, so the assumption of a semi-infinite medium is valid.

4.2 Ground Surface Temperature Beneath a PCM Thermal Barrier. To examine thermal protection from the PCM thermal barrier, an RPCM package was placed over the soil surface in the test cell. The flat plate heat exchanger was then installed to provide a controlled upper surface temperature for the PCM layer, denoted as $T_{u\text{PCM}}$, to simulate air temperature variations in a real foundation site. With thermal energy storage in the PCM layer, the surface temperature of the soil was modified, leading to changes in temperature in the test cell. Figure 8 shows the modified soil surface temperatures below the 20 mm thick PCM layer, denoted as $T_{b\text{PCM}}$, under a typical air temperature profile $T_{u\text{PCM}}$. It can be observed that the soil surface temperature range was greatly reduced by the PCM thermal barrier. The soil surface remains nearly constant at a certain temperature for two periods in each cycle, between the highest and lowest air temperatures (marked by the portion between two horizontal dashed lines in the figure). It can be observed that this constant temperature is about 18°C, which corresponds to the phase change temperature of the PCM. Results in Figs. 8 and 9 also suggest that the nearly constant temperature portion after the warm period is flatter than the previous portion before the temperature peak. This may be due to the difference in freezing and melting mechanisms of the PCM.

Figure 9 shows the results for the 10 mm thick PCM thermal barrier under the same experimental conditions, compared with results of the 20 mm thickness. Similar soil surface patterns were realized, with a further reduced temperature range and longer periods of constant soil surface temperatures. The amplitude of the simulated air temperature was 23°C. The amplitude of the soil surface temperature was reduced to 8.9°C, with the 10 mm PCM layer, and to 7.15°C with the 20 mm PCM layer. Analysis in the following will show that a PCM layer thickness of 27 mm may be able to eliminate the temperature amplitude at the soil surface.
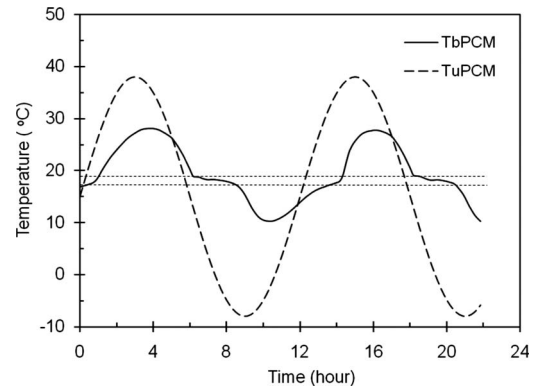
Different thermal effects of the PCM thermal barrier were realized under different air temperature conditions, as shown in Fig. 10, for four tests with the 20 mm thick PCM thermal barrier (labeled as tests (a), (b), (c), and (d)). Figure 10 shows the modified soil surface temperature profiles, compared with the air temperature profiles ($T_{u\text{PCM}}$ listed in Table 2) and phase change temperature of the PCM (18°C). In test (a), the soil surface temperature varies in a nearly sinusoidal fashion (without a clear constant temperature portion), and it remains below 18°C. In test (b), the soil surface temperature just reaches 18°C, and stays nearly constant at this temperature in the warm periods. Then it drops rapidly to a low temperature around 7.5°C in the cold periods. Test (c) shows a situation where the soil surface temperature rises to 26.5°C in the warm periods, followed by a nearly constant period around 18°C. Then it declines to a temperature of 12.3°C in the cold periods. In test (d), the soil surface temperature stays nearly constant around 18°C for a relatively long period in the cold periods, and then rises to 29°C in the warm periods. In this way, the soil surface temperature profile only has variations during warm periods, while variations in the cold periods were cut flat by effects of the PCM layer.

A method of freezing and melting degree hours can be used to interpret the observed behavior of the PCM layer under different air temperature conditions. This method is similar to the well-known concept of heating and cooling degree days in building
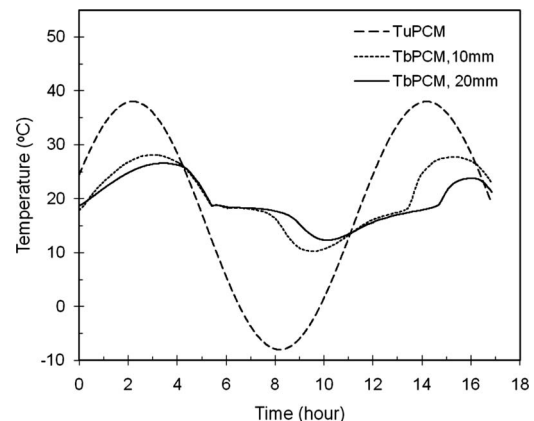
Fig. 9 Effects of PCM layer thickness on its thermal protection performance

(a)

(b)

(c)

(d)
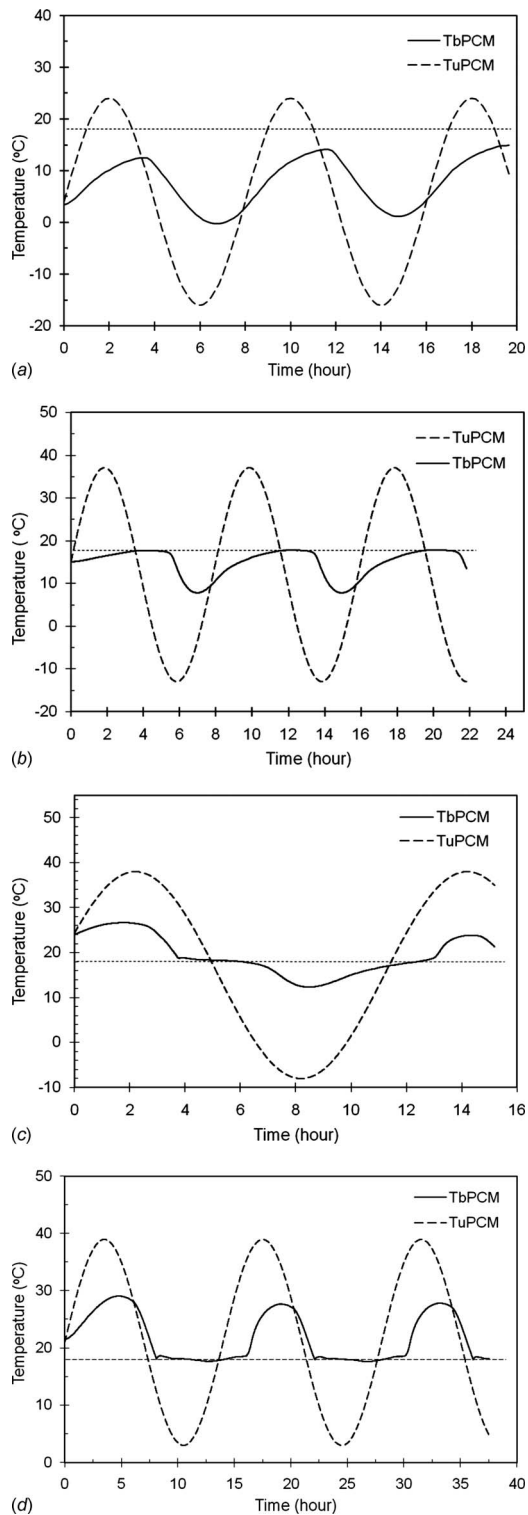
Fig. 10 Soil surface temperatures with a PCM thermal barrier of 20 mm, showing the effects of the PCM layer for different air temperature conditions

energy analysis. In the experiments, when the controlled surface temperature $T_{u\text{PCM}}$ is higher than the phase change temperature $T_{f\text{PCM}}$, the temperature difference multiplied by the duration of the period (in h) is calculated as melting degree hours (MDHs). The freezing degree hours (FDHs) is calculated for periods when $T_{u\text{PCM}}$ is lower than $T_{f\text{PCM}}$. Table 2 lists the melting and freezing degree hours for a full cycle of the simulated air temperature for

each test in Fig. 10.

The minimum melting or freezing degree time for a PCM layer can be obtained by rearranging Eq. (7) as follows:

$$t_{\text{melt}}(T_{s\text{PCM}} - T_{f\text{PCM}}) = \frac{H_{\text{PCM}}^2 \rho_{\text{PCM}} L_{\text{PCM}}}{2k_{\text{PCM}}} \quad (11)$$

From this equation, the critical melting or freezing degree hours can be calculated for the 20 mm RPCM as follows:

$$DH_c = \frac{(0.02)^2 \times 840 \times 195 \times 10^3}{2 \times 0.55} = 59563.64 \text{ deg s}$$

$$= 16.55 \text{ deg h} \quad (12)$$

As discussed in Sec. 2, the actual melting time may be different than the calculated value. In the present experiments, the soil has a similar conductivity as the PCM, but it has a much higher density and latent heat (333.7 kJ/kg for water in the soil) than the PCM. Therefore, the actual melting time would be much longer than the calculated result in Eq. (7). Consequently, the actual critical melting or freezing degree hours are expected to be much larger than 16.55 deg h to realize complete melting or freezing of the PCM layer.

Using this method, the number of MDH in test (a) is only 7.98, far less than the critical degree hours. Therefore, the PCM layer can only melt to a shallow top level in the warm periods, while its bottom remains frozen throughout the whole test, resulting in the modified soil surface temperature in Fig. 10(a). In test (b), the number of MDH (41.5) is large enough to fully melt the whole PCM layer, but not large enough to make the PCM bottom layer warmer than its phase change temperature. Therefore, the PCM bottom layer remains at 18°C for a short time of the warm period; it then cools down to freeze back. In test (c), the number of MDH is so large that the PCM layer is fully melted, and its temperature continues to increase, resulting in a soil surface temperature higher than 18°C. The number of FDH in test (c) is also very large, so the PCM layer can be fully frozen, and further cools down in the cold periods. Similarly, the soil surface temperature profile in test (d) can be understood by the large number of MDH (102.35) that makes the bottom layer of the PCM fully melted. It reaches a peak temperature higher than 18°C in the warm periods. The number of freezing degree days (60.33) is also large enough to fully freeze the PCM layer, but not sufficiently large to make its temperature continue to cool down, resulting in a flat temperature portion in the cold periods. For the current experiments, the actual critical degree hours for the 20 mm thick PCM layer would be around 60, i.e., 3.6 times the calculated number in Eq. (12). Based on this analysis, the critical degree hours of the PCM layer should be equal or larger than 107.13 in order to make the soil surface temperature in test (c) almost unchanged. This requires a thickness of 27 mm of the PCM layer.

4.3 Application of Compensation Function Method for Ground Temperature Prediction. In order to validate the compensation function method, the model was used to predict soil temperatures in the test cell for test (d) of Fig. 10. Temperature differences were compared with the initial soil temperature in the test cell, and only the cyclic temperature portion was analyzed (excluding the noncyclic starting period). The soil surface temperature difference $\theta'_{\text{gs}}(t)$ is shown by the solid line in Fig. 11. The dashed line is the following sinusoidal temperature profile, fitting the soil surface during warm periods:

$$\theta_{\text{gs}}(t) = -5.5 + 12 \sin(0.00012467t - 3.77748) \quad (13)$$

The first compensation function can be derived as

$$\theta_{\text{gsc1}}(t) = 4.05 \sin(0.000112384t - 0.4183872) \quad (14)$$

Figure 12 shows a comparison between the measured soil temperatures at 15 mm depth and the soil temperatures predicted by the compensation function method. The predicted temperature

Table 2 Summary of simulated air temperature conditions

Test	$T_{uPCM}(t)$	MDH	FDH	MDH/DH$_c$	FDH/DH$_c$	MDH/FDH
(a)	$4 + 20 \sin\left(\dfrac{2\pi}{480}t\right)$	7.98	122.32	0.48	7.39	0.07
(b)	$12 + 25 \sin\left(\dfrac{2\pi}{480}t + \dfrac{\pi}{2}\right)$	41.50	89.52	2.51	5.41	0.46
(c)	$15 + 23 \sin\left(\dfrac{2\pi}{720}t + 0.42\right)$	70.63	107.13	4.27	6.47	0.66
(d)	$21 + 18 \sin\left(\dfrac{2\pi}{840}t\right)$	102.35	60.33	6.19	3.65	1.70

profile generally agrees well with measured data, except a maximum discrepancy of 1.2 °C or 14% of the measured temperature range at this depth.

4.4 Thermal Effects of Metal Tower With Different Thermal Barriers on the Ground. Heat transfer in the foundation can be influenced in a local ground region by heat conduction through a metal structure partially buried in the ground. In this section, thermal effects of a metal tower are studied experimentally with the 10 mm PCM thermal barrier along the ground surface. The circular heat exchanger was installed onto the test cell, with the aluminum rod inserted into the center of the test cell. The circulating fluids through both the flat plate and circular heat exchangers were controlled with the same temperature variation, to simulate the air temperature passing over the ground surface and tower
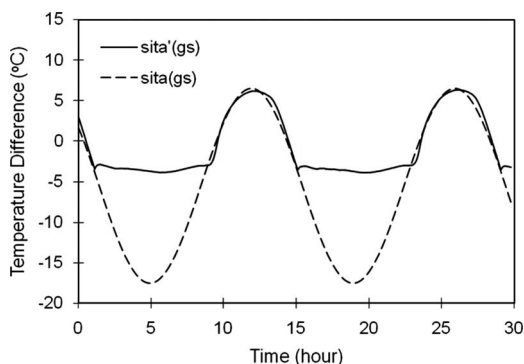
Fig. 11 Soil surface temperature under a PCM layer in the test cell, and the fitted sinusoidal temperature profile
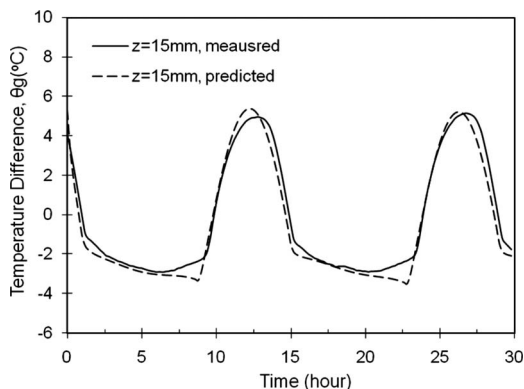
Fig. 12 Comparison between predicted (compensation function method) and measured data

structure.

Figure 13 shows measured temperature results at two locations ($R=7$ mm and $z=20$ mm, and $R=39$ mm and $z=20$ mm) of the same depth level, but different radial distances from the tower footing. Without the protection of a thermal barrier, soil at this location experienced a freezing period at a temperature of about -1 °C in the cold period. The PCM thermal barrier prevented soil freezing by reducing the soil temperature amplitude. Thermal effects of the tower can then be determined by comparing the temperature profiles at locations of different radial distances. The results indicated that the thermal barrier cannot prevent the thermal effects induced by the tower. On the contrary, it actually increases thermal effects of the tower. When there was no insulation, the thermal effect of the tower was only noticeable in the cold period, with lower temperatures at the location closer to the tower footing. An application of the PCM thermal barrier caused more thermal effects of the tower, as indicated by the larger difference between temperatures at $R=7$ mm and $R=39$ mm, where the former location experienced higher warm temperatures and lower cold temperatures than the latter. This may occur because the insulation only reduces heat transfer through the ground surface, but it cannot prevent heat conduction through the metal tower. The insulation layer creates a larger temperature difference between the atmosphere and the deeper levels of the foundation, thereby causing more heat conduction through the tower to the foundation.

These results confirm that thermal barriers on the ground surface can effectively reduce foundation temperature amplitudes by reducing heat conduction through the ground surface. But these thermal barriers cannot prevent heat conduction through the metal tower. They increase this heat conduction and lead to more sig-
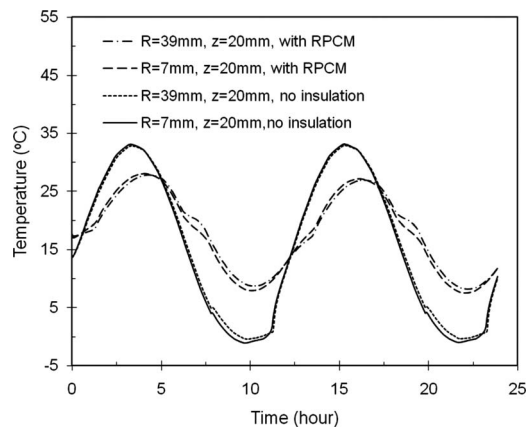
Fig. 13 Effects of PCM thermal barrier on temperature variations at two locations ($R=7$ mm and $z=20$ mm, and $R=39$ mm and $z=20$ mm) in the test cell

nificant thermal effects of the tower footing, although the magnitude of the temperature difference caused by the metal tower is much smaller than that caused by temperature variations along the ground surface. Other protection techniques, such as a ground cooling method with air ducts or solar radiation shields, could also be integrated with thermal barriers to further protect the foundation.

5 Conclusions

In this paper, a thermal barrier made of phase change material was shown to provide an excellent alternative to conventional insulation in ground heat transfer problems. It reduces the amplitude of temperature cycles in the foundation and can thereby effectively alleviate damage caused by seasonal freezing and thawing cycles. Under different air temperature conditions, the PCM thermal barrier provides different patterns of modified ground surface temperatures. The PCM parameters (thermal conductivity, latent heat, and thickness) could be designed for a particular foundation protection purpose, i.e., cold or warm preservation, using the melting and freezing degree-day analysis. When the desired ground surface temperature is achieved, i.e., nearly constant temperature profile in either cold or warm periods, the compensation function method may be used to predict ground temperatures at different depths in the foundation.

Thermal barriers can protect the permafrost foundation by reducing the thawing and freezing cycle in the active layer, but they cannot reduce heat conduction through the metal tower. On the contrary, it may increase this heat flow and enhance thermal effects of the metal tower, although the magnitude of temperature difference caused by the metal tower is much smaller than that caused by temperature variations along the ground surface. A comprehensive thermal protection strategy must be employed for permafrost structures with buried metal parts. The PCM thermal barrier can be integrated with other thermal protection techniques, such as conventional insulation, passive ground cooling ducts, solar radiation shields, and so forth to further protect the foundation.

Nomenclature

A = amplitude
D = distance, diameter (m or mm)
k = thermal conductivity (W/m°C)
L = latent heat (kJ/kg)
P = cyclic period (s, min, days, or months)
r = radial coordinate (m or mm)
R = radius (m or mm)
T = temperature (°C)
t = time (s, min, days, or months)
w = frequency
z = vertical coordinate (m or mm)
Z = depth (m or mm)

Greek

α = thermal diffusivity (m²/s)
β = intermediate variable in Eq. (1) and Eq. (4)
θ = temperature response or difference (°C)
λ = moisture content (%)
ρ = density (kg/m³)
ϕ = phase lag

Subscripts

b = buried metal rod or tower
f = fluid
flr = flour
g = ground
gs = ground surface
gsm = mean value at ground surface
i = initial condition
PCM = phase change material

References

[1] U.S. Arctic Research Commission Permafrost Task Force, 2003, "Climate Change, Permafrost, and Impacts on Civil Infrastructure," U.S. Arctic Research Commission, Special Report No. 01-03.
[2] Couture, R., Robinson, S. D., and Burgess, M. M., 2000, "Climate Change, Permafrost Degradation, and Infrastructure Adaption: Preliminary Results From a Pilot Community Case Study in the Mackenzie Valley," Geological Survey of Canada, Current Research 2000-B2.
[3] Krarti, M., Claridge, D. E., and Kreider, J. F., 1990, "ITPE Technique Applications to Time-Varying Three-Dimensional Ground-Coupling Problems," ASME J. Heat Transfer, 112(4), pp. 849–856.
[4] Furmanski, P., and Floryan, J. M., 1994, "A Thermal Barrier With Adaptive Heat Transfer Characteristics," ASME J. Heat Transfer, 116(2), pp. 302–310.
[5] Reid, R. L., and Evans, A. L., 1983, "Investigation of the Air Convection Pile as a Permafrost Protection Device," Proceedings of 4th International Conference on Permafrost, National Academy Press, Washington, DC, pp. 1048–1053.
[6] Esch, D. C., 1986, "Insulation Performance Beneath Roads and Airfields in Alaska," Proceedings of the Fourth International Specialty Conference, ASCE, Reston, VA, pp. 713–722.
[7] Feklistov, V. N., and Rusakov, N. L., 1996, "Application of Foam Insulation for Remediation of Degraded Permafrost," Cold Regions Sci. Technol., 24(2), pp. 205–212.
[8] Staudzs, A., 1982, "Frost and Permafrost: Effects and Remedial Work on Transmission Tower Foundations," Manitoba Hydro Report, Winnipeg, MB, Canada.
[9] Wen, Z., Sheng, Y., Ma, W., and Qi, J., 2005, "Evaluation of EPS Application to Embankment of Qinghai–Tibetan Railway," Cold Regions Sci. Technol., 41(3), pp. 235–247.
[10] Sheng, Y., Wen, Z., Ma, W., Liu, Y., Qi, J., and Wu, J., 2006, "Long-Term Evaluations of Insulated Road in the Qinghai-Tibetan Plateau," Cold Regions Sci. Technol., 45(1), pp. 23–30.
[11] Bardy, E. R., Mollendorf, J. C., and Pendergast, D. R., 2007, "Thermal Conductivity and Compressive Strain of Aerogel Insulation Blankets Under Applied Hydrostatic Pressure," ASME J. Heat Transfer, 129(2), pp. 232–235.
[12] Daigle, L., and Zhao, J. Q., 1999, "Effectiveness of Rigid Insulation for Thermal Protection of Buried Water Pipes in Rock Trenches," CSCE 1999 Annual Conference—First Cold Regions Specialty Conference, pp. 389–398.
[13] Khudhair, A. M., and Farid, M. M., 2004, "A Review on Energy Conservation in Building Applications With Thermal Storage by Latent Heat Using Phase Change Materials," Energy Convers. Manage., 45(2), pp. 263–275.
[14] Medina, M. A., King, J. B., and Zhang, M., 2008, "On the Heat Transfer Rate Reduction of Structural Insulated Panels (SIPs) Outfitted With Phase Change Materials (PCMs)," Energy, 33(4), pp. 667–678.
[15] Saha, S. K., Srinivasan, K., and Dutta, P., 2008, "Studies on Optimum Distribution of Fins in Heat Sinks Filled With Phase Change Materials," ASME J. Heat Transfer, 130(3), p. 034505.
[16] Weinstein, R. D., Kopec, T. C., Fleischer, A. S., D'Addio, E., and Bessel, C. A., 2008, "The Experimental Exploration of Embedding Phase Change Materials With Graphite Nanofibers for the Thermal Management of Electronics," ASME J. Heat Transfer, 130(4), p. 042405.
[17] Al-Hallaj, S., and Selman, J. R., 2002, "Thermal Modeling of Secondary Lithium Batteries for Electric Vehicle/Hybrid Electric Vehicle Applications," J. Power Sources, 110(2), pp. 341–348.
[18] Faghri, A., and Guo, Z., 2005, "Challenges and Opportunities of Thermal Management Issues Related to Fuel Cell Technology and Modeling," Int. J. Heat Mass Transfer, 48(19–20), pp. 3891–3920.
[19] Naterer, G. F., 2003, Heat Transfer in Single and Multiphase Systems, CRC, Boca Raton, FL.
[20] Duan, X., and Naterer, G. F., 2008, "Ground Thermal Response to Heat Conduction in a Power Transmission Tower Foundation," Heat Mass Transfer, 44(5), pp. 547–558.
[21] Duan, X., and Naterer, G. F., 2008, "Ground Heat Transfer From a Varying Line Source With Seasonal Temperature Fluctuations," ASME J. Heat Transfer, 130(11), p. 111302.
[22] Duan, X., and Naterer, G. F., 2009, "Heat Conduction With Seasonal Freezing and Thawing in an Active Layer Near a Tower Foundation," Int. J. Heat Mass Transfer, 52(7–8), pp. 2068–2078.

[23] El-Din, M. M. S., 1999, "On the Heat Flow Into the Ground," Renewable Energy, **18**(4), pp. 473–490.

[24] Zeng, H. Y., Diao, N. R., and Fang, Z. H., 2002, "A Finite Line-Source Model for Boreholes in Geothermal Heat Exchangers," Heat Transfer Asian Res., **31**(7), pp. 558–567.

[25] Ingersoll, L. R., Zobe, O. J., and Ingersoll, A. C., 1954, *Heat Conduction With Engineering, Geological and Other Applications*, University of Wisconsin Press, Madison, WI.

[26] Carslaw, H. S., and Jeager, J. C., 1993, *Conduction of Heat in Solids*, 2nd ed., Oxford University Press, New York.

[27] Canadian Climate Normals or Averages, 1971–2000, Environment Canada, http://climate.weatheroffice.ec.gc.ca/climate_normals/index_e.html

[28] Kline, S. J., and McClintock, F. A., 1953, "Describing Uncertainties in Single Sample Experiments," Mech. Eng. (Am. Soc. Mech. Eng.), **75**(1), pp. 3–8.

Optimal Heat Distribution Among Discrete Protruding Heat Sources in a Vertical Duct: A Combined Numerical and Experimental Study

T. V. V. Sudhakar
Research Scholar

Arun Shori
Undergraduate Student of NIT Trichy

C. Balaji[1]
Professor
e-mail: balaji@iitm.ac.in

S. P. Venkateshan
Professor

Heat Transfer and Thermal Power Laboratory,
Department of Mechanical Engineering,
Indian Institute of Technology Madras,
Chennai 600 036, India

This paper reports the results of experimental and numerical investigations of optimal heat distribution among the protruding heat sources under laminar conjugate mixed convection heat transfer in a vertical duct. A printed circuit board with 15 heat sources forms a wall of a duct. Three-dimensional governing equations of flow and heat transfer were solved in the flow domain along with the energy equation in the solid domain using FLUENT 6.3. A database of temperatures of each of the heat sources for different heat distributions is generated numerically. Artificial neural networks (ANNs) were used as a forward model to replace the time consuming complex computational fluid dynamics (CFD) simulations. The functional relationship between heat input distribution and the corresponding temperatures of the heat sources obtained by training the network is used to drive a genetic algorithm based optimization procedure to determine the optimal heat distribution. The optimal distribution here refers to the apportioning of a fixed quantity of heat among 15 heat sources, keeping the maximum of the temperatures of the heat sources to a minimum. Furthermore, the heat distribution corresponding to a set of specified target temperatures of the heat sources is obtained using a network that is trained and tested with a database of temperatures of the heat sources generated using FLUENT 6.3 in the range of total heat dissipation of 5–25 W. Using this network, it was possible to maximize the total heat dissipation from the heat sources for a given target temperature directly. In order to validate the optimization method, a low speed vertical wind tunnel has been used to carry out the mixed convection experiments for different combinations of heat distribution and also for the optimal heat distribution, and the temperatures of the heat sources were measured. The results of the numerical simulations, ANN, and the corresponding experimental results are in good agreement.
[DOI: 10.1115/1.3194762]

Keywords: mixed convection, protruding heat sources, three-dimensional, experimental, numerical, optimization, artificial neural networks, genetic algorithms

1 Introduction

In the present day context, thermal optimization plays a significant role in the cooling of electronic components, particularly when multiple components are placed on a printed circuit board (PCB). In such situations, the positions of various components relative to each other influence both the flow and heat transfer characteristics regardless of the mode of convection. The reliable operation of electronic components has depended on the ability to dissipate heat while maintaining their temperatures at acceptably lower values, and the temperature difference between the components must be as small as possible to reduce the thermal stresses to a minimum. In most of the electronic systems, the heat-dissipating components are arranged in arrays on a series of parallel PCBs that form vertical channels/ducts. Natural convection is still a better option for cooling the array of heat sources that dissipate heat at lower levels (heat flux of order of 1 W/cm^2) due to its inherent advantages such as no operating cost, quietness of operation, and

reliability. For higher heat generating components, forced convection is inevitable for cooling the components. The problem associated with forced convection heat transfer is the large pumping power requirements for driving the fluid (coolant) over the components. Mixed convection heat transfer mitigates the problems of forced convection and draws the advantages of both forced convection and natural convection. A number of studies have been carried out on heat transfer from multiple heat generating modules. Both experimental and numerical investigations on natural [1–7], forced [8–12], and mixed convection [13–16] heat transfer from multiple flush/protruding discrete heat sources have been reported in literature. A three-dimensional numerical study was conducted by Adam et al. [1] to investigate conjugate transport resulting from a 3×3 array of heated components on a horizontal substrate in a narrow aspect ratio enclosure. They reported that failure to include wall conduction and radiation in the analysis would result in an 80%–90% difference between the measured and simulated temperatures. Afrid and Zebib [2] numerically studied three-dimensional natural convection air cooling of multiple electronic components in an enclosure using a control volume finite difference analysis for a range of Rayleigh numbers from 3×10^6 to 3×10^7. Sathe and Joshi [3] presented numerical results for conjugate natural convection from a substrate mounted protruding heat source placed in a liquid filled enclosure for a wide

---

range of Rayleigh numbers, heat sources, and substrate thermal conductivities. It was concluded that immersion cooling in common dielectric fluids is advantageous over air cooling only if the thermal conductivity of the heat source was larger than that of the liquid. Wang et al. [4] numerically studied a two-dimensional, steady state laminar conjugate natural convection/conduction air cooling of a vertical plate with five wall-attached protruding, discretely heated integrated circuit (IC) packages. Tou et al. [5] studied a three-dimensional natural convection cooling on a 3×3 array of discrete heat sources flush mounted on one vertical wall of a rectangular enclosure filled with various liquids (Pr=5, 9, 25, and 130) and cooled by the opposite wall. The results showed that the flow field is complex and the heat transfer from the discrete heaters is not uniform. Flow visualization studies [6] clearly showed significant three-dimensional effects, and three-dimensional numerical predictions were in excellent agreement with the experimental data [7]. However, two-dimensional predictions overestimate the surface temperatures. Young and Vafai [8] experimentally investigated forced convection in a class of problems where protruding heat sources were placed on different geometries and reported a set of correlations characterizing the forced convection heat transfer of individual and array of multiple two-dimensional obstacles. An experimental study was carried out by Gupta and Jaluria [9] on liquid forced convective cooling of an inline array of heated modules. McEntire and Webb [10] carried out experimental investigations on two-dimensional flush mounted and protruding discrete heater configurations under local forced convection heat transfer and concluded that protruding heat sources yield higher heat transfer than the flush mounted heat sources for the same channel Reynolds number. Alex et al. [11] performed several experiments with both a single heat source and multiple heat sources in channels. Yadav and Kant [12] performed numerical and experimental investigations to study the effects of array size and substrate thermal conditions upon heat transfer characteristics of an array of heated modules subjected to buoyancy assisted convection cooling in air. Maheney et al. [13,14] investigated mixed convection heat transfer from a four row, inline array of 12 square heat sources mounted on the lower wall of a horizontal rectangular channel. Watson et al. [15] carried out a numerical study of laminar mixed convection heat transfer between a series of vertical aligned plates provided with planar heat sources. They noticed that the velocity profiles within the channel were skewed substantially toward the hot wall as the Richardson number (Ri) increases and k_s/k_f decreases. Dogan et al. [16] considered mixed convection heat transfer from flush mounted discrete heat sources inside a horizontal rectangular channel for their experimental investigation to study the surface temperature and Nusselt number distributions of the discrete heat sources for different Reynolds and Grashof numbers. A few more investigations, for instance, Refs. [17,18], were carried out on position optimization of the heat sources in different flow geometries under natural/forced/mixed convection heat transfer. All these investigations are restricted to two-dimensional calculations and invariably conjugate effects have not been taken into consideration.

From the review of the literature, it is seen that several numerical and experimental investigations on heat transfer from flush mounted and protruding heat sources have been conducted. One of the important conclusions from these studies is that for better cooling of the heated components, their placement plays a very important role. Even so, studies that have focused on the optimal heat distribution among multiple heat sources for their reliable operation are scarce in literature. In view of this, the present investigation considers the optimal heat distribution among 15 protruding heat sources mounted on a wall of vertical duct. Two variants of the optimization problem are considered: (i) the total power to be dissipated from the heat sources has been fixed and is to be distributed among all the heat sources in such a way that the maximum temperature of any of the heat sources is minimized and (ii) the total heat dissipation from the heat sources is to be maximized for a given target temperature.

2 Problem Description and Governing Equations

The problem considered in the present study is conjugate mixed convection heat transfer in a vertical duct with 15 protruding heat sources mounted on a wall. Each of the heat sources is assumed to generate heat at a constant rate. Figure 1(a) shows the geometry and the problem domain considered for the present investigation. Heat sources are uniformly mounted on the left wall of the duct with a pitch equal to half of the height of the heat source in both the horizontal and vertical directions. The heat sources are numbered, as shown in Fig. 1(b), 1–5 for the left and right columns and 6–10 for the middle column in the flow direction. The corresponding heat sources on the left and right columns generate the same amount of heat. The flow is assumed to be steady, laminar, and incompressible with constant properties, except for the change in density with temperature in the buoyancy term. The density changes are modeled with the use of the Boussinesq approximation. The medium under consideration is air and is assumed to be a radiatively nonparticipating medium. Viscous heat dissipation, compressibility effects, and contact resistance between the heat source and the substrate are considered to be negligible. To account for conjugate convection, the energy equation is solved for the solid domain as well. It is assumed that no temperature jump occurs at the solid-solid interface. Since the dimensions of the heat source are small compared with the dimensions of the substrate and a number of heat sources are placed in close proximity to each other on the substrate, the flow around the heat sources due to buoyancy effect can significantly influence the heat transfer characteristics. Based on the above assumptions, the governing equations for mass, momentum, and energy for a steady three-dimensional flow in the fluid domain and the energy equation in the solid region are as follows.

- Fluid:
- continuity equation,

$$\nabla \cdot \mathbf{V} = 0 \tag{1}$$

- momentum equation,

$$(\mathbf{V} \cdot \nabla)V = -\frac{\nabla_p}{\rho} + \nabla^2 V + g\beta(T - T_\infty) \tag{2}$$

- energy equation,

$$(\mathbf{V} \cdot \nabla)T = \alpha\nabla^2 T \tag{3}$$

- Solid:
- energy equation,

$$\nabla^2 T + \frac{Q_{\text{gen}}}{k_s} = 0 \tag{4}$$

2.1 Radiation Heat Transfer Model. The discrete ordinate (DO) radiation heat transfer model was used in the present numerical analysis as it can be applied to the entire range of optical thicknesses. Furthermore, it has several other advantages such as (i) moderate computational cost and (ii) modest memory requirements. Conceptually, with the discrete ordinate mode, the radiative transfer equation (RTE) is solved for a set of n different directions, with the integrals over these directions replaced by numerical quadratures. The DO model writes the RTE in the direction **s** in terms of spatial coordinates as in Eq. (5). The details of the DO model are available in Refs. [19,20],

$$\frac{dI(r,s)}{ds} + aI(r,s) = an^2\frac{\sigma T^4}{\pi} \tag{5}$$

where s is a component of **s**.
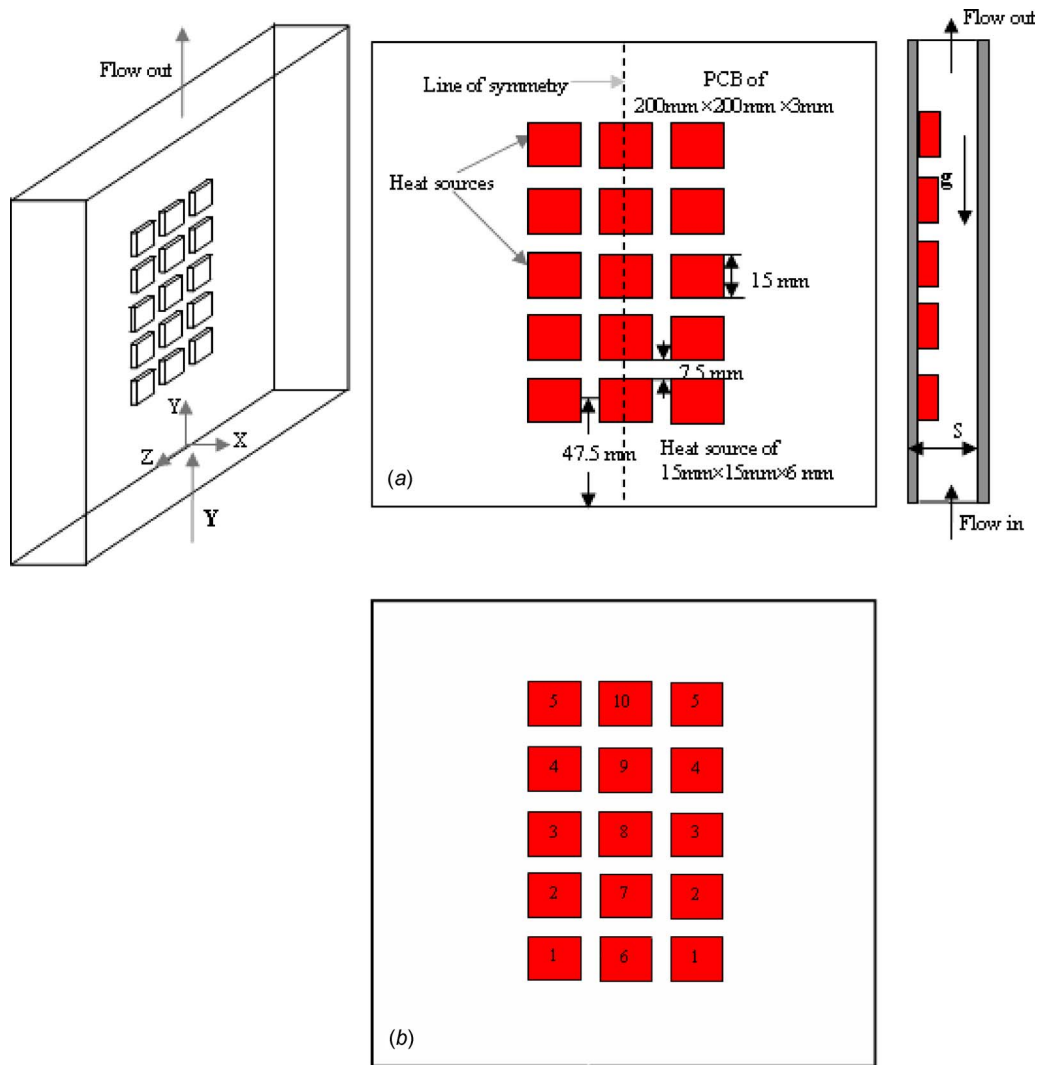
Fig. 1 (*a*) **Physical arrangement of the heat sources on a PCB considered in the present study.** (*b*) **Representation of position of heat sources on the substrate used for optimum heat distribution studies.**

In order to test the discrete ordinate model used in the present work, a three-dimensional clear channel with one plate heated and the other being adiabatic was considered. The heated plate loses heat by convection and radiation simultaneously. The physical dimensions of the geometry considered in the numerical simulations correspond to those used by Krishnan [21] in an experimental study. For air, the absorption coefficient a is taken to be 0. A comparison of the results of the numerical scheme with the discrete ordinate model, with the experimental results of Krishnan [21], for different combinations of temperatures and emissivities of the heated plate showed an excellent agreement with a correlation coefficient of over 0.99.

2.2 Problem Domain and Boundary Conditions

2.2.1 Solid Wall. No slip and impermeability conditions as given in Eq. (6) is applied to all fluid-solid surface interfaces,

$$U = V = W = 0 \tag{6}$$

and the solid surfaces other than the fluid-solid interfaces are assumed to be adiabatic,

$$\frac{\partial T}{\partial n} = 0 \tag{7}$$

2.2.2 Plane of Symmetry. As there is a plane of symmetry geometrically as well as thermally with respect to the *x-y* plane, only one-half of the domain is considered for numerical computations. The following conditions are imposed corresponding to the plane of symmetry:

$$\frac{\partial W}{\partial n} = 0, \quad \frac{\partial T}{\partial n} = 0 \tag{8}$$

2.2.3 Outlet. Outflow condition, which corresponds to zero diffusion for all flow variables, is imposed. Since the height to spacing ratio of the channel is high, the error associated with this boundary condition is small.

2.2.4 Inlet. The flow is one dimensional, with a uniform velocity of V_∞ and a uniform temperature of T_∞, and this translates to the following boundary conditions:

$$U = W = 0 \tag{9}$$

$$V = V_\infty \tag{10}$$

$$T = T_\infty \tag{11}$$

2.3 Grid. Different nonuniform structured grids were employed to establish grid independence. A mesh of 675,360 grids/cells is found to be good enough when the Reynolds number is 1200 and the modified Grashof number is 1.0×10^7. The thermal conductivity ratio of that PCB material used for the substrate and the heat sources plays a significant role on the mesh size. The mesh size used in the present analysis corresponds to a thermal conductivity ratio of 1. Further refinement in the grid does not show a significant change in any of the temperatures of the heat sources.

2.4 Numerical Scheme. Equations (1)–(5), together with the boundary conditions shown in Eqs. (6)–(11), form a set of coupled nonlinear partial differential equations and have been solved using FLUENT 6.3 including the radiation model. The numerical scheme adopted is a steady segregated solver with an implicit formulation and a first order up-winding scheme for the convective terms. The pressure and velocity equations are linked by the SIMPLE algorithm. A residual of 10^{-6} for the equations of continuity and momentum and for the radiation model and that of 1×10^{-12} for the energy equation have been employed as the convergence criteria. The overall energy and mass balance, upon convergence, were found to be observed within 0.01%. The details of the numerical scheme used in the present study are available in Ref. [20].

3 Experimental Setup

Figure 2 shows a schematic of the experimental setup used for the mixed convection experiments. The test rig is essentially a low speed vertical wind tunnel that can provide uniform flow with very low fluctuations in the flow velocity. The experimental setup consists of a diffuser, a settling chamber, a convergent part, and a test section. All these parts are assembled into a unit and supported in a stand, as shown in Fig. 2. A variable speed axial flow fan is mounted on a separate stand just below the diffuser section of the wind tunnel to avoid vibrations induced to the wind tunnel when the fan is turned on. A detailed description of the wind tunnel has been presented in Ref. [21].

3.1 Test Section. Two views of the test section used in the present study are shown in Fig. 3. The test section is made up of plywood consisting of four identical closed boxes. These boxes are filled with silica glass wool to reduce heat loss through them. One of the faces of these boxes is fixed with a PCB board of 3 mm thickness. The position of these boxes can be adjusted by means of a bolt-nut arrangement in the test section. The PCB faces of the two boxes form the walls of a channel, and the heat sources are embedded on one of these walls. The PCB faces of the other two boxes are used to close the channel sides, and thus the four boxes form a vertical duct with heat sources on one of its walls. The bottom (inlet) and top (outlet) faces of the test section are open to the atmosphere. A uniform velocity and fully developed flow conditions are ensured at both inlet and outlet faces of the duct, respectively. To prevent air leak from the corners of the duct, a rubber material is used on the sides of the two boxes that form the channel. The excess width of the channel due to the rubber material is filled with a PCB material that has a thickness equal to that of channel spacing. The dimensions and the material used for the test section and other components are given in Table 1.

3.2 Heat Source. The heat sources are made up of a plate of aluminum material that is cut into square blocks of sizes $15 \times 15 \times 6$ mm^3 with a square cavity at its center of size $11 \times 11 \times 4$ mm^3. A standard coil-type Nichrome wire is used as a heating element and is inserted in the cavity. Teflon tape is wound around the heating coil to avoid any metal to metal contact. The
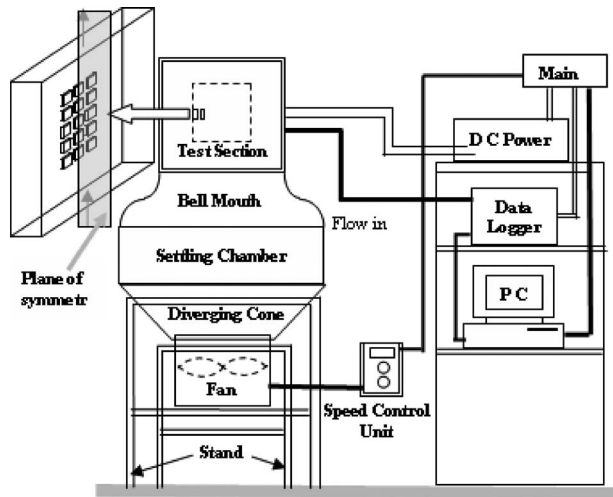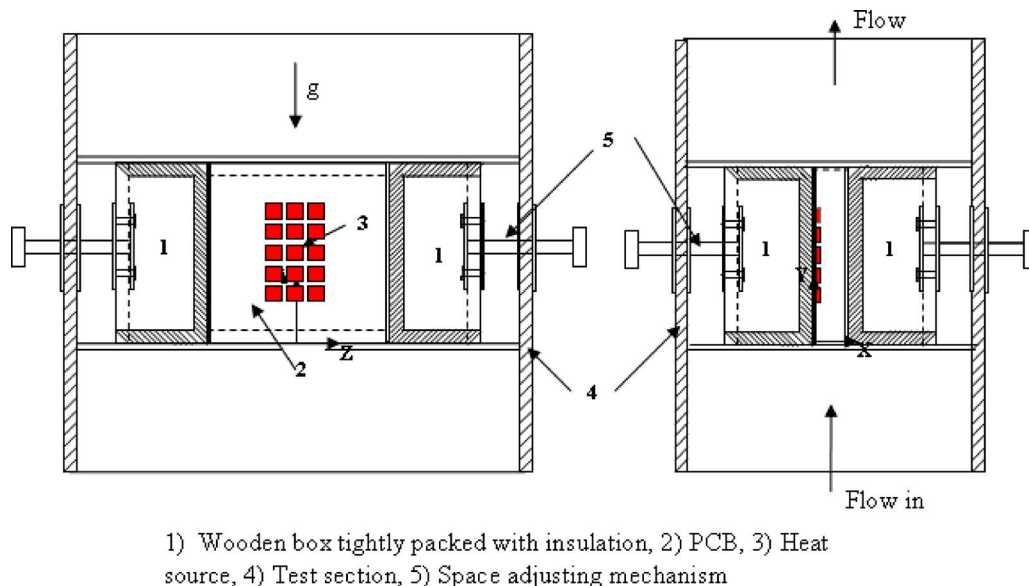

Fig. 2 Schematic of a low speed vertical wind tunnel along with the instrumentation used in the present study

1) Wooden box tightly packed with insulation, 2) PCB, 3) Heat source, 4) Test section, 5) Space adjusting mechanism

Fig. 3 Schematic of the test section used in the present investigation with heat source and other details

Table 1 Specification of materials used in the experimental investigation

Serial no.	Description	Material	Dimensions/specification
1	Test section	Plywood	$490 \times 400 \times 600$ mm^3
2	Substrate	PCB	$200 \times 200 \times 3$ mm^3
3	Heat source block	Aluminum	$15 \times 15 \times 6$ mm^3
4	Heating element	Nichrome	80/20 (coil type)
5	Thermocouples	K-type	32-AWG
6	Insulation	Silica wool	$\cdots$

Table 2 Results of the uncertainty analysis

Specification no.	Quantity measured/calculated	Uncertainty
1	Voltage (V)	0.01
2	Current (A)	0.02
3	Power (W)	0.24
4	Temperature (°C)	0.40
5	Velocity (m/s)	0.05
6	Emissivity	0.002

temperatures at one of the horizontal faces and the vertical face of each of the heat sources are measured by chromel-alumel K-type (32 AWG) thermocouples, which were inserted exactly 1 mm below and at the center of the plane surfaces of the blocks. All thermocouples are calibrated before fixing them into the grooves provided in the aluminum blocks, and they are connected to a PC based data acquisition system through compensating wires. The air gaps in the cavity and the grooves made for locating thermocouples are filled with a highly conducting thermal paste.

The heat sources are embedded onto the PCB. To ensure firm contact between the heat module and the PCB, the heat sources were fitted to the PCB with four brass screws of 2 mm diameter.

3.3 Instrumentation. The power input to each of the heaters is supplied from independently controlled dc power units, which have ranges of 0–12 V and 0–2.0 A, with resolutions of ± 0.01 V and ± 0.01 A, respectively. The velocity and temperature of the air inside the test section at the inlet to the duct are measured using a thermal anemometer (Airflow™ TA5). The uniformity of velocity upstream of the test plate is ascertained by traversing the anemometer across the duct length in the z direction and taking the readings at different locations. It is observed that the velocities measured at different locations across the entrance vary by less than 3%. Different air velocities are obtained by varying the speed of the axial flow fan mounted appropriately below the diffuser entry. As mentioned in Sec. 3.2, "K-type" (36 AWG) thermocouples are used for the measurement of the temperatures of the heat sources. All thermocouples are calibrated before fixing them into the grooves machined in the plates, and the measurement error is within $\pm 0.4 \degree$C. The experiments were repeated for several power input combinations to the heater and for different velocities.

3.4 Uncertainty Analysis. Uncertainties were estimated according to standard procedures outlined in Ref. [22]. In the present experimental study, 15 individual dc power units (0–12 V and 0–2 A) were used for heating 15 heat sources, and a separate dc power unit (0–300 V and 0–5 A) was used for heating the plate-heater assembly that was used for the measurement of surface emissivity. The error in the measurement of the voltage and the current will propagate as error in the power supplied to the respective elements. Furthermore, there are uncertainties in the temperature and velocity measurements. All the heaters were tested for their uniformity in their current carrying ability for a constant voltage in the range of 1–3 V, and the corresponding heat source temperatures were measured. The measured and estimated parameters and their uncertainties are given in Table 2. Emissivity values of the heat sources were independently estimated based on a transient cooling technique, wherein all parameters except the emissivity are treated as known. By using a least squares minimization between the experimentally obtained temperatures and the numerically generated temperatures for an assumed value of emissivity, the best estimates of emissivity were obtained. For a fuller discussion on the emissivity estimation procedure, see Ref. [21]. For the estimation of uncertainty in the measurement of emissivity, several tests were performed, and the emissivities so obtained

were averaged. This average value was taken to be the estimated value for the surface, and the standard deviation among the values was taken to be the error in the estimation of emissivity.

4 Artificial Neural Networks

Artificial neural networks (ANNs) can be trained to represent the relationships between inputs (heat input, for example) and outputs (temperatures), however complex, with a high degree of accuracy without requiring an explicit knowledge of the relationships between them. A detailed discussion on ANNs has been presented in Ref. [23]. However, for the sake of completeness, the salient features of ANN are explained here. ANN can be considered to be a form of nonlinear regression between one or more dependent variables and a set of independent variables. ANN consists of several layers with a large number of highly interconnected computational units called neurons. For the present investigation, a backpropagation feed-forward neural network or a multilayer perceptron (MLP) shown in Fig. 4 has been considered. Backpropagation is the most widely used learning process in neural networks today. In order to decide the architecture of the neural network, a code was written in MATLAB 7.0. The required weights for better network performance are obtained iteratively by changing the parameters such as momentum rate and learning rate.

4.1 Genetic Algorithms. Genetic algorithms (GAs) are adopted for the optimization of a given heat distribution among the heat sources considered in the present investigation. Genetic algorithms are believed to work based on the mechanism of natural selection and natural genetics to imitate living beings for solving optimization problems. Genetic algorithms were introduced by
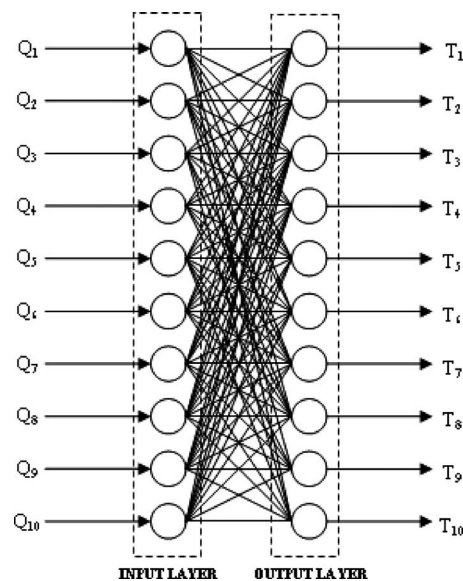
Fig. 4 Schematic of the neural network architecture employed for this study

Holland [24], and Goldberg [25] gave one of the most common and widely used forms of GA. The summary of this algorithm is as follows. The solution vector is called an individual or a chromosome. The individuals are generated through random selection. GA works with a randomly generated population of individuals, each of them representing a possible solution to a given optimization problem. A model (an objective function to be optimized) is used to evaluate the fitness of each individual. GA uses genetic operators, such as selection, crossover, and mutation, to generate new solutions from existing ones. After evaluating the fitness of each individual, fitter individuals are selected to reproduce offsprings for the next generation. The selection process is determined by the objective function values. Some of the selected individuals are chosen to find mates and undergo the crossover operation, which is a reproduction process that makes offsprings by exchanging their genes to improve the fitness of the next generation. Then, some of the offsprings are chosen for the operation of mutation that preserves the diversity of a population, while searching the design space that cannot be represented with the present population by changing some of the genes of a selected individual within the range of the design space. During each generation, these chromosomes evolve into a better fitness by applying an evolution operation called selection. The tournament selection has been adopted in the present investigation. From generation to generation, eventually, the chromosomes in the population aree converged.

The objective function used in the present optimization problem is to minimize the maximum of the temperatures of the heat sources. The objective function is represented mathematically by Eq. (12) with a constraint that the maximum power carried by any of the heat sources does not exceed 3.0 W and the total heat distribution is restricted to 15 W,

$$\text{Minimize: } \max(T_i) \tag{12}$$

The input parameters that are required in the genetic algorithm are population size, chromosome length, number of generations, and crossover and mutation rates along with the objective or fitness function. In the present study, the following values of parameters were used: initial population size, 100; number of generations, 300; crossover rate, 0.8; and mutation probability, 0.01.

The fitness function is generated based on the output of ANN, and this is coupled by the GA code. MATLAB again has been used to carry out the GA operations. Further discussion on GA is available in Refs. [26,27].

5 Results and Discussion

5.1 Validation of the Numerical Results With the Present Experimental Results. Mixed convection experiments are conducted for a wide range of modified Richardson numbers and Reynolds numbers $(0.4 < \text{Ri}^* < 16, \ 200 < \text{Re} < 1200)$. Numerical calculations were performed for a duct spacing of 10 mm and for the different heat distributions among the heat sources. The physical dimensions of the duct and heat sources are similar to those employed in the numerical study. As already mentioned, the hemispherical emissivity of the heater surface was measured experimentally, and this was also used in the numerical simulations. Figure 5 shows a comparison of the experimentally measured temperatures of the heat sources with the numerically predicted temperatures for a configuration of 15 heat sources for different heat duties at different inlet velocities in the range of modified Grashof and Reynolds numbers considered for the present investigation. There is a reasonably good agreement between experimental results and numerical predictions, with the maximum deviation being 20%. It is observed that the error between the experimentally measured heat source temperature and the numerically predicted temperatures is large at high values of heat generation rates at lower velocities and vice versa. This may be due to the increase in local disturbances in the flow, and flow may turn out to be turbulent.
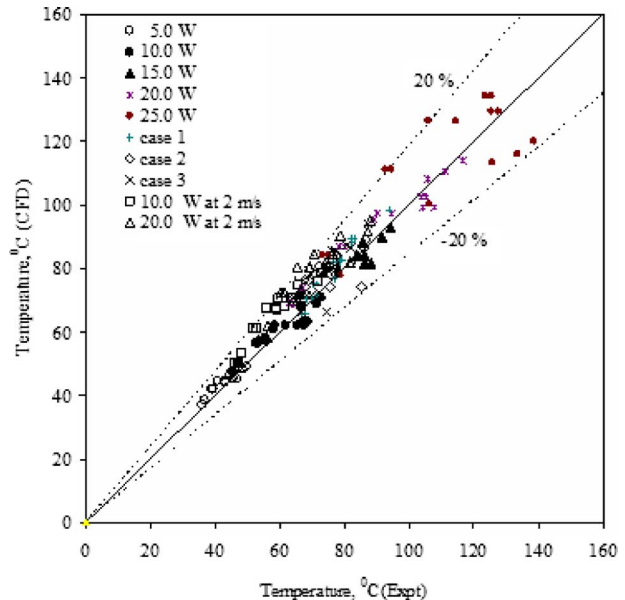
Fig. 5 Parity plot showing the agreement between measured and predicted heat source temperatures

5.2 Effect of Reynolds Number, Duct Spacing and Radiation on the Row Averaged Temperature of the Heat Sources. The influence of Reynolds number and duct spacing on the row averaged temperatures of the heat sources is experimentally investigated. The row averaged temperature is expressed as the temperature above the ambient temperature, which is referred to as the excess temperature. The variation in excess temperatures with Reynolds number is shown in Fig. 6 for different modified Grashof numbers. The row numbers 1–5 shown in Fig. 6 represent, respectively, the rows of heat sources located from the bottommost row to the top row. It is observed that the row averaged temperatures decrease as the Reynolds number increases irrespective of the row number and the modified Grashof number. Furthermore, there is a linear variation in the excess temperature with the modified Grashof number for the range of Reynolds numbers considered. For example, the excess temperatures of the heat sources located in the middle row for the modified Grashof numbers 2×10^6, 4×10^6, and 8×10^6 are 32, 57.7, and 89.3 °C, respectively, at a Reynolds number of 628, as seen in Figs. 6(a)–6(c). The temperature of the heat sources in each of the columns increases as the row number increases at Reynolds numbers above 1000 due to the fact that the heat sources on the downstream side experience the thermal environment developed by the heat sources on the upstream side, along with the heat generation by the heat sources themselves. For Reynolds numbers below 1000, the temperatures of the heat sources located in the top row are observed to be lower than the temperatures of the heat sources in the fourth row. This may be due to the influence of natural convection and radiation heat transfer from the heat sources located in the top row, as these heat sources are exposed directly to ambient through the outlet of the duct. Figure 7 shows the effect of duct spacing on the excess temperature. The spacing has a significant effect on the excess temperatures of the heat sources, particularly the heat sources located in row numbers 2–5. The effect of radiation on the row averaged temperature of the heat sources is also shown in Fig. 7 for a given spacing. It is observed that radiation has a significant effect on the excess temperatures particularly on the heat sources located in the rows in the downstream of the flow. Furthermore, the variation in the excess temperature of the heat source trend with and without radiation are the same. The fall in the temperatures at the top row for the no radiation case indicates that there may be a strong effect of buoy-
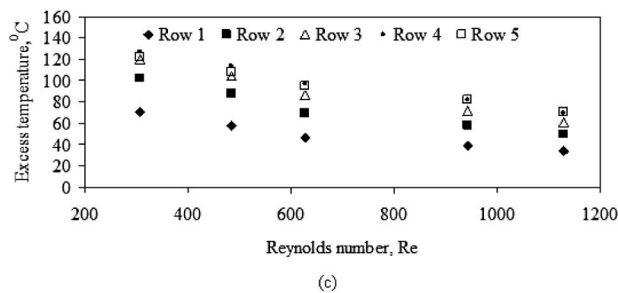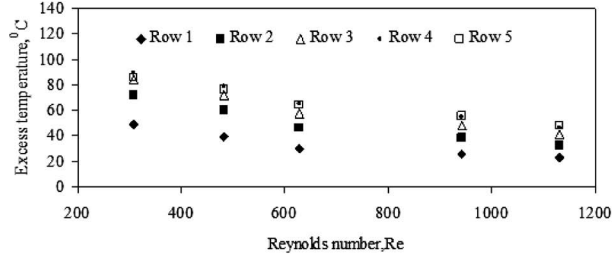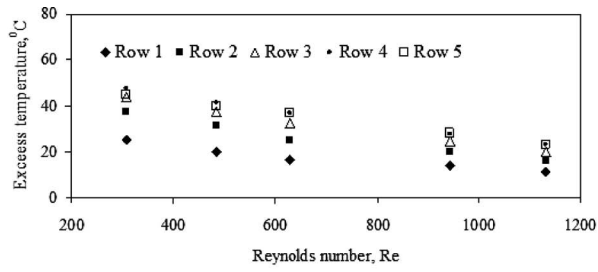
Fig. 6 Variation in row averaged temperatures with Reynolds number for different modified Grashof numbers: (*a*) 2×10^6, (*b*) 4×10^6, and (*c*) 6×10^6

Fig. 7 Effect of duct spacing on the row averaged temperatures of the heat sources with and without radiation

ancy on the cooling of heat sources at low Reynolds numbers. The numerically computed temperatures of the heat sources for uniform heat distribution are given in Table 3 along with the values predicted by the ANN and the experimentally measured temperatures. Due to the thermal interaction between the heat sources in the transverse direction, the temperature of the heat sources in the middle column is slightly higher than the corresponding adjacent heat sources in each of the rows. Under these conditions, the heat source that experiences the maximum temperature is the one present in the last but one row and in the middle column. This is designated as heat source number 9 (Fig. 1). In order to investigate the contribution of natural convection to the total heat transfer from the system, calculations were done for a few representative cases with the buoyancy switched off. It was observed that the maximum difference between the heat source temperature with and without buoyancy is around 6.5 °C. Hence, natural convection cannot be neglected for the range of parameters considered in the present study.

5.3 Optimization Studies

5.3.1 Minimization of Maximum Temperature for a Given Total Heat Duty. One of the major objectives of the present investigation, as mentioned earlier, is to obtain an optimal distribution of a given quantity of heat among the multiple heat sources. Fifteen heat sources of uniform size ($15 \times 15 \times 6$ mm^3) are mounted on the wall of the vertical duct with an equal spacing of 7.5 mm between the heat sources in both the streamwise and spanwise directions. The duct dimensions are fixed as $200 \times 200 \times 10$ mm^3. The total heat dissipation from the 15 heat sources used in the present investigation is also fixed at 15 W. A set of temperatures of the heat sources is obtained for different heat distributions generated randomly using "full" CFD simulations. The optimal heat distribution among the heat sources is the distribution that leads to a minimum of the maximum of the temperatures of all the heat sources. Considering the large number of possibilities for heat distributions, the use of CFD simulations alone for exercising the search for the optimum is a very formidable task from the point of view of both computational time and cost. With regard to the computational time for each simulation, one set of calculations for a heat distribution on a Pentium 4 machine with CPU 3.00 GHz and 4.0 Gbyte RAM took around 6 h. This shows that the simulations are computationally intensive when a greater number of solutions are required. For such problems, methods such as ANN are extremely useful in rapidly obtaining a relation between the input (here, it is a set of heat quantities supplied to the heat sources) and the output (here, it is a set temperatures corresponding to the heat quantities supplied to the heat sources). In this study, a network has been trained with 25 solutions generated for randomly selected heat distributions using full CFD solutions, and the trained network is then tested with 40 simulations. In the process of a random generation of heating values for the heat sources, the maximum heating value of any of the heat sources is restricted to 3.0 W. It is observed that regardless of the position of the heat source, which generates the maxi-

Table 3 Temperatures for uniform heat distribution among 15 heat sources

		Left column				Middle column				Right column		
		Temperature, T_i (°C)				Temperature, T_i (°C)				Temperature, T_i (°C)		
	Q_i (W)	ANN	CFD	Expt.	Q_i (W)	ANN	CFD	Expt.	Q_i (W)	ANN	CFD	Expt.
1	1	81.6	81.6	88.3	1	90.0	90.0	91.6	1	81.6	81.6	85.9
2	1	84.0	84.0	86.2	1	93.0	93.0	94.3	1	84.0	84.0	83.7
3	1	79.9	79.9	78.0	1	88.1	88.1	85.8	1	79.9	79.9	74.3
4	1	71.9	71.9	65.9	1	78.6	78.6	73.7	1	71.9	71.9	66.5
5	1	58.3	58.3	55.8	1	62.2	62.2	57.7	1	58.3	58.3	54.9

Table 4 Temperatures for optimum heat distribution among 15 heat sources (ANN plus GA)

	Left column					Middle column					Right column				
	Q_i (W)		Temperature, T_i (°C)			Q_i (W)		Temperature, T_i (°C)			Q_i (W)		Temperature, T_i (°C)			
	Num (GA)	Expt.	ANN	CFD	Expt.	Num	Expt.	ANN	CFD	Expt.	Num	Expt.	ANN	CFD	Expt.	
1	1.0948	1.107	77.3	77.1	84.0	0.6659	0.640	77.0	77.7	78.3	1.0948	1.089	77.3	77.1	82.7	
2	0.5879	0.592	73.5	73.3	75.1	0.5843	0.594	77.2	77.0	76.8	0.5879	0.584	73.5	73.3	72.9	
3	1.0272	1.021	77.3	77.1	78.0	0.0229	0.024	70.4	70.2	64.2	1.0272	1.081	77.3	77.1	74.9	
4	1.0342	1.035	77.1	76.7	72.7	0.6274	0.606	77.0	77.0	69.8	1.0342	1.010	77.1	76.7	70.5	
5	1.9968	2.015	77.0	76.0	76.3	1.6177	1.586	77.4	76.4	71.1	1.9968	2.054	77.0	76.0	75.9	

mum heat, i.e., 3.0 W, the maximum of the temperatures of the heat sources exceeds 135°C, which is unrealistic in the applications of electronic equipment, and hence an upper limit of 3 W has been chosen in the study.

The trained network was extensively tested for performance, and it was seen that the agreement between the data produced by the network and the data obtained from the numerical simulations is very good. The temperatures of the heat sources predicted by the neural network also showed an excellent match with the temperatures directly available from the numerical simulations for cases where the data from full CFD solutions were not used to train the network.

The network used in the present investigation has a linear relationship between the heat quantities supplied to the heat sources and the corresponding temperatures. The mathematical form of the relation between the heat quantities and the corresponding temperatures is given by

$$T_i = \sum_{j=1}^{10} a_{ij} Q_j + b_i \qquad (13)$$

where a_{ij} is the weighted parameter of each of the heat quantity Q_j (W) and b_i is the bias used for the heat source whose temperature is T_i (K).

The values of a_{ij} and b_i are obtained by training the network. Equation (13) has been used as a fitness function for the optimization part of the problem. MATLAB 7.1 has been used to determine the best possible heat distribution among the 15 heat sources using GA. The optimal heat distribution for $Q = 15$ W obtained by using GA is given in Table 4 along with the CFD predicted temperatures and experimentally measured values.

5.3.2 Maximization of Heat Duties for a Given Target Temperature. In Sec. 5.3.1, the optimal heat distribution of a total quantity of heat corresponding to the minimum of the maximum temperature of the heat sources was presented. However, an equally important problem concerns the distribution of heat such that ΣQ is maximized for a given target temperature. As mentioned earlier, the present study considers mixed convection heat transfer from protruding heat sources generating heat at a constant rate with conjugate effects including wall conduction and surface radiation. For given heat generation rates from each of the heat sources, determining the corresponding temperatures is a straightforward problem. However, the inverse problem i.e., finding the heat distribution among the heat sources for a set of target temperatures of the heat sources, is not trivial. An attempt is made to explore the possibility of finding the heat distribution for a set of target temperatures directly using artificial neural networks. A database of temperatures of the heat sources corresponding to the heat distributions is generated using the forward model. The heat distributions are generated randomly in the range of total heat dissipation of 5–25 W. A neural network similar to one shown in Fig. 5 has been trained and tested for predicting the heat distribution corresponding to a given set of target temperatures. The heat distributions for different but uniform target temperatures obtained using the network are presented in Table 5, along with the temperatures predicted numerically corresponding to these distributions. A sensitivity study has been conducted with different temperature data sets generated randomly with a standard deviation of 0.3°C. The sensitivity study reveals that there is no significant change in the total heat dissipation from the heat sources.

Table 6 presents the heat distribution for arbitrarily selected temperatures for the heat sources, keeping the maximum of these temperatures as equal to 353 K and the mean value at 345.5. The total heat dissipation from the heat sources is compared with the cases where all 15 heat sources are maintained at mean temperatures (i.e., 345.5 K) and at the maximum temperature of 353 K. It is observed that the heat dissipation is a maximum when all the heat sources are maintained at a constant maximum target temperature. This result is also evident from the optimization problem discussed in Sec. 5.3.1.

Table 5 Heat distribution for a given target temperature obtained from the solution of the inverse problem

Heat source number	Heat duty corresponding to the target temperatures obtained using ANN (Q_i, W)				Temperatures (T_i, K) predicted by CFD corresponding to Q_i			
	340 K	360 K	380 K	400 K				
1	0.8136	1.2294	1.6452	2.0610	340.0	360.0	379.5	398.7
2	0.6514	0.9851	1.3188	1.6525	340.0	359.9	379.4	398.5
3	0.7146	1.0789	1.4432	1.8075	339.9	359.8	379.2	398.3
4	0.8123	1.2243	1.6364	2.0484	339.8	359.6	379.0	398.1
5	1.6098	2.4167	3.2235	4.0303	339.5	359.1	378.5	397.6
6	0.4676	0.7125	0.9575	1.2025	340.0	360.0	379.4	398.5
7	0.3187	0.4875	0.6564	0.8253	339.9	359.9	379.2	398.4
8	0.3759	0.5727	0.7696	0.9664	339.9	359.8	379.2	398.2
9	0.4475	0.6783	0.9091	1.1399	339.8	359.6	379.0	398.0
10	1.2793	1.9220	2.5647	3.2075	339.5	359.1	378.4	397.5

Table 6 Effect of target temperatures on the total heat dissipation from the heat sources

Serial no.	$T_{\text{target}}=353$ K		$T_{\text{av}}=345.5$ K		$T_{\text{max}}=353$ K	
	Q_i (W)	T_i (K)	Q_i (W) (ANN)	T (K) (CFD)	Q_i (W) (ANN)	T (K) (CFD)
1	0.4581	336.2	0.9292	345.6	1.0880	353.2
2	0.4291	341.1	0.7442	345.5	0.8717	353.1
3	1.2608	353.0	0.8159	345.5	0.9551	353.0
4	0.9736	349.1	0.9269	345.3	1.0843	352.9
5	2.1008	349.3	1.8341	344.9	2.1423	352.4
6	0.6570	342.8	0.5357	345.6	0.6292	353.2
7	0.1919	343.3	0.3656	345.5	0.4301	353.1
8	0.5544	349.9	0.4306	345.4	0.5058	353.0
9	0.7007	349.2	0.5116	345.3	0.5998	352.9
10	0.8884	341.5	1.4580	344.9	1.7035	352.4
ΣQ_i	13.4372	⋯	13.8021	⋯	16.1512	⋯

The temperatures of the heat sources corresponding to the heat distributions obtained from ANN for a given target temperature have also been measured experimentally. The heat distributions corresponding to target temperatures of 340, 360, and 380 K given in Table 5 were applied to the heat sources in the respective experiments. Due to limitations in the measurement of voltage and current in each of the dc power units, the power supplied to each of the heaters deviates from the actual value by a maximum of 2%. The temperatures measured corresponding to the three target temperatures are given in Table 7. It is observed that the measured temperatures agree with those predicted by ANN to within 8%.

6 Conclusions

Three-dimensional numerical simulations were carried out to study laminar mixed convection with a view to determine the optimal heat duty among 15 heat sources mounted on a wall of a vertical duct. For accomplishing the optimization, ANNs are combined with GA for rapidity. Few numerical simulations are sufficient to train the network for reasonably accurate predictions of the temperatures for all possible heat distributions. It is observed that the temperatures of the heat sources for uniform heat distribution increase as we move downstream up to the fourth row, and the temperatures of the heat sources located in the middle column are high compared to the other, for wall heat sources. In consonance with the heat sources located on the downstream side, there is a need to generate heat at lower rates than the heat sources located on the upstream side to keep the maximum temperatures within limits. The optimal heat distribution among the heat sources was tested in a low speed wind tunnel, and the agreement between the temperatures of the heat sources measured experimentally and the temperatures predicted from numerical simulations is good. Additionally, the problem of maximization of heat dissipation from multiple heat sources for a given target temperature was again directly solved using another network, and the optima thus obtained were verified with the experiments and full CFD numerical simulations.

Table 7 Measured temperatures corresponding to the heat distribution obtained by ANN for the target temperatures 340, 360, and 380 K

Column	Heat source	Target temperatures (K)		
		340	360	380
Left	1	340.1	359.6	380.4
	2	339.7	358.4	379.4
	3	340.1	358.9	378.6
	4	340.0	357.8	376.2
	5	339.7	358.6	376.6
Middle	6	339.3	359.3	379.2
	7	336.9	355.2	373.0
	8	336.4	353.7	371.4
	9	336.9	353.7	370.8
	10	338.7	356.1	374.6
Right	1	339.2	358.6	379.0
	2	339.8	359.6	379.0
	3	339.3	358.4	376.8
	4	337.8	356.1	374.6
	5	338.8	358.1	378.6

Nomenclature

a = absorption coefficient, m^{-1}
A = wetted area of the heat source, m^2
AR = aspect ratio, H/S
C_p = specific heat, J/kg K
$\mathbf{g}$ = acceleration due to gravity, m/s^2
Gr^* = modified Grashof number, $g\beta\Delta T_{\text{ref}}h^3/\nu^2$
h = height of the heat source, m
$\bar{h}$ = average heat transfer coefficient, W/m^2 K
H = height of the duct/channel, m
I = total radiation intensity, W/m^2
k = thermal conductivity, W/m K
Nu = average Nusselt number, $\bar{h}S/k$
N = refractive index, coordinate axes (x, y, and z) as the case may be
p = pressure, N/m^2
$\mathbf{r}$ = position vector, m
$\mathbf{s}$ = direction vector
Q = heat transfer rate, W
Q_{gen} = volumetric heat generation, W/m^3
Ri^* = modified Richardson's number, Gr^*Pr
S = spacing between the walls of the channel, m
t_h = heat source thickness, mm
T = temperature, K
U = velocity in the X direction, m/s
V = velocity in the Y direction, m/s
$\mathbf{V}$ = velocity vector, m/s
W = velocity in the Z direction, m/s
x,y,z = coordinate directions, m

Greek Symbols

α = thermal diffusivity of the fluid, $k_f/\rho C_p$, m^2/s
β = isobaric cubic expansivity of the fluid, K^{-1}
ΔT_{ref} = $Q_{\text{gen}}(V/A)h/k_f$, K
ε = total hemispherical emissivity
ν = kinematic viscosity of fluid, m^2/s
ρ = density, kg/m^3
σ = Stefan–Boltzmann constant, 5.67×10^{-8} W/m^2 K^4

Subscripts

f = fluid
h = heat source
i = heat source number
max = maximum
ref = reference
s = solid
∞ = ambient/inlet

References

[1] Adams, V. H., Joshi, Y., and Blackburn, D. L., 1999, "Three-Dimensional Study of Combined Conduction, Radiation and Natural Convection From Discrete Heat Sources in a Horizontal Narrow-Aspect-Ratio Enclosure," ASME J. Heat Transfer, **121**, pp. 992–1001.

[2] Afrid, M., and Zebib, A., 1991, "Three-Dimensional Laminar and Turbulent Natural Convection Cooling of Heated Blocks," Numer. Heat Transfer, **19**, pp. 405–424.

[3] Sathe, S. B., and Joshi, Y., 1992, "Natural Convection Liquid Cooling of a Substrate Mounted Protrusion in a Square Enclosure," ASME J. Heat Transfer, **114**, pp. 401–409.

[4] Wang, H. Y., Penot, F., and Sauliner, B., 1997, "Numerical Study of Buoyancy—Induced Flow Along a Vertical Plate With Discretely Heated Integrated Circuit Packages," Int. J. Heat Mass Transfer, **40**, pp. 1509–1520.

[5] Tou, S. K. W., Tso, C. P., and Zhang, X., 1999, "3-D Numerical Analysis of Natural Convective Liquid Cooling of a 3×3 Heater Array in Rectangular Enclosures," Int. J. Heat Mass Transfer, **42**, pp. 3231–3244.

[6] Joshi, Y., Willson, T., and Hazard, S. J., 1989, "An Experimental Study of Natural Convection Cooling of an Array of Heated Protrusions in a Vertical Channel in Water," ASME J. Electron. Packag., **111**, pp. 33–40.

[7] Heindel, T. J., Ramadhyani, S., and Incropera, F. P., 1996, "Conjugate Natural Convection From an Array of Discrete Heat Sources: Part 1—Two- and Three-Dimensional Model Validation," Int. J. Heat Fluid Flow, **16**, pp. 501–510.

[8] Young, T. J., and Vafai, K., 1999, "Experimental and Numerical Investigation of Forced Convective Characteristics of Channel Mounted Obstacles," ASME J. Heat Transfer, **121**, pp. 34–42.

[9] Gupta, A., and Jaluria, Y., 1998, "Forced Convective Liquid Cooling of Array of Protruding Heated Elements Mounted in a Rectangular Duct," ASME J. Electron. Packag., **120**, pp. 243–252.

[10] McEntire, A. B., and Webb, B. W., 1990, "Local Forced Convective Heat Transfer From Protruding and Flush-Mounted Two-Dimensional Discrete Heat Sources," Int. J. Heat Mass Transfer, **33**, pp. 1521–1533.

[11] Joseph, A. T., Venkateshan, S. P., and Kuruvilla, G., 2001, "Experimental Studies on Cooling of Electronic Components in a Channel," Int. J. Transp. Phenom., **3**, pp. 103–118.

[12] Yadav, V., and Kant, K., 2007, "Air Cooling of Variable Array of Heated Modules in a Vertical Channel," ASME J. Electron. Packag., **129**, pp. 205–215.

[13] Mahaney, H. V., Incropera, F. P., and Ramadhyani, S., 1990, "Comparison of Prediction and Measure Mixed Convection Heat Transfer From an Array of Discrete Sources in a Horizontal Rectangular Channel," Int. J. Heat Mass Transfer, **33**, pp. 1233–1245.

[14] Mahaney, H. V., Ramadhyani, S., and Incropera, F. P., 1991, "Numerical Simulation of Three Dimensional Mixed Convection Heat Transfer From a Finned Array of Discrete Sources," Numer. Heat Transfer, **19**, pp. 125–149.

[15] Watson, J. C., Anand, N. K., and Fletcher, L. S., 1996, "Mixed Convection Heat Transfer Between a Series of Vertical Parallel Plates With Planar Heat Sources," ASME J. Heat Transfer, **118**, pp. 984–1218.

[16] Dogan, A., Sivrioglu, M., and Baskaya, S., 2005, "Experimental Investigation of Mixed Convection Heat Transfer in a Rectangular Channel With Discrete Heat Sources at the Top and at the Bottom," Int. J. Heat Mass Transfer, **32**, pp. 1244–1252.

[17] da Silva, A. K., Lorente, S., and Bejan, A., 2004, "Optimal Distribution of Discrete Heat Sources on a Plate With Laminar Forced Convection," Int. J. Heat Mass Transfer, **47**, pp. 2139–2148.

[18] Dias, T., Jr., and Milanez, L. F., 2006, "Optimal Location of Heat Sources on a Vertical Wall With Natural Convection Through Genetic Algorithms," Int. J. Heat Mass Transfer, **49**, pp. 2090–2096.

[19] Modest, M. F., 2003, *Radiative Heat Transfer*, 2nd ed., Academic, New York.

[20] Fluent Incorporated, 1990, *Fluent User's Guide*, Vol. 2, Lebanon, PA.

[21] Krishnan, A. S., 2005, "Experimental Studies on Free and Mixed Convection With Surface Radiation in Isolated and Parallel Vertical Heated Plates," Ph.D. thesis, Indian Institute of Technology Madras, Chennai, India.

[22] Holman, J. P., 2001, *Experimental Methods for Engineers*, 7th ed., McGraw-Hill, New York.

[23] Sudhakar, T. V. V., Balaji, C., and Venkateshan, S. P., 2009, "Optimal Configuration of Discrete Heat Sources in a Vertical Duct Under Conjugate Mixed Convection Using Artificial Neural Networks," Int. J. Therm. Sci., **48**, pp. 881–890.

[24] Holland, J. H., 1975, "Adaptation in Natural and Artificial Systems," Ann Arbor, The University of Michigan Press.

[25] Goldberg, D. E., 1989, "Genetic Algorithms in Search, Optimization, and Machine Learning," Addison-Wesley.

[26] Queipo, N., Devarakonda, R., and Humphery, J. A. C., 1994, "Genetic Algorithms for Thermo Sciences Research: Application to the Optimized Cooling of Electronic Components," Int. J. Heat Mass Transfer, **37**, pp. 893–908.

[27] Madadi, R., and Balaji, C., 2008, "Optimization of the Location of Multiple Discrete Heat Sources in a Ventilated Cavity Using Artificial Neural Networks and Micro Genetic Algorithm," Int. J. Heat Mass Transfer, **51**, pp. 2299–2312.

Subcooled Boiling Heat Transfer for Turbulent Flow of Water in a Short Vertical Tube

Koichi Hata[1]
Institute of Advanced Energy,
Kyoto University,
Gokasho, Uji,
Kyoto 611-0011, Japan
e-mail: hata@iae.kyoto-u.ac.jp

Suguru Masuzaki
National Institute for Fusion Science,
322-6 Oroshi-cho, Toki,
Gifu 509-5292, Japan

The subcooled boiling heat transfer and the critical heat flux (CHF) due to exponentially increasing heat inputs with various periods ($Q = Q_0 \exp(t/\tau)$, $\tau = 22.52$ ms–26.31 s) were systematically measured by an experimental water loop flow and observed by an infrared thermal imaging camera. Measurements were made on a 3 mm inner diameter, a 66.5 mm heated length, and a 0.5 mm thickness of platinum test tube, which was divided into three sections (upper, mid, and lower positions). The axial variations of the inner surface temperature, the heat flux, and the heat transfer coefficient from nonboiling to critical heat flux were clarified. The results were compared with other correlations for the subcooled boiling heat transfer and authors' transient CHF correlations. The influence of exponential period (τ) and flow velocity on the subcooled boiling heat transfer and the CHF was investigated and the predictable correlation of the subcooled boiling heat transfer for turbulent flow of water in a short vertical tube was derived based on the experimental data. In this work, the correlation gave 15% difference for subcooled boiling heat transfer coefficients. Most of the CHF data (101 points) were within 15% and −30 to +20% differences of the authors' transient CHF correlations against inlet and outlet subcoolings, respectively. [DOI: 10.1115/1.3194768]

Keywords: subcooled boiling heat transfer, turbulent flow of water, short vertical tube

1 Introduction

The knowledge of subcooled boiling heat transfer for turbulent flow of water is important to understand the mechanism of subcooled flow boiling critical heat flux (CHF) in a short vertical tube. Many researchers have experimentally studied the subcooled boiling heat transfer for turbulent flow of water in pipes and given the correlations for calculating subcooled boiling heat transfer coefficients [1–4].

In the previous works, we have already measured the transient CHF by exponentially increasing heat input ($Q_0 \exp(t/\tau)$, $\tau = 16.8$ ms–15.5 s), rampwise one ($Q = \alpha t$, $\alpha = 6.21 \times 10^8$–1.63 $\times 10^{12}$ W/m³ s) and stepwise one ($Q = Q_s$, $Q_s = 2.95 \times 10^{10}$ –7.67 × 10¹⁰ W/m³) for the SUS304 test tubes with rough, smooth, and mirror finished inner surfaces in the wide range of experimental conditions to establish the database for designing the divertor of a helical type fusion experimental device, which is large helical device (LHD) located in National Institute for Fusion Science, Japan [5–17]. Furthermore, we have given the transient CHF correlations against inlet and outlet subcoolings based on the effects of test tube inner diameter (d), flow velocity (u), inlet and outlet subcoolings ($\Delta T_{sub,in}$ and $\Delta T_{sub,out}$), ratio of heated length to inner diameter (L/d), and nondimensional reduced time ($\omega_p u/\{\sigma/g/(\rho_l - \rho_g)\}^{0.5}$) on CHF [15,17].

$$\text{Bo} = C_1 \left\{ \frac{d}{\sqrt{\sigma/g(\rho_l - \rho_g)}} \right\}^{-0.1} \text{We}^{-0.3} \left(\frac{L}{d}\right)^{-0.1} e^{-(L/d)/C_2 \text{Re}^{0.4}} \text{Sc}^{*C_3}$$
$$\times \left[1 + 11.4 \left\{ \frac{\omega_p u}{\sqrt{\sigma/g(\rho_l - \rho_g)}} \right\}^{-0.6} \right]$$

for inlet subcooling $(\Delta T_{sub,in} \geq 40$ K) (1)

$$\text{Bo} = 0.082 \left\{ \frac{d}{\sqrt{\sigma/g(\rho_l - \rho_g)}} \right\}^{-0.1} \text{We}^{-0.3} \left(\frac{L}{d}\right)^{-0.1} \text{Sc}^{0.7}$$
$$\times \left[1 + 6.34 \left\{ \frac{\omega_p u}{\sqrt{\sigma/g(\rho_l - \rho_g)}} \right\}^{-0.6} \right]$$

for outlet subcooling $(\Delta T_{sub,out} \geq 30$ K) (2)

where $C_1 = 0.082$, $C_2 = 0.53$, and $C_3 = 0.7$ for $L/d \leq$ around 40, and $C_1 = 0.092$, $C_2 = 0.85$, and $C_3 = 0.9$ for $L/d >$ around 40. The reduced times, ω_p, for exponentially increasing heat input, rampwise one, and stepwise one are τ, $t_{cr}/2$, and t_{cr}, respectively. Bo, We, Sc*, and Sc are boiling number ($= q_{cr,sub}/Gh_{fg}$), Weber number ($= G^2 d/\rho_l \sigma$), nondimensional inlet subcooling ($= c_{pl} \Delta T_{sub,in}/h_{fg}$), and nondimensional outlet subcooling ($= c_{pl} \Delta T_{sub,out}/h_{fg}$), respectively. Saturated thermophysical properties were evaluated at the outlet pressure. Most of the data for the exponentially increasing heat input (2824 points), the rampwise one (208 points), and the stepwise one (105 points) are within 15% difference of Eqs. (1) and (2), respectively.

Meanwhile, other workers obtained CHF data [18–20], which varied widely in the whole experimental range, although most of our CHF data are within the 15% difference of our CHF correlations. The burned out test surface showed that burnout occurred at a local position near the exit of the test tube. Distribution of temperature along the inner surface of the test tube would become more nonuniform at CHF. The inner surface temperature at the exit of the test tube would become higher when the outlet liquid temperature is higher than the inlet one. The nonuniformity for the inner surface temperature of the test tube may become the cause of the lower CHF. The axial variations of the inner surface temperature, the heat flux, and the heat transfer coefficient at CHF have been desired to clarify the mechanism of subcooled flow boiling CHF in a short vertical tube.

The present work has the following objectives: (1) to measure the subcooled boiling heat transfer for platinum test tube divided into three sections (upper, mid, and lower positions) and the CHF with a wide range of exponential periods (τ) and flow velocities
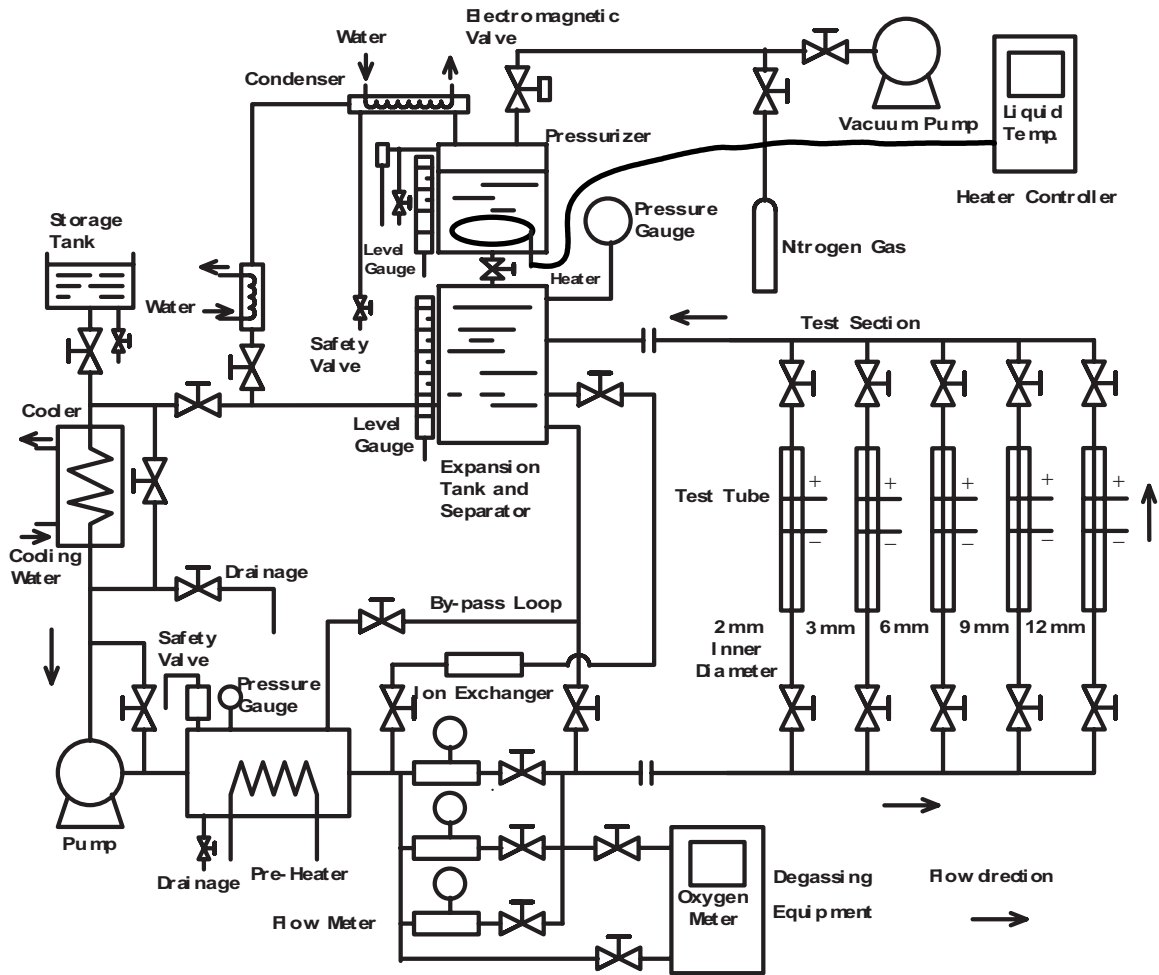
Fig. 1 Schematic diagram of experimental water loop

(u), (2) to clarify the axial variations of the inner surface temperature, the heat flux, and the heat transfer coefficient from nonboiling to CHF, (3) to derive the correlation of the subcooled boiling heat transfer in a short vertical tube based on the experimental data for platinum test tube with a commercial finish of inner surface, and (4) to discuss the mechanisms of the subcooled flow boiling critical heat flux in a short vertical tube.

2 Experimental Apparatus and Method

The schematic diagram of experimental water loop comprised of the pressurizer is shown in Fig. 1. The loop is made of SUS304 stainless steel and is capable of working up to 2 MPa. The loop has five test sections whose inner diameters are 2 mm, 3 mm, 6 mm, 9 mm, and 12 mm. Test sections were vertically oriented with water flowing upward. The test section of the inner diameter of 3 mm was used in this work. The circulating water was distilled and deionized with about 0.2 μS/cm specific resistivity. The circulating water through the loop was heated or cooled to keep a desired inlet temperature by preheater or cooler. The flow velocity was measured by a mass flow meter using a vibration tube (Nitto Seiko, CLEANFLOW 63FS25, Flow range=100 and 750 kg/min). The flow velocity was controlled by regulating the frequency of the three-phase alternating power source to the canned type circulation pump (Nikkiso Co., Ltd., Non-Seal Pump HT24B-B2, pump flow rate=75 m³/h and pump head=18 m). The water was pressurized by saturated vapor in the pressurizer in this work. The pressure at the inlet of the test tube was controlled within ±1 kPa of a desired value by using a heater controller of the pressurizer.

The cross-sectional view of the 3 mm inner diameter test section is shown in Fig. 2. The platinum (Pt) test tube with inner diameter of 3 mm and heated length of 66.5 mm, and with the commercial finish of inner surface was used in this work. The test tube has wall thickness, δ, of 0.5 mm. Four fine 0.07 mm diameter platinum wires were spot welded on the outer surface of the test tube as potential taps; the first one is at the position of 4.8 mm from the leading edge of the test tube, and the second to forth ones are at 19.2 mm, 18.8 mm, and 18.7 mm from the previous ones, respectively. The silver-coated 5 mm thickness copper-electrode plates to supply heating current were soldered to the surfaces of the both ends of the test tube. The both ends of test tube were electrically isolated from the loop by Bakelite plates of 14 mm thickness. The inner surface condition of the test tube was observed by the scanning electron microscope (SEM) photograph and inner surface roughness was measured by the surface texture measuring instrument (SURFCOM 120A) of Tokyo Seimitsu Co., Ltd., Mitaka, Tokyo, Japan. Figure 3 shows the result of SEM photograph of the inner surface of platinum (Pt) test tube. The inner surface roughness is measured 0.40 μm for average roughness, R_a, 2.20 μm for maximum roughness depth, R_{max}, and 1.50 μm for mean roughness depth, R_z.

The test tube was heated with an exponentially increasing heat input, $Q_0 \exp(t/\tau)$, supplied from a direct current source (Takasago Ltd., Kawasaki, Kanagawa, Japan, NL035-500R, DC 35 V-3000 A) through the two copper electrodes shown in Fig. 4. The value of the initial exponential heat input, Q_0, was set to be 1.5×10^7 W/m³ throughout the present experiments which was so low that no significant change in heater temperature occurred
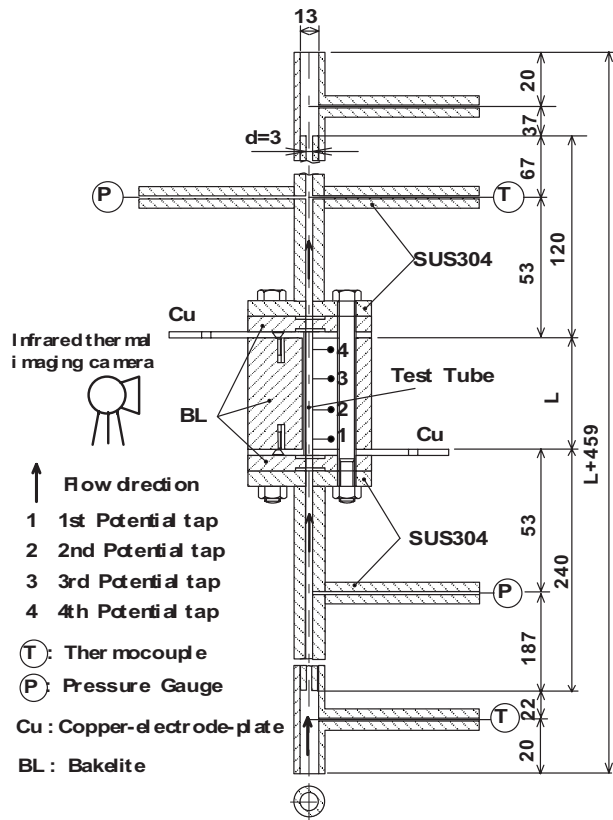
Fig. 2 Vertical cross-sectional view of 3 mm inner diameter test section

Fig. 4 Measurement and data processing system

during the early stage of the run. The exponential periods, τ, of the heat input ranged from 22.5 ms to 26.3 s. The common specifications of the direct current source are as follows. Constant-voltage (CV) mode regulation is 0.005%+3 mV of full scale, CV mode ripple is 500 μV rms or better and CV mode transient response time is less than 200 μs (typical) against 5% to full range change in load. The transient CHFs, $q_{\text{cr,sub}}$, were realized by the exponentially increasing heat input to the test tube. At the CHF, the test tube average temperature rapidly increases. The current for the heat input to the test tube was automatically cut off when the average temperature increased up to the preset tempera-

Fig. 3 Result of SEM photograph of platinum test tube

ture, which was several tens of K higher than corresponding CHF surface temperature. This procedure avoided actual burnout of the test tube.

The outer surface temperature of the test tube with heating was observed by an infrared thermal imaging camera (NEC Avio Infrared Technologies Co., Ltd., Shinagawa, Tokyo, Japan, Thermo Tracer TH9100WR). The accuracy is ±2% of reading. The outer surface of the test tube was uniformly painted black with black body spray (Japan Sensor Corporation, Minato, Tokyo, Japan, JSC-3, $\varepsilon = 0.94$) in this work.

The average temperature of the test tube was measured with resistance thermometry participating as a branch of a double bridge circuit for the temperature measurement. The output voltages from the bridge circuit together with the voltage drops across the two electrodes, across the potential taps of the test tube (first and second potential taps, second and third ones, and third and fourth ones), and across a standard resistance were amplified and then were sent via a D/A converter to a digital computer. These voltages were simultaneously sampled at a constant time interval ranging from 60 μs to 200 ms. The average temperatures of the test tube between the two electrodes and between adjacent potential taps (first and second potential taps, second and third ones, and third and fourth ones) were calculated with the aid of previously calibrated resistance-temperature relation, respectively. The average temperatures of the test tube between the two electrodes were compared with those between first and fourth potential taps and much difference for a heat loss could not be clearly observed in high subcooling range. The heat generation rates of the test tube between the two electrodes and between adjacent potential taps (first and second potential taps, second and third ones, and third and fourth ones) were calculated from the measured voltage differences between the two electrodes and between adjacent potential taps of the test tube, and that across the standard resistance, respectively. The surface heat fluxes between the two electrodes and between adjacent potential taps are the differences between the heat generation rate per unit surface area and the rate of change in energy storage in the test tube obtained from the faired average temperature versus time curve as follows:

$$q(t) = \frac{V}{S}\left(Q(t) - \rho c \frac{d\bar{T}}{dt}\right) \quad (3)$$

where ρ, c, V, and S are the density, the specific heat, the volume, and the inner surface area of the test tube, respectively.

The heater inner surface temperatures between the two electrodes and between adjacent potential taps were also obtained by solving the heat conduction equation in the test tube under the conditions of measured average temperature and surface heat flux of the test tube. All the calculations of the inner surface temperature were made by using the PHOENICS code [21]. Basic unsteady two-dimensional heat conduction equation for the test tube is as follows:

$$\rho c \frac{\partial T}{\partial t} = \frac{1}{r}\frac{\partial}{\partial r}\left(r\lambda \frac{\partial T}{\partial r}\right) + \frac{1}{r}\frac{dT}{d\theta}\left(\frac{\lambda}{r}\frac{\partial T}{\partial \theta}\right) + Q(t) \quad (4)$$

The calculation domain from test tube inner radius, r_i, to test tube outer radius, r_o, is radially divided into 500 grid points ($\Delta r = 1$ μm) and the time step, Δt, is given much smaller than 0.45 ms. The unsteady equation is numerically analyzed together with the following boundary conditions:

$$q(t) = -\lambda \left.\frac{\partial T}{\partial r}\right|_{r=r_i} \quad (5)$$

$$\left.\frac{\partial T}{\partial r}\right|_{r=r_o} = 0 \quad (6)$$

Furthermore, the solutions for the inner and outer surface temperatures of the test tube, T_s and T_{so}, are given by the steady one-dimensional heat conduction equation. The basic equation for the test tube is as follows:

$$\frac{d^2 T}{dr^2} + \frac{1}{r}\frac{dT}{dr} + \frac{Q}{\lambda} = 0 \quad (7)$$

then integration yields and the mean temperature of the test tube is obtained.

$$T(r) = -\frac{Qr^2}{4\lambda} + \frac{Qr_o^2}{2\lambda}\ln r + C \quad (8)$$

$$\bar{T} = \frac{1}{\pi(r_o^2 - r_i^2)}\int_{r_i}^{r_o} 2\pi r T(r)dr \quad (9)$$

Generating heat in the tube is equal to the thermal conduction and the test tube is perfectly insulated.

$$q = -\lambda \left.\frac{dT}{dr}\right|_{r=r_i} = \frac{(r_o^2 - r_i^2)Q}{2r_i}$$

$$\left.\frac{dT}{dr}\right|_{r=r_o} = 0 \quad (10)$$

The temperatures of the heater inner and outer surfaces, T_s and T_{so}, and C in Eq. (8) can be described as follows:

$$T_s = T(r_i) = \bar{T} - \frac{qr_i}{4(r_o^2 - r_i^2)^2\lambda} \times \left[4r_o^2\left\{ r_o^2\left(\ln r_o - \frac{1}{2}\right) \right.\right.$$
$$\left.\left. - r_i^2\left(\ln r_i - \frac{1}{2}\right)\right\} - (r_o^4 - r_i^4) \right] - \frac{qr_i}{2(r_o^2 - r_i^2)\lambda}(r_i^2 - 2r_o^2 \ln r_i)$$
$$(11)$$

$$T_{so} = T(r_o) = \bar{T} - \frac{qr_i}{4(r_o^2 - r_i^2)^2\lambda} \times \left[4r_o^2\left\{ r_o^2\left(\ln r_o - \frac{1}{2}\right) \right.\right.$$
$$\left.\left. - r_i^2\left(\ln r_i - \frac{1}{2}\right)\right\} - (r_o^4 - r_i^4) \right] - \frac{qr_i r_o^2}{2(r_o^2 - r_i^2)\lambda}(1 - 2 \ln r_o)$$
$$(12)$$

$$C = \bar{T} - \frac{qr_i}{4(r_o^2 - r_i^2)^2\lambda} \times \left[4r_o^2\left\{ r_o^2\left(\ln r_o - \frac{1}{2}\right) - r_i^2\left(\ln r_i - \frac{1}{2}\right)\right\} \right.$$
$$\left. - (r_o^4 - r_i^4) \right] \quad (13)$$

In case of the 3 mm inner diameter test section, before entering the test tube, the test water flows through the tube with the same inner diameter of the test tube to form the fully developed velocity profile. The entrance tube length, L_e, is given 240 mm ($L_e/d = 80$). The values of L_e/d for $d=3$ mm in which the center line velocity reaches 99% of the maximum value for turbulence flow were obtained from 9.8 to 21.9 by the correlation of Brodkey and Hershey [22] as follows:

$$\frac{L_e}{d} = 0.693 \, \mathrm{Re}_d^{1/4} \quad (14)$$

The inlet and outlet liquid temperatures were measured by 1mm outer diameter, sheathed, K-type thermocouples (Nimblox, sheath material: SUS316, hot junction: ground, response time (63.2%): 46.5 ms), which are located at the centerline of the tube at the upper and lower stream points of 262 mm and 53 mm from the tube inlet and outlet points. The outlet liquid temperatures and the outlet subcoolings for power transient experiment were made corrections in time to account for instrument lag because the locations of the vapor patches for the CHFs were almost observed near the tube outlet. The values of the time lag for $u = 4.01–13.3$ m/s were 13.25–3.98 ms. The inlet and outlet pressures were measured by the strain gauge transducers (Kyowa Electronic Instruments Co., Ltd., Chofu, Tokyo, Japan, PHS-20A, natural frequency: approximately 30 kHz), which were located near the entrance of conduit at upper and lower stream points of 53 mm from the tube inlet and outlet points. The thermocouples and the transducers were installed in the conduits, as shown in Fig. 2. The inlet and outlet pressures for $d=3$ mm were calculated from the pressures measured by inlet and outlet pressure transducers as follows [5]:

$$P_{in} = P_{ipt} - \{(P_{ipt})_{wnh} - (P_{opt})_{wnh}\} \times \frac{0.053}{0.106 + L} \quad (15)$$

$$P_{out} = P_{in} - (P_{in} - P_{opt}) \times \frac{L}{0.053 + L} \quad (16)$$

Outline of these equations is shown in the Appendix.

Experimental errors are estimated to be ± 1 K in inner tube surface temperature and $\pm 2\%$ in heat flux. Inlet flow velocity, inlet and outlet subcoolings, inlet and outlet pressures, and exponential period were measured within the accuracy $\pm 2\%$, ± 1 K, ± 1 kPa, and $\pm 2\%$, respectively.

3 Experimental Results and Discussion

3.1 Experimental Conditions. Transient heat transfer processes on the test tube that caused by the exponentially increasing heat inputs, $Q_0 \exp(t/\tau)$, were measured. The exponential periods, τ, of the heat input ranged from 22.52 ms to 26.31 s. The decrease in the exponential period means an increase in the rate of increasing heat input. The initial experimental conditions such as inlet flow velocity, inlet subcooling, inlet pressure, and exponential period for the flow boiling heat transfer and CHF experiments were
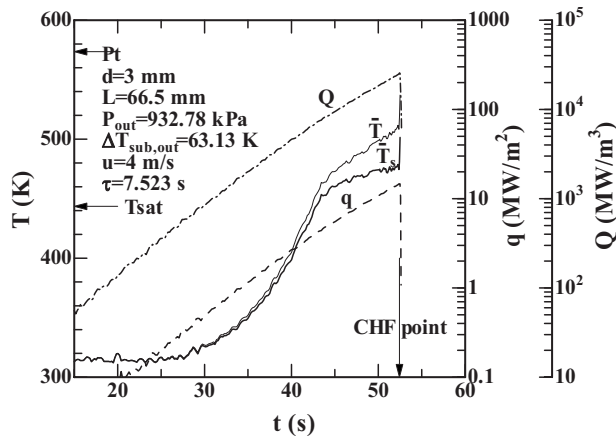
Fig. 5 Typical time variations in measured heat input per unit volume, Q, average temperature, $\bar{T}$, calculated heat flux, q, and inner surface temperature, $\bar{T}_s$, on the platinum test tube of d =3 mm and L=66.5 mm for the exponential period of 7.52 s, with the flow velocity of 4.0 m/s

Fig. 6 Typical heat transfer processes on the platinum test tube of d=3 mm and L=66.5 mm for the exponential period of around 8 s with the flow velocities of 4.0 m/s, 6.9 m/s, 9.9 m/s, and 13.3 m/s

determined independently each other before each experimental run.

The experimental conditions were as follows:

- heater material platinum
- surface condition commercial finish of inner surface
- surface roughness: 0.40 μm for R_a, 2.20 μm for $R_{\max}$, and 1.50 μm for R_z
- inner diameter (d): 3 mm
- heated length (L): 66.5 mm
- L/d: 22.17
- wall thickness (δ): 0.5 mm
- inlet flow velocity (u): 4.0 m/s, 6.9 m/s, 9.9 m/s, and 13.3 m/s
- inlet pressure (P_{in}): 739.26 kPa to 1064.48 kPa
- outlet pressure (P_{out}): 763.70 kPa to 986.85 kPa
- inlet subcooling $(\Delta T_{\text{sub,in}})$: 141.58 K to 156.93 K
- outlet subcooling $(\Delta T_{\text{sub,out}})$: 48.72 K to 150.70 K
- inlet liquid temperature (T_{in}): 295.26 K to 305.25 K
- exponentially increasing heat input (Q): $Q_0 \exp(t/\tau)$ and τ =22.52 ms−26.31 s

3.2 Heat Transfer Characteristics

3.2.1 Steady State Heat Transfer. Figure 5 is the typical time variation in the measured heat input per unit volume, Q, and average temperature, $\bar{T}$, and the calculated heat flux, q, and inner surface temperature, $\bar{T}_s$, with time for the platinum test tube of d=3 mm and L=66.5 mm at the flow velocity of 4.0 m/s. The test tube was heated with an exponentially increasing heat input with the period of 7.52 s. The heat flux becomes exponentially higher with an increase in the heat input per unit volume and reaches a maximum value, $q_{\text{cr,sub}}$, which is named the CHF. The average temperature of the test tube and the inner surface temperature are almost constant at first. They increase with the increase in the heat input and their increase rates become lower for the boiling initiation. They continue to increase up to the CHF and rapidly increase at the point. This phenomenon is shown in Fig. 6 as a plot of log q versus log $\Delta \bar{T}_{\text{sat}}$ $(=\bar{T}_s - T_{\text{sat}})$.

Figure 6 shows typical examples of the heat transfer curves for the exponential period, τ, of around 8 s on the platinum test tube of d=3 mm and L=66.5 mm at the inlet liquid temperature, T_{in}, of around 301.73 K and the flow velocities, u, of 4 to 13.3 m/s. At a fixed flow velocity, the heat flux gradually becomes higher with
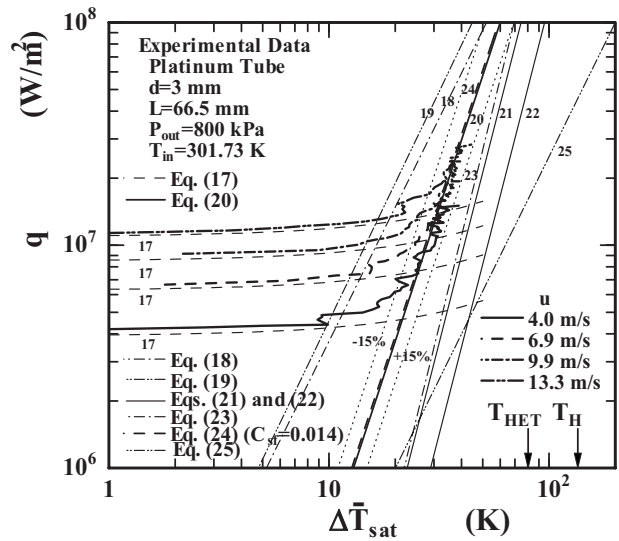
an increase in $\Delta \bar{T}_{\text{sat}}$ $(=\bar{T}_s - T_{\text{sat}})$ on the nonboiling forced convection curve derived from our correlation, Eq. (17) [23], up to the point where the slope begins to increase with heat flux following the onset of nucleate boiling.

$$\text{Nu}_d = 0.02 \ \text{Re}_d^{0.85} \ \text{Pr}^{0.4}\left(\frac{L}{d}\right)^{-0.08}\left(\frac{\mu_l}{\mu_w}\right)^{0.14} \quad (17)$$

All properties in the equation are evaluated at the average bulk liquid temperature, T_L, $[=(T_{\text{in}}+(T_{\text{out}})_{\text{cal}})/2]$, except μ_w, which is evaluated at the heater inner surface temperature. And the heat flux increases up to the CHF, where the heater surface temperature rapidly jumps from the nucleate boiling heat transfer regime to the film boiling one. The CHF and its superheat become higher with an increase in flow velocity. The nucleate boiling curves in higher heat flux range for each flow velocity agree with each other forming a single straight line on the log q versus log $\Delta \bar{T}_{\text{sat}}$ graph. The corresponding equation number is shown near each heat transfer curve on the graph.

The analytical solution of incipient boiling superheat given by Sato and Matsumura [24] is shown in the figure for comparison. The solution was derived based on the initiation model of bubble growth.

$$q = \frac{\lambda_l h_{fg}(T_s - T_{\text{sat}})^2}{8\sigma T_{\text{sat}}(v_g - v_l)} \quad (18)$$

For thermophysical properties, the saturated temperature, T_{sat}, is defined. The experimental data of the incipient boiling superheat for each flow velocity almost agree with the values predicted by Eq. (18).

The equation of incipient boiling superheat given by Bergles and Rohsenow [25] is also shown in the figure for comparison.

$$(\Delta T_{\text{sat}})_{\text{ONB}} = 0.556\left(\frac{q}{1082P^{1.156}}\right)^{0.463P^{0.0234}} \quad (19)$$

where q is the surface heat flux in W/m^2, P is the system pressure in bar and ΔT_{sat} is in K. The values of $(\Delta T_{\text{sat}})_{\text{ONB}}$ calculated from Eq. (19) are in good agreement with the experimental data of the incipient boiling superheat for each flow velocity.

The fully developed subcooled boiling curve for platinum test tube with a commercial finish of inner surface can be expressed by the following empirical correlation.

$$q = C\Delta\bar{T}_{sat}^n \qquad (20)$$

where C and n are coefficient and exponent, and equivalent to 463 and 3, respectively. The correlation can almost describe the fully developed subcooled boiling curves for the platinum test tube of $d=3$ mm and $L=66.5$ mm, with the commercial finish of inner surface at the outlet pressure of around 800 kPa obtained in this work within 15% difference under the wide range of flow velocities.

The corresponding curves derived from the correlations for fully developed subcooled boiling given by McAdams et al. [1], Jens and Lottes [2], Rohsenow [3], and Thom et al. [4] are also shown in Fig. 6 for comparison.

- McAdams et al. [1]:

$$\Delta T_{sat} = 22.62 q^{0.259}$$

for the dissolved gas concentration of 0.3 ml

of airper liter of water $\qquad (21)$

$$\Delta T_{sat} = 28.92 q^{0.259}$$

for the dissolved gas concentration of 0.06 ml

of airper liter of water $\qquad (22)$

where ΔT_{sat} is in K and q is in MW/m^2.

- Jens and Lottes [2]:

$$\Delta T_{sat} = 0.79 q^{0.25} e^{-P/6.2} \qquad (23)$$

where P is the absolute pressure in MPa, ΔT_{sat} is in K, and q is in W/m^2.

- Rohsenow [3]:

$$\frac{c_{pl}\Delta T_{sat}}{h_{fg}} = C_{sf}\left(\frac{q}{\mu_l h_{fg}}\sqrt{\frac{\sigma}{g(\rho_l - \rho_g)}}\right)^{0.33}\left(\frac{c_{pl}\mu_l}{\lambda_l}\right)^{1.7} \qquad (24)$$

where the various fluid properties are evaluated at the saturation temperature corresponding to the local pressure and C_{sf} is a function of the particular heating surface-fluid combination.

- Thom et al. [4]:

$$\Delta T_{sat} = 0.022 q^{0.5} e^{-P/8.6} \qquad (25)$$

where P is the absolute pressure in MPa, ΔT_{sat} is in K, and q is in W/m^2.

The values of n given by the correlation of McAdams et al. [1] and the one by Jens and Lottes [2] are about 30% larger than that of our correlation, although the correlation of Thom et al. [4] is about 30% smaller. The values calculated from our correlation are in good agreement with the corresponding values from Rohsenow correlation, Eq. (24), with $C_{sf}=0.014$ on the log q versus log $\Delta\bar{T}_{sat}$ graph.

The values of the lower limit of the heterogeneous spontaneous nucleation temperature, T_{het} [26], and the homogeneous spontaneous nucleation temperature, T_H [27], at the pressure of 800 kPa are shown in the figure for comparison. The inner surface temperature of the test tube at CHF with the flow velocity, u, of 13.3 m/s is 41.31 K and 96.03 K lower than the T_{het} and the T_H, respectively.

Figure 7 shows inner surface temperatures ($\bar{T}_{s1}$, $\bar{T}_{s2}$, and $\bar{T}_{s3}$—solid lines on the left side of the figure), heat fluxes (q_1, q_2, and q_3—solid lines on the right side of the figure) and heat transfer coefficients ($\bar{h}_1$, $\bar{h}_2$, and $\bar{h}_3$—broken lines on the right side of the figure) for first, second, and third positions of the sections between first and second potential taps, second and third ones, and third and fourth ones, and inlet and outlet liquid temperatures (T_{in} and T_{out}—broken lines on the left side of the figure) at the flow velocity, u, of 13.3 m/s with the heat flux, q, varied as a parameter.
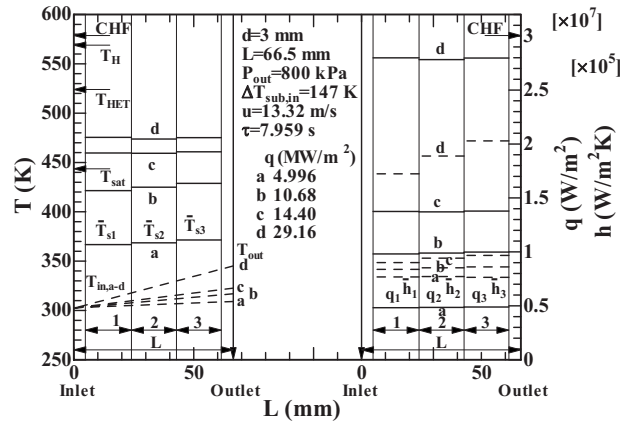
Fig. 7 Inner surface temperatures, heat fluxes, and heat transfer coefficients for first, second, and third positions of three sections, and inlet and outlet liquid temperatures with the exponential period of 8 s at the flow velocity of 13.3 m/s

The liquid temperatures at the center of each section (heated lengths, L, of 14.4 mm, 33.4 mm, and 52.15 mm) are linearly estimated from the values of the inlet liquid temperature, T_{in}, and outlet one, T_{out}. At low heat flux in the nonboiling region ($\Delta\bar{T}_{sat}$ < boiling initiation temperature), the inner surface temperatures for each position of the sections ($\bar{T}_{s1}$, $\bar{T}_{s2}$, and $\bar{T}_{s3}$) become gradually higher with an increase in the heated length from the leading edge of the test tube, whereas the heat fluxes (q_1, q_2, and q_3) are almost constant for each position of the sections. The increasing rate of the inner surface temperature shows nearly the same trend of that of the liquid temperature from the inlet to the outlet (T_{in} to T_{out}). The heat transfer coefficients for each position of the sections ($\bar{h}_1$, $\bar{h}_2$, and $\bar{h}_3$) become almost constant as shown in the figure. At high heat flux in the nucleate boiling region ($\Delta\bar{T}_{sat}$ > boiling initiation temperature), the inner surface temperatures (modified into larger than) for each position of three sections ($\bar{T}_{s1}$, $\bar{T}_{s2}$, and $\bar{T}_{s3}$) almost become constant, as well as the heat fluxes (q_1, q_2, and q_3), although the outlet liquid temperature (T_{out}) become much higher than the inlet one (T_{in}). The heat transfer coefficients ($\bar{h}_1$, $\bar{h}_2$, and $\bar{h}_3$) become gradually higher with an increase in the heated length.

Figure 8 shows the numerical solutions of the radius variations in the inner temperatures of the platinum test tube at the critical heat fluxes of 15.05 MW/m^2 and 28.3 MW/m^2 with the flow
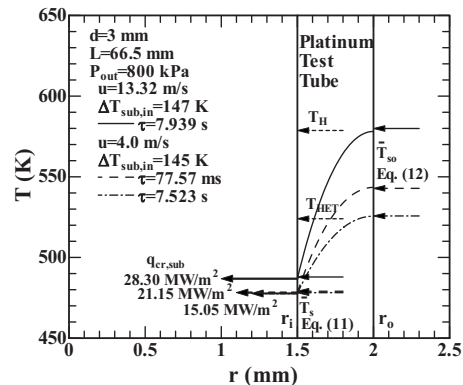
Fig. 8 Inner temperatures of platinum test tube at the critical heat fluxes of 15.1 MW/m^2, 21.2 MW/m^2, and 28.3 MW/m^2 for the exponential periods of 7.5 s, 77.6 ms, and 7.9 s with the flow velocities of 4 m/s, 4 m/s, and 13.3 m/s, respectively
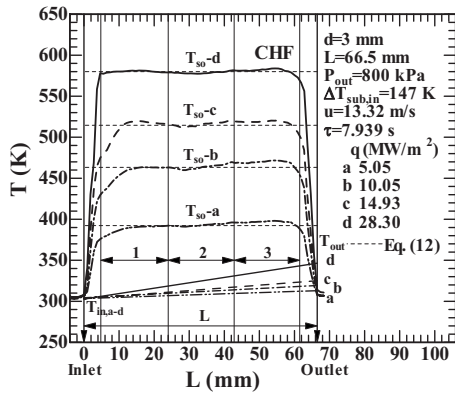
Fig. 9 Axial variations in outer surface temperature of the test tube observed by an infrared thermal imaging camera for the exponential period of 7.9 s, with the flow velocity of 13.3 m/s

Fig. 10 Time variations in measured heat input per unit volume, Q, average temperature, $\bar{T}$, calculated heat flux, q, and inner surface temperature, $\bar{T}_s$, on the platinum test tube of d =3 mm and L=66.5 mm for the exponential period of 77.57 ms with the flow velocity of 4.0 m/s

velocities of 4 m/s and 13.3 m/s for the exponential period of around 8 s, respectively. They become parabolically high with an increase in the radius from the inner surface temperatures, $\bar{T}_s$, to the outer surface temperatures, $\bar{T}_{so}$. The steady state values of the heater inner and outer surface temperatures calculated from Eqs. (11) and (12) are also shown as each arrow symbol in the figure for comparison. The numerical solutions of the inner and outer surface temperatures solved by the unsteady two-dimensional heat conduction equation, Eq. (4), are in good agreement with the values given by Eqs. (11) and (12), which are obtained from the steady one-dimensional heat conduction equation.

The outer surface temperature of the test tube was observed by an infrared thermal imaging camera. Figure 9 shows the axial variations in the outer surface temperature of the test tube, T_{so}, for the exponential period of 7.9 s at the flow velocity of 13.3 m/s with the heat flux varied as a parameter. For example, the outer surface temperature of the test tube for q=28.3 MW/m^2, which is almost the CHF value steeply increases from 303 K at the electrode of the inlet up to 580 K at the heated length of 5 mm from the leading edge of the test tube, and firmly keeps the constant value of about 580 K to about 5 mm short of the outlet of the test tube. Finally, it linearly falls down to 305 K at the electrode of the outlet again. The both ends of the platinum test tube were soldered to the copper-electrode plates which have a width of 80 mm, a length of 120 mm, and a thickness of 5 mm. The heat capacities of the copper-electrode plates with subcooled water flow would be far large in comparison with the joule heat of the test tube which has a wall thickness, δ, of 0.5 mm. The outlet liquid temperature (T_{out}=346.4 K) becomes 43.6 K higher than the inlet one (T_{in} =302.8 K) by the uniform heating of the test tube with q =28.3 MW/m^2. It is observed from this figure that the outer surface temperatures for 1st, 2nd, and 3rd positions of three sections almost become constant at high heat flux in the nucleate boiling region (q=14.93 and 28.3 MW/m^2) and gradually increase with an increase in the heated length at low heat flux in the nonboiling region (q=5.05 and 10.05 MW/m^2). The increasing rate of the outer surface temperature at low heat flux seems to be the same with that of the test water. It will be considered from this fact that the heat transfer coefficients on the inner surface of the test tube will be gradually high with an increase in the heated length at high heat flux in the nucleate boiling region and those will be almost constant for the heated length at low heat flux in the nonboiling region as mentioned above. The outer surface temperatures with ε=0.94 for first, second, and third positions of three sections were 10–20% lower than the values calculated from Eq. (12) for each heat flux, although the infrared thermal imaging camera has the

accuracy of $\pm2\%$ of reading. The temperature curves on the figure were uniformly revised to the values calculated from Eq. (12) and plotted.

3.2.2 Transient Heat Transfer. Figure 10 is the time variation in the measured heat input per unit volume, Q, and average temperature, $\bar{T}$, and the calculated heat flux, q, and inner surface temperature, $\bar{T}_s$, with time for the platinum test tube of d =3 mm and L=66.5 mm at the flow velocity of 4.0 m/s. The test tube was heated with an exponentially increasing heat input with the period of 77.57 ms. The heat flux becomes exponentially higher with an increase in the heat input per unit volume and reaches the CHF. The average temperature of the test tube and the inner surface temperature increase with the increase in the heat input, and their increase rates also become lower for the boiling initiation. They continue to increase up to the CHF and rapidly increase at the point. This transient phenomenon is shown in Fig. 11 as a plot of log q versus log $\Delta\bar{T}_{sat}$.
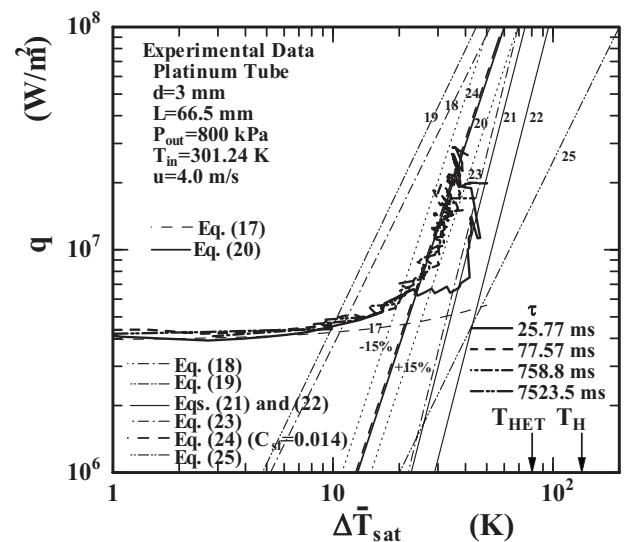
Fig. 11 Typical heat transfer processes on the platinum test tube of d=3 mm and L=66.5 mm for the exponential periods of 26 ms, 78 ms, and 759 ms, and 7.5 s with the flow velocity of 4.0 m/s
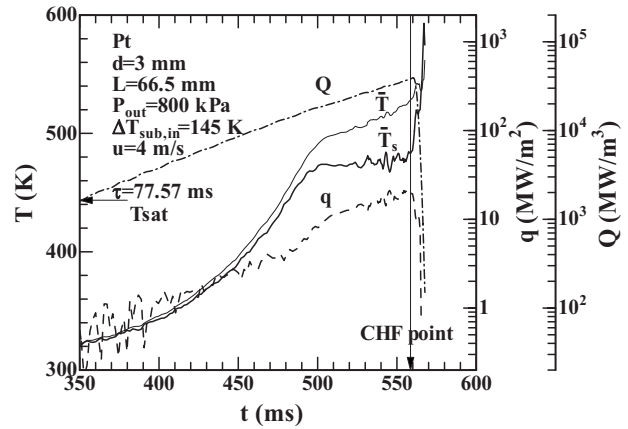
Fig. 12 Inner surface temperatures, heat fluxes, and heat transfer coefficients for first, second, and third positions of three sections, and inlet and outlet liquid temperatures with the exponential period of 77.6 ms at the flow velocity of 4 m/s

Fig. 13 The $q_{\text{cr,sub}}$ on the platinum test tube of $d=3$ mm and $L=66.5$ mm, with the commercial finish of inner surface at $\Delta T_{\text{sub,in}}=150$ K for $\tau=22.52$ ms-26.31 s

Figure 11 shows the typical heat transfer curves for the exponential periods, τ, of 25.8 ms, 77.6 ms, 758.8 ms, and 7.52 s on the platinum test tube o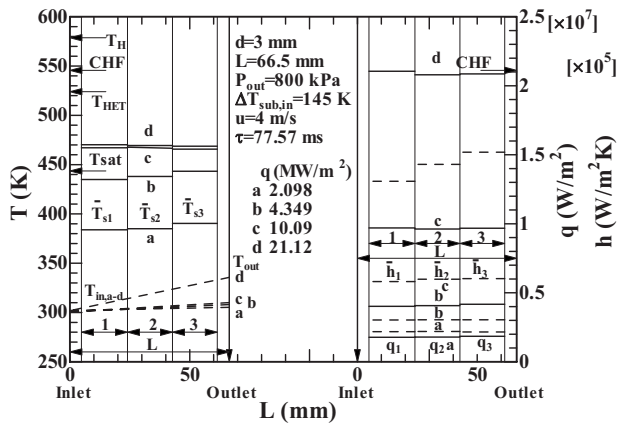f $d=3$ mm and $L=66.5$ mm at the inlet liquid temperature, T_{in}, of around 301.24 K and the flow velocity, u, of 4 m/s. For the wide range of exponential periods ($\tau=25.8$ ms-7.52 s), the heat flux becomes similarly higher with an increase in $\Delta \bar{T}_{\text{sat}}$ on the nonboiling forced convection curve derived from our correlation, Eq. (17). The nucleate boiling curves for the exponential period larger than 77.6 ms almost agree with each other forming a single straight line given by Eq. (20) on the log q versus log $\Delta \bar{T}_{\text{sat}}$ graph. The temperature overshoot for the exponential period of 25.8 ms becomes considerably larger than those for the exponential period larger than 77.6 ms because of the time lag of the activation of originally flooded cavity for the increasing rate of the heat input. The maximum value of the temperature overshoot for the exponential period, τ, of 25.7 ms becomes 46.63 K at $q=11.3$ MW/m^2, which is 33.8 K lower than the lower limit of the heterogeneous spontaneous nucleation temperature, T_{het}.

Inner surface temperatures ($\bar{T}_{s1}$, $\bar{T}_{s2}$, and $\bar{T}_{s3}$), heat fluxes (q_1, q_2, and q_3), and heat transfer coefficients ($\bar{h}_1$, $\bar{h}_2$, and $\bar{h}_3$) for 1st, 2nd, and 3rd positions of three sections; and inlet and outlet liquid temperatures (T_{in} and T_{out}) with the exponential period, τ, of 77.6 ms at the flow velocity, u, of 4 m/s are shown in Fig. 12. The experimental data for the transient heat input show nearly the same trend of dependence on the inner surface temperature, the heat flux, and the heat transfer coefficient for the steady state one, although the increasing rates of the inner surface temperature and the heat flux become very high. At low heat flux in the nonboiling region ($\Delta \bar{T}_{\text{sat}} <$ boiling initiation temp.), the inner surface temperatures for each position of three sections ($\bar{T}_{s1}$, $\bar{T}_{s2}$, and $\bar{T}_{s3}$) are gradually increased with an increase in the heated length from the leading edge of the test tube, whereas the heat fluxes (q_1, q_2, and q_3) are almost constant. The increasing rate of the inner surface temperature is the same as that of the liquid temperature from the inlet to the outlet (T_{in} to T_{out}). The heat transfer coefficients for each position of three sections ($\bar{h}_1$, $\bar{h}_2$, and $\bar{h}_3$) are almost constant. Meanwhile, at high heat flux in the nucleate boiling region ($\Delta \bar{T}_{\text{sat}} >$ boiling initiation temperature), the inner surface temperatures ($\bar{T}_{s1}$, $\bar{T}_{s2}$, and $\bar{T}_{s3}$) and the heat fluxes (q_1, q_2, and q_3) for each position of three sections almost become constant, although the outlet liquid temperature becomes much higher than the inlet
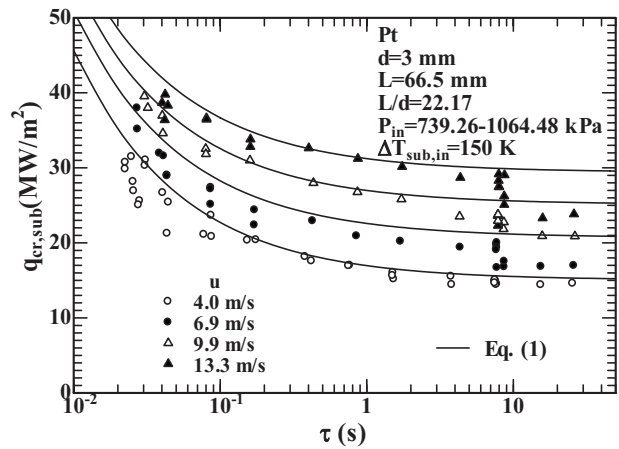
one. The heat transfer coefficients ($\bar{h}_1$, $\bar{h}_2$, and $\bar{h}_3$) become gradually high with an increase in the heated length.

The radius variation in the inner temperatures of the platinum test tube numerically obtained for the transient critical heat flux of 21.15 MW/m^2 at the flow velocity of 4 m/s with the exponential period of 77.6 ms are also shown in Fig. 8 for comparison. They were compared with the values of the inner and outer surface temperatures calculated from the steady one-dimensional heat conduction equation, Eqs. (11) and (12). The numerical solutions of the inner and outer surface temperatures are almost in good agreement with the steady state values given by Eqs. (11) and (12), although the exponential period ($\tau=77.57$ ms) becomes 100 times smaller.

3.3 Critical Heat Flux Characteristics

3.3.1 Inlet Subcooling. Figure 13 shows the transient CHFs, $q_{\text{cr,sub}}$, for the test tube inner diameter ($d=3$ mm), the heated length ($L=66.5$ mm), L/d (=22.17), and the wall thickness ($\delta=0.5$ mm) obtained for the exponential periods, τ, ranging from 22.52 ms to 26.31 s at the inlet subcooling, $\Delta T_{\text{sub,in}}$, of around 150 K. The transient CHFs, $q_{\text{cr,sub}}$, for the section between the two electrodes were shown in the figure. The exponential period represents the e-fold time of heat input. As shown in the figure, the $q_{\text{cr,sub}}$ are almost constant for the exponential periods from 800 ms to 26.31 s and they become higher with the decrease in the exponential period from around 800 ms. The corresponding curves for the flow velocities obtained from the transient CHF correlation against inlet subcooling, Eq. (1), are also shown in the figure for comparison. The $q_{\text{cr,sub}}$ appear to be well expressed by Eq. (1) for the wide range of the exponential periods tested here. The transient CHFs in the whole experimental range become higher with an increase in the flow velocity at a fixed exponential period.

For power transient experiments, the rate of increasing heat input is very high. It takes time to form the fully developed temperature profile in the test tube because the test tube has some heat capacity. Then the temperature profile in the thermal boundary layer on the test tube surface grows, and vaporization occurs. And furthermore, it is seen that the phenomenon occurs at some critical velocity in the vapor phase when the vapor jets start interfering with each other. It takes time to occur the hydrodynamic instability on the vapor-liquid interface at the CHF. Namely, it is explained to be as a result of the time lag of the formation of the transient critical heat flux for the increasing rate of the heat input.

The ratios of the transient CHF data for the platinum test tube of $d=3$ mm and $L=66.5$ mm with the commercial finish of inner surface to the corresponding values calculated from the transient
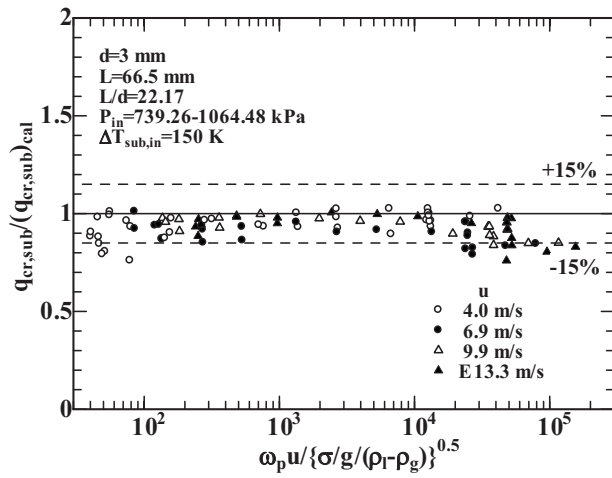
Fig. 14 Ratios of $q_{cr,sub}$ for the platinum test tube of d =3 mm and L=66.5 mm, with the commercial finish of inner surface (101 points) to corresponding values calculated by Eq. (1) versus $\omega_p u / \{\sigma / g / (\rho_l - \rho_g)\}^{0.5}$

CHF correlation against inlet subcooling, Eq. (1), are shown versus the nondimensional reduced time, $\omega_p u / \{\sigma / g / (\rho_l - \rho_g)\}^{0.5}$, in Fig. 14. Most of the data (101 points) for the $\omega_p u / \{\sigma / g / (\rho_l - \rho_g)\}^{0.5}$ ranging from 40.17 to 1.552×10^5 are within 15% difference of Eq. (1) for 141.58 K$\leq \Delta T_{sub,in} \leq$156.93 K.

3.3.2 Outlet Subcooling. The ratios of the transient CHF data for the wide range of exponential periods ($Q_0 \exp(t/\tau)$, τ =22.52 ms–26.31 s) to the corresponding values calculated from the transient CHF correlation against outlet subcooling, Eq. (2), are shown versus the nondimensional reduced time, $\omega_p u / \{\sigma / g / (\rho_l - \rho_g)\}^{0.5}$, in Fig. 15. Most of the data (101 points) for the platinum test tube of d=3 mm and L=66.5 mm with the commercial finish of inner surface are within -30 to $+20\%$ difference of Eq. (2) for $40.17 \leq \omega_p u / \{\sigma / g / (\rho_l - \rho_g)\}^{0.5} \leq 1.552$ $\times 10^5$ at 48.72 K$\leq \Delta T_{sub,out} \leq$150.70 K. The CHF data (32 points) for the SUS304 test tube with the mirror finished inner surface (R_a=0.14 μm) have been distributed within -30 to $+7.6\%$ difference of Eq. (2) for 71.4 K$\leq \Delta T_{sub,out} \leq$108.4 K [8], although the transient CHF correlations against inlet and outlet subcoolings, Eqs. (1) and (2) can describe the authors' published
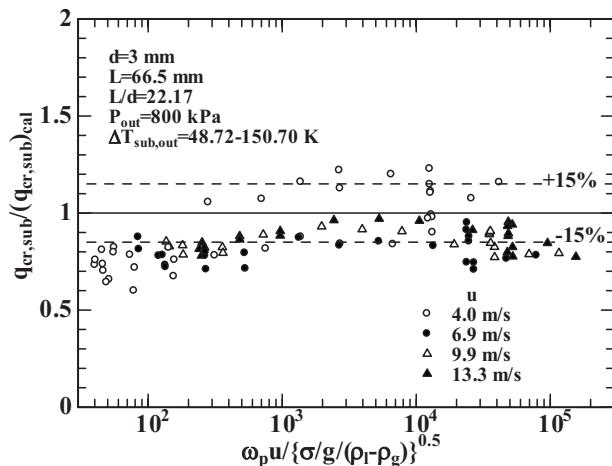
Fig. 15 Ratios of $q_{cr,sub}$ for the platinum test tube of d =3 mm and L=66.5 mm, with the commercial finish of inner surface (101 points) to corresponding values calculated by Eq. (2) versus $\omega_p u / \{\sigma / g / (\rho_l - \rho_g)\}^{0.5}$

CHF data (3137 points) on test tubes with rough and smooth finished inner surfaces (R_a=3.18 and 0.26 μm) for the wide range of test tube inner diameters (d=2–12 mm), heated lengths (L=22–149.7 mm), L/d (=4.08–74.85), outlet pressures (P_{out} =159 kPa–1.1 MPa), flow velocities (u=4.0–13.3 m/s), inlet subcoolings ($\Delta T_{sub,in}$=40–155 K), outlet subcoolings ($\Delta T_{sub,out}$ =30–140 K), and nondimensional reduced times (30.59 $\leq \omega_p u \{\sigma / g / (\rho_l - \rho_g)\}^{0.5} \leq 1.94 \times 10^5$) within 15% difference [5–17]. Reproducibility of the data for the test tube with a smoother inner surface needs further studies.

The shorter exponential period for various heat inputs induces instantaneously a very high heating rate in the test tube. We have supposed before this study that heating rate will affect the incipient boiling superheat and the nucleate boiling heat transfer up to the CHF. Incipient boiling superheat may shift to a high value at a high heating rate, and direct transition to film boiling may occur in such a case. This may be the cause of very low published data [18–20] that were about a half or lower of those given by our CHF correlations, Eqs. (1) and (2). However, neither a direct transition to film boiling nor a trend of a decrease in CHF with a decrease in the exponential period in a smaller exponential period range was observed on a platinum test tube of d=3 mm and L=66.5 mm with a commercial finish of inner surface (R_a=0.40 μm) used here even at the highest heating rate ($\omega_p u / \{\sigma / g / (\rho_l - \rho_g)\}^{0.5}$ =40.17) and the flow velocity (u=13.3 m/s) as shown in Figs. 13–15. It becomes very important to confirm the lower limit of the exponential period, τ, for the applicability of transient CHF correlations, Eqs. (1) and (2), to keep on high heat flux heat removal.

4 Conclusions

The subcooled boiling heat transfer and the CHF due to exponentially increasing heat inputs with various periods (Q =$Q_0 \exp(t/\tau)$, τ=22.52 ms–26.31 s) were systematically measured for the flow velocities (u=4.0–13.3 m/s), the inlet liquid temperatures (T_{in}=295.26–305.25 K) and the inlet pressures (P_{in}=739.26–1064.48 kPa). Measurements were made on a 3 mm inner diameter, a 66.5 mm heated length, and a 0.5 mm thickness of platinum test tube, which was divided into three sections (upper, mid, and lower positions). Experimental results lead to the following conclusions.

(1) The heat flux for the exponential periods, τ, ranging from 22.52 ms to 26.31 s becomes higher with an increase in $\Delta \bar{T}_{sat}$ ($=\bar{T}_s - T_{sat}$) on the nonboiling forced convection curve derived from our correlation, Eq. (17).

(2) The correlation of the subcooled boiling heat transfer for turbulent flow of water in a short vertical tube, Eq. (20), can almost describe the fully developed subcooled boiling curves for platinum test tube with a commercial finish of inner surface within 15% difference for the wide range of exponential periods from 22.52 ms to 26.31 s.

(3) At low heat flux in the nonboiling region ($\Delta \bar{T}_{sat}<$boiling initiation temperature), the heat transfer coefficients ($\bar{h}_1$, $\bar{h}_2$, and $\bar{h}_3$) and the heat fluxes (q_1, q_2, and q_3) for the upper, mid, and lower positions of three sections are almost constant for the exponential period, τ, ranging from 22.52 ms to 26.31 s. Meanwhile, at high heat flux in the nucleate boiling region ($\Delta \bar{T}_{sat}>$boiling initiation temperature), the inner surface temperatures ($\bar{T}_{s1}$, $\bar{T}_{s2}$, and $\bar{T}_{s3}$) and the heat fluxes (q_1, q_2, and q_3) for each position of three sections clearly become constant for various exponential periods.

(4) The outer surface temperatures, T_{so}, of the test tube steeply increase at the heated length of 5 mm from the leading edge of the test tube. After that those at low heat flux in the nonboiling region become gradually higher with an increase in the heated length and those at high heat flux in the

nucleate boiling region firmly keep the constant value to about 5 mm short of the outlet of the test tube. Finally, those linearly fall down at the electrode of the outlet again.

(5) Most of the CHF data (101 points) for the platinum test tube of $d=3$ mm and $L=66.5$ mm with the commercial finish of inner surface are within 15% difference of the transient CHF correlation against inlet subcooling, Eq. (1), for 141.58 K$\leq\Delta T_{\text{sub,in}}\leq156.93$ K and within -30 to $+20\%$ difference of the transient CHF correlation against outlet subcooling, Eq. (2), for 48.72 K$\leq\Delta T_{\text{sub,out}}\leq150.70$ K, respectively.

(6) Neither a direct transition to film boiling nor a trend of a decrease in CHF with a decrease in the exponential period in a smaller exponential period range was observed on the platinum test tube of $d=3$ mm and $L=66.5$ mm with the commercial finish of inner surface ($R_a=0.40$ μm) used here even at the highest heating rate ($\omega_p u/\{\sigma/g/(\rho_l-\rho_g)\}^{0.5}=40.17$) and the flow velocity ($u=13.3$ m/s).

Acknowledgment

Nomenclature

Bo = $=q_{\text{cr,sub}}/Gh_{fg}$, boiling number
C = constant in Eq. (8) and coefficient in Eq. (20)
C_1, C_2, C_3 = constant in Eq. (1)
C_{sf} = coefficient in Eq. (24)
c = specific heat, J/kg K
c_p = specific heat at constant pressure, J/kg K
d = test tube inner diameter, m
G = $=\rho_l u$, mass flux, kg/m^2 s
g = acceleration of gravity, m/s^2
h = $=q/(T_s-T_L)$, heat transfer coefficient, W/m^2 K
$\bar{h}$ = $=q/(\bar{T}_s-T_L)$, average heat transfer coefficient, W/m^2 K
h_{fg} = latent heat of vaporization, J/kg
L = heated length, m
L_e = entrance length, m
L_{ipt} = distance between inlet pressure transducer and inlet of the heated section, m
L_{opt} = distance between outlet pressure transducer and outlet of the heated section, m
n = exponent in Eq. (20)
Nu_d = Nusselt number, hd/λ
P = pressure, kPa
P_{in} = pressure at inlet of heated section, kPa
P_{ipt} = pressure measured by inlet pressure transducer, kPa
P_{out} = pressure at outlet of heated section, kPa
P_{opt} = pressure measured by outlet pressure transducer, kPa
Pr = $=c_p\mu/\lambda$, Prandtl number
Q = heat input per unit volume, W/m^3
Q_0 = initial exponential heat input, W/m^3
Q_s = step height of heat input per unit volume, W/m^3
q = heat flux, W/m^2
$q_{\text{cr,sub}}$ = transient critical heat flux for subcooled condition, W/m^2
R_a = average roughness, μm
Re_d = $=Gd/\mu$, Reynolds number
R_{max} = maximum roughness depth, μm

Rz = mean roughness depth, μm
r = radius, m
Δr = r-direction width of control volume, m
r_i = test tube inner radius, m
r_o = test tube outer radius, m
S = surface area, m^2
Sc = $=c_{pl}(\Delta T_{\text{sub,out}})_{\text{cal}}/h_{fg}$, $=c_{pl}\Delta T_{\text{sub,out}}/h_{fg}$, nondimensional outlet subcooling
Sc^* = $=c_{pl}\Delta T_{\text{sub,in}}/h_{fg}$, nondimensional inlet subcooling
T = temperature of the test tube, K
$\bar{T}$ = mean temperature of the test tube, K
T_H = homogeneous spontaneous nucleation temperature, K
T_{het} = lower limit of heterogeneous spontaneous nucleation temperature, K
T_{in} = inlet liquid temperature, K
T_L = $=(T_{\text{in}}+T_{\text{out}})/2$, $=(T_{\text{in}}+(T_{\text{out}})_{\text{cal}})/2$, average bulk liquid temperature, K
T_{out} = outlet liquid temperature, K
$(T_{\text{out}})_{\text{cal}}$ = calculated outlet liquid temperature, K
T_s = inner surface temperature, K
$\bar{T}_s$ = inside axial mean temperature, K
T_{sat} = saturation temperature, K
$\bar{T}_{\text{so}}$ = outside axial mean temperature, K
T_{so} = outer surface temperature, K
t = time, s
Δt = time step, s
t_{cr} = reduced time for stepwise heat input, s
$t_{\text{cr}}/2$ = reduced time for rampwise heat input, s
$\Delta \bar{T}_{\text{sat}}$ = $=\bar{T}_s-T_{\text{sat}}$, superheat, K
$\Delta T_{\text{sub,in}}$ = $=(T_{\text{sat}}-T_{\text{in}})$, inlet liquid subcooling, K
$\Delta T_{\text{sub,out}}$ = $=(T_{\text{sat}}-T_{\text{out}})$, outlet liquid subcooling, K
u = flow velocity, m/s
V = volume, m^3
We = $=G^2 d/\rho_l\sigma$, Weber number
α = coefficient of rampwise heat input, W/m^3 s
δ = wall thickness, m
λ = thermal conductivity, W/mK
μ = viscosity, Ns/m^2
μ_w = viscosity at the temperature of the tube wall, Ns/m^2
ρ = density, kg/m^3
σ = surface tension, N/m
τ = exponential period, s
ω_p = reduced time, s

Subscripts

cr = critical heat flux
g = vapor
in = inlet
out = outlet
l = liquid
sat = saturated conditions
sub = subcooled conditions
wnh = with no heating

Appendix

1 Inlet and Outlet Pressures: P_{in} and P_{out}. Figure 16 shows the time variations in the pressures measured by the inlet and outlet pressure transducers, P_{ipt} and P_{opt}, the inlet and outlet pressures calculated by Eqs. (15) and (16), P_{in} and P_{out}, heat flux, q, and heater inner surface temperature, $\bar{T}_s$, for $P_{\text{out}}=933$ kPa, $\Delta T_{\text{sub,out}}=63.13$ K and $u=4$ m/s. The values of P_{ipt} kept almost constant in the whole experimental range as they are controlled
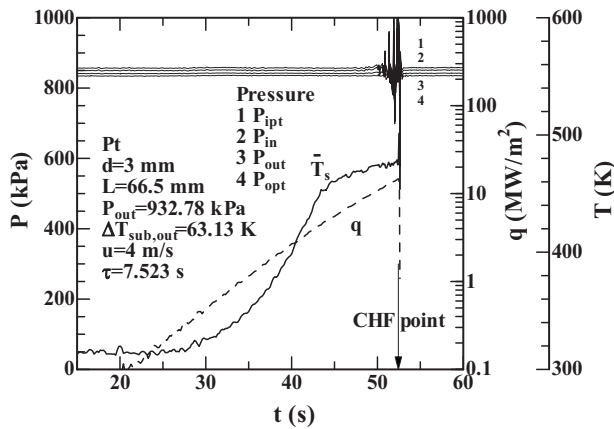
Fig. 16 Time variations in P_{ipt}, P_{opt}, P_{in}, P_{out}, q, and $\bar{T}_s$ for $P_{out}=933$ kPa, $\Delta T_{sub,out}=63.13$ K, and $u=4$ m/s

within ± 1 kPa of the desired value by using a heater controller of the pressurizer, although they oscillated violently near the CHF point. It is considered especially in case of the small diameter tube that the pressure drop in two-phase flow becomes larger than that in single phase due to the vapor bubble confined in the small diameter tube. However, the P_{opt} values showed almost the same ones, too. Therefore, we derived Eqs. (15) and (16) by the use of linear interpretation for the calculation of inlet and outlet pressures, P_{in} and P_{out}: the two-phase pressure drop could not be clearly observed in high subcooling range.

References

[1] McAdams, W. H., Kennel, W. E., Minden, C. S. L., Carl, R., Picornell, P. M., and Dew, J. E., 1949, "Heat Transfer at High Rates to Water With Surface Boiling," Ind. Eng. Chem., **41**(9), pp. 1945–1953.
[2] Jens, W. H., and Lottes, P. A., 1951, "Analysis of Heat Transfer Burnout, Pressure Drop and Density Data for High Pressure Water," Report No. ANL-4627.
[3] Rohsenow, W. M., 1952, "A Method of Correlating Heat-Transfer Data for Surface Boiling of Liquids," Trans. ASME, **74**, pp. 969–976.
[4] Thom, J. R. S., Walker, W. M., Fallon, T. A., and Reising, G. F. S., 1966, "Boiling in Subcooled Water During Flow Up Heated Tubes or Annuli," Proc. Inst. Mech. Eng., **180**, pp. 226–246.
[5] Hata, K., Shiotsu, M., and Noda, N., 2004, "Critical Heat Fluxes of Subcooled Water Flow Boiling Against Outlet Subcooling in Short Vertical Tube," Trans. ASME, Ser. C: J. Heat Transfer, **126**, pp. 312–320.
[6] Hata, K., Komori, H., Shiotsu, M., and Noda, N., 2004, "Critical Heat Fluxes of Subcooled Water Flow Boiling Against Inlet Subcooling in Short Vertical Tube," JSME Int. J., Ser. B, **47**(2), pp. 306–315.
[7] Hata, K., Komori, H., Shiotsu, M., and Noda, N., 2004, "Influence of Dissolved Gas Concentration on Subcooled Water Flow Boiling Critical Heat Flux in Short Vertical Tube," *Proceedings of the 12th International Conference on Nuclear Engineering*, Paper No. ICONE12-49194, pp. 1–10.
[8] Hata, K., Shiotsu, M., and Noda, N., 2004, "Subcooled Flow Boiling Critical Heat Flux in Short Vertical Tube (Influence of Inner Surface Roughness)," ASME Paper No. IMECE2004-61453.
[9] Hata, K., and Noda, N., 2005, "Subcooled Flow Boiling Heat Transfer and Critical Heat Flux in Short Vertical Tube With Mirror Finished Inner Surface," *Proceedings of the 11th International Topical Meeting on Nuclear Reactor Thermal Hydraulics*, Paper No. NURETH11-281, pp. 1–20.
[10] Hata, K., and Noda, N., 2006, "Thermal Analysis on Flat-Plate Type Divertor Based on Subcooled Flow Boiling Critical Heat Flux Data Against Inlet Subcooling in Short Vertical Tube," Trans. ASME, Ser. C: J. Heat Transfer, **128**, pp. 311–317.
[11] Hata, K., Shiotsu, M., and Noda, N., 2006, "Thermal Analysis on Mono-Block Type Divertor Based on Subcooled Flow Boiling Critical Heat Flux Data Against Inlet Subcooling in Short Vertical Tube," Plasma and Fusion Research, **1**, p. 017.
[12] Hata, K., Shiotsu, M., and Noda, N., 2006, "Critical Heat Flux of Subcooled Water Flow Boiling for High L/d Region," Nucl. Sci. Eng., **154**(1), pp. 94–109.
[13] Hata, K., Shiotsu, M., and Noda, N., 2006, "Influence of Heating Rate on Subcooled Flow Boiling Critical Heat Flux in a Short Vertical Tube," JSME Int. J., Ser. B, **49**(2), pp. 309–317.
[14] Hata, K., Shiotsu, M., and Noda, N., 2007, "Influence of Test Tube Material on Subcooled Flow Boiling Critical Heat Flux in Short Vertical Tube," Journal of Power and Energy Systems, **1**(1), pp. 49–63.
[15] Hata, K., and Noda, N., 2007, "Influence of Heat Input Waveform on Transient Critical Heat Flux of Subcooled Water Flow Boiling in a Short Vertical Tube," *Proceedings of the 12th International Topical Meeting on Nuclear Reactor Thermal Hydraulics*, Pittsburgh, PA, Paper No. NURETH12-050, pp. 1–18.
[16] Hata, K., Shiotsu, M., and Noda, N., 2008, "Transient Critical Heat Fluxes of Subcooled Water Flow Boiling in a Short Vertical Tube Caused by Exponentially Increasing Heat Inputs," Trans. ASME, Ser. C: J. Heat Transfer, **130**, p. 054503.
[17] Hata, K., and Masuzaki, S., 2009, "Influence of Heat Input Waveform on Transient Critical Heat Flux of Subcooled Water Flow Boiling in a Short Vertical Tube," Nucl. Eng. Des., (in press).
[18] Celata, G. P., Cumo, M., and Mariani, A., 1992, "Subcooled Water Flow Boiling CHF With Very High Heat Fluxes," Rev. Gen. Therm., **362**, pp. 29–37.
[19] Vandervort, C. L., Bergles, A. E., and Jensen, M. K., 1994, "An Experiment Study of Critical Heat Flux in Very High Heat Flux Subcooled Boiling," Int. J. Heat Mass Transfer, **37**, pp. 161–173.
[20] Mudawar, I., and Bowers, M. B., 1999, "Ultra-High Critical Heat Flux (CHF) for Subcooled Water Flow Boiling-I: CHF Data and Parametric Effects for Small Diameter Tubes," Int. J. Heat Mass Transfer, **42**, pp. 1405–1428.
[21] Spalding, D. B., 1991, *The PHOENICS Beginner's Guide*, CHAM Ltd., London, United Kingdom.
[22] Brodkey, R. S., and Hershey, H. C., 1988, *Transport Phenomena*, McGraw-Hill, New York, p. 568.
[23] Hata, K., and Noda, N., 2008, "Turbulent Heat Transfer for Heating of Water in a Short Vertical Tube," Journal of Power and Energy Systems, **2**(1), pp. 318–329.
[24] Sato, T., and Matsumura, H., 1963, "On the Conditions of Incipient Subcooled-Boiling With Forced Convection," Bull. JSME, **7**, pp. 392–398.
[25] Bergles, A. E., and Rohsenow, W. M., 1964, "The Determination of Forced-Convection Surface-Boiling Heat Transfer," Trans. ASME, Ser. C: J. Heat Transfer, **86**, pp. 365–372.
[26] Cole, C., 1979, *Homogeneous and Heterogeneous Nucleation in Boiling Phenomena*, Vol. 1, S. van Stralen and R. Cole, eds., Hemisphere, New York, p. 71.
[27] Lienhard, J. H., 1976, "Correlation of Limiting Liquid Superheat," Chem. Eng. Sci., **31**, pp. 847–849.

Optimal Distribution of Heat Sources in Convergent Channels Cooled by Laminar Forced Convection

E. Jassim
Mem. ASME
e-mail: ejassim@mun.ca

Y. S. Muzychka
Associate Professor
Mem. ASME
e-mail: yuri@engr.mun.ca

Faculty of Engineering and Applied Science,
Memorial University of Newfoundland,
St. John's, NL, A1B 3X5, Canada

The constructal theory is applied to the flow in a convergent channel. The primary goals of this work are to analyze the heat source distribution and generalize the formula concerning such configurations, to study the spacing between consecutive elements, and to verify the analysis by comparing the proposed configuration with numerical simulations. The results show that nonuniform distributions enhance the performance of the system by allowing the heat source element to work near its maximum condition. Furthermore, the optimal distribution occurs when the heat sources are placed closer to each other near the leading edge of the channel. While the literature shows that the spacing between any consecutive element increases as the sources move downstream from the leading edge, the present results proved that such conclusions are restricted, depending on the ratio of outlet to inlet freestream velocity. Accordingly, the spacing has a maximum value when the exit freestream velocity is more than twice that of the inlet. For design issues, the study also addresses the minimum heat required to achieve optimal system performance. The results show that the amount of heat needed by the system to work close to its optimal performance varies exponentially with the convergent angle and increases with the increase in the heating element's width. The comparison of the present distribution of the heat source elements with a regular one (fixed spacing) is performed numerically to demonstrate the efficiency of the proposed configuration. The results show that the present model forces the system to work more efficiently than the uniform distribution. [DOI: 10.1115/1.3194760]

Keywords: discrete heat source, constructal design, convective cooling, laminar flow, electronic cooling

1 Introduction

Internal forced convection is one of the major active topics in heat transfer due to the strong emphasis on the miniaturization of cooling and heating configurations. Recent research concentrated on the generation of optimal flow architecture as a mechanism by which the system achieves its maximal heat density objective under a finite number of constraints [1]; the primary goal being the strong emphasis on thermal efficiency, the success of which relies on the optimization of flow configuration. The challenge is not only to predict thermal and fluid behaviors, but also to simulate a sufficient number of flow configurations such that the influence of geometry on the performance is clear [2].

The appearance of constructal theory and design as a principle based approach to optimization of flow structure is worth considering. No configuration is favored a priori based on intuition. All configurations compete under a specified set of global constraints [3]. Many applications of this approach were published, and the main trends are reviewed in Ref. [1]. The description of the flow through a structure is not as valuable to assess as how the structure "morphs" in order to achieve its best global performance while meeting the prescribed constraints. The present work is just a small step in a series of studies in which the density of heat transfer has been optimized subject to volume constraints. Of particular interest is internal forced convection in a channel of variable cross section.

In this paper, we strive to extend the work reported in Ref. [2] by including the effect of variable freestream velocity and consider the fundamental problem of optimizing the distribution of discrete heat sources on a wall cooled with forced convection in a convergent duct. The work reports the effects of flow and geometry configurations that should be used in any design of such a system. Several works were done and several papers were published regarding heat transfer performance of walls with distributed heat sources [4–13]. Some have recognized the opportunity to improve global performance by optimizing the nonuniform distribution of discrete heat sources [6–11]. For example, Wang [8] theoretically studied the best placement of heat sources such that the minimum temperature requirement is satisfied with the least amount of total thermal energy input. Experimental studies were performed as well [10,13]. Da Silva et al. [2] studied this problem analytically and numerically, and showed that an optimal nonuniform distribution of heat sources exists, that it relies on flow strength or Reynolds number, and that when the heat sources are sparse, the optimization has a sizeable effect on the global performance.

2 Theoretical Analysis

The main concept of this work is attempting to unite the arrangement of discrete heat sources on a wall cooled by forced convection by considering a variable freestream velocity or what is called the "Jeffery–Hamel flow." Figure 1 shows the schematic of the problem. The inlet freestream of temperature T_∞ and velocity U_∞ are initially uniform at the inlet of a convergent channel of length L. The channel is heated at the wall by line heat sources of fixed strength q' (W/m). Each line heat source extends in the
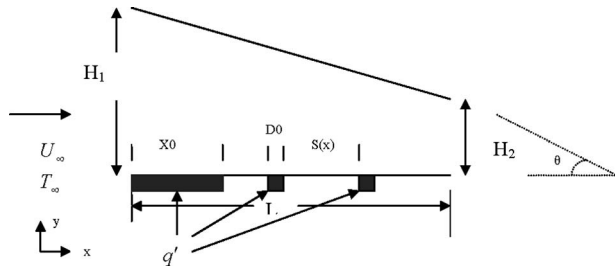
Fig. 1 Finite size heat sources on a convergent flow

Fig. 2 Number of heat elements ratio versus geometry

direction perpendicular to the figure. The flow is incompressible and two-dimensional in the laminar boundary layer regime since the spacing between the walls of the channel was chosen such that the boundary layers merge at the channel exit.

The appropriate spacing that leads the boundary layers to be distinct in all domains can be determined using the following correlation, which was developed by Morega and Bejan [14]:

$$\frac{H_{\mathrm{opt}}}{L} = 3.2\left(\frac{l}{L}\right)^{1/2} \mathrm{Pr}^{-1/4}\ \mathrm{Re}^{-1/2} \tag{1}$$

where H_{opt} is the spacing between the walls of the channel and l is the total length occupied by the heated section, i.e., the flush-mounted sources plus the unheated patches between them. Therefore, when the spacing between the channel walls is greater than H_{opt}, the problem becomes a laminar boundary layer problem.

Now, the number of heat sources per unit length is defined as

$$N' = \text{number of sources/length} \tag{2}$$

The constructal theory shows that the best system is accomplished when all its elements work as hard as the hardest working element [1]. In other words, if T_{max} is the maximum temperature occurring on the plate, and if it must not be exceeded at the hot spot, then the entire system should operate at T_{max}. Consequently, the question now is, what should be the distribution of the heat sources, such that the wall temperature is close to the allowed constraint, or

$$T_w(x) = T_{\mathrm{max}} = \text{const} \tag{3}$$

Suppose the density of line sources is sufficiently high, so that q' is the distribution of heat flow

$$q''(x) = q'N' \tag{4}$$

Equation (4) can be combined with the laminar boundary layer equation

$$\mathrm{Nu}_x = 0.332\ \mathrm{Pr}^{1/3}\ \mathrm{Re}_x^{1/2} \tag{5a}$$

or

$$\frac{q''x}{k(T_{\mathrm{max}} - T_\infty)} = 0.332\ \mathrm{Pr}^{1/3}\left(\frac{U_x x}{\nu}\right)^{1/2} \tag{5b}$$

such that

$$N'(x) = 0.332\frac{k}{q'}(T_{\mathrm{max}} - T_\infty)\mathrm{Pr}^{1/3}\left(\frac{U_x}{\nu x}\right)^{1/2} \tag{6}$$

The function $N'(x)$ represents the optimal configuration of heat sources. U_x can be formulated, assuming a locally steady flow, according to the conservation equation

$$U_x = \frac{U_\infty L}{L - (1 - H)X} \tag{7}$$

where the shape factor (H) is
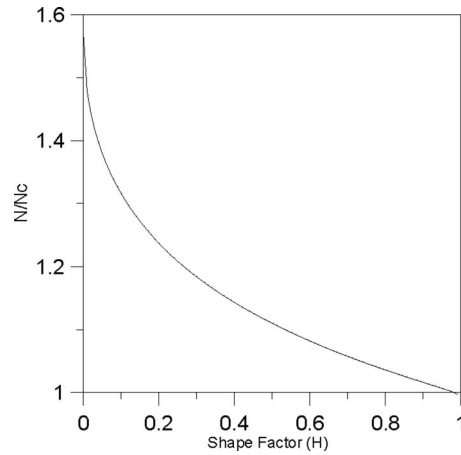
$$H = \frac{A_2}{A_1} = \frac{H_2}{H_1} \tag{8}$$

and hence,

$$N'(x) = 0.332\frac{k}{q'}(T_{\mathrm{max}} - T_\infty)\mathrm{Pr}^{1/3}\ \mathrm{Re}_L^{1/2}\left[\frac{1}{Lx - (1 - H)x^2}\right]^{1/2} \tag{9}$$

where

$$\mathrm{Re}_L = \frac{U_\infty L}{\nu} \tag{10}$$

Equation (9) implies that the heat sources must be located closer together when they are nearer the start of the boundary layer.

The total number of heat sources is

$$N = \int N'dx \tag{11}$$

After integrating we obtain

$$N = \underbrace{0.664\frac{k}{q'}(T_{\mathrm{max}} - T_\infty)\mathrm{Pr}^{1/3}\ \mathrm{Re}_L^{1/2}}_{\mathrm{I}}\underbrace{\left(\frac{\frac{\pi}{2} - \sin^{-1}(2H - 1)}{2\sqrt{1 - H}}\right)}_{\mathrm{II}} \tag{12}$$

Equation (12) represents the global discrete heat source distribution in a convergent flow. Term I symbolizes the total discrete heat distribution in a uniform freestream velocity "N_c" (i.e., constant control surface area) [2], while term II is related to the geometry of the channel; in other words

$$N = N_c\left(\frac{\frac{\pi}{2} - \sin^{-1}(2H - 1)}{2\sqrt{1 - H}}\right) \tag{13a}$$

or

$$\frac{N}{N_c} = \left(\frac{\frac{\pi}{2} - \sin^{-1}(2H - 1)}{2\sqrt{1 - H}}\right) \tag{13b}$$

It can be easily proven that as $H \to 1$, N will approach N_c. Therefore, N/N_c will approach 1 when the cross section area becomes constant, as shown in Fig. 2. Furthermore, $N \to 1.57N_c$ as $H \to 0$, which represents the Jeffery–Hamel flow or radial flow caused by lines of sources or sinks. In other words, the number of discrete
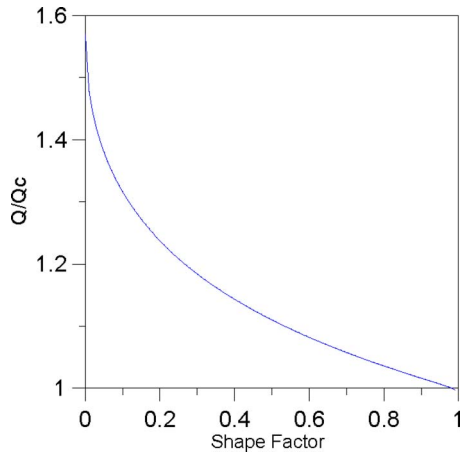
Fig. 3 Maximum heat ratio versus geometry

Fig. 4 Geometry angle effectiveness

sources, as an objective parameter, will increase with the inclination angle, or as a variable constraint parameter, grow when other constraints are fixed. However, it is limited according to

$$N_c \le N \le 1.57 N_c$$

or

$$1 \le \frac{N}{N_c} \le 1.57 \tag{14}$$

The rate of heat transfer from all discrete heat sources to the flow at T_∞ is given by

$$Q'_{max} = q' N = 0.664 k (T_{max} - T_\infty) Pr^{1/3} \; Re_L^{1/2} \left(\frac{\frac{\pi}{2} - \sin^{-1}(2H-1)}{2\sqrt{1-H}} \right) \tag{15}$$

or

$$\frac{Q'_{max}}{Q'_{c(max)}} = \left(\frac{\frac{\pi}{2} - \sin^{-1}(2H-1)}{2\sqrt{1-H}} \right) \tag{16}$$

where $Q'_{c(max)}$ stands for the total heat transfer rate from an isothermal wall at T_{max} when the channel has constant cross section area. Figure 3 demonstrates the maximum heat transfer ratio, which behaves identically as that of the number of sources in Fig. 2.

3 Number of Discrete Heat Sources in Terms of θ

Consider the stream flow through a variable cross-sectional area. The freestream velocity for convergent flow, Eq. (7) becomes

$$\frac{U_x}{U_\infty} = \frac{H_1}{H_1 - x \tan(\theta)} \tag{17}$$

where H_1 is the inflow vertical spacing. Let the factor F represent the ratio

$$F = \frac{\tan(\theta)}{H_1} \tag{18}$$

Hence,

$$\frac{U_x}{U_\infty} = \frac{1}{1 - Fx} \tag{19}$$

and the total number of heat sources (Eq. (13a)) becomes

$$\frac{N}{N_c} = \left[\frac{\frac{\pi}{2} - \sin^{-1}(1 - 2FL)}{2\sqrt{FL}} \right] \tag{20a}$$

As $\theta \to 0$, $F \to 0$ and Eq. (20a) becomes $N = N_c$, i.e., parallel plates. Analogously

$$\frac{Q'_{max}}{Q'_{c(max)}} = \left[\frac{\frac{\pi}{2} - \sin^{-1}(1 - 2FL)}{2\sqrt{FL}} \right] \tag{20b}$$

Figure 4 demonstrates total heat or number of discrete sources as a function of geometry angle for various H_1/L. The figure shows the influence of the convergent channel angle on heat transfer and on the number of heat sources. The relationship begins almost linear. However, when the angle becomes close to its maximum value, the heat transfer and number of heat sources increase exponentially to their maximum limit, which is always equal to $\tan^{-1}(H_1/L)$. Hence, for $H_1/L = 1$, $0 \le \theta \le 45$ deg, as shown in Fig. 4.

4 Local Spacing of Heat Source Elements

The physical implementation of the optimal distribution is restricted by a manufacturing constraint: There exists the smallest scale in the design—the D_o thickness of the line heat sources. Features smaller than D_o cannot be made. This constraint endows the design with structure or coarseness [2].

The spacing $S(x)$, defined as the local distance between two adjacent heat lines, varies with x in accordance with the optimal N' distribution function, see Eq. (9). Specifically, the plate length interval that corresponds to a single line heat source q' is $D_o + S(x)$. This means

$$N' \sim \frac{1}{D_o + S(x)} \tag{21}$$

The strength of one source (q') is spread uniformly over the finite thickness of the source ($q''_o = q'/D_o$). Unlike the function $q''(x)$ of Eq. (5b), which is the result of design, the heat flux q''_o here is a known constant. Furthermore, to acquire the rule for how the wall heating scheme should be constructed, we combine Eqs. (9) and (21)

$$\frac{1}{D_o + S(x)} = 0.332 \left(\frac{k(T_{max} - T_\infty)}{q'} \right) Pr^{1/3} \; Re^{1/2} \left[\frac{1}{Lx - (1-H)x^2} \right]^{1/2} \tag{22}$$

or
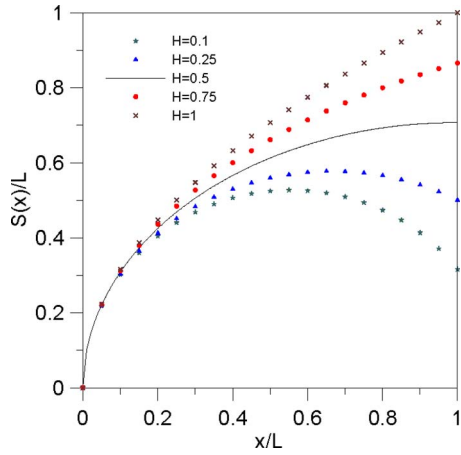
Fig. 5   Spacing between consecutive elements

$$\frac{S(x)}{L} = \frac{3q' \ \Pr^{-1/3} \ \mathrm{Re}^{-1/2}}{k(T_{\max} - T_\infty)} \left[\frac{Lx - (1 - H)x^2}{L^2}\right]^{1/2} - \frac{D_o}{L} \quad (23)$$

The spacing between any consecutive elements S varies along the direction of the flow, as shown in Fig. 5. However, one can recognize two regions of variation, the first region, which occurs when $H > 0.5$, concluded that the spacing increases when moving far from the leading edge. That includes the case study of Da Silva et al. [2], who considered a uniform stream velocity. Hence, both analyses are matches. The second region in the figure, which is bounded by the domain $(0 < H < 0.5)$, demonstrates that moving along the flow direction increases spacing to its maximum possible value and then starts to decrease. In other words, the maximum spacing exists when the freestream velocity at exit is more than double of the inlet's. The position of the maximum spacing can be found from the following equation:

$$\frac{x_{\max}}{L} = \frac{0.5}{1 - H} \quad H < 0.5 \quad (24a)$$

while the magnitude of the maximum spacing is proportional to

$$\frac{S_{\max}}{L} \sim \frac{0.5}{\sqrt{1 - H}} \quad (24b)$$

in the same domain, as shown in Fig. 6.

Equation (23) is not valid in the entire domain of x since it has negative values near the leading edge. It means that the analysis that is provided by Eqs. (1)–(4), (5a), (5b), (6)–(12), (13a), (13b), and (14)–(16) fails to describe the region $(0 \le x \le x_o)$ near the start
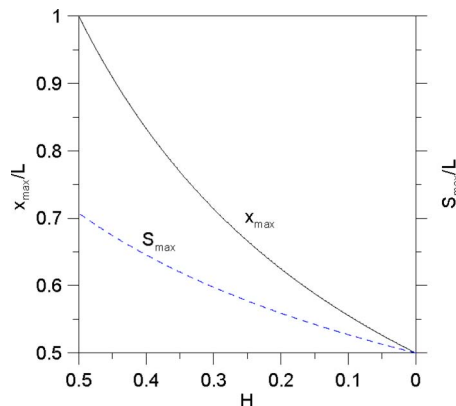
Fig. 6   Position and magnitude of maximum spacing
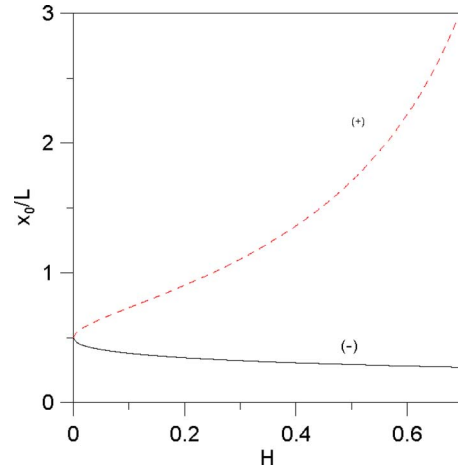
Fig. 7   Investigation of the continuous heat discrete equation

of the boundary layer. Hence, we use a logical approach that Eq. (23) is valid from the position where $(x = x_o)$ and at that location the spacing $S(x_o) = 0$.

Substituting in Eq. (23) and solving for x_0, one can determine the starting length for which Eq. (23) not valid. Thus,

$$\frac{x_o}{L} = \frac{1}{2(1 - H)}\left\{1 \pm \sqrt{1 - (1 - H)\left(\frac{2D_o}{3L}\Lambda\right)^2}\right\} \quad (25a)$$

where the dimensionless parameter (Λ) obtained from the formula

$$\Lambda = \frac{k(T_{\max} - T_o)}{q'}\Pr^{1/3} \ \mathrm{Re}^{1/2} \quad (25b)$$

To be considered, two restrictions must be satisfied by Eq. (25a) and (25b). These are the following.

(1) The range of the dependant variable must satisfy $0 \le x_o/L \le 1$.
(2) From the definition of continuous discrete heat source, x_o should vanish when D_o approaches zero.

Based on the above two facts, Eq. (25a) and (25b), with the plus sign, violates the second condition, and the first condition is violated in the domain $(H > 0.5)$ as well. In contrast, the equation with the minus sign satisfies both conditions, as shown in Fig. 7. Thus, the continuous discrete heat source equation would be

$$\frac{x_o}{L} = \frac{1}{2(1 - H)}\left\{1 - \sqrt{1 - (1 - H)\left(\frac{2D_o}{3L}\Lambda\right)^2}\right\} \quad (26)$$

Equation (26) is used as an estimation of the continuous portion of the discrete heat source from other parameters: shape factor, element thickness, and flow configuration.

It is worth commenting here that Eq. (26) is also valid in the case of uniform freestream velocity. Obviously by using the limiting algorithm with some algebra, one can come up with a formula similar to that of Ref. [2] with a simple discrepancy in the constant. The discrepancy is due to the different approach used in defining the spacing. The approach of Ref. [2] was based on the following criteria. Since D_o is the smallest length scale of the system, the spacing S cannot be smaller than D_o. Consequently, a longitudinal scale x_o must be defined where S is as small as D_o in an order of magnitude scale

$$S \sim D_o \quad \text{when} \quad x \sim x_o \quad (27)$$

Accordingly, Eq. (26) becomes
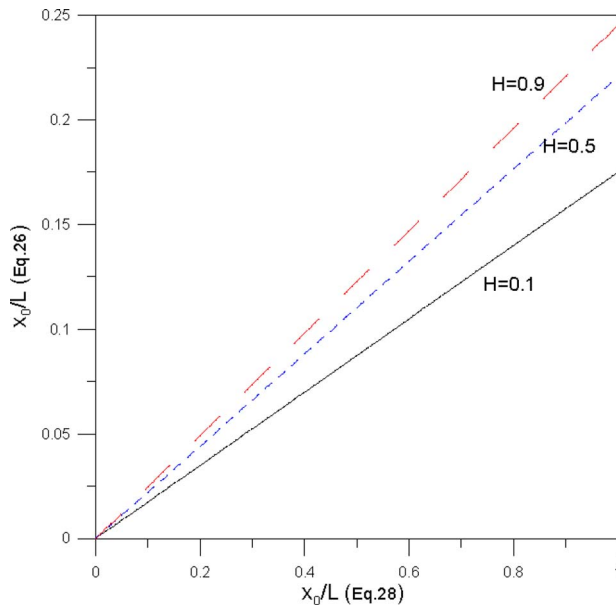
Fig. 8 Continuous heat discrete in different approaches

$$\frac{x_o}{L} = \frac{1}{2(1-H)}\left\{1 - \sqrt{1-(1-H)\left(\frac{4D_o}{3L}\Lambda\right)^2}\right\} \quad (28)$$

The comparison between Eqs. (26) and (28) showed that the discrepancy is only in the numerical value that appears in the term $(D_o/L)\Lambda$. Figure 8 shows the relation between these two equations and one can see that for the particular value of area ratio (H), the continuous discrete heat source obtained from each equation is linearly related to each other.

4.1 Design Criteria. Using Eq. (26), the correlation of the parameters that satisfies the condition can be formulated. The equation should satisfy two limits. The first condition, which involves the fact that the term inside the square root must not be negative, leads to the following inequality:

$$\phi \le \frac{3}{2\sqrt{1-H}} \quad \text{where} \quad \phi = \frac{D_0}{L}\Lambda \quad (29)$$

The second condition, which is based on the fact that the continuous discrete heat source must not be greater than the length of the channel ($0 \le x_o/L \le 1$), gives the following inequality:

$$\phi \le 3\sqrt{H} \quad (30)$$

Figure 9 shows the two conditions and clearly one can conclude that the latter encompasses both conditions. Hence, the design should be based on the second inequality, which with some algebra can be written as

$$\frac{q'}{k(T_{\max} - T_\infty)} \ge \frac{1}{3\sqrt{H}}\frac{D_0}{L}\text{Pr}^{1/3}\ \text{Re}^{1/2} \quad (31)$$

Introducing the heat transfer coefficient and using the average Nusselt number for laminar flow boundary layer, Eq. (31) becomes

$$\frac{q'}{hL(T_{\max} - T_\infty)} \ge \frac{1}{2\sqrt{H}}\frac{D_0}{L} \quad (32)$$

Defining the left hand side of Eq. (32) as the heat ratio, the ratio of the heat source of the elements per unit thickness to the heat absorbed by the fluid, one can predict the minimum heat required for designing the process of optimal distribution by knowing the shape factor and element width. Figure 10 illustrates the variation in the minimum heat ratio as a function of the shape factor for
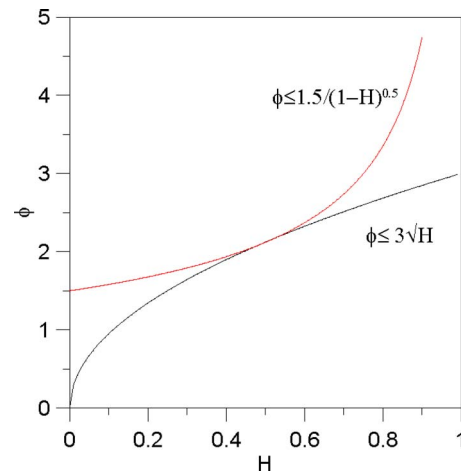
Fig. 9 Design region

different D_0/L. The figure concludes that the minimum value of the heat ratio increases linearly as the convergent angle increases (shape factor decreases) but the variation becomes exponential as the angle becomes larger, particularly when the shape factor descends below 0.5. Another conclusion can be acquired from the figure that the minimum magnitude of the heat ratio required to achieve optimal performance levels up when larger sizes of discrete sources are used.

5 Numerical Analysis

In this section we numerically simulate the flow and heat transfer in the vicinity of the wall with discrete heat sources for the case of variable freestream velocity. The wall of length L is the bottom side of a convergent channel of varying spacing H_1. The upper side was modeled as an adiabatic wall. The cold fluid is delivered into the channel with an inlet freestream velocity U_∞.

The commercial software, which is based on the finite volume method, was used in the simulation. The solver discretizes the mass, momentum, and energy equations in integrated form. The general form of the transport equation is
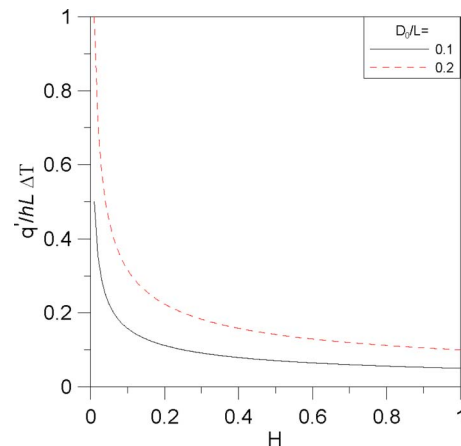
Fig. 10 Heat ratio as a function of the shape factor for various discrete source thicknesses
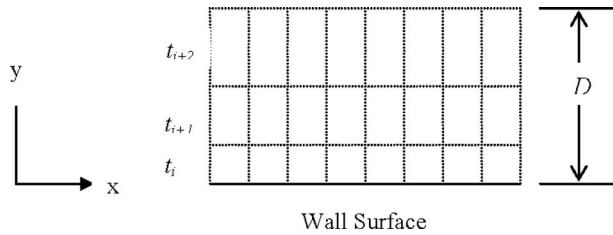
Fig. 11 Boundary layer meshing: (t_i) thickness of the first row and (t_{i+1}) thickness of the following row

$$\int_{\Delta t} \frac{\partial}{\partial t} \left(\int_{CV} \rho \phi dV \right) dt + \int_{\Delta t} \int_A n \cdot (\rho \phi u) dA dt$$

$$= \int_{\Delta t} \int_A n \cdot (\Gamma \text{ grad } \phi) dA dt + \int_{\Delta t} \int_{CV} S_\phi dV dt \quad (33)$$

Equation (33) is used as the starting point for computational procedures in the finite volume method. By setting φ equal to 1, u, v, and T, and selecting appropriate values for diffusion coefficient Γ and source terms, the mass, momentum, and energy equations in integral form are obtained.

The governing equations are transformed into algebraic equations for every cell. The discrete equation for 2D becomes

$$a_P \phi_P = a_w \phi_W + a_e \phi_E + a_s \phi_S + a_n \phi_N + b \quad (34)$$

$$a_P = a_w + a_e + a_s + a_n - b \quad (35)$$

where a stands for the coefficient of the property φ (diffusion and advection) and b is the source term coefficient.

5.1 Grid Test. A good initial grid design relies largely on an insight into the expected properties of the flow such as boundary layer, point of separation, or abrupt variation in a property [15]. The quality of the mesh plays a significant role in the accuracy and stability of the numerical computation. Obviously, the goal of any numerical simulation should be the optimization of both the discretization scheme as well as the grid generation scheme.

One of the most powerful techniques used recently to achieve this task is the *multigrid scheme*. The idea of a multigrid algorithm, which is considered in the present numerical technique, is to accelerate the convergence of a set of fine-grid discrete equations by computing corrections to these equations on a coarser grid, where the computation can be performed more economically. This process is applied recursively to an entire set of coarse-grid levels [16].

Because of the boundary layers in the present study, a nonuniform mesh was used in the y direction, and the smallest elements were placed close to the wall. Figure 11 shows the dimensions of a nonuniform grid. The parameters used were: first row $a = 0.1\delta$; the aspect ratio, the ratio of the two consecutive mesh thicknesses ($t_{i+1}/t_i = 1.2$), and the depth of the boundary layer meshing region (D) > δ. Starting from the wall, the height of the first grid row should be less than the boundary layer thickness to describe the flow in that region more precisely [17,18]. Based on that, an extension in the numerical domain is important to develop the boundary layer region so that at the channel entrance the boundary layer has a certain value and this value is greater than the height of the first grid lines. Hence, mesh independency was achieved when about 115 cells per unit dimension are used.

5.2 Results and Discussion. The working fluid used in the numerical studies was air and the boundary conditions at the inlet and outlet of the computational domain are as follows: the inlet velocity and temperature are 5 m/s and 20°C, respectively; the maximum system temperature is 60°C; and the exit ambient conditions are 1.01 bars and 25°C. The thermal boundary conditions on the heated wall are the uniform heat fluxes over each source and adiabatic over the wall sections located between heat sources.

Three different cases for three shape factors are addressed, namely, 0.25, 0.5, and 1 with $D_0/L = 0.1$, and the target was the temperature variation in the spacing between the consecutive elements. In each case, two software's runs have been performed: one with optimal spacing distribution of discrete heat sources and the other with fixed spacing; hence, the temperature profile of the entire wall can be predicted. It is worth noting here that according to the data used in the numerical simulation, the length of the continuous heat source required for the case ($H = 0.25$) is ($x_0/L \sim 0.32$). This distance is used in both simulations (i.e., fixed and optimal distributions) since our aim is just to present the virtue of using optimal spacing between consecutive elements. (x_0/L) for other cases is listed in Table 1.

Mass flow rate was chosen as the target criteria for investigating the convergence in addition to the residual errors of the transport and energy equations. Convergence was achieved when the difference between the inlet and outlet mass flow rates reaches a certain value; thus, a steady state condition is obtained. The number of iterations required to achieve this task depends on the initial guess, the type of the solver used (i.e., either implicit or explicit solver), and other criteria such as the complexity of the system and the abrupt changes in the flow conditions and properties.

For our examples, the initial guess was the inlet condition, whereas implicit solver was used in order to reach the convergence more rapidly. The residuals of continuity, momentum, and energy equations for the case of optimal distribution when ($H = 0.25$) is illustrated in Fig. 12. Although the residual of the continuity equation, for instance, is barely high, the difference in inlet/outlet mass flow rate is low, as presented in Table 1; thus, convergence occurs after ~43 steps. Table 1 shows the number of steps needed to reach the convergence, based on the mass flow rate, for each case when the optimal spacing is used.

As mentioned earlier, our aim is to prove that the optimal dis-

Table 1 Convergence of numerical simulations

$H = H_2/H_1$	x_0/L	Iteration steps	$\Delta m/m$ (%)
0.25	0.32	43	1.8×10^{-3}
0.5	0.278	56	5×10^{-5}
1	0.25	120	0
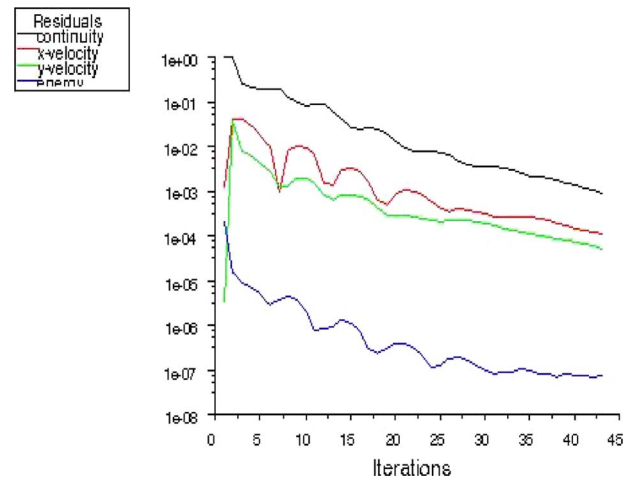
Fig. 12 Residual of transport equations as a function of iteration steps for $H = 0.25$

(a)

(b)

(c)
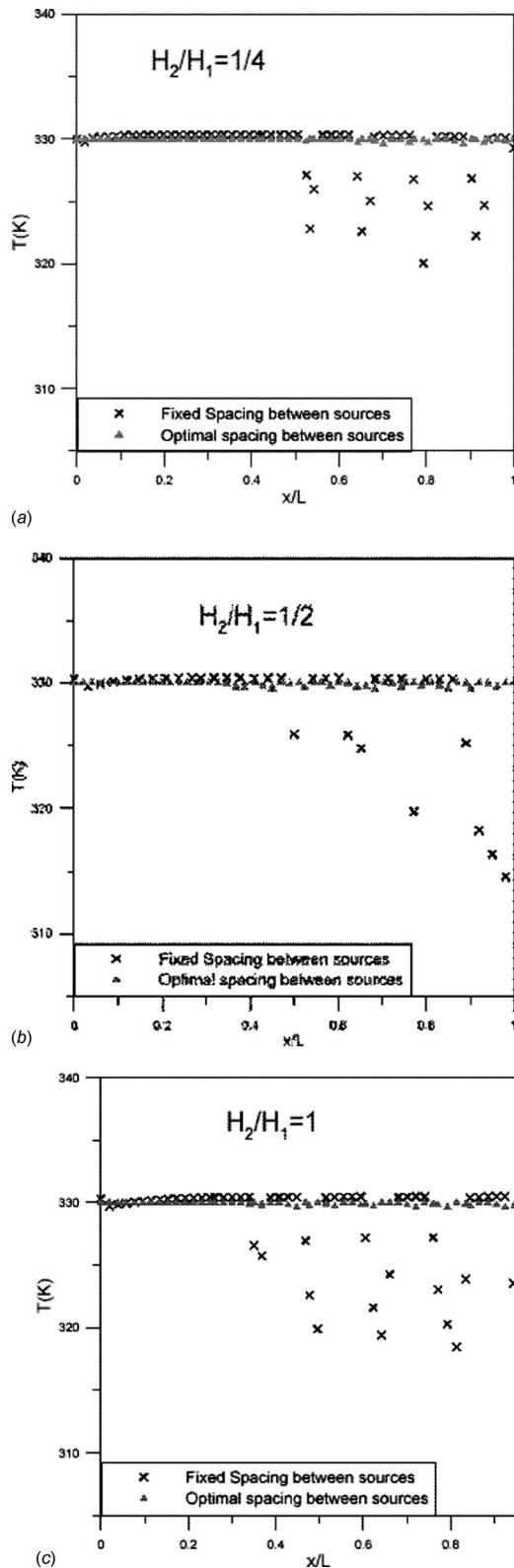
Fig. 13 Temperature distribution along the inside wall surface when (*a*) *H*=0.25, (*b*) *H*=0.5, and (*c*) *H*=1

tribution makes the system work at high performance, i.e., at $T_{\max}$. Figure 13(*a*) illustrates the temperature distribution along the spacing zones in the case when the shape factor is 0.25. The figure clearly proves that using the optimal distribution of the heating element and the spacing between them results in a better wall

temperature profile, which is almost uniform and at maximum value. In contrast, using different distributions leads to nonuniform temperature profile in the spacing zones, forcing the system to work far from its optimal performance. For the other two cases ($H=0.5$ and $H=1$), similar conclusions can be obtained, as shown in Figs. 13(*b*) and 13(*c*).

In summary, by applying the concept of the constructal theory, the thermal system can work more efficiently and close to the maximum possible performance.

6 Summary and Conclusions

The main problem of how to allocate discrete heat sources to the space on a wall of a convergent flow, cooled by forced convection is analyzed in this study. The objective is to optimize the configuration of the heat source distribution, to study the local spacing between the consecutive elements, and to provide model criteria for designing such systems.

The analysis showed that the heat sources should be distributed nonuniformly on the wall, which is in agreement with the previous works. Furthermore, the optimal spacing between heat sources relies not only on the Reynolds number but also on the channel shape factor as well. When the magnitude of the shape factor becomes less than 0.5, the heating elements move closer together near the trailing edge.

The analysis has also concluded that two distinct regions have been identified on the wall with optimally distributed heat sources. The first region is located upstream of a transition point x_0 close to the tip of the boundary layer. In this area, heat sources should be placed close to each other since the spaces between the sources in this area have a magnitude of zero. The second area is mounted downstream of x_0 and is characterized by a nonuniform distribution of heat sources. Finally, the result of the numerical analysis concluded that reducing the accumulated sources right after the leading edge improves the performance of the process by raising the wall temperature up closer to the highest possible value.

Nomenclature

$$A = \text{area, m}^2$$
$$D_h = \text{hydraulic diameter, m}$$
$$D_0 = \text{heat source size, m}$$
$$H = \text{shape factor}$$
$$H_1 = \text{inflow channel height, m}$$
$$H_2 = \text{outflow channel height, m}$$
$$k = \text{thermal conductivity, W m}^{-1}\text{ K}^{-1}$$
$$l = \text{total length occupied by the heated section}$$
$$L = \text{length, m}$$
$$N = \text{number of heat sources}$$
$$N' = \text{number of heat sources per unit length, m}$$
$$N_c = \text{number of heat sources at parallel plates}$$
$$\text{Nu} = \text{Nusselt number}$$
$$\text{Pr} = \text{Prandtl number}$$
$$q' = \text{heat transfer per unit length, W m}^{-1}$$
$$q'' = \text{continuously distributed heat flux, W m}^{-2}$$
$$q_0'' = \text{uniform heat flux over heat sources, W m}^{-2}$$
$$Q' = \text{total heat transfer rate, W m}^{-1}$$
$$S = \text{heat source spacing, m}$$
$$\text{Re} = \text{Reynolds number}$$
$$T = \text{temperature, K}$$
$$U = \text{velocity, m s}^{-1}$$
$$W = \text{channel width, m}$$
$$x, y = \text{Cartesian coordinates, m}$$
$$x_L = \text{entrance boundary layer length, m}$$
$$x_0 = \text{continuously heated region, m}$$

Greek Symbols

$$\varphi = \text{general property}$$
$$\delta = \text{boundary layer thickness, m}$$
$$\theta = \text{convergent angle, deg}$$

ν = kinematic viscosity, $m^2\ s^{-1}$

∞ = freestream subscript

Λ = dimensionless parameter

References

[1] Bejan, A., 2000, *Shape and Structure, From Engineering to Nature*, Cambridge University Press, Cambridge, UK.

[2] Da Silva, A. K., Lorente, S., and Bejan, A., 2004, "Optimal Distribution of Discrete Heat Sources on a Plate With Laminar Forced Convection," Int. J. Heat Mass Transfer, **47**(10–11), pp. 2139–2148.

[3] Da Silva, A. K., 2005, "Constructal Multi-scale Heat Exchangers," Ph.D. thesis, Duke University, Durham, NC.

[4] Incropera, F. P., Kerby, J. S., Moffatt, D. F., and Ramadhyani, S., 1986, "Convection Heat Transfer From Discrete Heat Sources in a Rectangular Channel," Int. J. Heat Mass Transfer, **29**, pp. 1051–1058.

[5] McEntire, A. B., and Webb, B. W., 1990, "Local Forced Convective Heat Transfer From Protruding and Flush-Mounted Two-dimensional Discrete Heat Sources," Int. J. Heat Mass Transfer, **33**, pp. 1521–1533.

[6] Mahaney, H. V., Interopera, F. P., and Ramadhyani, S., 1990, "Comparison of Predicted and Measured Mixed Convection Heat Transfer From an Array of Discrete Sources in a Horizontal Rectangular Channel," Int. J. Heat Mass Transfer, **33**, pp. 1233–1245.

[7] Shaw, H. J., and Chen, W. L., 1991, "Laminar Forced-Convection in a Channel With Arrays of Thermal Sources," Waerme- Stoffuebertrag., **26**, pp. 195–201.

[8] Wang, C. Y., 1992, "Optimum Placement of Heat Sources in Forced-Convection," ASME J. Heat Transfer, **114**, pp. 508–510.

[9] Gupta, A., and Jaluria, Y., 1998, "Forced Convective Liquid Cooling of Arrays of Protruding Heated Elements Mounted in a Rectangular Duct," ASME J. Electron. Packag., **120**, pp. 243–252.

[10] Tso, C. P., Xu, G. P., and Tou, K. W., 1999, "An Experimental Study on Forced Convection Heat Transfer From Flush Mounted Discrete Heat Sources," ASME J. Heat Transfer, **121**, pp. 326–332.

[11] Rahman, M. M., and Raghavan, J., 1999, "Transient Response of Protruding Electronic Modules Exposed to Horizontal Cross Flow," Int. J. Heat Fluid Flow, **20**, pp. 48–59.

[12] Sultan, G. I., 2000, "Enhancing Forced Convection Heat Transfer From Multiple Protruding Heat Sources Simulating Electronics Components in Horizontal Channel by Passive Cooling," Microelectron. J., **31**, pp. 773–779.

[13] Chen, S., Liu, Y., Chan, S. F., Leung, C. W., and Chan, T. L., 2001, "Experimental Study of Optimum Spacing Problem in the Cooling of Simulated Electronics Package," Int. J. Heat Mass Transfer, **37**, pp. 251–257.

[14] Morega, A. M., and Bejan, A., 1994, "Optimal Spacing of Parallel Boards With Discrete Heat Sources Cooled by Laminar Forced Convection," Numer. Heat Transfer, Part A, **25**(4), pp. 373–392.

[15] Versteeg, H. K., and Malalasekera, W., 2007, *An Introduction to Computational Fluid Dynamics*, 2nd ed., Pearson Education Limited, Harlow, Essex, UK.

[16] Jassim, E., Abedinzadegan Abdi, M., and Muzychka, Y., 2008, "Computational Fluid Dynamics Study for Flow of Natural Gas Through High-Pressure Supersonic Nozzles: Part 1. Real Gas Effects and Shockwave," Pet. Sci. Technol., **26**(15), pp. 1757–1772.

[17] White, F. M., 1991, *Viscous Fluid Flow*, 2nd ed., McGraw-Hill, New York.

[18] Schlichting, H., 1968, *Boundary-Layer Theory*, McGraw-Hill, New York.

Three-Dimensional Magnetic Fluid Boundary Layer Flow Over a Linearly Stretching Sheet

E. E. Tzirtzilakis

Assistant Professor
Department of Mechanical Engineering and Water Resources,
Technological Educational Institute of Messolonghi,
30 200 Messolonghi, Greece
e-mail: tzirtzi@iconography.gr

N. G. Kafoussias

Professor
Department of Mathematics,
Section of Applied Analysis,
University of Patras,
26 500 Patras, Greece
e-mail: nikaf@math.upatras.gr

The three-dimensional laminar and steady boundary layer flow of an electrically non-conducting and incompressible magnetic fluid, with low Curie temperature and moderate saturation magnetization, over an elastic stretching sheet, is numerically studied. The fluid is subject to the magnetic field generated by an infinitely long, straight wire, carrying an electric current. The magnetic fluid far from the surface is at rest and at temperature greater of that of the sheet. It is also assumed that the magnetization of the fluid varies with the magnetic field strength H and the temperature T. The numerical solution of the coupled and nonlinear system of ordinary differential equations, resulting after the introduction of appropriate nondimensional variables, with its boundary conditions, describing the problem under consideration, is obtained by an efficient numerical technique based on the common finite difference method. Numerical calculations are carried out for the case of a representative water-based magnetic fluid and for specific values of the dimensionless parameters entering into the problem, and the obtained results are presented graphically for these values of the parameters. The analysis of these results showed that there is an interaction between the motions of the fluid, which are induced by the stretching surface and by the action of the magnetic field, and the flow field is noticeably affected by the variations in the magnetic interaction parameter β. The important results of the present analysis are summarized in Sec. 6.
[DOI: 10.1115/1.3194765]

Keywords: FHD, magnetic fluid, three-dimensional flow, stretching sheet, low Curie temperature, moderate saturation magnetization

1 Introduction

The investigation of the two-dimensional flow problems, caused by a linearly stretching flat surface, in an otherwise quiescent incompressible fluid, has been proved of fundamental importance in recent years due to their applications in a number of mechanical and technological processes, and several authors have studied various aspects of this problem [1–10]. More specifically, the generalized three-dimensional boundary layer flow of a viscous and in an otherwise ambient incompressible viscous fluid, due to a stretching sheet, was also studied by Wang [11], Ariel [12], and Takhar et al. [13].

On the other hand, during the last decades, there is a steady growth in the study and applications of colloidal stable magnetizable fluids. The new scientific advances and the increasing importance of the technological applications of magnetic fluids, and especially of ferromagnetic ones, have led to widely dispersed growing research groups of many nationalities all over the world. The behavior of a ferrofluid, under the action of an applied magnetic field, is of fundamental importance not only in ferrohydrodynamics (FHD) but also in biomagnetic fluid dynamics (BFD) in which blood is investigated as a magnetic fluid. So, an extensive work has been done in this field, and some representative works can be found in Refs. [14–25].

However, it is known that a magnetic fluid, also known as a ferrofluid, is a suspension of ferromagnetic or ferrimagnetic particles in a carrier liquid (water-based or oil-based ferrofluids). In certain applications, such as in energy conversion devices, it is necessary to use a fluid with large pyromagnetic coefficient K, i.e.,

with a high saturation magnetization and a low Curie temperature T_c. So, the above mentioned magnetic particles are unsuitable for this purpose since they have Curie temperatures higher than the boiling point of the carrier liquid. To overcome this difficulty, some investigators [26–32] have synthesized fine particles of different types and obtained water-based magnetic fluids, such as EMG 901, EMG 909, and EMG 805, with large pyromagnetic coefficient K and moderately low curie temperatures T_c.

So, the purpose of the present work is to study the three-dimensional laminar and steady boundary layer flow of an electrically nonconducting and incompressible magnetic fluid, with low Curie temperature and moderate saturation magnetization, over a stretching sheet. The fluid is subject to the magnetic field generated by an infinitely long, straight wire oriented along the x-axis of a Cartesian coordinate system $Oxyz$. The wire carries an electric current I and it is placed parallel to the stretching surface (Oxy-plane) at a distance d below it. The magnetic fluid, far from the surface, is initially at rest and at temperature greater of that of the sheet. This physical problem concerns the FHD flow, but it can also be considered as a BFD flow as long as the conditions referred in Ref. [14] hold. It is also assumed that the magnetization varies with the magnetic field strength H and the temperature T according to the relation

$$M = KH(T_c - T) \tag{1}$$

and this relation is the one derived experimentally in Ref. [25], suggested in Ref. [14], and also used in Ref. [33].

The formulation of the problem is obtained by an analogous manner presented in Refs. [23,24], and the numerical solution is obtained by applying an efficient numerical technique based on the common finite difference method [34,35]. The obtained numerical results for a representative water-based magnetic fluid, with moderate saturation magnetization and low Curie tempera-
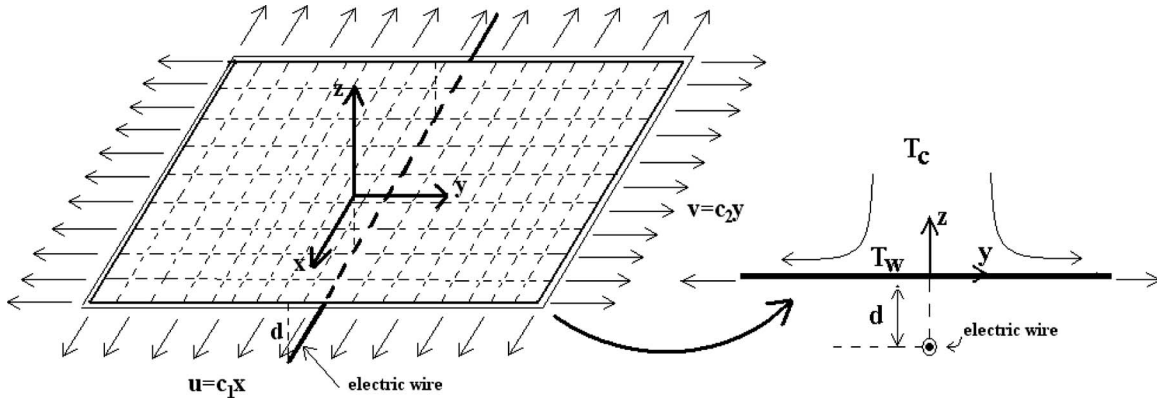
Fig. 1 Schematic representation of flow configuration

ture, are presented graphically for specific values of the parameters entering into the problem under consideration and analyzed in detail.

2 Mathematical Formulation

The steady, three-dimensional, incompressible, laminar boundary layer magnetic fluid flow, induced by the stretching of a highly elastic flat surface in two lateral directions, in an otherwise quiescent fluid is considered. The stretching surface is placed in the plane $z=0$, whereas the fluid occupies the upper half plane $z \geq 0$. The velocities of the stretching surface in the x- and y-directions, respectively, and therefore of the fluid in contact with it, and in a Cartesian coordinate system $Oxyz$, are given by

$$u = c_1 x, \quad v = c_2 y, \quad w = 0 \qquad (2)$$

where c_1 and c_2 are dimensional constants. The fluid temperature, far away from the sheet, is T_c, whereas the stretching surface is kept at a constant temperature T_w, less than T_c. The viscous and electrically nonconducting magnetic fluid is subject to the action of a magnetic field H, which is generated by an electric current with intensity I. The electric current is going through an infinite thin wire placed parallel to the x-axis and at a distance d below it. The electric current in the wire flows from the positive x-axis toward the negative, and a schematic representation of this flow configuration is presented in Fig. 1.

It is also assumed that this electric current in the wire gives rise to a magnetic field of sufficient strength to saturate the magnetic fluid so that the equilibrium magnetization is attained.

Under the above assumptions the equations governing the physical problem under consideration are the mass conservation, fluid momentum in the x-, y-, and z-directions, and energy equation and can be written as [14,15,18,23,24,33]

$$\frac{\partial u}{\partial x} + \frac{\partial v}{\partial y} + \frac{\partial w}{\partial z} = 0 \qquad (3)$$

$$\rho \left(u \frac{\partial u}{\partial x} + w \frac{\partial u}{\partial z} \right) = -\frac{\partial p}{\partial x} + \mu \left(\frac{\partial^2 u}{\partial x^2} + \frac{\partial^2 u}{\partial z^2} \right) \qquad (4)$$

$$\rho \left(v \frac{\partial v}{\partial y} + w \frac{\partial v}{\partial z} \right) = -\frac{\partial p}{\partial y} + \mu \left(\frac{\partial^2 v}{\partial y^2} + \frac{\partial^2 v}{\partial z^2} \right) + \mu_0 M \frac{\partial H}{\partial y} \qquad (5)$$

$$\rho w \frac{\partial w}{\partial z} = -\frac{\partial p}{\partial z} + \mu \frac{\partial^2 w}{\partial z^2} + \mu_0 M \frac{\partial H}{\partial z} \qquad (6)$$

$$\rho c_p \boldsymbol{q} \cdot (\boldsymbol{\nabla} T) + \mu_0 T \frac{\partial M}{\partial T} \left(v \frac{\partial H}{\partial y} + w \frac{\partial H}{\partial z} \right) = k \nabla^2 T + \mu \Phi \qquad (7)$$

In the above equation (7), Φ is the dissipation function, which, in the case under consideration, is given by the expression

$$\Phi = 2 \left[\left(\frac{\partial u}{\partial x} \right)^2 + \left(\frac{\partial v}{\partial y} \right)^2 + \left(\frac{\partial w}{\partial z} \right)^2 \right] + \left[\left(\frac{\partial v}{\partial z} \right)^2 + \left(\frac{\partial u}{\partial z} \right)^2 \right] \qquad (8)$$

The system of Eqs. (3)–(7) is subject to the following boundary conditions:

$$z = 0: \quad u = c_1 x, \quad v = c_2 y, \quad w = 0, \quad T = T_w \qquad (9)$$

$$z \to \infty: \quad u = 0, \quad v = 0, \quad T = T_c, \quad p + \rho \tfrac{1}{2} w^2 = p_\infty = \text{const} \qquad (10)$$

The terms $\mu_0 M (\partial H / \partial y)$ and $\mu_0 M (\partial H / \partial z)$ in Eqs. (5) and (6), respectively, represent the components of the magnetic force, per unit volume of the fluid, and depend on the existence of the magnetic gradient. When the magnetic gradient is absent these forces vanish. The second term, on the left-hand side of the energy equation (6), accounts for heating due to the adiabatic magnetization.

The components H_y, H_z of the magnetic field $\boldsymbol{H} = (H_y, H_z)$, due to the electric current flowing through the wire with intensity I, are given by

$$H_y(y,z) = -\frac{I}{2\pi} \frac{z+d}{y^2 + (z+d)^2} \qquad (11)$$

$$H_z(y,z) = \frac{I}{2\pi} \frac{y}{y^2 + (z+d)^2} \qquad (12)$$

Therefore, the magnitude $\|\boldsymbol{H}\| = H$, of the magnetic field, is given by

$$H(x,y,z) \equiv H(y,z) = [H_y^2 + H_z^2]^{1/2} = \frac{I}{2\pi} \frac{1}{\sqrt{y^2 + (z+d)^2}} \qquad (13)$$

It is reminded, once more, that when the applied magnetic field $\boldsymbol{H}$ is sufficiently strong to saturate the magnetic fluid, the magnetization M is, generally, determined by the fluid temperature T and the magnetic field strength H and, in the problem under consideration, it is expressed by relation (1), i.e., $M = KH(T_c - T)$.

3 Transformation of Equations

The mathematical analysis of the problem under study is simplified by introducing the following dimensionless coordinates:

$$\xi(x) = \left(\frac{c}{\nu} \right)^{1/2} x, \quad \zeta(y) = \left(\frac{c}{\nu} \right)^{1/2} y, \quad \eta(z) = \left(\frac{c}{\nu} \right)^{1/2} z \qquad (14)$$

where $c = (c_1 + c_2)/2$.

In addition, the corresponding velocity components of the fluid, defined by the expressions

$$u(\xi,\eta) = \sqrt{c\nu}\,\xi f'(\eta), \quad \upsilon(\zeta,\eta) = \sqrt{c\nu}\,\zeta g'(\eta),$$

$$w(\eta) = -\sqrt{c\nu}\,[f(\eta) + g(\eta)] \tag{15}$$

where $(\ )' = \partial(\ )/\partial\eta$ satisfy the continuity equation (3).

Finally, the dimensionless pressure (magnetic and static) $P(\xi,\zeta,\eta)$ and temperature $\Theta(\xi,\zeta,\eta)$ of the magnetic fluid are given by the following expressions:

$$P(\xi,\zeta,\eta) = \frac{p}{c\mu} = P_1(\eta) + \xi P_2(\eta) + \xi^2 P_3(\eta) + \zeta P_4(\eta) + \zeta^2 P_5(\eta)$$

$$+ \xi\zeta P_6(\eta) \tag{16}$$

$$\Theta(\xi,\zeta,\eta) = \frac{T_c - T}{T_c - T_w} = \Theta_1(\eta) + \xi\Theta_2(\eta) + \xi^2\Theta_3(\eta) + \zeta\Theta_4(\eta)$$

$$+ \zeta^2\Theta_5(\eta) + \xi\zeta\Theta_6(\eta) \tag{17}$$

As far as the magnetic field is concerned, the magnitude H of the magnetic field strength is given by the expression

$$H(\zeta,\eta) = \frac{I}{2\pi}\sqrt{\frac{c}{\nu}}\frac{1}{\sqrt{\zeta^2 + (\eta + \alpha)^2}} \tag{18}$$

where α is the dimensionless distance of the electric wire from the ξ-axis $(\alpha = d\sqrt{c/\nu})$.

For the calculation of the partial derivatives of the above expression, with respect to ζ and η, a similar procedure to that first used in Refs. [23,24] is followed. First, Eq. (18) is expanded in powers of ζ up to terms of the order of ζ^2. Hereafter, the corresponding derivatives are calculated by partial differentiation of the resulting expansion already mentioned. So, the partial derivatives of the magnetic field, with respect to ζ and η, are given by the following expressions:

$$\frac{\partial H}{\partial\zeta} = -\frac{c}{\nu}\frac{I}{2\pi}\frac{\zeta}{(\eta + \alpha)^3} \tag{19}$$

$$\frac{\partial H}{\partial\eta} = -\frac{c}{\nu}\frac{I}{2\pi}\frac{1}{(\eta + \alpha)^2}\left[1 - \frac{3}{2}\frac{\zeta^2}{(\eta + \alpha)^2}\right] \tag{20}$$

By substituting Eq. (1) and all the above expressions (14)–(20) into the momentum equations (4)–(6), and into the energy equation (7), and following standard procedure, the problem under consideration is finally described by the following system of ordinary differential equations:

$$f''' + (f + g)f'' - (f')^2 - 2P_3 = 0 \tag{21}$$

$$g'' + (f + g)g'' - (g')^2 - 2P_5 - \frac{\beta\Theta_1}{(\alpha + \eta)^4} = 0 \tag{22}$$

$$P_1' + f'' + g'' + (f + g)(f' + g') + \frac{\beta\Theta_1}{(\alpha + \eta)^3} = 0 \tag{23}$$

$$P_3' + \frac{\beta\Theta_3}{(\alpha + \eta)^3} = 0 \tag{24}$$

$$P_5' - \frac{2\beta\Theta_1}{(\alpha + \eta)^5} + \frac{\beta\Theta_5}{(\alpha + \eta)^3} = 0 \tag{25}$$

$$\Theta_1'' + \Pr(f + g)\Theta_1' + \frac{\lambda\beta(\Theta_1 - \varepsilon)}{(\alpha + \eta)^3}(f + g) + 2(\Theta_3 + \Theta_5) - 4\lambda[(f')^2$$

$$+ (g')^2 + f'g'] = 0 \tag{26}$$

$$\Theta_3'' + \Pr(f + g)\Theta_3' + \left[\lambda\beta\frac{f + g}{(\alpha + \eta)^3} - 2\Pr f'\right]\Theta_3 - \lambda(f'')^2 = 0 \tag{27}$$

$$\Theta_5'' + \Pr(f + g)\Theta_5' + \left[\lambda\beta\frac{f + g}{(\alpha + \eta)^3} - 2\Pr g'\right]\Theta_5 + \beta\lambda(\varepsilon - \Theta_1)$$

$$\times\left[\frac{2(f + g)}{(\alpha + \eta)^5} + \frac{g'}{(\alpha + \eta)^4}\right] = 0 \tag{28}$$

subject to the boundary conditions

$$\eta = 0: \quad f' = \delta_1, \quad g' = \delta_2, \quad f = g = 0, \quad \Theta_1 = 1, \quad \Theta_3 = \Theta_5 = 0 \tag{29}$$

$$\eta \to \infty: \quad f' = g' = 0, \quad P_1 \to P_\infty, \quad P_3 = P_5 = 0,$$

$$\Theta_1 = \Theta_3 = \Theta_5 = 0 \tag{30}$$

The dimensionless parameters appearing in these equations are defined as follows:

$$\Pr = \mu c_p/k \quad \text{(Prandtl number)}$$

$$\lambda = \frac{c\mu^2}{\rho k(T_c - T_w)} \quad \text{(viscous dissipation parameter)}$$

$$\varepsilon = T_c/(T_c - T_w) \quad \text{(dimensionless temperature parameter)}$$

$$\alpha = (c\rho/\mu)^{1/2}d \quad \text{(dimensionless distance)}$$

$$\beta = \frac{I^2}{4\pi^2}\frac{K\mu_o(T_c - T_w)\rho}{\mu^2} \quad \text{(dimensionless magnetic}$$

$$\text{interaction parameter)} \tag{31}$$

and the quantities δ_1 and δ_2 are also defined as

$$\delta_1 = c_1/c \quad \text{and} \quad \delta_2 = c_2/c \quad \text{where} \quad c = (c_1 + c_2)/2 \tag{32}$$

For equal speeds of stretching in the ξ- and ζ-directions, it is $c_1 = c_2 = c$ and therefore the corresponding boundary conditions for the functions f' and g' become $f'(0) = \delta_1 = 1$ and $g'(0) = \delta_2 = 1$. It is worth noting, however, that other cases could also be considered for these boundary conditions. For instance, when $c_1 = 0$ and $c_2 = 2c$ there is stretching only toward the ζ-direction (two-dimensional flow) and the corresponding boundary conditions become $f'(0) = \delta_1 = 0$ and $g'(0) = \delta_2 = 2$. However, in the problem under consideration, and due to the lack of space, only the most representative case $c_1 = c_2 = c$ is examined.

The system of Eqs. (21)–(28), subject to the boundary conditions (29) and (30), is a five-parameter $(\alpha, \beta, \lambda, \varepsilon, \Pr)$ coupled and nonlinear system of ordinary differential equations, describing the magnetic fluid flow over the stretching sheet when the magnetization of the fluid is given as a function of temperature T and magnetic field strength H.

4 Numerical Solution Method

For the numerical solution of the system of ordinary differential equations, of the problem under consideration, and for specific values of the dimensionless parameters appearing in it, a numerical technique is applied with the following characteristics. It is based on the common finite difference method with central differencing, a tridiagonal matrix manipulation, and an iterative procedure. The whole numerical scheme can be programed and applied easily, is stable, accurate, and rapidly converging. This solution methodology, for a system of three equations, is described in detail in Refs. [34,35]. It has also been extended, applied, and validated in Refs. [24,33].

In order to obtain and present numerical results, for the problem under consideration, and analyze them, the following assumptions are made for the magnetic fluid and the values of the dimensionless parameters, entering into the problem and defined in Eq. (31).

(a) The magnetic fluid is similar to that used in Ref. [32] (a water-based magnetic fluid Ferrotec™ EMG 805, 300 G,

with density $\rho = 1180$ kg/m^3, kinematical viscosity $\nu = 1.69 \times 10^{-6}$ m^2/s, coefficient of thermal diffusivity $a = 0.119 \times 10^{-6}$ m^2/s, and saturation magnetization $M_s = 15.61 \times 10^3$ A/m), but with low Curie temperature and moderate saturation magnetization. The Prandtl number of this fluid is equal to Pr=14.20.

(b) The temperature T_w of the stretching sheet is taken equal to 280 K, whereas the fluid temperature far away from the sheet is taken equal to $T_c = 340$ K. In such a case the dimensionless temperature parameter ε is equal to $\varepsilon = 5.667$.

(c) The dimensional constants c_1 and c_2 express the rate of stretching of the elastic sheet, per unit length, along the x- and y-axes, respectively. For equal speeds of stretching in x- and y-directions (or in ξ- and ζ-directions) it is taken as $c_1 = c_2 = c = 1$ and in such a case, the boundary conditions for the functions f' and g' become $f'(0) = \delta_1 = 1$ and $g'(0) = \delta_2 = 1$.

(d) The infinitely long and straight current carrying wire is placed at a distance $d = 0.01$ m below the x-axis and parallel to it. In such a case, the dimensionless distance a, defined by the relation $\alpha = (c/\nu)^{1/2}d$, is equal to $a = 7.69$.

(e) According to its definition and to the physical properties of the fluid under consideration, the viscous dissipation parameter λ is equal to $\lambda = 9.5234 \times 10^{-11}$.

(f) Finally, the dimensionless magnetic interaction parameter β, defined as $\beta = (I^2/4\pi^2)K\mu_o(T_c - T_w)\rho/\mu^2$, can also be defined as $\beta = M_s B_s a^2/c\mu$, where $M_s = H(0,0)K(T_c - T_w)$, $B_s = \mu_0 H(0,0)$, and $H(0,0)$ is the value of the magnetic field strength for $\zeta = \eta = 0$, that is, $H(0,0) = (I/2\pi) \cdot 1/d$.

According to the assumptions made for the properties of the magnetic fluid and the flow configuration, a plausible value for the dimensionless magnetic interaction parameter β that saturates the fluid is $\beta = 1.5 \times 10^5$. It is worth reminding here that the case $\beta = 0.0$ corresponds to the hydrodynamic flow.

For these values of the dimensionless parameters, entering into the problem under consideration, the obtained numerical results, concerning the dimensionless velocity field, temperature field, pressure, skin friction, and rate of heat transfer coefficients, are shown in Figs. 2–10 and analyzed in Sec. 5.

5 Analysis of the Results

The velocity components of the fluid, along the axes x, y, and z, respectively, are defined by expressions (15):

$$u(\xi, \eta) = \sqrt{c\nu}\xi f'(\eta), \quad \upsilon(\zeta, \eta) = \sqrt{c\nu}\zeta g'(\eta),$$

$$w(\eta) = -\sqrt{c\nu}[f(\eta) + g(\eta)]$$

It is clear that for a specific vertical plane, parallel, for instance, to the Oyz, e.g., $x = $const or $\xi = $const, the u-velocity component is a function only of the dimensionless variable $\eta = \eta(z)$. The same is true for the υ-velocity component, whereas the w-velocity component is a function only of the dimensionless variable η. So, the variations in the dimensionless velocity components

$$f'(\eta) = u(\xi, \eta)/\sqrt{c\nu}\xi, \quad g'(\eta) = \upsilon(\zeta, \eta)/\sqrt{c\nu}\zeta$$

$$\text{and} \quad -[f(\eta) + g(\eta)] = w(\eta)/\sqrt{c\nu} \quad (33)$$

against the dimensionless distance η from the surface of the stretching sheet are shown in Figs. 2–4, respectively. It is observed that inside the boundary layer over the stretching sheet, the velocity components $f'(\eta)$ and $g'(\eta)$ present the classical behavior of the velocity field taking their limiting value of zero far away from the stretching surface (Figs. 2 and 3). It is worth noting, however, that when the fluid is saturated by the applied magnetic field ($\beta \neq 0.0$) and inside the boundary layer ($0 < \eta < \eta_\infty = 6.0$), the velocity component $f'(\eta)$ is greater than the corresponding
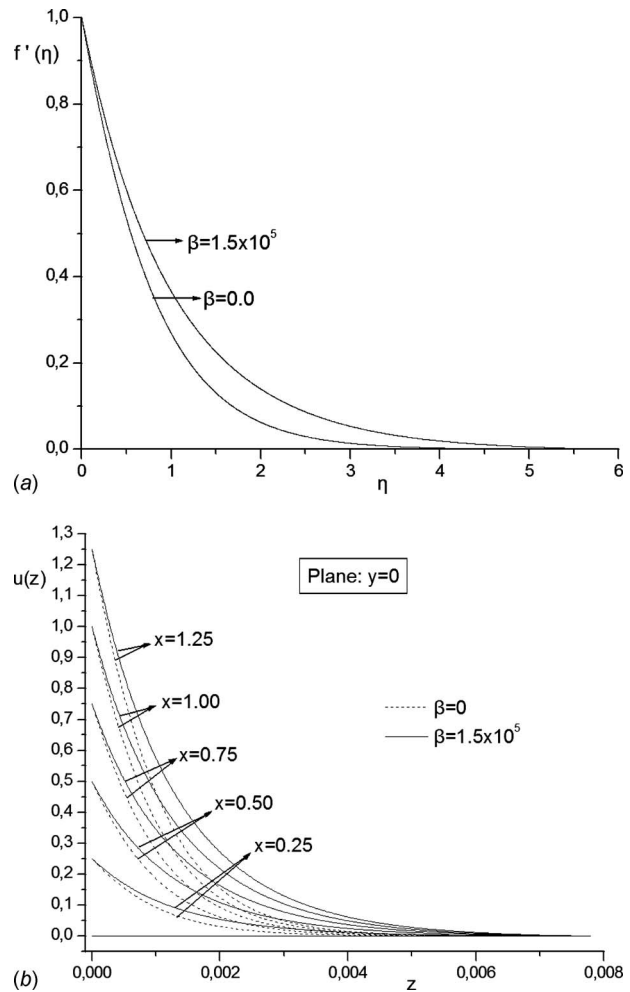
Fig. 2 (a) Dimensionless velocity component $f'(\eta)$ and (b) dimensional velocity component $u(z)$ at the plane $y=0$ and for different positions of x

one in hydrodynamics case (Fig. 2). However, the opposite is true for the velocity component $g'(\eta)$ (Fig. 3). This fact is due to the influence of the Kelvin force on the flow field in the y- and z-directions. This influence is also evident in Fig. 4, which presents the variations in the dimensionless velocity component in the z-direction. In the ferromagnetic case ($\beta \neq 0.0$) the components of magnetic force per unit volume act in the negative y-direction and in the positive z-direction, respectively, and oppose to the fluid motion that comes as a result of the stretching of the elastic surface. So, there is an interaction between the motions of the fluid that are induced by the stretching surface and by the action of the magnetic field. It is worth noting that in the ferromagnetic case and very close to the elastic sheet ($\eta \cong 0.5$) the velocity component in the y-direction ($g'(\eta)$) takes negative values, which means that in that region the flow is reversed. Quantitatively, when $\eta = 1.0$, for instance, and β increases from 0.0 to 1.5×10^5, the percentage changes (decrements) of the dimensionless velocity components $g'(\eta)$ (Fig. 3) and $-[f(\eta) + g(\eta)]$ (Fig. 4) are 138.75% and 42.8%, respectively.

The interaction between the motions of the fluid that are induced by the stretching surface and by the action of the magnetic field is also shown in Figs. 2(b) and 3(b). These figures present the variations in the dimensional velocity components $u(z)$ and $\upsilon(z)$ against z at different distances along the x- and y-axes, respectively. It is concluded that near the surface the magnetic field interacts with the fluid motion that comes as a result of the stretch-
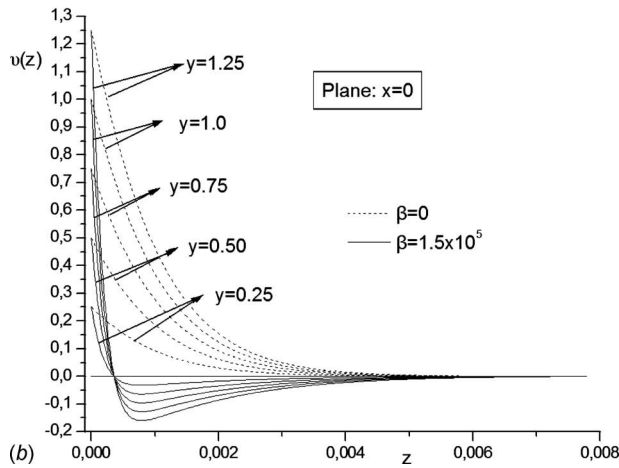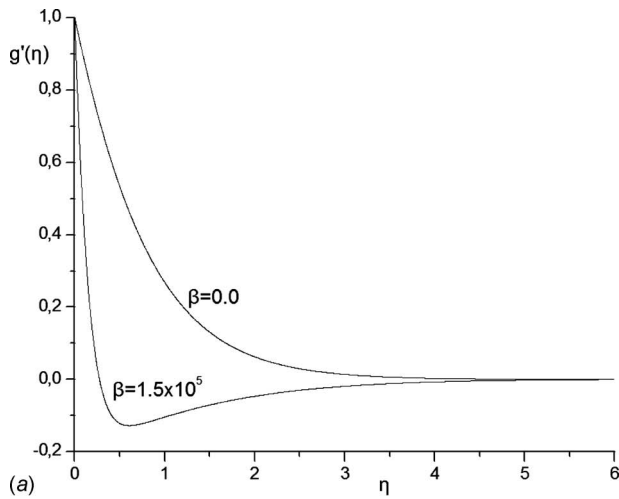
Fig. 3 (*a*) Dimensionless velocity component $g'(\eta)$ and (*b*) dimensional velocity component $\upsilon(z)$ at the plane $x=0$ and for different positions of y

ing of the elastic surface. This interaction increases the $u(z)$ velocity component but decreases the $\upsilon(z)$ velocity component. This different influence of the magnetic field on the velocity components u and υ is due to the orientation of the infinite electrical wire that is placed parallel to the x-axis.
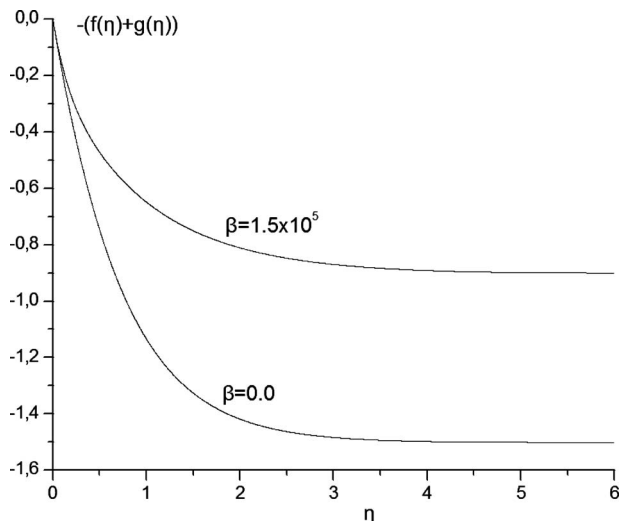
Fig. 4 Dimensionless velocity component $-[f(\eta)+g(\eta)]$
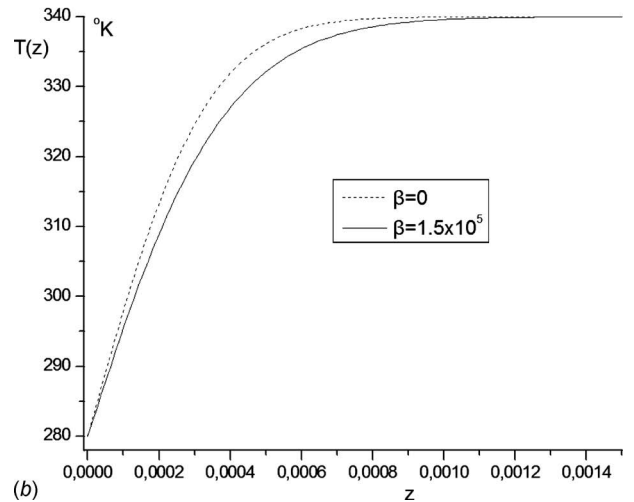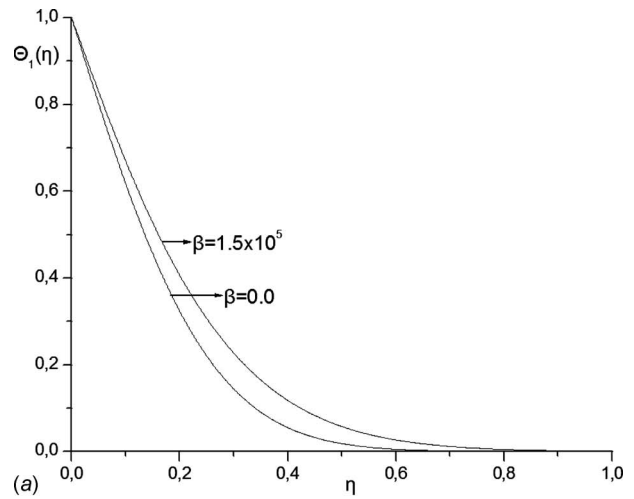
Fig. 5 (*a*) Dimensionless fluid temperature $\Theta_1(\eta)$ and (*b*) dimensional fluid temperature $T(z)$

The numerical analysis and the obtained numerical results showed that the dimensionless temperature $\Theta(\xi,\zeta,\eta)$ of the fluid is represented only by the dimensionless temperature $\Theta_1(\eta)$, e.g., $\Theta_i=0$, for $i=2,\ldots,5$. So, the dimensional temperature T can be expressed, according to Eq. (17), as
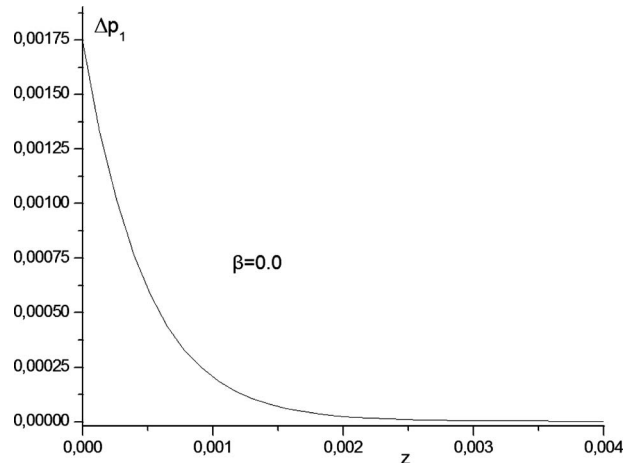
Fig. 6 Dimensional fluid pressure difference Δp_1 in the hydrodynamic case
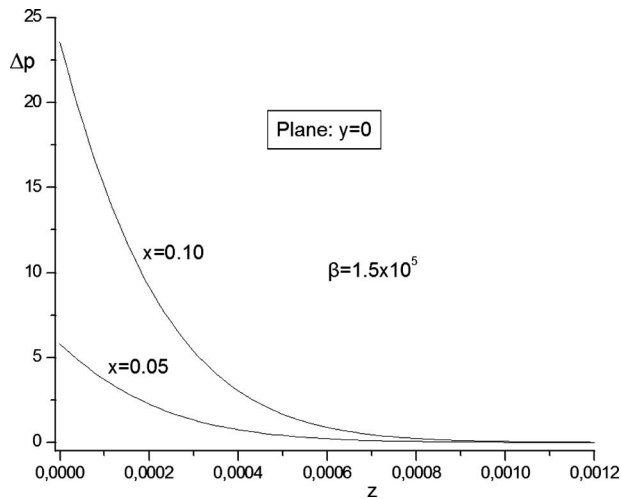
Fig. 7 Dimensional fluid pressure difference Δp in the ferromagnetic case at the plane $y=0$ and for different positions of x

Fig. 9 Dimensionless skin friction coefficient $g''(0)$

$$T(z) = T_c - (T_c - T_w)\Theta_1(\eta(z)) \tag{34}$$

Figure 5 shows the variations in the dimensionless temperature $\Theta_1(\eta)$ in the hydrodynamic case ($\beta=0.0$) as well as in the ferromagnetic one ($\beta=1.5\times10^5$). From this figure it is concluded that the thermal boundary layer thickness $\delta_{th}(\delta_{th}\sim0.8)$ is much smaller than the corresponding viscous boundary layer thickness $\delta_{vis}(\delta_{vis}\sim5.0$, and this is in agreement with the relation that compares these thicknesses with Prandtl number $Pr(\sqrt{Pr}\sim\delta_{vis}/\delta_{th})$. It is also concluded, from this figure, that the dimensionless temperature $\Theta_1(\eta)$ is greater in the ferromagnetic case than the corresponding one in the hydrodynamic case. However, this increment is not important since, for instance, for $\eta=0.2$, the percentage increment is only 1.2%. However, for the dimensional temperature $T(z)$ the opposite is true. The variation in the dimensional temperature $T(z)$ against the normal distance z, from the elastic surface, for $\beta=0$ (hydrodynamic case) and for $\beta=1.5\times10^5$ (ferromagnetic case) is shown in Fig. 5(b). It is concluded, from this figure, that the fluid temperature inside the thermal boundary layer is greater in the hydrodynamic case than that in the ferromagnetic one. So, the contribution, in the increase in fluid temperature, of the second term, on the left-hand side of the energy equation (6), which accounts for heating due to the adiabatic

magnetization, cannot counterbalance the decrement of temperature due to the variation in the velocity field in the ferromagnetic case. This was also verified by additional numerical calculations in which the contribution of this term was found to be not important.

The numerical analysis also showed that the dimensionless pressure $P(\xi,\zeta,\eta)$ is represented only by the function $P_1(\eta)$ in the hydrodynamic case and by the functions $P_1(\eta)$ and $P_3(\eta)$ in the ferromagnetic one. So, according to Eq. (16), the dimensional pressure difference $\Delta p=p-p_\infty$ is expressed as

$$\Delta p_1(z) = p(z) - p_\infty = c\mu P_1(\eta(z)) \tag{35}$$

in the hydrodynamic case and as

$$\Delta p(x,z) = p(x,z) - p_\infty = c\mu\left\{P_1(\eta(z)) + \frac{c}{\nu}x^2 P_3(\eta(z))\right\} \tag{36}$$

in the ferromagnetic one.

The variations in these functions are presented in Figs. 6 and 7, respectively. It is concluded that in the hydrodynamic case as well as in the ferromagnetic one, the dimensional pressure differences decrease to zero (or $p\to p_\infty$) as the distance from the stretching surface approaches infinity.

It is worth reminding here that in the ferromagnetic case by the term "pressure" the sum of the static and magnetic pressure of the

Fig. 8 Dimensionless skin friction coefficient $f''(0)$
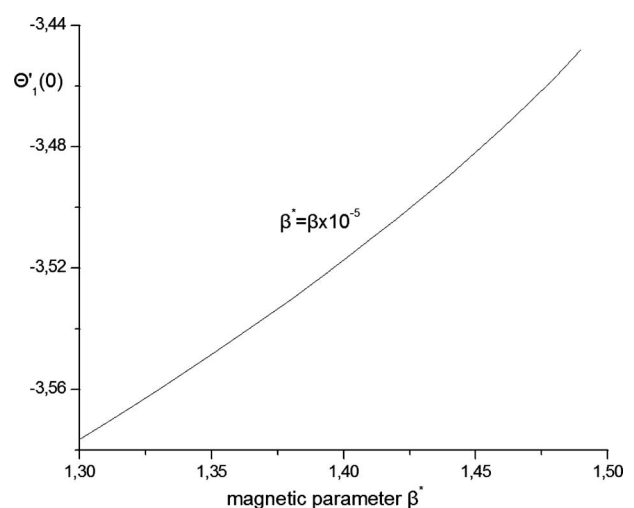
Fig. 10 Dimensionless wall heat transfer coefficient $\Theta_1'(0)$

011702-6 / Vol. 132, JANUARY 2010

Transactions of the ASME

fluid is insinuated. In such a case the magnetic pressure represents the energy density (internal energy per unit volume of the fluid) associated with the induced magnetic field by the electric current of the wire. Isolation of the static or magnetic pressure is not an easy task and requires modification of the initial governing equations of the mathematical model of FHD.

For the physical problem under study the shearing stresses and the rate of heat transfer, at the stretching elastic surface, are defined as follows:

$$(\tau_{zx})_w = \mu\left(\frac{\partial w}{\partial x} + \frac{\partial u}{\partial z}\right)_{z=0}, \quad (\tau_{zy})_w = \mu\left(\frac{\partial w}{\partial y} + \frac{\partial \nu}{\partial z}\right)_{z=0} \quad (37)$$

for the shearing stresses in the x- and y-directions, respectively, and

$$\dot{q}_w = -k\left(\frac{\partial T}{\partial z}\right)_{z=0} \quad (38)$$

for the rate of heat transfer at the sheet.

Using transformations (14), (15), and (17) the corresponding dimensionless quantities C_{f_ξ}, C_{f_ζ}, and Nu can be written as

$$C_{f_\xi} = f''(0) = \frac{(\tau_{zx})_w}{\mu c \xi}, \quad C_{f_\zeta} = g''(0) = \frac{(\tau_{zy})_w}{\mu c \zeta},$$

$$\text{Nu} = \Theta_1'(0) = \frac{\dot{q}_w}{k(T_c - T_w)\sqrt{c/\nu}} \quad (39)$$

The corresponding dimensional quantities can also be written as

$$(\tau_{zx})_w = \mu c \xi \cdot f''(0), \quad (\tau_{zy})_w = \mu c \zeta \cdot g''(0)$$

$$\text{and} \quad \dot{q}_w = k(T_c - T_w)\sqrt{c/\nu} \cdot \Theta_1'(0) \quad (40)$$

It was stated earlier that according to the assumptions made for the properties of the magnetic fluid and the flow configuration, a plausible value for the dimensionless magnetic interaction parameter β that saturates the fluid is $\beta = 1.5 \times 10^5$. It is worth examining, however, the behavior of the above mentioned dimensionless quantities $f''(0)$, $g''(0)$, and $\Theta_1'(0)$ supposing that the value of the magnetic interaction parameter β that saturates the magnetic fluid under consideration can vary from 1.3×10^5 to 1.5×10^5.

So, Fig. 8 shows the variation in the dimensionless skin friction coefficient $C_{f_\xi} = f''(0)$ against the magnetic interaction parameter β ($\beta^* = \beta \times 10^{-5}$). It is observed from this figure that $f''(0)$ increases as β increases, and this is in agreement with the variation in the velocity profile presented in Fig. 2. On the contrary, as it was expected from the analysis of the velocity field, the skin friction coefficient $g''(0)$ decreases with the magnetic interaction parameter β (Fig. 9). Finally, from Fig. 10, it is concluded that the amount of heat, per unit area and time $\dot{q}_w$ (or the dimensionless wall heat transfer parameter $\Theta_1'(0)$), flowing from the magnetic fluid to the elastic surface, that is, in the negative z-direction, decreases as the magnetic interaction parameter increases. This conclusion is in agreement with the results obtained from Fig. 5(b), showing the variation in the dimensional temperature $T(z)$ against the normal distance z from the elastic surface.

6 Conclusions

In the ferromagnetic case the velocity component $f'(\eta)$ is greater than the corresponding one in the hydrodynamic case. The opposite is true for the velocity component $g'(\eta)$. This fact is due to the influence of the Kelvin force on the flow field that is produced by the interaction between the motion of the fluid, which is induced by the stretching surface, and by the action of the magnetic field.

In the ferromagnetic case and very close to the elastic sheet, the velocity component in the y-direction takes negative values, which means that in that region the flow is reversed. The numerical analysis and the obtained numerical results showed that the

dimensionless temperature $\Theta(\xi, \zeta, \eta)$ of the fluid is represented only by the dimensionless temperature $\Theta_1(\eta)$, and the dimensional temperature of the fluid is greater in the hydrodynamic case than the corresponding one in the ferromagnetic case. On the other hand, the dimensionless pressure $P(\xi, \zeta, \eta)$ is represented only by the function $P_1(\eta)$ in the hydrodynamic case and by the functions $P_1(\eta)$ and $P_3(\eta)$ in the ferromagnetic one. Finally, the magnetostatic pressure inside the boundary layer and the shearing stresses and the rate of heat transfer, on the stretching elastic surface, are noticeably affected by the variations in the magnetic interaction parameter β.

Nomenclature

a = thermal diffusivity, $m^2 \, s^{-1}$
α = dimensionless distance
B = magnetic induction, Wb/m^2
B_s = saturation magnetic induction, Wb/m^2
c_1, c_2, c = dimensional constants, s^{-1}
c_p = specific heat at constant pressure, $J \, kg^{-1} \, K^{-1}$
d = distance of the wire from the x-axis, m
∇ = $(\partial/\partial x, \partial/\partial y, \partial/\partial z)$
∇^2 = $(\partial^2/\partial x^2 + \partial^2/\partial y^2 + \partial^2/\partial z^2)$ (Laplacian operator)
f', g' = dimensionless velocity components in the x- and y-directions
H = magnetic field intensity, $A \, m^{-1}$
I = electric current intensity, A
K = pyromagnetic coefficient, K^{-1}
k = thermal conductivity, $J \, s^{-1} \, m^{-1} \, K^{-1}$
M = fluid magnetization, $A \, m^{-1}$
M_s = saturation magnetization, $A \, m^{-1}$
P = dimensionless (magnetic and static) pressure
$P_\infty = p_\infty/c\mu$ = dimensionless pressure far away from the sheet
Pr = Prandtl number
p = fluid pressure (magnetic and static), $N \, m^{-2}$
p_∞ = fluid pressure far away from the sheet, $N \, m^{-2}$
q = (u, v, w), velocity field
T = fluid temperature, K
T_c = Curie temperature (fluid temperature far away from the sheet), K
T_w = stretching sheet temperature, K
x, y, z = Cartesian coordinates, m
u, v, w = velocity components in the x, y, z-direction, $m \, s^{-1}$

Greek

β = dimensionless magnetic interaction parameter
δ_1, δ_2 = dimensionless constants
ε = dimensionless temperature parameter
ξ, ζ, η = dimensionless coordinates
Θ = dimensionless temperature
λ = viscous dissipation parameter (dimensionless)
μ = dynamic viscosity, $kg \, m^{-1} \, s^{-1}$
μ_0 = magnetic fluid permeability, $N \, A^{-2}$
ν = kinematical viscosity, $m^2 \, s^{-1}$
π = $3.14159\cdots$
ρ = fluid density, $kg \, m^{-3}$
Φ = dissipation function, s^{-2}

References

[1] Crane, L. J., 1970, "Flow Past a Stretching Plate," Z. Angew. Math. Phys., **21**, pp. 645–647.
[2] Gupta, P. S., and Gupta, A. S., 1977, "Heat and Mass Transfer on a Stretching Sheet With Suction and Blowing," Can. J. Chem. Eng., **55**, pp. 744–746.
[3] Chakrabarti, A., and Gupta, A. S., 1979, "Hydromagnetic Flow, Heat and Mass Transfer Over a Stretching Sheet," Q. Appl. Math., **33**, pp. 73–78.
[4] Carragher, P., and Crance, L. J., 1982, "Heat Transfer on a Continuous Stretching Sheet," Z. Angew. Math. Mech., **62**, pp. 564–565.
[5] Dutta, B. K., Roy, P., and Gupta, A. S., 1985, "Temperature Field in Flow

Over a Stretching Sheet With Uniform Heat Flux," Int. Commun. Heat Mass Transfer, **12**, pp. 89–94.

[6] Jeng, D. R., Chang, T. C. A., and DeWitt, K. J., 1986, "Momentum and Heat Transfer on a Continuous Moving Surface," ASME J. Heat Transfer, **108**, pp. 532–539.

[7] Dutta, B. K., 1989, "Heat Transfer From a Stretching Sheet With Uniform Suction and Blowing," Acta Mech., **78**, pp. 255–262.

[8] Andersson, H. I., 1995, "An Exact Solution of the Navier-Stokes Equations for MHD Flow," Acta Mech., **113**, pp. 241–244.

[9] Chiam, T. C., 1996, "Heat Transfer With Variable Conductivity in a Stagnation-Point Flow Towards a Stretching Sheet," Int. Commun. Heat Mass Transfer, **23**, pp. 239–248.

[10] Vajravelu, K. A., and Hadjinicolaou, A., 1997, "Convective Heat Transfer in an Electrically Conducting Fluid at Stretching Surface With Uniform Free Stream," Int. J. Eng. Sci., **35**, pp. 1237–1244.

[11] Wang, C. Y., 1984, "The Three-Dimensional Flow Due to a Stretching Flat Surface," Phys. Fluids, **27**, pp. 1915–1917.

[12] Ariel, P. D., 2003, "Generalized Three-Dimensional Flow Due to a Stretching Sheet," Z. Angew. Math. Mech., **83**, pp. 844–852.

[13] Takhar, H. S., Chamka, A. J., and Nath, G., 2001, "Unsteady Three-Dimensional MHD—Boundary-Layer Flow Due to the Impulsive Motion of a Stretching Surface," Acta Mech., **146**, pp. 59–71.

[14] Tzirtzilakis, E. E., 2005, "A Mathematical Model for Blood Flow in Magnetic Field," Phys. Fluids, **17**, p. 077103.

[15] Neuringer, J. L., and Rosensweig, R. E., 1964, "Ferro Hydrodynamics," Phys. Fluids, **7**, pp. 1927–1937.

[16] Neuringer, J. L., 1966, "Some Viscous Flows of a Saturated Ferro Fluid Under the Combined Influence of Thermal and Magnetic Field Gradients," Int. J. Non-Linear Mech., **1**, pp. 123–127.

[17] Bailey, R. L., 1983, "Lesser Known Applications of Ferro Fluids," J. Magn. Magn. Mater., **39**, pp. 178–182.

[18] Rosensweig, R. E., 1985, *Ferro Hydrodynamics*, Cambridge University Press, Cambridge, MA.

[19] Rosensweig, R. E., 1987, "Magnetic Fluids," Annu. Rev. Fluid Mech., **19**, pp. 437–463.

[20] Arrot, A. S., Heinrich, B., and Templeton, T. L., 1989, "Phenomenology of Ferromagnetism: I. Effects of Magnetostatics on Susceptibility," IEEE Trans. Magn., **25**(6), pp. 4364–4373.

[21] Eringen, A. C., and Maugin, G. A., 1990, *Electrodynamics of Continua II: Fluids and Complex Media*, Springer, New York.

[22] Li, X. L., Yao, K. L., and Liu, Z. L., 2007, "Numerical Study on the Magnetic Fluid Flow in a Channel Surrounding a Permanent Magnet Under Temperature

Field," Mod. Phys. Lett. B, **21**(19), pp. 1271–1283.

[23] Andersson, H. I., and Valnes, O. A., 1998, "Flow of a Heated Ferro Fluid Over a Stretching Sheet in the Presence of a Magnetic Dipole," Acta Mech., **128**, pp. 39–47.

[24] Tzirtzilakis, E. E., and Kafoussias, N. G., 2003, "Biomagnetic Fluid Flow Over a Stretching Sheet With Non Linear Temperature Dependent Magnetization," ZAMP, **54**, pp. 551–565.

[25] Matsuki, H., Yamasawa, K., and Murakami, K., 1977, "Experimental Considerations on a New Automatic Cooling Device Using Temperature Sensitive Magnetic Fluid," IEEE Trans. Magn., **13**(5), pp. 1143–1145.

[26] Matsuki, H., and Murakami, K., 1987, "Performance of an Automatic Cooling Device Using a Temperature-Sensitive Magnetic Fluid," J. Magn. Magn. Mater., **65**, pp. 363–365.

[27] Nakatsuka, K., Hama, H., and Takahashi, J., 1990, "Heat Transfer in Temperature-Sensitive Magnetic Fluids," J. Magn. Magn. Mater., **85**, pp. 207–209.

[28] Upadhyay, T., Upadhyay, R. V., Mehta, R. V., Aswal, V. K., and Goyal, P. S., 1997, "Characterization of a Temperature-Sensitive Magnetic Fluid," Phys. Rev. B, **55**(9), pp. 5585–5588.

[29] Upadhyay, R. V., Mehta, R. V., Parekh, K., Srinivas, D., and Pant, R. P., 1999, "Gd-Substituted Ferrite Ferrofluid: A Possible Candidate to Enhance Pyromagnetic Coefficient," J. Magn. Magn. Mater., **201**, pp. 129–132.

[30] Mukhopadhyay, A., Gangulu, R., Sen, S., and Puri, I. K., 2005, "A Scaling Analysis to Characterize Thermomagnetic Convection," Int. J. Heat Mass Transfer, **48**, pp. 3485–3492.

[31] John, T., Rannacher, D., and Engel, A., 2007, "Influence of Surface Tension on the Conical Meniscus of a Magnetic Fluid in the Field of a Current-Carrying Wire," J. Magn. Magn. Mater., **309**, pp. 31–35.

[32] Fruh, W.-G., 2005, "Using Magnetic Fluids to Simulate Convection in a Central Force Field in the Laboratory," Nonlinear Processes Geophys., **12**, pp. 877–889.

[33] Tzirtzilakis, E. E., and Tanoudis, G. B., 2003, "Numerical Study of Bio Magnetic Fluid Flow Over a Stretching Sheet With Heat Transfer," Int. J. Numer. Methods Heat Fluid Flow, **13**(7), pp. 830–848.

[34] Kafoussias, N. G., and Williams, E. W., 1993, "An Improved Approximation Technique to Obtain Numerical Solution of a Class of Two-Point Boundary Value Similarity Problems in Fluid Mechanics," Int. J. Numer. Methods Fluids, **17**, pp. 145–162.

[35] Kafoussias, N. G., and Williams, E. W., 1995, "Thermal-Diffusion and Diffusion-Thermo Effects on Mixed Free-Forced Convective and Mass Transfer Boundary Layer Flow With Temperature Dependent Viscosity," Int. J. Eng. Sci., **33**(9), pp. 1369–1384.

Haydar Eren
Department of Mechanical Engineering,
University of Firat,
Elazig 23119, Turkey
e-mail: haydar@firat.edu.tr

Nevin Celik[1]
Department of Mechanical Engineering,
University of Minnesota,
MN 55455
e-mail: nevincelik23@gmail.com

Seyba Yildiz
Department of Mechanical Engineering,
University of Firat,
Elazig 23119, Turkey
e-mail: seybayildiz@yahoo.com

Aydın Durmus
Department of Mechanical Engineering,
University of Ondokuz Mayis,
Samsun 55139, Turkey
e-mail: adurmus@omu.edu.tr

Heat Transfer and Friction Factor of Coil-Springs Inserted in the Horizontal Concentric Tubes

The goal of this investigation is to obtain definitive information about the heat transfer characteristics of circular coil-spring turbulators. This is achieved by measuring the wall temperatures on the inner tube of the exchanger. Also the inlet and outlet temperatures and pressure loss of the fluid are measured. These results are parametrized by Reynolds numbers ($2500 < Re < 12,000$), outer diameters of the springs ($D_s = 7.2$ mm, 9.5 mm, 12 mm, and 13 mm), numbers of the springs ($n = 4$, 5, and 6), and the incline angles of the springs ($\theta = 0$ deg, 7 deg, and 10 deg). Additionally, another goal of this work is to quantify the friction factor f of the turbulated heat exchanger system with respect to aforementioned parametric values. As a result, it is found that increasing spring number, spring diameter, and incline angle result in significant augmentation on heat transfer, comparatively 1.5–2.5 times of the results of a smooth empty tube. By the way, friction factor increases 40–80 times of the results found for a smooth tube. Furthermore, as a design parameter, the incline angle has the dominant effect on heat transfer and friction loss while spring number has the weakest effect. [DOI: 10.1115/1.3194771]

Keywords: heat exchanger, coil-spring, turbulator, heat transfer, pressure drop

1 Introduction

Heat exchangers are widely used in industry, especially in heating, ventilation and air-conditioning (HVAC) processes as evaporator, condenser, heater, refrigerator, etc. The answer why we use the heat exchangers is to obtain the highest heat transfer rate by implementing active or passive methods. If the heat transfer is improved by adding energy to the system, the process is called an active method. However, if the heat transfer is improved without adding any energy, it is called a passive method. Some examples of active methods are using mechanical auxiliary elements, rotating the surface, mixing the fluids with mechanical accessories, and constituting electrostatic areas in the flow area. Passive methods comprise covering or changing the heat transfer surface and forming some projecting parts of the rough surfaces.

In order to increase the heat transfer rates by passive methods the surface can be extended in various ways. Fabricating a finned-surface is a harder and more complex process than attaching a turbulator to the system. Therefore, investigators prefer to use different shapes, sizes, and numbers of turbulators in many applications.

In the present study, coil-springs inserted in a concentric tube are used to promote convective heat transfer. Coil-spring insert tubes have been used as one of the passive heat transfer enhancement techniques and are the most widely used tubes in several heat transfer applications, for example, heat recovery processes, air conditioning and refrigeration systems, chemical reactors, and food and dairy processes. The pitch of the coil-wire [1–9], the diameter of the coil-wire [3,4,6–8], and the length and the segmentation of the coil-spring [10] have been the investigated parametric values. Table 1 summarizes existing studies of forced convection heat transfer in a coil-spring insert heat exchanger. The table indicates the geometrical properties of the coil-spring used and the data presented in the cited articles.

The effect of coil-wire insert on the enhancement of heat transfer tends to decrease as Reynolds number increases [1,3–5]. At low Reynolds numbers, coil-spring insert has a significant effect on the enhancement of heat transfer [1] and wire coils behave as a smooth tube but accelerate transition to critical Reynolds numbers down to 700 [7]. Transition from laminar to turbulent flow occurs at a lower Reynolds number in the coiled wire-insert tube than in a smooth one. Heat transfer from coiled wires may be different from a coiled straight wire for two reasons: (i) the varying angle between flow direction and heat transfer surface, and (ii) the effects of helix geometry on the flow profile [2].

The geometry of the coil-spring is also an important parameter on the heat transfer. Coiled-square spring provides higher heat transfer than the circular one does under the same conditions [3]. When any snail-type swirl generator is mounted on the entrance of the tube, there is an increase in heat transfer and friction loss over the tube [5].

The friction factor obtained from the tube with coil-wire insert is significantly higher than that without a coil-wire insert [1–5]. Wire coils increase pressure drop up to nine times and heat transfer up to four times compared with the empty smooth tube [7]. The use of coil-spring causes a high pressure drop increase, which depends mainly on spring pitches and wire thickness, and also provides considerable heat transfer augmentations [3–5].

Coil-spring-type turbulators generate almost-periodic vortices into the flow while increasing the heat transfer rate. The vortex shedding frequencies decrease and the maximum amplitudes of pressure fluctuation of vortices produced by coiled wire turbulators occur with small pitches [2].

To the best of the authors' knowledge, the published papers in archival journals include only one coil, which is stated in the inner tube of the exchanger and its outer surface mates to the inner surface of the tube. The case that contains more than one spring has not been mentioned yet. Also the size of each spring and the locations of all springs in the tube have not been focused. The present work is an experimental investigation into the effects of the numbers ($n = 4$, 5, and 6), incline angles ($\theta = 0$ deg, 7 deg, and 10 deg), and outer diameters of the springs ($D_s = 7.2$ mm, 9.5 mm, 12 mm, and 13 mm) for heat transfer and pressure drop by using spring coils as turbulators in a heat exchanger whose inner tube is

---

Table 1 Literature survey of coil-springs

Authors	Diameter of wire (mm)	Diameter of inner tube (mm)	Pitch (mm)	Length (mm)	Observed data
Naphon [1]	1	7.8	3.18 5.08	2000	Heat transfer coefficient Heat transfer rate
Yakut and Sahin [2]	4	50	10 20 30	1240	Strouhal number Entropy generation Nusselt number
Promvonge [3,4]	2 3	47.5	15 20	1250	Nusselt number Friction factor
Promvonge [5]	5	47	20 30 40	1500	Nusselt number Friction factor
Prasad [6]	0.813 0.813 0.813 0.813 1.016 1.016 1.016 1.016 1.575 1.575 1.575 1.575	14	8.47 5.08 3.63 2.82 8.47 5.08 3.63 2.82 8.47 5.08 3.63 2.82	2200	Nusselt number Friction factor Exergy destruction
Garcia et al. [7]	1.34 1.45 1.40 1.68 1.79 1.82	18	21.12 48.32 30.66 46.22 33.57 25.31	2830	Nusselt number Friction factor
Agrawal et al. [8]	0.65 1 1.5	12.7	6.5 10 13	850	Heat transfer coefficient
Ozceyhan [9]	2	18	9 18 36	72	Temperature Thermal stress ratio
Shoji et al. [10]	1.5	13.8	15	1000 500 300	Effects of the lengths and segmetation on heat transfer

heated by constant temperature water vapor on all surfaces. Varying Reynolds number from 2500 to 12,000 means that turbulent flow is considered as a flow region. The results obtained from the tube with coil-spring insert are compared with those without coil-spring insert. Also the results are compared with those obtained in literature. New correlations for the Nusselt number and friction factor are proposed.

2 Experimental Setup

Figure 1 presents the schematic view of the whole setup. The experimental setup is divided into three main parts: (i) air facility, (ii) test section and instruments, and (iii) data acquisition system. The air is sucked by a centrifugal fan and its speed is regulated by an inverter (EKAMAT A-2000). At the exit of the fan a rotameter is used to acquire the measurements of volumetric flow rate of the air (DWYER, 100–700 l/min). Pressure differences between the inlet and outlet of the exchanger are measured by an incline manometer.

The test section is a classical type double tube heat exchanger of which the outer surface of the inner tube is heated by the condensation of a stream of flowing water vapor. After passing the condensing surface, the residual water vapor is discharged to the ambient. In order to avoid the issue of noncondensable gases, the steam generator is operated for a considerable period of time prior to its use as a heating medium.

The inner and outer diameters of the inner tube are, respectively, 60 mm and 62 mm and the length of the tube is 900 mm. As an outer tube, a 1-mm-thick flat plate with dimensions of 700×1200 mm^2 is rolled to obtain a circular tube with a diameter of 210 mm.

Turbulators inserted in the horizontal concentric tube are coil-springs. Figure 2 shows detailed instructions about the coil-springs. In literature *coil diameter* or *wire diameter* terms [1–9] are generally used to define the diameter of the coil-wire, whereas in the present paper the *diameter of the spring* term (D_s) defines the outer diameter of spring pretending to be a rod, as seen in Fig. 2(a). Cross sections of the spring are presented both from front-side view and left-side view in the figure. In Fig. 2(b) the incline angles of the springs are shown schematically.
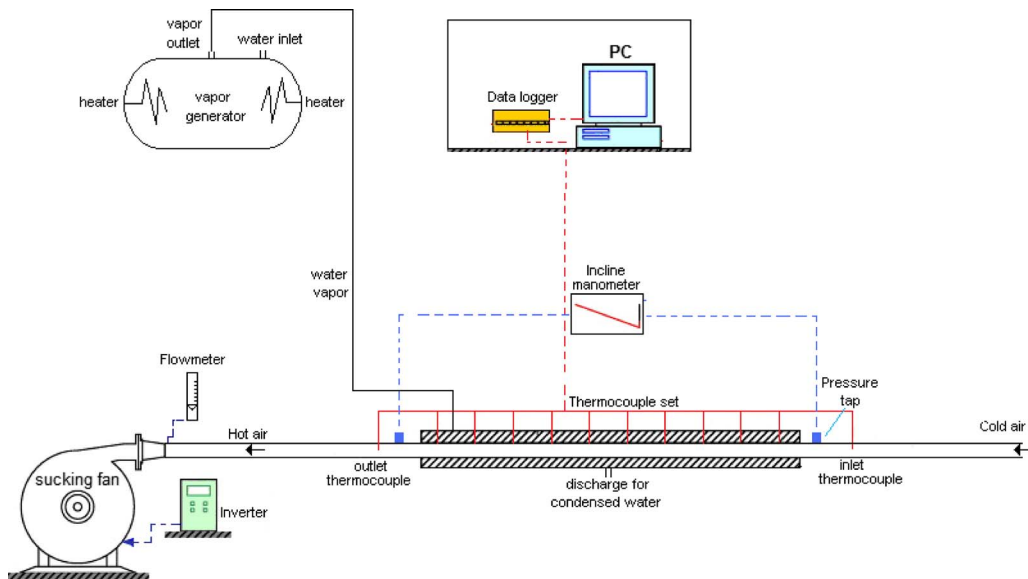
Fig. 1 Schematic view of the whole setup

The outer surface of the inner tube was maintained at a constant temperature ($100\,^{\circ}$C) by continuous contact with saturated water vapor introduced and filled into the annular space between the inner and outer tubes and discharged by a channel, like a teapot.
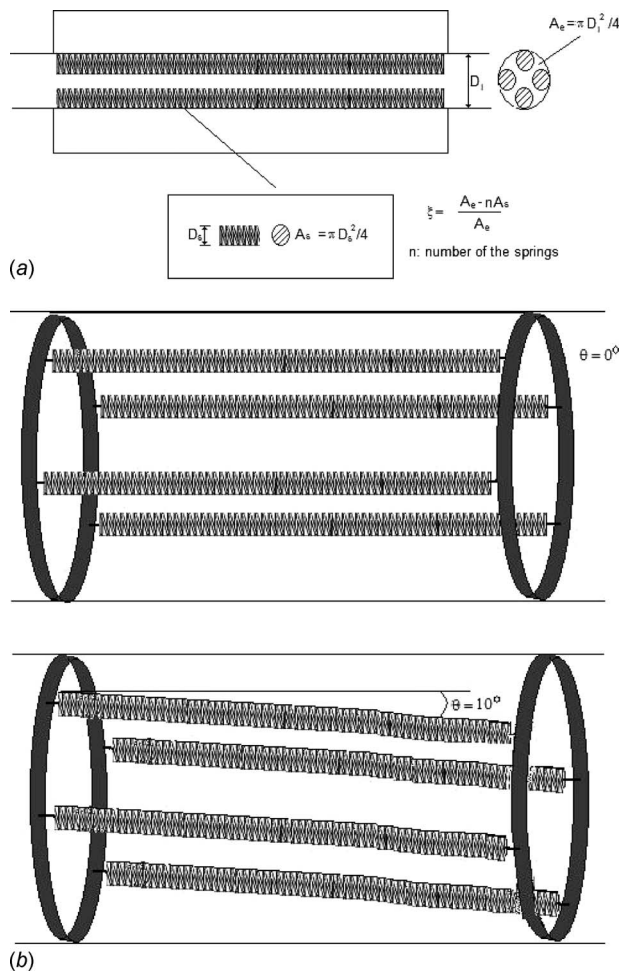
Fig. 2 Specifications of the springs: (*a*) dimensions of the springs and (*b*) incline angle of the springs

The surface temperatures were measured by *T*-type thermocouples located every 50 mm distance along the tube length. 18 thermocouples were placed on the local wall of the tube and 18 thermocouples were placed around the tube to measure the circumferential temperature variation, which was found to be negligible. The mean local wall temperature was determined by means of calculations based on the readings of the *T*-type thermocouples. The inner and outer temperatures of air were also measured at certain points inside the tube. Temperature measurements were made by using a personal computer aided data logger device (CAMPBELL CR10X) in conjunction with *T*-type thermocouples.

3 Data Deduction

3.1 Nusselt Number, Reynolds Number, and Friction Factor. The experiments are performed for the steady state conditions. Each test run takes nearly 30 min. Heat transfer and pressure loss data are parametrized with the Reynolds number, which is varied from 2500 to 12,000. Re number is found based on the volumetric flow rate of air

$$\mathrm{Re} = \frac{4\dot{V}}{\pi D_i \nu} \tag{1}$$

where ν is kinematic viscosity of the air and D_i is the inner diameter of the inner tube.

The average Nusselt number is found by logarithmic mean temperature difference (LMTD)

$$\mathrm{LMTD} = \frac{\Delta T_1 - \Delta T_2}{\ln\left(\dfrac{\Delta T_1}{\Delta T_2}\right)} \tag{2}$$

where ΔT_1 is the difference between mean wall temperature and inlet temperature of the air ($\Delta T_1 = T_w - T_i$), and ΔT_2 is the difference between mean wall temperature and outlet temperature of the air ($\Delta T_2 = T_w - T_o$). The mean wall temperature T_w was determined by means of calculations based on the readings of the *T*-type thermocouples.

The net heat is obtained by subtracting the heat loss from the gained heat, which occurred because of the water vapor on the surface. The outer surface of the test tube was well insulated and necessary precautions were taken to prevent leakages from the system. Thus, the convection heat transfer to the surrounding is neglected. Also the conductive heat loss through the thickness of

the copper tube, as well as radiation between the air and copper surface, is neglected. The mentioned neglected heat rates are less than 0.5% of the total heat obtained by heating the surface by water vapor.

Net heat is equal to the heat transfer rate, which occurred by LMTD

$$\dot{V}\rho C_p(T_o - T_i) = h_m A(\text{LMTD})$$

$$h_m = \frac{(\dot{V}\rho)C_p(T_o - T_i)}{(\pi D_i L)\text{LMTD}}$$

(3)

where the fluid properties C_p, ρ, and k are found based on bulk temperature of the air.

Then average Nusselt number can be calculated as follows:

$$\text{Nu} = \frac{h_m D_i}{k}$$

(4)

The measured pressure loss is used to calculate the friction factor

$$\Delta p = f\frac{L}{D_i}\rho\frac{V^2}{2}$$

(5)

In order to compare the experimental results of the turbulated tube, a smooth tube flow is also tested. In addition, the well-known empirical formulas of Dittus–Boelter and Blasius are used for comparisons [11].

$$\text{Nu} = 0.023 \times (\text{Re})^{0.8} \times (\text{Pr})^{0.4}$$

(6)

$$f = 0.316 \ \text{Re}_{D_i}^{-0.25} \quad (\text{Re}_{D_i} \le 2 \times 10^4)$$

(7)

where Prandtl number is considered according to the average of inlet and outlet temperatures.

3.2 Uncertainty Analysis. The well-known uncertainty analysis method introduced by Kelvin and McClintock [12] is used to estimate the total uncertainty of the parametric values: Nu, Re, and f.

According to Eqs. (1)–(4) Nu is a function of a number of *independent* variables (ρ, C_p, k, L, $\dot{V}$, T_i, T_o, and T_w)

$$\text{Nu} = \frac{\dot{V}\rho C_p}{\pi k L}\ln\left(\frac{T_w - T_i}{T_w - T_o}\right)$$

and each of those variables has individual uncertainty ($w_r, w_{Cp}, \ldots, w_{Tw}$). This can be viewed as a weighted root mean squared sum of the individual uncertainties. The total uncertainty in the result, w_{Nu}, is found as follows:

$$\omega_{\text{Nu}} = \left[\left(\frac{\partial \text{Nu}}{\partial \rho}\omega_\rho\right)^2 + \left(\frac{\partial \text{Nu}}{\partial Cp}\omega_{Cp}\right)^2 + \left(\frac{\partial \text{Nu}}{\partial k}\omega_k\right)^2 + \left(\frac{\partial \text{Nu}}{\partial L}\omega_L\right)^2 \right.$$
$$+ \left(\frac{\partial \text{Nu}}{\partial \dot{V}}\omega_{\dot{V}}\right)^2 + \left(\frac{\partial \text{Nu}}{\partial T_i}\omega_{T_i}\right)^2 + \left(\frac{\partial \text{Nu}}{\partial T_o}\omega_{T_o}\right)^2$$
$$\left. + \left(\frac{\partial \text{Nu}}{\partial T_w}\omega_{T_w}\right)^2\right]^{1/2}$$

(8)

Similar calculations can also be made for friction factor f (Eq. (5)) and Reynolds number Re (Eq. (1))

$$\omega_f = \left[\left(\frac{\partial f}{\partial \rho}\omega_\rho\right)^2 + \left(\frac{\partial f}{\partial D_i}\omega D_i\right)^2 + \left(\frac{\partial f}{\partial L}\omega_L\right)^2 + \left(\frac{\partial f}{\partial \dot{V}}\omega_{\dot{V}}\right)^2 \right.$$
$$\left. + \left(\frac{\partial f}{\partial \Delta p}\omega_{\Delta p}\right)^2\right]^{1/2}$$

(9)

Table 2 Uncertainties of dependent and independent parameters

	Uncertainties (%)		
	Present study	Peng and Peterson[a]	Asan and Namli[b]
Independent variables			
Inlet temperature of fluid, ω_{T_i} (%)	±1.49	–	±1.53
Outlet temperature of fluid, ω_{T_o} %)	±2.9	–	±3.2
Wall temperature of tube, ω_{T_w} (%)	±1.49	±1	±1.53
Pressure drop, $\omega_{\Delta p}$ (%)	±3.3	±1.5	±3.32
Volumetric flow rate of air, $\omega_{\dot{V}}$ (%)	±3.5	±1.5	±3.5
Diameter of the inner tube, ω_D (%)	±1	–	±1
Length of the tube, ω_L (%)	±1.5	–	±1.5
Others, ω_{ρ,n,k,C_p} (%)	±0.20	–	±0.20
Dependent variables			
Nusselt number, ω_{Nu} (%)	±15	±16	±18
Friction factor, ω_f (%)	±10	±10	±10
Reynolds number, ω_{Re} (%)	±4	±8	±4

[a]Reference [14].
[b]Reference [13].

$$\frac{\omega_{\text{Re}}}{\text{Re}} = \left[\left(\frac{\partial \text{Re}}{\partial \nu}\omega_\nu\right)^2 + \left(\frac{\partial \text{Re}}{\partial D_i}\omega D_i\right)^2 + \left(\frac{\partial \text{Re}}{\partial \dot{V}}\omega_{\dot{V}}\right)^2\right]^{1/2}$$

(10)

The uncertainty of each variable was estimated by the help of instruments' catalogs and published papers in literature [13,14]. Then the total uncertainties for each independent variable were found for Nu, f, and Re as ±15%, ±10%, and ±4%, respectively. Comparing these results to the ones in archival journals it will be seen that the results are agreeable. For instance, Peng and Peterson [14] found 16%, 10%, and 8% uncertainties for Nu, f, and Re, respectively. Asan and Namli [13] found 18%, 10%, and 4% for the aforementioned parameters. Both results are agreeable with those obtained in the present work. Table 2 presents the comparisons to literature. It also exhibits the uncertainty of each independent variable. As can be seen from the table, pressure, volumetric flow rate of the air, and the outlet temperature of the fluid are the major uncertainty sources. The highest effect on the total uncertainty of Nusselt number is outlet temperature, with the level 55%. For friction factor and Re number major uncertainties are caused by volumetric flow rate of the fluid. The effect of volumetric flow rate of fluid on Reynolds number is 63%, while it is 20% on friction factor.

4 Results and Discussions

4.1 Results for a Smooth Tube. In this section, first, the verification of the experimental results will be presented. The presentation begins with a display of the validation of the results for a smooth tube. The Nusselt number Nu and friction factor f obtained from the present smooth tube are, respectively, compared with the correlations of Dittus–Boelter (Eq. (6)) and Blasius (Eq. (7)) [11]. Figures 3(a) and 3(b) show these comparisons. In the figures, the present results agree reasonably well within 8.5% for Nusselt number correlation of Dittus–Boelter. However, for the friction factor, there is 20.5% deviation between the present results and the correlation of Blasius, which is quite high. The present results are correlated for the Nusselt number and friction factor of the smooth tube as follows:

$$\text{Nu} = 0.158 \ \text{Re}^{0.6} \ \text{Pr}^{0.4}$$

(11)

$$f = 71.24 \ \text{Re}^{-0.84}$$

(12)
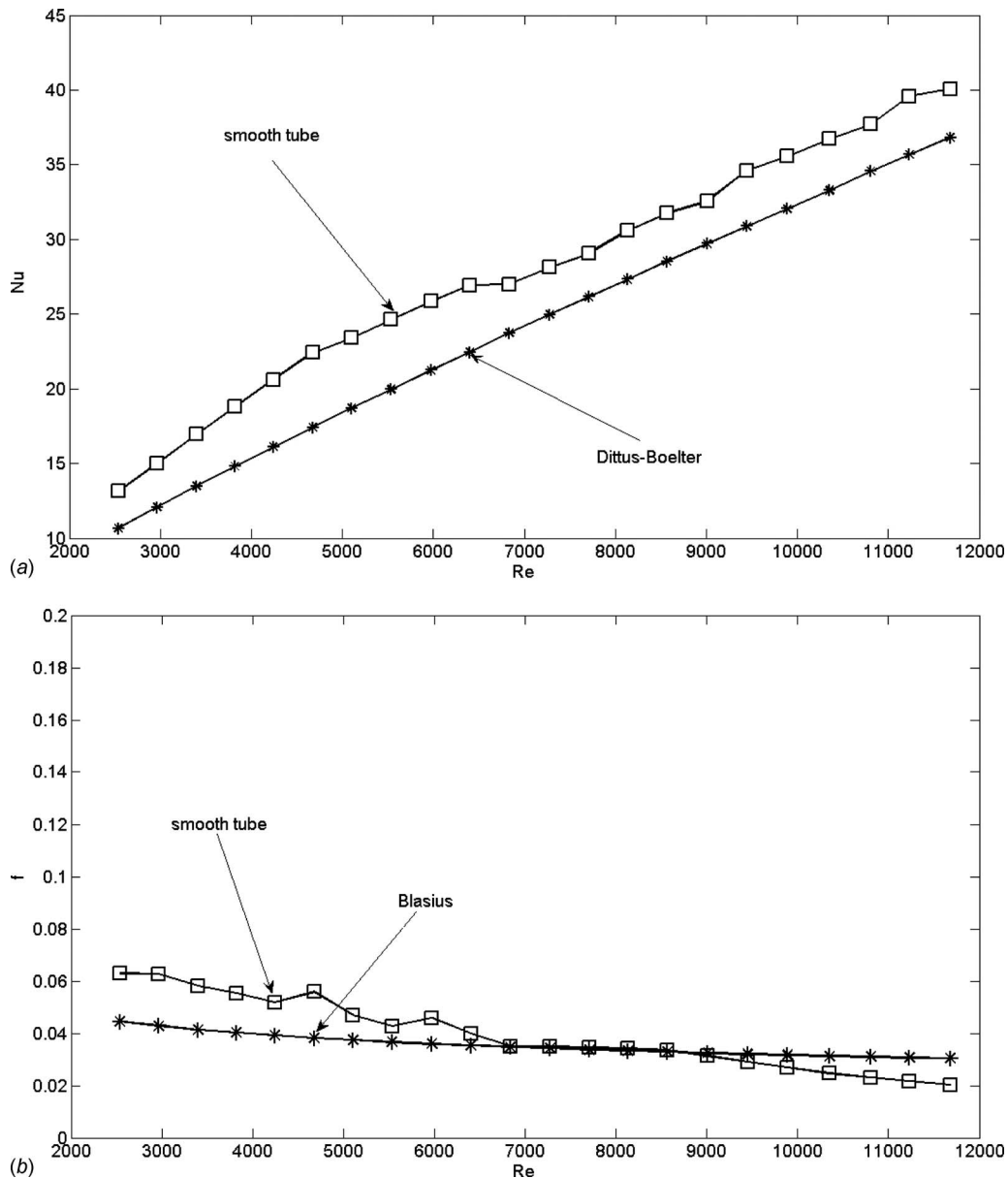
Fig. 3 Verification of the results for a smooth tube and empirical correlations: (*a*) Nu number results versus Dittus–Boelter correlation's results, and (*b*) *f* friction factor results versus Blasius correlation's results

4.2 Effects of Design Parameters. The design parametric values investigated in this work are coil-spring size (diameter), number of the springs, and incline angle of the springs. Three graphs are plotted to show the effects of these three parameters on Nusselt number in Figs. 4(*a*)–4(*c*). Also the results of the smooth empty tube and empirical correlation of Dittus–Boelter are added into figures.

As seen from Figs. 4(*a*)–4(*c*), coil-springs yield a considerable heat transfer enhancement with a similar trend in comparison with the smooth tube. Careful inspection of the curves in Fig. 4(*a*) indicates that the rate of increase in Nu with Re is more or less the same for all diameters. The most important point in the curves of Fig. 4(*a*) is the distance between the lines of each diameter. Although the three lines regarding D_s=7.2 mm, 9.5 mm, and 12 mm have the same distance between each other, the lines for D_s =12 mm and 13 mm are quite closer. The reason is related to the magnitude of the diameter. Subtracting the diameters, it is found that the difference between D_s=9.5 and D_s=7.2 is 2.3 mm and the

difference between D_s=12 mm and D_s=9.5 mm is 2.5 mm. Hence the curves for D_s=7.2, 9.5, and 12 are stated with an equal distance from each other. Since the difference between the curves of D_s=12 mm and 13 mm is only 1 mm, the gap is not as large as the others.

In Fig. 4(*b*) the effects of the number of the springs is presented, and it is shown that the increasing rate of Nusselt number with Re number shows similar trends for all *n* values.

In Fig. 4(*c*) the incline angle effect is shown. It is observed that Nusselt number increases monotonically with the incline angle. The increment trend is approximately the same for each angle.

For all cases Nu number increases with increasing Re number, since the coiled wire turbulators interrupt the development of the boundary layer of the fluid flow and increase the degree of flow turbulence [3].

Considering Figs. 4(*a*)–4(*c*) it can be briefly said that when three design parameters increase, heat transfer increases too. However, it is important to know that which parameter has the
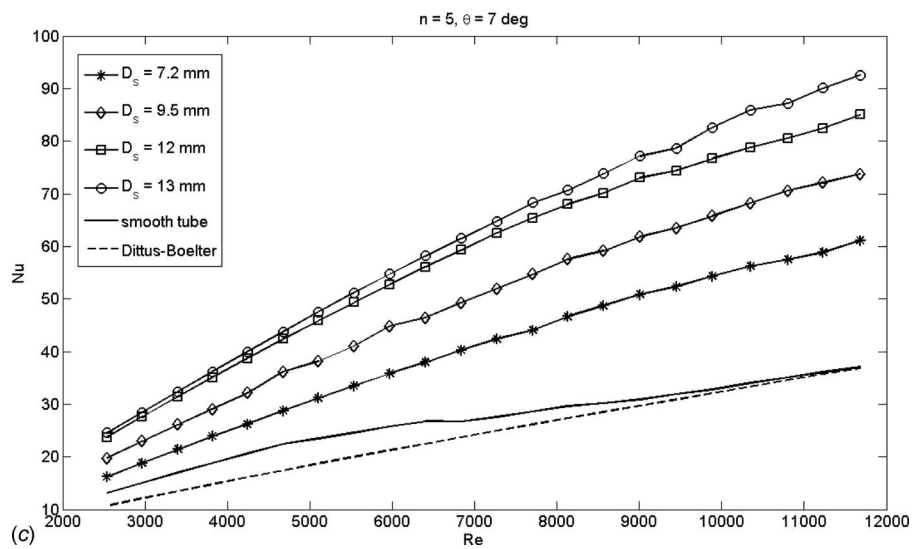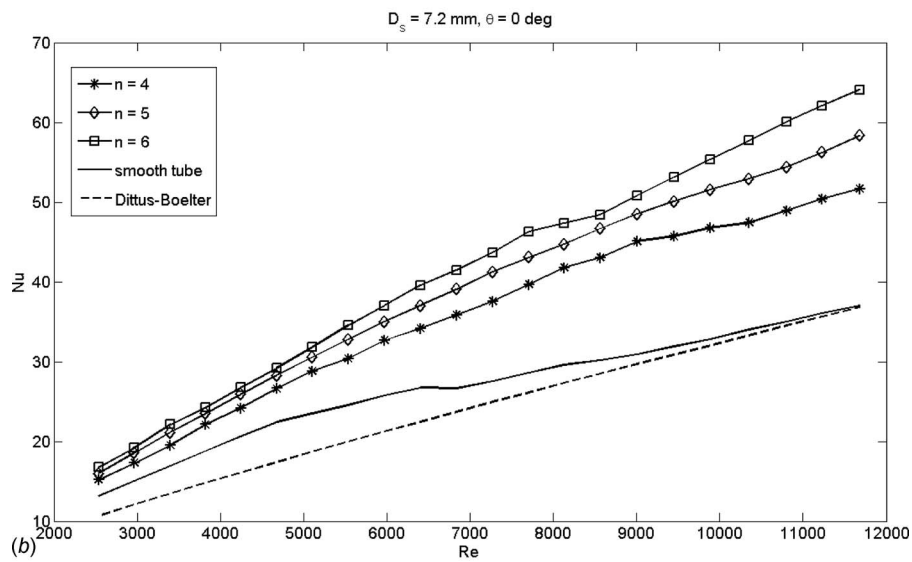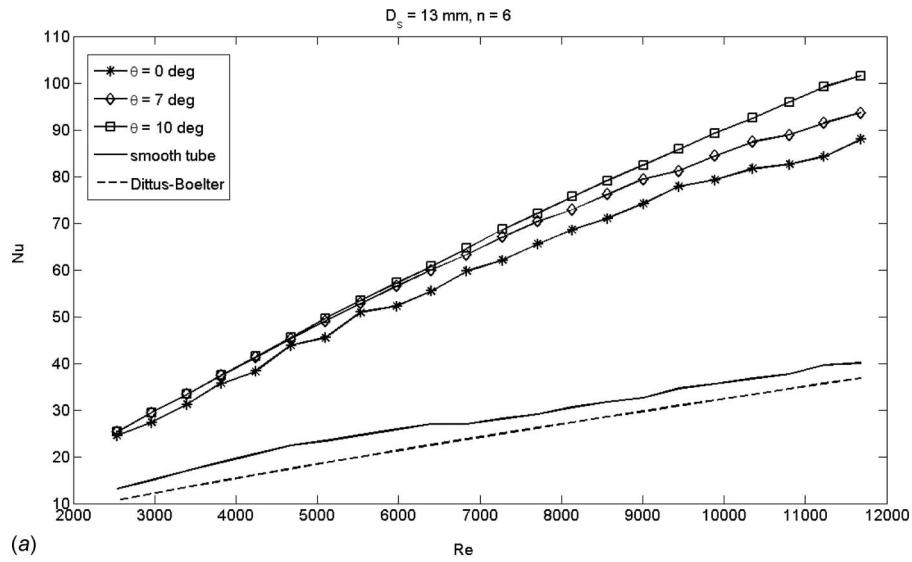
Fig. 4 Nu number versus Re number with respect to (*a*) incline angles, for *D_s*=13 mm and *n*=6; (*b*) number of springs, for *D_s*=7.2 mm and *θ*=0 deg; and (*c*) diameter of the springs, for *n*=5 and *θ*=7 deg

Table 3 Cross-section factor, ξ, of each turbulator case

Diameter of the springs, D_s (mm)	Numbers of the springs, n	Cross-section factor, ξ
7.2	4	0.942
	5	0.928
	6	0.914
9.5	4	0.900
	5	0.875
	6	0.850
12	4	0.840
	5	0.800
	6	0.760
13	4	0.812
	5	0.765
	6	0.718

highest effect on thermal performance, in other words, which is dominant in thermal enhancement effect of the spring turbulators. In order to evaluate the independent design parameters' effects on Nusselt number, a statistical correlation analysis is performed.

The number and the diameter of the springs affect the fluid passing area magnitude but the incline angle has no effect on the sizes of the flow passing area. So they should be considered together. A new term *cross-section factor* represented with the Greek letter ξ is generated to show the fluid passing area in the tube

$$\xi = \frac{A_e - n \cdot A_s}{A_e} \quad (13)$$

where A_e is the cross-section area of the empty tube ($A_e = 2827.43$ mm^2), and A_s is the cross-section area of each spring, assuming that each spring is like a rod with diameters $D_s = 7.2$ mm, 9.5 mm, 12 mm, and 13 mm (see Fig. 2(a)). Finally, n is the number of the springs located inside the tube ($n = 4$, 5, and 6). In Table 3 the values of ξ are listed. The effect of the incline angle is given with "$1 + \tan \theta$" as shown in Fig. 2(b).

The software program STATISTICA 5.0 is used to estimate correlation coefficients. Nonlinear estimation method is used in the analysis. The Nusselt number correlation is found for the range of Reynolds number $2500 < \mathrm{Re} < 12,000$, Pr=0.7, and $L/D_i = 15$ as follows:

$$\mathrm{Nu} = 0.023 \ \mathrm{Re}^{0.83} \ \mathrm{Pr}^{0.4} \ \xi^{-1.64}(1 + \tan \theta)^{0.93} \quad (\mathrm{Pr} = 0.71) \quad (14)$$

In Fig. 5, the predicted values versus observed values of Nusselt number are plotted. Agreeable regression coefficients are obtained ($R^2 = 0.98$). Also the average, maximum, and minimum errors are in agreeable ranges.

From the correlation it is seen that incline angle has an exponent 0.93 while Re has an exponent value of 0.83. This shows that incline angle is more effective than Re number. It is worthy to note that the correlation coefficient 0.83 for Re number is very close to that in Dittus–Boelter (0.8). The cross-sectional area for the fluid passing through the tube decreases when the number of the spring and the diameter of the spring increase. Nu number increases with this diminishing fluid area. This area effect seems to be the dominant parameter since it has the highest exponent, 1.64. However, it does not give any idea about the effect of number of spring and diameter separately on Nusselt number. Hence another correlation of Nu dependent on n is generated by assuming spring diameter to be constant ($D_s = 7.2$ mm)

$$\mathrm{Nu} = 10.8 n^{0.24} \quad (15)$$

then the number n is assumed to be constant ($n = 5$) and the correlation of Nu-D_s is found as

$$\mathrm{Nu} = 3.9 D_s^{0.72} \quad (16)$$

It is apparent that the diameter's effect is greater than the number's effect. Eventually, sorting the parameters' effects from high to low, the order is as (1) the incline angle, (2) diameter, and (3) the number of the coil-springs.

Now, it is time to focus on pressure loss by means of friction factor. For all tested cases, the use of coil-spring results in a substantial increase in friction factor. Since the coil-springs pretend to be a second tube in the test tube, the contact of the working fluid with the surface area of the test tube is higher due to the longer
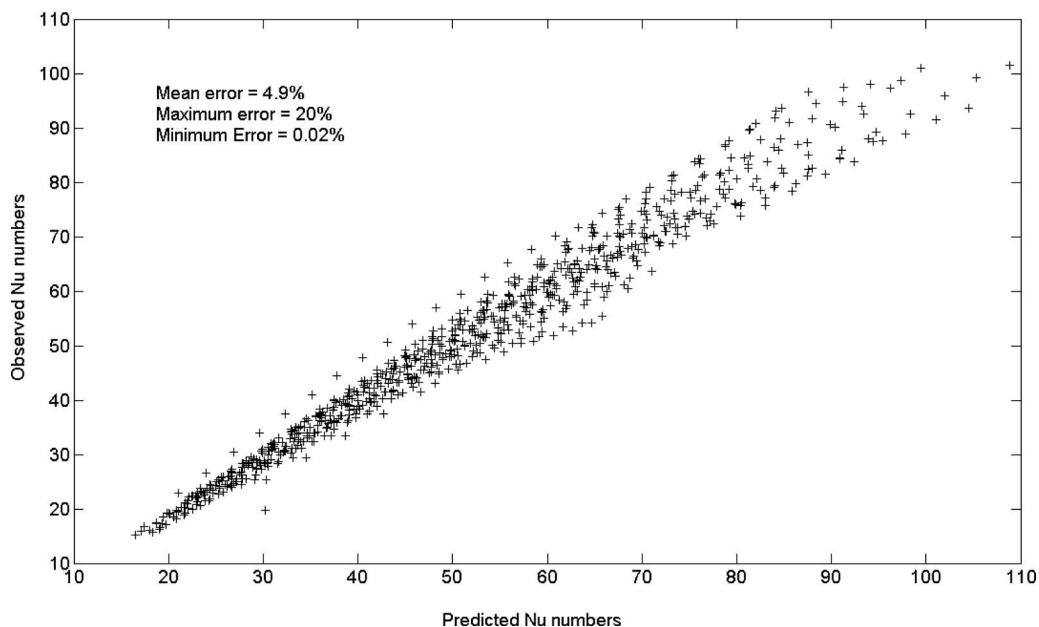
Fig. 5 Correlation results for predicted Nu number versus observed Nu number
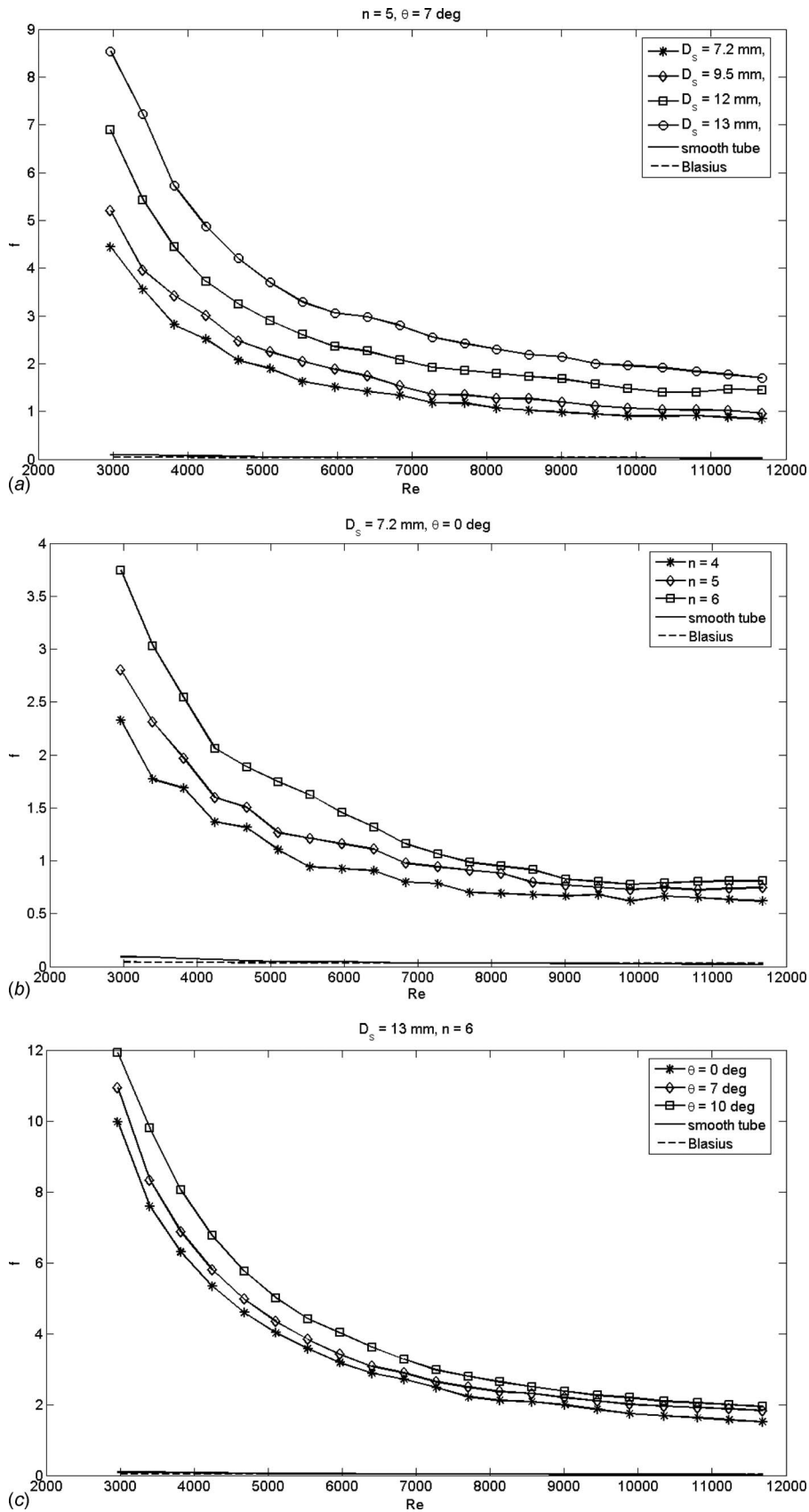
Fig. 6 Friction factor *f* versus Re number with respect to (*a*) incline angles, for D_s =13 mm and *n*=6; (*b*) number of springs, for D_s=7.2 mm and θ=0 deg; and (*c*) diameter of the springs, for *n*=5 and θ=7 deg
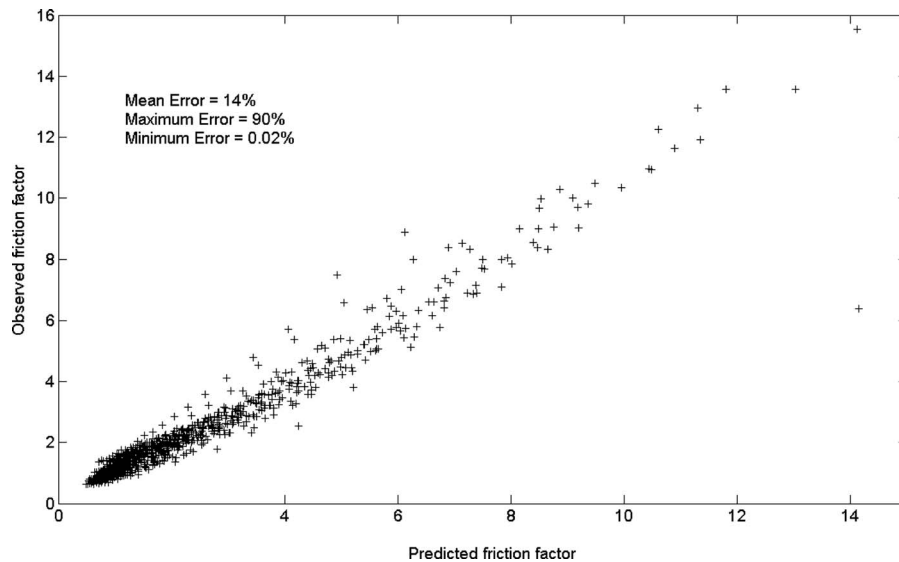
Fig. 7 Correlation results for predicted friction factor versus observed friction factor

flow path and residence time, leading to higher friction loss [2,3].

In Figs. 6(a)–6(c), f-Re variations of the coil-springs' diameters, numbers, and incline angles are plotted. As mentioned above, the friction factor increase in all cases, however, is much higher than that of the smooth tube. These increments can be attributed to dissipation of the dynamic pressure of the fluid due to higher surface area and flow blockage of the coil-spring along the tube wall [1–5].

Friction factor tends to decrease with the increase in Reynolds number in the range 2000–9000. Above this value the decrement rate nearly keeps constant or becomes less.

It is found that there is a reduction in the friction factor while using less coil-spring and smaller spring diameter and incline angle. The highest value of friction factor is observed for D_s =13 mm, n=6, and θ=10 deg, while the lowest value is for D_s =7.2 mm, n=4, and θ=0 deg. Sequencing the design parameters' effects from high to low, it will be seen that the most effective design parameter on the friction factor enhancement is incline angle, the second dominant parameter is diameter, and finally the least effect is caused by changing the number of the coil-springs, as previously observed in heat transfer.

A correlation including all of the effective parameters on friction factor is obtained as follows:

$$f = 210{,}767\ \mathrm{Re}^{-1.4}\ \xi^{-3.26}(1 + \tan\ \theta)^{1.82} \qquad (17)$$

Equation (17) is valid for the experimental conditions of 2900 < Re < 12,000, Pr=0.7, and L/D_i=15. The exponents of Reynolds number, cross-section factor, and incline angle show that their effects on friction factor increment are much more than their effects on heat transfer increment.

In Fig. 7 the comparison of observed values by the tests and the predicted values by the correlation (Eq. (17)) is presented. The regression coefficient is 0.98, which is high enough to be scientifically acceptable, and the mean, maximum, and minimum deviations between the observed and predicted values are 14%, 90%, and 0.02%.

4.3 Performance Evaluation. It will now be focused on the enhancement of heat transfer and friction loss by means of Nu number ratio, $Nu/Nu_0$, and friction factor ratio, f/f_0, which are, respectively, defined as the ratio of the observed augmented results of Nu and f to the results of the smooth tube of Nu_0 and f_0. Nusselt number ratio is plotted against Reynolds number in Figs. 8(a)–8(d) and friction factor ratio versus Reynolds number is plotted in Figs. 9(a)–9(d). The subfigures (a), (b), (c), and (d), respec-

tively, represent the coil-spring diameters D_s=7.2 mm, 9.5 mm, 12 mm, and 13 mm. Each of these subfigures consists of three parts, with each part corresponding to a specific value of incline angle θ. These graphs extend over a Reynolds number Re range from 2500 to 12,000, spring diameters n=4, 5, and 6, and incline angles from θ=0 deg, 7 deg, and 10 deg.

From Figs. 8(a)–8(d) it is apparent that Nusselt number ratios are generally above unity in all cases, indicating that the use of coil-springs is advantageous over the smooth tube. Nusselt number ratio Nu/Nu_0 tends to increase with the increase in Reynolds number from 2500 to 7000 for all turbulators and then nearly keeps constant or has a slight decrease for higher Reynolds numbers.

Among all cases, the maximum value of Nu/Nu_0 is obtained as 2.5 for D_s=13 mm, θ=10 deg, and n=6, and the minimum value is obtained as 1.5 for D_s=7.2 mm, θ=0 deg, and n=4. These results show a good agreement compared to literature. For example, in Promvonge's study [3], average enhancement of heat transfer rate is found to be about 2.1 times more than that of the smooth tube. In Naphon's experiments [1], enhancement of heat transfer varied between 1.5 and 2 times according to the pitch size.

From Figs. 9(a)–9(d) it is observed that the friction factor ratio tends to decrease for Re < 9000 for all the turbulators applied. For Re > 9000 it slightly decreases or keeps constant. The average f/f_0 values for D_s=7.2 mm, with the incline angle θ=0 deg, are 23, 27, and 32, for n=4, 5, and 6, respectively. For θ=7 deg, the increase in the friction factor is 29, 36, and 43 times of the friction factor for a smooth tube. Finally for θ=10 deg the increments are 32, 41, and 51 times. In literature Promvonge [3–5] used only one coil-spring with zero incline angle. He found that for circular coils, friction factor ratio is 7.5, which is three times smaller than the lowest average value found in the present paper. This deviation is directly related to the design parameters, such as spring numbers and incline angle, applied in the present study.

5 Conclusions

In the present work, springs are located along the inner tube of a heat exchanger. These springs behave like turbulators and, hence, cause some heat transfer enhancement. The major results of the experiments are as follows.

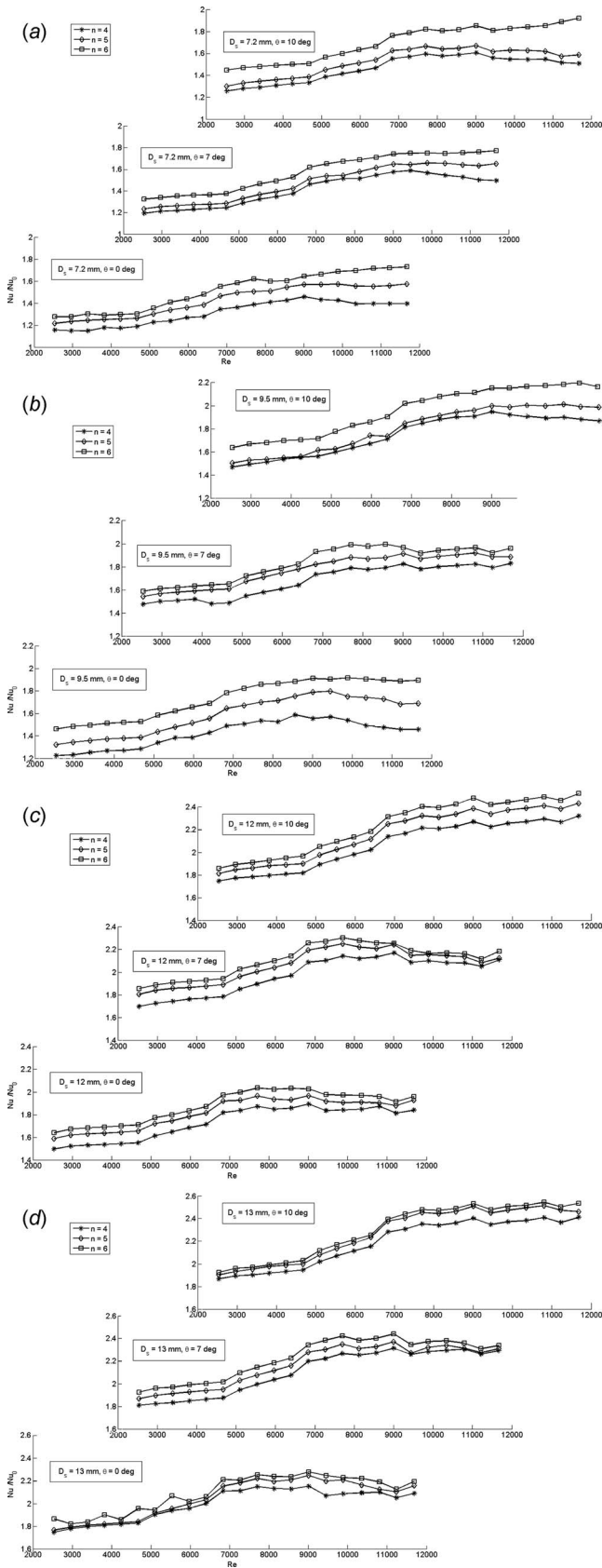- Turbulators not only produce more turbulence than the smooth tube but also increase heat transfer area.

Fig. 8 Ratio of augmented Nu number to the smooth tube Nu number, Nu/Nu₀: (a) D_s=7.2 mm, (b) D_s=9.5 mm, (c) D_s=12 mm, and (d) D_s=13 mm
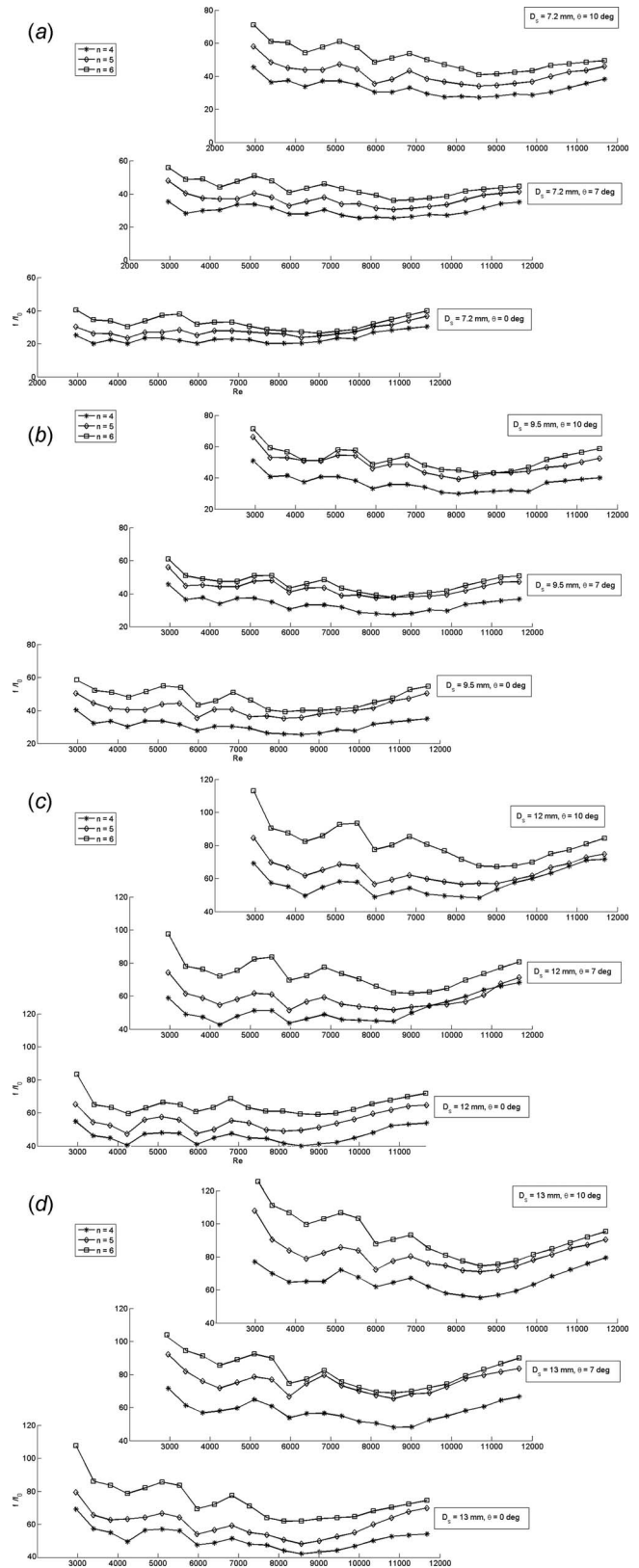
Fig. 9 Ratio of augmented friction factor to the smooth tube friction factor, f/f_0: (a) D_s=7.2 mm, (b) D_s=9.5 mm, (c) D_s=12 mm, and (d) D_s=13 mm

- Incline angle of the coil-springs stated along the tube has an impetus on heat transfer and pressure loss. For the smallest incline angle of the springs $\theta=0$ deg heat transfer and friction factor have the lowest values, while for $\theta=10$ deg the heat transfer and friction factor have the highest values.
- Second the diameter of the springs has a great effect on heat transfer and friction loss. Increasing the diameter causes significant increases in heat transfer and friction loss.
- The heat transfer and friction factor increase with increasing spring numbers, n, but the effect of n is not as powerful as the effects of diameter and incline angle.
- Heat transfer increases with increasing Re. However, the friction loss also increases. The recommendation of the authors is to make an optimization analysis for diminishing the friction loss.

Nomenclature

A = peripheral heat transfer area of the inner tube ($A = \pi D_i L$) (m^2)

A_e = cross-sectional area for the empty tube ($A_e = \pi D_i^2 / 4$) (m^2)

A_s = cross-sectional area for spring based on the outer diameter ($A_s = \pi D_s^2 / 4$) (m^2)

C_p = specific heat (J kg^{-1} K^{-1})

D_i = inner diameter of the inner tube (mm)

D_s = outer diameter of the spring (m)

f = friction factor

f_0 = friction factor for a smooth empty tube

h_m = average heat transfer coefficient (W m^{-2} K^{-1})

k = thermal conductivity of the air (W m^{-1} K^{-1})

L = length of the inner tube (m)

LMTD = logarithmic mean temperature difference (K)

n = number of the springs

Nu = Nusselt number

Nu$_0$ = Nusselt number for a smooth empty tube

Δp = pressure loss (Pa)

Pr = Prandtl number

R^2 = regression coefficient

Re = Reynolds number

T_i = temperature of air at the inlet (K)

T_0 = temperature of air at the outlet (K)

T_w = wall temperature of the inner tube (K)

V = mean velocity of the air (m/s)

Greek Letters

$\dot{V}$ = volumetric flow rate of the air (m s^{-3})

ρ = density of the air (kg m^{-3})

ν = kinematic viscosity of air (N m s^{-1})

θ = incline angle of the spring (deg)

ω = uncertainty (%)

ξ = nondimensional cross-section factor

References

[1] Naphon, P., 2006, "Effect of Coil-Wire Insert on Heat Transfer Enhancement and Pressure Drop of the Horizontal Concentric Tubes," Int. Commun. Heat Mass Transfer, **33**, pp. 753–763.

[2] Yakut, K., and Sahin, B., 2004, "The Effects of Vortex Characteristics on Performance of Coiled Wire Turbulators Used for Heat Transfer Augmentation," Appl. Therm. Eng., **24**, pp. 2427–2438.

[3] Promvonge, P., 2008, "Thermal Performance in Circular Tube Fitted With Coiled Square Wires," Energy Convers. Manage., **49**(5), pp. 980–987.

[4] Promvonge, P., 2008, "Thermal Enhancement in a Round Tube With Snail Entry and Coiled-Wire Inserts," Int. Commun. Heat Mass Transfer, **35**(5), pp. 623–629.

[5] Promvonge, P., 2008, "Thermal Augmentation in Circular Tube With Twisted Tape and Wire Coil Turbulators," Energy Convers. Manage., **49**, pp. 2949–2955.

[6] Prasad, R. C., 1994, "Performance Evaluation Using Exergy Analysis—Application to Wire-Coil Inserts in Forced Convection Heat Transfer," Int. J. Heat Mass Transfer, **37**(15), pp. 2297–2303.

[7] Garcia, A., Vicente, P. G., and Viedma, A., 2005, "Experimental Study of Heat Transfer Enhancement With Wire Coil Inserts in Laminar-Transition-Turbulent Regimes at Different Prandtl Numbers," Int. J. Heat Mass Transfer, **48**, pp. 4640–4651.

[8] Agrawal, K. N., Kumar, A., Behabadi, M. A. A., and Varma, H. K., 1998, "Heat Transfer Augmentation, by Coiled Wire Inserts During Forced Convection Condensation of R-22 Inside Horizontal Tubes," Int. J. Multiphase Flow, **24**(4), pp. 635–650.

[9] Ozceyhan, V., 2005, "Conjugate Heat Transfer and Thermal Stress Analysis of Wire Coil Inserted Tubes That Are Heated Externally With Uniform Heat Flux," Energy Convers. Manage., **46**, pp. 1543–1559.

[10] Shoji, Y., Sato, K., and Oliver, D. R., 2003, "Heat Transfer Enhancement in Round Tube Using Coiled Wire: Influence of Length and Segmentation," Heat Transfer Asian Res., **32**(2), pp. 99–107.

[11] Incropera, F. P., and Dewitt, D. P., 1988, *Fundamentals of Heat and Mass Transfer*, Wiley, New York.

[12] Kline, J., and McClintock, F. A., 1953, "Describing Uncertainties in Single-Sample Experiments," Mech. Eng. (Am. Soc. Mech. Eng.), **75**, pp. 3–8.

[13] Asan, H., and Namli, L., 1997, "Uncertainty Analysis of the Experimental Studies of Heat Transfer and Pressure Loss," ULIBTK'97, 11th National Heat Science and Techniques Congress, Edirne, Turkey, pp. 369–378.

[14] Peng, X. F., and Peterson, G. P., 1996, "Convective Heat Transfer and Flow Friction for Water Flow in Microchannel Structures," Int. J. Heat Mass Transfer, **39**, pp. 2599–2608.

Exergy Study of Fouling Factors in Heat Exchanger Networks

Zunlong Jin[1]
e-mail: zljin@zzu.edu.cn

Qiwu Dong

Minshan Liu

Thermal Energy Engineering Research Center,
Zhengzhou University,
Zhengzhou 450002, P.R. China

Selection of fouling factors is somewhat arbitrary in heat exchanger networks (HENs) synthesis. Fouling factors were reconsidered in this article for heat exchanger networks design. An objective function based on exergoeconomic analysis was introduced to assess optimal less conservative fouling factors. The objective took account of exergy consumption expense and heat exchanger capital cost at the same time. The exergy consumption of heat transfer in HENs was calculated using subsection integral on balanced composite curves. The proposed method was applied to an industrial case. Numerical results indicated that the optimal less conservative fouling factors were 80% of the original values and the heat transfer area of the system saved 350 m^2 compared with root design. So it is necessary to reconsider the values of fouling factors for HENs design and that exergoeconomic analysis is useful in determining the optimal less conservative fouling factors. [DOI: 10.1115/1.3194766]

Keywords: heat exchanger networks, fouling factors, exergoeconomic analysis

1 Introduction

Heat exchanger network (HEN) syntheses play an important role in controlling energy consumption and costs. Recent years have witnessed a rapid development in this field. As nature phenomena, fouling of heat transfer equipment has long plagued energy-related industries. Increasing energy and raw material costs, declining availability of high-quality cooling water, and environmental restrictions limiting the use of certain additives that could be used to mitigate fouling have combined to increase the importance of understanding fouling phenomena in the design and operation of industrial heat exchangers [1]. This is an interesting issue in HEN syntheses as well. More and more literatures on this subject were published in recent years [2–5].

Increasing energy and capital costs have made it imperative to ensure that as little energy and capital as possible was consumed by a chemical plant. The synthesis of HENs subject to fouling is thus worthy of being investigated. The traditional approach to fouling is to add area for contingency in heat exchanger. Practically, heat exchanger designs allowances for fouling through "fouling factors." The most widely used data on fouling factors were published by the Tubular Exchanger Manufacturers Association (TEMA), which provided lots of experienced fouling data for different kinds of fluids. However, selection of fouling factors was somewhat arbitrary and there have been several limitations. Specifying a large fouling factor produces a conservative overdesign, which may produce problems. For example, an oversize in heat exchanger will reduce flow velocity causing an increased rate of fouling to occur and there is too much area for the required heat duty at start up. Could we do better?

The normal design often selects certain fouling factors. These values can be called original design setting. Since fouling deposits build up over time, the original fouling factors represent terminal values and they represent that at the point when some clean action should be taken. The exchanger is overdesigned for the initial operation. Generally, the target temperatures of process streams with somewhat tolerance are permitted to keep within a certain range, which provides the chance to think over less conservative fouling factors. But the question is: How much is the suitable

fouling factor. Wang and Sunden [5] employed the method of trade-off optimization between the utility consumption and capital cost in which the optimal fouling factor is dependent on the capital saving and the utility consumption increase. However, in previous literature, the optimal objective function was expressed by the sum of hot utility and cold utility for the energy consumption, which took no account of exergy consumption. Actually, it was not reasonable.

Exergy reflects that usefulness or value of energy. In the process of heat transfer, energy is conservational, but exergy is consumed or destroyed due to irreversible phenomena. In fact, it is the exergy consumption that impels the process of heat transfer. Therefore, it is more reasonable to price exergy rather than energy as the annual operating expense, which trades off with the capital cost in determining the optimal synthesis. Work linking exergy and economics was carried out for several decades and a lot of research on exergy linked with economics was done, which made the concept of exergoeconomic [6] well appreciated (for more detailed review, see Ref. [7]).

In this article, an approach based on exergoeconomic analysis was introduced to determine the optimum less conservative fouling factors. Exergy consumption expense acted as operating costs of HENs in the objective function. Finally, the proposed method was applied to an industrial case, and encouraging results have been obtained.

2 Methodology

2.1 Less Conservative Fouling Factor. The fouling layer has a high thermal resistance with respect to other resistances in the system, which increases the resistance to heat transfer and reduces the overall effectiveness. So, overdesign is made for the added resistance due to fouling.

Currently, the most widely used data on fouling resistance are published by TEMA, which provides a listing of experience-based fouling factors. But selection of fouling factors is somewhat arbitrary. Recently, a coming has been formed to re-evaluate these fouling factors.

It is possible to select less conservative fouling factor, R_f^*, based on the original value. Accordingly, there will be the equation as follows:

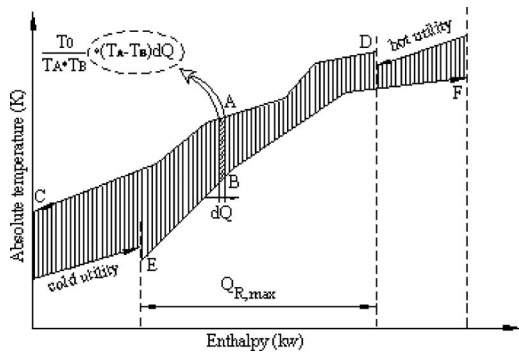$$R_f^* = \frac{1}{U_f^*} - \frac{1}{U_c} \tag{1}$$

Fig. 1 Balanced composite curves for exergy consumption calculation

where R_f^* is the less conservative thermal resistance due to fouling, U_f^* is the overall heat transfer coefficient with less conservative fouling considered, U_c is the clean overall heat transfer coefficient.

Less conservative fouling factors result in less heat transfer surface margin with less capital costs and bigger impetus of heat transfer is needed because of the below design performance. The exergy consumption increases with the increase of the degree of irreversibility accordingly. The proper value will be determined through a trade-off way between capital cost saving and exergy consumption increasing. If the annual saving is the biggest, the fouling factors are the optimal conservative fouling values.

2.2 Calculation of Exergy Consumption in HENs. During the process of heat transfer in HENs, the temperature of process stream is changing continuously. So, it is difficult to calculate exergy loss at every heat exchange point. Apparently, it is not rational to use mean temperature difference in process stream for calculation of exergy consumption. A new method is proposed here.

As demonstrated in Fig. 1, point A and point B on hot composite curve and cold composite curve are selected at random, respectively. The exergy consumption of heat transfer between A and B is calculated by using the differential element

$$\frac{T_0}{T_A \cdot T_B}(T_A - T_B)dQ \qquad (2)$$

where T_A is the absolute temperature of point A (K), T_B is the absolute temperature of point B (K), and T_0 is the absolute temperature of assumed environment (here 298 K is assumed).

The exergy consumption of the whole process of heat transfer in HENs is calculated by using integration on the whole process.

However, it is shown that the hot and cold composite curves are composed of several lines. There are several different integral equations. Integration can be done apart from the hot end of the balanced composite curves and moving upwards the curves between plumb corresponding hot and cold curves. That is,

$$I = \int_0^{Q_1} \frac{T_0}{T_A \cdot T_B}(T_A - T_B)dQ + \int_{Q_1}^{Q_2} \frac{T_0}{T_A \cdot T_B}(T_A - T_B)dQ + \cdots$$
$$+ \int_{Q_{N-1}}^{Q_N} \frac{T_0}{T_A \cdot T_B}(T_A - T_B)dQ \qquad (3)$$

where T_A and T_B are changed continuously with the line relations between the absolute temperature and the enthalpy.

2.3 Objective Function Based on Exergoeconomic Analysis. In the process of heat transfer, exergy loss occurs due to irreversibility. Exergy loss increases with the increase in the degree of irreversibility and this kind of exergy loss is inevitable. However, according to the first law of thermodynamics, the en-

Table 1 Cost data of heat exchanger network

Items	Cost data
Capital cost of HEN (US$)	$10000 + 350A$ (m^2)
Electricity price (US$)	0.04/kW h
Operation time	7200 h/year

ergy is conservational but the quality is decreased. Therefore, many researchers [8] recognize that exergy, not energy, is the commodity of value in an energy system. Consequently, it is more reasonable to assign prices to exergy-related variables.

The economic assessment includes exergy consumption expense and heat exchanger capital costs. In the objective function, exergy consumption expense substitutes for hot and cold utility energy costs as the operating costs. Annualized saving is used as the economic objective for selecting optimal less conservative fouling factors. Less surface margin is achieved because of less conservative fouling factors and the capital costs are reduced accordingly. Consequently, exergy consumption is increased because of greater heat transfer driving force needed with the below design performance. So, there will be an optimal trade-off between exergy consumption expense and heat exchanger capital costs. When the annual saving is the biggest, the fouling factors are the optimal less conservative fouling values. So the objective function based on exergoeconomic analysis is expressed as follows.

For objective function,

$$\max C = C_{I,\text{save}} - C_{\text{ex,increase}} \qquad (4)$$

where C is the annual cost savings, $C_{I,\text{save}}$ is the capital cost savings, $C_{\text{ex,increase}}$ is the exergy consumption increase.

As for exergoeconomic analysis, it is important to find a sound method for exergy price setting. Many papers for exergy price settings were published in literatures and significant work was done (for more details, see Refs. [9–12]). In this work, exergy is priced by electrical price. Electrical energy is totally convertible to work in theory. The annual exergy consumption expense is obtained by multiplying the unit price of electrical energy and operating hours and exergy consumption. Table 1 gives the cost data [4].

3 Case Study

This case study was initially selected from an ammonia synthesis plant. During the process of CO conversion, a large amount of heat was released. The conversion gas with high temperature was let off from converter. The HENs for heat recovery have been designed and the conversion gas was used to generate high-pressure steam. The high-pressure steam was used to heat some cold streams and to supply heat for reboilers. The grassroot design is shown in Fig. 2. The areas of exchangers E1, E2, E3, E4, E5, E6, E7, E8, E9, E10, E11, and E12 are 162 m^2, 610.8 m^2, 111.9 m^2, 3.6 m^2, 187 m^2, 506 m^2, 336 m^2, 41 m^2, 520 m^2, 1056 m^2, 848 m^2, and 536 m^2, respectively.

The targeting was redone over the temperature scale 20–38°C as the $\Delta T_{\min}$ of the HENs and the targeting results are given in Fig. 3. The figure indicates that the exergy consumption decreases when the heat transfer area needs to be increased. These data can be used to value exergy consumption in the process of heat transfer. The redesign area of the heat recovery system is changed due to different fouling factors selected.

When the HEN system was redesigned using 0–100% of the original setting fouling factors, exergy consumption in the process of heat transfer needed was larger in order to maintain the controlled target temperature. At the same time, the area needed by the system was decreased due to less conservative fouling factors. This variation was shown in Figs. 4 and 5.
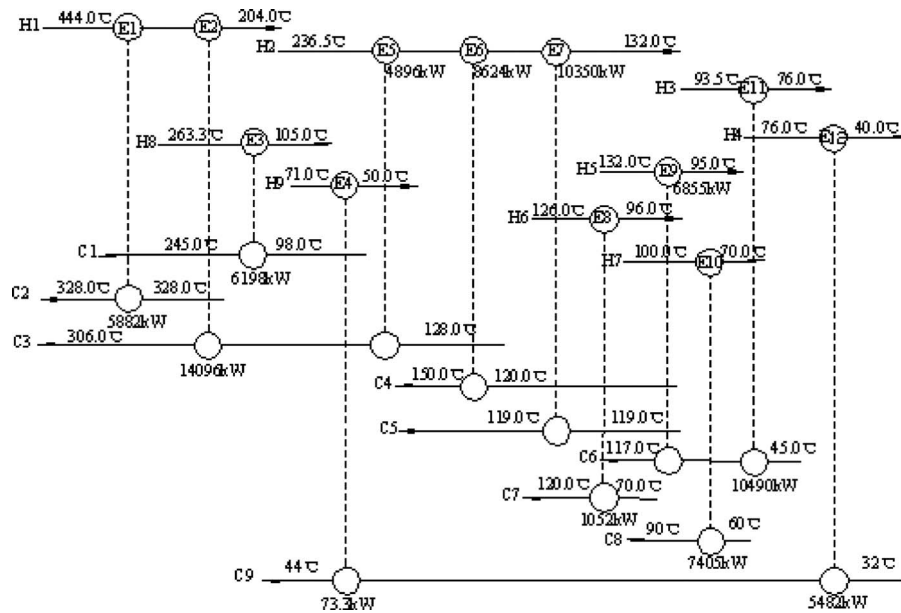
Fig. 2 HENs of grassroot design in local site

In order to value the potential of less conservative fouling factors, trade-off between exergy consumption increase and heat transfer area saving should be established. The results were shown in Fig. 6 from which it can be shown that the optimal less conservative fouling factors are at 80% of the original values. At the same time, redesign area of the system decreased from 4918.3 m^2 to 4568.3 m^2. That is to say, the new system saved 350 m^2 of heat transfer area. If some measures of heat transfer enhancement have been taken, there would be larger area saved. So, it indicates that consideration of less conservative fouling factors will result in notable saving.

4 Conclusions

This work presented a method of calculation of exergy consumption in heat transfer of HENs. An objective function based on exergoeconomic analysis was introduced to assess optimal less fouling factor, based on trade-off between exergy consumption expense and heat exchanger capital cost. The proposed method was applied to an industrial case and encouraging results were
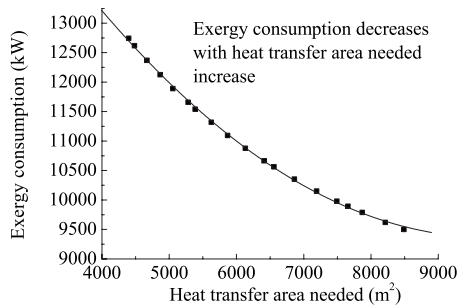
Fig. 3 Exergy consumption versus heat transfer area needed
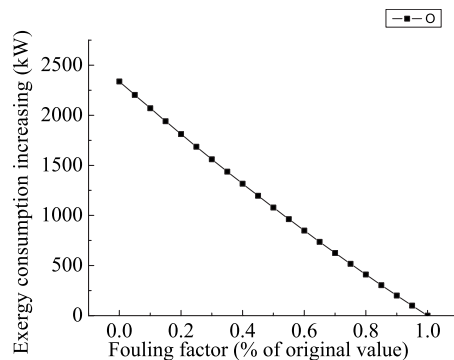
Fig. 5 Exergy consumption increasing versus fouling factor
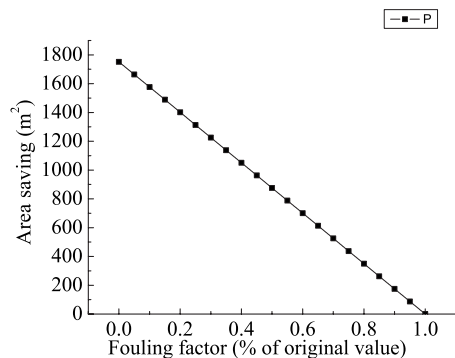
Fig. 4 Area saving versus fouling factor
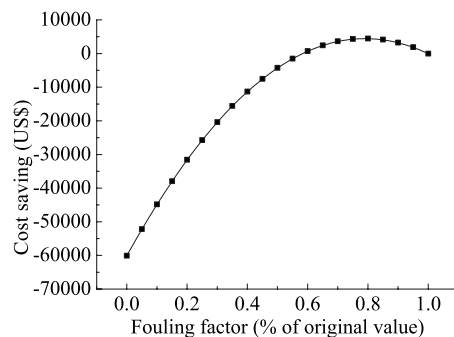
Fig. 6 Cost saving versus fouling factor

obtained, and it was shown that potential usefulness of exergoeconomic analysis in determining the optimal less conservative fouling factor.

Nomenclature

C = annual cost saving (US\$/year)

$C_{I,\text{save}}$ = capital cost saving (US\$/year)

$C_{\text{ex,increase}}$ = exergy consumption increasing (US\$/year)

R_f^* = less conservative thermal resistance due to fouling ($\text{m}^2\,\text{K/W}$)

U_f^* = overall heat transfer coefficient with less conservative fouling considered ($\text{W/m}^2\,\text{K}$)

U_c = clean overall heat transfer coefficient ($\text{W/m}^2\,\text{K}$)

T_A = absolute temperature of point A (K)

T_B = absolute temperature of point B (K)

T_0 = absolute temperature of assumed environment (K)

References

[1] Garrett-Price, B. A., Smith, S. A., and Watts, R. L., 1985, *Fouling of Heat Exchangers*, Noyes, Park Ridge, NJ.

[2] Fryer, P., Melo, L. F., et al., eds., 1988, *Fouling Science and Technology*, Kluwer Academic, Dordrecht, The Netherlands.

[3] Kotjabasakis, E., and Linnhoff, B., 1986, "Sensitivity Tables for the Design of Flexible Processes (1)—How Much Contingency in Heat Exchanger Networks is Cost-Effective?," Chem. Eng. Res. Des., **64**, pp. 197–211.

[4] Ravagnani, M. A. S. S., da Silva, A. P., and Andrade, A. L., 2003, "Detailed Equipment Design in Heat Exchanger Networks Synthesis and Optimization," Appl. Therm. Eng., **23**, pp. 141–151.

[5] Wang, L. K., and Sunden, B., 2001, "Detailed Simulation of Heat Exchanger Networks for Flexibility Consideration," Appl. Therm. Eng., **21**, pp. 1175–1184.

[6] Tsatsaronis, G., Moran, M. J., and Sciubba, E., eds., 1987, *Proceedings of the Fourth International Symposium on Second Law Analysis of Thermal Systems*, Rome, Italy, May 25–29, pp. 81–87.

[7] Rosen, M. A., 2002, "Exergy and Economics: Is Exergy Profitable?," Int. J. Exergy, **2**, pp. 218–220.

[8] Rosen, M. A., and Dincer, I., 2003, "Exergoeconomic Analysis of Power Plants Operating on Various Fuels," Appl. Therm. Eng., **23**, pp. 643–658.

[9] Rosen, M. A., and Dincer, I., 2003, "Exergy-Cost-Energy-Mass Analysis of Thermal Systems and Processes," Energy Convers. Manage., **44**, pp. 1633–1651.

[10] Ayres, R. U., Ayres, L. W., and Martinás, K., 1998, "Exergy, Waste Accounting, and Life-Cycle Analysis," Energy, **23**, pp. 355–363.

[11] Shah, A. J., Carey, V. P., Bash, C. E., and Patel, C. D., 2008, "Exergy Analysis of Data Center Thermal Management Systems," ASME J. Heat Transfer, **130**(2), p. 021401.

[12] Haseli, Y., Dincer, I., and Naterer, G. F., 2008, "Exergy Analysis of Condensation of a Binary Mixture With One Noncondensable Component in a Shell and Tube Condenser," ASME J. Heat Transfer, **130**(8), p. 084504.

Heat Transfer Characteristics of a Swirling Laminar Impinging Jet

Koichi Ichimiya
Mechanical Systems Engineering Division,
Interdisciplinary Graduate School of Medicine
and Engineering,
University of Yamanashi,
Takeda-4, Kofu,
Yamanashi 400-8511, Japan
e-mail: ichimiya@yamanashi.ac.jp

Koji Tsukamoto
Yamaha Marine Co. Ltd.,
1400 Nippashi, Hamamatsu,
Shizuoka 432-8528, Japan

This paper describes the characteristics of the heat transfer and flow of a swirling laminar impinging jet in a comparatively narrow space with a confined wall. Air is impinged on a flat surface with constant wall temperature. The heat transfer and flow field were analyzed numerically by solving three-dimensional governing equations. Heat transfer experiment and flow visualization were also performed. Numerical heat transfer was compared with experimental results. Temperature distribution and velocity vectors in the space were obtained for various swirl numbers at Reynolds number $Re = 2000$. The numerical and experimental results show that the swirling jet enhances or depresses the local heat transfer, and the average Nusselt number ratio with and without swirl takes a peak at a certain swirl number. [DOI: 10.1115/1.3211870]

Keywords: impinging jet, swirl, heat transfer enhancement, swirl number

1 Introduction

Jet impingement systems received considerable attention and comprehensible reviews are available [1,2]. There are many factors which affect the local heat transfer and mass transfer, namely, the nozzle shape [3], the attitude [4], the number [5], and so on. These studies have been confined to nonswirling flows. The swirl can markedly affect the flow characteristics near the impingement surface. Huang et al. [6] numerically calculated the effect of introducing swirl in the jet flow and heat transfer under a laminar impinging jet. The center-line axial velocity decays more rapidly and increases in the spreading rate of the jet with increase in swirl number. A recirculating bubble is formed on the impingement plate at the stagnation point for swirl number above 0.43. The Stanton number decreases slightly with the swirl number from 0 to 0.2. Ward and Mahmood [7] experimented on heat and mass transfer. Mass transfer rates were determined using naphthalene technique. The Chilton–Colburn analogy was employed to infer the corresponding heat transfer coefficients. They found that the swirl reduced the heat transfer and the average Nusselt number was correlated by a simple power-law dependence on swirl number, Reynolds number, and nozzle-to-plate space. Wicker and Eaton [8] investigated a passive particle dispersion control technique in which longitudinal vortices were injected into a developing coaxial swirling jet with sufficient annular swirl. Wen and Jang [9] performed heat transfer and flow visualization experiments to investigate the performance of two swirling jets, namely, longitudinal swirling and cross swirling. The heat transfer rate increased as the jet spacing decreases owing to the reduction in the impingement surface area. Cross swirling supplied the better heat transfer performance than that of the longitudinal swirling. The percentage increase in the heat transfer enhancement approached to the range of 9–14%. Ichimiya and Tsukamoto [10] carried out the heat transfer characteristics of a circular turbulent impinging jet with a swirl using air as a working fluid. Swirling was generated by air from two-inserting nozzles on the side surface of the main nozzle. The swirl effect was remarkable in higher jet spacing and brought about the peak heat transfer enhancement at a certain momentum ratio. Recently, heat transfer removal or improvement is requested in a narrow space corresponding to a compact facility with low power, low noise and low vibration. In such a meaning, the research on a swirling impinging jet is needed in laminar flow situation and in dimensionless space $h/D < 1$.

In the present study, a laminar, swirling impinging air jet in a confined flow passage was examined numerically and experimentally for various swirl numbers at fixed Reynolds number. Local and average heat transfer and flow characteristics were examined. Thermal performance was evaluated on the average Nusselt number ratio with and without swirl for various swirl numbers.

2 Numerical Analysis

Figure 1 shows the coordinate system. This is composed of three-dimensional circular system (r, θ, z) and the origin is the center point on impingement surface. The gravity works along the negative direction of z-axis. Nozzle diameters $D = 30$ mm, space $h = 10$ mm, radius of flow passage $R_n = 75$ mm, and peripheral direction $\theta = 0 - 360$ deg. Fluid is incompressible and Newtonian fluid without heat generation. Impingement surface temperature is $T_w = 50 °C$ and upper wall of flow passage is insulated thermally.

The conservation of mass

$$\frac{1}{r}\frac{\partial rU}{\partial r} + \frac{1}{r}\frac{\partial V}{\partial \theta} + \frac{\partial W}{\partial z} = 0 \tag{1}$$

The conservation of momentum

$$\frac{\partial U}{\partial t} + \frac{1}{r}\frac{\partial rUU}{\partial r} + \frac{1}{r}\frac{\partial VU}{\partial \theta} + \frac{\partial WU}{\partial z} - \frac{VV}{r}$$
$$= -\frac{1}{\rho}\frac{\partial P}{\partial r} + \frac{1}{r}\frac{\partial r\tau_{rr}}{\partial r} + \frac{1}{r}\frac{\partial \tau_{\theta r}}{\partial \theta} + \frac{\partial \tau_{zr}}{\partial z} - \frac{\tau_{\theta\theta}}{r} \tag{2}$$

$$\frac{\partial V}{\partial t} + \frac{1}{r}\frac{\partial rUV}{\partial r} + \frac{1}{r}\frac{\partial VV}{\partial \theta} + \frac{\partial WV}{\partial z} - \frac{UV}{r}$$
$$= -\frac{1}{\rho r}\frac{\partial P}{\partial \theta} + \frac{1}{r^2}\frac{\partial r^2\tau_{r\theta}}{\partial r} + \frac{1}{r}\frac{\partial \tau_{\theta\theta}}{\partial \theta} + \frac{\partial \tau_{z\theta}}{\partial z} \tag{3}$$

$$\frac{\partial W}{\partial t} + \frac{1}{r}\frac{\partial rUW}{\partial r} + \frac{1}{r}\frac{\partial VW}{\partial \theta} + \frac{\partial WW}{\partial z}$$
$$= -\frac{1}{\rho}\frac{\partial P}{\partial z} + \frac{1}{r}\frac{\partial r\tau_{rz}}{\partial r} + \frac{1}{r}\frac{\partial \tau_{\theta z}}{\partial \theta} + \frac{\partial \tau_{zz}}{\partial z} - g \ \beta(T - T_o) \tag{4}$$

where

$$\tau_{rr} = 2\nu\frac{\partial U}{\partial r} \quad \tau_{\theta\theta} = 2\nu\left(\frac{1}{r}\frac{\partial V}{\partial \theta} + \frac{U}{r}\right) \quad \tau_{zz} = 2\nu\frac{\partial W}{\partial z}$$
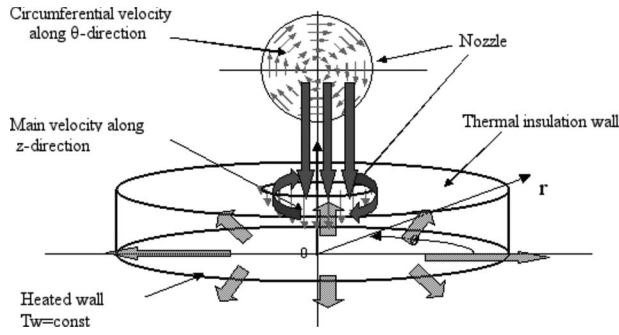
Fig. 1 Coordinate system

$$\tau_{r\theta} = \tau_{\theta r} = \nu\left(\frac{\partial V}{\partial r} - \frac{V}{r} + \frac{1}{r}\frac{\partial U}{\partial \theta}\right) \quad \tau_{\theta z} = \tau_{z\theta} = \nu\left(\frac{1}{r}\frac{\partial W}{\partial \theta} + \frac{\partial V}{\partial z}\right)$$

$$\tau_{zr} = \tau_{rz} = \nu\left(\frac{\partial U}{\partial z} + \frac{\partial W}{\partial r}\right)$$

The conservation of energy

$$C_p\rho\left(\frac{\partial T}{\partial t} + \frac{1}{r}\frac{\partial rUT}{\partial r} + \frac{1}{r}\frac{\partial VT}{\partial \theta} + \frac{\partial WT}{\partial z}\right) = \frac{1}{r}\frac{\partial rq_r}{\partial r} + \frac{1}{r}\frac{\partial q_\theta}{\partial \theta} + \frac{\partial q_z}{\partial z} \tag{5}$$

where

$$q_r = \lambda\frac{\partial T}{\partial r}, \quad q_\theta = \frac{\lambda}{r}\frac{\partial T}{\partial \theta}, \quad q_z = \lambda\frac{\partial T}{\partial z}$$

The Boussinesq approximation was applied in buoyancy term in momentum equation. Thermal radiation was neglected in energy equation. Temperature dependence was considered on the thermal conductivity and kinematic viscosity of air. At nozzle exit, air whose temperature was $T_{in}=20°C$, was jetted with z-component and peripheral velocity components. The z-directional velocity is fully developed. Peripheral velocity V is as follows:

$$0 < r < r_t: \quad V = cr$$
$$r_t < r < R_n: \quad V = cr\{1 - (1 - r_t/r)/(1 - r_t/R_n)\} \tag{6}$$

where r_t means the distance where the swirl effect appears and c is determined by the mass conservation.

Swirl number, Sw, is determined by next equation.

$$\text{Sw} = G_\theta/(G_z D/2) \tag{7}$$

where

$$G_\theta = \int \rho r V W 2\pi r dr \quad \text{and} \quad G_z = \int \rho W^2 2\pi r dr$$

At $t=0$, the air is quiescent and the temperature is $T_o=20°C$. At the exit of flow passage, the second derivative of temperature and the first derivative of velocity were zero.

The unsteady three-dimensional governing equations were solved numerically with the control volume method. The system is geometrically symmetrical. However, the computational domain is whole area ($\theta=0–360°$) because of the inclusion of the buoyancy force and the swirl flow. The velocity and pressure were gained using the SIMPLE algorithm [11] and the QUICK scheme with the third order upper wind method [12]. The number of meshes were $75(r) \times 360(\theta) \times 10(z)$. One mesh is $\Delta r=1$ mm, $\Delta\theta=1.0$ deg, and $\Delta z=1$ mm. However, the first step from the impingement surface is $\Delta z=0.5$ mm. The time step Δt is 10^{-4} s to 10^{-3} s for numerical stability. Solution accuracy was studied
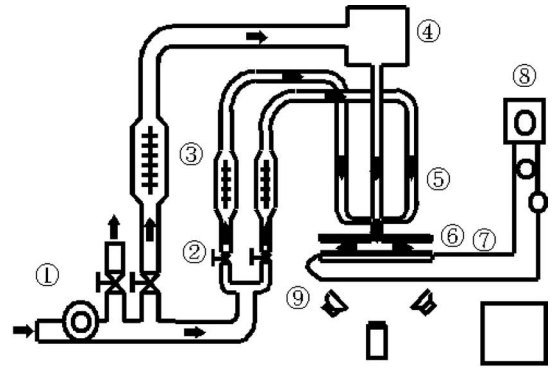
① Blower ②Valve ③Flow Meter ④Mixing Chamber
⑤Nozzle ⑥Stainless Steel Foil ⑦Liquid Crystal
⑧Slide Regulator ⑨Halogen Lamp ⑩C.C.D. Camera
(a)

(b)
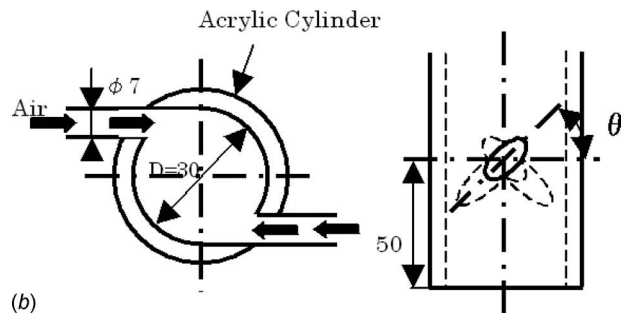
Fig. 2 Experimental apparatus: (a) a schematic diagram and (b) two-inserting nozzles for swirl generation

from solutions on successive refined grids. The root mean square error defined by Fletcher [13] was less than 0.05 for a grid employed to predict the velocity and temperature.

Calculation was performed at the following conditions: Reynolds number Re=2000, space $h=10$ mm, and swirl number Sw=0.410, 0.675, and 1.186.

The numerical results were evaluated by the velocity vector, the temperature distribution, and the local and average Nusselt numbers.

3 Experiment

Figure 2(a) shows a schematic diagram of the experimental apparatus. The apparatus was composed of the flow delivery passage, the heated section including the impingement surface, and the temperature measuring system. After the air was compressed in a blower, air was divided into three flow passages. One was an axial air supply and the other two were an angular air supply connected to the side surface of a circular nozzle for the generation of a swirl flow. The inner diameter of the main nozzle was $D=30$ mm. The upper wall, set at the same level of the nozzle, was made of acrylic resin and is thermally insulated. The impingement section was composed of a stainless steel foil, a thermosensitive liquid crystal sheet, and a transparent acrylic plate. These are closely connected by binding tapes with transparency 99%. The foil was heated electrically. The impingement surface temperature was measured by transforming the color intensity of the thermosensitive liquid crystal sheet to the corresponding temperature. The back side of the impingement section was illuminated by four halogen lamps. These lamps were equipped with infrared radiation absorption filters to prevent radiative heating of the thermosensitive liquid crystal. The color image was converted into an

1 [m/s] →
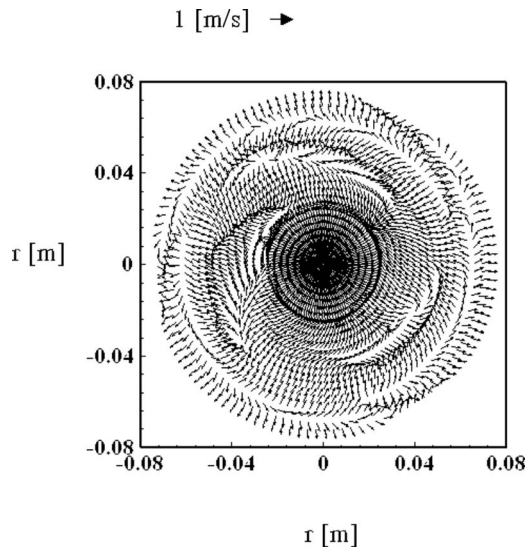
Fig. 3 Velocity vector (Sw=1.186)

(a)

(b)

Fig. 5 Flow visualization (Sw=1.08) (a) swirl flow at the nozzle exit and (b) flow across the flow passage

electrical signal by a CCD camera. The relationship between temperature and color intensity was calibrated in advance. The local heat flux was corrected by considering the thermal conduction in the impingement section using the detailed temperature distribution and the local Nusselt number was obtained by using the net heat flux. Figure 2(b) shows two-inserting nozzles on the side surface of the main nozzle for the generation of a swirl flow. The inner diameter of an inserting nozzle is $D=7$ mm. The θ in the figure is an inserting angle and is from 0 deg to 60 deg. The distance from the end of the main nozzle to the inserting nozzle is 50 mm.

The flow visualization was performed using a smoke injection method.

Experiments were carried out in the following conditions: the Reynolds number at nozzle exit Re=1900, the space between nozzle and impingement surface $h=10$ mm, and the swirl numbers Sw=0.31, 0.6, and 1.08.

4 Results and Discussions

4.1 Flow. In the first stage, the numerical results were presented.

Figure 3 shows the velocity vector at $z=0.5$ mm from the impingement surface (r,θ) for swirl number Sw=1.186. The origin (0,0) corresponds to the nozzle center. Radial flow runs coaxially from $r=0$ mm to $r=25$ mm. After that peripheral flows are generated and are rolled up to $r=60$ mm. In the present case, the swirl spreads to the downstream region

Figure 4 shows velocity vector and temperature distribution across the section for Sw=1.186. The $r=0$ means the nozzle cen-

ter and $r=0-15$ mm is the nozzle radius. After the jet from the nozzle impinged on the flat heated surface, fluid rises up from $r=25$ mm and approaches to upper wall. A recirculating flow is generated near the impingement surface from $r=30$ mm to $r=50$ mm. The flow is divided into three: perpendicular flow to the impingement surface, radial flow after impingement, and peripheral flow by the swirl. Fluid temperature increased there and thermal stratified layer is generated. Therefore, local temperature gradient becomes low at the impingement surface. Comparatively, low temperature fluid is involved at $r=60$ mm.

Figures 5(a) and 5(b) show the flow visualization. Figure 5(a) presents the swirl generation from two-inserting nozzle on the side surface of the main nozzle. This swirl jet was released from the main circular nozzle. Figure 5(b) shows the flow situation after the swirl jet impinged on the heated surface. The picture shows that the flow rises up corresponding to Fig. 4 and a recirculating bubble is generated at the downstream region. Therefore, the flow visualization verifies qualitatively with numerical results.

4.2 Heat Transfer. Figure 6 shows the isothermal lines at $z=0.5$ mm from the impingement surface for swirl number Sw=1.186 corresponding to Figs. 3 and 4. The origin (0,0) corresponds to the nozzle center. The temperature at a half-mesh from the impingement surface, T is expressed by $T=T_w-(q\delta/\lambda)$ where q is the local heat flux, δ is a half-mesh away from the impinge-
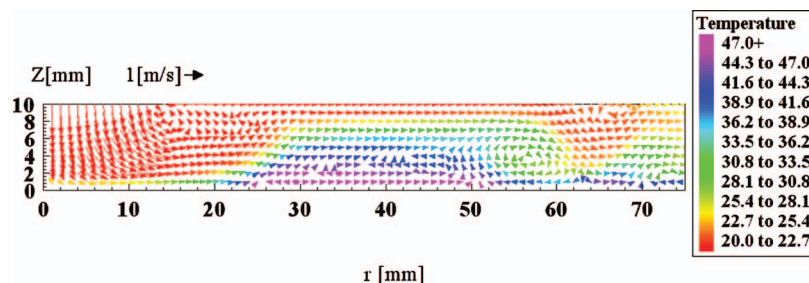
Fig. 4 Velocity vector and temperature distribution across the section (Sw=1.186)
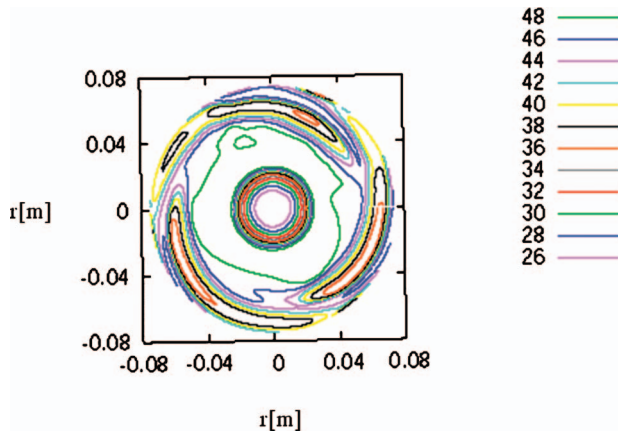
Fig. 6 Isothermal lines (Sw=1.186)

Fig. 8 Local Nusselt umber (experiment) (Sw=1.08)

ment surface, and λ is the thermal conductivity of air. Therefore, the temperature corresponds to the local heat flux. Coaxial isothermal lines in Fig. 6 correspond to coaxial radial flow presented in Fig. 3. Swirl affects in the downstream region because the swirl number is comparatively high. Temperature distribution is divided into three peripherally closed-isothermal lines regions in radial direction $r=40-60$ m.

Figure 7 shows the local Nusselt number distribution corresponding to isothermal lines for Sw=1.186, shown in Fig. 6. Local heat transfer is high beneath the nozzle because axial flow impinged. The high swirl number brings about the recirculation bubble. The plateau region can be found from $r=30$ mm to $r=50$ mm corresponding to the recirculating flow region. Flow mixing is promoted and heat transfer is recovered at downstream region by swirling at the nozzle.

Figure 8 shows the two-dimensional distribution of the local Nusselt number (Sw=1.08) by experiment. The local Nusselt number is high and is almost coaxial beneath the nozzle. It decreases along the flow direction and recovers at downstream region because of a swirl effect. This behavior of experimental results agrees with that of numerical results.

In the next step, the local Nusselt numbers was averaged peripherally. The average Nusselt numbers are presented along radial direction for various swirl numbers in Fig. 9. Sw=0 means normal impinging jet without swirl. In the case of Sw=0.410 and 0.675, heat transfer is improved and particularly oscillates downwards due to the swirl. In the case of Sw=1.186, heat transfer is depressed rapidly due to a rising flow and a recirculating flow

corresponding to Fig. 4 and increases near $r=60$ mm because a high swirl number means the high spreading rate of the jet to downstream region.

Figure 10 shows the peripherally averaged Nusselt number by experiment along radial direction. The -●- line denotes the value without swirl (Sw=0). The values in Sw=0.31 and 0.6 are higher than those in Sw=0 and present the heat transfer improvement. However, in Sw=1.08, it decreases from the center $r=0$ mm to $r=60$ mm and recovers in the downstream region $r=60-75$ mm. This behavior agrees nearly with numerical values, although there is a little difference near the exit.

In addition, the peripherally averaged Nusselt numbers were averaged along radial direction from $r=0$ to $r=65$ mm to evaluate the thermal performance. The relationship between the average Nusselt number ratio with and without swirl and various swirl numbers is shown in Fig. 11. The symbols ●, ▲, and ■ mean without the swirl, the numerical results with the swirl, and the experimental results with the swirl, respectively. The value higher than 1 means heat transfer improvement and the value lower than
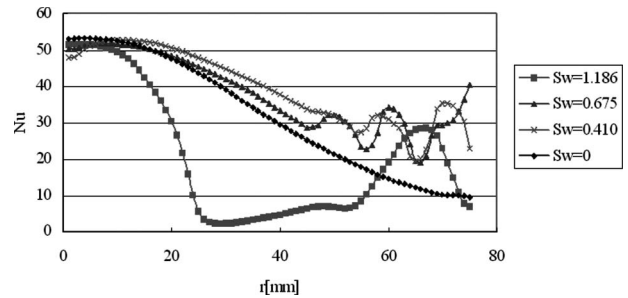
Fig. 9 Peripherally averaged Nusselt number (numerical calculation)
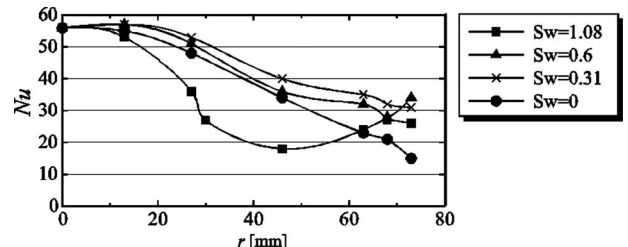
Fig. 10 Peripherally averaged Nusselt number (experiment)

Fig. 7 Local Nusselt number (numerical calculation) (Sw=1.186)
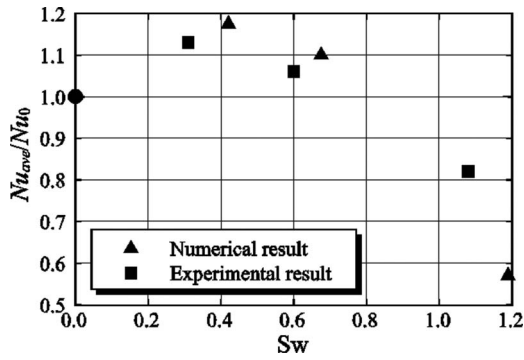
Fig. 11 Average Nusselt number ratio

1 does heat transfer depression. According to Fig. 11, Nu_{ave}/Nu_o increases with Sw, takes a peak near $Sw \cong 0.40$ and after that it decreases with increase of Sw. This behavior is same in both numerical and experimental results. This means that the swirl number, which maximizes the heat transfer, exists. The peak swirl number depends on the Reynolds number and the space between nozzle and impingement surface. Consequently, a swirl brings about both heat transfer enhancement and depression.

5   Conclusions

Heat transfer and flow characteristics of swirl-type impinging jet were numerically and experimentally evaluated using the velocity vector, the flow visualization, the temperature distribution, the local Nusselt number, and the average Nusselt number ratio with and without swirl. Concluding remarks are as follows.

(1) The swirl at nozzle exit brings about both heat transfer improvement and depression.
(2) The average Nusselt number ratio with and without swirl takes a peak at a certain swirl number.
(3) The flow acceleration and flow mixing promotion near the impingement surface by a swirl brings about heat transfer enhancement.
(4) The rising flow and recirculating flow by a swirl bring about heat transfer depression.

Nomenclature

C_p = specific heat, J/kg K
D = nozzle diameter, mm or m
H = space between nozzle and impingement surface, mm or m
Nu = local Nusselt number, $\alpha D/\lambda$
Nu_{ave} = average Nusselt number
Nu_o = Nusselt number without swirl
Re = Reynolds number at nozzle exit, uD/ν
R_n = distance from the center to the exit of flow passage
Sw = Swirl number (refer to Eq. (7))
r, θ, z = coordinate system
T = temperature, °C or K
T_{in} = air temperature at nozzle exit
T_o = air temperature at initial condition
T_w = impingement surface temperature
U = velocity along radial direction, m/s
V = velocity along peripheral direction, m/s
W = velocity along axial direction, m/s
α = heat transfer coefficient, W/m^2 K
λ = thermal conductivity of air, W/m K
ν = kinematic viscosity of air, m^2/s
ρ = density of air, kg/m^3

References

[1] Martin, H., 1977, "Heat and Mass Transfer Between Impinging Gas Jets and Solid Surface," *Advances in Heat Transfer*, Vol. 13, J. P. Hartnett and T. F. Irvine, eds., Academic, New York.
[2] Viskanta, R., 1993, "Heat Transfer to Impinging Isothermal Gas and Flame Jets," Exp. Therm. Fluid Sci., **6**, pp. 111–134.
[3] Ichimiya, K., 2003, "Heat Transfer Characteristics of an Annular Turbulent Impinging Jet With a Confined Wall Measured by Thermosensitive Liquid Crystal," Heat Mass Transfer, **39**, pp. 545–551.
[4] Ichimiya, K., 1995, "Heat Transfer and Flow Characteristics of an Oblique Turbulent Impinging Jet Within Confined Walls," Trans. ASME, Ser. C: J. Heat Transfer, **117**, pp. 316–322.
[5] Ichimiya, K., and Hosaka, N., 1992, "Experimental Study of Heat Transfer Characteristics Due to Confined Impinging Two-Dimensional Jets," Exp. Therm. Fluid Sci., **5**, pp. 803–807.
[6] Huang, B., Douglas, W. J. M., and Mujumdar, A. S., 1978, "Heat Transfer Under a Laminar Swirling Impinging Jet—A numerical Study," *Proceedings of the Sixth International Heat Transfer Conference (Toronto)*, pp. 311–316.
[7] Ward, J., and Mahmood, M., 1982, "Heat Transfer From a Turbulent, Swirling, Impinging Jet," *Proceedings of the Seventh International Heat Transfer Conference (Munchen)*, pp. 401–408.
[8] Wicker, R. B., and Eaton, J. K., 1999, "Effect of Injected Longitudinal Vorticity on Particle Dispersion in a Swirling, Coaxial Jet," Trans. ASME, Ser. C: J. Heat Transfer, **121**, pp. 766–772.
[9] Wen, M. Y., and Jang, K. J., 2003, "An Impingement Cooling on a Flat Surface by Using Circular Jet With Longitudinal Swirling Strips," Int. J. Heat Mass Transfer, **46**, pp. 4657–4667.
[10] Ichimiya, K., and Tsukamoto, K., 2006, "Heat Transfer From an Inflow-Type Swirling Turbulent Impinging Jet," JSME Int. J., **49**, pp. 995–999.
[11] Patankar, S. V., 1980, *Numerical Heat Transfer and Fluid Flow*, Hemisphere, London.
[12] Leonald, B. P., 1980, "The QUICK Algorithm," *Computer Methods in Fluids*, Pentech, Plymouth, UK.
[13] Fletcher, C. A. J., 1988, *Computational Techniques for Fluid Dynamics I*, *Springer Series in Computational Physics*, Springer, Berlin.

Thermal Properties for Bulk Silicon Based on the Determination of Relaxation Times Using Molecular Dynamics

Javier V. Goicochea
Department of Mechanical Engineering,
Carnegie Mellon University,
Pittsburgh, PA 15213

Marcela Madrid
Pittsburgh Supercomputing Center,
Pittsburgh, PA 15213

Cristina Amon
Department of Mechanical and Industrial
Engineering,
University of Toronto,
Toronto, ON, M5S 1A4, Canada

Molecular dynamics simulations are performed to estimate acoustical and optical phonon relaxation times, dispersion relations, group velocities, and specific heat of silicon needed to solve the Boltzmann transport equation (BTE) at 300 K and 1000 K. The relaxation times are calculated from the temporal decay of the autocorrelation function of the fluctuation of total energy of each normal mode in the ⟨100⟩ family of directions, where the total energy of each mode is obtained from the normal mode decomposition of the motion of the silicon atoms over a period of time. Additionally, silicon dispersion relations are directly determined from the equipartition theorem obtained from the normal mode decomposition. The impact of the anharmonic nature of the potential energy function on the thermal expansion of the crystal is determined by computing the lattice parameter at the cited temperatures using a NPT (i.e., constant number of atoms, pressure, and temperature) ensemble, and are compared with experimental values reported in the literature and with those computed analytically using the quasiharmonic approximation. The dependence of the relaxation times with respect to the frequency is identified with two functions that follow the functional form of the relaxation time expressions reported in the literature. From these functions a simplified version of relaxation times for each normal mode is extracted. Properties, such as group and phase velocities, thermal conductivity, and mean free path, needed to further develop a methodology for the thermal analysis of electronic devices (i.e., from nano- to macroscales) are determined once the relaxation times and dispersion relations are obtained. The thermal properties are validated by comparing the BTE-based thermal conductivity against the predictions obtained from the Green–Kubo method. It is found that the relaxation times closely resemble the ones obtained from perturbation theory at high temperatures; the contribution to the thermal conductivity of the transverse acoustic, longitudinal acoustic, and longitudinal optical modes being approximately 30%, 60%, and 10%, respectively, and the contribution of the transverse optical mode negligible.
[DOI: 10.1115/1.3211853]

1 Introduction

In pure semiconductor materials, such as silicon and germanium, which are the main components of modern transistors—including silicon on insulator, silicon on silicon-germanium, and strained silicon—the thermal transport is described in terms of quantized lattice vibrations or phonons [1]. Phonons undergo different collisions or scattering mechanisms (e.g., phonon-phonon, phonon-impurities, phonon-boundaries, and phonon-defects), which play a crucial role on describing how the heat is transported in the crystalline structure. These interactions are conveniently represented by the relaxation time (τ_m) of each interacting phonon mode (m). The relaxation time is defined as the time it takes to return to equilibrium when one phonon mode has been perturbed. Under the single-mode relaxation time (SMRT) approximation every phonon is assigned a relaxation time corresponding to the net effect of the scattering mechanisms coexisting in a particular situation. This allows replacing the scattering term in the Boltzmann transport equation (BTE) by

$$-v_{g,m} \cdot \nabla T \frac{\partial n_m}{\partial T} + \left(\frac{\partial n_m}{\partial t} \right)_{\text{scattering}} \rightarrow \left(\frac{\partial n_m}{\partial t} \right)_{\text{scattering}} = \frac{n_m^o - n_m}{\tau_m} \qquad (1)$$

where T is the temperature, t is the time, n_m is the phonon mode occupation number, and n_m^o is the equilibrium phonon occupation number given by the Bose–Einstein distribution. The left part of Eq. (1) represents the BTE equation for a mode m under a temperature gradient.

Several phenomenological models exist to estimate phonon relaxation times. Unfortunately, the complexity of the scattering mechanisms affects their reliability in situations outside the range for which they were developed. Particular considerations have to be taken to avoid large discrepancies when applied to different semiconductor materials [2–6]. Furthermore, important simplifications and assumptions are involved in their derivation such as isotropic crystal, elastic continuum behavior, piecewise linear dispersion relations, third-order anharmonic expansions, etc. Errors associated with these assumptions can be hidden by the use of fitting parameters [5,7,8]. In these models, the contribution of the optical modes to thermal conductivity has been considered negligible. Different authors [9–13] have pointed out that optical phonons can have a significant effect on the creation of hot spots during transient Joule heating events due to the confinement of phonons, which can severely impact performance and reliability of transistors and other electronic devices. Notable are the works of Pop et al. [11,14] and more recently Rowlette and Goodson

[12], who have developed nonequilibrium electron and electron-phonon transport models, respectively, applicable to nanometer-scale field-effect transistors. In addition, Sinha et al. [13] studied the scattering mechanisms of longitudinal optical phonons at hotpots in silicon using molecular dynamics (MD).

Using molecular dynamics, Ladd et al. [15] calculated the relaxation times from the autocorrelation function of the fluctuation of the potential energy. The later was obtained from the normal modes decomposition of the system over a period of time. Later, McGaughey and Kaviany [8] modified this approach by considering the fluctuation of the total energy (potential+kinetic) of each mode. They applied the method to compute the relaxation times of argon for a range of temperatures from 20 K to 80 K and was validated using the Green–Kubo method for thermal conductivity. Similarly, Sun and Murthy [16] reported transverse acoustic (TA) and longitudinal acoustic (LA) phonon relaxation times using an environmental-dependent interatomic potential (EDIP) for silicon. Third- and fourth-order polynomial functions were used to fit the relaxation times of the TA and LA modes, respectively. More recently, Henry and Chen following the same procedure have also used the EDIP potential to determine the relaxation times of silicon at different molecular temperatures and symmetry directions (i.e., [100], [110], and [111]).

In this work, as a first step to develop a methodology capable of integrating all scales involved in the thermal analysis of electronic devices (i.e., from nano- to macroscales) [17], we estimate different thermal properties of silicon at 300 K and 1000 K. These are obtained from the determination of the relaxation times for the acoustical and optical normal modes and the dispersion relations of bulk silicon in the $\langle 100 \rangle$ family of directions. Here, we apply and extend the method reported by McGaughey and Kaviany [8] for silicon, in which the relaxation times are calculated from the temporal decay of the autocorrelation function of the fluctuation of total energy of each normal mode. These properties can be used as input for other less time consuming numerical tools, such as lattice Boltzmann, phonon Monte Carlo, etc., to perform transient and steady state thermal predictions on a variety of situations. For simplicity, we have used the word *phonon* instead of *normal mode*, however, note that the phonon's energy is quantized, while the energy of a normal mode computed with MD is a continuous function.

Silicon and germanium crystallize into a diamond structure (i.e., fcc lattice with two atoms per unit cell). To maintain this structure, the interatomic potential function between silicon atoms must include two- and three-body terms. As a result, the numerical determination of the forces between silicon atoms is computationally demanding. The presence of two atoms per unit cell produces optical modes, which double the number of normal modes. Moreover, the thermal conductivity of silicon is several orders of magnitude greater than that for argon, resulting in much longer correlation times. These characteristics make the application of the method to silicon challenging.

The advantages of using molecular simulations to compute the relaxation times are that (i) no assumptions about the nature of the thermal transport are required; (ii) the anharmonic nature of the potential energy function is captured as a function of temperature; (iii) no explicit simplification about the lattice structure or the contribution of anharmonic terms is made; (iv) well documented interatomic potentials for silicon and other semiconductor materials are available in the literature (e.g., Stillinger–Weber (SW) [18], Tersoff [19], or EDIP [20]); and (v) the method can be extended to other materials and geometries with relative facility. In this work, we use the Stillinger–Weber potential for silicon [18].

As illustrated in the flow chart shown in Fig. 1, we start building our model by assessing the impact of the anharmonic nature of the potential energy function over the thermal expansion of the crystal. The lattice parameter (a) is determined using MD in the NPT ensemble (i.e., constant number of atoms, pressure, and temperature) at 300 K and 1000 K. The values of the lattice parameter
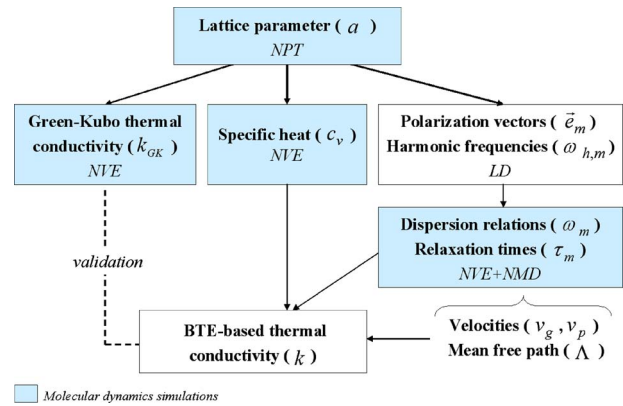
Fig. 1 Flow chart of calculations performed in this work

at different temperatures are compared with those obtained experimentally and analytically with the quasiharmonic approximation (QHMK). Once the lattice parameter is determined, we compute the specific heat per degree of freedom (c_v), the Green–Kubo thermal conductivity (k_{GK}), the dispersion relations (ω_m), and the relaxation times (τ_m) using MD in the NVE ensemble (i.e., constant number of atoms, volume, and energy) at 300 and 1000 K. We identify the dependence of the relaxation times on the frequency by means of two fitted functions. Using the MD relaxation times and the normal mode decomposition we determine other thermal properties that complement our model, such as group (v_g) and phase (v_p) velocities, mean free path (Λ) of each mode, and the BTE-based thermal conductivity (k). We validate our model by comparing the BTE-based thermal conductivities with those previously predicted using the Green–Kubo method at the studied temperatures.

This work is structured as follows. In Sec. 2 we review the different relaxation time expressions commonly used in thermal models, and how these can be computed using MD and the normal mode decomposition. Details of the four types of MD simulations needed to construct our model are given in Sec. 3. Then, in Secs. 4 and 5, we present the MD results for the relaxation times, dispersion relations, BTE-based thermal conductivity, and other thermal properties. Section 6 shows the validation of our properties, whereas Sec. 7 presents the limitations to further use our model in other numerical tools. Lastly, the summary and conclusions of our findings are given in Sec. 8.

2 Literature Review

2.1 Phonon Relaxation Time Expressions. Herring [21] derived relaxation time expressions in the acoustic limit of the form $1/\tau(q) \propto q^c T^{5-c}$, where T is the temperature and c is a parameter that depends on the crystal class (e.g., cubic, orthorhombic, etc.) and on the phonon branch (for silicon $c=1$ for transverse modes and $c=2$ for longitudinal modes). For low-frequency longitudinal modes, the relaxation times are proportional to the square of the frequency and cube of the temperature (i.e., $1/\tau(q) \propto q^2 T^3 \propto \omega^2 T^3$), while at high temperatures (i.e., $T > \theta_D$, where θ_D is the Debye temperature) the dependence is linear in temperature (i.e., $1/\tau(q) \propto \omega^2 T$). Additionally, for transverse modes at high temperature the dependence on frequency is linear (i.e., $1/\tau(q) \propto \omega T$).

Klemens [22] derived relaxation times expressions for Umklapp-processes using a generalized interaction matrix ($c(q,q',q'')$) assumed to be a function of the Grüneisen parameter and the cube of the participating mode frequencies (i.e., $c(q,q',q'') \propto \gamma \omega \omega' \omega''$). The resulting relaxation time expressions took the form

$$1/\tau \propto \omega^2 T^3 \exp(-\theta_D/\alpha T) \quad \text{and} \quad 1/\tau \propto \omega^2 T \qquad (2)$$

for low and high temperatures, respectively [22]. Carruthers [23], on the other hand, suggested a simple solution to the BTE in steady state where the relaxation times are taken to be $1/\tau = b(T)\omega^2 + I\omega^4$. The first and second terms represent the relaxation times due to phonon-phonon and phonon-impurity scattering, respectively, and $b(T)$ and I are fitted constants.

Despite the fact that the relaxation times for acoustic modes have been broadly studied in the literature, the study of relaxation times for optical modes has been very limited. Klemens [24] and Ecsedy and Klemens [25] derived simple expressions for the relaxation times of these modes. Their derivations embrace important assumptions such as long-wave limit (i.e., $q \sim 0$) and negligible group velocity (i.e., flat dispersion). The resulting expressions are proportional to

$$1/\tau \propto \omega \quad \text{and} \quad 1/\tau \propto [(\omega_O - \omega)/\omega_D]^2 \omega^2 T \tag{3}$$

where ω_O and ω_D are constants related to the average frequency of all optical modes and the Debye frequency, respectively.

Several decades later, Han and Klemens [26] proposed a two-stage model for thermal conductivity at low temperatures, which considers dispersion between the frequency and wave vector. The model provides an estimation of the thermal conductivity using just one fitted value—the Grüneisen parameter (γ). The functional form of the general relaxation time expression used in their model is

$$\frac{1}{\tau_U} \propto \gamma^2 \int_{q'} dS' \int \frac{d\Delta\omega}{v_g} \omega\omega'\omega''\delta_t(\Delta\omega)\exp\left(\frac{-\hbar\omega'}{k_B T}\right) \tag{4}$$

where $\hbar$ is the Plank constant, k_B is the Boltzmann constant, $\Delta\omega$ is a term related to resonance condition equal to $\omega + \omega' - \omega''$, δ_t is a delta function, and S' is the surface over which the selection rules are satisfied simultaneously (valid only for three-phonon scattering). For interactions of the type transverse+transverse$\leftrightarrow$longitudinal, after applying the corresponding energy and quasi-momentum conservation rules, the expression takes the form

$$\frac{1}{\tau_U} \propto \gamma^2 \omega_i \omega_T (\omega_i + \omega_T) r_c^2 \exp\left(\frac{-\hbar\omega_T}{k_B T}\right) \tag{5}$$

while for interactions of the type transverse+longitudinal$\leftrightarrow$longitudinal, the expression takes the form

$$\frac{1}{\tau_U} \propto \gamma^2 \omega_i (\omega_L - \omega_i) \omega_L r_c^2 \exp\left(\frac{-\hbar\omega_T}{k_B T}\right) \tag{6}$$

In these equations, the integral over S' is reduced to a circle of radius r_c, and ω_T and ω_L are the values of the frequency for the transversal and longitudinal modes at the edge of the first Brillouin zone (BZ).

2.2 MD Relaxation Times Determination. Under the harmonic approximation, the total energy of each mode m for a classical system can be written as [27]

$$E_{m,t} = \frac{\omega_{h,m}{}^2 Q_m^*(\mathbf{q},\lambda) Q_m(\mathbf{q},\lambda)}{2} + \frac{\dot{Q}_m^*(\mathbf{q},\lambda)\dot{Q}_m(\mathbf{q},\lambda)}{2} \tag{7}$$

where $\omega_{h,m}$ is the harmonic frequency, and the first and second terms on the right hand side of the equation represent the potential energy and kinetic energy of the mode m, respectively. $Q_m(\mathbf{q},\lambda)$ is a normal mode of the system given as [8,27]

$$Q_m(\mathbf{q},\lambda) = N_u^{-1/2} \sum_i M_i^{1/2} \exp(-\mathbf{q}\cdot\vec{r}_{i,0}) e_m^*(\mathbf{q},\lambda)\cdot\vec{u}_i(t) \tag{8}$$

where N_u is the number of atoms, M_i is the mass of atom i, and λ corresponds to the mode polarization (longitudinal or transverse) described by the polarization vector $e_m^*(\mathbf{q},\lambda)$, i.e., its complex conjugate. $\mathbf{r}_{i,0}$ is the equilibrium position of atom i, and $\mathbf{u}_i(t)$ is the relative displacement of atom i at time t from its equilibrium position ($\mathbf{u}_i(t) = \mathbf{r}_i(t) - \mathbf{r}_{i,0}$).

From the normal mode decomposition, the total energy $E_{m,t}$ of each normal mode (Eq. (7)) is computed during a MD simulation. Once the total energy $E_{m,t}$ of each mode is obtained for each time step in the MD simulation, the autocorrelation of the deviation of total energy from its mean value ($\delta E_{m,t} = E_{m,t} - \bar{E}_m$) is computed. The normalized autocorrelation produces a temporal decaying function, which is fitted with an exponential function, where the time constant is τ_m.

3 Methodology

Details of each type of MD simulation are presented next. In all of the simulations periodic boundary conditions are established in all directions, and five independent runs (i.e., using different starting atomic velocities) are conducted for each molecular domain and temperature studied.

The lattice parameter of the silicon crystal is obtained by means of MD simulations using a NPT (extended formulation) ensemble at zero-pressure. We perform MD simulations using 2.5×10^6 time steps, from which 4.0×10^5 steps correspond to equilibration.

The specific heat is computed using the procedure reported in Ref. [8], with the difference that the temperature is varied in $\pm 0.5\%T$ increments over a $\pm 1\%T$ range around the temperatures of interest. Each simulation involves 4.5×10^6 time steps, from which 3.0×10^5 steps correspond to equilibration, with time steps of 0.5×10^{-15} s. The sensitivity of the specific heat and the lattice parameter to the domain size is studied with three different molecular domains of increasing size, from $\eta = 3$ (216 atoms) to $\eta = 5$ (1000 atoms), where η is the number of unit cells in each atomic direction, corresponding to $N = 8\eta^3$ atoms. For the specific heat a total of 25 simulations are required per temperature studied and molecular domain.

The Green–Kubo thermal conductivity (described in Sec. 6) and the relaxation times are obtained using 17.1×10^6 time steps with time steps of 0.5×10^{-15} s for a total simulation length of 8550 ps. Data are collected after 3.0×10^5 steps of equilibration. A domain of $\eta = 4$ (512 atoms) is used to compute the thermal conductivity at the studied temperatures. The specific heat, the Green–Kubo thermal conductivity, the anharmonic dispersion relations, and the relaxation times are obtained using NVE ensembles. To verify the absence of simulation cell size artifacts, the Green–Kubo thermal conductivity was determined at 300 K for different domain sizes (i.e., $\eta = 4$, 6, and 8) and compared with reported values in Ref. [28].

To obtain the relaxation times of the acoustical and optical modes, molecular domains of increasing size, from $\eta = 4$ (512 atoms) to $\eta = 10$ (8000 atoms), are used. The normal mode decomposition (NMD) is obtained during the MD simulations for the [100], [010], and [001] directions. Data are collected every eight steps (after equilibration). Sensitivity analyses were performed to avoid variations in the results due to the number of data points collected.

As shown in Fig. 1, the harmonic frequencies (ω_h) and polarization vectors ($e_m^*(\mathbf{q},\lambda)$) are obtained in advance from the lattice dynamic (LD) decomposition of the SW interatomic potential. All autocorrelation functions are computed as a postprocessing step. The calculations of autocorrelation functions are speeded-up using an algorithm based on the fast Fourier transform [29]. For each simulation, all collected data ($2^{21} = 2.097.152$ data points for each mode) are used to compute the autocorrelation functions. For each direction, there are $(\eta+1)^*pb$ autocorrelation functions to be computed per MD simulation, where pb is the number of phonon branches (acoustic and optical) times the number of polarizations (one longitudinal and two degenerate transverse) for a silicon crystal ($pb = 6$).

The autocorrelation functions for all directions ([100], [010], and [001]) of the five independent runs are averaged. This leads to 15 data sets for the longitudinal polarization and 30 for the transverse polarization. Due to the size of each data file (>1 Gb), a

Table 1 Lattice parameter computed with MD at various temperatures

T (K)	η	No. of atoms	a (Å)	σ_a (Å)	$\bar{P}$ (bar)	ρ (kg/m³)	c_v/k_B
0			5.4300			2330.64	1.00
300	3	216	5.4376	1.01×10^{-4}	$<5 \times 10^{-5}$	2320.93	
	4	512	5.4373	1.19×10^{-4}	$<4 \times 10^{-5}$	2321.23	1.0103
	5	1000	5.4377	8.84×10^{-5}	$<3 \times 10^{-5}$	2320.72	
400	4	512	5.4393	7.17×10^{-5}	$<6 \times 10^{-5}$	2318.69	1.0136
600	4	512	5.4428	1.75×10^{-4}	$<1 \times 10^{-4}$	2314.26	1.0250
800	4	512	5.4464	9.24×10^{-5}	$<2 \times 10^{-4}$	2309.61	1.0364
1000	3	215	5.4495	3.85×10^{-4}	$<5 \times 10^{-3}$	2305.75	
	4	512	5.4496	3.52×10^{-4}	$<4 \times 10^{-4}$	2305.57	1.0498
	5	1000	5.4496	2.17×10^{-4}	$<4 \times 10^{-4}$	2305.52	

T: temperature.
a: lattice parameter.
σ_a: standard deviation of a.
$\bar{P}$: average pressure at the end of the simulation.
ρ: density.
c_v/k_B: nondimensional specific heat per degree of freedom.

Fig. 2 Temperature dependence of the lattice parameter for the SW potential

subset of 2048 points is collected to further fit the exponential decay function. The relaxation times of each mode are extracted from the fitted functions.

The dispersion relations are calculated *directly* from our MD results using the equipartition of the potential and kinetic energy associated with each normal mode [27], as

$$\omega_m^2 = \frac{\langle \dot{Q}_m(q,\lambda)\dot{Q}_m(-q,\lambda)\rangle}{\langle Q_m(q,\lambda)Q_m(-q,\lambda)\rangle} \tag{9}$$

where the angular brackets represent a time average of the square of the potential (denominator) and kinetic energy (numerator) of the mode m. $\dot{Q}_m(q,\lambda)$ is the time derivative of $Q_m(q,\lambda)$.

Other alternatives have been proposed to estimate dispersion relations; however, they require additional postprocessing steps after the MD simulation. Maruyama [30] used the autocorrelation function of the velocities of the atoms, while McGaughey and Kaviany [8] computed the dispersion relations from the autocorrelation function of the potential energy of each mode. Our approach is straightforward once the normal mode decomposition is obtained. The procedure for obtaining the remaining properties is presented in Sec. 5.

4 Molecular Dynamics Results

4.1 Lattice Parameter and Specific Heat. The results of lattice parameter and specific heat obtained from the MD simulations are presented in Table 1. It can be observed that the sensitivity of the lattice parameter to the domain size is minimal. The standard deviation of the lattice parameter (σ_a) only affects its fourth decimal position. The average value of the ensemble pressure ($\bar{P}$) at the end of the simulations was always lower than 5×10^{-3} bar (worst case). Due to the low sensitivity of the results to the domain size, the lattice parameter for other temperatures (i.e., 400 K, 600 K, and 800 K) is determined using $\eta=4$.

Figure 2 shows the change in the lattice parameter with respect to the temperature obtained from different methods. Our results (▲) are in excellent agreement with those from Broughton and Li [31], who use MD with the SW potential along with a constrained NPT method, and fall between the experimental values reported in Ref. [32] and our analytical results (solid line) for the SW potential computed with the QHMK method (described in Ref. [33]).
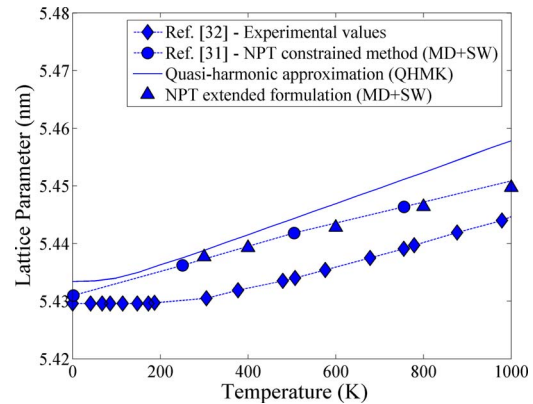
The extended formulation and the constrained methods are different algorithms to solve the set of equations that describe a NPT ensemble [34].

The small difference between our results and those from Broughton and Li can be attributed to the short extent of their simulations. This is especially important at high temperatures where the anharmonic contribution of the potential is more relevant. As the temperature decreases, our MD results are closer to the values obtained from the QHMK. QHMK overpredicts the value of the lattice parameter and does not capture the anharmonic contribution of the potential energy function. On the other hand, the SW potential does not reproduce the slope of the lattice parameter with respect to the temperature obtained experimentally. We have obtained similar results (within 0.0001%) at zero and at atmospheric pressure (1 atm).

As reported in Table 1, the values of the specific heat are slightly higher than those expected for a classical system and increase as the temperature of the molecular system is increased. This behavior is due to an increase in the anharmonicity of the potential energy function with temperature. To corroborate these results, the specific heat is also computed using the fluctuation of the kinetic energy (K) for a microcanonical ensemble as $Cv/Nk_B = [3/2 - N(\langle K^2\rangle - \langle K\rangle^2)\langle K\rangle^{-2}]^{-1}$, where N is the number of atoms in the simulation and the angle brackets represent average values [35,36]. Values for the nondimensional specific heat per degree of freedom of 1.034 and 1.054, with standard deviations of 1.318×10^{-2} and 8.127×10^{-3} were obtained at 300 K and 1000 K, respectively.

4.2 Relaxation Times Results. In this section, we first analyze the behavior of the relaxation times for each branch and polarization with respect to the frequency at 300 K and 1000 K. We present our results in terms of the inverse relaxation time (IRT), defined as $1/\tau$, also known as the relaxation rate or scattering frequency. Then, for 1000 K, we identify their dependence on the frequency by means of two fitted functions, a low-order ($1/\tau(\omega)=a^*\omega^2+b^*\omega$) polynomial, and a power function ($1/\tau(\omega)=a^*\omega^b$). These functions are chosen according to Matthiessen's rule and following the functional form of the relaxation expressions suggested by Herring and Klemens (Eqs. (2)–(6)) and Sun and Murthy [16]. We compare these results with those obtained at 300 K using the same fitting functions. In general, we found that the relaxation times exhibit a complex dependence on frequency, as has also been reported in previous works using different interatomic potentials [8,15]. For MD, it has been suggested that the interaction between modes, which produce the different shapes of the relaxation time curves, is controlled by internal resonance [37].

Figure 3 shows the IRT corresponding to the LA and longitudinal optical (LO) modes as a function of frequency at 300 K and
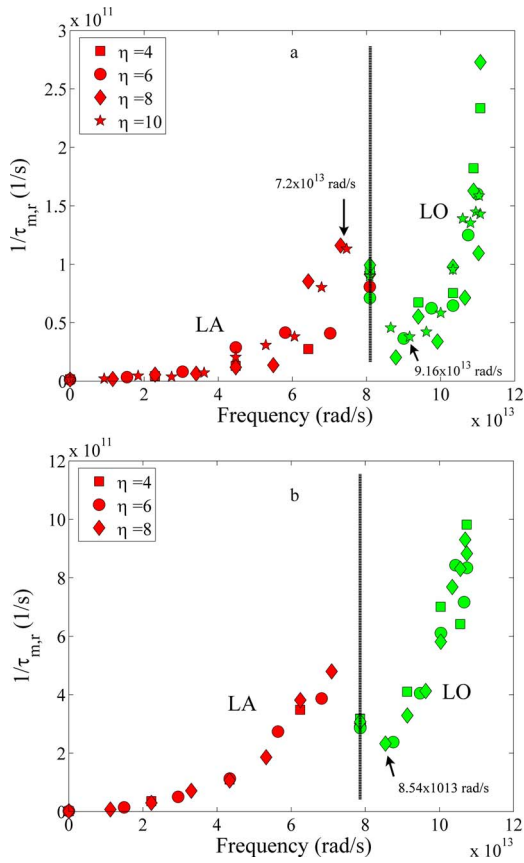
Fig. 3 Relaxation rates as a function of the frequency for LA and LO modes at 300 K (*a*) and 1000 K (*b*). The vertical line indicates the first Brillouin zone.

Fig. 4 Relaxation rates as a function of the frequency for TA and TO modes at 300 K (*a*) and 1000 K (*b*)

1000 K. The symbols represent domains of different sizes. At 300 K the values of the IRT are lower than those corresponding to 1000 K, albeit the different scale used. At both temperatures, it is observed that there is a common trend in all IRT curves. In general, the IRT for the LA mode increases with frequency reaching a maximum around 7.2×10^{13} rad/s, and then decreasing until the boundary of the first BZ (for $q=2\pi/a$). The IRT for the LO mode, first decreases from its value at the BZ until a minimum close to 9.16×10^{13} rad/s (for $\eta=10$) and 8.54×10^{13} rad/s (for $\eta=8$) at 300 K and 1000 K, respectively, and then increases with a larger slope than the LA mode. At the boundary of the BZ, the IRT values are equal. This similitude is due to identical polarization vectors, i.e., the polarization vectors produce undistinguishable modes. At 300 K, the lower anharmonicity of the potential energy function results in IRT values that are more disperse than those at 1000 K, for the same number of allowed interacting phonons.

Figure 4 shows the IRT corresponding to the TA and transverse optical (TO) modes as a function of frequency at 300 and 1000 K. Here, the IRT values at 300 K are lower than those corresponding to 1000 K.

A common trend is observed for the TA modes at both temperatures. There is a change of slope in the IRT values close the BZ boundary, this change is small at 1000 K, but it is more notorious at 300 K. In fact, at 300 K, the IRT values for the TA mode decrease after the peak around 3.54×10^{13} rad/s (for $\eta=10$), until a constant value at the BZ. At the BZ, the values of the IRT between the two vibration branches differ. In Figs. 3 and 4, for the same value of the wave vector, the frequency of the modes is shifted as the temperature is increased. This is more evident at the edge of the BZ for the LA modes.

Due to the narrow frequency range of the LO and TO modes, their behavior is not clearly observable in Figs. 3 and 4. Figure 5
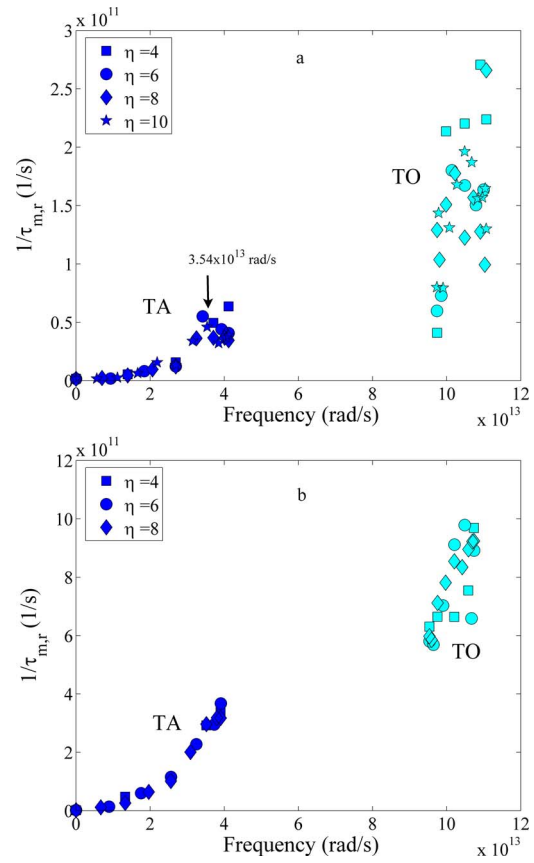
shows the relaxation rates of these modes with respect to the reduced (nondimensional) wave vector ($q^*=q/(2\pi/a)$), for 300 K ($\eta=10$) and 1000 K ($\eta=8$). In this figure, $q^*=0$ corresponds to a frequency value of 1.107×10^{14} rad/s (at 300 K) and 1.075×10^{14} rad/s (at 1000 K) for both branches. For 300 K and $q^*=1$, the frequency is 8.09×10^{13} rad/s and 9.742×10^{13} rad/s for the LO and TO modes, respectively. While at 1000 K and $q^*=1$ the frequency is 7.86×10^{13} rad/s and 9.54×10^{13} rad/s for the LO and TO modes, respectively. The change in the frequency with temperature is explained in Sec. 5. Again, the values of the IRT for both modes are lower for 300 K. The LO and TO curves decrease from their value at the BZ ($q^*=1$) and then increase as the wave vector decreases. When wave vector approaches zero ($q^* \rightarrow 0$), the values of the IRT trend to be constant and almost
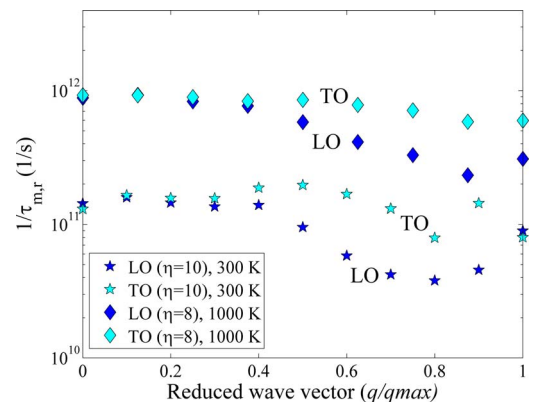
Fig. 5 Relaxation rates for LO and TO modes at 300 K and 1000 K with respect to the reduced wave vector
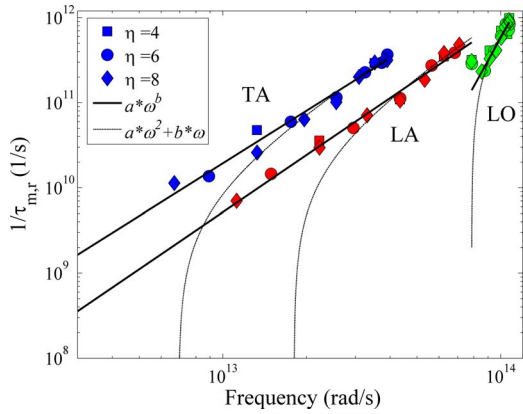
Fig. 6 Fitted relaxation rates at 1000 K. Log-log scale.

Fig. 7 Relaxation rates as a function of the wave vector for the LO and TO modes at 1000 K

equal for both modes. At 300 K the IRT is approximately 1.349×10^{11} s^{-1}, while for 1000 K is 9.120×10^{11} s^{-1}. This similitude might be due to the flat nature of the dispersion relation as $q^* \to 0$. Lastly, the TO mode exhibits a larger sensitivity with respect to the number of phonons present in the molecular domains used in the simulations.

It is interesting to note that the IRT curves (Figs. 3–5) do not exhibit the discontinuities of orders of magnitude found in the relaxation times models proposed by Holland [38], Han and Klemens [26], and Gomes [28]. Only changes of the slope for the LA, LO, and TA modes near the edge of the BZ are observed. These can be produced by the ability of certain modes to interact with others at specific ranges of frequency and wave vector, whereas in the cited models the discontinuities are produced by the functional form of the dispersion relation assumed and by how the fitting parameters are determined. For argon, McGaughey and Kaviany [8] reported relaxation time curves that do not exhibit discontinuities.

To identify the functional dependence of the different polarization modes, we fit the results with a lower-order polynomial and a power function. The values of the IRT at the boundary of BZ for the LA and LO modes are not included. A small correction is applied latter. We start identifying the functional dependence at 1000 K.

Figure 6 shows the values of the IRT and the fitted functions with respect to the frequency for the TA, LA, and LO modes at 1000 K. The TO mode is not included to facilitate visualization. The polynomial functions produce negative values of the IRT for low frequencies of the TA and LA modes. The source of the negative values is the sign of coefficient b in the polynomial function. A negative sign for this coefficient would produce negative values for IRT when $\omega < b/a$. Conversely, the power functions produce only positive values of the relaxation times, which yield to infinite
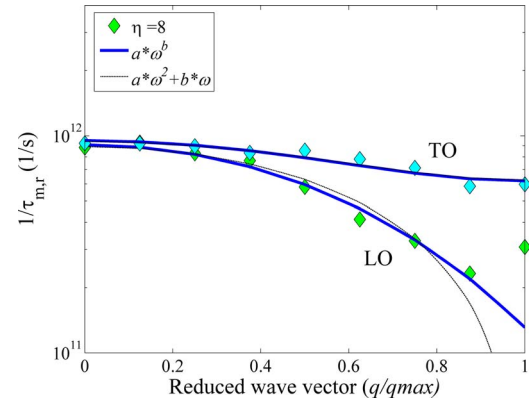
as the frequency trends to zero. In the limit of zero frequency the IRT is zero.

Table 2 presents the values of the coefficients obtained after the curve fitting. The quality of the fitting is measured in terms of the sum of square errors (SSE) in log-log space and the coefficient of determination (R^2). Only functions that produce positive relaxation times are shown.

It can be observed that the power function fits the MD results well. The value of the exponents for the TA and LA modes (2.0513 and 2.2245, respectively) are in agreement with those of the phonon relaxation expressions obtained by Klemens at high temperatures (Eq. (2)) and with Eqs. (5) and (6). Likewise, the exponents also agree with those used by Henry and Chen [39] to fit their relaxation times with temperature. In contrast, the exponents for the LO and TO (equal to 6.2074 and 3.6216, respectively) are higher than those predicted by Eq. (2). Nevertheless, the exponent of the TO mode is similar to the predictions of Hans and Klemens [26] and Ecsedy and Klemens [25] (Eq. (3)). The expressions obtained in Refs. [26,25] were derived assuming that the dispersion curves of the optical modes intercept those of the longitudinal modes and four-phonon interactions, respectively. The later was considered to be important at high temperatures ($T > \theta_D$) [1,27].

The polynomial function only produce positive values for the LO and TO modes. Figure 7 shows the MD results and the fitted curves for IRT as a function of the wave vector for the LO and TO modes. The ability to fit these modes with the polynomial suggests that the power function might be too simple to capture their behavior completely. However, if higher order polynomials or more complex functions are used to better fit the behavior of the relaxation times (as in Ref. [16]), their physical meaning should be analyzed in detail. The IRT for the LO and TO modes is fitted

Table 2 Fitting results for $1/\tau(\omega)$ at 1000 K

Branch	Function	SSE	R^2	a (s^{-1}/rad^b)	b
TA	$a^*\omega^b$	0.5242	0.9758	exp(−37.71546)	2.0513
LA	$a^*\omega^b$	0.3418	0.9850	exp(−44.21843)	2.2245
LO	$a^*\omega^b$	0.0244	0.9870	exp(−173.0092)	6.2074
TO	$a^*\omega^b$	0.0231	0.9076	exp(−89.4238)	3.6216
LO	$a^*\omega^2 + b^*\omega$	0.1433	0.9672	2.8777×10^{-16} (s^{-1}/rad^2)	-2.2598×10^{-2} (s^{-1}/rad)
TO	$a^*\omega^2 + b^*\omega$	0.0218	0.9188	1.8670×10^{-16} (s^{-1}/rad^2)	-1.1258×10^{-2} (s^{-1}/rad)

SSE: sum of square errors.
R^2: coefficient of determination.
a and b: fitted functions coefficients.

Table 3 Fitting results for $1/\tau(\omega)$ at 300 K

Branch	Function	SSE	R^2	a (s^{-1}/rad^b)	b
TA	$a^*\omega^b$	2.5107	0.9273	exp(−34.8400)	1.8920
LA	$a^*\omega^b$	6.0148	0.8746	exp(−39.5487)	2.0153
LO	$a^*\omega^b$	0.4477	0.8564	exp(−179.8710)	6.3574
TO	$a^*\omega^b$	0.5991	0.3533	exp(−92.8887)	3.6727
TA	$a^*\omega^2+b^*\omega$	2.5538	0.8059	2.6893×10^{-17} (s^{-1}/rad^2)	2.0393×10^{-5} (s^{-1}/rad)

SSE: sum of square errors.
R^2: coefficient of determination.
a and b: fitted functions coefficients.

using only the results obtained for $\eta=8$. As shown in Table 2, the coefficient of determination (R^2) indicates that it is more difficult to obtain a good fit for TO mode.

Table 3 presents the numerical results obtained at 300 K. Only results for $\eta=10$ are considered for the LO and TO modes. Since the polynomial functions of the LA, LO, and TO modes predict negative values of the IRT, they are not reported in the table. The exponents for all modes are remarkably similar to those obtained at 1000 K. For the TA and LA modes these are equal to 1.8920 and 2.0153, respectively, while for the TO and LO are 6.3574 and 3.6727.

From Tables 2 and 3, the coefficient of determination (R^2) for the different modes indicates that fitting the results at 300 K is more challenging than at 1000 K. This is also true for optical modes, where well-behaved IRT curves are difficult to obtain for small molecular domains (as shown in Figs. 3 and 4). For optical modes the difficulty might be related to their range of interacting frequencies and to the number of phonons available in a given molecular domain. Optical modes have narrower frequency ranges (e.g., from 8×10^{13} rad/s to 11×10^{13} rad/s and 10×10^{13} rad/s to 11×10^{13} rad/s for the LO and TO modes, respectively, in the [100] direction) that constrain their interaction with other phonons. Although at high temperatures ($T>\theta_D$) the anharmonicity of the potential energy function might enhance their interactions with other phonons, it is expected that larger molecular domains would result in better IRT curves for these modes.

Two additional sets of MD simulations were carried out at 300 K to verify the sensitivity of the exponents (b), reported in Table 3, for different initial conditions (velocities). Each set consists of five independent simulations per domain size (i.e., $\eta=4$, 6, 8, and 10) for a total of 40 additional runs. These were performed following the description given in Sec. 3. Only results for $\eta=10$ were considered for the optical modes.

We found that the new exponents are in excellent agreement with those reported in Table 3. For each simulation set, values of 1.9147, 2.0245, 6.3101, and 3.8229 and 1.8976, 2.0319, 6.2605, and 3.8041 were obtained for the TA, LA, LO, and TO modes, respectively. The maximum difference between these values with those reported in Table 3 is less than 4.08% corresponding to the TO modes, while the rest exhibits a difference lower that 1.5%. Furthermore, as described in Sec. 6, no simulation cell size artifacts were observed in our simulations.

5 Phonon and Thermal Properties

Using the normal mode decomposition and/or the relaxation times obtained from the MD simulations, in this section, we compute different phonon and thermal properties such as dispersion relations, group and phase velocities, thermal conductivity, and phonon mean free path. The last three of these properties are determined using the fitted power functions obtained in Sec. 4. As we shall see, the thermal expansion and the anharmonic nature of the SW potential modify the magnitude and behavior of the thermal properties of the crystal.

5.1 Dispersion Relations. Figure 8 shows the dispersion relations of silicon at 300 K and 1000 K for the [100] direction. They are compared with the analytical dispersion relations obtained using the equilibrium lattice parameter (5.43 Å) at 0 K. It is found that as the temperature is increased, the frequency of the modes changes. The change is produced by two competing effects associated with the anharmonic nature of the potential energy function [27]. For a given value of the lattice parameter, the increase in the temperature yields a linear increase in the normal mode's frequency (related to the fourth-order term in the Taylor expansion of the potential energy). This situation occurs at 300 K, where the change in the lattice parameter from its equilibrium value is small. At this temperature, the frequency of the LA and LO modes are higher than at 0 K for values close to $q^*=1$. At the same time, the increase in the temperature results in thermal expansion, which causes the normal mode frequencies to decrease. At 300 K and 1000 K, this is evident for the TA and TO modes for the entire frequency spectrum and for values close to $q^*=0$ for the LO mode. At 1000 K, the reduction in the frequency due to the thermal expansion surpasses the linear increase in the frequency, and all modes experience a decrease in their frequency. The deviation from the harmonic values of the TA and TO modes is found to be significant at both temperatures and in a lower degree for the LA and LO modes. Conversely, these changes are found to be underestimated by the quasiharmonic approximation. In fact, the values of the dispersion relations obtained using the lattice parameter at 0 K and those determined at 300 K and 1000 K are only lower by 0.9%. On the other hand, for solid argon the deviation was found to be important for the LA modes for all temperatures and only at relative high temperatures (80 K) for TA modes
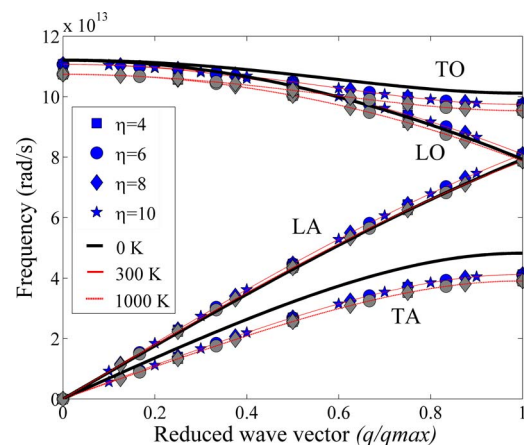
Fig. 8 Dispersion relations obtained at 300 K and 1000 K. The thick solid line represents the analytical dispersion relation obtained at 0 K using the equilibrium lattice parameter. The MD results (thin solid and dashed lines) are fitted using a fourth-order polynomial. The symbols represent domains of different sizes.
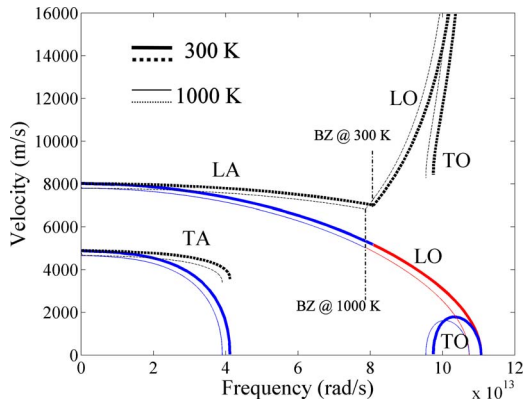
Fig. 9 Group (solid lines) and phase (dashed lines) velocities at 300 K (bold lines) and 1000 K (thin lines) in the [100] direction

[8]. The change in the dispersion relation, besides modifying the behavior and magnitude of other thermal properties, can affect the frequency and wave vector ranges over which the scattering events occur, altering the value of the relaxation times. Although the thermal expansion is one of the important competing effects, it has never been included before in the theoretical derivation of the relaxation time expressions [40].

5.2 Group and Phase Velocities. The group and phase velocities are defined as $v_g = \partial \omega / \partial q$ and $v_p = \omega / q$, respectively. These are obtained numerically by fitting the MD dispersion relations with fourth-order polynomials. The thin solid and dashed lines in Fig. 8 are the fitted curves. Figure 9 shows the group and phase velocities for the [100] direction as a function of frequency at 300 K and 1000 K. It can be observed that the change in the frequencies in the dispersion relations affects the behavior and magnitude of both velocities. At 300 K the group velocity for all modes is larger than at 1000 K, while the phase velocity is larger only for the LA and TA modes. The group velocity is zero for the TA and TO modes at the edge of the BZ and at $q^* = 0$ for the LO and TO modes.

The increase in the phase velocity of the LO and TO modes is produced because the value of the wave vector tends to zero, while the frequency remains high. The TO mode has the lower group velocity. The maximum and minimum values of group velocity for each branch are reported in Table 4.

5.3 Phonon Mean Free Path. The phonon mean free path is computed as the product of the group velocities and the relaxation times of each mode as $\Lambda_m(\omega) = v_g(\omega)^* \tau_m(\omega)$. In our case, the relaxation times are obtained from the power functions, while the group velocities are computed as described before.

The phonon mean free path for all modes and temperatures as a function of frequency is shown in Fig. 10. At both temperatures the power functions capture well the behavior of the data. As

Table 4 Maximum and minimum values of the group velocity at different temperatures

	0 K		300 K		1000 K	
	$v_{g,max}$ (m/s)	$v_{g,min}$ (m/s)	$v_{g,max}$ (m/s)	$v_{g,min}$ (m/s)	$v_{g,max}$ (m/s)	$v_{g,min}$ (m/s)
TA	5913	0	4887	0	4663	0
LA	7607	5378	8002	5156	7789	5021
LO	5378	0	5164	0	5047	0
TO	1492	0	1800	0	1625	0

$v_{g,max}$ and $v_{g,min}$: maximum and minimum group velocities for each branch.
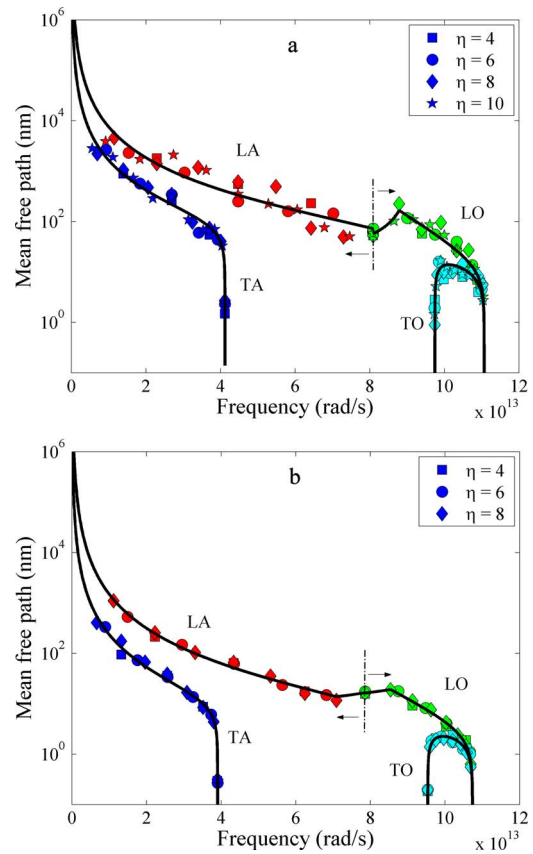
Fig. 10 Phonon mean free path at 300 K (a) and 1000 K (b) as a function of the frequency. The arrows and the dashed lines represent the edge of the Brillouin zone.

mentioned before, more dispersion in the results is observed at 300 K, which is a consequence of the relaxation times obtained at 300 K (as shown in Figs. 3(a) and 4(a)).

Reported values of the phonon mean free path are still subject of discussion. At 1000 K the silicon phonon mean free path is estimated from the kinetic theory to be 30 nm, while at room temperature Ju and Goodson [41] suggested a value of 300 nm. Escobar et al. [9] using a Debye-based model have estimated the phonon mean free path to be 41 nm at 300 K. It is observed that as the frequency is increased, the phonon mean free path for the LA and TA modes decrease from several hundred nanometers (or more) at the low-frequency range to tens of nanometers at the BZ for the LA mode. For the transverse modes, even smaller values at BZ are found. Due to the low group velocity and relaxation times, the TO mode exhibits on average the lowest value of the mean free path.

For the LO mode at 300 K and 1000 K, the relaxation time values have been corrected to capture the change of slope in its IRT close to the BZ, while at 1000 K the LA mode is the only one adjusted. There are no discontinuities in the reported mean free path values, with the values for the LA and LO modes at the BZ being almost equal. At the BZ, the obtained mean free path at 300 K and $\eta = 10$ are 56.23 nm and 57.54 nm for the LA and LO modes, respectively. At 1000 K the BZ values obtained for $\eta = 8$ are 16.60 nm and 16.40 nm for the LA and LO modes, respectively. Recall that our estimation of the phonon mean free path only includes phonon-phonon scattering events. At $T < \theta_D$ other scattering processes, such as impurity and defect scattering, can further reduce the values of the mean free path reported here.

5.4 Thermal Conductivity. Using the relaxation time approximation, the steady state BTE (Eq. (1)) for phonons can be

Table 5 Thermal conductivity predicted using Eqs. (10) and (11)

T (K)	k (W/m K)	k_{TA} (W/m K)	k_{LA} (W/m K)	k_{LO} (W/m K)	k_{TO} (W/m K)	k_{GK} (W/m K)	$\sigma(k_{GK})$ (W/m K)	k' (W/m K)
300	379.66	128.615 (33.87%)	212.151 (55.87%)	35.80 (9.429%)	3.092 (0.815%)	350.67	17.38 (4.90%)	362.549
1000	62.928	18.876 (29.99%)	37.055 (58.88%)	6.535 (10.38%)	0.459 (0.73%)	52.36	11.16 (21.31%)	60.092

k: BTE-based thermal conductivity (Eq. (10)).

k_{TA}, k_{LA}, k_{LO}, and k_{TO}: thermal conductivity contribution of the transverse and longitudinal acoustic and optical modes, respectively.

$\sigma(k_{GK})$: standard deviation of the Green–Kubo thermal conductivity.

k': corrected BTE-based thermal conductivity.

solved for n_m. From the resulting expression, assuming isotropic phonon dispersion and integrating over all phonon modes, the thermal conductivity k for silicon can be expressed using the Fourier law of heat conduction as [6]

$$k = \frac{4\pi}{3} \frac{1}{(2\pi)^3} \left[2 \int_0^{\omega_{TA,max}} \left(c_v \frac{v_g}{v_p^2} \tau_r \right)_{TA} \omega^2 d\omega \right.$$
$$+ \int_0^{\omega_{LA,max}} \left(c_v \frac{v_g}{v_p^2} \tau_r \right)_{LA} \omega^2 d\omega + 2 \int_{\omega_{TO,min}}^{\omega_{TO,max}} \left(c_v \frac{v_g}{v_p^2} \tau_r \right)_{TO} \omega^2 d\omega$$
$$\left. + \int_{\omega_{LO,min}}^{\omega_{LO,max}} \left(c_v \frac{v_g}{v_p^2} \tau_r \right)_{LO} \omega^2 d\omega \right] \qquad (10)$$

In the equation, each term represents the contribution to the thermal conductivity from the TA, LA, LO, and TO modes, respectively. $\omega_{TA,max}$, $\omega_{LA,max}$, $\omega_{TO,max}$, $\omega_{LO,max}$, $\omega_{TO,min}$, and $\omega_{LO,min}$ are the limits of integration defined at $q^*=0$ and $q^*=1$, given from the condition that the mean free path should be longer than one half of its wavelength [8], and c_v is the specific heat per mode at constant volume (see Table 1). Once the specific heat, relaxation times, and group and phase velocities are specified, the thermal conductivity can be predicted using Eq. (10). Table 5 shows the predicted thermal conductivity.

For more than 40 years, there has been a controversy between the relative contributions to the total thermal conductivity of the transverse and longitudinal modes of semiconductor materials such as silicon and germanium. Pioneer works from Holland [38] and Hamilton and Parrott [42], who used a variational method, suggest that the TA modes are the dominant heat carriers at high temperatures. Mazumder, using a Monte Carlo method that incorporates the relaxation times from Holland, has found that the TA modes are the dominant ones at temperatures above 100 K. However, such results have been contradicted when more refined models for thermal conductivity are employed [5,7]. Sood and Roy [5] used a model based on Tiwari's equation (similar to Eq. (10)) concluded that LA phonons dominate heat transport in germanium at high temperatures, their contribution being more than 75% for $T > \theta_D$. Their results have been also corroborated by Ju and Goodson [41] for silicon near room temperature. Chung et al. [7] found that Holland's model fails to predict the thermal conductivity of germanium at high temperatures, when the dispersion relations, group and phase velocities, v_g/v_p^2 ratio, and the impurity scattering are rigorously modeled. Using MD and the EDIP potential, Henry and Chen [39] also determined that the contribution to the thermal conductivity of LA modes is greater than that for the TA modes being 45% and 30%, respectively. Here we found that at both temperatures, the contribution from the TA and LA modes represents roughly 90% of the total contribution, being about 30% from the TA mode and lower than 60% from the LA mode, while the relative contribution of LO mode is approximately 10%. These results are in excellent agreement with recent ab initio predictions

by Broido et al. [43] who reported that acoustic modes provide 95% of the contribution to the thermal conductivity. Although, we do not apply quantum corrections to the thermal conductivity, their application per mode basis would further reduce the contribution of high-frequency modes (i.e., optical modes). We also found that as the temperature is increased from 300 K to 1000 K, the contribution from the TA mode lowers approximately 3% (from 33.87% to 29.99%), while the one from the LA increases by almost the same amount (from 55.87% to 58.88%). All other modes remain unaffected. The reduction in the contribution from the TA mode can be attributed to the reduction of its group velocity, as described previously.

Although we mentioned that the TO mode at 300 K and 1000 K is more difficult to fit, their impact over the total thermal conductivity is less than 1% (as shown in Table 5). However, while the contribution from TO modes can be neglected in steady state situations, in transient regimes their capacitive character will be more relevant. This mode can store heat with almost no dissipation. Hence, any heat transferred to this mode will remain confined for long periods of times, leading to the creation of hot spots.

6 Validation

In order to validate our model for silicon, we compare the thermal conductivity results (obtained from the MD relaxation times) with those predicted using the Green–Kubo method at the studied temperatures. The Green–Kubo method has been extensively used in equilibrium molecular dynamics to determine the thermal conductivity of dielectric materials [8,44,45]. The thermal conductivity (k_{GK}) is computed from the decay of the fluctuations of the heat current vector ($\boldsymbol{J}$) given by

$$k_{GK} = \frac{1}{k_B V T^2} \int_0^\infty \frac{\langle \boldsymbol{J}(t) \cdot \boldsymbol{J}(0) \rangle}{3} dt \qquad (11)$$

where V is the volume of the molecular ensemble, and $\langle \boldsymbol{J}(t) \cdot \boldsymbol{J}(0) \rangle$ is the heat current autocorrelation function. The expression of the heat current depends on the type of interatomic potential function used. For the SW potential the heat current is given in Ref. [44].

Table 5 reports the thermal conductivities predicted with this method at the studied temperatures. At both temperatures the values of the thermal conductivity computed with the relaxation time model agree well with the ones from the Green–Kubo method (reported in Ref. [28] for silicon and the SW potential). These values were also compared with those for larger domain sizes (i.e., $\eta=6$ and $\eta=8$), and no simulation cell size artifacts were observed. Specifically, for all domains considered, the thermal conductivity was about 350 W/m K (i.e., 351 W/m K, 342 W/m K, and 355 W/m K with standard deviations of 4.90%, 7.41%, and 7.16% for $\eta=4$, 6, and 8, respectively). These estimations fall within 1 standard deviation of the thermal conductivity obtained in Ref. [28] for $\eta=10$. This behavior is in agreement with the results presented by Sun and Murthy [46], who showed that the

value of the bulk thermal conductivity for silicon using the EDIP potential at 300 K converges for molecular domains larger than $\eta > 3$ (i.e., >216 atoms).

It is important to note that the isotropic model assumed in Eq. (10) overestimates the volume of the BZ by a factor of $V_{\text{iso}}/V_{\text{BZ}} = \pi/3 \sim 1.0472$ [8]. The real volume of the first BZ is $32\pi^3/a^3$, while the volume from the spherical volume associated to the isotropic model is $32\pi^4/(3a^3)$. Hence, the thermal conductivity can be further corrected ($k \rightarrow k'$) to account for the real volume of the first BZ. After correcting the values (last column of Table 5), the difference between k' and k_{GK} is 3.39% and 14.76% at 300 K and 1000 K, respectively. Both values are within 1 standard deviation of the predicted values of the Green–Kubo method.

7 Limitations

MD is a classical method. For weak anharmonicities, normal modes have an energy according to the equipartition theorem of $k_B T$. In a quantum system, on the other hand, the phonon occupation number is a function of the temperature and frequency, and the energy is quantized in units of $\hbar\omega$. These differences affect the values of the properties estimated using MD, especially the specific heat, temperature, and thermal conductivity. At temperatures below the Debye's temperature (estimated to be 645 K for silicon [44]), quantum effects are particularly important due to the freezing of high-frequency modes, while at high temperatures ($T > \theta_D$) the predictions of both systems are expected to converge.

Although our model reproduces very well the Green–Kubo predicted thermal conductivity, its further application in other numerical tools would require quantum corrections to rescale these properties.

8 Summary and Conclusions

Using molecular dynamics simulations, different phonon and thermal properties of silicon needed to solve the BTE (including group and phase velocities, phonon mean free path, and BTE-based thermal conductivity) were determined from the estimation of the relaxation times for the acoustical and optical modes and the dispersion relations of bulk silicon at 300 K and 1000 K. The relaxation times are determined from the normal decomposition of the motion of the atoms during a given period of time. No fitting parameters were needed to estimate the relaxation times from MD. Their behavior was identified with two functions (i.e., a polynomial and a power function of the frequency) that follow the expression derived from time-dependent perturbation theory. The properties were validated comparing the BTE-based thermal conductivity against the predictions obtained from the Green–Kubo method.

We found that the polynomial function fails to capture the behavior of the relaxation times at low frequencies for the TA and LA modes at 1000 K and for the LA at 300 K. At low frequencies, unrealistic values (negative) of the relaxation rates are obtained when the polynomial is applied to these modes. The power function, on the other hand, captures well the behavior of the relaxation times for both temperatures. However, the TO mode was difficult to fit with the power function at 300 K. At both temperatures the value of the exponents of the power functions for the different modes are remarkably similar. For the TA and LA modes, these are approximately equal to 2.0, in agreement with theoretical predictions obtained from time-dependent perturbation theory for U-processes at high temperatures, while for the TO and LO modes, the higher value in their exponents suggests that high-order phonon interactions might be responsible for such behavior, or that more complex functions are required to capture their comportment.

The relaxation times are inversely proportional to the temperature of the molecular system, being lower at 1000 K. A lower value of the relaxation times implies lower thermal conductivity. This agrees with the experimental results for semiconductor devices for the studied temperatures and with the results obtained for the thermal conductivity from our model and the Green–Kubo method.

For both temperatures, the relaxation rates do not exhibit noticeable discontinuities with respect to the frequency, as was found using the relaxation time modes of Holland or Han and Klemens. Only changes of the slope for the LA, LO, and TA modes are observed near the edge of the BZ. The relaxation times at the BZ for the LA and LO modes are almost equal. We believe this is produced since the polarization vectors at the edge of BZ for both modes are equal, making them indistinguishable.

It is observed that the anharmonic nature of the potential energy and the thermal expansion are responsible for the change of the dispersion relations with temperature. At 300 K where the thermal expansion is small, the frequency of the LA and LO modes increases near the BZ, while at 1000 K all modes experience a decrease in their vibration frequency. The deviation from the harmonic values of the TA and TO modes is found to be significant at both temperatures and in a lower degree for the LA and LO modes. Our estimation of the thermal expansion of the silicon crystal falls between reported experimental results and the analytical results based in the quasiharmonic approximation, where the latter does not include the anharmonic nature of the Stillinger–Weber potential at high temperatures.

The change in the dispersion relations affects the behavior and magnitude of group and phase velocities of the normal modes with respect to frequency. As the temperature is increased from 300 K to 1000 K, the group velocity decreases and shifts to the left in the frequency spectrum. A similar behavior is observed in the phase velocity for the LA and TA modes.

At both temperatures a power function of the frequency captures well the behavior of the phonon mean free path with respect to the frequency. On average, the TO mode exhibits the lowest mean free path, followed (in order) by the LO, TA, and LA. As the frequency is increased, the mean free path for the LA and TA modes decreases from hundreds (or more) to tens (or less) of nanometers. It is found that at the edge of the BZ the mean free path for the LA and LO coincide and are equal to ~ 56 nm at 300 K (for $\eta = 10$) and ~ 16 nm at 1000 K (for $\eta = 8$).

From the thermal conductivity results obtained using our model, we found that at both temperatures, the contribution from the TA and LA modes to the overall thermal conductivity represents roughly 90%, being about 30% from the TA mode and lower than 60% from the LA mode, while the relative contribution of LO mode is 10%. The contribution from the TO mode for both temperatures is negligible (less 1%). These results are in excellent agreement with recent ab initio predictions for silicon by Broido et al. [43], who determined that acoustic modes provide 95% of the contribution to the thermal conductivity.

A good agreement is obtained between our results for thermal conductivity with the predictions obtained from the Green–Kubo method at the studied temperatures. A difference of 4.6% and 14.76% in these results is obtained at 300 K and 1000 K, respectively, validating in this way our model.

Nomenclature

a = lattice parameter (Å)
a and b = fitted coefficients

c_v/k_B = nondimensional specific heat per degree of freedom

e^* = polarization vector (complex conjugate)

$E_{m,t}$ = total energy of each normal mode (J)

$\hbar$ = Planck constant (J s/rad)

k = BTE-based thermal conductivity (W/m K)

k' = corrected BTE-based thermal conductivity (W/m K)

k_B = Boltzmann constant (kg/s^2 K)

k_{GK} = Green–Kubo thermal conductivity (W/m K)

M_i = mass of atom i (kg)

n_m = phonon mode occupation number

N_u = number of atoms

$\bar{P}$ = average pressure at the end of the simulation (bar)

q and $\boldsymbol{q}$ = wave vector (1/m)

Q = normal mode

$\boldsymbol{r}_i$ and $\boldsymbol{r}_{i,0}$ = instant and equilibrium position of atom i (m)

t = time (s)

T = temperature (K)

$\boldsymbol{u}_i(t)$ = relative displacement of atom i at time t from its equilibrium position (m)

v_g and v_p = group and phase velocities (m/s)

V = volume of molecular ensemble (m^3)

Greek Symbols

η = number of unit cells

θ_D = Debye temperature (K)

λ = mode polarization (longitudinal or transverse)

Λ = mean free path (m)

ρ = density (kg/m^3)

σ = standard deviation

τ_m = relaxation time (s)

ω = frequency (rad/s)

ω_h = harmonic frequency (rad/s)

Subscripts

m = phonon mode

max = maximum

min = minimum

References

[1] Ziman, J., 1960, *Electrons and Phonons: The Theory of Transport Phenomena in Solids* (The International Series of Monographs on Physics), Clarendon, New York.

[2] Holland, M. G., 1964, "Phonon Scattering in Semiconductors From Thermal Conductivity Studies," Phys. Rev., **134**(2A), pp. A471–A480.

[3] Liu, W., and Asheghi, M., 2005, "Thermal Conduction in Ultrathin Pure and Doped Single-Crystal Silicon Layers at High Temperatures," J. Appl. Phys., **98**, p. 123523.

[4] Liu, W., Etessm-Yazdani, K., Hussin, R., and Asheghi, M., 2006, "Modeling and Data for Thermal Conductivity of Ultrathin Single-Crystal SOI Layers at High Temperature," IEEE Trans. Electron Devices, **53**(8), pp. 1868–1876.

[5] Sood, K. C., and Roy, M. K., 1993, "Longitudinal Phonons and High-Temperature Heat Conduction in Germanium," J. Phys.: Condens. Matter, **5**, pp. 301–312.

[6] Tiwari, M. D., and Agrawal, B. K., 1971, "Analysis of the Lattice Thermal Conductivity of Germanium," Phys. Rev. B, **4**(10), pp. 3527–3532.

[7] Chung, J. D., McGaughey, A. J. H., and Kaviany, M., 2004, "Role of Phonon Dispersion in Lattice Thermal Conductivity Modeling," ASME J. Heat Transfer, **126**, pp. 376–380.

[8] McGaughey, A. J., and Kaviany, M., 2004, "Quantitative Validation of the Boltzmann Transport Equation Phonon Thermal Conductivity Model Under the Single-Mode Relaxation Time Approximation," Phys. Rev. B, **69**(9), p. 094303.

[9] Escobar, R. A., Ghai, S. S., Jhon, M. S., and Amon, C. H., 2006, "Multi-Length and Time Scale Thermal Transport Using the Lattice Boltzmann Method With Applications to Electronics Cooling," Int. J. Heat Mass Transfer, **49**, pp. 97–107.

[10] Narumanchi, S. V. J., Murthy, J. Y., and Amon, C. H., 2006, "Boltzmann Transport Equation-Based Thermal Modeling Approaches for Hotspots in Microelectronics," Int. J. Heat Mass Transfer, **42**(6), pp. 478–491.

[11] Pop, E., Sinha, S., and Goodson, K., 2006, "Heat Generation and Transport in Nanometer-Scale Transistors," Proc. IEEE, **94**(8), pp. 1587–1601.

[12] Rowlette, J., and Goodson, K., 2008, "Fully Coupled Nonequilibrium Electron-Phonon Transport in Nanometer-Scale Silicon FETs," IEEE Trans. Electron Devices, **55**(1), pp. 220–232.

[13] Sinha, S., Schelling, P. K., Phillpot, S. R., and Goodson, K. E., 2005, "Scattering of g-Process Longitudinal Optical Phonons at Hotspots in Silicon," J. Appl. Phys., **97**(2), p. 023702.

[14] Pop, E., Dutton, R. W., and Goodson, K. E., 2005, "Monte Carlo Simulation of Joule Heating in Bulk and Strained Silicon," Appl. Phys. Lett., **86**(8), p. 082101.

[15] Ladd, A., Moran, B., and Hoover, W. G., 1986, "Lattice Thermal Conductivity: A Comparison of Molecular Dynamics and Anharmonic Lattice Dynamics," Phys. Rev. B, **34**, pp. 5058–5064.

[16] Sun, L., and Murthy, J. Y., 2005, "Molecular Dynamics Simulation of Phonon Transport in EDIP Silicon," pp. 1–6, ASME Paper No. HT2005-72200.

[17] Goicochea, J. V., Madrid, M., and Amon, C., 2008, "Hierarchical Modeling of Heat Transfer in Silicon-Based Electronic Devices," Thermal and Thermomechanical Phenomena in Electronic Systems, ITHERM, Orlando, FL, pp. 1006–1017.

[18] Stillinger, F. H., and Weber, T. A., 1985, "Computer Simulation of Local Order in Condensed Phases of Silicon," Phys. Rev. B, **31**(8), pp. 5262–5271.

[19] Tersoff, J., 1988, "Empirical Interatomic Potential for Silicon With Improved Elastic Properties," Phys. Rev. B, **38**, pp. 9902–9905.

[20] Bazant, M. Z., Kaxiras, E., and Justo, J. F., 1997, "Environment-Dependent Interatomic Potential for Bulk Silicon," Phys. Rev. B, **56**(14), pp. 8542–8552.

[21] Herring, C., 1954, "Role of Low-Energy Phonons in Thermal Conduction," Phys. Rev., **95**(4), pp. 954–965.

[22] Klemens, P. G., 1951, "The Thermal Conductivity of Dielectric Solids at Low Temperatures," Proc. R. Soc. London, Ser. A, **208**(1092), pp. 108–133.

[23] Carruthers, P., 1961, "Theory of Thermal Conductivity of Solids at Low Temperatures," Rev. Mod. Phys., **33**(1), pp. 92–138.

[24] Klemens, P. G., 1966, "Anharmonic Decay of Optical Phonons," Phys. Rev., **148**(2), pp. 845–848.

[25] Ecsedy, D. J., and Klemens, P. G., 1977, "Thermal Resistivity of Dielectric Crystals Due to Four-Phonon Processes and Optical Modes," Phys. Rev. B, **15**(12), pp. 5957–5962.

[26] Han, Y.-J., and Klemens, P. G., 1993, "Anharmonic Thermal Resistivity of Dielectric Crystals at Low Temperatures," Phys. Rev. B, **48**, pp. 6033–6042.

[27] Dove, M. T., 1993, *Introduction to Lattice Dynamics* (Cambridge Topics in Mineral Physics and Chemistry), Cambridge University Press, New York.

[28] Gomes, C., 2005, "Molecular Dynamics Study of Silicon Thin Films Thermal Conductivity," Ph.D. thesis, Carnegie Mellon University, Pittsburgh, PA.

[29] Press, W. H., Vetterling, W. T., Teukolsky, S. A., and Flannery, B. P., 1992, *Numerical Recipes in FORTRAN: The Art of Scientific Computing*, Cambridge University Press, New York.

[30] Maruyama, S., 2003, "A Molecular Dynamics Simulation of Heat Conduction of a Finite Length Single-Walled Carbon Nanotube," Nanoscale and Microscale Thermophysical Engineering, **7**(1), pp. 41–50.

[31] Broughton, J. Q., and Li, X. P., 1987, "Phase Diagram of Silicon by Molecular Dynamics," Phys. Rev. B, **35**(17), pp. 9120–9127.

[32] Herrero, C. P., 2001, "Quantum Atomistic Simulations of Silicon and Germanium," J. Mater. Res., **16**(9), pp. 2505–2512.

[33] Zhao, H., Tang, Z., Li, G., and Aluru, N. R., 2006, "Quasiharmonic Models for the Calculation of Thermodynamic Properties of Crystalline Silicon Under Strain," J. Appl. Phys., **99**(6), p. 064314.

[34] Nosé, S., 1984, "A Unified Formulation of the Constant Temperature Molecular Dynamics Methods," J. Chem. Phys., **81**(1), pp. 511–519.

[35] Allen, M. P., and Tildesley, D. J., 1987, *Computer Simulation of Liquids*, Clarendon, Oxford, UK.

[36] Pearson, E. M., Halicioglu, T., and Tiller, W. A., 1985, "Laplace-Transform Technique for Deriving Thermodynamics Equations From the Classical Microcanonical Ensemble," Phys. Rev. A, **32**(5), pp. 3030–3039.

[37] McGaughey, A. J. H., 2004, "Phonon Transport in Molecular Dynamics Simulations: Formulation and Thermal Conductivity Prediction," Ph.D. thesis, University of Michigan, Ann Arbor, MI.

[38] Holland, M. G., 1963, "Analysis of Lattice Thermal Conductivity," Phys. Rev., **132**(6), pp. 2461–2471.

[39] Henry, A. S., and Chen, G., 2008, "Spectral Phonon Transport Properties of Silicon Based on Molecular Dynamics Simulations and Lattice Dynamics," J. Comput. Theor. Nanosci., **5**(2), pp. 141–152.

[40] Klemens, P. G., 1969, "Theory of Thermal Conductivity of Solids," *Thermal Conductivity*, Academic, London.

[41] Ju, Y. S., and Goodson, K. E., 1999, "Phonon Scattering in Silicon Thin Films With Thickness of Order 100 nm," Appl. Phys. Lett., **74**(20), pp. 3005–3007.

[42] Hamilton, R. A. H., and Parrott, J. E., 1969, "Variational Calculation of the Thermal Conductivity of Germanium," Phys. Rev., **178**(3), pp. 1284–1292.

[43] Broido, D. A., Malorny, M., Birner, G., Mingo, N., and Stewart, D. A., 2007, "Intrinsic Lattice Thermal Conductivity of Semiconductors From First Principles," Appl. Phys. Lett., **91**(231922), pp. 1–3.

[44] Gomes, C., Madrid, M., Goicochea, J. V., and Amon, C., 2006, "In-Plane and Out-of-Plane Thermal Conductivity of Silicon Thin Films Predicted by Molecular Dynamics," ASME J. Heat Transfer, **128**(11), pp. 1114–1121.

[45] Schelling, P. K., Phillpot, S. R., and Keblinski, P., 2002, "Comparison of Atomic-Level Simulation Methods for Computing Thermal Conductivity," Phys. Rev. B, **65**, p. 144306.

[46] Sun, L., and Murthy, J. Y., 2006, "Domain Size Effects in Molecular Dynamics Simulation of Phonon Transport in Silicon," Appl. Phys. Lett., **89**, p. 171919.

Molecular-Scale Mechanism of Thermal Resistance at the Solid-Liquid Interfaces: Influence of Interaction Parameters Between Solid and Liquid Molecules

Daichi Torii[1]
e-mail: torii@microheat.ifs.tohoku.ac.jp

Taku Ohara
e-mail: ohara@ifs.tohoku.ac.jp

Kenji Ishida
e-mail: ishida@microheat.ifs.tohoku.ac.jp

Institute of Fluid Science,
Tohoku University,
2-1-1 Katahira,
Aoba-ku,
Sendai, Miyagi 980-8577, Japan

The solid-liquid interfacial thermal resistance is getting more and more important as various solid-liquid systems are utilized in nanoscale, such as micro electro-mechanical systems/nano electro-mechanical systems (MEMS/NEMS) with liquids and nanoparticle suspension in liquids. The present paper deals with the transport of thermal energy through the solid-liquid interfaces, and the goal is to find a molecular-scale mechanism that determines the macroscopic characteristics of the transport phenomena. Nonequilibrium molecular dynamics simulations have been performed for systems of a liquid film confined between atomistic solid walls. The two solid walls have different temperatures to generate a steady thermal energy flux in the system, which is the element of macroscopic heat conduction flux. Three kinds of liquid molecules and three kinds of solid walls are examined, and the thermal energy flux is measured at the control surfaces in the liquid film and at the solid-liquid interfaces. The concept of boundary thermal resistance is extended, and it is defined for each degree of freedom of translational motion of the molecules. It is found that the interaction strength between solid and liquid molecules uniformly affects all boundary thermal resistances defined for each degree of freedom; the weaker interaction increases all the resistances at the same rate and vice versa. The boundary thermal resistances also increase when the solid and liquid molecules are incommensurate, but the incommensurability has a greater influence on the boundary thermal resistances corresponding to the molecular motion parallel to the interface than that for the normal component. From these findings it is confirmed that the thermal resistance for the components parallel to the interface is associated with the molecular-scale corrugation of the surface of the solid wall, and that the thermal resistance for the component normal to the interface is governed by the number density of the solid molecules that are in contact with the liquid. [DOI: 10.1115/1.3211856]

Keywords: thermal energy transfer, thermal resistance, solid-liquid interface, crystal plane, surface corrugation

1 Introduction

Boundary resistance against thermal energy transfer across the solid-liquid interfaces is one of the key issues in modern nanoscale thermal and fluid engineering, as a determining factor in nanoscale thermal devices, as well as in micropores filled with liquid and a liquid with nanoparticle suspension called "nanofluids."

When the characteristic length reduces to nano-order where the macroscopic continuous theory cannot be applied, analyses on the molecular-scale become essential and meaningful. They offer molecular-scale mechanisms of the observing phenomena, leading us to real understandings of them. Moreover, this knowledge is expected to help us a lot in "designing" and controlling the phenomena as required.

There are few studies done for thermal resistance at the solid-liquid interfaces using the microscopic approach and their findings are not sufficient to picture the whole phenomenon clearly. The pioneering work was done by Maruyama and Kimura [1], who reported a temperature jump resulting from the thermal resistance at the solid-liquid interfaces. They showed that the thermal resistance is higher when the solid is less wet to the liquid by controlling the strength of the bond between solid and liquid molecules in their molecular dynamics (MD) simulation. The same tendency has been confirmed by several other researchers by means of both MD simulations [2,3] and experiments [4]. In addition to the confirmation of the correlation between boundary resistance and the wettability, Xue et al. [2] found that the solid-liquid boundary resistance as a function of the wettability exhibits two different profiles depending on whether the surface is wettable or not. Barrat and Chiaruttini discuss in their paper [3], as well as in Bocquet and Barrat's review [5], the analogy of the thermal resistance length or so-called Kapitza length (thermally equivalent length in liquid) with the hydrodynamic slip length. More recently, Kim et al. [6] characterized the thermal resistance length as a function of not only the surface wettability, but also of the thermal oscillation frequency, the wall temperature, the thermal gradient, and the

channel height. Moreover, an empirical model for the thermal resistance length was developed by which some temperature distributions in their nanochannels were predicted successfully.

On the other hand, we have been working on thermal boundary resistances from the viewpoint of molecular motions. Ohara [7] derived the energy that is transferred between a pair of molecules at every moment as a function of the velocities of the two molecules and the intermolecular force acted on them. He showed that the accumulation of this intermolecular-transferred energy for all the pairs of molecules involved plus the accumulation of the energy transported by motions of the molecules equal quantitatively to the macroscopic heat flux. We have been employing this concept of intermolecular energy transfer to the issue of the thermal resistance at the solid-liquid interfaces and obtained various findings. In our earlier study, for example, Ohara and Suzuki [8] found that the intermolecular-transferred energy between a solid molecule and a liquid molecule apart for a certain distance reverses, or has a negative contribution, to the macroscopic heat flux.

We conducted another series of MD simulations [9] to find molecular-scale mechanisms that govern the characteristics of the thermal energy transfer at the solid-liquid interfaces. The simulation system consists of a liquid film of a few nanometer thickness confined between two sliding solid walls. Four types of solid walls were employed, which have different crystal planes on the surface, hence, different surface corrugations in molecular-scale. We defined the thermal boundary resistance for each Cartesian component by two elements: (1) the accumulation of the intermolecular-transferred energy, which we call thermal energy flux in this paper, by molecular motions in the corresponding direction, and (2) the jump in the temperature distribution at the interface where the temperature is based on the kinetic energy of the molecular motions in the corresponding direction. It was found that the characteristics of the thermal energy transfer in the direction parallel to the interface is strongly associated with molecular-scale corrugation on the solid surface; the more corrugated the surface, the less boundary resistance. In contrast, the thermal energy transfer by the molecular motion normal to the interface is governed by the number density of solid molecules in contact with the liquid that participate in energy transfer processes. The overall thermal boundary resistance is determined by the characteristics of the thermal energy transfer for the three Cartesian components as elements. The momentum transfer (velocity slip characteristics) at the solid-liquid interfaces was also discussed in this paper and it was concluded that the molecular-scale governing factor for the momentum transfer is the same as that of the thermal energy transfer for the component parallel to the interface, i.e., the molecular-scale corrugation on the solid surface in the direction of the momentum. In this respect, the
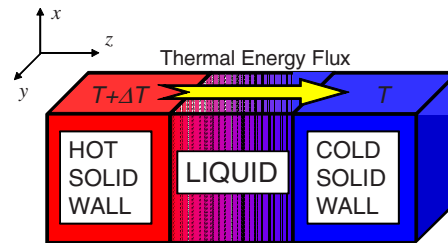
Fig. 1 Simulation system for the energy transfer through the solid-liquid interfaces

momentum transfer is one aspect of the thermal energy transfer and the two characteristics are not entirely correlated to each other as a principle.

Regarding the characteristics of the thermal energy transfer, a dependency on the slip velocity was observed in the simulation results [9]. Therefore, we performed additional MD simulations of a similar system [10], but without shear this time to eliminate the influence of the momentum transfer on the characteristics of the thermal energy transfer. Although the obtained thermal resistances were different (it was found later that the thermal boundary resistance increases with the increase in the velocity slip at the interface), the basic molecular-scale mechanisms that govern the characteristics of the thermal energy transfer for each Cartesian component held true.
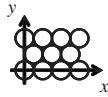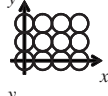
Argon was the only kind of liquid molecule employed in the previous simulations [10], however, it is not just interesting, but it will be a practical need to know how the mechanisms of thermal resistance found in our previous researches are affected by parameters for intermolecular potential between solid and liquid molecules. Therefore, in the present paper, further MD simulations have been performed for the same system (without shear) with two different sets of solid-liquid interaction parameters, and the results are reported in comparison with the previous study [10].

2 Molecular Dynamics Simulation

The simulation system employed in the present study is shown in Fig. 1. The system consists of two parallel solid walls and a liquid film between them. The temperature of the left solid wall is kept higher than that of the right throughout the simulation time in order to generate a steady thermal energy flux in the system. Periodic boundary conditions were applied in the x and y directions.

The three solid walls examined in the simulation are shown in Table 1. They all have an identical face-centered cubic (FCC) structure, and their (1,1,1), (1,0,0), and (1,1,0) crystal planes con-

Table 1 Solid walls employed in the simulation

	Surface molecular density	Surface crystal plane	Surface molecular configuration	Number of atoms in x and y directions	Number of layers in z direction	Number of atoms in a pair of walls
A	largest	FCC (1,1,1)		20×20	7	5600
B	↑ ↓	FCC (1,0,0)		20×17	8	5440
C	small	FCC (1,1,0)		20×12	11	5280

Table 2 Parameters for the model of liquid molecules. Subscripts "LL" and "LS" denote interactions between liquid molecules and those between liquid and solid molecules, respectively. All values are based on those of argon, which are σ_{Ar} =3.405×10⁻¹⁰ m, ε_{Ar}=1.67×10⁻²¹ J, and m_{Ar}=6.63×10⁻²⁶ kg. The equilibrium distance between two solid molecules r_{eq} is 2.77×10⁻¹⁰ m.

	Case 1	Case 2	Case 3
σ_{LL}	σ_{Ar}	σ_{Ar}	$2\sigma_{Ar}$
σ_{LS}	$(\sigma_{Ar}+r_{eq})/2$	$(\sigma_{Ar}+r_{eq})/2$	$(2\sigma_{Ar}+r_{eq})/2$
ε_{LL}	ε_{Ar}	ε_{Ar}	ε_{Ar}
ε_{LS}	ε_{Ar}	$\varepsilon_{Ar}/2$	ε_{Ar}
m	m_{Ar}	m_{Ar}	m_{Ar}

tact the liquid, which are named A–C, respectively. Each solid wall is constructed using 7–11 layers of solid molecules in such a manner that the thickness in the z direction was almost identical, which is around 1.6 nm, for the three types of solid walls. No intentional control of molecular motion, such as temperature control, was applied in the calculation of molecular motion of solid and liquid molecules. However, the phantom molecule method [1] was applied to model a semi-infinite solid having a constant temperature. The phantom molecules are placed outside the layers of solid molecules and excited by the random force of Gaussian distribution with a standard deviation whose magnitude is determined by the target temperature. The integrated interaction acting on the solid molecules from an isothermal semi-infinite solid is represented by the interaction between the solid molecules and the phantom molecules. The target temperature of the hot and cold solid walls was selected to be 155 K and 85 K, respectively, which are just below the critical point and just above the triple point of the liquid employed in the present simulation in the bulk state. The interaction between solid molecules was modeled using a harmonic potential, with the potential parameters and mass values being those for platinum: the spring constant was 46.8 N/m, the equilibrium distance r_{eq}=2.77×10⁻¹⁰ m, and the mass m=3.24 ×10⁻²⁵ kg. The dimensions of the basic cell in the x and y directions were fixed to 5.0 nm approximately in every case by arranging 12–20 solid atoms in each direction.

A total of three types of liquid molecules were selected for simulation. They are all monatomic molecules, interacting by the Lennard-Jones (12-6) potential. The first specie of liquid molecule, which is the one employed in the previous study [10], is equivalent to argon. The interaction between a solid molecule and a liquid molecule is also modeled by the Lennard-Jones (LJ) potential; σ_{LS} was selected to be the mean of σ_{LL} and the equilibrium distance between solid molecules r_{eq}, and ε_{LS} was assumed to be equal to ε_{LL}. The second and third species have the same parameters as the first one, but has one exception for each. The second one has a weaker solid-liquid interaction; ε_{LS} was set to be half of that of the first specie. This corresponds to the case where liquid is less wet to solid. For the third specie, σ_{LL} was doubled. This corresponds to the case where equilibrium distance between liquid molecules is larger for a fixed lattice constant of the solid. These parameters are collected in Table 2. Moreover, the simulation system with each parameter set is called as "Case 1," or Case 2 or Case 3, as shown in Table 2. The thickness of the liquid film, defined by the distance in the z direction between the time-averaged positions of solid molecule layers, each of which contacted the liquid film at each end, was equated to $15\sigma_{Ar}$ =5.108 nm. The number of constituent molecules of the liquid film (listed in Table 3) was determined by trial and error in such a way that the pressure of the liquid was small enough not to influence the liquid structure or thermal energy transfer. The resulting pressure of each simulation system was within the range of ±2 MPa. The pressure of the liquid was calculated by accumulating the forces in the z direction acting on the solid walls. In all the MD simulations, every LJ potential was truncated at 5σ.

The data for analyses were obtained by simulations with a time step of 2.5×10⁻¹⁵ s for 2×10⁶ steps for Case 1, 3×10⁶ steps for Case 2, or 4×10⁶ steps for Case 3, after an equilibrium state was established by an equilibration run for each preceding 1×10⁶ steps. The simulation time was determined so as to obtain all the data sufficiently reliable. Among all the values measured here, the energy flux required the longest simulation time in this respect. Since the fluctuation of the value was even more dominant in the case the magnitude of energy flux was less, the simulation time was set longer for systems with smaller energy flux. The equilibration of the system was confirmed by the stability of the profiles of energy, temperature, and number density of molecules.

3 Results for a Platinum-Argon System (Case 1)

Since the results for Case 1 were already published [10], they were summarized here only briefly.

Figure 2 shows number density distributions of liquid molecules along the z direction, which is normal to the liquid film. Trapped by the potential of solid molecules, liquid molecules form a layered structure in the vicinities of the interfaces (top figure). Hereafter, the layer of molecules that contact the solid surface is referred to as the "liquid contacting layer," and its peak is called "first peak." The bottom figure is a comparison among cases with solid walls A–C in the region adjacent to the left solid

Table 3 Total number of liquid molecules and positions of peaks in their number density distributions for each simulation condition. Positions of peaks listed here are mean values of z position of the peak for hot solid wall side and $15\sigma_{Ar}-z$ position of the peak for cold solid wall side.

	Solid wall	Number of liquid molecules in the system	Nondimensionalized by σ_{Ar}		Nondimensionalized by σ_{LS}	
			Position of first peak	Position of second peak	Position of first peak	Position of second peak
Case 1	A	2330	0.884	1.838	0.975	2.027
	B	2300	0.864	1.816	0.953	2.003
	C	2330	0.746	1.674	0.823	1.847
Case 2	A	2230	0.888	1.884	0.979	2.078
	B	2200	0.878	1.875	0.969	2.067
	C	2200	0.802	1.782	0.884	1.965
Case 3	A	325	1.364	3.229	0.970	2.295
	B	320	1.355	3.205	0.963	2.278
	C	330	1.293	3.140	0.919	2.232
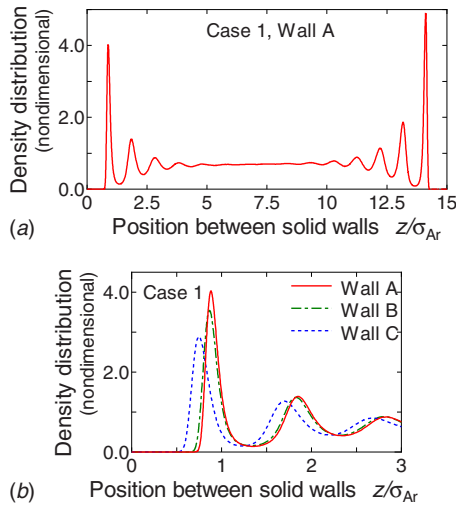
Fig. 2 The number density distribution of liquid molecules (Case 1); (*a*) the case with solid wall A over the whole range of liquid film (top panel) and (*b*) the comparison among cases with walls A–C in the vicinity of the left solid-liquid interface (bottom panel)

Fig. 3 The distribution of temperature in the liquid film and the solid walls (Case 1) in the case with solid wall A (top panel) and C (bottom panel)

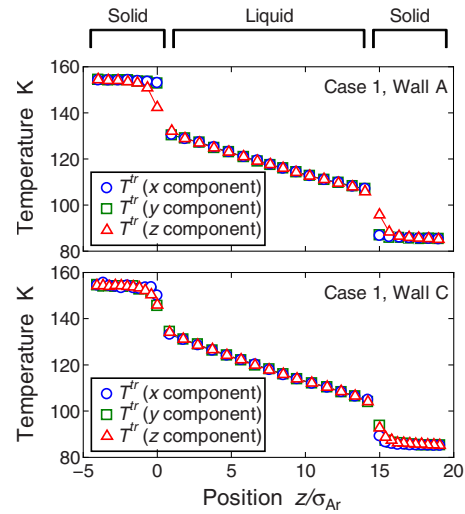surface. The position of the first peak in the *z* axis is nearest to the solid surface for the case with wall C, and farthest with wall A, as listed in Table 3. This is correlated with the number density of the surface molecules of the solid wall, which is A>B>C; most liquid molecules in the liquid contacting layers are captured in the "pits" of the potential made by solid molecules, and the first peak gets close to the solid surface as the pits become deeper or as the number density of the surface molecules is smaller.

The control surfaces in the liquid film, defined to measure the energy flux, were all parallel to the liquid film and they were placed where this number density distribution performs its local minima. In the center region of the film, where the distribution is more or less flat, they were located at a constant interval, just like those in the vicinities of the interfaces.

Temperature profiles of the system are shown in Fig. 3. Here, the temperature is defined for each degree of freedom of molecular motion based on the kinetic energy distributed to each degree of freedom. A series of plots connected by lines in the center of the graphs denote the data averaged over the molecules belonging to each molecular layer or slab between the two adjacent control surfaces. A series of plots at both sides of the graphs denote the data for molecular layers of the solid walls. A uniform temperature gradient is observed in the liquid film. The temperature difference among the degrees of freedom of molecular motions is

remarkable in the layers of solid molecules near the solid-liquid interfaces, which shows that the system is in a highly nonequilibrium state where the equipartition law of energy does not hold. The temperature jump at the solid-liquid interface is defined here as the temperature difference between the layers of solid molecules and liquid molecules contacting each other over the interface. Moreover, this temperature jump can also be defined for each degree of freedom of molecular motion. For the case with wall A, the *z* component of the temperature jump is smallest. For the case with C, on the other hand, the *y* component represents the smallest jump followed by the *z* component, indicating that the energy transfer by the molecular motion along the *y* axis is activated by the molecular-scale corrugation on the solid surface along the same axis. The concrete values of these temperature jumps are collected in Table 4.

The thermal energy flux in the *z* direction J_z that passes through a control surface S_{xy} is given by [7]

$$J_z S_{xy} = \sum_i \left[\left(\frac{1}{2} m \boldsymbol{v}_i^2 + \phi_i \right) / 1 \right] \frac{v_{i,z}}{|v_{i,z}|} + \frac{1}{2} \sum_i \sum_{j>i} [\boldsymbol{F}_{ij} \cdot (\boldsymbol{v}_i + \boldsymbol{v}_j)] \frac{z_{ij}}{|z_{ij}|}$$

$$\phi_i = \frac{1}{2} \sum_j \phi_{ij} \qquad (1)$$

where m and $\boldsymbol{v}$ denote the mass and velocity vector, respectively. $\boldsymbol{F}_{ij}$ and z_{ij} are the intermolecular force vector between molecules

Table 4 Measured and calculated values for each simulation condition

	Solid wall	Temperature jump at the interface (K)				Energy flux at the interface (MW/m²)				Boundary thermal resistance ×10⁻⁶(m² K/W)			
		Average	*x*	*y*	*z*	Total	*x*	*y*	*z*	Overall	*x*	*y*	*z*
Case 1	A	17.6	21.3	21.3	10.2	451.9	30.9	27.2	393.8	0.039	0.690	0.784	0.026
	B	16.2	19.5	19.7	9.3	374.9	35.0	34.1	305.8	0.043	0.558	0.577	0.031
	C	12.9	16.3	10.8	11.6	536.1	41.0	147.1	347.9	0.024	0.398	0.073	0.033
Case 2	A	24.5	28.3	28.0	17.1	227.0	12.4	12.0	202.7	0.108	2.290	2.343	0.085
	B	22.8	22.8	26.6	14.9	174.9	15.3	13.6	146.0	0.130	1.487	1.953	0.102
	C	21.1	24.7	19.2	19.4	255.0	15.7	65.9	173.4	0.083	1.571	0.292	0.112
Case 3	A	18.6	24.9	24.8	6.0	78.7	2.3	1.9	74.5	0.236	10.777	12.823	0.081
	B	19.6	25.6	25.6	7.7	75.6	3.7	3.9	68.0	0.260	6.946	6.614	0.113
	C	14.3	18.3	15.5	9.1	103.2	3.0	27.9	72.3	0.139	6.187	0.557	0.126
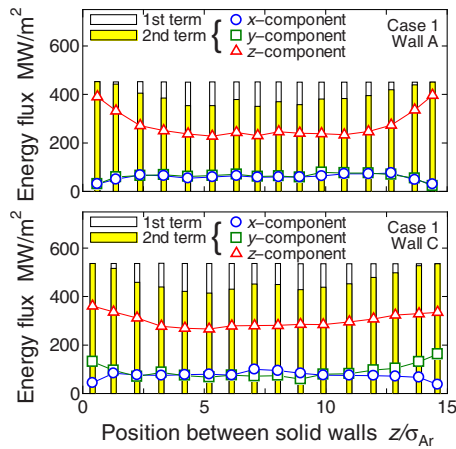
Fig. 4 Contributions of each degree of freedom of molecular motion to the total energy flux observed in the liquid film and at the solid-liquid interfaces (Case 1) with solid wall A (top panel) and C (bottom panel). "1st term" and "2nd term" correspond to those in the right side of Eq. (1).

i and j and the distance along the z axis between molecules i and j, respectively. The first term on the right hand side of Eq. (1) represents the transport of energy of molecules due to their motion; the summation is to be made over the molecules that pass through the control surface in a unit period of time. The second term represents the energy transfer due to changes of molecular energy by intermolecular forces acting between a pair of molecules; the double summation is to be made over all pairs of molecules that hold the control surface between them at a certain moment. This second term can further be decomposed into three corresponding degrees of freedom of molecular motion, i.e., the x, y, and z, in such a manner as

$$F_{ij} \cdot v_i = F_{ij,x} \cdot v_{i,x} + F_{ij,y} \cdot v_{i,y} + F_{ij,z} \cdot v_{i,z} \qquad (2)$$

each of which represents the intermolecular energy transfer by the molecular motion along the x, y, and z axis, respectively.

Figure 4 shows each contribution of the thermal energy flux at each control surface in the system. The rightmost and leftmost bars and plots denote the data for the solid-liquid interfaces. Although the total amount of thermal energy flux is uniform throughout the liquid film, the contribution of each component does not exhibit uniform distribution. In other words, the thermal energy flux is uniform in its quantity, but differs in "quality," which is focused on here in this study. The second term of Eq. (1) dominates the first one throughout the liquid film. In the central region of the film, the z component is about three times as large as the other two in the second term. That is to say, in the bulk liquid the molecular motion parallel to the direction of the energy flux makes the largest contribution. The composition of the thermal energy flux changes as its getting closer to the solid-liquid interface, which is apparently an influence of the solid wall. For the case with wall A, the z component of the second term becomes even larger, while the x and y components decrease. For the case with wall C, on the other hand, the only decreasing component is x, and the increase in the y component is remarkable as the position gets closer to the solid-liquid interface. This feature with wall C comes from the molecular-scale corrugation on the surface of the solid wall. The interval between rows of solid molecules on the surface is large along the y axis for the case with wall C (see Table 1). Larger interval means deeper pits of the potential of the solid molecules that traps liquid molecules, and deeper pits make it easier for molecules to transfer energy by the movement or oscillation along the identical axis, which results in a larger contribution to the thermal energy flux. This large contribution is consistent with the smaller temperature jump shown in Fig. 3.
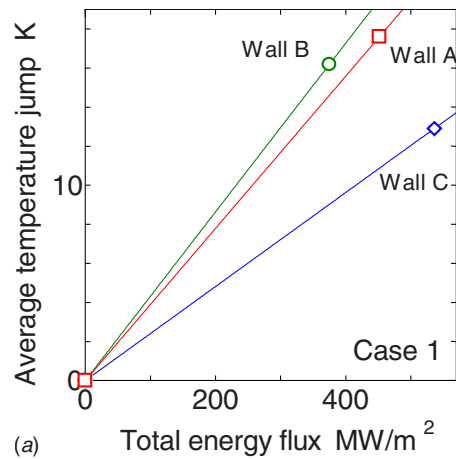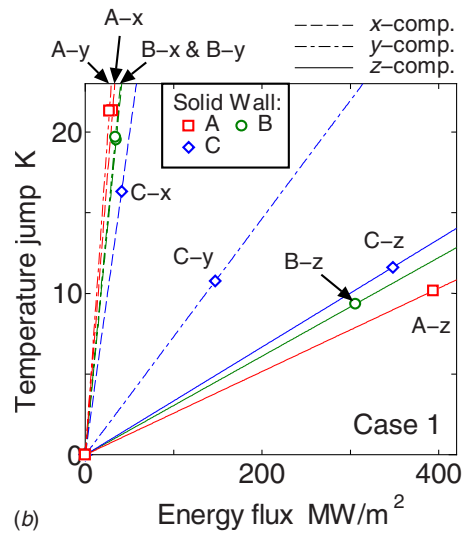

Fig. 5 The thermal boundary resistance at the solid-liquid interface (Case 1); (a) the average temperature jump versus the total energy flux (top panel) and (b) the temperature jump versus the energy flux for each degree of freedom (bottom panel)

The thermal resistance at the solid-liquid interfaces is examined in Fig. 5 with its value listed in Table 4. As it is already described, the temperature jump can be defined for each degree of freedom, and the thermal energy flux at the interface, where only the second term of Eq. (1) has a value, can also be decomposed to the contributions of each freedom of molecular motion. The bottom panel of Fig. 5 shows the individual plots of the temperature jump for each degree of freedom against each corresponding contribution to thermal energy flux for three kinds of solid walls. The average temperature jump among the three degrees of freedom versus the total energy flux passing the interface is plotted in the top figure. The thermal boundary resistance for each solid wall, which is defined by the ratio of the temperature jump to the thermal energy flux, corresponds to the gradient of the correlation line in the top figure. As is shown in the figure, the resistance for wall B is the largest, followed by walls A and C.

The thermal boundary resistance for each component is defined here as the gradient of each straight line in the bottom panel of Fig. 5. First, by taking a look at the lines for the x and y components, one would tell that all the lines are almost vertical (high resistance) except for the y component of wall C. It was this component whose corresponding contribution to the thermal energy flux had a relatively large magnitude in Fig. 4. The reason for the large contribution was explained above in relation to the
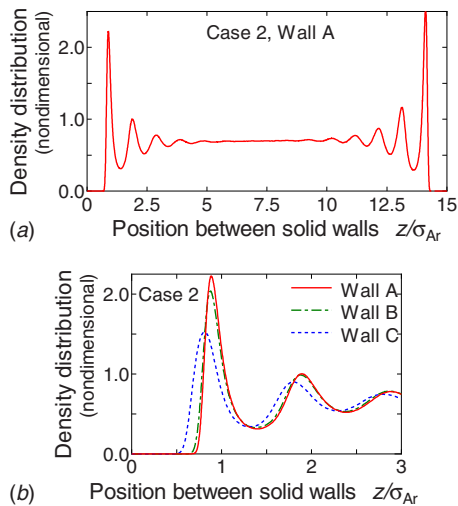
Fig. 6 The number density distribution of liquid molecules (Case 2); (*a*) the case with solid wall A over the whole range of liquid film (top panel) and (*b*) the comparison among cases with walls A–C in the vicinity of the left solid-liquid interface (bottom panel)

Fig. 7 The number density distribution of liquid molecules (Case 3); (*a*) the case with solid wall A over the whole range of liquid film (top panel) and (*b*) the comparison among cases with walls A–C in the vicinity of the left solid-liquid interface (bottom panel)

molecular-scale corrugation of the solid surface, and the same explanation can be applied here to the thermal resistance. It is, therefore, summarized that the boundary resistance for the components parallel to the interface are strongly associated with the molecular-scale corrugation of the potential surface of solid surface, which liquid molecules experience according to the positional change in each direction. For the z component, on the contrary, the corrugation of the potential surface of the solid wall is not an influencing factor. The major factor for the z component of the thermal energy flux is the number density of solid molecules on the wall surface, i.e., the number of molecules that can participate in the energy transfer. As a result, the thermal boundary resistance for the z component is the lowest for wall A, which has the highest number density of molecules on the surface, and then increases in the order $B < C$. The boundary resistance for each of the x, y, and z components is governed by those different factors, respectively, and the extent of the contribution of each component to the total energy flux is another factor to determine the overall influence of the solid surface structure on the total boundary resistance shown in the top panel of Fig. 5.

4 Parameter Study (Cases 2 and 3)

Here in this section, results for the other two cases, i.e., Cases 2 and 3, are shown and the influence of interaction between solid molecules and liquid ones are discussed, comparing them with the results obtained for Case 1 in Sec. 3.

The number density distribution of liquid molecules for Case 2 is nearly the same as Case 1 except for the region near the solid-liquid interface, which is shown in Fig. 6. The heights of the peaks in the vicinities of the interfaces are almost exactly half of those for Case 1, which means that the solid molecules can trap only half the number of molecules at a moment when the depth of the solid-liquid potential well is reduced to half. As shown in the bottom panel, the positions of the first peaks for different walls, whose concrete values are listed in Table 3, exhibit the same tendency as Case 1.

Figure 7 is the same analysis done for Case 3. Since the equilibrium distance between liquid molecules is twice as long as that for Case 1 or Case 2, the distance between the two neighboring peaks in Fig. 7 are about twice as large, resulting in the formation of only seven molecular layers in the film. What is unique for Case 3 is that the peaks for liquid contacting layers are isolated from the rest of the distribution. It tells that molecules in liquid
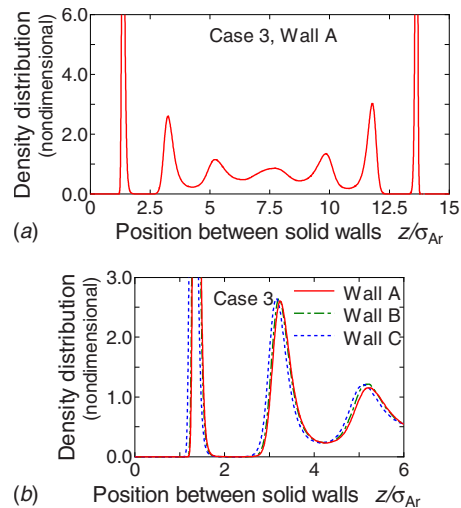
contacting layers do not diffuse toward the center of the liquid film in the z direction. This is, for one thing, caused by the shift of the liquid contacting layer away from the solid surface, leaving a larger gap between the inmost layer of the solid molecules and the liquid contacting layer. The larger gap allows more solid molecules to exert force on the liquid molecules in the direction normal to the solid surface to affect and limit the motion of the liquid molecules. The second reason is the lower temperature of the liquid in reduced units. The temperature conditions in the current simulations are kept the same on the dimensional scale, so the nondimensional temperature that determines the thermodynamic state of the liquid is lower for the liquid with a larger equilibrium distance. The isolation of the peaks of the liquid contacting layers is due to the solidification of the liquid molecules. The difference in distributions of liquid molecules according to the different solid walls shown in the bottom panel of Fig. 7 is not large as compared to those of Cases 1 and 2. This is because liquid molecules that have a larger equilibrium distance experience the variation in the molecular-scale corrugation on the solid surfaces to be relatively smaller.

Figure 8 shows the temperature distribution for Case 2. Independent on the solid wall employed, the gradients of the distribution lines in the liquid are now smaller, leaving larger temperature jumps than Case 1. This indicates that the thermal boundary resistance is larger than that of Case 1, which will be confirmed later in relation to the magnitude of energy flux. The differences among the x, y, and z components are the same as Case 1.

The temperature distribution exhibits a very unique feature for Case 3, especially for the case with wall C, as shown in Fig. 9. On the top panel for wall A, the temperature difference among the three components is very large in the liquid contacting layers. What makes it possible is the large equilibrium distance between liquid molecules compared to the range of movement of molecules in the z direction in the liquid contacting layers. Liquid molecules in the liquid contacting layers are so separated apart in the x and y directions that little force can be acted in the z direction between a pair of molecules in a liquid contacting layer. This means that the movement of molecules along the z axis in liquid contacting layers is scarcely governed by the interaction with molecules in the same liquid contacting layer. Therefore, the exchange of thermal energy among the degrees of freedom of molecular motion, the x, y, and z, is insufficient to help the equilibration of thermal energy among these degrees, which result in the large
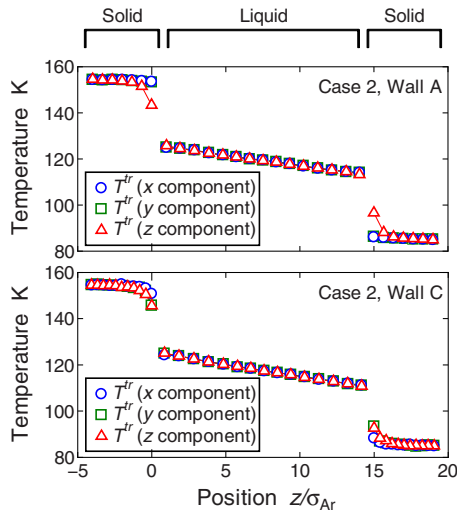
Fig. 8 The distribution of temperature in the liquid film and the solid walls (Case 2) in the case with solid wall A (top panel) and C (bottom panel)

Fig. 10 Contributions of each degree of freedom of molecular motion to the total energy flux observed in the liquid film and at the solid-liquid interfaces (Case 2) with solid wall A (top panel) and C (bottom panel). "1st term" and "2nd term" correspond to those in the right side of Eq. (1).

difference in the ensemble-averaged kinetic energy distributed for the three degrees of freedom of molecular motion. For the case with wall C, temperature jump is relatively small for all the three components, and there is a remarkable temperature difference between the liquid contacting layer and the liquid molecular layer next to it for all components.

The profiles of the thermal energy flux for Cases 2 and 3 are shown in Figs. 10 and 11, respectively. The profiles for Case 2 are almost exactly the same as those for Case 1 except for their magnitudes, which are approximately half of those for Case 1. The magnitude of the energy flux is the smallest for Case 3; it is around 100 MW/m^2 or less. Although the contribution profiles for Cases 1 and 3 look alike, the x and y components for wall A and the x component for wall C at the solid-liquid interfaces contribute only 2.5–3.0 % to the total energy flux for Case 3, while they were 6.0–8.0 % for Case 1. The only component that is parallel to the interface and still has a comparable contribution is the y component for wall C. The decrease in contribution owes it to the larger equilibrium distance of solid-liquid molecules in comparison with that between two solid molecules r_{eq}. For liquid

molecules with a larger solid-liquid equilibrium distance, the pits in the potential surface made by solid molecules are relatively smaller and the liquid molecules do not experience the corrugation as much as they do in the case of a smaller solid-liquid equilibrium distance. Therefore, all the solid walls are more slippery for the molecules of Case 3, resulting in a lesser contribution of the molecular motion parallel to the interface to thermal energy flux. Judging from the stable contribution of the y component of wall C, on the contrary, the liquid molecules still seem to "feel" the surface in this direction as corrugated. However, when the equilibrium distance between solid-liquid molecules becomes even larger, which is usually accompanied with a larger equilibrium distance between the liquid molecules themselves, the liquid molecules will be expected to lose the sensitivity for corrugation totally and feel the solid surface in any direction parallel to the solid surface as slippery, resulting in having all the energy flux, transferred by the z component, at the interface.

In the same way as in Sec. 3, the average temperature jump is plotted against the total energy flux in Fig. 12 for the three cases with all solid walls (the concrete values for the plots can be found in Table 4). Regardless of the solid walls employed, Case 1 ex-
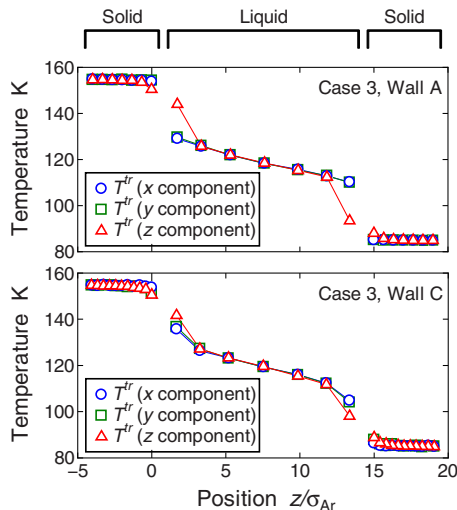
Fig. 9 The distribution of temperature in the liquid film and the solid walls (Case 3) in the case with solid wall A (top panel) and C (bottom panel)
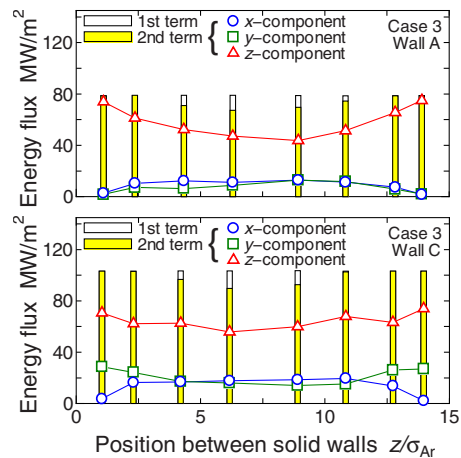
Fig. 11 Contributions of each degree of freedom of molecular motion to the total energy flux observed in the liquid film and at the solid-liquid interfaces (Case 3) with solid wall A (top panel) and C (bottom panel). "1st term" and "2nd term" correspond to those in the right side of Eq. (1).
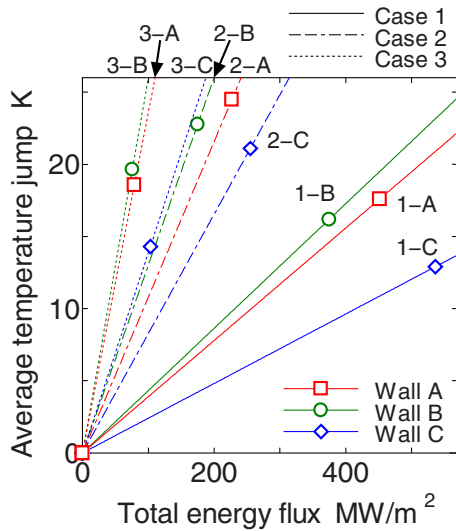
Fig. 12 The boundary thermal resistance; the average temperature jump versus the total energy flux for Cases 1–3

hibits the lowest resistance, which is followed by Cases 2 and 3. Case 2 shows a higher boundary resistance than Case 1, since the solid molecules cannot trap and hold the liquid molecules as well as they do for Case 1, causing lesser chances of exchanging energy between a pair of solid and liquid molecules. The same results can be found in many literatures [1,2]. There are two reasons for the highest boundary resistance of Case 3; one is the lower number density of the liquid molecules in the liquid contacting layers because of the enlarged equilibrium distance between liquid molecules and the other reason is that the solid wall is more "slippery" to liquid molecules. For each case, the system with wall B shows the highest boundary resistance, while wall C represents the lowest.

For Case 2, the thermal resistances for each component have the same trend as for Case 1, with all values of the resistance shifting to the larger side but keeping the same magnitude relation to each other. Therefore, only the plot for Case 3 is shown here in Fig. 13, although the concrete values of the thermal resistance are collected in Table 4 for both cases, Cases 2 and 3. The tendency seen in Fig. 13 is similar to that for Case 1 in Fig. 5, but for Case 3 the lines for the z components lie more horizontally and vertical
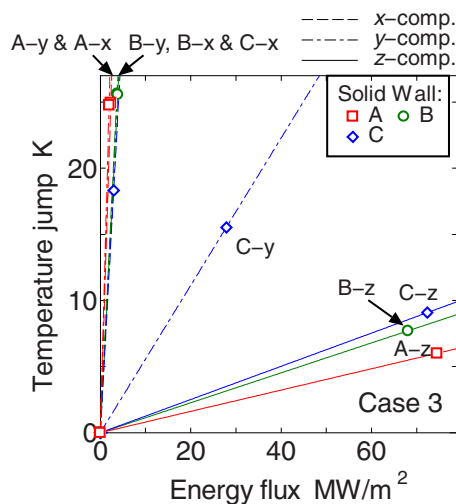

Fig. 13 The boundary thermal resistance; the temperature jump versus the energy flux for each degree of freedom for Case 3

lines are even more straightened up, showing that the molecular motion perpendicular to the interface plays a much more important role when the equilibrium distance between liquid molecules becomes relatively larger than the molecular-scale corrugation on the solid surface.

5 Concluding Remarks

Molecular dynamics simulations have been performed for a system composed of a pair of parallel solid walls and a liquid film interposed between the walls, which are kept at different temperatures. The simulations were done for the combinations of three kinds of solid walls and three kinds of liquid molecules. The thermal energy transfer at the solid-liquid interface has been analyzed, and molecular-scale mechanisms that govern the interfacial thermal resistance are elucidated.

The results have revealed that certain components of energy transfer, which are due to the molecular motion in directions parallel to the solid-liquid interface, are governed by surface corrugation at the molecular-scale, i.e., the unevenness on the potential surface formed by the surface solid molecules that liquid molecules experience by the positional change in the relevant direction. On the other hand, the component of energy transfer due to the molecular motion in the direction perpendicular to the surface, which is the major component of thermal energy flux at the interface, is governed by the molecular number density on the solid surface.

From the parameter study, it was found that the weakened interaction between solid and liquid molecules enlarges the boundary resistance, but it does not have any significant influence on the phenomena and their mechanism qualitatively. The larger equilibrium distance between liquid molecules was also found to make the thermal resistance higher due to the two reasons; the smaller number density of liquid molecules that contact the solid surface (which mainly reduces the efficiency of energy transport by the molecular motion perpendicular to the interface) and the reduction in the relative scale of the unevenness of the potential surface on the solid surface, which is essential in energy transfer by the molecular motion parallel to the interface.

Nomenclature

J = thermal energy flux (W/m^2)
r_{eq} = equilibrium distance between solid molecules (m)
S = area of a control surface (m^2)
ε = energy parameter of the LJ potential (J)
ϕ = intermolecular potential energy (J)
σ = length parameter of the LJ potential (m)

Subscripts and Superscripts

Ar = parameters for argon
i and j = ith and jth molecules
LL = interaction between liquid molecules
LS = interaction between a liquid molecule and a solid one
tr = translational motion

References

[1] Maruyama, S., and Kimura, T., 1999, "A Study on Thermal Resistance Over a Solid-Liquid Interface by the Molecular Dynamics Method," Therm. Sci. Eng., **7**(1), pp. 63–68.

[2] Xue, L., Keblinski, P., Phillpot, S. R., Choi, S. U.-S., and Eastman, J. A., 2003, "Two Regimes of Thermal Resistance at a Liquid-Solid Interface," J. Chem. Phys., **118**(1), pp. 337–339.

[3] Barrat, J.-L., and Chiaruttini, F., 2003, "Kapitza Resistance at the Liquid-Solid Interface," Mol. Phys., **101**(11), pp. 1605–1610.

[4] Ge, Z., Cahill, D. G., and Braun, P. V., 2006, "Thermal Conductance of Hydrophilic and Hydrophobic Interfaces," Phys. Rev. Lett., **96**(18), p. 186101.

[5] Bocquet, L., and Barrat, J.-L., 2007, "Flow Boundary Conditions From Nano- to Micro-Scales," Soft Matter, **3**, pp. 685–693.

[6] Kim, B. H., Beskok, A., and Cagin, T., 2008, "Molecular Dynamics Simulations of Thermal Resistance at the Liquid-Solid Interface," J. Chem. Phys., **129**(17), p. 174701.

[7] Ohara, T., 1999, "Intermolecular Energy Transfer in Liquid Water and Its Contribution to Heat Conduction: A Molecular Dynamics Study," J. Chem. Phys., **111**(14), pp. 6492–6500.

[8] Ohara, T., and Suzuki, D., 2000, "Intermolecular Energy Transfer at a Solid-Liquid Interface," Microscale Thermophys. Eng., **4**(3), pp. 189–196.

[9] Ohara, T., and Torii, D., 2005, "Molecular Dynamics Study of Thermal Phenomena in an Ultrathin Liquid Film Sheared Between Solid Surfaces: The Influence of the Crystal Plane on Energy and Momentum Transfer at Solid-Liquid Interfaces," J. Chem. Phys., **122**(21), p. 214717.

[10] Torii, D., Ohara, T., and Ishida, K., 2006, "Solid-Liquid Boundary Resistance: A Molecular Dynamics Study on Intermolecular Energy Transfer at Solid-Liquid Interfaces," *Proceedings of the 13th International Heat Transfer Conference*, Begell House, Redding, CT, p. 287.

Measurement of the Heat Capacity of Copper Thin Films Using a Micropulse Calorimeter

Jun Yu
e-mail: junyu@dlut.edu.cn

Zhen'an Tang

Fengtian Zhang

Haitao Ding

Zhengxing Huang

Department of Electronic Engineering,
Dalian University of Technology,
Dalian, Liaoning 116024, China

This paper presents a micropulse calorimeter for heat capacity measurement of thin films. Optimization of the structure and data processing methods of the microcalorimeter improved the thermal isolation and temperature uniformity and reduced the heat capacity measurement errors. Heat capacities of copper thin films with thicknesses from 20 nm to 340 nm are measured in the temperature range from 300 K to 420 K in vacuum of 1 mPa. The specific heat of the 340 nm Cu film is close to the literature data of bulk Cu. For the thinner films, the data shows that the specific heat increases with the decreasing of film thickness (or the average crystalline size). [DOI: 10.1115/1.3211864]

1 Introduction

Thermal properties of thin films may be significantly different from the corresponding bulk material data [1]. Various experiment techniques have been developed for measuring the thermal properties of thin films, including flash method [2], 3ω method [3,4], ac calorimetry [5], and scanning thermal microscopy (SThM), etc. [6]. Over the past 10 years, suspending membrane based microcalorimeters have been developed for measuring the heat capacity of ultrathin films with thickness from the nanometer scale to submicrometer scale, as thin films in this scale can hardly be measured with the traditional calorimeters [7,8]. The basic structure of a microcalorimeter is a suspending membrane with a heater and thermometer on it. With this structure, the microcalorimeter has very small heat capacitance and it is quasi-adiabatic. These conditions are essential for the thin-film heat capacity measurement because the heat capacity of the thin films is small (from several nano-J K^{-1} to micro-J K^{-1}). ac calorimetries and the relaxation method are used to measure heat capacities of thin films from several Kelvin to room temperature [9–13]. High heating/cooling rate is another important thermal property of the microcalorimeter. The ultrafast heating rate reduces the influence of heat loss of the calorimeter during the measurement, thus, enables fast scanning calorimetry in a wide temperature range. Various kinds of ultrafast scanning calorimetries are developed such as thin-film differential scanning calorimetry (TDSC) [14–17], high temperature scanning nanocalorimeter [18,19], and nonadiabatic ultrafast nanocalorimetry [20,21]. In our previous work [22], we developed a thin-film microcalorimeter, which can measure the heat capacity of submicrometer-thick thin films. The thin-film microcalorimeter uses pulse calorimetry in which heat loss, temperature uniformity, and random noise are the main factors leading to the measurement errors. In this paper, structure of the microcalorimeter and the data processing method are optimized to improve the heat capacity measurements. The thin-film micropulse calorimetry is applied to the measurement of heat capacities of the copper thin films with thicknesses from 20 nm to 340 nm. The specific heat of the sample films are calculated and compared with the literature data of bulk copper.

2 Microcalorimeter Design and Fabrication

The microcalorimeter is a freestanding 88×88 μm^2 square membrane suspended above the silicon substrate by six beams, as shown in Fig. 1. The membrane is made from a $SiO_2/SiN/SiO_2$ sandwich structure, which is the typical dielectric layer for freestanding thin films. The membrane is designed to be around 2 μm thick in order to ensure sufficient mechanical strength after released from the substrate. A zigzag polysilicon thin-film resistor lies on the membrane, acting as both heater and thermometer. It is preferred to use thin-film thermometer rather than the thermocouple because the former can record the average temperature of the membrane with rapid response. The thin-film resistor has four ends so that the average temperature of the square membrane can be precisely measured with the four-point method. Four main beams 98 μm in length and 20 μm in width support the four ends of the resistor at two diagonal corners. Two assistant beams 68 μm in length and 10 μm in width support the other two corners of the membrane to improve the mechanical strength and symmetry of the microcalorimeter.

Using three-dimensional finite element analyses (FEAs) with ANSYS software, the thermal simulations of the microcalorimeter were performed. The suspending parts, including the center membrane and the beams with the same geometry of the designed calorimeter, are the structure used for the simulation. The beams of the calorimeter are anchored on Si substrate with good thermal conductivity. Therefore, the beams' anchors were fixed to be at a constant temperature $T_0 = 298$ K in the simulation. The material parameters needed for the simulation are listed in Table 1. The thermal conductivities of thin films are smaller than the relative bulk materials, and the conductivity data of SiO_2, SiN_x, and poly-Si are from Ref. [23].

The electrical voltage stimulation is applied at the resistor's ends on beams 3 and 6. The microcalorimeter works in a vacuum, so the heat transfer by convection and conduction through gas is neglectable. When the temperature of the calorimeter is less than 450 K, the thermal radiation is also neglectable because result from a simulation including a 0.5 surface radiation ratio shows less than a 1% change in the temperature compared with a simulation without considering thermal radiation. The heat loss through the beams of the calorimeter is the dominate heat loss, and it is unavoidable because the beams are required for mechanical supporting of the suspending membrane and electrical collecting of the heater/thermometer. Longer beams provide better thermal isolation but poor mechanical strength. In our previous work,
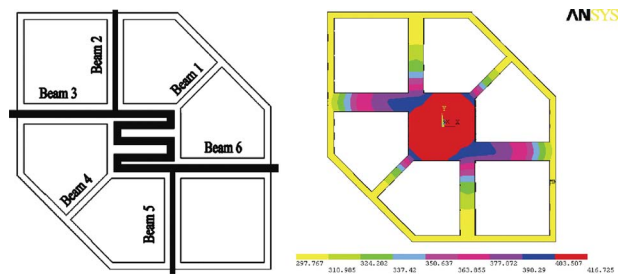
Fig. 1 Structure of the microcalorimeter and FEA temperature distribution

Fig. 2 Microcalorimeter: (*a*) fabrication process flow, (*b*) SEM photo, and (*c*) with sample film

the main beams were 54 μm in length, and simulation results showed that the average temperature of the center membrane reached 411.6 K (maximum temperature was 416.5 K) in 1ms with 4.6 mW of electrical heating power at an ambient temperature of 298 K in a vacuum. Fabrication experiments show that the microcalorimeter presents satisfactory mechanical strength when the beams are below 100 μm. The strength problems, such as broken beams, the membrane sticking to the substrate, and the distortion of the membrane, become serious when the length of the beams is above 120 μm. Therefore, the length of the main beams is optimized to 98 μm in this work. The FEA results show that with 4.2 mW, the average temperature of the center membrane reaches 412.7 K in 1 ms, where the maximum temperature is 416.7 K; the temperature distribution is shown in Fig. 1. The results show that the center membrane has good temperature uniformity. Almost no temperature gradient exists along the thickness direction of the thin free standing membrane. The new microcalorimeter with optimized structure has better thermal isolation and temperature uniformity compared with the previous one.

Most microcalorimeters are fabricated by bulk silicon micromachining technique [7–10,14–21], and the dimensions' uniformity of the calorimeters is poor because the precision of the mechanical fabrication processes, such as double side alignment and wet etch of silicon substrate, is typically in the order of tens of micrometers. By contrast, the surface micromachining technique provides better control on the size of the device and improves the mechanical strength of the suspending membrane [24]. In this paper, surface micromachining technology is used to fabricate the microcalorimeter, as illustrated in Fig. 2(*a*). A thin layer of thermal oxide is first grown on the (100) *n* type silicon wafer. Then a sacrificial layer of low pressure chemical vapor deposition (LPCVD) polysilicon 1 μm in thickness is deposited and patterned. Polysilicon is chosen as the sacrificial layer because it can withstand the consequent high temperature processes (over 600 °C), while other common sacrificial materials, such as aluminum [25] and polyimide [26], will melt at the high temperatures. The next step is plasma enhanced chemical vapor deposition (PECVD) deposition of the $SiO_2/SiN/SiO_2$ multilayer and 850 °C densification of the multilayer in nitrogen. Then the polysilicon thin-film resistor is deposited and patterned followed by the fabrication of contact holes, aluminum leads, and pads. After the deposition of a PECVD SiO_2 layer for passivation, etching windows are opened by reactive ion etching (RIE) and plasma etching (PE) of the dielectric multilayer. Finally, the polysilicon sacrificial

layer is etched with an improved tetramethylammonium hydroxide (TMAH) etching method [27] to release the membrane and beams of the microcalorimeter from the substrate, and the gap between the membrane and the substrate is about 1 μm. The scanning electron microscope (SEM) (JSM-6360LV, JEOL) photo of the fabricated microcalorimeter is shown in Fig. 2(*b*).

The copper thin-film samples are sputtered on the microcalorimeter. The sample film should be loaded just on the center square of the suspending membrane where the temperature distribution is the most uniform. However, the traditional patterning processes of deposition plus etching is not a suitable method for the sample loading because the processes contaminate the freestanding membrane with some copper film or photoresist attached on the underside of the membrane or inserted into the gap between the membrane and the substrate, which seriously influenced the accuracy of the heat capacity measurement. Therefore, the "silicon shadow mask" technique is adopted [8]. The silicon shadow mask is a silicon wafer with apertures fabricated by inductive coupled plasma (ICP). This shadow mask is aligned with the microcalorimeters and then sample films can be sputtered in the center membrane of the microcalorimeters through the apertures on the silicon shadow mask. The copper films were sputtered from a 99.99% pure Cu target in atmosphere of argon at 0.8 Pa at room temperature with a rf magnetron sputter (S3X-80B, Institute of Microelectronics of Chinese Academy of Sciences, Beijing, China). A microcalorimeter with the sample film on its center is shown in Fig. 2(*c*).

3 Micropulse Calorimetry

The thermal properties of the microcalorimeter are measured at first. The relationship between the resistance and temperature of the resistor is linear in the temperature range of 273–420 K, and the temperature coefficient of resistance (TCR) α is 800–1100 ppm °C^{-1}. At higher temperatures, the TCR of the resistor drops gradually, and reliability of the polysilicon becomes poor, which limits the temperature range of the measurement.

The thermal property of the microcalorimeter is greatly related to the air pressure because the thermal conductance of the air between the membrane and the silicon substrate changes dramatically with the change in air pressure [28]. As shown in Fig. 3, with 0.7 mA heating current, temperature of the calorimeter changes from 298 K to 393 K while the air pressure changes from 1 atm to 10^{-1} Pa, respectively. Below 10^{-1} Pa, the thermal conductance of the air is negligible. In this paper, all measurements are carried out in a vacuum of 10^{-3} Pa, and heat loss by gas convection and conduction is negligibly small.

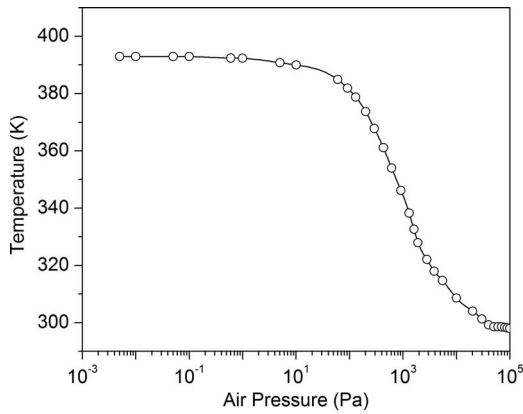**Table 1 Material parameters used in FEA simulation**

Material	ρ (kg m^3)	c_p (J kg^{-1} K^{-1})	k [21] (W K^{-1} m^{-1})
SiO$_2$	2270	710	1.17
SiN$_x$	2840	700	1.55
Poly-Si	2330	700	34.5

Fig. 3 The microcalorimeter's temperature dependence on air pressure at $I=0.7$ mA

Fig. 5 Typical power curves during a test run

The relationship between the temperature and the power consumption P of the microcalorimeter in steady state in vacuum is shown in Fig. 4. With less than 0.4 mW heating power, the temperature of the microcalorimeter is elevated to 400 K from room temperature, indicating that the microcalorimeter has excellent thermal isolation. The temperature linearly increases with the increasing of the power consumption.

Pulse calorimetry is an ultrafast calorimetry usually used in a temperature range from room temperature up to several thousand Kelvin [29]. According to nonsteady-state heat transfer equation with internal heat source, power balance for the center membrane of the calorimeter can be expressed as

$$\frac{V_R^2}{R} = C \cdot \frac{dT}{dt} + Q_{\text{loss}} \tag{1}$$

where V_R is the voltage across the heater, R is resistance of the heater, C is the sum of heat capacity of the sample and the membrane, T is average temperature of the membrane, t is time, and Q_{loss} is the heat loss of the membrane. Here, V_R and R are measured as functions of time, and T is derived from R with the previously calibrated TCR.

As the temperature of the membrane is higher than the temperature of the beams, the heat loss Q_{loss} is the total heat power transferred from the membrane to the beams. Some of this heat power is absorbed by the beams to increase their temperature, and some are transferred to the substrate. The heating power generated by the resistors on beams 3 and 6 partially compensate for the heat loss through these two beams, and it makes the temperature of beams 3 and 6 to be higher than the temperature of beams 2 and 4. The heat loss during the rapid heating period is unavailable because the temperature distribution and heat transfer of the beams

is hard to be measured or calculated from an analytic solution. At steady state, Q_{loss} equals to the power consumption P, thus, the approximation $Q_{\text{loss}}=P$ was used in Eq. (1). As shown in Fig. 4, the steady-state power consumption is directly proportional to the average temperature of the microcalorimeter, confirming that the heat transfer of the calorimeter is primarily the heat conduction of the six supporting beams. Then the heat loss can be expressed as

$$Q_{\text{loss}} = P = G_s \cdot (T - T_0) \tag{2}$$

where G_s represents the equivalent thermal conductance of the beams, and T_0 is the ambient temperature, respectively.

As a matter of fact, temperature distribution of the microcalorimeter at steady-state is not entirely the same as the temperature distribution at nonsteady-state, thus, the approximation $Q_{\text{loss}}=P$ will cause systematic error. In order to minimize this error, pulse calorimetry is applied. In this paper, the heating rate of the microcalorimeter is 100–200 K ms^{-1} with heating power of 3–4 mW in vacuum. Figure 5 shows the typical heating power ($Q_{\text{in}}=V_R^2/R$), the temperature ($T=(R-R_0)/\alpha R_0$, where R_0 is the heater resistance at $0\,^\circ$C), the power loss ($Q_{\text{loss}}=P(T)$, refer to Fig. 4), and the absorbed power ($Q_{\text{absorb}}=Q_{\text{in}}-Q_{\text{loss}}$) by the calorimeter to increase its temperature during a test run. With a heating power of 3.9 mW, temperature increases from 300 K to 420 K in 0.85 ms. $Q_{\text{loss}}=P(T)$ increases with temperature, and Q_{absorb} decreases consequently. With the pulse calorimetry, the proportion of Q_{loss} in the heating power is small, thus, the systematic error induced by the Q_{loss} approximation is significantly reduced.

Figure 6 shows a schematic of the experimental setup used for heat capacity characterization of thin films with the microcalorimeter. During the pulse calorimetry measurement, the microcalorimeter is placed in a vacuum chamber. A standard resistor r is placed in series with the heater, so that resistance of the heater is calculated by $R=rV_R/V_r$. The power required for the measure-

Fig. 4 Temperature versus power consumption
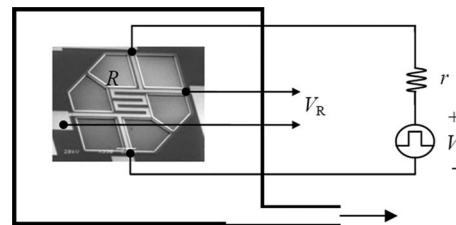
Fig. 6 A schematic of the experimental setup used for heat capacity characterization of thin films with the microcalorimeter

Fig. 7 Typical temperature data and the exponential fitting curve

Fig. 8 Heat capacity of three adjacent microcalorimeters

ment is only several milliwatts. Function generator (Agilent HP33120A) is used to provide the heating voltage pulse V, and the amplified V_r and V_R are monitored by a two-channel oscilloscope (Agilent HP54616B) in real-time. A test run is done in about 1 ms. The average data of 100 test runs with the same experimental setups is used as the final data for the thermal analysis to minimize the random noise.
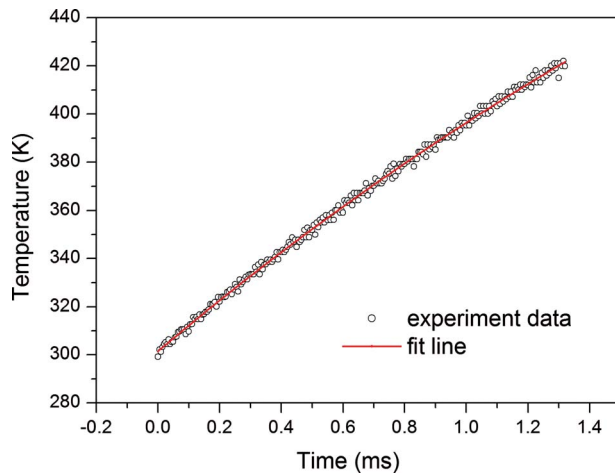
In order to calculate the heat capacity, the derivative of the temperature to time dT/dt shall be calculated first. As noise exists in the measured data, direct calculation of $\Delta T/\Delta t$ between two sample points is not feasible. Our previous works used nonlinear least-squares subregional fitting. But this method also magnifies the noise, and the results are related to how the subregion is made. A more reasonable curve fitting is required to effectively reduce the error caused by the derivation computation. Combining Eqs. (1) and (2) we obtain

$$Q_{in} = C \cdot \frac{dT}{dt} + G_s \cdot (T - T_0) \qquad (3)$$

Then, take Q_{in}, C, and G_s as constant in a small temperature range, T is obtained as

$$T = \exp\left[-\frac{G_s}{C} \cdot (t + D)\right] + \frac{Q_{in}}{G_s} + T_0 \qquad (4)$$

where D is a constant. Therefore, exponential fitting is more suitable for the temperature curve. Figure 7 is a typical temperature curve, the circles are the measurement data, and the line is the exponential fitting curve. The fitting is satisfactory.

Finally the heat capacity can be obtained by

$$C = \frac{Q_{in} - Q_{loss}}{dT/dt} \qquad (5)$$

The heat capacity of the thin-film samples is from the difference between heat capacity curve C_{empty} of an empty calorimeter and the heat capacity curve $C_{empty+film}$ of a sample loaded calorimeter: $C_{film} = C_{empty+film} - C_{empty}$. The only difference between the two calorimeters is the sample film in the center membrane. The beams of the calorimeters are the same, and the systematic error caused by the uncertainty of heat loss through the beams is significantly reduced with this differential method of determining C_{film}.

4 Results and Discussion

Heat capacity of the empty microcalorimeter is about 21.7 nJ K^{-1} at 300 K, and 26.0 nJ K^{-1} at 420 K. Figure 8 illustrates heat capacity of three adjacent microcalorimeters. Because sizes of the calorimeters are well controlled during the surface micromachining fabrication, the differences in heat capacities among the adjacent calorimeters are within 0.3 nJ K^{-1}. Therefore, in the measurements, the empty calorimeter and the sample loaded calorimeter are two adjacent calorimeters in one chip.
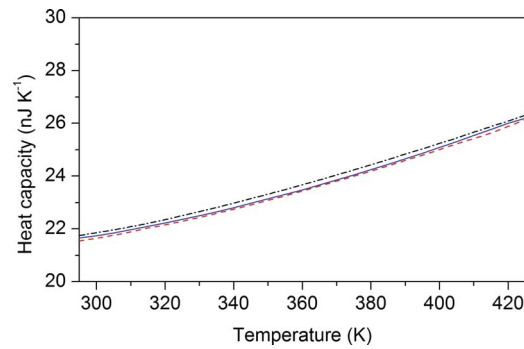
Copper films of different thicknesses from 20 nm to 340 nm were sputtered on the sample zones of the microcalorimeters. X-ray diffraction (XRD) measurements were performed on a Shimadzu XRD-6000 diffractometer using CuKa ($\lambda = 1.5406$ Å) radiation. The average crystalline sizes of the copper films were estimated from the (111) face with the Scherrer equation [30]. Table 2 lists the average crystalline size of the films. The crystalline diameter d increases with the increase in film thickness.

Heat capacity measurements were carried out in a 10^{-3} Pa vacuum. Figure 9 shows the measured heat capacity of the films. The heat capacity of a thicker Cu film is larger than a thinner film because it occupies a larger mass. The heat capacity of the Cu films regularly increases when temperature increases from 300 K to 420 K.

In order to extract the specific heat ($c_p = C/m$) of the copper films, mass (m) of the films shall be known. It is a tough task to measure the mass of the thin-film sample that is in nanograms. We

Table 2 Average crystalline size and c_p of the Cu films

No.	Thickness (nm)	d (nm)	c_p at 300 K (J kg^{-1} K^{-1})
1	340	48	390
2	155	40	396
3	110	36	425
4	80	29	468
5	60	24	449
6	50	22	472
7	20	16	615
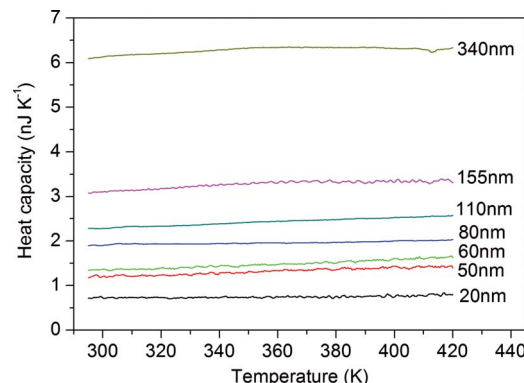
Fig. 9 Heat capacity of the copper films
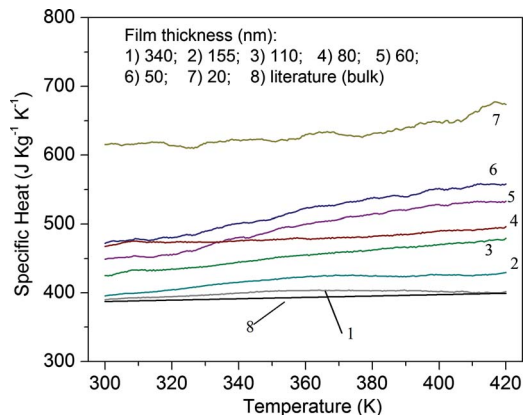
Fig. 10 Specific heat of the copper films

calculated the mass by the product of film volume and density. A microscope is used to capture the sample area. Thicknesses of the film are measured by a profiler (Kosaka ET4000). As the sample film is deposited on a suspending membrane, direct measurement of its thickness by profiler is not applied because the membrane may distort a little and be scratched during the measurement. A neighboring dummy film grown in the same deposition of the sample film and located on flat substrate is measured with the profiler to obtain the thickness of the sample film, and the measurement error is 5 nm. Thus relative errors of thickness are 25% for the 20 nm film and 1.5% for the 340 nm film, respectively. Then the volume of the sample film is the product of the area and the thickness. Another Cu film from the same deposition covering the whole surface of a silicon wafer is prepared, the volume and mass of this large area thin film are measured, and density of the film is calculated. The measured densities of the copper films are within ±5% of the literature value of 8960 kg m^{-3}. Therefore, the literature density value is adopted to generate the mass of the sample film. The dominant source of uncertainty of the specific heat value comes from the estimation of the film mass, as the uncertainty of the volume and density is large, especially for the ultrathin films.

The calculated specific heat $c_{p\,\text{film}}$ for the Cu films compared with the literature $c_{p\,\text{bulk}}$ values of bulk Cu is shown in Fig. 10. The c_p for the 340 nm Cu film is close to the literature data of 387 J kg^{-1} K^{-1} for bulk Cu [31]. For the thinner films, an enhanced specific heat is observed, and the specific heat of the films at 300 K is listed in Table 2. The specific heat of samples 4, 5, and 6 are close to or even cross each other, since their microstructures are close to each other with crystalline sizes of 20–30 nm and film thicknesses of 50–80 nm.

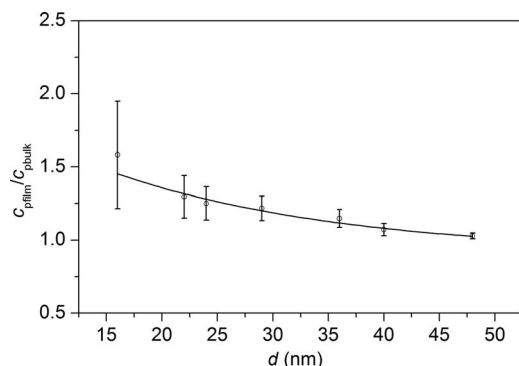Figure 11 shows the trend of the enhanced specific heat

Fig. 11 $c_{p\,\text{film}}/c_{p\,\text{bulk}}$ versus the crystalline diameter d at $T = 350$ K

$c_{p\,\text{film}}/c_{p\,\text{bulk}}$ at 350 K concerned with the film crystalline size. As discussed above, the measurement of uncertainty mainly comes from the uncertainty of film mass and heat capacity difference among microcalorimeters, and it grows larger for the thinner films. The specific heat tends to increase with the decrease in crystalline size. This is in agreement with previous investigations on metal nanocrystalline materials [22,32,33]. Some researchers suggest that the enhanced specific heat may be caused by impurities, the softening of surface phonons and the contribution of the grain-boundary component [32–35]. The measured specific heat of a substance at constant pressure includes two parts: one part is the internal energy increaser term (the specific heat under the restraint of constant volume, c_v), another part is the dilation term. Above room temperature, c_v of copper is mainly related to lattice vibrations. Molecular-dynamics simulations on nanomaterials [36,37] find that partial density of states (DOS) of the atoms at the surface or grain boundaries shift to the low frequency region compared with that of the atoms in the center due to dimensional constraint, resulting in the increase in c_v with the decreasing crystalline diameter. In addition, XRD analyses on nanocrystalline [38] suggest that the grain-boundary components and defects in nanocrystalline result in an evident increase in the thermal-expansion coefficients (TECs), following the d^{-1} rule, where d is the average crystalline diameter. The increase in TEC is also observed in thin copper and other metal films [39] related to the crystallite sizes of the films. In the sputtered copper films, there are large amount of grain boundary, defects, surface, and interface components. The c_v and TEC of these components increase with the decrease in crystalline diameter. Therefore, heating the copper thin film may require more heat not only to increase its internal energy but also to enable the film to do work in expanding compared with bulk copper material, which in turn leads to the enhanced specific heat.

5 Conclusions

A microcalorimeter with nJ K^{-1} sensitivity is developed, and a pulse calorimetry system is constructed for thin-film heat capacity measurement. The microcalorimeter has a very small heat capacity (21.7 nJ K^{-1} at 300 K) and can be heated up at an ultrafast heating rate (100–200 K ms^{-1}) with only several milliwatts in a vacuum, which satisfying the requirements of micropulse calorimetry. Optimization on the structure and data processing methods of the microcalorimeter improved the thermal isolation, temperature uniformity, and calculation errors, and these efforts efficiently reduced the heat capacity measurement error. The heat capacities of the polycrystalline copper thin films with a thickness of 20 nm to 340 nm are measured in the temperature range from 300 K to 420 K in a vacuum of 10^{-3} Pa. The specific heat of the sample films is estimated. Results show that the specific heat of the copper films increases with the decrease in crystalline size and film thickness. We suggest that the grain boundary, defects, surface, and interface components of the films are responsible for the enhancement of the specific heat. Comparing with the size effect on the thermal conductivity of a nanothin film, which is usually more than one order of magnitude smaller than the bulk value, the enhanced heat capacity of thin films is relatively small. Thus simply using specific heat value of bulk copper in thermal models for microsystems is still acceptable in most cases.

Nomenclature

α = temperature coefficient of resistance (ppm °C^{-1})

C = heat capacity (nJ K^{-1})
c_p = specific heat at constant pressure (J kg^{-1} K^{-1})
c_v = specific heat at constant volume (J kg^{-1} K^{-1})
D = constant
d = crystalline diameter (nm)
G = equivalent thermal conductance (W K^{-1})
I = electric current (mA)
m = mass (kg)
P = power consumption at steady state (mW)
Q = thermal power (mW)
T = temperature (K)
t = time (ms)
V = voltage (μm^3)
λ = X-ray wavelength (Å)

Subscripts

absorb = absorbed by the calorimeter to increase its temperature
bulk = copper bulk material
empty = empty calorimeter
film = copper sample film
in = input
loss = heat loss from the calorimeter to the surrounding
R = resistance of heater/thermometer
r = standard resistance
s = solid beams

References

[1] Cahill, D. G., Ford, W. K., Goodson, K. E., Mahan, G. D., Majumdar, A., Maris, H. J., Merlin, R., and Phillpot, S. R., 2003, "Nanoscale Thermal Transport," J. Appl. Phys., **93**(2), pp. 793–818.
[2] Maillet, D., Moyne, C., and Remy, B., 2000, "Effect of a Thin Layer on the Measurement of the Thermal Diffusivity of a Material by a Flash Method," Int. J. Heat Mass Transfer, **43**(21), pp. 4057–4060.
[3] Jain, A., and Goodson, K. E., 2008, "Measurement of the Thermal Conductivity and Heat Capacity of Freestanding Shape Memory Thin Films Using the 3ω Method," ASME J. Heat Transfer, **130**, p. 102402.
[4] Hopkins, P. E., and Phinney, L. M., 2009, "Thermal Conductivity Measurements on Polycrystalline Silicon Microbridges Using the 3ω Technique," ASME J. Heat Transfer, **131**, p. 043201.
[5] Huang, Z. X., Tang, Z. A., Xu, Z. Q., Ding, H. T., and Gu, Y. Q., 2004, "In-Plane Thermal Diffusivity Measurement of Thin Films Based on the Alternating-Current Calorimetric Method Using an Optical Reflectivity Technique," Chin. Phys. Lett., **21**(4), pp. 713–715.
[6] Cahill, D. G., Goodson, K. E., and Majumdar, A., 2002, "Thermometry and Thermal Transport in Micro/Nanoscale Solid-State Devices and Structures," ASME J. Heat Transfer, **124**, pp. 223–241.
[7] van Herwaarden, A. W., 2005, "Overview of Calorimeter Chips for Various Applications," Thermochim. Acta, **432**, pp. 192–201.
[8] Denlinger, D. W., Abarra, E. N., Allen, K., Rooney, P. W., Messer, M. T., Watson, S. K., and Hellman, F., 1994, "Thin Film Microcalorimeter for Heat Capacity Measurements From 1.5 to 800 K," Rev. Sci. Instrum., **65**(4), pp. 946–959.
[9] Allen, K., and Hellman, F., 1999, "Specific Heat of C$_{60}$ and K$_3$C$_{60}$ Thin Films for $T = 6 – 400$ K," Phys. Rev. B, **60**(16), pp. 11765–11772.
[10] Fominaya, F., Fournier, T., Gandit, P., and Chaussy, J., 1997, "Nanocalorimeter for High Resolution Measurements of Low Temperature Heat Capacities of Thin Films and Single Crystals," Rev. Sci. Instrum., **68**(11), pp. 4191–4195.
[11] Bourgeois, O., Skipetrov, S. E., Ong, F., and Chaussy, J., 2005, "Attojoule Calorimetry of Mesoscopic Superconducting Loops," Phys. Rev. Lett., **94**, p. 057007.
[12] Fon, W. C., Schwab, K. C., Worlock, J. M., and Roukes, M. L., 2005, "Nanoscale Phonon-Coupled Calorimetry With Sub-Attojoule/Kelvin Resolution," Nano Lett., **5**(10), pp. 1968–1970.
[13] Song, Q. L., Cui, Z., Xia, S. H., Chen, Z. F., and Zhang, J. G., 2004, "Measurement of SiN$_x$ Thin Film Thermal Property With Suspended Membrane Structure," Sens. Actuators, A, **112**, pp. 122–126.
[14] Lai, S. L., Ramanath, G., and Allen, L. H., 1997, "Heat Capacity Measurements of Sn Nanostructures Using a Thin-Film Differential Scanning Calorimeter With 0.2 nJ Sensitivity," Appl. Phys. Lett., **70**(1), pp. 43–45.
[15] Olson, E. A., Efremov, M. Y., Zhang, M., Zhang, Z., and Allen, L. H., 2003, "The Design and Operation of a MEMS Differential Scanning Nanocalorimeter for High-Speed Heat Capacity Measurements of Ultrathin Films," J. Microelectromech. Syst., **12**(3), pp. 355–364.
[16] Efremov, M. Y., Olson, E. A., Zhang, M., Schiettekatte, F., Zhang, Z., and Allen, L. H., 2004, "Ultrasensitive, Fast, Thin-Film Differential Scanning Calorimeter," Rev. Sci. Instrum., **75**(1), pp. 179–191.
[17] Efremov, M. Y., Olson, E. A., Zhang, M., Schiettekatte, F., Zhang, Z., and Allen, L. H., 2004, "Thin-Film Differential Scanning Nanocalorimetry: Heat Capacity Analysis," Thermochim. Acta, **412**(1–2), pp. 13–23.
[18] Lopeandia, A. F., Cerdo, L. I., Arana, L. R., Jensen, K. F., Munoz, F. J., and Rodriguez-Viejo, J., 2005, "Sensitive Power Compensated Scanning Calorimeter for Analysis of Phase Transformations in Small Samples," Rev. Sci. Instrum., **76**, p. 065104.
[19] Lopeandia, A. F., Gutierrez, E. L., Viejo, J. R., and Munoz, F. J., 2007, "Design Issues Involved in the Development of a Membrane-Based High-Temperature Nanocalorimeter," Microelectron. Eng., **84**, pp. 1288–1291.
[20] Minakov, A. A., Herwaarden, A. W., Wien, W., Wurm, A., and Schick, C., 2007, "Advanced Nonadiabatic Ultrafast Nanocalorimetry and Superheating Phenomenon in Linear Polymers," Thermochim. Acta, **461**, pp. 96–106.
[21] Minakow, A. A., Morikawa, J., Hasimoto, T., Huth, H., and Schick, C., 2006, "Temperature Distribution in a Thin-Film Chip Utilized for Advanced Nanocalorimetry," Meas. Sci. Technol., **17**, pp. 199–207.
[22] Yu, J., Tang, Z. A., Zhang, F. T., Wei, G. F., and Wang, L. D., 2005, "Investigation of a Microcalorimeter for Thin-Film Heat Capacity Measurement," Chin. Phys. Lett., **22**, pp. 2429–2432.
[23] Andrea, T., and Sarro, P. M., 1999, "Measurement of Thermal Conductivity and Diffusivity of Single and Multiplayer Membranes," Sens. Actuators, A, **76**, pp. 323–328.
[24] Chan, C. H., Yan, G., Sheng, L., Sharma, R. K., Tang, Z., Sin, J. K. O., Hsing, I. M., and Wang, Y., 2002, "An Integrated Gas Sensor Technology Using Surface Micro-Machining," Sens. Actuators B, **82**, pp. 277–283.
[25] Chang, K., Lin, R., and Deng, I., 2007, "Design of Low-Temperature CMOS-Process Compatible Membrane Fabricated With Sacrificial Aluminum Layer for Thermally Isolated Applications," Sens. Actuators, A, **134**(2), pp. 660–667.
[26] Pham, H. T. M., Bagolini, A., Boer, C. R., Laros, J. M. W., Pakula, L., French, P. J., and Sarro, P. M., 2003, "Polyimide Sacrificial Layer for an All-Dry Post-Process Surface Micromachining Module," The 12th International Conference on Solid State Sensors, Actuators and Microsystems, Boston, MA, Jun. 8–12, pp. 813–816.
[27] Yan, G. Z., Chan, P. C. H., Hsing, I. M., Sharma, R. K., and Sin, J. K. O., 2000, "An Improved TMAH Si-Etching Solution Without Attacking Exposed Aluminum," *Proceedings of the 13th IEEE International Micro Electro Mechanical Systems Conference (MEMS 2000)*, Miyazaki, Japan, pp. 562–567.
[28] Yu, J., Tang, Z. A., Chan, P. C. H., Wei, G. F., Wang, L. D., and Yan, G. Z., 2005, "Thermal Analysis of Silicon Micromachining Based Micro Hotplates," Chin. J. Semicond., **26**(1), pp. 192–196.
[29] Cezairliyan, A., Anderson, A. C., Bonnell, D. W., Brooks, C. R., Chasanov, M. G., Ditmars, D. A., Fischer, D. F., Kirby, R. K., Kraftmakher, Ya. A., Leibowitz, L., Loriers-Susse, C., Margrave, J. L., Martin, D. L., Miller, A. P., Montgomery, R. L., Mraw, S. C., Stansbury, E. E., Stephenson, B., Sundareswaran, P. C., and Westrum, E. F., 1988, *Specific Heat of Solids*, C. Y. Ho, ed., Hemisphere, New York, p. 323.
[30] Guinier, A., 1963, *X-Ray Diffraction*, W. H. Freeman, San Francisco, CA, p. 121.
[31] Touloukian, Y. S., and Buyco, E. H., 1970, *Specific Heat: Metallic Elements and Alloys*, IFI/Plenum, New York.
[32] Rupp, J., and Birringer, R., 1987, "Enhanced Specific-Heat-Capacity (c_p) Measurements (150–300 K) of Nanometer-Sized Crystalline Materials," Phys. Rev. B, **36**(15), pp. 7888–7890.
[33] Lopeandia, A. F., Pi, F., and Rodriguez-Viejo, J., 2008, "Nanocalorimetric Analysis of the Ferromagnetic Transition in Ultrathin Films of Nickel," Appl. Phys. Lett., **92**, p. 122503.
[34] Sun, N. X., and Lu, K., 1996, "Heat-Capacity Comparison Among the Nanocrystalline, Amorphous, and Coarse-Grained Polycrystalline States in Element Selenium," Phys. Rev. B, **54**, pp. 6058–6061.
[35] Balogh, J., Kemeny, T., Vincze, I., Szabo, S., Beke, D. L., and Toth, J., 1999, "Comment on "Grain-Boundary Structure and Magnetic Behavior in Nanocrystalline Ball-Milled Iron"," Phys. Rev. B, **59**, pp. 14786–14787.
[36] Meyer, R., Lewis, L. J., Prakash, S., and Entel, P., 2003, "Vibrational Properties of Nanoscale Materials: From Nanoparticles to Nanocrystalline Materials," Phys. Rev. B, **68**, p. 104303.
[37] Zhang, Y., Cao, J. X., Xiao, Y., and Yan, X. H., 2007, "Phonon Spectrum and Specific Heat of Silicon Nanowires," J. Appl. Phys., **102**, p. 104303.
[38] Zhao, Y. H., and Lu, K., 1997, "Grain-Size Dependence of Thermal Properties of Nanocrystalline Elemental Selenium Studied by X-Ray Diffraction," Phys. Rev. B, **56**(22), pp. 14330–14337.
[39] Kuru, Y., Wohlschlögel, M., Welzel, U., and Mittemeijer, E. J., 2008, "Coefficients of Thermal Expansion of Thin Metal Films Investigated by Non-Ambient X-Ray Diffraction Stress Analysis," Surf. Coat. Technol., **202**, pp. 2306–2309.

F. X. Alvarez[1]
Departament de Física,
Universitat Autònoma de Barcelona,
08193 Bellaterra, Catalonia, Spain
e-mail: xavier.alvarez@uab.cat

D. Jou
Departament de Física,
Universitat Autònoma de Barcelona,
08193 Bellaterra, Spain;
Institut d'Estudis Catalans,
Carme 47,
08001 Barcelona, Catalonia, Spain
e-mail: david.jou@uab.es

Boundary Conditions and Evolution of Ballistic Heat Transport

We analyze the effects of boundary conditions on the evolution of ballistic heat transport in four theoretical models and propose that a Fourier equation with an effective size-dependent thermal conductivity is a good candidate for the description of ballistic transport when boundary conditions are suitably imposed. [DOI: 10.1115/1.3156785]

1 Introduction

The transition from diffusive-to-ballistic heat transport is a relevant topic in nanosystems [1,2]. Many studies are focused on a steady-state effective thermal conductivity, which depends on the Knudsen number, i.e., on the ratio of the mean free path ℓ to the characteristic length L of the system. For $\ell/L \ll 1$ the regime is diffusive and for $\ell/L \gg 1$ it is ballistic. However, nonsteady states are also of much technological interest because of the high-frequency operation of many microdevices.

It is widely accepted that classical heat transport equations like Fourier equation (FE) or Maxwell–Cattaneo equation (MCE) are not valid at the ballistic regime when the mean free path of the carriers is of the same order as the typical size of the system. There are two main reasons for this inadequacy. First, the high value of bulk thermal conductivity predicts much higher fluxes than those obtained in experiments, and second, the boundary conditions usually imposed on these equations lead to an excessively high flux in the temperature imposition side.

Several approaches have been used to model the heat evolution on these systems [1] starting from microscopic bases. These equations are usually cumbersome and numerical methods are needed to obtain their solutions; thus, looking for simpler phenomenological equations leading to reasonable predictions may be useful from the practical point of view as they offer a preliminary approach, which may be refined later by means of cumbersome but more precise methods after having in a fast and efficient way the most promising physical conditions for the device operation.

Here, we analyze some of these proposals to understand the origin of their differences with respect to the classical equations. This knowledge could help us to obtain simpler equations allowing us to obtain analytical approximate expressions easier for practical purposes. For the sake of a more direct comparison, we use the same system in all cases, that is, a unidimensional rod initially at a homogeneous temperature T_c, which at time $t=0$ is suddenly put in contact with a heat source at temperature T_h at $x=0$ and kept at $T=T_c$ at $x=1$.

Apparently, this situation should not present a special problem regarding boundary conditions, but in physical terms, its implications are rather different in the ballistic regime than in the classical (diffusive) regime. Whereas in the latter the heat remains initially in a thin layer of a width comparable to the mean free path and heats it very fast in such a way that its temperature rapidly approaches that of the source wall, in the ballistic regime heat is

rapidly distributed in the whole system. Thus, the classical situation corresponds to imposing a temperature at $x=0$, whereas in the ballistic domain it seems more suitable to represent this situation as imposing a heat flux on the mentioned wall.

In this article we show that by a suitable choice of the boundary conditions and the use of an effective thermal conductivity that takes under consideration the size of the system we can reduce the difference between thermodynamical and kinetic approaches. We examine the role of these boundary conditions in four models proposed for the dynamical description of ballistic heat transport by Joshi and Majumdar [3], Chen [4,5], Naqvi and Waldenstrøm [6], and Alvarez and Jou [7,8]. The two first ones stem from solutions of the Boltzmann equation, whereas the two latter ones focus their interest at a more macroscopic and phenomenological level.

2 Heat Transfer Equations

Although the starting point for all the models in this analysis is the same, that is, the Boltzmann equation, the methods to solve it are different in each proposal. In this section we briefly sketch how to obtain the different equations starting from the Boltzmann equation, with the aim to unify them giving a general scope of the topic. For a detailed explanation of each model we recommend the original references of each author [3,5,6,8].

The Boltzmann transport equation for the velocity distribution function f of the energy carriers in the relaxation time approximation is

$$\frac{\partial f}{\partial t} + \mathbf{v} \cdot \frac{\partial f}{\partial \mathbf{r}} = \frac{f - f_0}{\tau} \tag{1}$$

where $\mathbf{v}$ is the group velocity, τ is the relaxation time, and f_0 is the equilibrium distribution function.

From the distribution function we can obtain the energy moments by multiplying it by $\hbar\omega\mathfrak{D}$ and $\mathbf{v}\hbar\omega\mathfrak{D}$, where $\mathfrak{D}$ is the phonon density of states and ω is the frequency of phonons, and integrating in the frequency. The first moment is the mean energy ϵ,

$$\epsilon = \int_\Omega \int_0^{\omega_D} \sum_p f_q(x,t)\hbar\omega_p(q)\mathfrak{D}(\omega)d\omega d\Omega \tag{2}$$

and the second is the heat flux q by

$$q = \int_\Omega \int_0^{\omega_D} \sum_p v_p(\theta,\phi)f_q(x,t)\hbar\omega_p(q)\mathfrak{D}(\omega)d\omega d\Omega \tag{3}$$

where $d\Omega = \sin\theta d\theta d\phi$ is the differential solid angle, ω_D is the Debye frequency, and the sum is over different polarization branches. By multiplying all terms of the Boltzmann equation by

---

the corresponding factors and integrating we obtain the transport equation for these moments. The first two equations, corresponding to the mentioned moments, are

$$\int \frac{\partial f}{\partial t} \hbar \omega \mathfrak{D} d\omega d\Omega + \int \mathbf{v} \cdot \frac{\partial f}{\partial \mathbf{r}} \hbar \omega \mathfrak{D} d\omega d\Omega = \int \frac{f - f_0}{\tau} \hbar \omega \mathfrak{D} d\omega d\Omega$$

(4)

and

$$\int \frac{\partial f}{\partial t} \mathbf{v} \hbar \omega \mathfrak{D} d\omega d\Omega + \int v^2 \cdot \frac{\partial f}{\partial \mathbf{r}} \hbar \omega \mathfrak{D} d\omega d\Omega$$

$$= \int \frac{f - f_0}{\tau} \mathbf{v} \hbar \omega \mathfrak{D} d\omega d\Omega$$

(5)

In both expressions the sum over polarizations is implicit and we have grouped all integrals under the same symbol. After integrating these equations we obtain their thermodynamic correspondences

$$\frac{\partial \epsilon}{\partial t} + \nabla \cdot q = 0$$

(6)

and

$$\tau \frac{\partial q}{\partial t} + \lambda \nabla \cdot T = -q$$

(7)

Equations (6) and (7) are, respectively, the energy conservation and the transport equation for heat flux. Equation (7) is the Maxwell–Cattaneo equation. We can combine Eqs. (6) and (7) and using the relation $d\epsilon = c_v dT$ with c_v as the specific heat per unit volume we obtain the hyperbolic heat equation.

$$\tau \frac{\partial^2 T}{\partial t^2} + \frac{\partial T}{\partial t} = \alpha \frac{\partial^2 T}{\partial x^2}$$

(8)

If we consider that heat flux variations are not important in Eq. (7), that is, $\tau \partial q / \partial t \ll q$, we obtain instead of the hyperbolic equation the classical

$$\frac{\partial T}{\partial t} = \alpha \frac{\partial^2 T}{\partial x^2}$$

(9)

These classical steps can be generalized to obtain more general equations to describe heat transfer through more general systems like nanoscale devices. We can find the equations for higher-order moments (namely, the flux of the heat flux, related to the integral of $\mathbf{vv}\hbar\omega$, and in general, the flux of order n, $\mathbf{Q}^{(n)}$, related to $\mathbf{v} \cdots^{(n)} \mathbf{v} \hbar \omega$) and then combine all of them into the zero order equation (energy conservation) to obtain the heat equation of order n [9]. If we go to the second order we can obtain, for example, the Guyer–Krumhansl equation [9,10].

The order n of the moment expansion to be used in a model must be higher as the mean free path of the carriers becomes longer. For systems with ballistic phonons, where the mean free path is of the order of the device, we should go to very high orders. In Refs. [8,9] it is shown how to work with an infinite order moment expansion by Fourier transforming all the equations and grouping them analytically into a continued-fraction expansion leading to a size-dependent effective thermal conductivity. The resulting equation is

$$\frac{\partial T}{\partial t} = -\lambda(L)\nabla^2 T$$

(10)

with the size-dependent thermal conductivity given by

$$\lambda(L) = \frac{\lambda_0 L^2}{2\pi^2 \ell^2}\left(\sqrt{1 + \frac{4\pi^2 \ell^2}{L^2}} - 1\right)$$

(11)

From here we have considered that highly nonequilibrium expressions are obtained by considering higher-order moment expansions. Other methodologies propose to find different expressions by splitting the whole distribution function in subsystems containing different kinds of particles. This method is used in two of the equations that were analyzed. Joshi and Majumdar [3] divided the system in two systems with particles traveling in the positive and negative directions, respectively, to the heat flow direction, and Chen [5] split it in a diffusive group of carriers with a very short mean free path and a ballistic group of carriers with a large mean free path.

Following the same nomenclature as Refs. [3,5] we define the phonon intensity I from the distribution function f by

$$I(\omega, \theta, \phi, x, t) = \sum_p v_p(\theta, \phi) f_q(x, t) \hbar \omega_p(q) \mathfrak{D}(\omega)$$

(12)

where v is the phonon group velocity, $\hbar\omega$ is the phonon energy, and $\mathfrak{D}$ is the density of states. θ and ϕ represent the azimuthal and polar angles and p is the polarization.

Multiplying the Boltzmann equation by $v\hbar\omega\mathfrak{D}$ we can write the equation for the phonon intensity

$$\frac{\partial I_\omega}{\partial t} + \mathbf{v} \cdot \nabla_x I_\omega = \frac{I_\omega^0 - I_\omega}{\tau_\omega}$$

(13)

This expression is equivalent to Eq. (5) in the moment expansion. Joshi and Majumdar [3] and Chen [5] solved this equation by using the separation of the whole system in subsystems with different properties. Joshi and Majumdar [3] split the system in a distribution function for the carriers traveling in the direction of the heat flux I^+ and another distribution with phonons going in the opposite direction I^-.

In Chen's model [5], the phonon intensity is split in diffusive and ballistic parts $I = I^d + I^b$. Both distributions follow expressions similar to Eq. (13) with only one difference, that is, the diffusive distribution relaxes to I_{0d} while the ballistic distribution relaxes to 0. The final ballistic-diffusive equation (BDE) obtained after integration is

$$\tau \frac{\partial^2 \theta}{\partial t^2} + \frac{\partial \theta}{\partial t} = \alpha \nabla^2 \theta - \nabla \cdot q_b$$

(14)

where θ is the temperature defined from the energy stored in the ballistic part of the system and q_b is the ballistic heat flux obtained numerically from solving the Boltzmann equation describing the behavior of I^b. This last process is possible due to the fact that ballistic phonons relax to 0 and their distribution function has an exponential form. One of the main drawbacks of this method is that the splitting of the system in parts makes it difficult to define a temperature on the whole system.

In Secs. 2.1–2.3 we describe the solution of the four models in a simple unidimensional rod that helps us to compare their results.

2.1 Equation of Phonon Radiative Heat Transfer (EPRT). As commented before, Joshi and Majumdar [3] solved the Boltzmann equation in a unidimensional rod in the x axis by splitting the phonon energy-flux distribution in two contributions. Concretely, in a unidimensional rod we have a distribution for phonons traveling in the positive x direction I_ω^+ and the other for phonons in the opposite direction I_ω^-. The equations for the corresponding distributions, following the same nomenclature as in Ref. [3], take the form

$$\frac{\partial I_\omega^\pm}{\partial t} + v\mu \frac{\partial I_\omega^\pm}{\partial x} = \frac{\frac{1}{2}\int_{-1}^{1} I_\omega d\mu - I_\omega^\pm}{\tau_\omega}$$

(15)

where ω is the phonon frequency, v is the phonon group velocity, $\mu = \cos\theta$ is the cosine of the azimuthal angle between velocity of phonons and the direction of heat propagation, and τ_ω is the re-

laxation time for phonons of frequency ω at temperature T.

The boundary values imposed by these authors on the mentioned unidimensional rod problem are, for $t > 0$,

$$I_\omega^+(t, \omega, x = 0) = I_\omega^0(T_h) \tag{16}$$

$$I_\omega^-(t, \omega, x = 1) = I_\omega^0(T_c) \tag{17}$$

where $I_\omega^0(T)$ is the Bose–Einstein equilibrium distribution at temperature T.

To obtain the temperature of their solution there is the drawback that the actual distribution function does not follow any equilibrium distribution form. To avoid this, they calculate the temperature of an equilibrium Bose–Einstein distribution that has the same mean energy as the phonon distribution of their solution. This is a reasonable choice but one has to be aware of the fact that in the integral average process, the detailed information contained in the distribution function is lost.

The solutions for this method are not represented in this article but they are very similar to those obtained by Chen [5], plotted in Fig. 2. It can be observed that a significant modification in the temperature profile as the size of the system is reduced and a reduction in the heat flux profiles both in the transient behavior and the stationary state with respect to those corresponding to the classical situation. This is physically meaningful because a reduction in this kind is found in actual systems at steady states.

2.2 Ballistic Diffusive Equation (BDE). Chen [4,5] developed a BDE approach to gradually introduce ballistic phonons in the equations as the size of the system becomes small enough. He also started from the Boltzmann equation but split the distribution function in two parts: one for ballistic phonons, traveling large distances after they collide, and the other for classical diffusive phonons. In the unidimensional rod, Chen [4,5] included a ballistic phonon source at the hot end. Due to the low collision rate, ballistic phonons decay slowly as they go through the system. Ballistic phonons, when colliding with an internal part of the system, act like a heat source in the diffusive equation, which takes the final form

$$\tau \frac{\partial^2 T}{\partial t^2} + \frac{\partial T}{\partial t} = \alpha \frac{\partial^2 T}{\partial x^2} - \frac{\partial q_b}{\partial x} \tag{18}$$

where q_b is the heat flux coming from ballistic phonons. This flux is obtained from the ballistic expression also coming from the starting Boltzmann equation. Note that the last term on the right-hand side of Eq. (18) can be understood as an energy supply to the system and, consequently, is an imposed value on the diffusive equation. The boundary conditions are taken to be

$$\tau \frac{\partial T}{\partial t} + T = \pm \frac{2\ell}{3} \frac{\partial T}{\partial x} \tag{19}$$

where ℓ is the mean free path of the phonons. The positive and negative signs in the right-hand side correspond to the left or right ends of the system, respectively.

BDE approach achieves a good agreement with the EPRT solutions. However, as Chen said in Ref. [5], the model suffers from an ill definition of temperature, as in the process of dividing the system and then calculating the temperature one often is not sure of the meaning of this equilibrium value. In order to minimize the effects of this temperature choice, Chen [4,5] rescaled the obtained value to compare different solutions.

Chen [4,5] based his development on a Maxwell–Cattaneo-like equation instead of choosing a Fourier-like equation. MCE is a wave equation, and the solutions coming from it are recognizable by the appearance of a wave front traveling through the system. Instead, in EPRT, solutions do not show any trace of these wave fronts. The amplitude of the obtained wave front is smaller than the one obtained by classical MCE because the heat source in BDE is spatially distributed over the system instead of being injected across the boundary surface.

2.3 New Heat Equation (NHE). Naqvi and Waldenstrøm [6] proposed to use a modified Fourier equation obtained from a Brownian motion approach. Their proposal is to include a relaxational time dependence on the diffusivity. Their new heat equation (NHE) has the form

$$\frac{\partial T}{\partial t} = \alpha(1 - e^{-t/\tau_R}) \frac{\partial^2 T}{\partial x^2} \tag{20}$$

It is a little difficult, from the physical point of view, to think about an explicitly time-dependent thermal conductivity, as it implies a synchronization between the imposition of a heat source and this bulk parameter. In spite of this, Eq. (20) leads to temperature profiles that fit correctly to EPRT solutions without artificial wave fronts, in contrast to BDE.

Although the physical meaning of the NHE is doubtful, we have included it in this study because the time-dependent factor has some common aspects with our proposed boundary equations.

3 Boundary Conditions

In order to obtain an improved version of Fourier equation valid for nanoscale systems, we focus our attention on an aspect from the previous equations that, from our point of view, has not been sufficiently studied in the bibliography, namely, the boundary condition selection.

When Joshi and Majumdar [3] and Chen [4,5] compared their solutions with that obtained from classical FE and MCE they did not emphasize enough the fact that the boundary conditions are not equivalent in the different equations. For the classical models the differential equations are

$$\frac{\partial T}{\partial t} = \alpha \frac{\partial^2 T}{\partial x^2} \tag{21}$$

with α the classical bulk heat diffusivity for the FE and

$$\tau_R \frac{\partial^2 T}{\partial t^2} + \frac{\partial T}{\partial t} = \alpha \frac{\partial^2 T}{\partial x^2} \tag{22}$$

for the MCE. They suggested to use the usual initial and boundary conditions

$$t = 0, \quad T = T_c, \quad \text{and} \quad T(x = 0) = T_h, \quad T(x = 1) = T_c \tag{23}$$

in both equations. These implies an abrupt and instantaneous temperature rise from the low initial value to the high heat source temperature while, in their models [3–5], they used a gradual increase in temperature at the heated side as a consequence of the fact that their imposed conditions are fluxes (I^0 in EPRT and q_b in Chen's [4,5] model) rather than temperatures. As a consequence, the authors compare different situations and could not strictly conclude that their models are a better approach to heat conduction when ballistic phonons are considered.

4 Extended Fourier Equation (EFE)

As previously commented, the main drawbacks of using the Fourier equation to describe heat transport on nanosystems are basically the high bulk thermal conductivity and the impossibility to describe the behavior of ballistic phonons. In small systems, boundary effects reduce the thermal conductivity from its bulk value, and a contact with a heat source is more likely an imposed flux than an imposed temperature.

Here, we propose to use the Fourier-like equation (10) with the effective thermal conductivity $\lambda(L)$ and change the boundary conditions and the thermal conductivity in order to compare the corresponding results with those of the presented models. For the thermal conductivity we use Eq. (11), which describes the reduction in the bulk conductivity by the small size of the system. Concerning the boundary conditions, a detailed analysis must be made. For $x = 1$ we suggest to use the same boundary conditions as Chen [4,5], that is, Eq. (19) with the minus sign. This is a reasonable choice as it states that the difference between the radiation

heat going outside at T from the system and the incoming heat at $T_c=0$ is precisely the heat supplied for the system by diffusion.

In contrast, the boundary condition at $x=0$ adds up a difficulty when analyzed from the Fourier classical point of view. When Chen [4,5] modeled the boundary at $x=0$, he imposed the same equation as the one chosen for $x=1$ as he considered that there is no heat source for the diffusive phonons. This is a reasonable choice if one considers that the heating of the system is not coming from the boundary but from an energy supply in the differential equation (18). However, this is not a suitable choice for an extended Fourier equation (EFE) as we are not adding the heat supply of the ballistic term in Chen's [4,5] equation. Consequently we have to add the heat flux supply in Chen's [4,5] proposal for this side.

Here we suggest to analyze the boundary conditions starting from the relaxational equation

$$\tau \frac{\partial \Delta T}{\partial t} + \Delta T = qR \qquad (24)$$

where $\Delta T = T_h - T$ is the difference between the source temperature T_h and the instantaneous temperature at the frontier of the system, q is the heat flux, and R is the boundary heat resistance. The right-hand term expresses that the temperature difference does not tend to zero but to a value depending on the transport properties of the contact materials. As we are now focusing on the evolution equations we differ a detailed study of this term, giving it for the moment the meaning of a jump of temperature at the boundary when stationary state is reached. Naqvi and Waldenstrøm [6] modeled this situation by imposing the conditions $T(-\delta_x,0)=T_h$ and $T(1+\delta_x,0)=T_c$, where δ_x is a length calculated from Chen's [4,5] solutions. These conditions state that T_h is actually imposed at a distance δ_x before $x=0$, and T_c is imposed δ_x after $x=1$ to modelize the jump temperature at the walls due to thermal boundary resistance. It must be noted that the general solution of the homogeneous case of Eq. (24) (that is $R=0$) has the same form as the correction time-dependent factor accompanying thermal diffusivity in NHE (20).

It is widely accepted that steady-state solution of Fourier classical equation for the temperature profile is valid in nanosystems if one introduces the concept of thermal boundary resistance at the interfaces, so Eq. (24) seems a more suitable choice in order to compare the solution of Fourier equation with that obtained from Boltzmann based formalisms.

We can rearrange Eq. (24) in the form

$$\tau \frac{\partial T}{\partial t} + T = T_h - qR \qquad (25)$$

That condition has a similar form as the boundary condition (19) proposed by Chen [4,5] if we note that it is a differential equation that raises exponentially the temperature from the initial value to an asymptotic value. In Chen's [4,5] condition, this final value depends on the temperature gradient and in the final solution, a balance between the rise on the temperature and its local gradient is achieved.

5 Discussion and Results

In Fig. 1 we plot the solutions obtained from EFE (21) with Eqs. (25) and (19) as boundary conditions for $x=0$ and $x=1$ at different flow regimes expressed by the Knudsen number (ℓ/L). The value of the thermal boundary resistance in Eq. (25) is selected in order for the final solution to converge to the same temperature value as the EPRT solution.

In Figs. 2 and 3 we plot the equivalent plots for the ballistic-diffusive equation and EPRT, respectively, with those plotted in Fig. 1. The plots for NHE are not included in this article as they are similar to those of EPRT at least in the one-dimensional situation examined here.

(a)

(b)

(c)
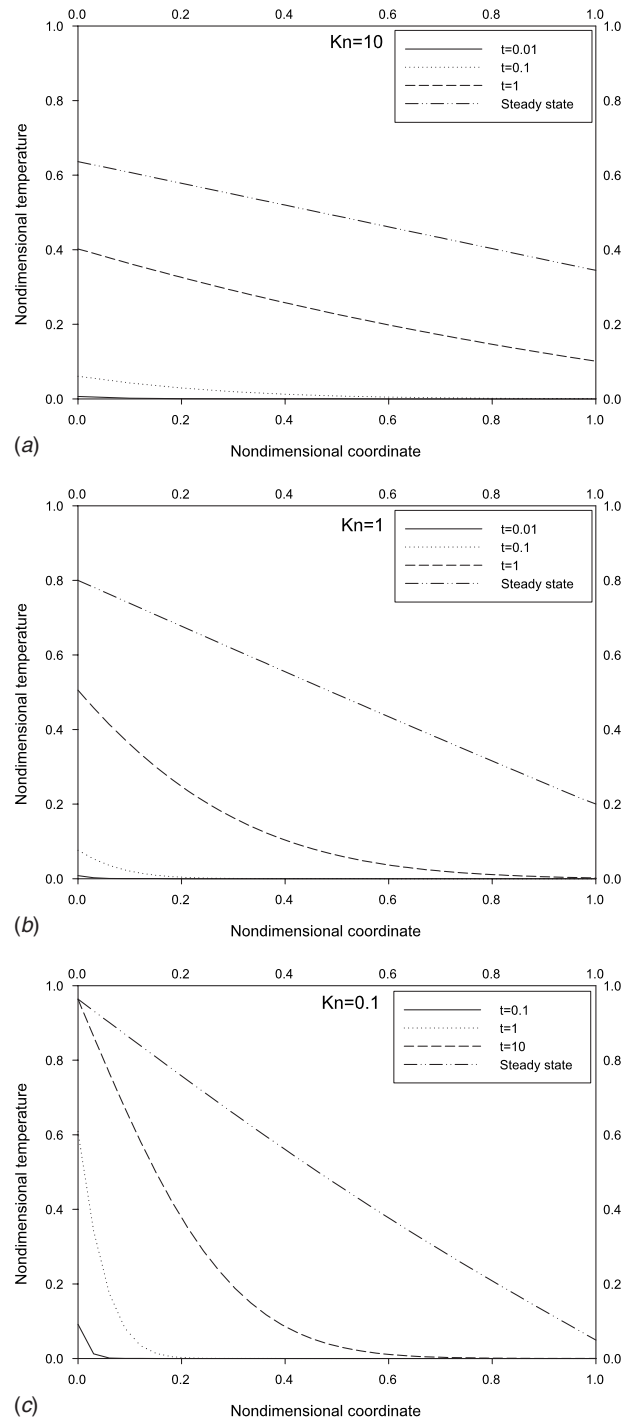
Fig. 1 1 Plots showing temperature profiles at different nondimensionalized times for different flow regimes depending on its Knudsen number. Profiles are obtained following Eq. (21) with boundary conditions (19) and (25) at the $x=1$ and $x=0$ ends, respectively, with $T_{0i}=1$ and $T_{1i}=0$. Thermal conductivity is given by Eq. (11).

In experimental devices, Joule heating in a metal is usually used as a heat source [11]. In this kind of experiments the controlled parameters are voltage and intensity. In our opinion, boundary condition (25) seems to be more realistic to model this kind of imposed heating, as the system in contact with the heat source feels a heat flux and not an abrupt change in its tempera-

(a)

(b)

(c)
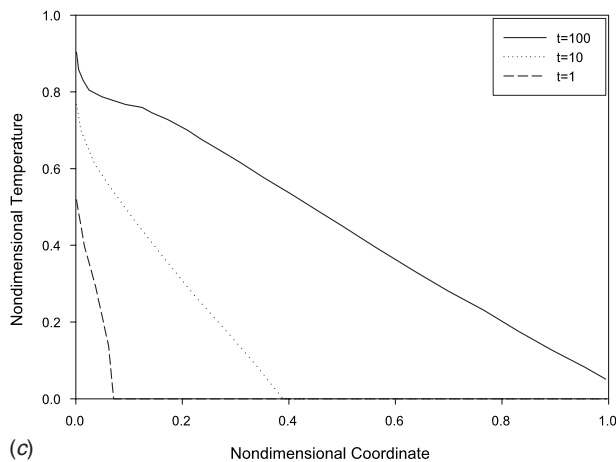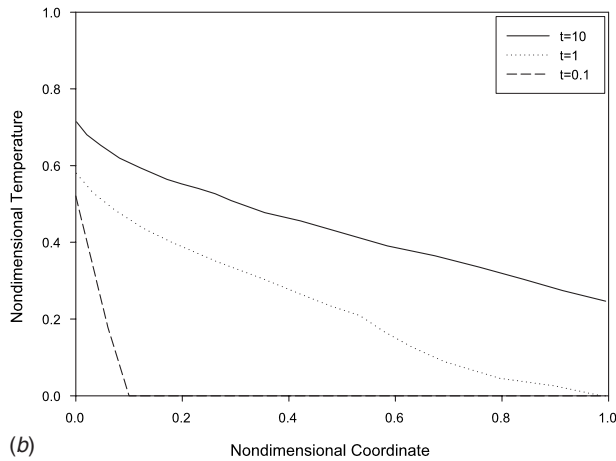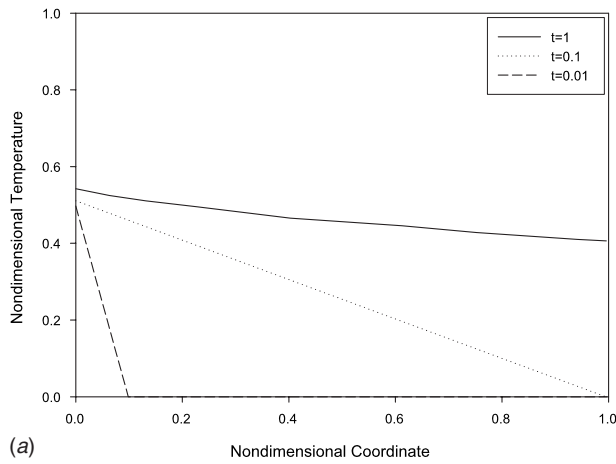
Fig. 2 Plots showing temperature profiles at different nondi-mensionalized times for different flow regimes depending on its Knudsen number for ballistic-diffusive equation. Profiles are obtained following Eq. (18) with boundary conditions (19) at the $x=1$ and $x=0$ ends with $T_{0i}=1$ and $T_{1i}=0$.

Fig. 3 Plots showing temperature profiles at different nondi-mensionalized times for different flow regimes depending on its Knudsen number for EPRT equation. Profiles are obtained following Eq. (15) with boundary conditions (16) and (17) at the $x=1$ and $x=0$ ends with $T_h=1$ and $T_c=0$.

ture as our interest is in the dynamical equations describing the transient behavior after a sudden rise of temperature at the boundary $x=0$.

It can be seen that EFEs with the boundary conditions (19) and (25) have similar solutions to those of EPRT and Chen's [4,5] models and lead us to conclude that their solutions differ from classical solutions by the fact that heat enters the system in a gradual way and not abruptly, as conditions (23) indicate. It also

indicates that it is not necessary that heat enters in a distributed way as the ballistic term in Chen's [4,5] model imposes.

Some differences appear between BDE and EPRT solutions (Fig. 2) and that of EFE (Fig. 1) at the side where the heat enters the system. Following EPRT [3] on this side, at $t=0$ we have a distribution formed by half of the carriers at temperature T_h and the other half of the carriers at temperature T_c. Thus, one obviously obtains for the joint temperature $T=(T_c+T_h)/2$. This is the boundary condition at $t=0$, but as time evolves, heat enters into

the system coming from the energy exchange between the positive and the negative distributions I_ω^+ and I_ω^- (particles going to the right and those going to the left). This heat exchange is due to the collision term and is observable in the solution as the temperature at $x=0$ rises. The positive distribution is always kept at T_h but the distribution in I_ω raises its temperature with time. As a result, EPRT solution raises abruptly the temperature at $t=0$ from T_c to $(T_h+T_c)/2$ on $x=0$ and afterward it rises continuously to the final temperature. With our boundary condition instead, temperature rises always in a continuous form from T_c at $t=0$ as the heat gradually enters the system. It must be noted that despite this difference, the general trends of the temperature profiles do not change significantly and mainly that steady-state profiles are identical in both equations.

A criticism that could be made to Eq. (25) is that boundary resistance is a new parameter imposed over the system, and the accuracy of the approach depends on this new value. But by the comparison between Eqs. (25) and (19) it seems reasonable to interpret the resistance term as some value related to the equilibrium between radiation and diffusion on the system's boundaries.

A second point to be analyzed is the definition of temperature in all of the models. In EPRT and Chen's [4,5] models, an equilibrium equivalent value is obtained. This leads the authors to warn about the fact that temperature does not have their usual thermodynamic meaning. An unsuitable choice in the definition of temperature can lead to an incorrect interpretation of the final results. In our thermodynamical based model, temperature is consistently defined, as thermodynamical relations are still valid. Anyway, the most suitable definition of temperature among the several possible definitions out of equilibrium is still an open problem, which receives an increasing attention (for a wide review on temperature in nonequilibrium situations, see Ref. [12]).

6 Conclusions

We have seen that a suitable modelization of the boundary conditions allows us to use an extended Fourier equation to model heat conduction at the ballistic regime. An important question to discuss is whether it is better to start from the Boltzmann equation to solve it for the distribution function, and then obtain thermodynamical values by integration, or directly obtain an averaged equation with effective transport coefficients for the thermodynamic quantities in order to obtain the equation for the mean value of these parameters.

In nonequilibrium thermodynamic models, the second approach is more usual, that is, the behavior of the distribution in terms of the velocity does not offer much corrections to the thermodynamic mean values after the average process. Nonequilibrium formalisms imply as well a way to calculate thermodynamical properties far from equilibrium by the use of successive corrections depending on the transport properties. This kind of formalism has the advantage of being self-consistent from the thermodynamic perspective, maintaining thermodynamical relations intact, and al-

lows us to speak of values like temperature without the need of a definition depending on the requirements of the model.

Nomenclature

α = thermal diffusivity
c_v = specific heat
$\mathfrak{D}$ = density of states
I = intensity of the phonon energy flux
Kn = Knudsen number
ℓ = mean free path of phonons
f = velocity distribution function
L = characteristic length of the device
λ_0 = bulk thermal conductivity
$\lambda(L)$ = size-dependent effective thermal conductivity
q = heat flux
R = thermal boundary resistance
T_h = applied temperature
T_c = base temperature
τ = relaxation time
v = phonon velocity

References

[1] Zhang, Z., 2007, *Nano/Microscale Heat Transfer*, McGraw-Hill, New York.
[2] Cahill, D. C., Ford, W. K., Goodson, K. E., Mahan, G. D., Majumdar, A., Maris, H. J., Merlin, R., and Phillpot, S. R., 2003, "Nanoscale Thermal Transport," J. Appl. Phys., **93**(2), pp. 793–818.
[3] Joshi, A. A., and Majumdar, A., 1993, "Transient Ballistic and Diffusive Phonon Heat Transport in Thin Films," J. Appl. Phys., **74**(1), pp. 31–39.
[4] Chen, G., 2001, "Ballistic-Diffusive Heat-Conduction Equations," Phys. Rev. Lett., **86**(11), pp. 2297–2300.
[5] Chen, G., 2002, "Ballistic-Diffusive Equations for Transient Heat-Conduction From Nano to Macroscales," ASME J. Heat Transfer, **124**, pp. 320–328.
[6] Naqvi, K. R., and Waldenstrøm, S., 2005, "Brownian Motion Description of Heat Conduction by Phonons," Phys. Rev. Lett., **95**, p. 065901.
[7] Alvarez, F. X., and Jou, D., 2007, "Memory and Nonlocal Effects in Heat Transport: From Diffusive to Ballistic Regimes," Appl. Phys. Lett., **90**, p. 083109.
[8] Alvarez, F. X., and Jou, D., 2008, "Size and Frequency Dependence of Effective Thermal Conductivity in Nanosystems," J. Appl. Phys., **103**(9), p. 094321.
[9] Jou, D., Casas-Vázquez, J., and Lebon, G., 2001, *Extended Irreversible Thermodynamics*, 3rd ed., Springer-Verlag, Berlin.
[10] Jou, D., and Casas-Vazquez, J., 1990, "Nonequilibrium Absolute Temperature, Thermal Waves and Phonon Hydrodynamics," Physica A, **163**(1), pp. 47–58.
[11] Li, D., Wu, Y., Fan, R., Yang, P., and Majumdar, A., 2003, "Thermal Conductivity of Si/SiGe Superlattice Nanowires," Appl. Phys. Lett., **83**(15), pp. 3186–3188.
[12] Casas-Vázquez, J., and Jou, D., 2003, "Temperature in Non-Equilibrium States: A Review of Open Problems and Current Proposals," Rep. Prog. Phys., **66**(11), pp. 1937–2023.

Sensitivity of the Human Comfort Equation and of Free Convection in a Vertical Enclosure as Examples of the Use of Global Sensitivity to Evaluate Parameter Interactions

A. F. Emery
e-mail: emery@u.washington.edu

M.-H. H. Wu

A. M. Mescher

Department of Mechanical Engineering,
University of Washington,
Seattle, WA 98195-2600

Many models of engineering and scientific systems involve interactions between and among the parameters, stimuli, and physical properties. The determination of the adequacy of models for predictions and for designing experiments generally involves sensitivity studies. Good designs mandate that the experiments be sensitive to the parameters sought with little interaction between them because such interaction generally confuses the estimation and reduces the precision of the estimates. For design purposes, analysts frequently want to evaluate the sensitivities of the predicted responses to specific variables, but if the variables interact it is often difficult to separate the effects. Global sensitivity is a technique by which one can evaluate the magnitude of the interactions between multiple variables. In this paper, the global sensitivity approach is applied to the human comfort equation and to free convection in a rectangular enclosure. It is found that when occupants are uncomfortable, there is little interaction and that one can predict the effects of changing several environmental conditions at once by adding the separate effects. But when occupants are comfortable, there is a large interaction and the effects cannot be treated separately. Free convective heat transfer in an enclosure is a function of the Rayleigh number Ra and the aspect ratio H/W, and the flow field changes from unicellular to multicellular as Ra increases. There is a strong interaction for $H/W \leq 2$ but little for $H/W \geq 2$. [DOI: 10.1115/1.3194759]

Keywords: sensitivty, global sensitivity, interactions, uncertainty, free convection, human comfort

1 Introduction

Mathematical models to simulate or describe scientific and engineering systems involve constants or material properties, which we term "parameters," and forcing functions such as ambient conditions and energy inputs, which we term "stimuli." We will use the term "variables" to refer to both parameters and stimuli.

Estimates of the sensitivity of the model to the different variables are widely used in the development of the model, in the interpretation of the results, and in the evaluation of the model. Most of the sensitivity studies are based upon *local* sensitivities found from the first derivative of the response to the variable, which is the first term of the Taylor series expansion of the response with respect to the variables.

With few exceptions, the response of such models is affected by nonlinear interactions between the variables. When a response is said to involve an "interaction," it is meant that the response cannot be characterized as a sum of functions, each of which is a function of only one variable. A precise mathematical definition of interactions is given in Sec. 6. Local sensitivities are insufficient to evaluate the interactions. In addition, it is not clear what metric should be used to characterize the interactions. One might compare the second order terms in Taylor's series to the first order terms, but even then what magnitude is indicative of a strong interaction is unknown.

As examples of interactions, we investigate two problems:

(a) the sensitivity of the comfort model that is used as an indication of the thermal comfort level of a homogeneous group of people
(b) the sensitivity of the laminar two dimensional free convection flow in a vertical enclosure

The comfort equation is not familiar to many in the heat transfer community and is reasonably complicated, and we begin the paper with its development. On the other hand, the free convection problem is well known, and the sensitivities examined will be presented at the end of the paper without a detailed discussion of the model.

2 The Comfort Model

The comfort model is based upon work done by Fanger [1] with university students in the 1960s. It was found from laboratory tests in a controlled environment that the subjects stated that they were comfortable when their skin temperature and the evaporative heat lost were related to their metabolic heat generation level by

Table 1 Thermal sensations

State	PMV	PPD (%)
Cold	−3	
Cool	−2	76
Slightly cool	−1	27
Neutral	0	5
Slightly warm	1	27
Warm	2	76
Hot	3	

$$T_{skin} = A_{sk} + B_{sk}M = 35.7 - 0.028(M - W) \quad (1a)$$

$$Q_{sweat} = A_{sw} + B_{sw}M = 0.42((M - W) - 58.15) \quad (1b)$$

These equations were derived by fitting the data shown in Fig. 1 and subtracting the respiration and passive skin diffusion losses from the evaporative losses. While the fit of the skin temperature is reasonable, $r^2 = 0.62$, that of the evaporative loss is clearly very poor, $r^2 = 0.4$, raising questions about the impact of uncertainties in the coefficients of Eq. (1b). Given values of ambient air temperature and velocity, mean radiant temperature, relative humidity, metabolic rate, and clothing resistance, one solves the nonlinear equation energy conservation equation (Eq. (2)) for the convective and radiant heat losses per unit surface area,

$$\frac{T_{sk} - T_{cl}}{R_{cl}} = h_c(T_{cl} - T_a) + \sigma\epsilon(T_{cl}^4 - T_{mr}^4) \quad (2)$$

For a given metabolic heat generation rate M and mechanical work W (almost always taken to be equal to 0), the heat load L is defined to be the difference between $M - W$ and the heat which would be lost under comfortable conditions through clothing, sweating, diffusion from the skin, and respiration. Metrics known as the predicted mean vote (PMV) and predicted percent dissatisfied (PPD) are defined in terms of L by Eqs. (3b) and (3c) with their characteristics given in Table 1,

(a)

Metabolic rate (kcal/hr/m^2)

(b)

Metabolic rate (kcal/hr/m²)

Fig. 1 (*a*) **Skin temperature as a function of metabolic rate.** (*b*) **Evaporative heat loss as a function of metabolic rate.**

$$L = M - W - 3.05(5.733 - 6.99(M - W) - P_a) - \underbrace{0.42((M - W) - 58.15)}_{\text{sweating}} - \underbrace{0.0173M(5.867 - P_a)}_{\text{latent respiration}}$$

where the first bracketed term is labeled *diffusion through skin*

$$- \underbrace{0.0014M(34 - T_a)}_{\text{dry respiration}} - \underbrace{3.96 \times 10^{-8}f_{cl}(T_{cl}^4 - T_{mr}^4)}_{\text{radiation}} - \underbrace{f_{cl}h_c(T_{cl} - T_a)}_{\text{convection}} \quad (3a)$$

$$\text{PMV} = L(0.303e^{-0.036M} + 0.028) \quad (3b)$$

$$\text{PPD} = 100 - 95e^{-0.03353\text{PMV}^4 - 0.2179\text{PMV}^2} \quad (3c)$$

The constants in Eq. (3) were derived from physiological data, and their evaluation is fully described in Ref. [1]. The PMV equation was found by least-squares fitting of the comfort sensation values to the computed values of L (p. 113 of Ref. [1]) and the PPD from a probit analysis (p. 130 of Ref. [1]). These equations clearly show how complex the evaluation of the PMV and PPD and the nature of the interaction are, but not its extent.

3 Validity of the Comfort Equation

Discussions of the use and validity of the thermal comfort equations can be found in Humphreys and Nicol [2], deDear and Brager [3], Brager and deDear [4], and Parsons [5]. There have

been many studies of the thermal comfort of people that have included sufficient information to compute the PMV. Some of the studies have supported the equations, while others have found discrepancies. deDear and Brager's [3] seminal review of the literature showed that the PMV is unbiased when used to predict comfort in air conditioned buildings but overestimated the subjective warmth sensations of people in naturally ventilated buildings. Humphreys and Nicol [2] performed statistical analyses of the data, concluded that the range of applicable variables was much less than that suggested by ASHRAE [6] and ISO [7] (e.g., the ambient air temperature should be in the range of 10–30°C), and suggested other limits (e.g., the air temperature should not exceed 19°C). Brager and de Dear [4] described some ten different effects which constitute potential explanations for the differences observed between predicted and observed thermal sensations. They also showed that comfort is statistically related to the exter-
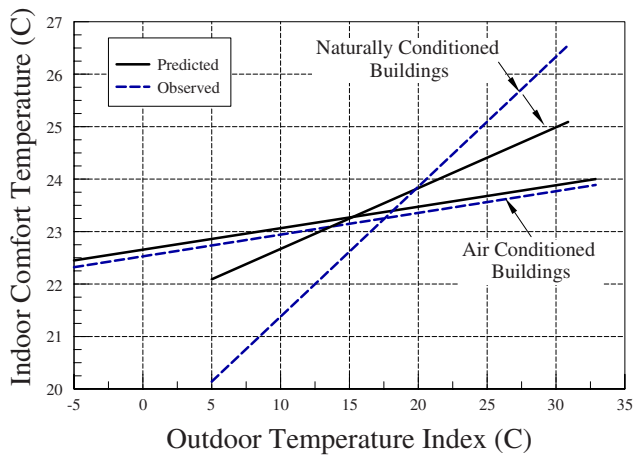
Fig. 2 Comparison of predicted and observed thermal sensations in air conditioned and naturally ventilated buildings (adapted from Ref. [5])

Fig. 3 (a) PPD(I_{cl}, V) for PPD evaluated at the comfort conditions for M=1 met, rh=50%. (b) $f_{12}(I_{cl}, V)$ for PPD evaluated at the comfort conditions for M=1 met, rh=50%.

nal climate with the occupants showing some form of adaptation related to their expectations conditioned on the external temperatures.

Some of the discrepancies may be attributed to measurement errors of the PMV, some to such a simple equation representing a complex physical, psychological, and physiological system and some to the application of a steady state model to a constantly changing dynamic system. Rohles [8] looked at the comfort equation from the point of view of a psychologist. He said that "we all respond the same when exposed to extreme hot and extreme cold. It is at the so called 'comfortable' temperatures that we differ the most." He concludes with the statement, "Although we may apply heat transfer equations to people, they break down when we consider the subtleties involved in human thermal comfort, not to mention the subjective nature of its measurement. In conclusion, recognition of this subjectiveness is paramount and basic to future studies of humans and their thermal environments."

Figure 2 compares the predicted and observed thermal sensations for occupants in air conditioned and naturally ventilated buildings. In controlled environments, the comfort equation does well, but in naturally ventilated buildings the discrepancy is large.

In spite of the concerns voiced by Rohles [8] and others and of the recognition of the level of error associated with the PMV model, it is the current international standard for designing for comfort and we will investigate its sensitivities to uncertainties in the variables and to determine under what conditions these variables interact.

4 Local Sensitivity

Sensitivity is generally thought of as the change in the response when variable changes, i.e., the slope of the response surface. Let the N varying parameters be denoted by x_i, $1 \leq i \leq N$, and let X denote the set of these parameters. x_i^0 represents a nominal value of x_i, and $\delta x_i = x_i - x_i^0$ is a change in x_i. Expanding the response $R(x_1, \ldots, x_N)$ about the nominal values in a Taylor series, for example, for two variables, gives

$$R(x_1, x_2) = R_0 + \frac{\partial R}{\partial x_1} \delta x_1 + \frac{\partial R}{\partial x_2} \delta x_2 + \frac{1}{2} \left(\frac{\partial^2 R}{\partial x_1^2} \delta^2 x_1 + \frac{\partial^2 R}{\partial x_2^2} \delta^2 x_2 \right.$$
$$\left. + 2 \frac{\partial^2 R}{\partial x_1 \partial x_2} \delta x_1 \delta x_2 \right) \quad (4)$$

The scaled local sensitivities are defined as
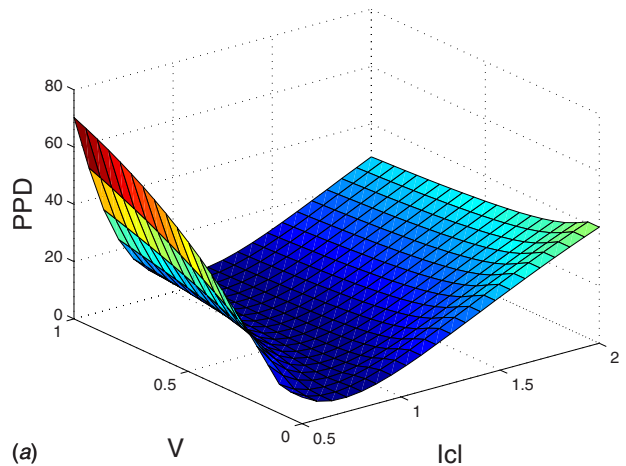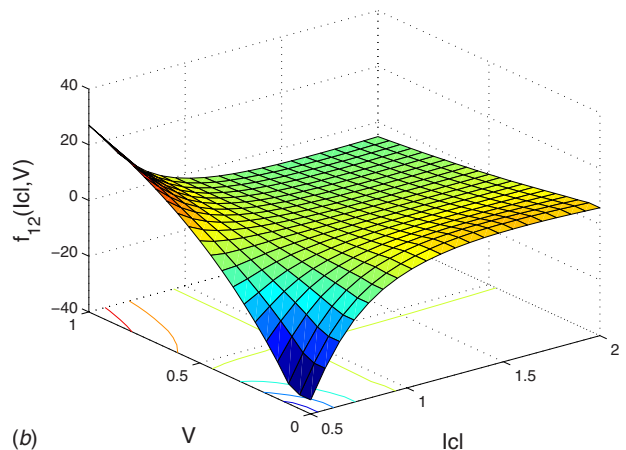
$$s_i = x_i^0 \frac{\partial R}{\partial x_i} \quad (5)$$

While the scaled sensitivities give one a feeling for the nature of the surface, they are strong functions of $x_1^0, \ldots, x_n^0$ and may not give an accurate picture of the nature of the response surface. For the response surface plot shown in Fig. 3, the evaluation of the sensitivities for $I_{cl} \leq 1$ at small values of the air velocity gives a picture very different from that for $I_{cl} > 1$, where the surface is very smooth.

5 Global Sensitivity

Since δR depends upon the direction one moves on the response surface and the extent of the move, a better metric is needed for rapidly varying responses. *Global* sensitivity is defined in terms of the impact that a change in a variable has upon δR and is measured in terms of the fraction of the variance of R due to a specific variable. For smooth response surfaces where the first order terms of the Taylor series are a good representation of δR, if the variables $x_i, \ldots, x_N$ are statistically independent we have

$$S_1 = \text{global sensitivity of } R \text{ to changes in } x_1 \approx \frac{s_1^2 \sigma'^2(x_1)}{V_X[R(X)]}$$
$$(6)$$

where $\sigma'(x_1)$ is the coefficient of variation of x_1 and $V_X[R(X)]$ is the variance of R, defined as

$$V_X[R(X)] = \int_X [R(X) - E_X[R(X)]]^2 p(X) dX$$

$$\text{where } E_X[R(X)] = \int_X R(X) p(X) dX \quad (7)$$

$E_X[R(X)]$ is the expected (average) value of $R(X)$ and $p(X)$ is the joint probability of $x_1, \ldots, x_N$.

If the second or higher order terms are important, then evaluating $\mathcal{S}_i$ using Eq. (6) is not sufficient and some method must be developed to account for the higher order terms and for the variation in S_i over the response surface.

Sobol [9] introduced the idea of expanding the response in the form

$$R(x_1, \cdots, x_N) = f_0 + \sum_{i=1,N} f_i(x_i) + \sum_{i=1,N} \sum_{j>i} f_{ij}(x_i, x_j)$$
$$+ \sum_{i=1,N} \sum_{j>i} \sum_{k>j,i} f_{ijk}(x_i, x_j, x_k)$$
$$+ \ldots f_{ijk\cdots N}(x_i, x_j, x_k, \cdots, x_N) \quad (8)$$

where

$$f_0 = \int R(x_1, \cdots, x_N) p(x_1, \cdots, x_N) dx_1, \cdots, dx_N \quad (9a)$$

$$f_1(x_1) = \int R(x_1, \cdots, x_N) p(x_2, \cdots, x_N) dx_2, \cdots, dx_n - f_0 \quad (9b)$$

where all functions except f_0 are orthogonal and of a zero mean. f_0 is the average value of R, f_i describes the dependence of R on x_i alone, and f_{ij} represents the second order interaction between x_i and x_j, f_{ijk}, the third order interactions, etc.[1] The interaction terms, f_{ij}, are found by extending the procedure shown for $f_1(x_1)$ [9].

In terms of the representation of the second order Taylor series, the functions $f_0, f_1(x_1), f_2(x_2)$ and $f_{12}(x_1, x_2)$ are

$$f_0 = R_0 + \frac{1}{2} \left(\frac{\partial^2 R}{\partial x_1^2} \sigma^2(x_1) + \frac{\partial^2 R}{\partial x_2^2} \sigma^2(x_2) \right) \quad (10a)$$

$$f_1(x_1) = \frac{1}{2} \frac{\partial^2 R}{\partial x_1^2} (\delta^2 x_1 - \sigma^2(x_1)) \quad (10b)$$

$$f_2(x_2) = \frac{1}{2} \frac{\partial^2 R}{\partial x_2^2} (\delta^2 x_2 - \sigma^2(x_2)) \quad (10c)$$

$$f_{12}(x_1, x_2) = \frac{\partial^2 R}{\partial x_1 \, \partial x_2} \delta x_1 \delta x_2 \quad (10d)$$

The function f_{12} is related to the twist of the response surface, and it is hard to visualize this. Figure 3(b) shows the behavior of f_{12} for $x_1 = I_{cl}$ and $x_2 = V_{air}$ for the PPD evaluated at the comfort conditions. (The integrations required were done numerically by sampling the PPD on a fine grid.) Comparing the values of f_{12} with the values of PPD, it is clear that there are significant interactions.

Since the functions are orthogonal and of a zero mean, the variance is given by the sum of the expectations of the square of each of the terms.

---

[1]Sobol considered only uniform probability distributions of x_i, but the method is easily generalized.

$$V_X[R(X)] = \sum_{i=1,N} E_i[f_i(x_i)^2] + \sum_{i=1,N} \sum_{j>i} E_{ij}[f_{ij}(x_i, x_j)^2] + \ldots$$

$$(11)$$

where $E_i[\ ]$ represents the integration with respect to x_i only and $E_{ij}[\ ]$ represents the integration with respect to x_i and x_j.

Using the definitions of f_i, f_{ij}, etc., it can be shown that the global sensitivities, which are the expected values of $f_{i,\ldots,N}^2$, are given by

$$\mathcal{S}_i \equiv \frac{V_i[E_{-i}[R|x_i]]}{V_X[R(X)]} = \frac{\int_{x_i} [E_{-i}[R(X|x_i)] - E[R(X)]]^2 p(x_i) dx_i}{V_X[R(X)]}$$

$$(12a)$$

where $R|x_i$ means that $R(X)$ is a function of all of the parameters except for x_i, which is held fixed, and E_{-i} means that the expectation (integration) is taken over all variables except for x_i. $V_i[E_{-i}[\ R|x_i)]]$ represents how much the total variance is reduced by knowing x_i; that is, it is the sensitivity of R to x_i.

The second order effects are found from

$$\mathcal{S}_{i,j} = \frac{V_{i,j}[E_{-i,j}[R|x_{i,j}]]}{V_X[R(X)]} \quad (12b)$$

Considering all possible sensitivities, we find

$$1 = \underbrace{\sum_i \mathcal{S}_i}_{\text{first order effects}} + \underbrace{\sum_i \sum_{j>i} \mathcal{S}_{i,j}}_{\text{second order effects}} + \underbrace{\sum_i \sum_{j>i} \sum_{i,j,k>j} \mathcal{S}_{i,j,k}}_{\text{third order effects}} \cdots \quad (13)$$

where there is a total of 2^N terms in this expression. The sum of the first order effects will be less than 1 by virtue of interactions between the parameters.

Saltelli et al. [10] defined a *total effect sensitivity* for x_i as

$$\mathcal{S}_i^T = 1 - \frac{V_{-i}[E_i[R|x_{-i}]]}{V_X[R(X)]} \quad (14)$$

This total effect represents the expected resulting variance that would be left if all parameters except x_i were known. Thus, it represents the effect of parameter x_i by itself and in its pair interactions with x_j, its triplet interactions with x_j and x_k, etc. These two sensitivities, $\mathcal{S}_i$ and $\mathcal{S}_i^T$, give a rather complete picture of the effect of x_i on the response of the system. Both are scaled to be between 0 and 1. For $\mathcal{S}_i$, a value of 0 means that x_i has no effect, and a value of 1 means that it constitutes the entire variability of the response. The sum of $\mathcal{S}_i$ is always less than 1 because of the neglect of the interactions. The sum of $\mathcal{S}_i^T$ is always greater than 1 because the interactions are multiply counted. For independent parameters, $\mathcal{S}_i \leq \mathcal{S}_i^T$.

5.1 Implementation. The evaluation of the sensitivities (Eqs. (12a), (12b), and (14)) can be a computationally challenging task for models that are complex. Saltelli et al. [10] suggested using Sobol's pseudo–Monte Carlo technique to perform the necessary integrations. Monte Carlo integration typically requires many thousands of evaluations for reasonable accuracy. In both this problem and others, we have found that Gaussian quadrature is more efficient and more accurate. For this study, we assumed that the parameters are independent with normal distributions. For this case and for models that are reasonably smooth with respect to the parameters, five or at most seven quadrature points have proven to be sufficient. For six parameters, this requires 7776 and 279,936 evaluations. The comfort model is simple enough that this is not a major problem. However, for more complicated models, such as in the free convection problem, it can clearly be an insurmountable stumbling block. Oakeley and O'Hagan [11] successfully used Gaussian processes to reduce the number of evaluations.
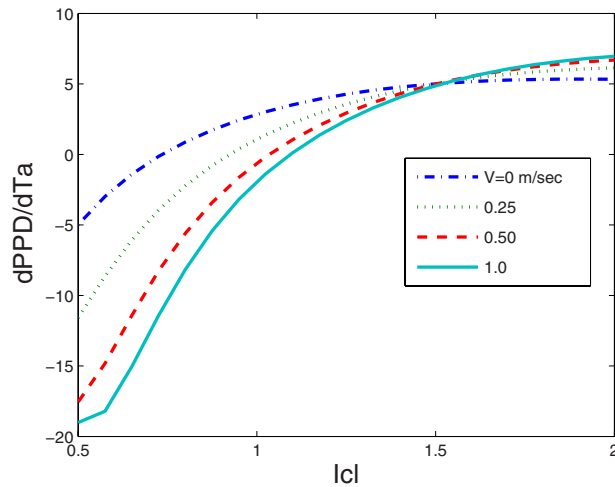
Fig. 4 *dPPD/dT$_a$* for *M*=1 met, rh=50%

Legend: V=0 m/sec; 0.25; 0.50; 1.0. Y-axis: dPPD/dTa. X-axis: |cl|

often occur in groups, e.g., Reynolds or Nusselt numbers. When this happens, cross derivative terms appear in the Taylor series. As a result of these cross derivatives, parameter estimation problems may become much more complex, depending upon the magnitude and the character of the interactions.

Clearly, the values of PMV and PPD are strong functions of both velocity and clothing (Fig. 3). Consider a room full of people with different clothings and thus different reported values of PMV and levels of dissatisfaction. If the model is additive, then as the air velocity changes, each will report the same change in PMV and PPD, regardless of their value of I_{cl}. Thus, the heating, ventilating, and air conditioning (HVAC) system operator need not worry about how V and I_{cl} will interact in causing changes in the responses of individuals. While we will later show that the PMV is only slightly affected by interactions, i.e., the model is primarily additive, a plot of *dPPD/dT$_a$* (Fig. 4), suggests that the model for PPD is not additive, displaying some unknown degree of interaction, especially at low values of I_{cl}. Unfortunately, simply looking at graphs such as that in Fig. 4 does not enable one to quantify the degree of interaction.

6 Additive Models

If the response R to a set of variables, $x_1, x_2, \cdots, x_n$, can be represented as the sum of functions, each of only one variable, as shown in Eq. (15), the model is said to be an "additive model,"

$$R(x_1, x_2, \ldots, x_N) = f_0 + f_1(x_1) + f_2(x_2) + \cdots f_N(x_N) \qquad (15)$$

where the constituent functions $f_i(x_i)$ may be complex nonlinear functions of the single parameter x_i. Additive models have several very desirable characteristics; among the most important are the following:

(a) The behavior of the model with respect to any single parameter, x_j, can be determined without specifying any of the other parameters.
(b) The maximum/minimum response is simply the sum of the maximum/minimum values of each of the constituent functions.
(c) The sensitivities and the confidence intervals of estimated parameters are easily determined.
(d) Error analyses are simple to conduct.

Unfortunately, models of technical systems are rarely additive. Instead, the model is usually a function of several parameters that

7 Global Sensitivity of PMV and PPD

The comfort equation (Eq. (2)) is based upon the equations for skin temperature (Eq. (1a)) and for sweating (Eq. (1b)). These were derived from the data shown in Fig. 2. Since the coefficients derived from a linear regression are linked together, i.e., a change in the weighting of the data or of a data point will lead to a change in both coefficients, the coefficients are correlated. If a change is made in A_{sk}, it must be accompanied by a change in B_{sk}. Consequently, questions that come to mind are: How sensitive are PMV and PPD to the constants in these equations? Do these constants interact in defining the PMV and PPD?

The sensitivities listed in Table 2 were based upon the 95% confidence limits shown in the figures. The entries are for the PMV and PPD affected by the variability in the skin equation only, by the variability in the sweating equation only, and then by the combined effect of the variabilities in both equations. The diagonal entries, e.g., in the second row for the entry in the third column labeled B_{sk} and in the column labeled B_{sk}, are the first order sensitivities. The off-diagonal entries, e.g., for the entry in the third column labeled B_{sk} and in the column labeled A_{sk}, are the second order interaction sensitivities.

From Table 2, it appears that there is no interaction for PMV, but it is considerable for PPD. Although these results may appear

Table 2 Global sensitivity to the constants in the skin and sweat equations evaluated at the comfort conditions for M=1, I_{cl}=1, V=0.5 m/s, and rh=50% with A_{sk}, B_{sk}, A_{sw}, and B_{sw} varying over the 95% confidence range

			A_{sk}	B_{sk}	A_{sw}	B_{sw}	Sum of interactions
PMV	Sk and Sw	A_{sk}	0.20	0.00	0.00	0.00	0.00
	Both	B_{sk}	0.00	0.05	0.00	0.00	0.00
	Uncertain	A_{sw}	0.00	0.00	0.00	0.01	0.01
		B_{sw}	0.00	0.00	0.01	0.75	0.01
PMV	Sk only	A_{sk}	0.79	0.00			0.01
		B_{sk}	0.00	0.21			0.01
	Sw only	A_{sw}			0.00	0.01	0.01
		B_{sw}			0.01	0.99	0.01
PPD	Sk and Sw	A_{sk}	0.02	0.31	0.00	0.44	0.47
	Both	B_{sk}	0.31	0.01	0.00	0.12	0.51
	Uncertain	A_{sw}	0.00	0.00	0.02	0.01	0.01
		B_{sw}	0.44	0.12	0.01	0.35	0.51
PPD	Sk only	A_{sk}	0.42	0.55			0.55
		B_{sk}	0.55	0.03			0.55
	Sw only	A_{sw}			0.04	0.03	0.03
		B_{sw}			0.03	0.93	0.03

Table 3 Values of PMV and PPD for $M=2$ with $T_{mr}=T_a$, $V=0.5$ m/s, rh=50%, $I_{cl}=1$ clo with T_a, T_{mr}, V, rh, M, and I_{cl} having a standard deviation of 10% or 20%

		PMV				PPD			
COV	T_a (°C)	Local value	Expected value	σ of PMV	Sum of interactions	Local value	Expected value	σ of PPD	Sum of interactions
0.1	25	1.23	1.23	0.38	0.01	38.4	40.0	17.6	0.01
0.2	25	1.23	1.23	0.80	0.03	38.4	44.3	29.1	0.08
0.1	Neutral	0.00	0.00	0.36	0.00	5.0	7.9	3.8	0.79
0.2	Neutral	0.00	0.00	0.78	0.02	5.0	17.6	17.0	0.71

surprising at first, they are easily explained in part. For the PMV, from Eq. (4) we see that it is proportional to the load L, which is a linear function of the constants, A_{sw} and B_{sw} in Eq. (1b). The convective and radiative losses are proportional to the skin temperature T_{sk}, which is also a linear function of the constants in Eq. (1a). Thus, there should be no interactions between these constants, in agreement with the values shown in Table 2.

By contrast, the PPD is a nonlinear function of the PMV and thus of the constants. As discussed more fully in the following section, when occupants are comfortable its sensitivity is strongly affected by the interactions. Because of the interaction between the constants A_{sw}, B_{sw}, A_{sk}, and B_{sk}, one must be careful to ensure that the regression is a valid representation of the data. Unfortunately, the lack of correlation of the evaporative heat loss, $r=0.4$, raises serious doubts about the validity of the thermal model for computing the level of dissatisfaction. On the other hand, the PMV shows little interaction and thus appears to be a more reliable result.

Table 2 and subsequent tables of sensitivities are interpreted as follows: For the row labeled A_{sk}, the entries in the fourth column are the sensitivities of the PMV to A_{sk} and the entries in the fifth column are the interaction between A_{sk} and B_{sk}. The entries in the eighth column are the total interaction between A_{sk} and the other parameters. Thus, for PMV there is no interaction between A_{sk} and the other parameters. However, there is an interaction between A_{sw} and B_{sw}.

The lack of interaction for the PMV means that one can estimate the change in the PMV by simply adding the changes due to V and I_{cl}. This is true whether one is uncertain about the coefficients in the sweating or the skin temperature equations or both. However, the uncertainty in the PPD is dominated by the uncertainty in B_{sw} and its interactions and the interaction of A_{sk} and B_{sk}. Neither of these latter two coefficients is important in themselves, only in their interactions; i.e., the sensitivity of the PPD to A_{sk} is only 0.02, but that to the interaction between A_{sk} and B_{sk} is 0.31.

8 Global Sensitivity and Interactions Associated With the Environmental Variables

In a typical office environment, it is unreasonable to expect that all the occupants will be at the same level of activity, M, or wearing the same clothing, I_{cl}. As a consequence, there will be a range of PMV and PPD values. What we are interested in is the expected value, i.e., the average values, and the variance of these values. In particular, we would like to know how the spread of PMV and PPD values is affected by the range of environmental values. This, of course, will be dependent upon the probability density distributions of the parameters. In these calculations, all the variables were independent and normally distributed about the nominal values.

For linear models, local sensitivity yields an accurate estimate of the effects of the parameters. Unfortunately, the comfort model has a complex nonlinear dependency on the variables. Estimating the effects, and particularly the coefficients of Eq. (4), is complex and depends upon the magnitude and the character of the interactions.

We assume that all of the variables are uncertain with coefficients of variation ranging from 0% (deterministic) to 20%. For a nominal value of $M=2$, and the values of T_a shown in column 2, the values of PMV and PPD are given in Table 3. Listed are the local values (i.e., the deterministic values), the expected values, the standard deviation over the range of the uncertainty of the parameters, and the sum of all of the interactions. The results are surprising. For $M=2$, the comfortable temperature is $T_a=17.4$. For $T_a=25$, which is outside of the comfort range, $-0.5 \leq \text{PMV} \leq 0.5$, the expected value differs negligibly from the local value (the deterministic value), and the variation in the PMV (indicated by its standard deviation) and the interactions between M and T_a are unimportant.

In view of the complexity of the thermal comfort equations, this does not appear to make sense. The PMV is proportional to L, the difference between the metabolic heat generation and that which would be lost under comfort conditions. M enters in through the metabolic rate and the skin temperature at comfort. T_a enters strongly through the convective and radiative loss terms and to a lesser degree through the ambient vapor pressure. Product terms of the form MT_a and MP_a are clearly sources of interaction. However, one must remember that the interactions derived from global sensitivity are not response interactions but sensitivity interactions. Figure 5 is a plot of the response surface as a function of T_a and M at the comfort condition.

Although not shown, the PMV is greater for $T_a=25$, but the nature of the surface is very similar. We see that the slopes, $dPMV/dM$ and $dPMV/dT_a$, are essentially constant over the entire surface, and thus the interactions are negligible.

The situation is much different with the PPD, which is a symmetrical function of the PMV. For $T_a=25$, the PMV varies from 0.5 to 2.5 over the range of M and T_a, and the PPD varies from 10% to 90% and has almost constant slopes, giving negligible interactions. However, if the occupants are at a comfortable average, the PMV varies from -1 to 0.8, and the PPD surface is a near quadratic (Fig. 5(b)) with substantial variations in slope over the range of M and T_a. Consequently, a very large interaction is reported. In addition, the expected value of PPD is much larger than the 5% associated with a comfortable condition and with a large standard deviation.

Table 4 lists the different interactions when occupants are uncomfortable, $T_a=25°C$, and comfortable, $T_a=17.4°C$. For both situations, there were no interactions for the PMV, and the global sensitivities listed in column 2 are essentially the same as the local sensitivities.

The entries for the PPD are shown as a matrix of values, i.e., the row labeled T_a and the column labeled M show the value of $S_{T_a,M}$. The dominant interactions are between T_a and M, with smaller interactions between T_a and I_{cl} and T_a and T_{mr}. As expected, the interactions dominate the PPD at the comfortable state.

It is surprising that the sensitivities of both PMV and PPD to V, the local air speed, is so small. The velocity enters only in through the convective heat transfer coefficient associated with the clothing heat transfer. Because of the relatively large clothing resistance for all $I_{cl}>0.5$, the overall resistance is only slightly af-
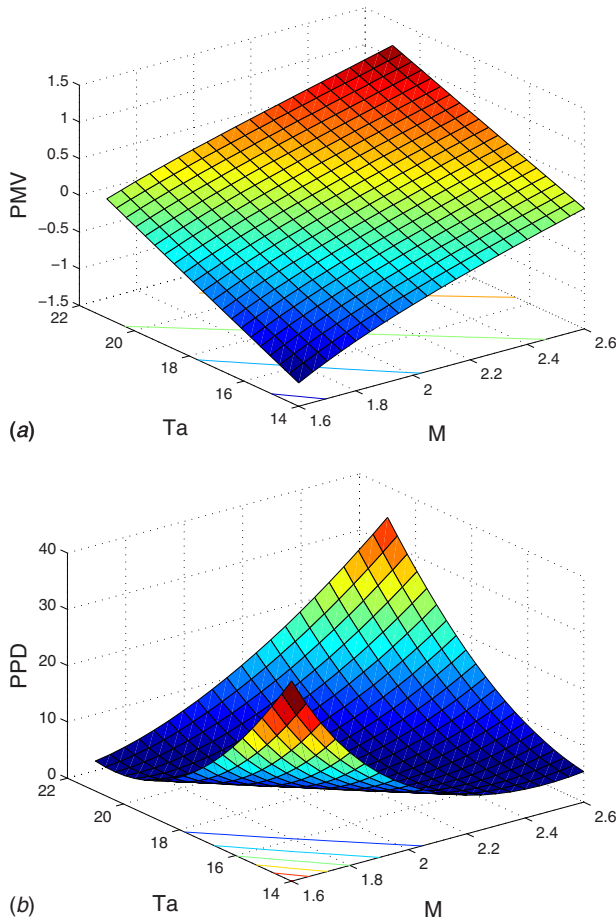
Fig. 5 (*a*) PMV response surfaces for $T_{rm} = T_a$, $V = 0.5$ m/s, and $I_{cl} = 1$ clo. (*b*) PPD response surfaces for $T_{rm} = T_a$, $V = 0.5$ m/s, and $I_{cl} = 1$ clo.

Table 4 (a) Sensitivity to environmental variables at $T_a = T_{mr} = 25$, $V = 0.5$ m/s, rh = 50%, $M = 2$, and $I_{cl} = 1$ clo with T_a, T_{mr}, V, rh, M, and I_{cl} having a 10% standard deviation. (b) Sensitivity to environmental variables at $T_a = T_{mr} = 17.4°C$ (comfortable) $V = 0.5$ m/s, rh = 50%, $M = 2$, and $I_{cl} = 1$ clo with T_a, T_{mr}, V, rh, M, and I_{cl} having a 10% standard deviation.

					PPD			
	PMV	T_a	T_{mr}	V	rh	M	I_{cl}	Sum of interactions
(a)								
T_a	0.64	0.65	0.00	0.00	0.00	0.00	0.00	0.00
T_{rm}	0.11	0.00	0.10	0.00	0.00	0.05	0.02	0.00
V	0.00	0.00	0.00	0.00	0.00	0.00	0.00	0.00
rh	0.01	0.00	0.00	0.00	0.00	0.00	0.00	0.00
M	0.21	0.00	0.05	0.01	0.00	0.20	0.19	0.00
I_{cl}	0.04	0.00	0.00	0.00	0.00	0.00	0.04	0.00
(b)								
T_a	0.32	0.06	0.04	0.00	0.00	0.34	0.13	0.51
T_{mr}	0.05	0.04	0.00	0.00	0.00	0.05	0.02	0.11
V	0.00	0.00	0.00	0.00	0.00	0.00	0.01	0.01
rh	0.00	0.00	0.00	0.00	0.00	0.00	0.00	0.00
M	0.45	0.34	0.05	0.01	0.00	0.12	0.19	0.59
I_{cl}	0.17	0.13	0.02	0.00	0.00	0.19	0.03	0.35

fected and in fact changes in clothing temperature due to the changes in V are usually compensated by offsetting changes in the radiative loss.

9 Free Convection: Uncertainty and Additivity

Lest one be led to believe that the existence of significant interactions depends upon the unique shape of the response surface as shown by the PPD, Fig. 3(*b*), we also examined the case of two dimensional laminar free convection in a rectangular region for Rayleigh numbers of 1000 to 10^6 and aspect ratios of H/W from 1 to 10. The experimental correlations are [12]

$$\mathrm{Nu} = 0.18\left(\frac{\mathrm{Pr}}{0.2 + \mathrm{Pr}}\mathrm{Ra}\right)^{0.29}, \quad 1 \leq H/W \leq 2; \quad \frac{\mathrm{RaPr}}{0.2 + \mathrm{Pr}} > 10^3 \tag{16a}$$

$$\mathrm{Nu} = 0.22\left(\frac{\mathrm{Pr}}{0.2 + \mathrm{Pr}}\mathrm{Ra}\right)^{0.28}(H/W)^{-0.25}, \quad 2 \leq H/W \leq 10; \quad 10^3$$
$$\leq \mathrm{Ra} \leq 10^{10} \tag{16b}$$

$$\mathrm{Nu} = 0.42\mathrm{Ra}^{1/4}\mathrm{Pr}^{0.012}(H/W)^{-0.3}, \quad 10 \leq H/W \leq 40; \quad 10^4 \leq \mathrm{Ra}$$
$$\leq 10^7 \tag{16c}$$

and the dependence upon H/W indicated by the two equations (Eqs. (16*a*) and (16*b*)) suggests that there will be a significant change in the response as H/W increases from 1 to greater than 2. Figure 6 clearly shows how the response surface for $H/W = 1$ varies as the Rayleigh number increases and how that for $H/W = 2$ is almost flat and lacking in twist. The twist apparent in the response surfaces for $H/W = 1$ suggests that the interaction may be important.

It is not easy to predict when interactions would exist. Equation (16*a*) shows no effect of H/W, while Eq. (16*b*) indicates a strong interaction between Ra and H/W. Evaluating the terms in the Taylor series for Eq. (16*b*) gives

$$\frac{\delta \mathrm{Nu}}{\mathrm{Nu}} = \underbrace{0.28\frac{\delta \mathrm{Ra}}{\mathrm{Ra}} - 0.25\frac{\delta H/W}{H/W}}_{\text{first order}}$$
$$\underbrace{- 0.1148\left(\frac{\delta \mathrm{Ra}}{\mathrm{Ra}}\right)^2 - 0.070\frac{\delta \mathrm{Ra}}{\mathrm{Ra}}\frac{\delta H/W}{H/W} + 0.15625\left(\frac{\delta H/W}{H/W}\right)^2}_{\text{second order}}$$

and it would appear that the interaction as indicated by the cross derivative at a point where the fractional change in Ra and H/W is equal, i.e., $\delta \mathrm{Ra}/\mathrm{Ra} = \delta H/W/H/W = P$, would be substantial, equaling $0.070P^2$ as compared with the sum of the remainder of the second order terms of $0.04145P^2$.

Computations of the flow field and heat transfer were made with FIDAP [13] and COMSOL [14] using a graded mesh of 51 $\times$ 51 for $H/W = 1$ and 51×153 for $H/W = 10$. For the square region, $H/W = 1$, we have the benchmark results of de Vahl Davis [15] to validate our numerical results. The results are compared in Table 5 with only the maximum velocity in the *x*-direction differing from the benchmark results.

Since the flow field changes substantially as the Rayleigh number increases (Fig. 7), we anticipated that there would be substantial interactions. We then computed the second order interactions for the heat transfer, Nu average, maximum Nu, minimum Nu, maximum velocities, and stream function in terms of Rayleigh number and aspect ratio. Since for $H/W = 1$ the system evolves from one of pure conduction at low Ra to a unicellular flow at modest Ra and finally to a bicellular flow at high Ra, we anticipated substantial interaction effects as measured by the values of the second order interaction between Ra and H/W, denoted by $\mathcal{S}_{12}$.

(a)

(b)

(c)
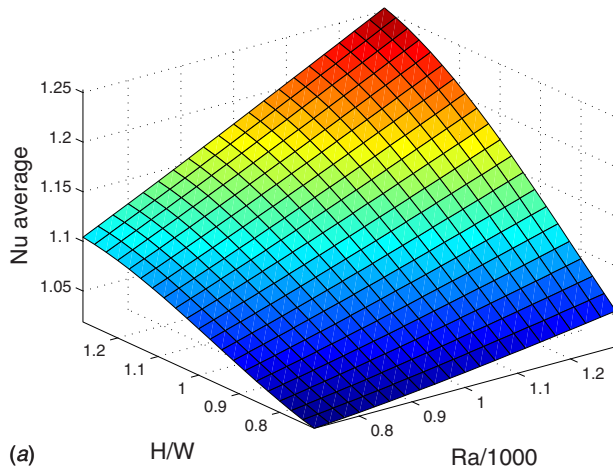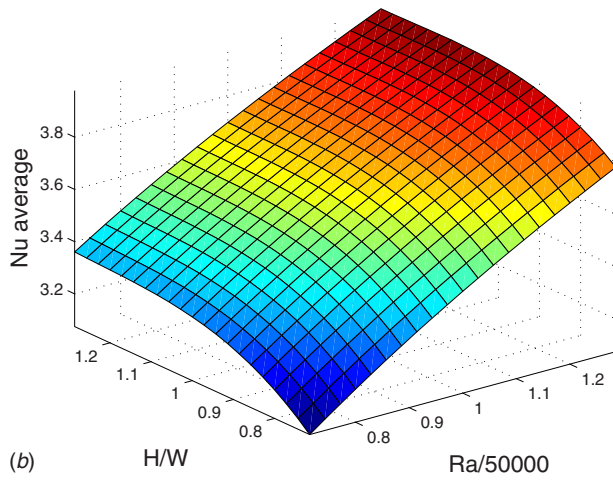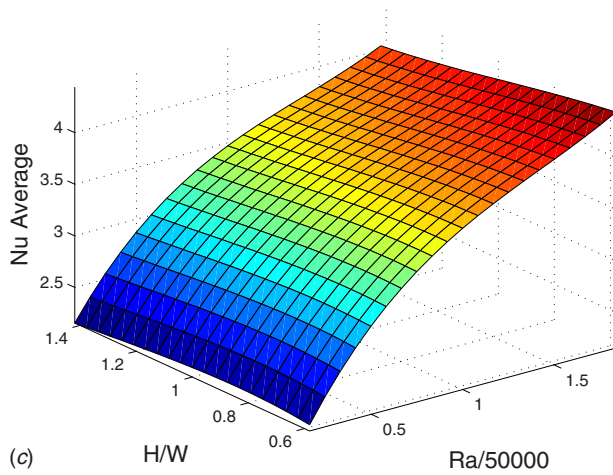
Fig. 6 (*a*) Response surface of average Nu for nominal values of *H/W*=1 and Ra= 10^3. (*b*) Response surface of average Nu for nominal values of *H/W*=1 and Ra= 5×10^4. (*c*) Response surface of average Nu for nominal values of *H/W*=2 and Ra $=5 \times 10^4$.

We have found from previous studies that when the second order sensitivities exceed a few percent, there are significant interactions. It might appear that a few percent is a very small amount, but remember that S_{12} is a root mean square value, and relatively large deviations of the response surface from an additive model often do not lead to large values of $\mathcal{S}_{12}$.

Table 5   Comparison with benchmark values for *H/W*=1

	Ra	U_{max}	V_{max}	Maximum Str
FIDAP	10^4	0.192	0.233	0.060
COMSOL	10^4	0.192	0.233	0.060
Benchmark	10^4	0.193	0.233	
FIDAP	10^5	0.165	0.257	0.036
COMSOL	10^5	0.165	0.257	0.036
Benchmark	10^5	0.130	0.257	0.036
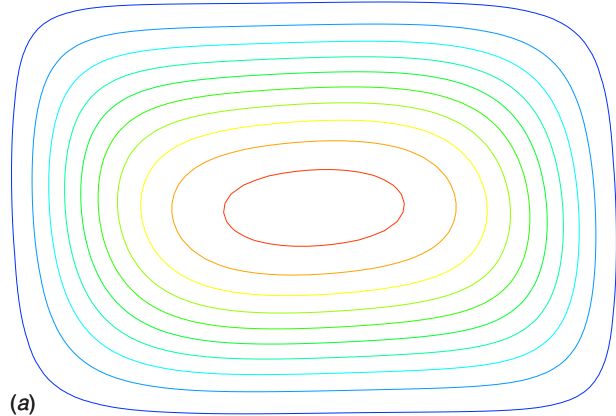
(a)
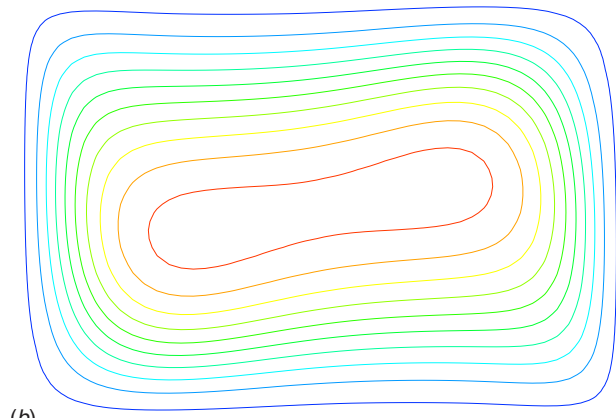
(b)
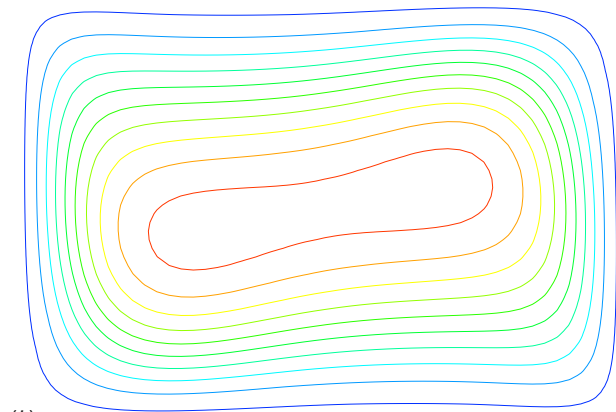
(b)

Fig. 7 (*a*) Streamlines for Ra=10^4. (*b*) Streamlines for Ra =71,430. (*c*) Streamlines for Ra=1,128,570.

9.1 Uncertainty. Consider the case where one is uncertain about the aspect ratio and the Ra number and is interested in the behavior of the average heat transfer. Let the Rayleigh number and the enclosure width be normally distributed about the nominal

Table 6 Values of S_{12} for Ra=10^5

H/W	Nu_{av}	Nu_{max}	Nu_{min}	U_{max}	V_{max}	Maximum Str
0.9–1.1	4.8×10^{-4}	2.2×10^{-4}	2.4×10^{-4}	8.3×10^{-5}	2.2×10^{-4}	1.5×10^{-3}
0.5–1.5	3.8×10^{-2}	3.1×10^{-2}	3.9×10^{-2}	1.2×10^{-2}	6.6×10^{-3}	6.5×10^{-2}
1.5–2.5	4.6×10^{-3}	3.9×10^{-4}	1.3×10^{-3}	7.6×10^{-2}	4.8×10^{-3}	2.8×10^{-2}

values with a standard deviation of 10% for Ra and a standard deviation in H equal to 10% of W. The second order sensitivities of the average Nusselt number, the maximum and minimum heat fluxes on the hot wall, the maximum vertical and horizontal velocities, and the maximum streamline value for variations in aspect ratio H/W and Rayleigh number are listed in the first line of Table 5. Comparable values were obtained when the uncertainties were characterized by uniform distributions.

Even though the twist of the response surfaces suggests that there might be significant second order interactions, none were predicted over the range of Ra and H/W studied. In other words, all responses were of additive models. That is, any curve on the surface at a specific value of H/W is essentially parallel to that at any other value of H/W, although displaced vertically. Consequently, the effect of the cross derivative, $\partial^2 R/\partial Ra\,\partial H/W$, is negligible.

9.2 Additivity. The results shown in the first line of Table 6 are primarily due to the relative linearity of the response surfaces when the deviation from the nominal values is small—an assumption used in the majority of engineering analyses. To determine whether the response is additive over a larger range of Ra and H/W, computations were made for a uniform distribution with a 50% standard deviation, and the results are shown in Fig. 8.

Table 6 lists the effects of the different quantities for the two cases, nominal values of $H/W=1$ and 2. The interactions for $0.5 \leq H/W \leq 1.5$ for the Nusselt numbers have an order of magnitude higher than that for $1.5 \leq H/W \leq 2.5$, while the velocity interactions are only slightly different.

10 Conclusions

The global sensitivity approach can be applied to any model whose response is a function of several variables that either have a range of values or are uncertain with a known probability
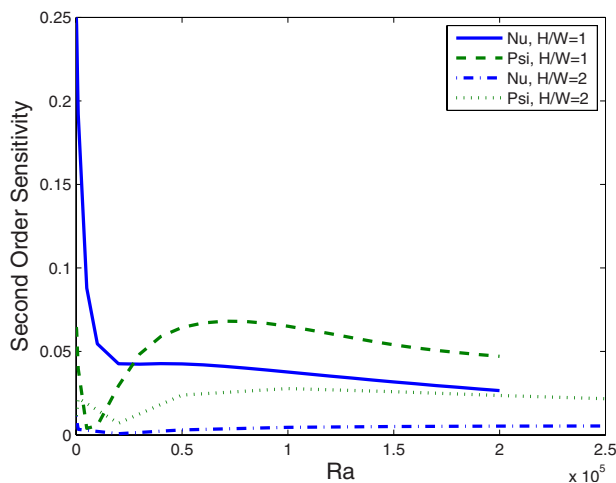
Fig. 8 Second order Interactions for average Nu and maximum stream function

density function. For example, some future applications will be to turbulent flow and its dependence upon parameters of the k-ϵ model. Once one has determined the level of interactions, then it might be possible to design experiments that have reduced interactions and will lead to more precise estimates of the parameters.

The comfort problem emphasizes the need to understand the basic nature of the model. The difference between the sensitivities when occupants are uncomfortable and those when they are comfortable is remarkable. When uncomfortable one can move toward comfort by changing one or more environmental parameters, and the change in the PMV and PPD is not affected by interactions. On the other hand, when moving away from the comfortable condition, the change in the PPD is strongly affected by interactions while the change in the PMV is not. This is because PPD is symmetrical with respect to the PMV; i.e., there is an equal dissatisfaction regardless of whether one is hot or cold. It would not be surprising to observe similar results for any variable that is a symmetric function—for example, the kinetic or potential energies of structures or the dissipation of turbulent energies.

In the free convection problem, the interaction between the driving force, the Rayleigh number, and the enclosure shape, H/W, is initially very large as the flow departs from pure conduction. As the Ra increases, the temperature field stabilizes while the circulatory pattern continues to evolve. The heat transfer is characterized by rising and falling boundary layers and is affected primarily by the vertical velocities, with both having reduced sensitivities. The horizontal velocities and the stream function continue to show the interactions of Ra and H/W on the evolving flow.

Although Eq. (16a) suggests that there is no effect of H/W, this is probably because limited experimental results are available particularly for $H/W \leq 1$. The global sensitivity analysis clearly indicates that there is an interaction when H/W is near 1 but not at 2. Figure 9 shows the behavior of Nu versus Ra for different values of H/W, and the lack of interaction for $1 < H/W < 2$ contrasts markedly with the strong interaction for $0.2 < H/W < 2$.

It is important to recognize that sensitivity represents how a response varies with respect to variables and is a measure of the gradient of the response surface, not of its magnitude. The global sensitivity approach is aimed at determining how the gradient is affected by interactions between the variables, not how they affect the magnitude of the response, that is, how far the model of the response differs from the additive model. Because the estimation of the interactions is often computationally challenging, as in the free convection study, considerable thought should be given as to the need for evaluating them before embarking on the study. When designing experiments to estimate physical properties or boundary conditions, this may require a considerable analysis of the role of each parameter sought.

Acknowledgment

(a)

(b)
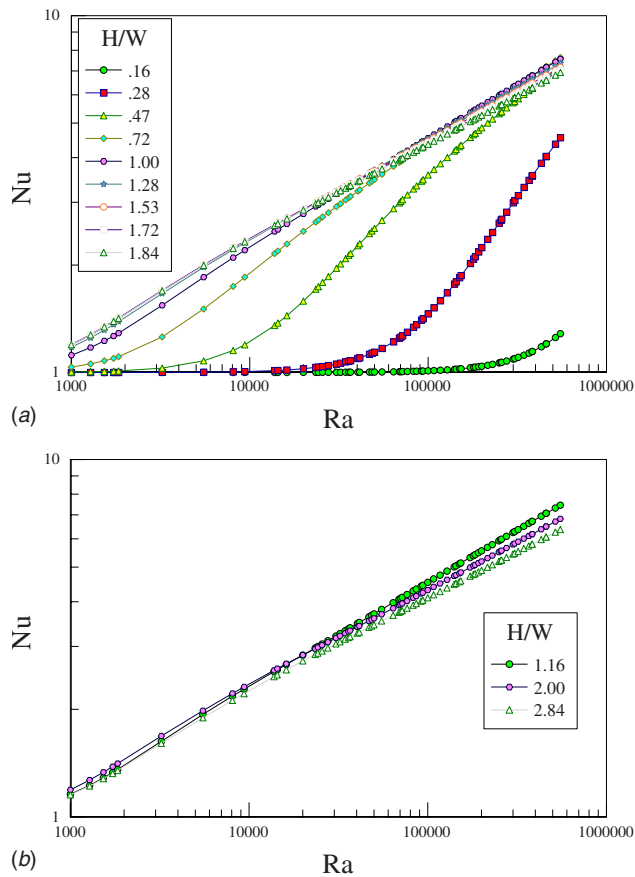
Fig. 9 (*a*) **Nu versus Ra from simulations for** *H/W*=1. (*b*) **Nu versus Ra from simulations for** *H/W*=2.

Nomenclature

A_{sk}, B_{sk} = constants in the T_{sk} equation
A_{sw}, B_{sw} = constants in the Q_{sw} equation
$\mathrm{COV}(v)$ = coefficient of variation$=\sigma(x)/E[x]$
$E[y]$ = expected value of y
f_{cl} = clothing form factor [3]
h_c = convective heat transfer coefficient, W/m² C
H = height of enclosure
H/W = aspect ratio
I_{cl} = clothing insulation, clo
L = thermal load, W/m²
M = metabolic heat production, W/m²
Nu = Nusselt number based on W
Q = heat lost, W/m²

$p(x)$ = probability density distribution of x
P_a = vapor pressure, kPa
R = response
R_{cl} = clothing resistance$=0.8I_{cl}$
Ra = Rayleigh number based on W
$\sigma(x_i)$ = standard deviation of x_i
$\sigma'(x_i)$ = coefficient of variation$=\sigma(x_i)/E[x_i]$
s_i = first order sensitivity
s_i = first order global sensitivity
S_i^T = first order total global sensitivity
$S_{i,j}$ = second order sensitivity
T_a = ambient air temperature
T_{cl} = clothing temperature
T_{mr} = mean radiant temperature
U, V = horizontal and vertical velocities in the enclosure
V = air velocity
$V[y]$ = variance of y
W = work, W/m², width of enclosure
x_i = ith variable
σ = Stefan–Boltzmann constant

References

[1] Fanger, P. O., 1970, *Thermal Comfort*, McGraw-Hill, New York.
[2] Humphreys, M. A., and Nicol, J. F., 2002, "The Validity of ISO-PMV for Predicting Comfort Votes in Every-Day Thermal Environments," Energy Build., **34**, pp. 667–684.
[3] deDear, R. J., and Brager, G. S., 2002, "Thermal Comfort in Naturally Ventilated Buildings: Revisions to ASHRAE Standard 55," Energy Build., **34**, pp. 549–561.
[4] Brager, G. S., and deDear, R. J., 1998, "Thermal Adaptation in the Built Environment: A Literature Review," Energy Build., **27**, pp. 83–96.
[5] Olesen, B. W., and Parsons, K. C., 2002, "Introduction to Thermal Comfort Standards and to the Proposed New Version of EN ISO 7730," Energy Build., **34**(6), pp. 537–548.
[6] 2004, ASHRAE Standard 55-2004—Thermal Environmental Conditions for Human Occupancy, ASHRAE Inc., Atlanta, GA.
[7] 1994, ISO 7730, "Moderate Thermal Environments—Determination of the PMV and PPD Indices and Specification of the Conditions for Thermal Comfort," ISO, Geneva.
[8] Rohles, F. H., 2007, "Temperature and Temperament, A Psychologist Looks at Comfort," ASHRAE J., **49**, pp. 14–22.
[9] Sobol, I. M., 1993, "Sensitivity Estimates for Nonlinear Mathematical Models," Mathematical Modeling and Computational Experiment, **1**(4), pp. 407–414.
[10] Saltelli, A., Tarantola, S., Campolongo, F., and Ratto, M., 2004, *Sensitivity Analysis in Practice*, Wiley, New York.
[11] Oakley, J. E., and O'Hagan, A., 2004, "Probabilistic Sensitivity Analysis of Complex Models: A Bayesian Approach," J. R. Stat. Soc. Ser. B (Stat. Methodol.), **66**, pp. 751–769.
[12] Incropera, F. P., and DeWitt, D. P., 2000, *Introduction to Heat Transfer*, Wiley, New York.
[13] FIDAP, Fluent Inc., Lebanon, NH.
[14] COMSOL, COMSOL, Inc., Palo Alto, CA.
[15] de Vahl Davis, G., and Jones, I. P., 1983, "Natural Convection in a Square Cavity: A Comparison Exercise," Int. J. Numer. Methods Fluids, **3**, pp. 227–248.

Natural Convection Inside a Bidisperse Porous Medium Enclosure

Arunn Narasimhan[1]
Assistant Professor
e-mail: arunn@iitm.ac.in

B. V. K. Reddy
e-mail: bvkreddy680@gmail.com

Department of Mechanical Engineering,
Heat Transfer and Thermal Power Laboratory,
Indian Institute of Technology Madras,
Chennai 600036, India

Bidisperse porous medium (BDPM) consists of a macroporous medium whose solid phase is replaced with a microporous medium. This study investigates using numerical simulations, steady natural convection inside a square BDPM enclosure made from uniformly spaced, disconnected square porous blocks that form the microporous medium. The side walls are subjected to differential heating, while the top and bottom ones are kept adiabatic. The bidispersion effect is generated by varying the number of blocks (N^2), macropore volume fraction (ϕ_E), and internal Darcy number (Da_I) for several enclosure Rayleigh numbers (Ra). Their effect on the BDPM heat transfer (Nu) is investigated. When Ra is fixed, the Nu increases with an increase in both Da_I and Da_E. At low Ra values, Nu is strongly affected by both Da_I and ϕ_E. When N^2 is fixed, at high Ra values, the porous blocks in the core region have negligible effect on the Nu. A correlation is proposed to evaluate the heat transfer from the BDPM enclosure, Nu, as a function of Ra_ϕ, Da_E, Da_I, and N^2. It predicts the numerical results of Nu within ±15% and ±9% in two successive ranges of modified Rayleigh number, $Ra_\phi Da_E$.
[DOI: 10.1115/1.3192134]

1 Introduction

A porous medium with macrosized pores whose solid matrix itself is replaced by another porous medium with microsized pores can be considered as a bidisperse or bidispersed porous medium (BDPM). Chen et al. [1] defined a BDPM to be composed of clusters of large particles that are agglomerates of small particles. In a BDPM, the micro- and macropores are usually connected and the same fluid permeates through these pores [2].

Several applications of BDPM exist including modeling of aquifers, absorbent catalyst pellets, proton exchange membrane (PEM) fuel cells, porous wicks in heat pipes, geothermal energy extraction, and microreactors and modeling of granular mixtures. Mass diffusion in such BDPM has been studied by Burghardt et al. [3], where chemical reactors were modeled as BDPM. Yu and Cheng [4] modeled BDPM as fractals, although BDPM offers only a two step reduction when compared with standard fractal objects. Experiments were also reported in Refs. [1,5,6] that determined the effective thermal conductivity of such a BDPM.

Recently, Nield and Kuznetsov [7–11] investigated forced convection heat transfer in a BDPM filled channel in thermally developing region, thermally developed region, and BDPM coupled conduction in plane slabs bounding the channel, respectively. Analytical solutions for a two-velocity, two-temperature model were presented in each case. The local Nu depended strongly on the BDPM thermal conductivity ratio but was only moderately dependent on the velocity ratio in the two bidisperse pore scales. In Refs. [12,13], the onset of natural convection and the effect of combined vertical and horizontal heterogeneities on the onset of convection in a horizontal BDPM heated uniformly from below were studied, while in Refs. [14,15], the natural convection in a BDPM bounded by a vertical flat plate was investigated. These studies utilized an extended Brinkman model with two velocities coupled with a two-temperature model. The critical Ra was reported as a function of BDPM interface momentum transfer, permeability ratio, thermal conductivity and heat capacity ratios, volume fractions, and interface heat transfer coefficient. In the vertical flat plate bounding the BDPM case, a similarity solution confined to leading edge was presented. In Ref. [16] the work reported in Ref. [12] was extended to investigate the possibility of oscillatory convection by using a highly accurate Chebyshev–Tau numerical method. A global stability threshold was reported below which instabilities cannot arise.

The manner in which the natural convection flow and heat transfer are influenced when obstacles (solid/porous blocks) are placed within an enclosure is of contemporary research interest [17–19]. Natural convection inside enclosures with solid obstacles approximates many applications such as ventilation in grain silos, buildings, and storage places for heat generating containers. The numerical simulations in Ref. [17] showed the effect of the intrusion of blocks within the side-wall thermal boundary layers, thereby inhibiting convection. The simulation results in Ref. [18] showed that the strong hindrance effect of the blocks on the convection process is found only beyond a minimum number of blocks for a given Rayleigh number.

Specific to the present study, an enclosure filled with distributed solid blocks immersed in a convecting fluid can be treated as a porous medium enclosure. This was attempted in Ref. [18] for interpreting the total Nu results. Extending this concept, an enclosure filled with distributed blocks made of a microscale porous medium with macrosized gaps separating the blocks can be modeled as a BDPM enclosure. This proposed idea essentially combines the two recent developments in natural convection discussed above: enclosures with distributed blocks and a BDPM.

Investigating natural convection inside such a BDPM enclosure using numerical simulations is the objective of the present investigation. The permeability of the porous blocks (termed the internal permeability Da_I) and the enclosure permeability (identified as the external permeability Da_E) are the two major parameters that are considered to influence the BDPM enclosure heat transfer (Nu) results for several Ra numbers.

2 Geometry and Problem Formulation

The system being investigated is shown as a two-dimensional schematic in Fig. 1(*a*). It consists of a fluid-saturated square enclosure containing several conducting square porous obstacles.
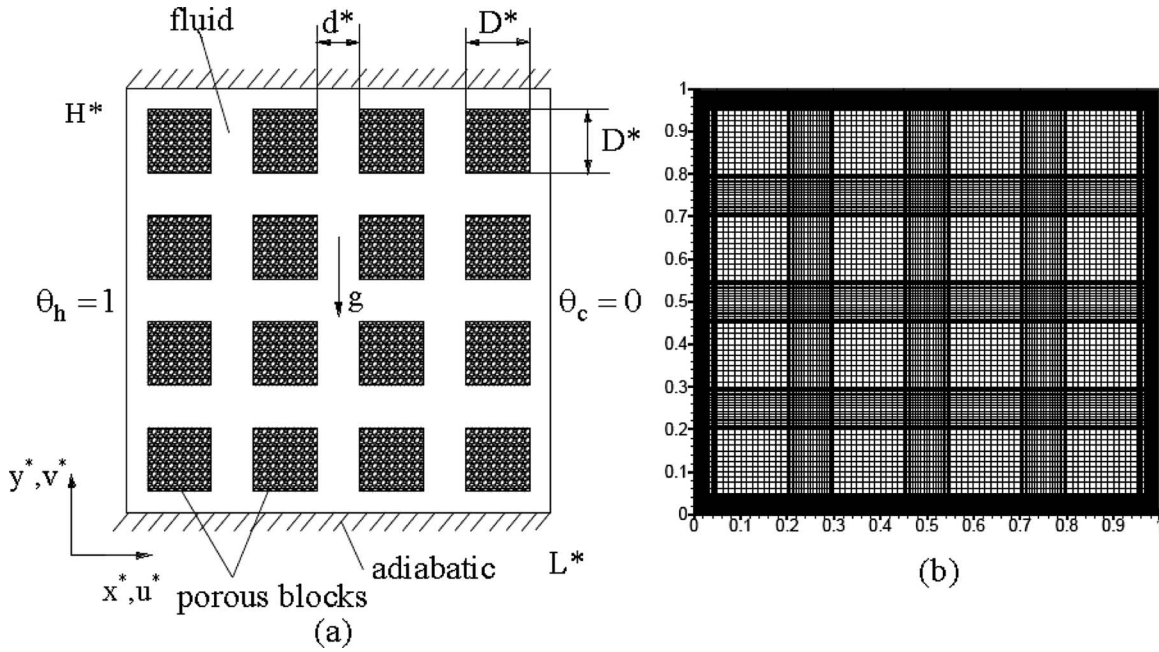
Fig. 1 Schematic of enclosure configuration with 4×4 porous block array (a) Geometry (b) Mesh

They are disconnected and distributed uniformly within the enclosure, which is itself subjected to a horizontal temperature difference ($\Delta\theta = \theta_h - \theta_c$) applied at the walls, as shown in Fig. 1(a). The resulting natural convection of the fluid due to buoyancy effects results in a flow within the enclosure through the micropores in the porous blocks and macropores within enclosure.

The flow is governed by the two-dimensional version of the three conservation equations: mass, momentum (modified Navier–Stokes), and the energy transport subject to certain assumptions. The Oberbeck–Boussinesq approximation, where the local density varies only with temperature and only within the buoyancy term, is invoked. Further, the Newtonian fluid retains its phase with constant thermophysical properties. The steady convection flow is incompressible and laminar. The blocks are made of homogeneous and isotropic porous media with constant thermophysical properties. The convecting fluid and the porous matrix are in local thermal equilibrium.

The governing equations are nondimensionalized using the following terms:

$$x^* = \frac{x}{L}, \quad y^* = \frac{y}{L}, \quad u^* = \frac{u}{(\alpha/L)(\text{Ra Pr})^{1/2}}, \quad v^* = \frac{v}{(\alpha/L)(\text{Ra Pr})^{1/2}}$$

$$p^* = \frac{(p - p_{\text{ref}})}{\rho(\alpha/L)^2 \, \text{Ra Pr}}, \quad \theta = \frac{T - T_c}{T_h - T_c}, \quad \text{Da}_I = \frac{K_I}{L^2}, \quad \text{Pr} = \frac{\nu}{\alpha},$$

$$\text{Ra} = \frac{g\beta(T_h - T_{\text{ref}})L^3}{\nu\alpha} \tag{1}$$

where the reference values for pressure (p_{ref}) and temperature (T_{ref}) have been taken as atmosphere pressure and cold wall temperature, respectively.

Employing the above terms, the nondimensional governing equations for mass, momentum in the x^* and y^* directions, and heat transport in porous media are as follows:

$$\frac{\partial u^*}{\partial x^*} + \frac{\partial v^*}{\partial y^*} = 0 \tag{2}$$

$$u^*\frac{\partial u^*}{\partial x^*} + v^*\frac{\partial u^*}{\partial y^*} = -\phi^2\frac{\partial p^*}{\partial x^*} + \phi\left(\frac{\text{Pr}}{\text{Ra}}\right)^{1/2}\left(\frac{\partial^2 u^*}{\partial x^{*2}} + \frac{\partial^2 u^*}{\partial y^{*2}}\right)$$
$$-\left[\left(\frac{\text{Pr}}{\text{Ra}}\right)^{1/2}\frac{\phi^2}{\text{Da}_I} + \frac{c_F\phi^{1/2}}{\sqrt{\text{Da}_I}}\sqrt{v^{*2} + u^{*2}}\right]u^* \tag{3}$$

$$u^*\frac{\partial v^*}{\partial x^*} + v^*\frac{\partial v^*}{\partial y^*} = -\phi^2\frac{\partial p^*}{\partial y^*} + \phi^2\theta + \phi\left(\frac{\text{Pr}}{\text{Ra}}\right)^{1/2}\left(\frac{\partial^2 v^*}{\partial x^{*2}} + \frac{\partial^2 v^*}{\partial y^{*2}}\right)$$
$$-\left[\left(\frac{\text{Pr}}{\text{Ra}}\right)^{1/2}\frac{\phi^2}{\text{Da}_I} + \frac{c_F\phi^{1/2}}{\sqrt{\text{Da}_I}}\sqrt{v^{*2} + u^{*2}}\right]v^* \tag{4}$$

$$u^*\frac{\partial \theta}{\partial x^*} + v^*\frac{\partial \theta}{\partial y^*} = \frac{(\gamma(1-\phi)+\phi)}{(\text{Ra Pr})^{1/2}}\left(\frac{\partial^2 \theta}{\partial x^{*2}} + \frac{\partial^2 \theta}{\partial y^{*2}}\right) \tag{5}$$

Inside the macropore region Eqs. (3)–(5) are also solved by setting $\phi = 1$ and by setting the last term in Eqs. (3) and (4) to zero.

The associated boundary conditions for Eqs. (2)–(5) with respect to the geometry shown in Fig. 1(a) are as follows.

At the hot wall

$$x^* = 0: \quad u^* = v^* = 0, \quad \theta = 1 \tag{6}$$

At the cold wall

$$x^* = 1: \quad u^* = v^* = 0, \quad \theta = 0 \tag{7}$$

And at the upper and lower walls

$$y^* = 0, 1: \quad u^* = v^* = 0, \quad \frac{\partial \theta}{\partial y^*} = 0 \tag{8}$$

At the interface between the macropores and the porous blocks the following conditions are imposed:

$$\theta_{\text{cf}} = \theta_{\text{pm}}, \quad \left(\frac{\partial \theta}{\partial n}\right)\bigg|_{\text{cf}} = \frac{k_{\text{pm}}}{k_{\text{cf}}}\left(\frac{\partial \theta}{\partial n}\right)\bigg|_{\text{pm}} \tag{9}$$

and

$$u_{\text{cf}}^* = u_{\text{pm}}^*, \qquad \left.\left(\frac{\partial u^*}{\partial n}\right)\right|_{\text{cf}} = \frac{\mu_e}{\mu_{\text{cf}}}\left.\left(\frac{\partial u^*}{\partial n}\right)\right|_{\text{pm}} \tag{10}$$

where n denotes the direction normal to the corresponding wall of each porous block.

Further, for an enclosure of unit aspect ratio (i.e., $H = L$ in Fig. 1), once the macropore volume fraction ϕ_E of the enclosure and the number of solid/porous blocks N^2 placed within it are known, the block size (D^*) and the channel width (δ) can be determined uniquely using the relations

$$\phi_E = 1 - N^2 D^{*2} \tag{11}$$

and

$$\delta = \frac{1 - D^* N}{N} \tag{12}$$

where the latter is obtained by observing that the enclosure wall has the same length as N channel widths and N blocks.

The enclosure with solid conducting blocks may be treated as an equivalent porous medium enclosure without losing the generality of the results. The permeability K_E of this equivalent porous medium can be calculated using the Carman–Kozeny relationship [20,2]. K_E will be a function of the macropore volume fraction, the number of blocks (macroporous medium particle length scale), and the gap width (macropore length scale). The nondimensional version of this relationship can be written as

$$\text{Da}_E = \frac{K_E}{L^2} = \frac{1}{180}\frac{\phi_E^3 D^{*2}}{(1 - \phi_E)^2} \tag{13}$$

where Da_E is the nondimensional representation of the permeability of the solid block-filled enclosure when treated as a porous medium.

While treating an enclosure with distributed blocks as a homogeneous porous medium modeled using a volume averaging approach for the conservation equations, it is essential to transform the variables valid in a continuum model to corresponding variables valid over a porous continuum. For instance, the buoyancy force that is valid for each point in a continuum model is now essentially valid for each point but defined over a porous continuum. Similarly, although the permeability for the porous medium model can be found using Eq. (13), it needs to be corrected for the square shape of the blocks, as Eq. (13) is valid for a packed bed of spheres treated as a porous medium. Following the method suggested in Ref. [21], the Rayleigh and Darcy numbers should be modified and are written as

$$\text{Ra}_\phi = 0.144 \ \text{Ra}^{1.208} \quad \text{and} \quad \text{Da}_E = 1.005 \ \text{Da}_{\text{eq}}^{1.208} \tag{14}$$

where Da_{eq} is calculated from Eq. (13).

As in the BDPM enclosure the solid blocks are replaced with a microporous medium, one can expect Da_E to depend on Da_I, the nondimensional permeability of the microporous medium.

3 Solution Methodology

The numerical simulations are performed using the finite volume formulation of Eqs. (2)–(5) together with the associated boundary conditions given in Eqs. (6)–(10). The convective terms of Eqs. (2)–(5) are discretized using a hybrid scheme and the diffusion terms with the central difference scheme. The pressure and velocity terms of Eqs. (2)–(4) are coupled using the SIMPLE algorithm [22] and are solved iteratively with alternative direction implicit (ADI) method using the tridiagonal matrix algorithm.

The convergence criteria (the difference between consecutive iterations at each cell center) for the mass, momentum, and energy equations are set as 10^{-5}, 10^{-5}, and 10^{-8}, respectively. Suitable grids are chosen after performing grid independence tests of the steady state results for all the numbers of blocks ($N = 3-8$) considered and are given in Table 1. The nonuniform, orthogonal, cosine grid used is shown for $N = 4$ case in Fig. 1(b). Based on the

Table 1 Grid independence study for all the cases at Ra=10^8, Da$_I$=10^{-4}, Pr=1, γ=1, ϕ_E=0.64, and ϕ_I=0.5 (boldface indicates grids chosen for further simulations)

| $N \times N$	Grid size	Nu	Percentage error $\dfrac{\lvert\text{Nu}_{\text{new}} - \text{Nu}_{\text{old}}\rvert}{\text{Nu}_{\text{new}}} \times 100$
3×3	45×45	30.3744	
	89×89	30.5533	0.59
	177×177	30.6791	0.41
	221×221	30.7053	0.09
4×4	57×57	30.4451	
	113×113	30.5849	0.46
	225×225	30.6863	0.33
	337×337	30.7256	0.13
6×6	81×81	30.5326	
	121×121	30.5037	0.09
	201×201	30.5047	0.003
	321×321	30.5194	0.04
8×8	105×105	30.6318	
	157×157	30.5502	0.27
	207×207	30.5286	0.07
	261×261	30.5196	0.03

results in Table 1, a 177×177 grid is used for all the cases to perform further simulations. In order to check the steady state energy balance consistency for the numerical results, a numerical parameter (Nu_c/Nu_h) was defined, and the final results are found to validate as $\text{Nu}_c/\text{Nu}_h = 0.999$. The present numerical simulation results are also validated with published results [18]. The validation is given in Table 2.

4 Results and Discussion

Streamlines and isotherms inside the BDPM enclosure for Ra $= 10^5$ are shown in Fig. 2 for several Da$_I$ values. Here, $N^2 = 16$ and $\phi_E = 0.64$, with the corresponding block size D^* evaluated from Eq. (11). The microphase porous blocks are shown as thin continuous-walled squares in these figures. At the monodisperse limit when the control volume forming the microphase porous blocks is solid (Da$_I \rightarrow 0$), the convection flow is restricted to the

Table 2 Comparison of the present results with Ref. [18] for Pr=1, γ=1, and ϕ_E=0.64

Ra	Blocks N^2	Reference [18] Nu	Present results Nu
10^5	9	1.383	1.405
	16	1.233	1.251
	36	1.098	1.113
	64	1.051	1.053
10^6	9	6.164	6.277
	16	4.274	4.385
	36	2.626	2.682
	64	2.223	2.249
10^7	9	16.087	15.931
	16	15.258	15.142
	36	11.798	11.928
	64	8.094	8.096
10^8	9	31.797	30.545
	16	31.180	30.132
	36	30.689	29.60
	64	29.394	28.137
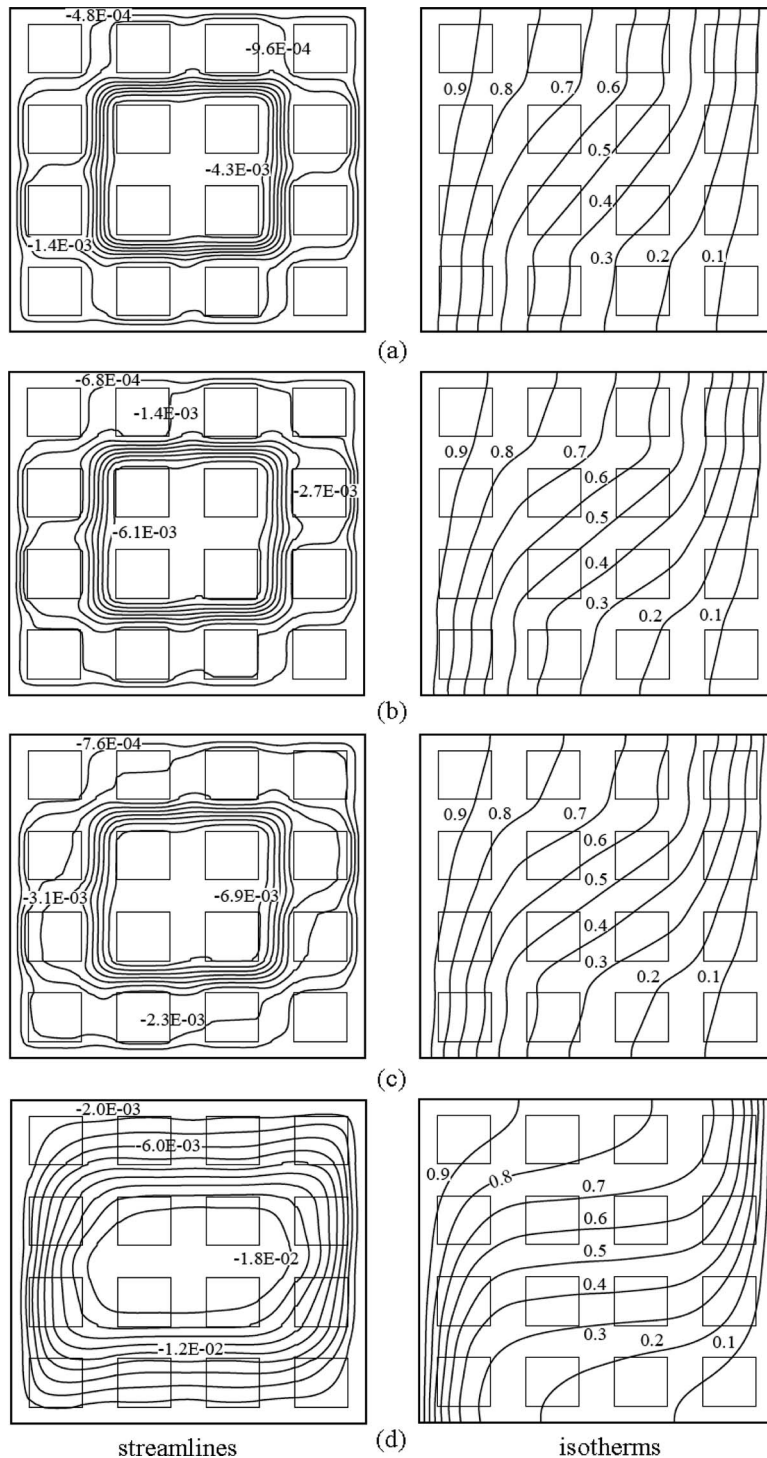
Fig. 2 Streamlines and isotherms for BDPM enclosure with a 4×4 porous block array at Ra=10^5, Da$_E$=2.53×10^{-4}, Pr=1, γ=1, ϕ_E=0.64, and ϕ_I=0.5, for several Da$_I$ values: (a) solid blocks, (b) 10^{-7}, (c) 10^{-5}, and (d) 10^{-3}

macropores, as seen in Fig. 2(a). Since for the BDPM γ=1, the wall-to-wall heat transfer is dominated by the convection flow. However, this highly restricted flow at Da$_I$→0 results in very little convection heat transfer, as shown by the isotherms in Fig. 2(a). As Da$_I$ increases, the resulting bidispersivity allows the flow through the porous blocks, as seen in Figs. 2(b) and 2(c), and eventually results in a clear fluid flow and isotherm pattern in the enclosure displayed in Fig. 2(d).

Figure 3 shows the effect of Da$_I$ on velocity and temperature profiles at the y^*=0.4 section of the enclosure for the 4×4 solid/porous block case with the corresponding parameters shown in Fig. 2. For Ra=10^5, as the bidispersivity effect is increased through the increase in Da$_I$, velocity peaks in Fig. 3(a) near the hot and cold walls increase until they finally resemble the clear fluid enclosure profile. The flow migrates from the core region to
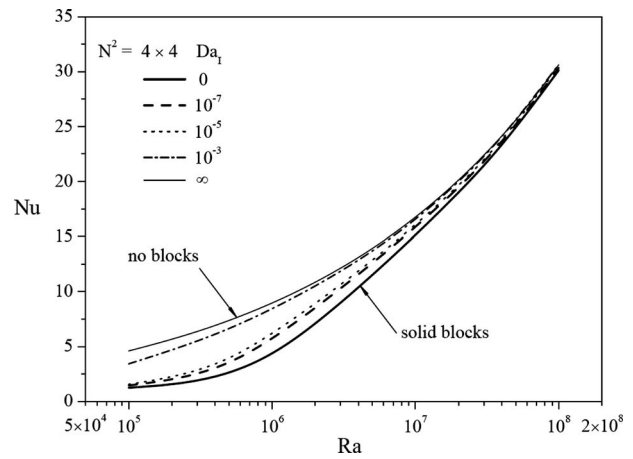
(a)

(b)
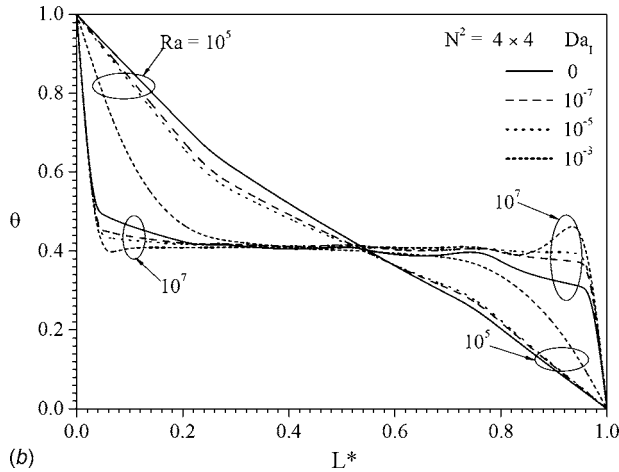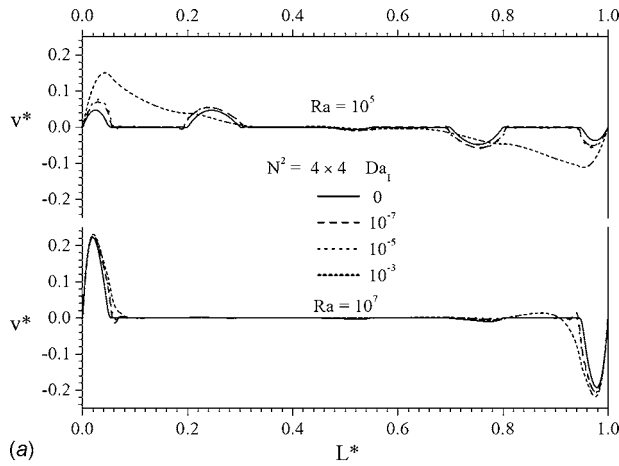
Fig. 3 Effect of internal Darcy number (Da_I) on the local velocity and temperature profiles at $y^*=0.4$ for 4×4 ($Da_E=2.53\times10^{-4}$, Pr=1, $\gamma=1$, $\phi_E=0.64$, and $\phi_I=0.5$)

Fig. 4 Nu variation with Rayleigh number (Ra) for case 4×4 (at $Da_E=2.53\times10^{-4}$, Pr=1, $\gamma=1$, $\phi_E=0.64$, and $\phi_I=0.5$)

walls. At higher Ra=10^7, for almost all Da_I values, the velocity peaks appear near the walls resulting in a wall boundary layer flow with a relatively stationary core region. From Fig. 3(b) it is seen that at Ra=10^5, an increase in the bidispersivity effect through an increase in Da_I causes an increased temperature gradient at the walls due to the increased flow through the micropores in the blocks. This results in enhanced rates of wall heat transfer. For higher Ra values (Ra=10^7), providing a similar bidisperse effect through increased Da_I values does not increase the heat transfer significantly, as much of the flow happens through the wall boundary layer. However, because of stronger convection at Ra=10^7, the heat transfer for all Da_I values is higher than that at Ra=10^5.

The above effect is evident from the Nu versus Ra plot in Fig. 4. It can be observed in Fig. 4 that by increasing the Da_I the effect of bidispersivity on the Nu is stronger at lower Ra values and progressively reduces as Ra increases. The bidispersion effect operates between the two asymptotes of $Da_I\to0$ where the enclosure with the solid blocks becomes a monodisperse porous medium and $Da_I\to\infty$ where convection persists in the enclosure without the porous medium.

The bidispersivity effect can also be brought in by varying the external or macropermeability of the BDPM. The macropermeability Da_E can be modified by either changing the external or macropore volume fraction ϕ_E (by varying the size of the microporous blocks) or by changing N^2, the number of distributed

porous blocks. By changing the macroporosity ϕ_E for fixed Da_I and N^2, the resulting bidisperse effect on the Nu versus Ra is shown in Fig. 5.

For a fixed block quantity, $N^2=16$, lower values of ϕ_E delay the convection until higher Ra is reached. For instance, at the lowest $\phi_E=0.36$, for solid blocks ($Da_I\to0$), Nu$\gg1$ only beyond Ra $\sim10^6$. As the ϕ_E is increased by reducing the size of the microporous blocks, the corresponding increase in the macropore channel width δ causes an increase in the effective permeability Da_E, resulting in stronger convection flow.

It is also observed that for a fixed block quantity, $N^2=16$, similar Nu versus Ra behavior can be obtained for $\phi_E=0.36$ and porous blocks with $Da_I=10^{-4}$ and $\phi_E=0.64$ case with $Da_I\to0$. It can be concluded that a similar bidispersion effect can be created by maintaining an identical enclosure external permeability (Da_E) through suitable combination of variation in ϕ_E and Da_I.

Next, the bidispersion effect is created through variation in the external permeability (Da_E, see Eq. (13)) by changing N^2, the number of porous blocks in the enclosure, while keeping ϕ_E invariant at 0.64 and Da_I at 10^{-4}. The N^2 values used are 9, 36, and 64, with the corresponding reduction in the size (D^*) of the individual blocks, as calculated in Eq. (11). This progressively reduces the external permeability Da_E of the BDPM. The corresponding streamlines and isotherms are shown in Fig. 6 for Ra $=10^7$. Interestingly, since bidispersion allows the flow through the
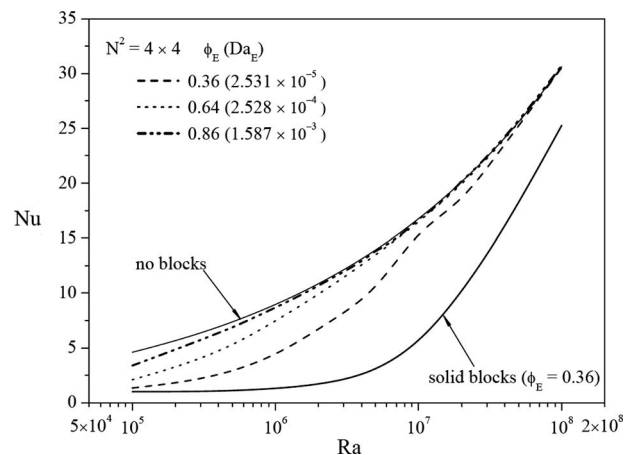
Fig. 5 Effect of external porosity (ϕ_E) on Nu variation with Rayleigh number for case 4×4 (at $Da_I=10^{-4}$, Pr=1, $\gamma=1$, and $\phi_I=0.5$)
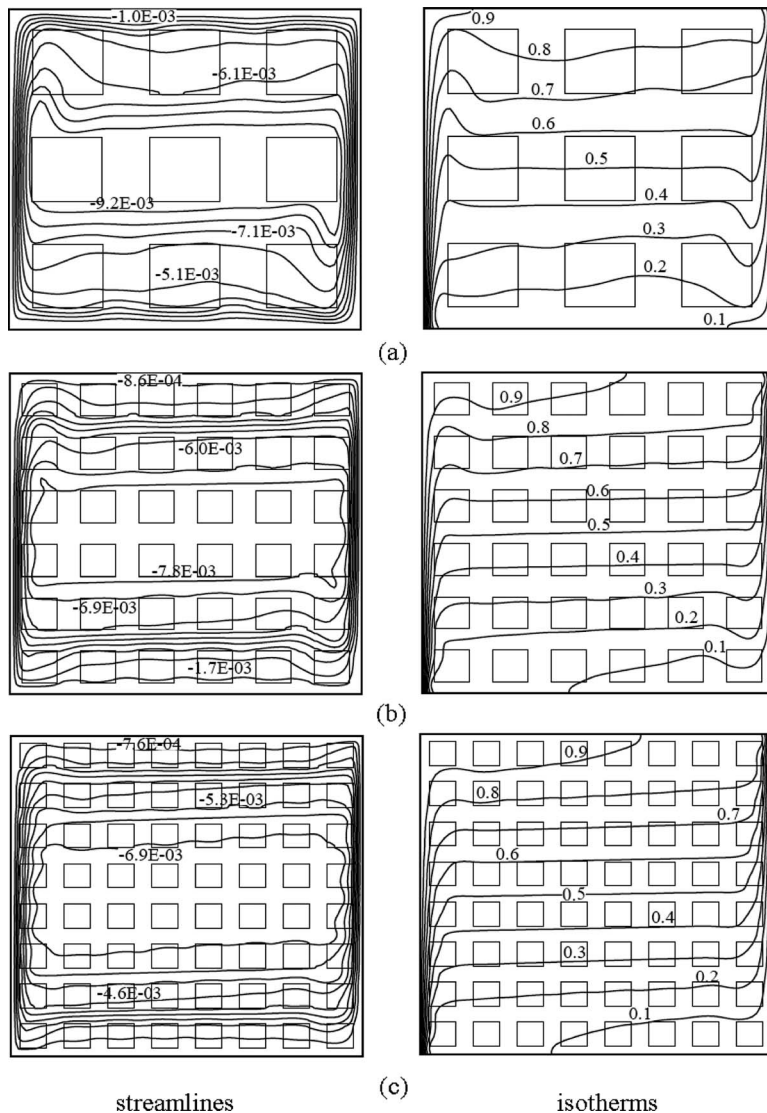
Fig. 6 Streamlines and isotherms for enclosure with different numbers of blocks (at Ra=10⁷, Da$_I$=10⁻⁴, Pr=1, γ=1, ϕ_E=0.64, and ϕ_I=0.5): (a) 3×3, Da$_E$=4.495×10⁻⁴, (b) 6×6, 1.124×10⁻⁴, and (c) 8×8, 6.321×10⁻⁵

porous blocks and also around them through the macropores, the depth of convection (in the horizontal direction along the X-axis) induced by buoyancy near the hot and cold walls remains almost invariant from $N^2=9$ case, where convection happens through the macropores, to $N^2=64$, where convection happens through the micropores in the column of blocks adjacent to the walls.

One can expect similar temperature gradients near the walls for these cases, which indeed is observed in the temperature profiles of Fig. 7(b), shown for two cases, Ra=10⁷ and Ra=10⁵, at the $y^*=0.42$ section of the enclosure. However, the change in flow pattern is particularly pronounced for lower Ra, as seen in the temperature profile for Ra=10⁵ in Fig. 7, where the bidispersivity effect is manifested also due to Da$_I$.

Although the Ra remains fixed for these cases, for a fixed ϕ_E, as the number of porous blocks increases, the modified BDPM Rayleigh number RaDa$_E$ correspondingly decreases. The variation in Nu with RaDa$_E$ for various numbers of blocks and internal Darcy number values is shown in Fig. 8. Convection is usually enhanced with increasing Ra for a given macropore volume fraction and external permeability Da$_E$. However, the effect of bidis-

persion due to N^2 and Da$_I$ as observed to be distinct at higher Ra values is not so in the lower Ra range, where the combined effect of Da$_I$ and Da$_E$ yields nonunique Nu values.

To summarize the bidispersion effects discussed above, an inset of the Nu results for the reduced range of $0 \le$ RaDa$_E \le 5 \times 10^3$ is shown in Fig. 9. In addition, the plot includes the Da$_I$ effect on the Nu for several Da$_E$ numbers. By controlling the extent of bidispersivity through modifications in external (macroscale) and internal (microscale) permeabilities, the desired overall heat transfer can be achieved. For instance, a Nu~20 can be achieved for a fixed Ra for the combinations of $N^2=64$, Da$_I=0$ and $N^2=36$, Da$_I=10^{-7}$. This effect of bidispersivity, however, diminishes for an increase in RaDa$_E$ ($>5 \times 10^3$), as shown in Fig. 8.

When Ra is fixed, a decrease in external permeability Da$_E$ by increasing from $N^2=9$ to $N^2=64$ decreases the flow rate and in turn the heat transfer within the enclosure. This conclusion can be obtained from the results in Fig. 9 itself in the following way. For a constant Ra=10⁷, with $N^2=9$ and Da$_I=0$, one could predict the Nu from the ordinate of Fig. 9, as marked by point A in the figure.
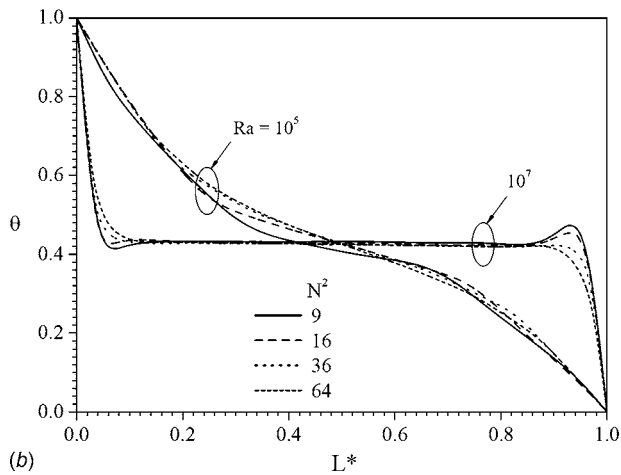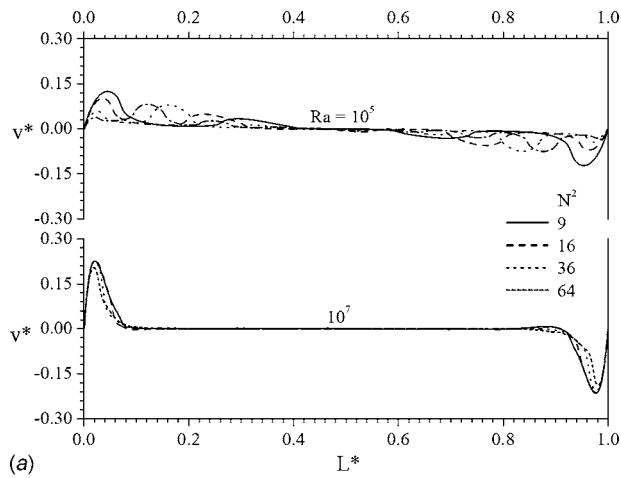
Fig. 7 Effect of number of porous blocks (N^2) on the local velocity and temperature profiles at $y^*=0.42$ (at $Da_I=10^{-4}$, Pr $=1$, $\gamma=1$, $\phi_E=0.64$, and $\phi_I=0.5$)

For this same Ra, in the $N^2=36$ case, the corresponding Nu is smaller, as marked by point B, since the external permeability Da_E is reduced as the macropore gap size is reduced. A similar argument leads to an even lower Nu for the same value of Ra when the number of the blocks increases to $N^2=64$, as marked by point C.
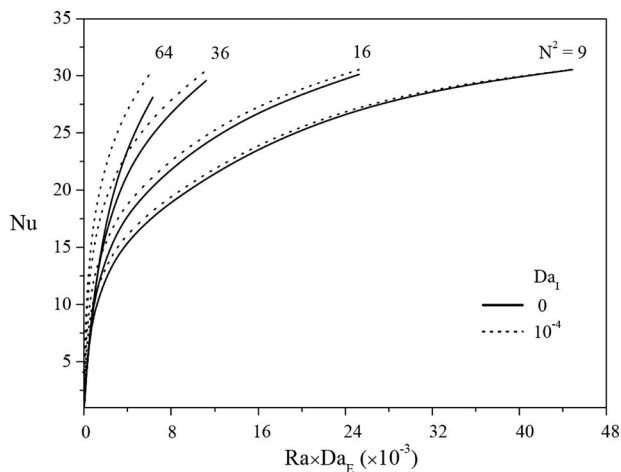
Fig. 8 Nu variation with modified Rayleigh number (Ra×Da$_E$) for all the block cases (at Pr=1, $\gamma=1$, $\phi_E=0.64$, and $\phi_I=0.5$)
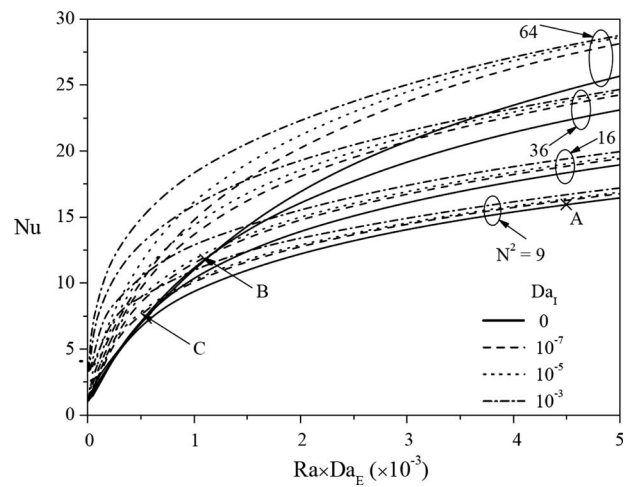
Fig. 9 Nu variation with modified Rayleigh number (Ra×Da$_E$) for all the block cases (at Pr=1, $\gamma=1$, $\phi_E=0.64$, and $\phi_I=0.5$)

Based on the data presented in Figs. 8 and 9, a correlation is proposed to predict the average Nusselt number Nu for the BDPM enclosure as a function of Rayleigh number Ra_ϕ and external Darcy number Da_E, both defined in Eq. (14). The correlation is written as

$$Nu = 0.577(Ra_\phi Da_E)^{0.5}, \quad 10 \leq Ra_\phi Da_E \leq 200$$
$$Nu = 0.37 \ Ra_\phi^{0.25} Da_E^{0.07}, \quad 200 < Ra_\phi Da_E \leq 10^5 \tag{15}$$

where the Da_E is separately modeled as a function of the number of blocks N and the internal Darcy number Da_I and is written as

$$Da_E = \frac{4.1 \times 10^{-3}}{N^2} + 0.007 \ Da_I^{0.32} \tag{16}$$

The correlation in Eq. (15) is valid for fixed macropore volume fraction ($\phi_E=0.64$) and micropore volume fraction ($\phi_I=0.5$) within the parameter range: $3 \leq N \leq 8$ and $0 \leq Da_I \leq 10^{-7}$. It predicts with a correlation coefficient of 0.98 the Nu data set generated by numerical simulations within $\pm 15\%$ and $\pm 9\%$ for $10 \leq Ra_\phi Da_E \leq 200$ and $200 < Ra_\phi Da_E \leq 10^5$, respectively. The parity plot for the data and correlation prediction is shown in Fig. 10.

The Da_E in Eq. (16) is a modified version of Eq. (13), the Carmen–Kozeny relation for the permeability of packed bed of spheres treated as a porous medium. When $Da_I=0$, the Da_E in Eq. (16) reduces to Eq. (13), the correct asymptotic behavior for enclosure with solid square blocks treated as a monodisperse porous medium of packed bed of connected spheres. Appropriately, within the range for $10 \leq Ra_\phi Da_E \leq 200$, the proposed correlation, Eq. (15), asymptotically reduces to the existing correlation for Nu for a monodisperse porous medium, as stated in Eq. (7.38), p. 289, in Ref. [2]. Beyond $Ra_\phi Da_E \geq 200$, there is no reference case for verification.

5 Conclusions

Steady natural convection inside a side-wall heated square enclosure filled with a bidisperse porous medium is investigated using numerical simulations. Uniformly distributed conducting porous blocks were treated as the BDPM. The bidispersion effect is studied by varying the internal Darcy number Da_I of the porous blocks and the external Darcy number of the macropores Da_E.

The bidispersion effect operates between the two asymptotes of $Da_I \rightarrow 0$, where the enclosure with the solid blocks reduces to a monodisperse porous medium, and $Da_I \rightarrow \infty$, where the enclosure is without the porous medium. As Da_I increases, the resulting bidispersivity allows more flow through the micropores. Corre-
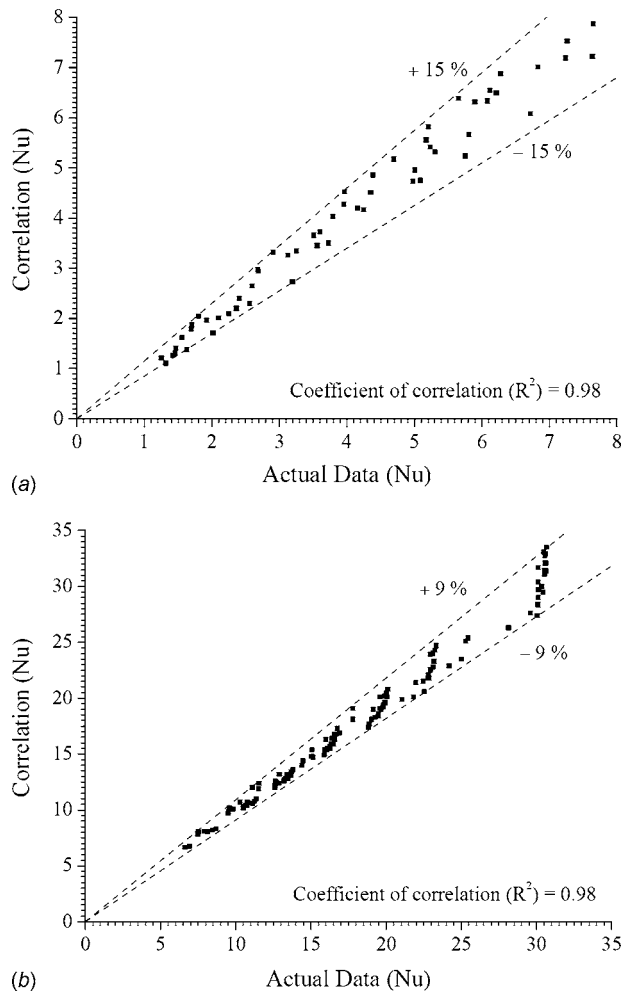
Fig. 10 Parity plot of predicted versus actual values for BDPM Nusselt number (Nu)): (a) $10 \leq \mathrm{Ra}_\phi \mathrm{Da}_E \leq 200$ and (b) $200 < \mathrm{Ra}_\phi \mathrm{Da}_E \leq 10^4$

Nomenclature

$$
\begin{aligned}
c_P &= \text{specific heat at a constant pressure, J kg}^{-1}\text{ K}^{-1} \\
c_F &= \text{Forchheimer coefficient, dimensionless} \\
d &= \text{macropore channel width, m} \\
d^* &= \text{macropore channel width, dimensionless} \\
D &= \text{porous/solid block size, m} \\
D^* &= \text{porous/solid block size, dimensionless} \\
\mathrm{Da} &= \text{Darcy number } (K/L^2), \text{ dimensionless} \\
g &= \text{acceleration due to gravity, m s}^{-2} \\
H &= \text{height of the enclosure, m} \\
H^* &= \text{height of the enclosure, dimensionless} \\
k &= \text{thermal conductivity, W m}^{-1}\text{ K}^{-1} \\
K &= \text{permeability of the porous medium, m}^2 \\
L &= \text{width of the enclosure, m} \\
L^* &= \text{width of the enclosure, dimensionless} \\
N &= \text{number of blocks in the first column of the } N \\
&\quad \times N \text{ block configuration} \\
\mathrm{Nu} &= \text{averaged Nusselt number} \\
&\quad (hL/k_f = -\int_0^1 \partial\theta/\partial x^*|_{x^*=0} dy^*), \text{ dimensionless} \\
p &= \text{pressure, N m}^{-2} \\
p^* &= \text{pressure, dimensionless} \\
\mathrm{Pr} &= \text{Prandtl number, } (\nu/\alpha) \\
\mathrm{Ra} &= \text{Rayleigh number, } (g\beta(T_h - T_c)L^3/(\alpha\nu)_f) \\
T &= \text{temperature, K} \\
u, v &= \text{velocity components along the } x\text{- and } y\text{-axes,} \\
&\quad \text{respectively, m s}^{-1} \\
u^*, v^* &= \text{velocity components along the } x\text{- and } y\text{-axes,} \\
&\quad \text{respectively, dimensionless} \\
x, y &= \text{coordinates, m} \\
x^*, y^* &= \text{coordinates, dimensionless}
\end{aligned}
$$

Greek Symbols

$$
\begin{aligned}
\alpha &= \text{thermal diffusivity, m}^2\text{ s}^{-1} \\
\beta &= \text{coefficient of thermal expansion, K}^{-1} \\
\delta &= \text{macropore channel width, dimensionless} \\
\gamma &= \text{thermal conductivity ratio } (k_s/k_f), \\
&\quad \text{dimensionless} \\
\phi &= \text{porosity, dimensionless} \\
\mu &= \text{dynamic viscosity, kg m}^{-1}\text{ s}^{-1} \\
\nu &= \text{kinematic viscosity, m}^2\text{ s}^{-1} \\
\theta &= \text{temperature, dimensionless} \\
\rho &= \text{density, kg m}^{-3}
\end{aligned}
$$

Subscripts

$$
\begin{aligned}
c &= \text{cold wall} \\
cf &= \text{clear fluid} \\
e &= \text{effective} \\
E &= \text{external} \\
f &= \text{fluid} \\
h &= \text{hot wall} \\
I &= \text{internal} \\
pm &= \text{porous media} \\
s &= \text{solid}
\end{aligned}
$$

spondingly, for all Ra, the Nu increases between $\mathrm{Da}_I \to 0$ and $\mathrm{Da}_I \to \infty$. The bidispersivity effect on Nu is stronger at lower Ra values and progressively reduces as the Ra increases.

The bidispersion effect through modification in Da_E is performed by two methods: by varying the external or macropore volume fraction ϕ_E through change in the size of the microporous blocks and by varying N^2, the number of distributed microporous blocks. For a fixed ϕ_E, the flow rate decreases with an increase in N^2 as the Da_E of the BDPM decreases. The effect is to reduce the Nu.

Using a modified Rayleigh number $\mathrm{Ra}_\phi \mathrm{Da}_E$ that subsumes the effect of Da_I, N^2, and ϕ_E, the effect of bidispersion on the BDPM enclosure average heat transfer Nu is summarized. For $\mathrm{Ra}_\phi \mathrm{Da}_E < 200$, Da_I and ϕ_E have significant effect on the Nusselt number. For $\mathrm{Ra}_\phi \mathrm{Da}_E > 200$, Nu is only marginally affected by these parameters, showing a weak increase with an increase in Ra_ϕ.

A correlation is developed to capture the bidispersion effects on the convection heat transfer Nu of the BDPM enclosure. It incorporates the effects of macro- and micropore convection effects through Da_E, which is a function of internal (micropore) Darcy number (Da_I) and number of blocks (N^2). The correlation predicts Nu results with a correlation coefficient of 0.98 within $\pm 15\%$ and $\pm 9\%$ for $10 \leq \mathrm{Ra}_\phi \mathrm{Da}_E \leq 200$ and $200 < \mathrm{Ra}_\phi \mathrm{Da}_E \leq 10^5$, respectively.

References

[1] Chen, Z. Q., Cheng, P., and Hsu, C. T., 2000, "A Theoretical and Experimental Study on Stagnant Thermal Conductivity of Bi-Dispersed Porous Media," Int. Commun. Heat Mass Transfer, **27**, pp. 601–610.

[2] Nield, D. A., and Bejan, A., 2006, *Convection in Porous Media*, 3rd ed., Springer-Verlag, New York.

[3] Burghardt, A., Rogut, J., and Gotkowska, J., 1988, "Diffusion Coefficients in Bidisperse Porous Structures," Chem. Eng. Sci., **43**, pp. 2463–2476.

[4] Yu, B., and Cheng, P., 2002, "A Fractal Permeability Model for Bi-Dispersed Porous Media," Int. J. Heat Mass Transfer, **45**, pp. 2983–2993.

[5] Chen, Z. Q., Cheng, P., and Zhao, T. S., 2000, "An Experimental Study of Two Phase Flow and Boiling Heat Transfer in Bi-Dispersed Porous Channels," Int. Commun. Heat Mass Transfer, **27**(3), pp. 293–302.

[6] Cao, X. L., Cheng, P., and Zhao, T. S., 2002, "Experimental Study of Evaporative Heat Transfer in Sintered Copper Bidispersed Wick Structures," J. Thermophys. Heat Transfer, **16**(4), pp. 547–552.

[7] Nield, D. A., and Kuznetsov, A. V., 2004, "Forced Convection in a Bi-

Disperse Porous Medium Channel: A Conjugate Problem," Int. J. Heat Mass Transfer, **47**, pp. 5375–5380.

[8] Nield, D. A., and Kuznetsov, A. V., 2005, "Heat Transfer in Bidisperse Porous Media," *Transport Phenomena in Porous Media III*, D. Ingham and I. Pop, eds., Pergamon, Oxford, pp. 34–59.

[9] Nield, D. A., and Kuznetsov, A. V., 2005, "Thermally Developing Forced Convection in a Channel Occupied by a Porous Medium Saturated by a Non-Newtonian Fluid," Int. J. Heat Mass Transfer, **48**, pp. 1214–1218.

[10] Nield, D. A., and Kuznetsov, A. V., 2005, "A Two-Velocity Two-Temperature Model for a Bi-Dispersed Porous Medium: Forced Convection in a Channel," Transp. Porous Media, **59**, pp. 325–339.

[11] Kuznetsov, A. V., and Nield, D. A., 2006, "Thermally Developing Forced Convection in a Bidisperse Porous Medium," J. Porous Media, **9**, pp. 393–402.

[12] Nield, D. A., and Kuznetsov, A. V., 2006, "The Onset of Convection in a Bidisperse Porous Medium," Int. J. Heat Mass Transfer, **49**, pp. 3068–3074.

[13] Nield, D. A., and Kuznetsov, A. V., 2007, "The Effect of Combined Vertical and Horizontal Heterogeneity on the Onset of Convection in a Bidisperse Porous Medium," Int. J. Heat Mass Transfer, **50**, pp. 3329–3339.

[14] Nield, D. A., and Kuznetsov, A. V., 2008, "Natural Convection About a Vertical Plate Embedded in a Bidisperse Porous Medium," Int. J. Heat Mass Transfer, **51**, pp. 1658–1664.

[15] Rees, D. A. S., Nield, D. A., and Kuznetsov, A. V., 2008, "Vertical Free Convective Boundary-Layer Flow in a Bidisperse Porous Medium," ASME J. Heat Transfer, **130**, p. 092601.

[16] Straughan, B., 2009, "On the Nield-Kuznetsov Theory for Convection in Bidisperse Porous Media," Transp. Porous Media, **77**, pp. 159–168.

[17] Merrikh, A. A., and Mohamad, A. A., 2001, "Blockage Effects in Natural Convection in Differentially Heated Enclosures," J. Enhanced Heat Transfer, **8**, pp. 55–72.

[18] Merrikh, A. A., and Lage, J. L., 2005, "Natural Convection in an Enclosure With Disconnected and Conducting Solid Blocks," Int. J. Heat Mass Transfer, **48**, pp. 1361–1372.

[19] Bhave, P., Narasimhan, A., and Rees, D. A. S., 2006, "Natural Convection Heat Transfer Enhancement Using Adiabatic Block: Optimal Block Size and Prandtl Number Effect," Int. J. Heat Mass Transfer, **49**, pp. 3807–3818.

[20] Kozeny, M., 1927, "Uber kapillare Leitung des Wassers im Boden," Sitzungsber. Akad. Wiss. Wien, Math.-Naturwiss. Kl., Abt. 2A, **136**, pp. 271–306.

[21] Braga, E. J., and de Lemos, M. J., 2005, "Heat Transfer in Enclosures Having a Fixed Amount of Solid Material Simulated With Heterogeneous and Homogeneous Models," Int. J. Heat Mass Transfer, **48**, pp. 4748–4765.

[22] Patankar, S., 1980, *Numerical Heat Transfer and Fluid Flow*, Taylor & Francis, London.

Study and Optimization of Horizontal-Base Pin-Fin Heat Sinks in Natural Convection and Radiation

D. Sahray

H. Shmueli

G. Ziskind

R. Letan

Department of Mechanical Engineering,
Heat Transfer Laboratory,
Ben-Gurion University of the Negev,
P.O. Box 653,
Beer-Sheva 84105, Israel

This paper aims at deeper understanding of heat transfer from horizontal-base pin-fin heat sinks with exposed edges in free convection of air. The effects of fin height and fin population density are studied experimentally and numerically. The sinks are made of aluminum, and there is no contact resistance between the base and the fins. All the sinks studied have the same base dimensions and are heated using foil electrical heaters. The fins have a constant square cross section, whereas the fin height and pitch vary. The heat input is set, and temperatures of the base and fins are measured. In the corresponding numerical study, the sinks and their environment are modeled using the FLUENT 6.3 software. The results show that heat-transfer enhancement due to the fins is not monotonic. The differences between sparsely and densely populated sinks are assessed quantitatively and analyzed for various fin heights. Also analyzed is the heat flux distribution at the edges and center of the sink. A relative contribution of outer and inner fin rows in the sink is assessed, together with the effect of fin location in the array on the heat-transfer rate from an individual fin. By decoupling convection from radiation, a dimensional analysis of the results for natural convection is attempted. A correlation presenting the Nusselt number versus the Rayleigh number is suggested, where the "clear" spacing between fins serves as the characteristic length. [DOI: 10.1115/1.3156791]

Keywords: pin fin, natural convection, optimum fin population, correlation

1 Introduction

Due to the low cost and high reliability, fin heat sinks are broadly used for thermal management of various applications. Accordingly, very extensive literature exists on the subject [1,2]. Still, fin sink performance in natural convection and radiation is to be investigated because it depends strongly on the sink orientation and fin configuration [3–7]. Recent literature points to a growing interest in heat sinks with a horizontal base in natural convection [8,9], where fin spacing affects air flow patterns and heat-transfer rates to the surroundings.

The existing literature on fin heat sinks in natural convection concerns mostly plate fins, although pin fins provide better performance, as shown by Sparrow and Vemuri [3]. Their research has established a number of important results for pin-fin heat sinks in natural convection, concerning sink orientation, additivity of natural convection and radiation, and existence of optimum fin population. In particular, they showed that a horizontal-base sink with upward-facing fins outperforms an identical sink with a vertical base and horizontal fins. The work on pin-fin heat sinks was continued by Zografos and Sunderland [10,11] for vertical and inclined bases. The ratio of the fin diameter to the center-to-center spacing was considered, and it was established that the optimum value of this ratio is about 1/3, whereas heat transfer from more densely populated sinks is less effective. Aihara et al. [12] performed a detailed study of vertical-base sinks suggesting a correlation based on the effective array length and lateral fin spacing. Fisher and Torrance [13] considered a system of a pin-fin heat sink and a chimney, and discussed limits of pin-fin cooling in natural convection. Huang et al. [14] studied horizontal-base sinks

with four different fin spacings, from 2 mm to 8 mm, fin cross section of 2×2 mm^2 and the fin heights of 2 mm to 10 mm. They considered also various sink orientations and discussed the corresponding optimum sink "porosities."

Our ongoing extensive investigation focuses on horizontal-base heat sinks with in-line arrays of pin fins of a square cross section [15,16]. Sahray et al. [15] explored experimentally two heat sinks, namely, of $9 \times 9 = 81$ fins and $16 \times 16 = 256$ fins, while the base size was the same, 100×100 mm^2. In addition, a smooth plate of the same size was considered. The numerical simulation indicated that in such systems an optimum exists, beyond which an increasing number of fins inhibits rather than enhances the heat-transfer rate. However, the experimental data were still too few to fully validate the numerical findings. Sahray et al. [16] explored experimentally four heat sinks, namely, of $8 \times 8 = 64$ fins, $9 \times 9 = 81$ fins, $11 \times 11 = 121$ fins, and $16 \times 16 = 256$ fins, with the same fin height of 10 mm. In parallel, nine heat sinks have been simulated in the numerical study, ranging from $6 \times 6 = 36$ fins to $16 \times 16 = 256$ fins. The existence of the optimum fin population was demonstrated for a constant fin height. Also explored was the effect of sink edges on the total heat-transfer rates.

In the present study, the effects of fin height and fin population density on the performance of a horizontal-base pin-fin heat sink with edges exposed to the ambient are studied both experimentally (11 sinks) and numerically (27 sinks). The numerical model, which reconstructs meticulously the physical one, is validated versus the experimental results. Then, the optimum array configurations obtained in the experimental work are confirmed numerically. Detailed analysis is done of the contributions of fin rows and individual fins to the total heat transfer from the sink, as related to the air flow patterns. The contributions of free convection and radiation are decoupled, and the results for free convection are generalized and correlated through a dimensional analysis.
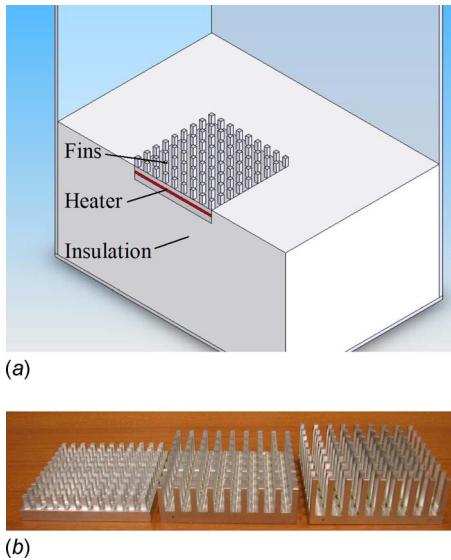
Fig. 1 Physical model of the sink and its surroundings: (*a*) schematic view of the sink and domain and (*b*) examples of the heat sinks

2 Physical and Numerical Models

2.1 Physical Model. The present study is based on the configuration shown in Fig. 1. The experimental model consists of a pin-fin heat sink and insulation enclosed in a relatively large box open from above, Fig. 1(*a*). In the figure, the insulation and outer box are partially removed in order to show the sink structure. The heat sinks, some of which are shown in Fig. 1(*b*), are made of aluminum 6061 blocks by machining, in order to prevent any contact resistance between the base and the fins. The base dimensions are 100×100 mm^2, and its thickness is 10 mm. The fin cross section is 4×4 mm^2 in all cases, whereas the fin height, H, is 10 mm, 20 mm, or 30 mm. From below, an electrical foil heater is attached to the base. The heater is pressed to the base by an additional aluminum plate. The plate dimensions are 100×100 mm^2, and its thickness is 5 mm.

In the experiments, four different sinks were studied for $H = 10$ mm and $H = 20$ mm, while for $H = 30$ mm three sinks were explored. Thus, the total number of experimental cases is eleven, as presented in Table 1.

The insulation is made of expanded polystyrene (EPS) and has the thermal conductivity of $k_{\text{ins}} = 0.034$ W/m K according to the manufacturer's data. The insulation thickness is 100 mm on each side of the sink, and about 135 mm under the sink. The sink is enclosed in the insulation so that the upper surface of the base is

Table 1 Summary of the experimental cases

Fin height H (mm)	Array (fins)	Pitch S (mm)	Pitch to width ratio, S/W
10	$8 \times 8 = 64$	14	3.5
	$9 \times 9 = 81$	12	3.0
	$11 \times 11 = 121$	10	2.5
	$16 \times 16 = 256$	6	1.5
20	$7 \times 7 = 49$	16	4.0
	$8 \times 8 = 64$	14	3.5
	$9 \times 9 = 81$	12	3.0
	$11 \times 11 = 121$	10	2.5
30	$7 \times 7 = 49$	16	4.0
	$8 \times 8 = 64$	14	3.5
	$9 \times 9 = 81$	12	3.0

mounted flush with the upper surface of the insulation, which does not touch the fins, thus allowing flow of air from the edges to the fin array. The outer Perspex box dimensions are about $400 \times 400 \times 400$ mm^3, and the wall thickness is 5 mm, with the thermal conductivity of 0.2 W/m K.

The power inputs explored in the present study varied in the range from 3 W to 16 W. The temperature of the sink, T_w, was monitored during the experiments, using eight T-type thermocouples. Additional thermocouples monitored temperatures in the insulation and ambient air at various locations. All thermocouples were connected to a Fluke Hydra data acquisition unit.

Uncertainties in experimental results were estimated using the method of Kline and McClintock [17]. The primary experimental parameters included the temperatures of the sink, T_w, and the air, T_∞, the voltage applied to the heater, U, and the resulting current, I. Based on the accuracy of the instrumentation used, the uncertainties were estimated as being within $\pm 0.3\,°$C and ± 0.3 W for the temperature difference, $\Delta T = T_w - T_\infty$, and the input power, $q = UI$, respectively.

2.2 Numerical Model. The numerical model follows, in a most complete and detailed manner, the features and dimensions of the physical model of Fig. 1(*a*). This approach has been successfully used by the authors for comparable problems in the past [18,19]. It is characterized by maximum possible similarity between the simulation and experiment. Actually, each and every component of the numerical model represents a careful reconstruction of its physical prototype. Thus, the dimensions of the heat sinks, including individual fins, as well as of the insulation and outer box, are exactly the same as in reality. The material properties used in the simulations are based on aluminum 6061, expanded polystyrene, and Perspex for the sinks, insulation, and outer box, respectively. In particular, the sink is modeled exactly as it was built in reality: it had a heat-generating core ("foil heater"), while its remaining volume, both on the upper ("base" and "fins") and lower ("plate") sides, is represented as a "conducting wall."

While eleven different heat sinks are explored in the experiments and "reproduced" in the simulation, 16 additional sinks are also explored numerically. Thus, the total of 27 heat sinks have been simulated in the numerical study, ranging from $6 \times 6 = 36$ fins to $16 \times 16 = 256$ fins for each of the three fin heights explored. The full geometry is numerically simulated in every case.

In the simulations, the basic conservation equations of continuity, momentum and energy are solved numerically, using the FLUENT 6.3 computational fluid dynamics (CFD) software. The steady-state form of these equations is as follows.

For continuity,

$$\frac{\partial}{\partial x_i}(\rho u_i) = 0 \tag{1}$$

For momentum,

$$\frac{\partial}{\partial x_j}(\rho u_i u_j) = -\frac{\partial p}{\partial x_i} + \frac{\partial \tau_{ij}}{\partial x_j} + \rho g_i \tag{2}$$

For energy,

$$\frac{\partial}{\partial x_i}(\rho u_i h) = \frac{\partial}{\partial x_i}\left(k\frac{\partial T}{\partial x_i}\right) + u_i\frac{\partial p}{\partial x_i} \tag{3}$$

where ρ is the density, u_i is the velocity component in the i-direction, p is the static pressure, x_i is a Cartesian coordinate, τ_{ij} is the stress tensor, g_i is the gravitational acceleration in the i-direction, h is the static enthalpy, k is the thermal conductivity, and T is the temperature. Since the flow is buoyancy-driven, the momentum equation, Eq. (2), was redefined in using the following relation for the vertical x_2-direction: $p' = -\rho_0 g x_2 + p$, where ρ_0 is the reference density taken at ambient temperature and atmospheric pressure. The Boussinesq approximation is not used, and

the density-temperature relation was provided as an input.

It should be noted that the three-dimensional numerical calculations are performed for the system as a whole. This means that the velocity fields, the temperature distributions in the air (convection), the temperature distributions in the heat sink and insulation (conduction), and radiation exchange between various components are modeled simultaneously. Accordingly, the appropriate boundary conditions are used. For the momentum equation (air) no-penetration and no-slip are assumed at all the solid boundaries (exposed sink and insulation surfaces and box inner walls), with the pressure boundary condition $p'=0$ imposed at the upper boundary of the system. Following Dubovsky et al. [18] and Kazansky et al. [19], boundary conditions for the energy equation are based on the experimental parameters: The heat input to the sink is set as in the corresponding experiment, whereas beyond the boundaries of the domain the ambient temperature is assigned. The set of conditions is made complete by assuming that the heat-transfer coefficients from the outer walls and bottom of the Perspex box are 8 W/m^2 K and 5 W/m^2 K, respectively [18]. No additional condition, e.g., at the interfaces between various components of the system, is used.

Surface-to-surface radiation inside the system and from the system to the surroundings is taken into account through a so-called discrete transfer radiation model (DTRM). The net radiation heat flux from the surface is then computed as a sum of the reflected portion of the incident radiation heat flux, $q_r''^{-}$, and the emissive power of the surface

$$q_r''^{+} = (1-\varepsilon_w)q_r''^{-} + \varepsilon_w \sigma T_w^4 \qquad (4)$$

where T_w is the surface temperature in Kelvin, ε_w is the wall emissivity, which should be assigned as a boundary condition, and $\sigma = 5.669 \times 10^{-8}$ W/m^2 K^4 is the Stefan–Boltzmann constant. The radiation heat flux, Eq. (4), is incorporated in the prediction of the wall surface temperature. For example, for the heat sink the boundary condition is the heat flux from below, and the temperature of the upper surface, including fins, is established in the simulations using the result of Eq. (4). Since the sink emissivity could not be measured directly, various emissivities were explored in the simulations. The emissivity of the insulation and Perspex walls is taken as 0.9 [15].

In the numerical solution, pressure-based solver is used. Pressure-velocity coupling is applied. "PRESTO!" discretization is used for the pressure. Second-order upwind discretization is used for the momentum and energy.

The software enables the calculation of the overall rate of change of the internal energy of the air, as well as the calculation of the overall heat input/output at any boundary. Thus, these results served to ensure the overall energy balance of the system.

It is worth noting that some instability could be expected in the system, as is typical for natural convection caused by heating from below. Indeed, a simulation typically achieved the stage at which the average sink temperature would vary within $\pm 0.3\,^\circ$C. This was considered as accurate enough for the purposes of the present study, and the mean value was recorded. In some cases, a time-dependent form of the conservation equations, Eqs. (1)–(3), was also used for the sake of comparison, yielding final mean values practically identical to those obtained from the time-independent computations.

The grid used in the simulations is not uniform. It is important to provide a finer grid near the boundaries, especially at the base and fins. Thus, the grid of variable step is used. The total number of cells depends on fin population density. The grid had been carefully refined, until no further change was detected. For the most densely populated sinks of 256 fins, it was necessary to model the flow in rather narrow passages of 2 mm wide, as shown in Fig. 2. Special attention has been paid to the height of the computational domain, as its horizontal dimensions were defined by the dimensions of the box. This was done following the analysis of similar systems, presented by Jaluria and Torrance [20]. The
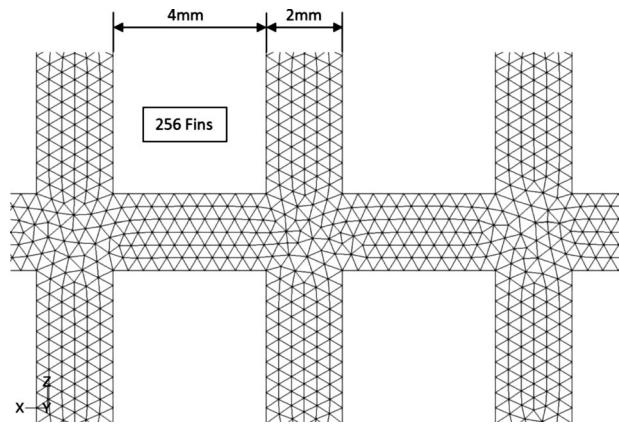

Fig. 2 Example of the grid

domain height was increased over the outer box height, with the "pressure outlet" boundary condition imposed not only on the upper boundary but also on the vertical "extensions" of the box walls. Only minor changes in the sink temperature were observed, as compared with the domain height equal to the box height. For instance, when the domain height was twice the box height, for the heat inputs explored experimentally, the differences in sink temperatures were within $1.0–2.5\,^\circ$C, increasing with the heat input. Thus, this deviation never exceeded 5% of the measured and simulated temperature difference. Moreover, the uncoupled results for natural convection, which were of special interest, were practically identical for different domain heights. For this reason, and taking into account very long computation times, it has been decided to set the upper boundary of the domain at the opening of the box.

As mentioned above, the approach adopted in the present study is based on a numerical model, which (1) reconstructs the physical model in its entirety, (2) assumes simultaneous simulation for various components of the system, and (3) couples convection and radiation. In addition, the finned structure requires a very large overall number of grid elements, reaching 4.5×10^6 for the fins 30 mm high. Therefore, extensive computing resources were required. The authors were allowed access to a specially assembled workstation featuring the Intel(R) Core(TM)2 Quad CPU @ 2.66 GHz processors and 8.00 GB RAM. Still, a typical simulation could take up to 40 h, whereas the main parametric study alone included 135 simulations: 27 sinks at 5 different heat inputs each.

3 Results and Discussion

3.1 Experimental Results. Figure 3 shows summary of the experimental results for all 11 arrays. The temperature difference between the sink and the surroundings, $\Delta T = T_w - T_\infty$, serves as the dependent variable, shown as the function of the fin population, while the fin height and the heat input serve as parameters. In this study, the sink, for which this difference is lower for the same heat input, is considered as the better performing one. One can see that, as expected, the arrays with higher fins perform better at the same number of fins for any given heat input. As for the effect of the fin population density, its effect is obviously not monotonic. Figure 3 shows that for the fin height of $H=10$ mm the sink temperature is always lower at the same heat input when the array consists of 81 fins. Both the less dense array of 64 fins and the more dense arrays of 121, and 256 fins have higher temperatures. Figure 3 also indicates that the sink of 81 fins generally outperforms both the denser and "looser" sinks for the fin height of $H=20$ mm as well, although the differences here are less pronounced. Finally, Fig. 3 shows that at the fin height of $H=30$ mm the sink of 81 fins also performs better than the less dense sinks of 49 and 64 fins. We note here that due to the technical limitations it was not possible
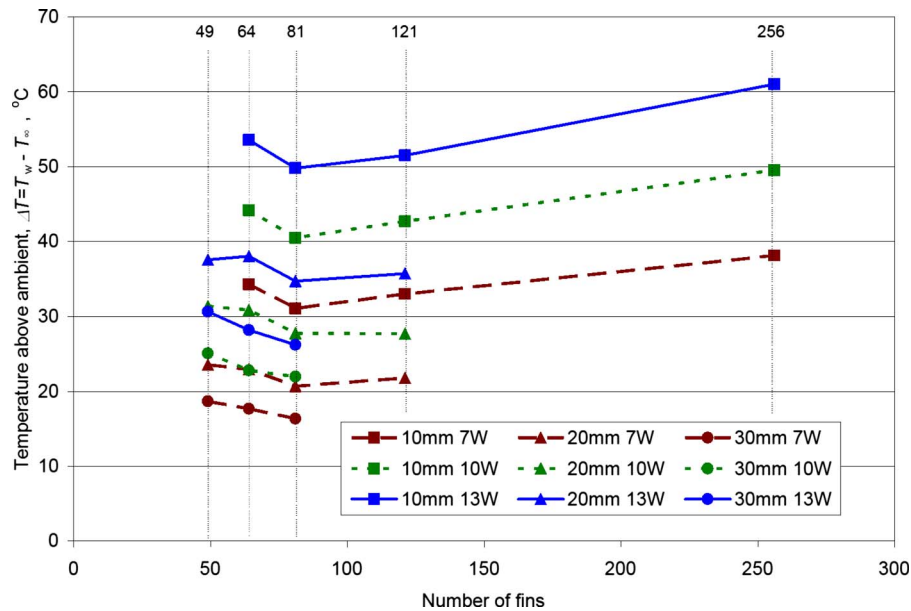
Fig. 3 Summary of the experimental results for the sinks of Table 1 at various heat inputs

to manufacture sinks of 256 fins for the height of 20 mm and of 121/256 fins for the height of 30 mm. However, the trend in sink performance is well pronounced, as will be shown also via numerical modeling below.

3.2 Comparison and Validation of the Numerical Findings. As mentioned above, numerical simulations were first performed for all 11 cases studied experimentally. In those simulations, the heat inputs were taken identical to the nominal experimental ones—the exact values of the latter could be slightly different because of the equipment used. Examples of the comparison between the experimental and numerical results are shown in Fig. 4. One can see from Fig. 4(a) that the agreement is generally rather good at ε=0.45, for the array of 81 fins at all three heights. Specifically, the difference in all cases except one is within 1 °C. Similar results were obtained also for all other arrays, as illustrated in Fig. 4(b), where the comparison is done for various fin populations and heights. Actually, these results had validated the numerical model. On this basis, all other cases are simulated with the same emissivity value of 0.45, which looks quite reasonable considering the machining used in the process of manufacturing. It should be noted that, as shown by Sparrow and Vemuri [3], the effective emissivity of a pin-fin system is higher than the assigned emissivity of its surface because it comprises partially enclosed cavities rather than exposed surfaces.

3.3 Parametric Investigation. Following the validation of the numerical simulations, a full parametric investigation was performed, on nine sinks of 36, 49, 64, 81, 100, 121, 144, 196, and 256 fins, having three different heights of 10 mm, 20 mm, and 30 mm, and heat inputs of 4 W, 7 W, 10 W, 13 W, and 16 W for each sink. Thus, the total number of cases amounted to 135, where in every case the full geometry was simulated. The results are summarized in Figs. 5(a)–5(c) for the fin heights of 10 mm, 20 mm, and 30 mm, respectively.

Similar to the experimental findings, the results of Fig. 5 show that the sink performance depends strongly on the fin height: An increase in the latter leads to a lower sink temperature at the same heat input. It is also clear that the effect of the fin population density on the performance is not monotonic: the latter is first improved with the population density, and then degrades, defining an optimal array(s).

To demonstrate the thermal effectiveness of the fins with re-

spect to a base without fins, a horizontal flat plate was simulated for the same heat inputs and surface emissivity. The size of the plate was equal to the size of the sink base. The results, also presented in Fig. 5, show that all the sinks considered herein perform better than the plate: the temperature of the flat plate is always much higher than the temperatures of the heat sinks, for the same heat input. Among them, the loosest sink of 36 fins and the densest one of 256 fins yield the closest results to those for the plate. The result for the loosest sink seems obvious, as the contribution of fins diminishes in comparison with the contribution of the base. On the other hand, the denser the sink, the narrower the passages between the fins; thus, the heat is removed by the air mostly from the fin tips. In the densest limit, the fins are so close together that they almost form on their upper surface the base, namely, a flat plate. Obviously, additional heat is removed from the vertical surfaces at the outside perimeter. We note also that the results for a flat horizontal plate served for an additional validation of the numerical method [15].

3.4 Optimal Configuration. The numerical results of Fig. 5 indicate that, for all three heights, an array of 9×9=81 fins yields the lowest temperature of the sink for the base and fin dimensions explored in the present study. However, the format of Fig. 5 makes it somewhat difficult to assess these results clearly. Therefore, the results of Fig. 5 are presented in a normalized form in Fig. 6, where the fin pitch, S, normalized with the fin width, W, serves as the independent variable. The dependent variable is the normalized temperature, defined as the temperature above the ambient for the heat sink, ΔT_{sink}, divided by the temperature above ambient for the flat plate, ΔT_{plate}, at the same heat input, as parameters serve the heat input and the fin height.

One can see from Fig. 6 that the results for different heat inputs practically coincide at the same fin height when the normalized representation is used. The lowest sink temperature, corresponding to the optimal performance, is obtained at $S/W=3$, which for $W=4$ mm corresponds to the pitch, S, of 12 mm, i.e., to the heat sink with 9×9=81 fins. This result is in a complete agreement with the experimental findings. The results of Figs. 5 and 6 are also consistent with the findings of Sparrow and Vemuri [3] who show that (1) for a horizontal-base pin-fin heat sink, there exists an optimum fin population, which yields a maximum of the combined-mode heat-transfer rate for a given base area at a given
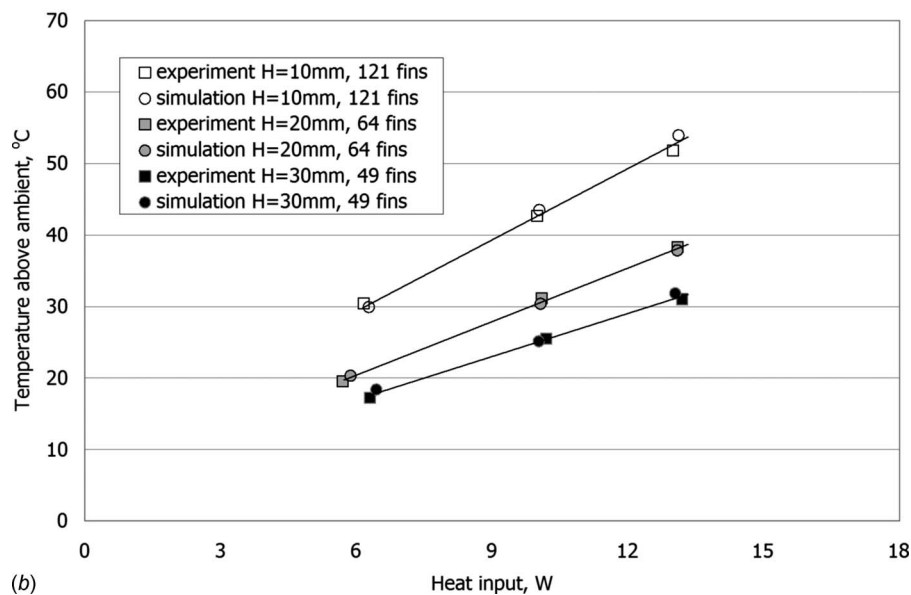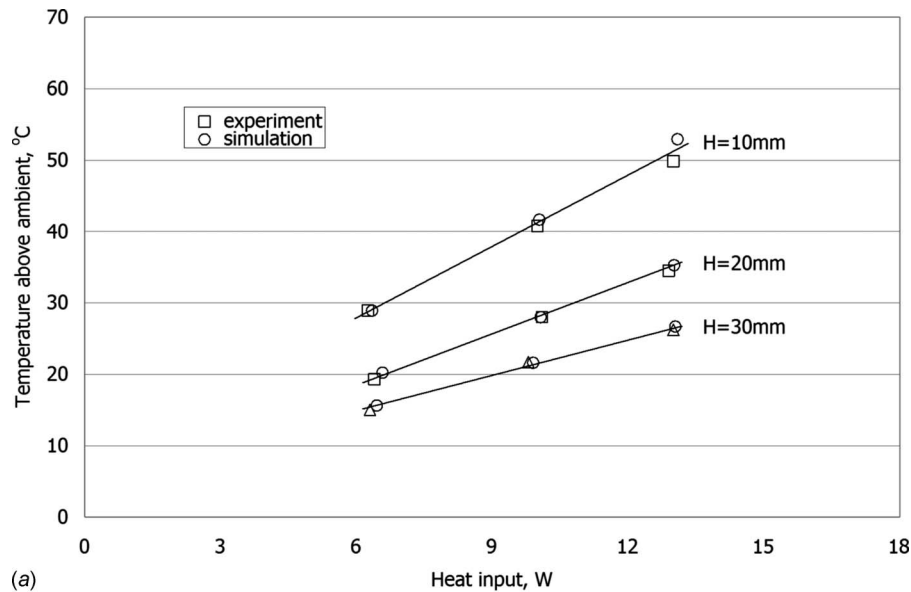
Fig. 4 Validation via comparison of experimental and numerical results: (a) for the array of 81 fins and various fin heights and (b) for a variety of population-height combinations

temperature difference, and (2) for a sink with a given base and fin dimensions, the optimal fin population is practically independent of the temperature difference with the surroundings.

3.5 Local Heat Flux Distribution. Due to the high thermal conductivity of the sink material and relatively high thermal resistance in natural convection and radiation to the surroundings, the temperature of the sink base is essentially uniform, and the fin efficiency approaches unity. However, the local heat flux from the base and the fins is highly nonuniform, varying from the periphery to the center and from one fin to another. This result is demonstrated in Figs. 7–9.

Figure 7 presents examples of the local heat flux distribution on the base. In all cases, the total heat input is 13 W. Each column includes sinks of the same height. In each row the arrays are the same, whereas the height varies. It appears that the resulting distribution is symmetric in all cases, apparently reflecting the symmetry that exists in the flow field. One can see that when the fin population is loose, the heat flux is rather high at the sink edges and reduces gradually toward the center. For the denser popula-

tions, the peripheral regions become narrower, and the major part of the base issues a rather uniform but low heat flux. When the population is very dense, the only region where the local heat flux is significant is the narrow strip outside the fin array. The effect of fin height is such that for the higher fins the local heat flux from the base is lower, but its variation from the periphery to the center remains gradual, except for the very dense sinks, where the contribution of the base is already insignificant even for the smallest fin height of $H=10$ mm.

Considering the decrease in the local heat flux from the upper surface of the base for higher fins, one should bear in mind that in the latter case the total heat-transfer rate obviously increases due to the increased heat-transfer surface of the almost isothermal fins. This result has been already illustrated in Figs. 5 and 6. Thus, it is worth noting that the heat flux distribution on the upper surface of the base does not represent the heat transfer from the sink, since the heat loss takes place mostly from the fins. However, the higher local heat flux from the inner regions of the base surface indicates
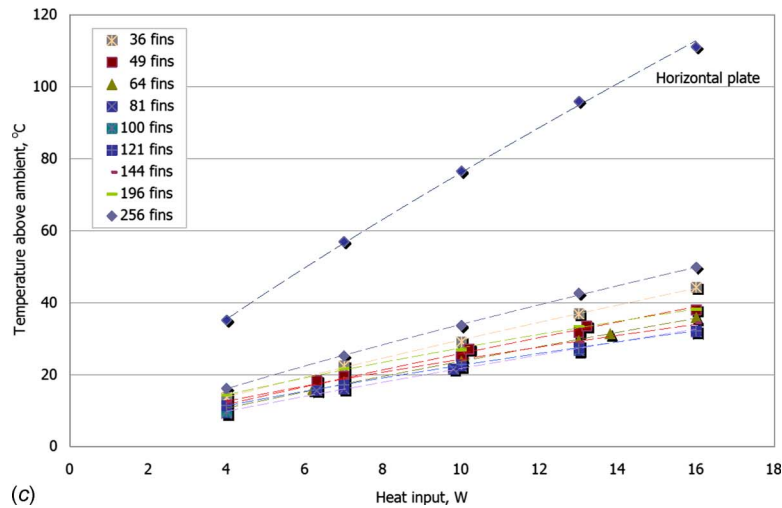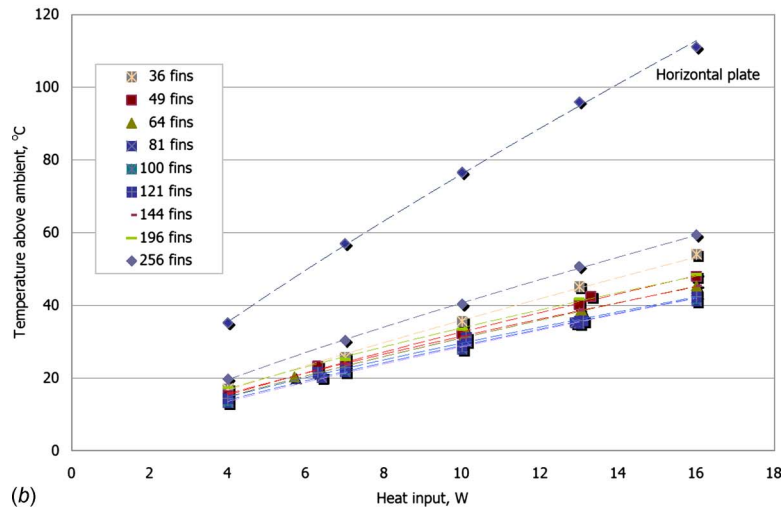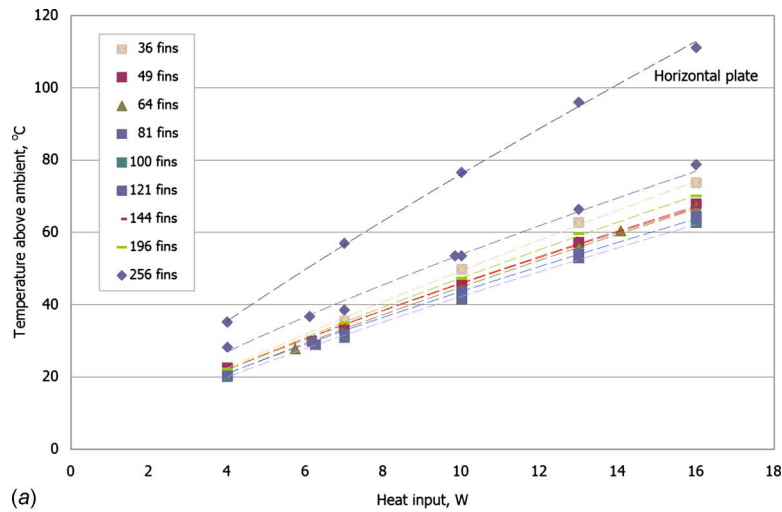
Fig. 5 Complete numerical results for various fin heights: (a) H=10 mm, (b) H=20 mm, and (c) H=30 mm

that the air flow at those locations is relatively strong and also affects the fins located there, as illustrated in Figs. 8 and 9.

3.6 Effect of Fin Location. Figure 8 provides an insight into the heat transfer-distribution between different fins in the sink. The figure shows the relative contributions of various fins to the total convection-radiation heat loss from the sink. In Fig. 8(a), examples of the results are presented for the arrays of $8 \times 8 = 64$ fins and $11 \times 11 = 121$ fins of $H=10$ mm, i.e., the same ones as shown in the left column of Fig. 7. It is essential to note that the "rows" are defined in the following manner: the "first row" de-
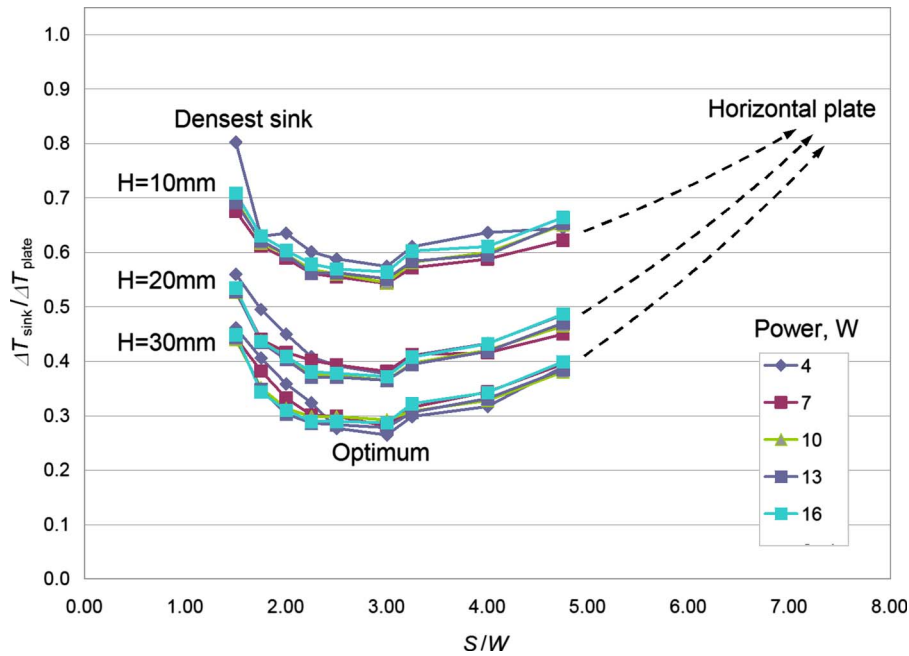
Fig. 6 Normalized numerical results for different fin arrays

notes all the fins located at the outside perimeter of the sink, the "second row" means the next row inside, and so on. For instance, for the presented sink of $11 \times 11 = 121$ fins, this means that the rows from first to fifth count 40, 32, 24, 16 and 8 fins, respectively.

One can see from Fig. 8(a) that the base contribution decreases when fin population increases. The figure shows that the contribution of the first row is always dominant, about half of the total heat-transfer rate in this case, while the inner rows' contributions are almost negligible, e.g., only 4% and 2% of the total for the fourth and fifth rows of $11 \times 11 = 121$ fins, and 4% of the total for the fourth row of $8 \times 8 = 64$ fins, respectively. However, as the number of fins in a row decreases from outside to inside, it is worth it to check the heat-transfer rate per an individual fin in the row. This is done in Fig. 8(b), where the heat transfer per fin is shown for the same arrays of 121 fins and 64 fins of $H = 10$ mm. The results are presented in a normalized form: The heat-transfer rate per fin in a given row is divided by the heat-transfer rate per an averaged fin.

The results of Fig. 8 show that in horizontal-base pin-fin heat sinks, the outer rows, which are exposed to free flow of ambient air, contribute the major part to heat losses. From a practical point of view, this result suggests that such heat sink could perform without inner fins at all. Indeed, the results of Fig. 9 prove the validity of this assumption. In the figure, the performance of the heat sink of $11 \times 11 = 121$ fins from Figs. 7 and 8 is compared with the performance of a similar sink from which the fourth and fifth rows have been removed, reducing the number of fins to 96. Figure 9(a) shows that in both cases, the external fins contribute a major share of the total heat transfer to the surroundings, whereas the internal fins are redundant, and even the third row contributes only 8% of the total heat transfer, Fig. 8(a). The typical flow patterns for both cases are shown in Fig. 9(b), for the plane located 4.5 mm off the plane of symmetry of the sink. This is done in order to present the flow in the passages between the in-line fins shown at the background. As illustrated in Fig. 9(b), the cool air flows into the sink, both with and without the internal fins, mostly from the sides, and the flow patterns in both cases are similar and resemble, in general, an "inverse" stagnation flow from the sides toward and up the vertical axis. One can see from Fig. 9(c) that the resulting overall performance of the two sinks is essentially

the same: their temperatures for the same heat inputs are practically identical. The simulation indicates that for this example, where the fin height is 10 mm and the heat input is 10 W, the air enters the sink at about 10 cm/s, but its velocity is reduced by an order of magnitude at the sink center. This, together with the fact that the air temperature increases as it flows across the sink, makes the internal fins highly inefficient in those configurations in which the outside perimeter of the fins is exposed to the ambient.

4 Dimensional Analysis of Natural Convection

4.1 Uncoupling of Natural Convection. The experimental and numerical results presented above indicate that while the contribution of radiation to the heat transfer from the sink is significant, it probably does not affect the trends related to sink optimization. Following Sparrow and Vemuri [3], we can note that the sinks explored in the present study are practically isothermal, and radiation is directed mostly from the outer contour of the sink to the surroundings that absorb it almost completely. For these reasons, it becomes both possible and worth it to explore the natural convection contribution separately.

Figure 10 shows the heat-transfer rate by free convection only, for all the cases presented in Fig. 5. Since, as discussed above, the heat sink is practically isothermal under the conditions of the present study, it has been decided to use the temperature difference as the abscissa and the natural convection heat flux as the ordinate. The results for each case have been calculated from the simulated total heat-transfer rate, q, equal to the heat generation rate, by subtracting from it the heat-transfer rate by radiation and also the heat losses through the insulation.

For any given sink, the insulation losses' share decreased with an increase in the heat input or in the fin height. This share typically varied with the fin population, being smaller for the better performing sink. Specifically, the insulation losses comprised 10–20%, 10–25%, and 20–30% of the total heat input, for the sinks with the fin height of 30 mm, 20 mm, and 10 mm, respectively.

For the emissivity of 0.45, the relative radiation contribution amounted to 15–40% of the total heat transfer to the surroundings, depending on the heat input and sink configuration. For the same sink, this share is higher for a lower heat input. For the same fin population, the radiation share is typically smaller for the higher
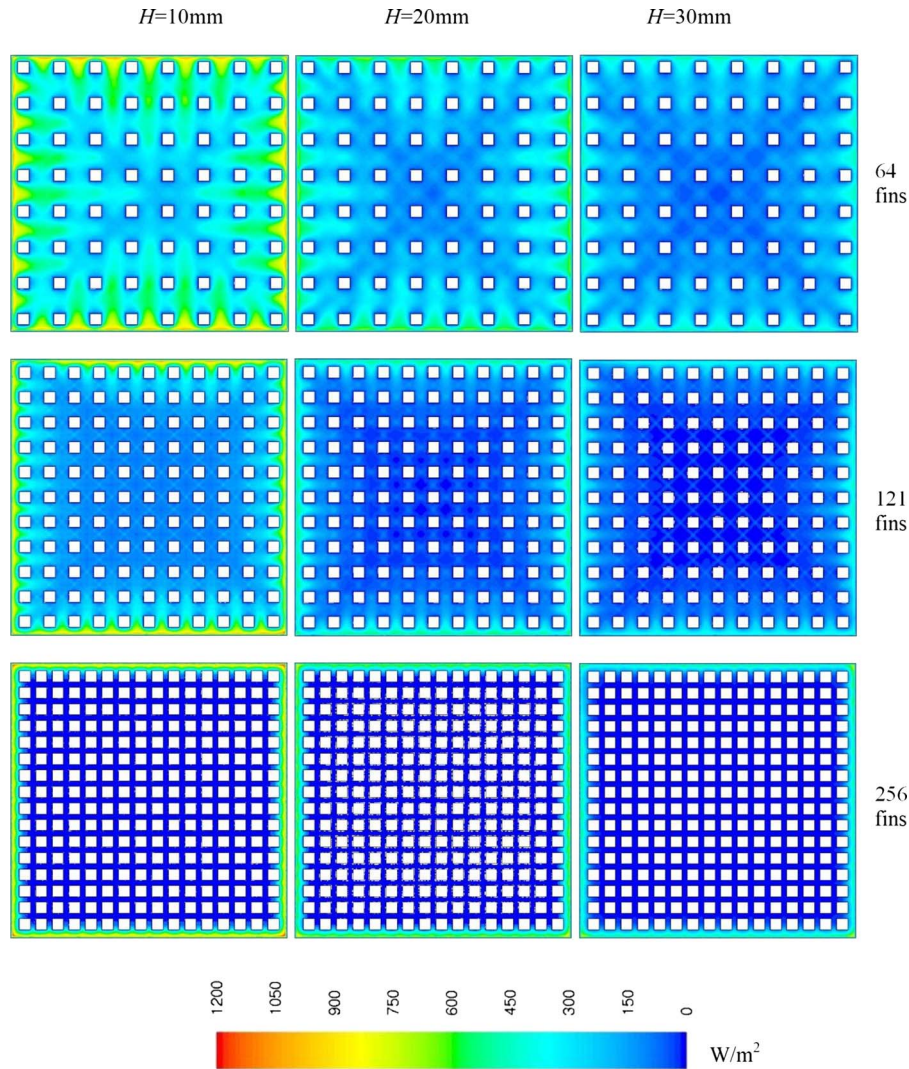
Fig. 7 Heat flux distribution for different fin heights and populations at 13 W heat input

fins. For a given-fin-height sink, the relative contribution of radiation is usually higher for both loose and dense sinks than it is for the intermediate sinks. The latter result could be explained by the fact that in a loose sink the surfaces have higher exposure to the surroundings, while in a dense sink the interfin spacings behave like cavities, and the effective emissivity is much higher than the nominal one [3].

In order to illustrate the uncoupled contributions of free convection and radiation, predicted in Ref. [3], the horizontal flat plate case has been simulated not only with $\varepsilon = 0.45$, but also with an additional emissivity of 0.2. Although the total heat-transfer rate was expectedly different in the two cases, Fig. 10 shows that the losses by natural convection follow exactly the same law, indicating that radiation does not interfere with free convection in this case. Additional data on this subject were presented in Ref. [16]. One can see also that the heat-transfer rate in all cases, including the plate and the sinks, expresses the dependence on the temperature difference, which is characteristic to natural convection: It increases nonlinearly due to the dependence of the heat-transfer coefficient on the temperature difference.

The results of Fig. 10 show that the free convection contribution to the total heat-transfer rate, for the sinks explored in the experimental study, follows the same trends as those discovered earlier for the total heat-transfer rate itself. One can see that the

optimum of free convection remains with the 81 fin sink, like in the measured and simulated combined results discussed above. We note that due to the form of representation, the upper curve in each of the three figures stands for the higher heat sink performance, while the lower curve corresponds to the flat plate. All other cases fall between the latter curve and the one for the optimal sink.

4.2 Dimensional Analysis. It is possible to represent the results for natural convection in a dimensionless form, defining the Nusselt and Rayleigh numbers based on the clear spacing between the fins, $\delta = S - W$

$$\mathrm{Nu}_\delta = \frac{h_c \delta}{k} \tag{5}$$

$$\mathrm{Ra}_\delta = \frac{g \beta \Delta T \delta^3}{\nu^2} \mathrm{Pr} \tag{6}$$

where h_c is the mean convective heat-transfer coefficient, calculated as the mean heat flux by convection only, divided by the temperature difference between the sink and the ambient, ΔT; k is the thermal conductivity of air, β is the volumetric expansion coefficient, ν is the kinematic viscosity, and Pr is the Prandtl num-
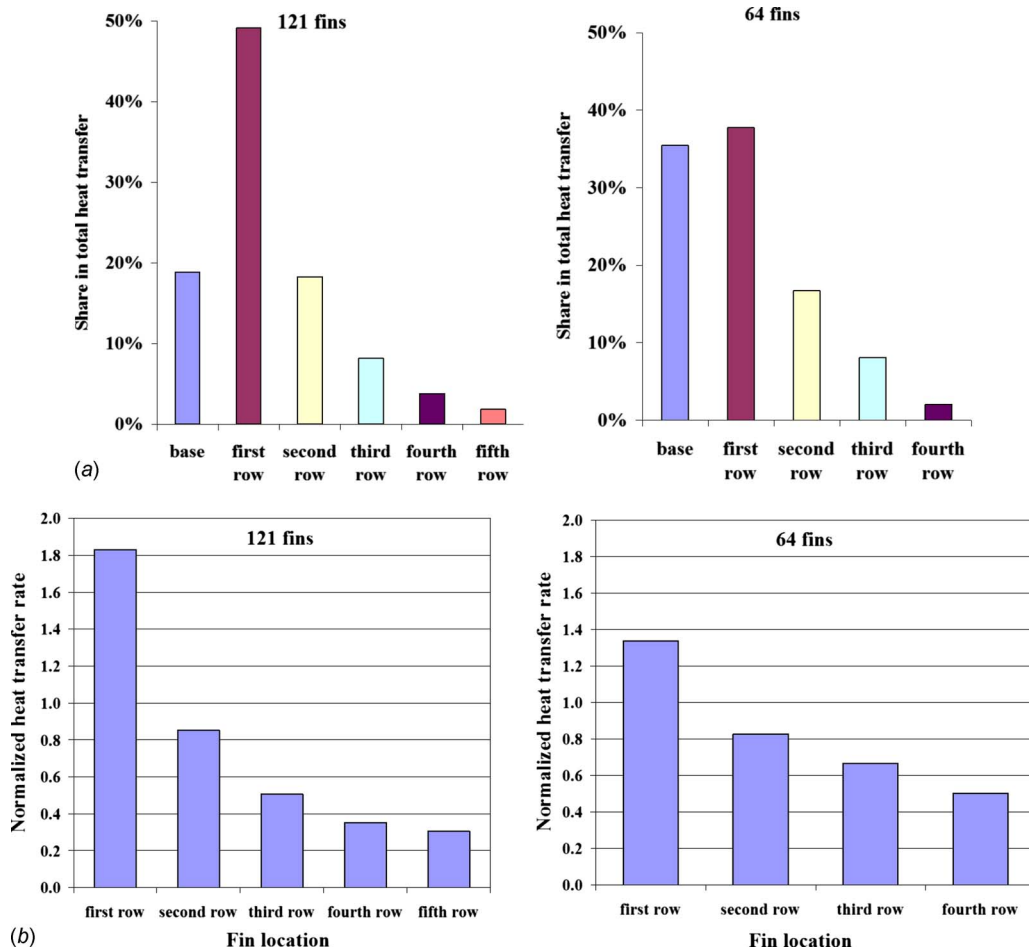
Fig. 8 Contribution of different rows and individual fins to the total heat output at 16W input (first row=all fins located at the outside perimeter of the sink): (a) different rows and (b) individual fins

ber. We note that the heat flux is calculated using the total exposed area of the sink, namely, the sum of the base and fin-side areas.

Figure 11(a) shows separately the results for the three different heights in a dimensionless form. One can see that for each height the results can be approximated by curves that follow the same relation

$$\text{Nu}_\delta = C \ \text{Ra}_\delta^{1/2} \left\{ 1 - \exp\left[-\frac{7000}{\text{Ra}_\delta} \right] \right\}^{1/3} \qquad (7)$$

where the constant C was determined using a statistical analysis. The best fit for the cases with $H=10$, 20, and 30 mm yielded the following values of C: 0.04523, 0.05661, and 0.06271, with R^2 of 0.99142, 0.99443, and 0.99036, respectively. We note here that the form of the suggested correlation, Eq. (7), had been inspired by the results for natural convection between two parallel vertical plates, initiated by Elenbaas [21] and recently discussed by Bar-Cohen et al. [22].

The remarkable similarity of the curves for different heights indicates that it is possible to obtain a general correlation that encompasses all the cases studied herein. For this purpose, the ratio of the fin width to its height, W/H, is used as an additional dimensionless parameter, leading to a "modified" Nusselt number, $\text{Nu}_\delta(W/H)^{1/3}$, plotted in Fig. 11(b). One can see that the results for different fin heights now converge, and can be approximated by the following correlation:

$$\text{Nu}_\delta = \frac{1}{30}\left(\frac{H}{W}\right)^{1/3} \text{Ra}_\delta^{1/2}\left\{ 1 - \exp\left[-\frac{7000}{Ra_\delta} \right] \right\}^{1/3} \qquad (8)$$

This correlation is valid for the horizontal-base heat sinks with rectangular pin fins when the fin efficiency is close to unity, and $\text{Ra}_\delta < 14,000$. While it is obtained for a base of 100×100 mm^2, and for a single fin width of 4 mm, the correlation indicates the general role of fin height and fin population density in sink performance when the outside perimeter of the fins is exposed to ambient. We note that the correlation does not apply to the extreme cases, which converge to a horizontal plate without fins.

An important issue that has been left beyond the scope of the present investigation is the effect of the base size on the sink performance. It is obvious that a larger or smaller sink will perform in a similar manner only if the flow field remains similar, i.e., air enters from the sink edges, moves toward its center, and then flows up. However, as the base size increases, the flow field may change drastically, featuring, for instance, air inflow from above at the inner parts of the sink. As a result, the sink thermal performance would differ from that reported in the present study. This problem, which is also related to a broader question of sink scale-up, will be addressed in a future study.

5 Closure

Heat transfer by free convection and radiation from horizontal-base pin-fin heat sinks, exposed to ambient at their perimeters, has
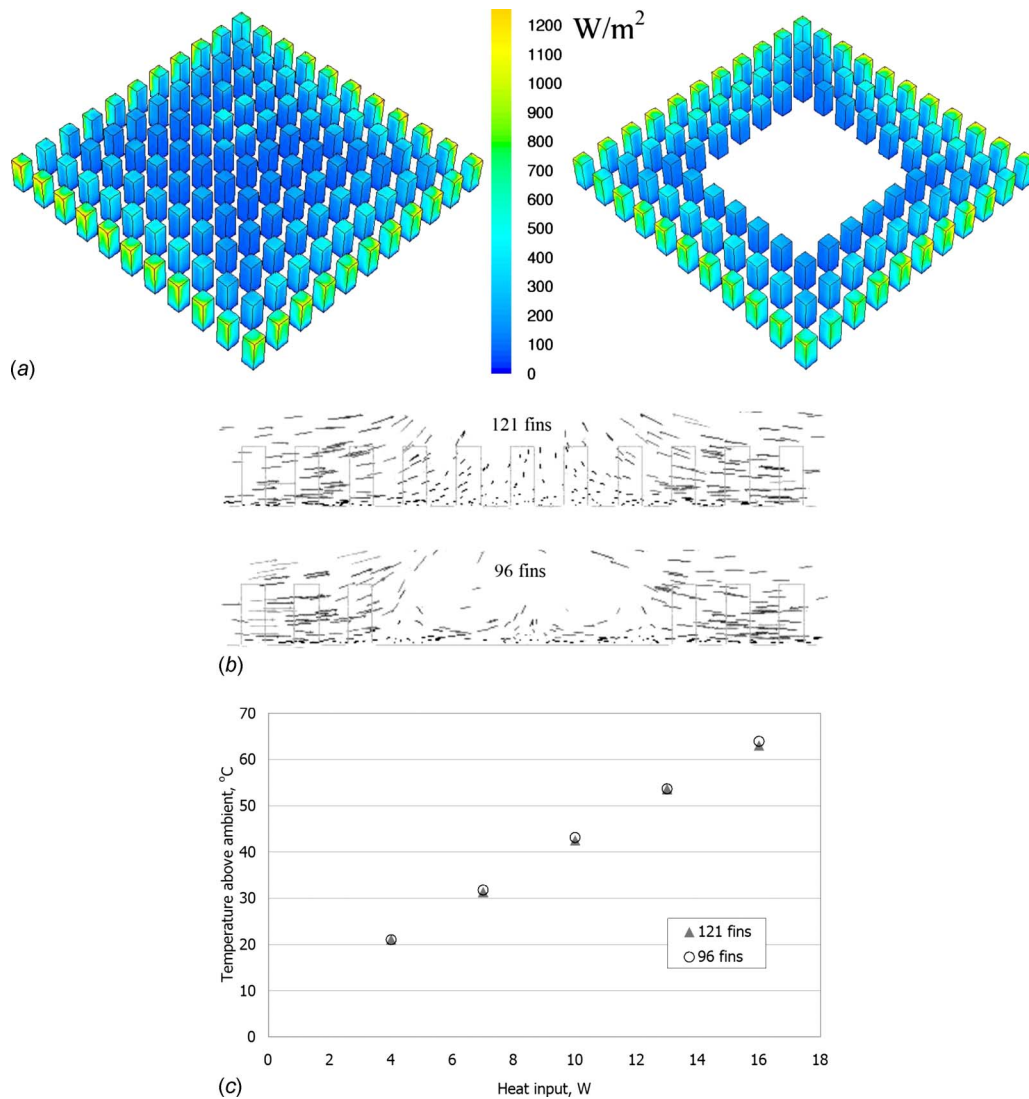
Fig. 9 Results for sinks with (121) and without (96) internal fins: (a) typical heat flux distribution for the fins at 10 W heat input, (b) typical flow field across the sink, and (c) overall comparison

been studied experimentally and numerically. The effects of fin height and fin population density on the performance of the sinks have been investigated at various heat inputs.

It has been found that the heat-transfer enhancement by the fins increases up to a certain fin population density, and then decreases, demonstrating an optimum array at various fin heights. The results also show that in horizontal-base pin-fin heat sinks the outer rows, which are exposed to free flow of ambient air, contribute the major part of the total heat transfer to the surroundings. Moreover, an individual outer-row fin contributes much more than an inner fin.

The free convection contribution to the combined heat transfer has been decoupled from that of radiation, and generalization of the results has been achieved for all cases explored in the work. This generalization is based on the Rayleigh and Nusselt numbers, defined for the "clear" spacing between the fins as the characteristic length. The fin width-to-height ratio serves as an additional dimensionless parameter.

The results of the present study may contribute to the optimal design of pin-fin heat sinks in natural convection and radiation. They also serve as a basis for a broader study, in which the effects of base dimensions are being explored in the context of sink scale-up.

Nomenclature

g = gravitational acceleration (m/s^2)
h = specific enthalpy (J/kg)
h_c = mean convective heat-transfer coefficient (W/m^2 K)
H = fin height (m)
I = electric current (A)
k = thermal conductivity (W/m K)
Nu = Nusselt number
p = static pressure (Pa)
Pr = Prandtl number
q = power, heat-transfer rate (W)
Ra = Rayleigh number
S = pitch (m)
T = temperature (K or °C)
u = velocity (m/s)
U = voltage (V)
W = fin width (m)
x = Cartesian coordinate (m)

Greek Letters

β = volumetric expansion coefficient (1/K)
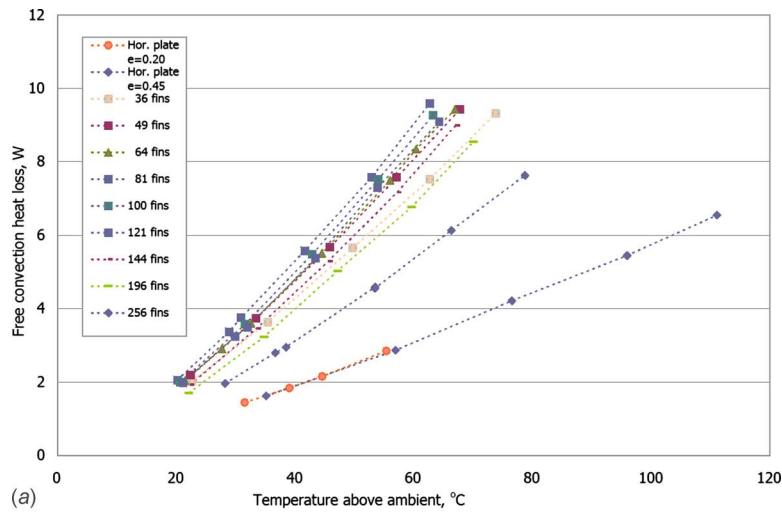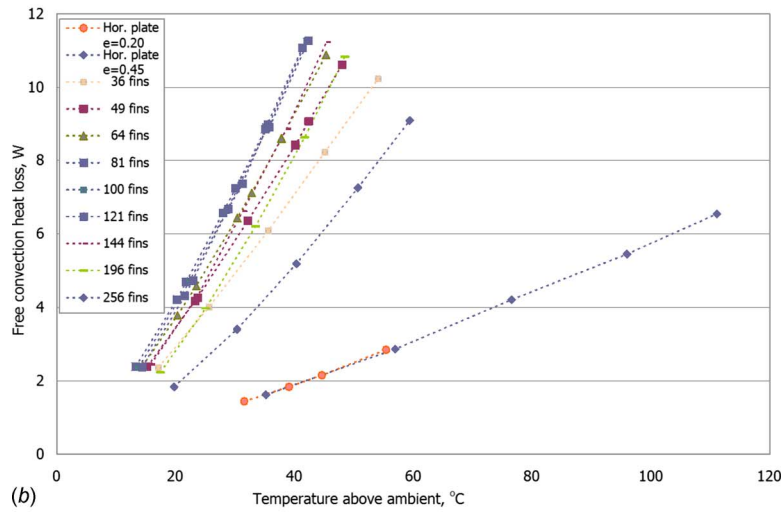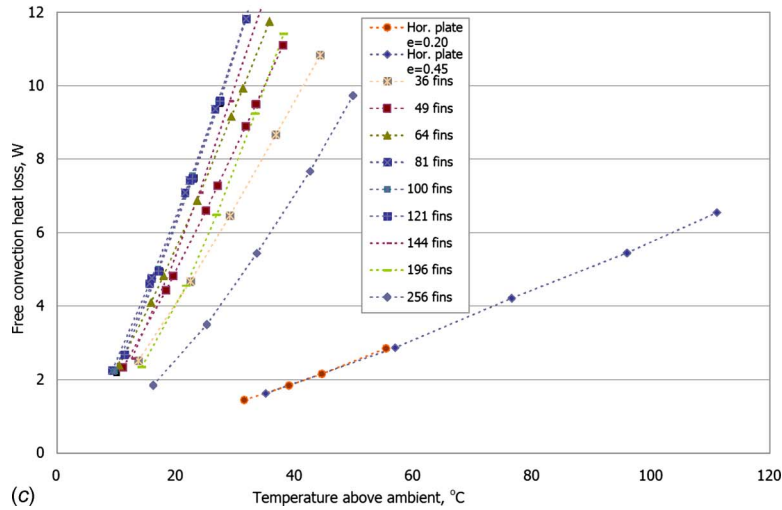
Fig. 10 Simulated heat loss by natural convection only: (*a*) *H*=10 mm, (*b*) *H*=20 mm, and (*c*) *H*=30 mm

δ = "clear" spacing between fins (m)
Δ = difference
ε = emissivity
ν = kinematic viscosity (m^2/s)
ρ = density (kg/m^3)

σ = the Stefan–Boltzmann constant (W/m^2 K^4)
τ = stress tensor (N/m^2)

Subscripts
conv = convective

Fig. 11 Generalized results (a) sinks with various fin heights and (b) overall correlation
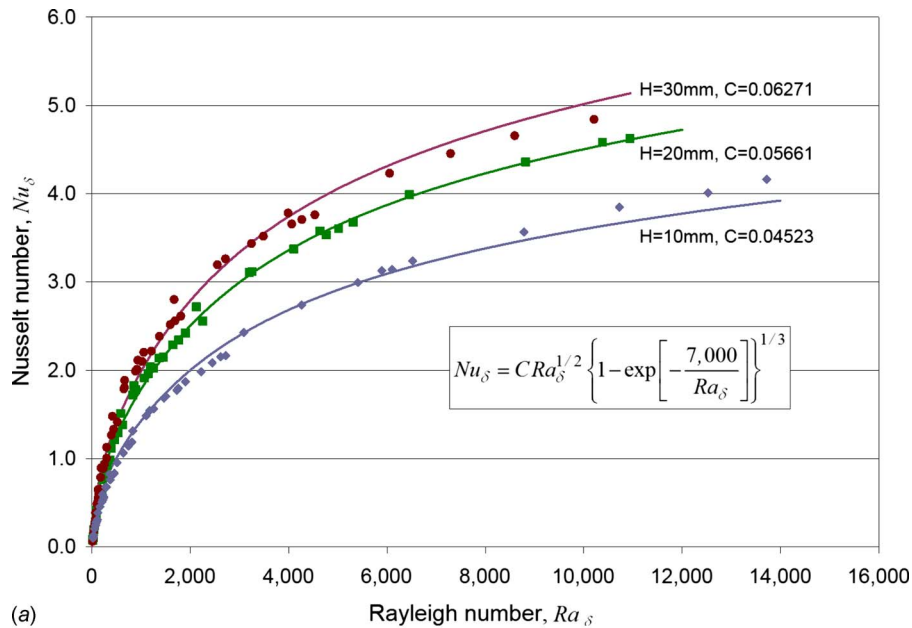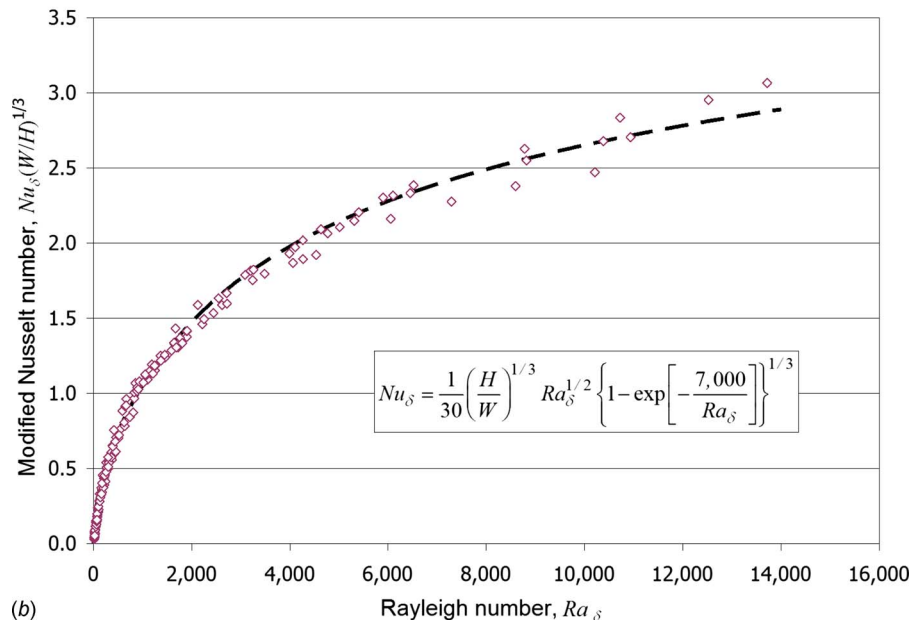
ins = insulation
r = radiation
w = wall
∞ = ambient

References

[1] Bar-Cohen, A., and Kraus, A. D., 1995, *Design and Analysis of Heat Sinks*, Wiley, New York.

[2] Kraus, A. D., Aziz, A., and Welty, J., 2001, *Extended Surface Heat Transfer*, Wiley, New York.

[3] Sparrow, E. M., and Vemuri, S. B., 1986, "Orientation Effects on Natural Convection/Radiation Heat Transfer From Pin-Fin Arrays," Int. J. Heat Mass Transfer, **29**, pp. 359–368.

[4] Yüncü, H., and Anbar, G., 1998, "An Experimental Investigation on Performance of Rectangular Fins on a Horizontal Base in Free Convection Heat Transfer," Heat Mass Transfer, **33**(5), pp. 507–514.

[5] Kwak, C. E., and Song, T. H., 2000, "Natural Convection Around Horizontal Downward-Facing Plate With Rectangular Grooves: Experiments and Numerical Simulations," Int. J. Heat Mass Transfer, **43**, pp. 825–838.

[6] Güvenç, A., and Yüncü, H., 2001, "An Experimental Investigation on Performance of Fins on a Vertical Base in Free Convection Heat Transfer," Heat Mass Transfer, **37**, pp. 409–416.

[7] Yazicioğlu, B., and Yüncü, H., 2007, "Optimum Fin Spacing of Rectangular Fins on a Vertical Base in Free Convection Heat Transfer," Heat Mass Transfer, **44**, pp. 11–21.

[8] Mobedi, M., and Yüncü, H., 2003, "A Three Dimensional Numerical Study on Natural Convection Heat Transfer From Short Horizontal Rectangular Fin Array," Heat Mass Transfer, **39**(4), pp. 267–275.

[9] Harahap, F., and Rudianto, E., 2005, "Measurements of Steady-State Heat Dissipation From Miniaturized Horizontally-Based Straight Rectangular Fin Arrays," Heat Mass Transfer, **41**, pp. 280–288.

[10] Zografos, A. I., and Sunderland, J. E., 1990, "Natural Convection From Pin Fins," Exp. Therm. Fluid Sci., **3**, pp. 440–449.

[11] Zografos, A. I., and Sunderland, J. E., 1990, "Numerical Simulation of Natural Convection From Pin-Fin Arrays," ASME Paper No. HTD-157.

[12] Aihara, T., Maruyama, S., and Kobayakawa, S., 1990, "Free Convective/ Radiative Heat Transfer From Pin-Fin Arrays With a Vertical Base Plate (General Representation of Heat Transfer Performance)," Int. J. Heat Mass Transfer, **33**, pp. 1223–1232.

[13] Fisher, T. S., and Torrance, K. E., 1998, "Free Convection Limits for Pin-Fin Cooling," ASME J. Heat Transfer, **120**, pp. 633–640.

[14] Huang, R.-T., Sheu, W.-J., and Wang, C.-C., 2008, "Orientation Effect on

Natural Convective Performance of Square Pin Fin Heat Sinks," Int. J. Heat Mass Transfer, **51**, pp. 2368–2376.

[15] Sahray, D., Magril, R., Dubovsky, V., Ziskind, G., and Letan, R., 2006, "Natural Convection Heat Transfer From Pin Fin Heat Sinks With Horizontal Base," *Proceedings of 13th International Heat Transfer Conference*, Sydney, Australia.

[16] Sahray, D., Magril, R., Dubovsky, V., Ziskind, G., and Letan, R., 2007, "Study of Horizontal-Base Pin-Fin Heat Sinks in Natural Convection," *Proceedings of ASME InterPACK '07*, Vancouver, Canada, Jul. 8–12.

[17] Kline, S. J., and McClintock, F. A., 1953, "Describing Uncertainties in Single-Sample Experiments," Mech. Eng. (Am. Soc. Mech. Eng.), **75**, pp. 3–8.

[18] Dubovsky, V., Ziskind, G., Druckman, S., Moshka, E., Weiss, Y., and Letan, R., 2001, "Natural Convection Inside Ventilated Enclosure Heated by Downward-Facing Plate: Experiments and Numerical Simulations," Int. J. Heat Mass Transfer, **44**, pp. 3155–3168.

[19] Kazansky, S., Dubovsky, V., Ziskind, G., and Letan, R., 2003, "Chimney-Enhanced Natural Convection From a Vertical Plate: Experiments and Numerical Simulations," Int. J. Heat Mass Transfer, **46**, pp. 497–512.

[20] Jaluria, Y., and Torrance, K. E., 1986, *Computational Heat Transfer*, Hemisphere, Washington, DC.

[21] Elenbaas, W., 1942, "The Dissipation of Heat by Free Convection: the Inner Surface of Vertical Tubes of Different Shapes of Cross-Section," Physica (Amsterdam), **9**(8), pp. 865–874.

[22] Bar-Cohen, A., Bahadur, R., and Iyengar, M., 2006, "Least-Energy Optimization of Air-Cooled Heat Sinks for Sustainability - Theory, Geometry and Material Selection," Energy, **31**, pp. 579–619.

Experimental and Numerical Determination of Thermal Radiative Properties of ZnO Particulate Media

P. Coray

Solar Technology Laboratory,
Paul Scherrer Institute,
5232 Villigen, Switzerland

W. Lipiński

Department of Mechanical Engineering,
University of Minnesota,
Minneapolis, MN 55455

A. Steinfeld[1]

Department of Mechanical and Process
Engineering,
ETH Zurich,
8092 Zurich, Switzerland;
and
Solar Technology Laboratory,
Paul Scherrer Institute,
5232 Villigen, Switzerland
e-mail: aldo.steinfeld@ethz.ch

The radiative characteristics of dependently scattering packed-beds of ZnO particles, applied in the design of high-temperature solar thermochemical reactors, were investigated experimentally. ZnO samples of varying thickness were exposed to a continuous beam of near monochromatic thermal radiation in the 0.5–1 μm wavelength range. The overall transmitted fraction measured as a function of sample thickness s obeys an exponential trend exp(−As), with the fit parameter A ranging from 4000 ± 100 m⁻¹ at 555 nm to 2100 ± 100 m⁻¹ at 1 μm. In the forward directions, the measured intensity distribution is approximately isotropic, whereas in the backward directions it is well approximated by a Henyey–Greenstein equation with asymmetry factors g ≈ −0.4 at 555 nm and g ≈ −0.1 at 1 μm. A Monte Carlo ray-tracing model of the experimental setup is employed to extract the extinction coefficient and the scattering albedo for the case of a nongray absorbing-scattering medium. [DOI: 10.1115/1.3194763]

Keywords: radiation, radiometry, radiative spectroscopy, Monte Carlo, zinc oxide, packed-bed

1 Introduction

The two-step water-splitting thermochemical cycle based on the ZnO/Zn redox reactions is considered for solar hydrogen generation [1]. It encompasses the endothermal dissociation of ZnO using concentrated solar radiation as the energy source of high-temperature process heat, followed by the non-solar exothermal hydrolysis of Zn. The solar chemical reactor features ZnO particles directly exposed to high-flux solar irradiation that serve the functions of radiant absorbers and chemical reactants [2].

Packed-beds containing chemically reacting particles subjected to high-flux irradiation are encountered in solar reactor applications [3]. These packed-beds, which often involve metal oxide particles, are characterized by their low thermal conductivity and their high attenuation of thermal radiation, which leads to large temperature gradients and, consequently, to a nonuniform rate of chemical reaction. Thus, heat transfer within the packed-bed becomes the limiting-controlling mechanism, affecting negatively the energy conversion efficiency of the solar thermochemical process. Of special interest is the thermal dissociation of ZnO at above 1700 K, performed in a packed-bed exposed to intense thermal radiation incident from the top under conditions that are typical of ablation processes [2,4]. Radiative properties such as the extinction coefficient, the scattering albedo, and the scattering phase function are needed to model thermal radiation-chemistry interactions for anticipating the consequences of a given design decision on the reactor's performance, and for optimizing the reactor design for maximum energy conversion efficiency. In general, the composition and structure of the reacting media encountered in solar chemical reactors are complex, and the properties should be determined by combined experimental-theoretical studies.

Previous pertinent studies of the radiative properties in particulate media include a review of experimental work up to 1991 and scattering analysis of collimated radiation [5], experimental characterization of radiative properties of disperse systems [6], and experimental determination of the extinction coefficient of packed-beds [7–10] and dense media [11,12], and a method to enhance transmittance of such media [13].

In this paper, a combined experimental and numerical study on radiative properties of ZnO packed-beds is presented. Experimentally measured radiative fluxes are compared with those obtained by Monte Carlo computations to determine the extinction coefficient $\beta_\lambda = \kappa_\lambda + \sigma_{s\lambda}$, the scattering albedo $\omega_\lambda = \sigma_{s\lambda}/\beta_\lambda$, and the scattering phase function Φ_λ, needed to solve the equation of radiative transfer (RTE) [14]

$$\frac{\mathrm{d}I_\lambda}{\mathrm{d}s} = \kappa_\lambda I_{b\lambda} - \beta_\lambda I_\lambda + \frac{\sigma_{s\lambda}}{4\pi}\int_{4\pi} I_\lambda(\hat{\mathbf{s}}_i)\Phi_\lambda(\hat{\mathbf{s}}_i,\hat{\mathbf{s}})d\Omega_i \qquad (1)$$

2 Experimental Setup

Two configurations of the experimental setup used in this study are shown schematically in Figs. 1 (setup No. 1) and 2 (setup No. 2). The main hardware components are as follows: (No. 1) a dual Xe-arc/Cesiwid-glowbar lamp as a source of radiation, (No. 2) a double monochromator (Acton Research Spectra Pro Monochromator SP-2355 series) with monochromator exit slit (No. 2′), (Nos. 3 and 5) two imaging lens pairs (MgF₂, focal lengths $f = 75$ mm and $f = 150$ mm), (No. 4) a sample, (No. 6) a detector (Si/PC-HgCdTe sandwich with thermoelectric cooler) mounted on a rotary arm, (No. 6′) a detector (Si, uncooled) mounted directly behind the sample, (No. 7) an optical chopper to modulate the radiation leaving the monochromator, (No. 8) a lock-in amplifier to measure the modulated signal, and (No. 9) a PC data acquisition system. This setup enables measurements in the spectral range from 0.3 μm to 4 μm with a spectral resolution of less than ±1 nm.
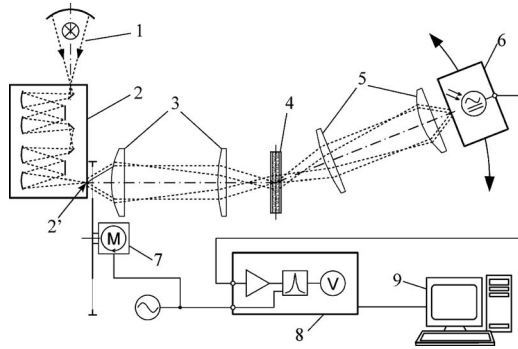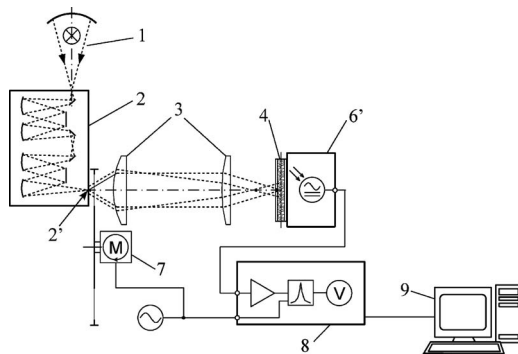
Fig. 1 Experimental setup No. 1 with a rotary detector. Components: (No. 1) dual Xe-arc/Cesiwid-glowbar lamp, (No. 2) double monochromator, (No. 2′) monochromator exit slit, (Nos. 3 and 5) imaging lens pairs, (No. 4) sample, (No. 6) rotary detector, (No. 7) optical chopper, (No. 8) lock-in amplifier, and (No. 9) data acquisition system.

Fig. 3 Normalized volume-based particle size distribution function f(a) and the corresponding cumulative volume distribution function F(a) of ZnO particles as a function of particle radius a

Due to the expected high attenuation of the ZnO packed-bed, the setup was operated at maximum throughput in the wavelength range between 555 nm and 1 μm, with spectral resolutions of ±15 nm and ±30 nm, respectively.
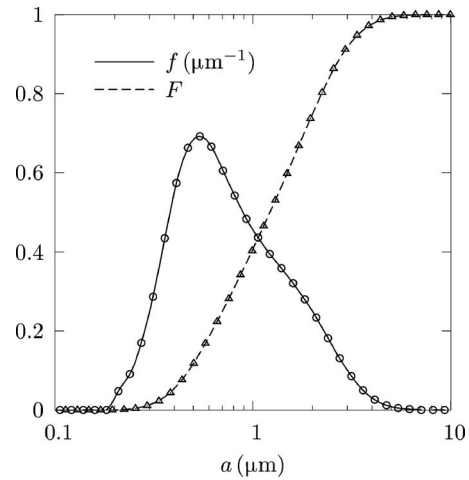
In setup No. 1 (Fig. 1), which is used for directional measurements, the radiation leaving through the 3×4 mm^2 sized monochromator exit slit is first projected onto the sample with a magnification factor of 2. On the opposite side of the sample an identical lens pair is used to project the radiation from the sample onto the detector. At this setting, the maximum acceptance angle for detection of an incoming ray measured with respect to the optical axis is less than 4 deg.

In setup No. 2 (Fig. 2) the main difference is that the detector is placed directly behind the sample with no additional optics between the sample and detector. This results in a ray acceptance angle of 50–60 deg, which in turn increases the detector signal, thus allowing measurements at sample optical thicknesses larger than with setup No. 1.
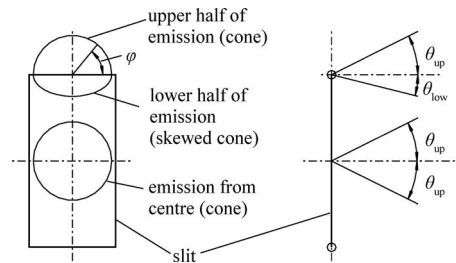
The samples of 24×24 mm^2 cross section were prepared by pressing ZnO powder to a target volume fraction of f_v $=40-45\%$ (the actual range was between 34% and 51%). To support the packed-bed of ZnO after pressing and prevent it from breaking, it was placed between two parallel ISO 8037/1 standard compliant microscopy slides. The normalized volume-based particle size distribution function $f(a)$ and the corresponding cumulative volume distribution function $F(a)$ of the ZnO particles,

Fig. 4 Directions of emission from the monochromator exit slit: left—front view of the monochromator exit slit; right—cross section of the monochromator exit slit

$$F(a) = \int_0^a f(a^*)\mathrm{d}a^*, \quad F(\infty) = 1 \qquad (2)$$

were obtained by laser scattering particle size analysis (Horiba LA-950) and are shown in Fig. 3. The Sauter mean particle radius a_{32}, volume median radius a_{VM}, and the maximum radius a_{max} are 0.95 μm, 1.21 μm, and 6.6 μm, respectively. At a wavelength of $\lambda=555$ nm this corresponds to particle size parameters $\xi \equiv \pi d/\lambda$ of 4.6, 13.7, and 75. For the present particle size and volume fraction range, the scattering regime is dependent [15], which considerably complicates the theoretical prediction of the radiative properties.

3 Monte Carlo Analysis

Solving for the radiative fluxes measured by the two setups was done by a Monte Carlo ray-tracing simulation [16], written in FORTRAN 2003. A large number of stochastic rays are launched at the rectangular exit slit of the second stage of the double monochromator. The starting points **p** are distributed uniformly over the slit.[2] A ray's emission direction is expressed as a function of its distance from the optical axis and the monochromator $f_\#$. At the center of the slit the ray emission direction is uniformly distributed over a cone with opening angle $\theta = \pm \arctan(0.5/f_\#)$. For off center rays the inward pointing half of this cone of emission becomes skewed to an elliptical base, which is sketched in Fig. 4.

Fig. 2 Experimental setup No. 2 with a fixed detector. Components: (Nos. 1–4 and 7–9) as in Fig. 1, (No. 6′) fixed detector.

[2]Underlined variables (**p** and **u**) indicate local lens system coordinates. **u** contains the slopes with respect to the optical axis and is not a unit vector.

As indicated in Fig. 4 two characteristic opening angles, θ_{up} and θ_{low}, are used to determine the direction of emission. For all starting points $\underline{p}$ the outward pointing angle is θ_{up} = arctan($0.5/f_\#$). The inward pointing angle θ_{low} is a linear function of distance from the slit center (i.e., the magnitude of $\underline{p}$). At the center of the slit θ_{low} = −arctan($0.5/f_\#$) and at the upper edge of the slit θ_{low} = −arctan($0.25/f_\#$).

Using θ_{up} and θ_{low} and the starting point $\underline{p}$, the ray circumferential angle φ and cone angle θ are determined by

$$\varphi = \pi\Re_\varphi, \quad \theta = \theta_{up}\Re_\theta - (1 - \Re_\theta)\left|\begin{pmatrix} \theta_{up}\cos(\varphi) \\ \theta_{low}\sin(\varphi) \end{pmatrix}\right| \quad (3)$$

The angles θ and φ resulting from Eq. (3) are aligned with respect to a radial coordinate system that is transformed into the lens coordinate system by using

$$\underline{p} = \begin{pmatrix} \underline{p}_1 \\ \underline{p}_2 \end{pmatrix}, \quad \underline{u} = \begin{pmatrix} \underline{p}_2\cos(\varphi) + \underline{p}_1\sin(\varphi) \\ -\underline{p}_1\cos(\varphi) + \underline{p}_2\sin(\varphi) \end{pmatrix}\frac{\tan(\theta)}{|\underline{p}|} \quad (4)$$

The lens system is modeled based on a paraxial approximation [17]. At each lens the ray direction is transformed from $\underline{u}$ to $\underline{u}'$ as shown in Eq. (5). Rays with positions $\underline{p}$ exceeding the lens clear aperture are discarded from further ray tracing.

$$(\underline{u}'_1 \; \underline{u}'_2) = (-f^{-1} \; 1) \cdot \begin{pmatrix} \underline{p}_1 & \underline{p}_2 \\ \underline{u}_1 & \underline{u}_2 \end{pmatrix} \quad (5)$$

The microscopy slides (windows) containing the packed-bed are treated as nonabsorbing and modeled using the Fresnel equations.

For modeling the dependently scattering packed-bed medium, it is assumed that the equation of radiative transfer, Eq. (1), for a pseudocontinuum of uniform properties may be applied. While strict derivations of the RTE do not necessarily include the case of dependent scattering, there are indications that the RTE can still be used, provided that appropriate radiative properties (β_λ, ω_λ, and Φ_λ) are employed [6,12]. It is further assumed that transition effects, which may occur when a ray passes the packed-bed boundaries, are negligible in comparison to the absorption and scattering events occurring inside the medium. The collision-based Monte Carlo method is used to solve for the radiative intensities described by the equation of radiative transfer [14,16]. Hence, the attenuation path length s is computed via

$$s = -\frac{1}{\beta_\lambda}\ln\Re_s \quad (6)$$

At the location of attenuation, another random number condition is checked to decide whether absorption or scattering occurs. If the condition

$$\Re_\omega \geq \omega_\lambda \quad (7)$$

is satisfied, the history of the ray is terminated. Otherwise, the ray is scattered and the scattering direction is obtained from

$$\varphi = 2\pi\Re_{\varphi_{sca}}, \quad \Re_{\theta_{sca}} = \frac{1}{2}\int_0^{\theta_{sca}}\Phi(\theta^*_{sca})\sin\theta^*_{sca}d\theta^*_{sca} \quad (8)$$

where θ_{sca} is the scattering cone angle, measured with respect to the direction of the incident ray, and φ is a circumferential angle.

Rays leaving the sample are traced until they either reach the detector surface or get lost. In case of the rotary detector lens system (Fig. 1), the rays are transformed into a local lens coordinate system and traced using Eq. (5).

Although a number of models for the theoretical prediction of radiative properties in the presence of dependent scattering have been presented in literature [6,15], none of the existing methods was found to be ideal for the present case of polydispersed ZnO particles sized on the order of the radiation wavelength. In a more heuristic than theoretical attempt to get a first estimate for the effective radiative properties (β_λ, ω_λ, and Φ_λ), a scaling approach similar to the one made in Ref. [18] and later applied in Ref. [19] is taken. The approach consists of first obtaining the independent scattering properties of polydispersed ZnO particles by applying the Mie solutions [14,15,20,21] and then individually scaling the absorption and scattering coefficients while leaving the phase function unchanged. Thus, the unscaled absorption, scattering and extinction coefficients, and the scattering phase function are calculated as

$$\{\kappa_\lambda, \sigma_{sca,\lambda}, \beta_\lambda\} = 0.75f_v\int_0^\infty\frac{\{Q_{abs}, Q_{sca}, Q_{ext}\}}{a}f(a)da \quad (9)$$

$$\Phi_\lambda(\theta) = \frac{0.75f_v}{\sigma_{sca,\lambda}}\int_0^\infty\frac{Q_{sca}\Phi_\lambda(a,\theta)}{a}f(a)da \quad (10)$$

In Eqs. (9) and (10), $Q_{abs}(a)$, $Q_{sca}(a)$, $Q_{ext}(a)$, and $\Phi_\lambda(a,\theta)$ are obtained by using the BHMIE subroutine from Ref. [21].

As shown in Sec. 4, the aforementioned approach based on scaling of independent properties gives results, which are too inaccurate for the purpose of subsequent solar reactor design calculations. The option of getting better results by trying to perform a more sophisticated theoretical prediction of radiative properties is, due to the involved complexity, beyond the scope of this work. Therefore a more empirical approach is pursued. This empirical approach makes use of an approximate scattering phase function consisting of a variation of the double Dirac-delta approximation[3] [14]

$$\Phi(\theta) = 2f_{fwd}\delta(1 - \cos(\theta)) + 2f_{bwd}\delta(1 + \cos(\theta)) + (1 - f_{fwd}$$
$$- f_{bwd})\Phi^*(\theta) \quad (11)$$

The non-Dirac part of Eq. (11), Φ^*, is modeled as a forced symmetric Henyey–Greenstein shaped phase function

$$\Phi^{**}(\theta) = \frac{1 - g'^2}{[1 + g'^2 - 2g'\,\text{sgn}(\cos\theta)\cos\theta]^{3/2}} \quad (12)$$

$$\Phi^*(\theta) = \int_0^\theta\Phi^{**}(\theta^*)\sin(\theta^*)d\theta^*/\int_0^\pi\Phi^{**}(\theta^*)\sin(\theta^*)d\theta^* \quad (13)$$

The reason for not leaving Φ^* isotropic is that using values of g' between 0 and 0.5 leads to an improved agreement with the measurement results in backward direction. To keep the number of variable parameters as low as just necessary for a good fit, the asymmetry factor

$$g = \overline{\cos(\theta)} = \frac{1}{4\pi}\int_{4\pi}\Phi(\theta)\cos(\theta)d\Omega \quad (14)$$

of Φ^* is set to $g(\Phi^*) = 0$ by forcing a symmetric shape. The other two components in Eq. (11), f_{fwd} and f_{bwd}, are the for- and backward-scattered fractions. The extinction coefficient β, scattering albedo ω, for- and backward-scattered fractions f_{fwd} and f_{bwd}, and shape g' are then determined by an iterative trial-and-error based best fit to the measurement results.

4 Results

Eight packed-beds of thickness between 0.85 mm and 2.65 mm were scanned at four wavelengths λ = 555 nm, 650 nm, 800 nm, 900 nm, and 1000 nm. Figure 5 shows the detector signal with sample (i.e., packed-bed and two windows), q, normalized by the signal without sample, q_0, plotted against the packed-bed thickness. Within the region of measurements the signal is approximated by an exponential fit with coefficients A_1 and A_2. It can also be seen that the signal attenuation decreases with increasing

---

[3]In the subsequent text, the spectral subscript λ will be omitted for brevity.
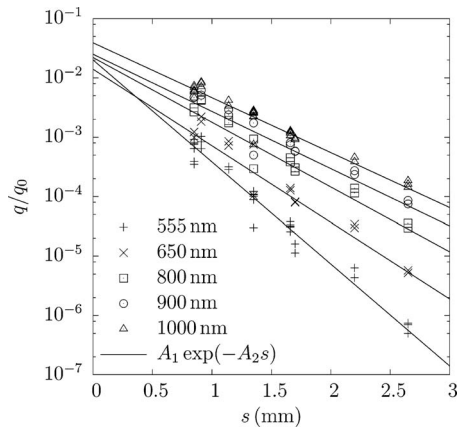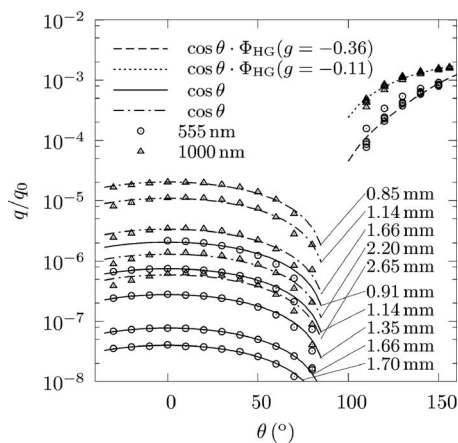
Fig. 5 Measured normalized signal q/q_0 versus packed-bed thickness s. Data obtained with setup No. 2.

Fig. 7 Measured data (points) versus Mie phase function based simulation (lines). The normalized signal q/q_0 is plotted as a function of viewing angle θ for two sample thicknesses s. The wavelength is 555 nm. Further details in Table 1.

wavelength, as expected from the decreasing absorption index of ZnO [22]. This is reflected in the fit coefficient A_2. At 555 nm $A_2=4000\pm100$ m^{-1} and at 1 μm $A_2=2100\pm100$ m^{-1}.
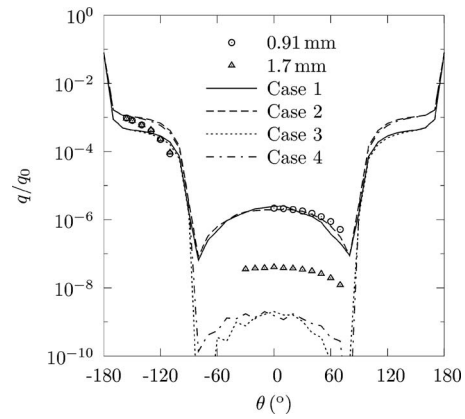
The directional distribution of radiation around the sample for the two wavelengths $\lambda=555$ nm and 1000 nm is shown in Fig. 6. In forward direction, i.e., at angles smaller than 90 deg, the detector signal is approximately proportional to the cosine of the viewing angle, indicating diffuse behavior. In backward direction it was found that the signal is roughly proportional to the product of the cosine of the viewing angle and a Henyey–Greenstein type phase function with asymmetry factor $g=-0.4$ at 555 nm and $g=-0.1$ at 1000 nm.

A first set of simulation runs was carried out based on a scattering phase function obtained by the Mie solution for polydispersed particles shown in Fig. 3. The phase function Φ was left unchanged while the extinction coefficient β and scattering albedo ω were adapted to give a best fit to the measurements. A typical result is shown in Fig. 7 and Table 1. It shows that when matching the measured signal in backward direction, the attenuation in forward direction turns out higher than measured. However, it was also observed that an increased albedo leads to increased agreement in forward direction, at the cost of poorer agreement in backward direction.

The results obtained by trying to scale independent scattering onto the measured dependent scattering results, Fig. 7, were judged to be too crude for further use in engineering design calculations. Therefore, simulation runs finding a best fit for the ap-

proximate double Dirac-delta phase function, Eq. (11), were performed. An initial parameter analysis showed that in order to get a good solution with the existing measurement data, the forward-scattered fraction must be artificially forced to zero, $f_{\text{fwd}}:=0$. This is because the employed sample preparation equipment does not allow manufacturing packed-bed samples thin enough to measure a pronounced forward peak. Without such a peak resolving the forward-scattered fraction is not possible, because f_{fwd} would be strongly correlated with σ_s and consequently also with β, ω, and f_{bwd}. Hence it is important to note that β, ω, and f_{bwd} are bound to $f_{\text{fwd}}:=0$, which, in a sense, makes them apparent properties. If the measurement data would allow resolving a conceptual "true" f_{fwd} and in turn a "true" σ_s, then the expected relation between the present apparent σ_s and the true σ_s is $\sigma_{s.\text{apparent}}=\sigma_{s.\text{true}}$ $(1-f_{\text{fwd.true}})$. Note that if f_{bwd} were zero, then the aforementioned $\sigma_{s.\text{apparent}}$ would be equivalent to the one obtained with the well known transport approximation described in Refs. [20,23].

An intermediate result for $\lambda=1000$ nm, $f_{\text{fwd}}:=0$, $f_{\text{bwd}}=0.8$ and 0.9, $g'=0.25$, $\beta=35,000$, and $\omega=0.999$ is shown in Figs. 8 and 9. In Fig. 8 the signal in forward direction is observed as a function of thickness for one viewing angle only. It shows that there first is a steep decay of the signal before gradually taking on the log-linear slope of the measurement data points. This zone of initial steep decay is interpreted as the region where radiation is predominately attenuated by scattering with only little augmentation by incoming scattering. Once a sufficient amount of scattered radiation is available incoming scattering begins to contribute, which leads to the observed reduced slope.

In backward direction, shown in Fig. 9, it appears that a good agreement can be reached for a backward Dirac peak, f_{bwd}, between 0.8 and 0.9. This would imply that at $\lambda=1000$ nm between 80% and 90% of all scattered radiation has a scattering angle θ close to 180 deg. In the simulation the signal at 180 deg becomes very strong. Having an experimentally measured signal in that direction will therefore be of great importance for further improv-

Fig. 6 Measured normalized signal q/q_0 as a function of viewing angle θ for different packed-bed thicknesses at $\lambda=555$ nm and 1000 nm. Data obtained with setup No. 1.

Table 1 Extinction coefficients, scattering albedos, and path lengths for Cases 1–4 shown in Fig. 7

	β (m^{-1})	ω	s (mm)
Case 1	25.0×10^3	0.85	0.91
Case 2	43.0×10^3	0.95	0.91
Case 3	25.0×10^3	0.85	1.7
Case 4	43.0×10^3	0.95	1.7
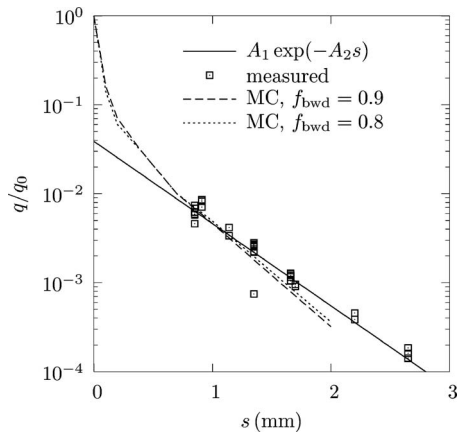
Fig. 8 Measured data (points) versus model phase function based simulation (lines). The normalized signal q/q_0 is plotted as a function of sample thickness s. The data were obtained with setup No. 2 (forward direction) at a wavelength of 1000 nm.

ing and verifying the approximate phase function. Experimental support for the existence of a strong backward peak can presently be drawn from previous studies on radiative properties of compacted zinc oxide powder [24]. For wavelengths between 0.5 μm and 1 μm, the reported normal spectral reflectance of compacted zinc oxide powder is in the range 80–99%. The main parameters affecting the normal spectral reflectance in Ref. [24] are compaction pressure and particle size distribution.

5 Conclusion

We have measured radiation exiting through dependently scattering samples of densely packed-beds of ZnO, with the aim of using these data to find volume-averaged radiative properties required in the equation of radiative transfer. A collision-based Monte Carlo ray-tracing model was used to find a best-match extinction coefficient β and scattering albedo ω for a given input scattering phase function. Two modeling approaches were taken to find an appropriate phase function Φ. The first was based on a Mie solution for an independently scattering cloud of particles. With this Mie phase function it was not possible to reach agreement in both forward and backward directions simultaneously. Therefore, a second modeling approach was based on an approximate phase function with a symmetric component and an addi-
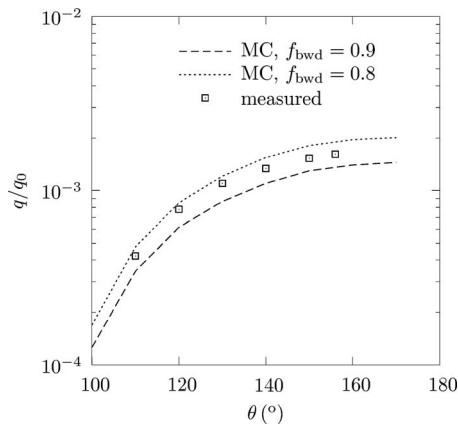

Fig. 9 Measured data (points) versus model phase function based simulation (lines). The normalized signal q/q_0 is plotted as a function of viewing angle θ. The data were obtained with setup No. 1 (backward direction) at a wavelength of 1000 nm.

tional backward Dirac peak. For this phase function it was possible to achieve a good match with both back and forward measurements, provided more than 80% of the radiative energy would be backscattered.

Future studies will focus on measurements at high temperatures to determine the radiative properties of porous materials encountered in solar thermochemical reactors such as packed-beds of ZnO, C, and $CaCO_3$, and reticulate porous ceramics.

Acknowledgment

Nomenclature

A_1 = coefficient of the exponential fit $A_1 \exp(-A_2 s)$
A_2 = coefficient of the exponential fit $A_1 \exp(-A_2 s)$, m^{-1}
a = particle radius, m
f = lens focal length, m
f_{bwd} = Dirac backward-scattered fraction
f_{fwd} = Dirac forward-scattered fraction
f_v = volume fraction
g = asymmetry factor
$\mathbf{p}$ = ray starting point, m
q = detector signal ("radiative flux"), arbitrary units
q_0 = detector signal without sample at 0 deg viewing angle, arbitrary units
$\Re$ = random number
RTE = equation of radiative transfer
I_λ = spectral radiative intensity, W m^{-3} sr^{-1}
Q = efficiency factor
s = path length, m; packed-bed thickness, m
T = transmittance
$\mathbf{u}$ = ray direction

Greek Symbols

β = extinction coefficient, m^{-1}
δ = Dirac-delta function
ε = porosity
θ = polar angle (cone angle), deg
κ = absorption coefficient, m^{-1}
λ = wavelength, m
ξ = size parameter
σ_s = scattering coefficient, m^{-1}
φ = azimuthal angle (circumferential angle), deg
Φ = scattering phase function
Ω = solid angle, sr
ω = scattering albedo

Subscripts

abs = absorption
ext = extinction
HG = Henyey–Greenstein
i = incident
MC = Monte Carlo method
sca = scattering
VM = volume median
λ = spectral

References

[1] Steinfeld, A., 2002, "Solar Hydrogen Production Via a 2-Step Water-Splitting Thermochemical Cycle Based on Zn/ZnO Redox Reactions," Int. J. Hydrogen Energy, **27**, pp. 611–619.
[2] Schunk, L., Haeberling, P., Wepf, S., Wuillemin, D., Meier, A., and Steinfeld, A., 2008, "A Solar Receiver-Reactor for the Thermal Dissociation of Zinc Oxide," ASME J. Sol. Energy Eng., **130**, p. 021009.
[3] Steinfeld, A., and Palumbo, R., 2001, "Thermochemical Process Technology,"

Encyclopedia of Physical Science and Technology, Vol. 15, R. A. Meyers, ed., Academic, San Diego, CA, pp. 237–256.

[4] Müller, R., Lipiński, W., and Steinfeld, A., 2008, "Transient Heat Transfer in a Directly-Irradiated Solar Chemical Reactor for the Thermal Dissociation of ZnO," Appl. Therm. Eng., **28**(5–6), pp. 524–531.

[5] Agarwal, B. M., and Mengüç, M. P., 1991, "Forward and Inverse Analysis of Single and Multiple Scattering of Collimated Radiation in an Axisymmetric System," Int. J. Heat Mass Transfer, **34**, pp. 633–647.

[6] Baillis, D., and Sacadura, J.-F., 2000, "Thermal Radiation Properties of Dispersed Media: Theoretical Prediction and Experimental Characterization," J. Quant. Spectrosc. Radiat. Transf., **67**, pp. 327–363.

[7] Kamiuto, K., Iwamoto, M., Nishimura, T., and Sato, M., 1991, "Radiation-Extinction Coefficients of Packed-Sphere Systems," J. Quant. Spectrosc. Radiat. Transf., **45**, pp. 93–96.

[8] Jones, P. D., McLeod, D. G., and Dorai-Raj, D. E., 1996, "Correlation of Measured and Computed Radiation Intensity Exiting a Packed Bed," ASME J. Heat Transfer, **118**, pp. 94–102.

[9] Lopes, R., Moura, L. M., Baillis, D., and Sacadura, J.-F., 2001, "Directional Spectral Emittance of a Packed Bed: Correlation Between Theoretical Prediction and Experimental Data," ASME J. Heat Transfer, **123**, pp. 240–248.

[10] Kuhn, J., Korder, S., Arduini-Schuster, M. C., Caps, R., and Fricke, J., 1993, "Infrared-Optical Transmission and Reflection Measurements on Loose Powders," Rev. Sci. Instrum., **64**, pp. 2523–2530.

[11] Ishimaru, A., and Kuga, Y., 1982, "Attenuation Constant of a Coherent Field in a Dense Distribution of Particles," J. Opt. Soc. Am., **72**, pp. 1317–1320.

[12] Hespel, L., Maiguy, S., and Greffet, J.-J., 2003, "Radiative Properties of Scattering and Absorbing Dense Media: Theory and Experimental Study," J. Quant. Spectrosc. Radiat. Transf., **77**, pp. 193–210.

[13] Lipiński, W., Guillot, E., Olalde, G., and Steinfeld, A., 2008, "Transmittance Enhancement of Packed-Bed Particulate Media," Exp. Heat Transfer, **21**(1),

pp. 73–82.

[14] Modest, M. F., 2003, *Radiative Heat Transfer*, 2nd ed., Academic, San Diego, CA.

[15] Tien, C. L., and Drohlen, B. L., 1987, "Thermal Radiation in Particulate Media With Dependent and Independent Scattering," Annu. Rev. Numer. Fluid Mech. Heat Transfer, **1**, pp. 1–32.

[16] Farmer, J. T., and Howell, J. R., 1998, "Comparison of Monte Carlo Strategies for Radiative Transfer in Participating Media," *Advances in Heat Transfer*, Vol. 31, J. P. Harnett and T. F. Irvine, eds., Academic, San Diego, CA, pp. 333–429.

[17] Gross, H., 2005, *Handbook of Optical Systems*, Vol. 1, Wiley-VCH, Weinheim, Germany.

[18] Singh, B. P., and Kaviany, M., 1992, "Modelling Radiative Heat Transfer in Packed Beds," Int. J. Heat Mass Transfer, **35**(6), pp. 1397–1405.

[19] Dombrovsky, L., Schunk, L., Lipiński, W., and Steinfeld, A., 2009, "An Abation Model for the Thermal Decomposition of Porous Zinc Oxide Layer Heated by Concentrated Solar Radiation," Int. J. Heat Mass Transfer, **52**, pp. 2444–2452.

[20] Dombrovsky, L. A., 1996, *Radiation Heat Transfer in Disperse Systems*, Begell House, New York.

[21] Bohren, C. F., and Huffman, D. R., 1983, *Absorption and Scattering of Light by Small Particles*, Wiley, New York.

[22] Dombrovsky, L. A., Lipiński, W., and Steinfeld, A., 2007, "A Diffusion-Based Approximate Model for Radiation Heat Transfer in a Solar Thermochemical Reactor," J. Quant. Spectrosc. Radiat. Transf., **103**(3), pp. 601–610.

[23] Kaviany, M., 1995, *Principles of Heat Transfer in Porous Media*, Springer, New York.

[24] Touloukian, Y. S., and DeWitt, D. P., 1972, *Thermal Radiative Properties—Nonmetallic Solids*, IFI/Plenum, New York.

Non-Darcy Mixed Convection With Thermal Dispersion in a Saturated Porous Medium

V. V. Sobha[1]

Department of Engineering Mathematics,
Andhra University,
Visakhapatnam, 530 003 India

R. Y. Vasudeva

Department of Applied Mathematics,
Andhra University,
Visakhapatnam, 530 003 India

K. Ramakrishna

Department of Mechanical Engineering,
K.L. College of Engineering,
Guntur, 522 502 India

K. Hema Latha

Department of Mathematics,
V.R. Siddhartha Engineering College,
Vijayawada, 520 007 India

Thermal dispersion due to local flows is significant in heat transfer with forced convection in porous media. The effects of parametrized melting (M), thermal dispersion (D), inertia (F), and mixed convection (Ra/Pe) on the velocity distribution, temperature, and Nusselt number on non-Darcy, mixed convective heat transfer from an infinite vertical plate embedded in a saturated porous medium are examined. It is observed that the Nusselt number decreases with increase in melting parameter and increases with increase in thermal dispersion. [DOI: 10.1115/1.3194761]

1 Introduction

In the present work, melting with thermal dispersion, which is a necessary secondary effect due to local fluid flow in the tortuous paths that exist in the porous medium [1,2] on non-Darcy, mixed convective heat transfer from an infinite vertical plate embedded in a saturated porous medium, is studied. Both aiding and opposing flows are examined. The Forchheimer extension for flow equations in steady state is considered and the coefficient of thermal diffusivity is assumed as the sum of the molecular diffusivity and the thermal diffusivity due to mechanical dispersion. Similarity solution for the governing equations is obtained. The equations are numerically solved using the Runge–Kutta fourth order method coupled with shooting technique. There is a large literature in this area and we will mention those that are, in our opinion, most relevant for reasons of print-space restrictions. The problem of mixed convection in melting from a vertical plate of uniform temperature in a saturated porous medium was studied by Gorla et al. [3]. They found that the melting process is analogous to mass injection and blowing near the boundary and thus, reduces the

heat transfer through the solid-liquid interface. In Ref. [4] Tashtoush studied the magnetic and buoyancy effects on melting from a vertical plate by considering the Forchheimer extension. He examined the velocity and temperature profiles and heat transfer rate of the melting phenomena associated with uniform wall temperature using the collocation finite element method. He has analyzed the effect of inertial forces on flow and heat transfer. However, Nield [5] recently pointed out that it is not possible to produce a magnetic field strong enough for the magnetic drag to be significant in comparison with the Darcy drag for a practical porous medium. Recently, Cheng and Lin [6] studied the melting effect on mixed convective heat transfer from a solid porous vertical plate with uniform wall temperature embedded in the liquid saturated porous medium, using the Runge–Kutta–Gill method and Newton's iteration for similarity solutions. They established the criteria for (G_r/R_e) values for forced, mixed, and free convection from an isothermal vertical plate in porous media with aiding and opposing external flows in the melting process.

2 Mathematical Formulation

A mixed convective heat transfer in a non-Darcian porous medium saturated with a homogeneous Newtonian fluid adjacent to a vertical plate is considered. This plate constitutes the interface between the liquid and solid phases during melting inside the porous matrix. The plate is at a constant temperature T_m, at which the material of the porous matrix melts. The x-y coordinate system is attached to the vertical plate, as shown in the Fig. 1. The solid phase occupying the region $y < 0$ is at temperature $T_0 < T_m$. A thin boundary layer exists close to the right of the vertical plate and the temperature changes smoothly through this layer from T_m to T_∞ ($T_m < T_\infty$), which is the temperature of the fluid phase.

Taking into account the effect of the thermal dispersion, the governing equations for steady non-Darcy flow in a saturated porous medium can be written as follows:

The continuity equation is

$$\frac{\partial u}{\partial x} + \frac{\partial v}{\partial y} = 0 \tag{1}$$

The momentum equation [4] is

$$\frac{\partial u}{\partial y} + \frac{2C\sqrt{K}}{v} u \frac{\partial u}{\partial y} = -\frac{Kg\beta}{v} \frac{\partial T}{\partial y} \tag{2}$$

The energy equation [7] is

$$u \frac{\partial T}{\partial x} + v \frac{\partial T}{\partial y} = \frac{\partial}{\partial y}\left(\alpha \frac{\partial T}{\partial y}\right) \tag{3}$$

Thermal diffusivity $\alpha = \alpha_m + \alpha_d$, where α_m is the molecular diffusivity and α_d is the dispersion thermal diffusivity due to mechanical dispersion. As in the linear model proposed by Plumb [8], the dispersion thermal diffusivity α_d is proportional to the velocity component, i.e., $\alpha_d = \gamma u d$, where γ is the dispersion coefficient and d is the mean particle diameter.

The boundary conditions for this problem are

$$y = 0, \quad T = T_m, \quad k \frac{\partial T}{\partial y} = \rho[h_{sf} + c_s(T_m - T_0)]v \tag{4}$$

$$y \to \infty, \quad T \to T_\infty, \quad u = u_\infty \tag{5}$$

The stream function ψ with $u = \dfrac{\partial \psi}{\partial y}$ and $v = -\dfrac{\partial \psi}{\partial x}$ (6)

renders the continuity equation (Eq. (1)) satisfied and Eqs. (2) and (3) transform to

$$\frac{\partial^2 \psi}{\partial y^2} + 2\frac{C\sqrt{K}}{v}\left(\frac{\partial \psi}{\partial y}\right)\left(\frac{\partial^2 \psi}{\partial y^2}\right) = -\frac{kg\beta}{v}\frac{\partial T}{\partial y} \tag{7}$$
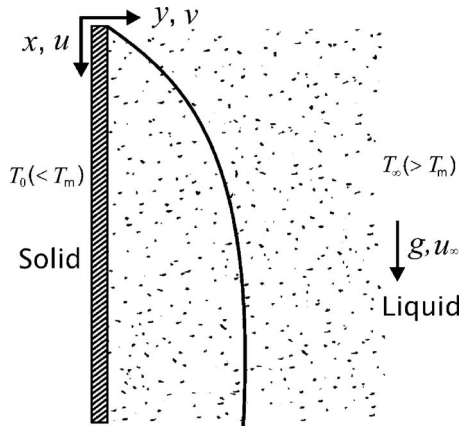
Fig. 1 Schematic diagram of the problem

Table 1 Comparison of present results with the values obtained by Gorla et al. [3] and Cheng and Lin [6] for the melting strength M=2 and F=0 for different mixed convection parameter values in an aiding external flow

Parameter		$f'(0)$	$f'(0)$	$f'(0)$	$\theta'(0)$	$\theta'(0)$	$\theta'(0)$
M	$\dfrac{\mathrm{Ra}}{\mathrm{Pe}}$	Gorla et al. [3]	Cheng and Lin [6]	Present	Gorla et al. [3]	Cheng and Lin [6]	Present
2.0	0.0	1.000	1.000	1.000	0.2799	0.2706	0.27062
	1.4	2.400	2.400	2.400	0.3823	0.3801	0.3801
	3.0	4.000	4.000	4.000	0.4754	0.4745	0.4745
	8.0	9.000	9.000	9.000	0.6902	0.6902	0.69019
	10.0	11.00	11.00	11.00	0.7594	0.7594	0.75939
	20.0	21.00	21.00	21.00	1.038	1.038	1.0384

$$\frac{\partial \psi}{\partial y}\frac{\partial T}{\partial x} - \frac{\partial \psi}{\partial x}\frac{\partial T}{\partial y} = \frac{\partial}{\partial y}\left[\left(\alpha_m + \gamma\frac{\partial \psi}{\partial y}d\right)\frac{\partial T}{\partial y}\right] \qquad (8)$$

Introducing the similarity variables as

$$\psi = f(\eta)(\alpha_m u_\infty x)^{1/2} \qquad (9)$$

$$\eta = \left(\frac{u_\infty x}{\alpha_m}\right)^{1/2}\left(\frac{y}{x}\right) \qquad (10)$$

$$\theta(\eta) = \frac{T - T_m}{T_\infty - T_m} \qquad (11)$$

the momentum (Eq. (7)) and energy equations (Eq. (8)) are reduced to

$$(1 + Ff')f'' + \frac{\mathrm{Ra}_x}{\mathrm{Pe}_x}\theta' = 0 \qquad (12)$$

$$(1 + Df')\theta' + \left(\frac{1}{2}f + Df''\right)\theta' = 0 \qquad (13)$$

where the prime symbol denotes the differentiation with respect to the similarity variable η, and $\mathrm{Ra}_x/\mathrm{Pe}_x$ is the mixed convection parameter, which is taken as positive when the buoyancy is aiding the external flow and as negative when the buoyancy is opposing the external flow.

$$\mathrm{Ra}_x = \frac{g\beta K(T_\infty - T_m)x}{\nu\alpha_m} \qquad (14)$$

$$\mathrm{Pe}_x = \frac{u_\infty x}{\alpha_m} \qquad (15)$$

$$F = \frac{2C\sqrt{K}u_\infty}{\nu} \qquad (16)$$

$$D = \frac{\gamma d u_\infty}{\alpha_m} \qquad (17)$$

Taking into consideration the thermal dispersion effect together with melting, the boundary conditions (Eq. (4)) take the form

$$\eta = 0, \quad \theta = 0, \quad f(0) + \{1 + Df'(0)\}2M\theta'(0) = 0 \qquad (18)$$

$$\eta \to \infty, \quad \theta = 1, \quad f' = 1 \qquad (19)$$

where

$$M = \frac{c_f(T_\infty - T_m)}{h_{sf} + c_s(T_m - T_0)} \qquad (20)$$

From the conditions in Eq. (18), we can recover the conditions when thermal dispersion is absent [3].

The local heat transfer rate from the surface of the plate is given by

$$q_w = -k\left[\frac{\partial T}{\partial y}\right]_{y=0} \qquad (21)$$

The Nusselt number

$$\mathrm{Nu} = \frac{hx}{k} = \frac{q_w x}{k(T_m - T_\infty)} \qquad (22)$$

where k is the effective thermal conductivity of the porous medium, which is the sum of the molecular thermal conductivity k_m and the dispersion thermal conductivity k_d [7]. Substituting Eqs. (11) and (21) into Eq. (22), the modified Nusselt number is obtained as

$$\frac{\mathrm{Nu}_x}{(\mathrm{Pe}_x)^{1/2}} = [1 + Df'(0)]\theta'(0) \qquad (23)$$

In the absence of inertia and thermal dispersion, we get the Nusselt number for pure melting phenomenon in the Darcy medium [3].

3 Solution Procedure

The dimensionless equations (Eqs. (12) and (13)) together with the boundary conditions (Eqs. (18) and (19)) are solved numerically by means of the fourth order Runge–Kutta method coupled with the shooting technique. The solution, thus, obtained is matched with the given values of $f'(\infty)$ and $\theta(0)$. In addition, the boundary condition $\eta \to \infty$ is approximated by $\eta_{\max} = 7$, which is found sufficiently large for the velocity and temperature to approach the relevant freestream properties. This choice of $\eta_{\max}$ helps to compare the present results with these of earlier researchers. Table 1 shows a comparison of the results obtained through the stated procedure with those obtained in Refs. [3,6] for the Darcian conditions.

From Table 1, it is clear that the present study is in complete agreement with the results of Cheng and Lin [6].

4 Conclusions

In problems of heat transfer in porous media under forced convection, thermal dispersion due to local flows in the tortuous paths of the medium is significant. In this paper, the effect of thermal dispersion, i.e., the effect of heat transfer due to hydrodynamic mixing of the interstitial fluid at the pore scale is incorporated by using Plumb's linear model in the governing equations and a numerical solution of the problem is obtained using the shooting
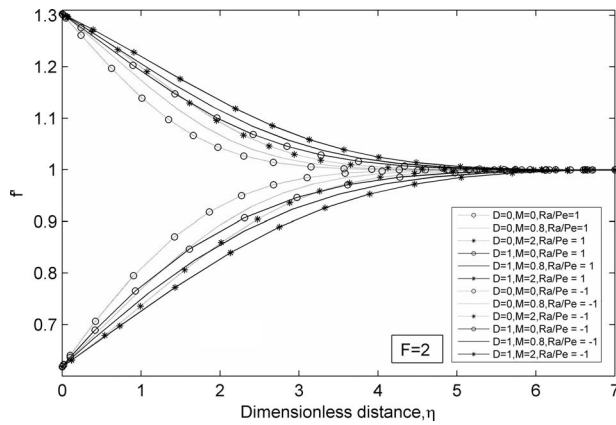
Fig. 2 The effect of thermal dispersion and melting on the velocity distribution in both aiding and opposing flows
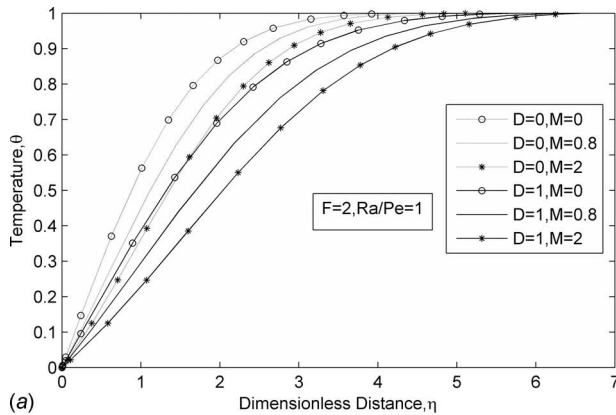
Fig. 3 The effect of melting and thermal dispersion on the temperature distribution

Fig. 4 Variation in the local Nusselt number with the melting parameter for different values of thermal dispersion and mixed convection parameters
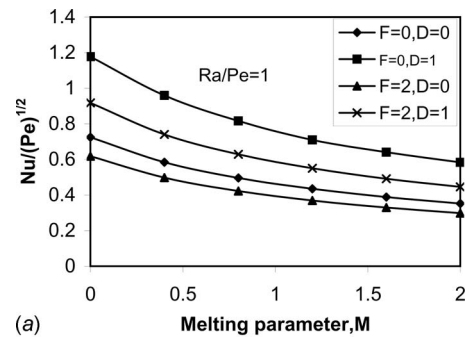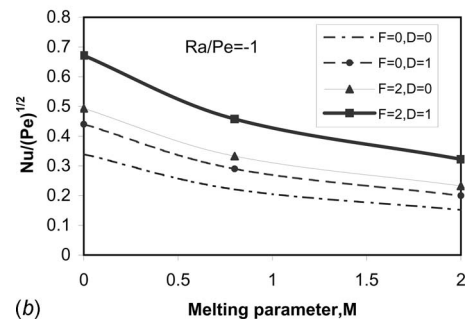
Fig. 5 Variation in the local Nusselt number with the melting parameter for different values of thermal dispersion and inertia parameters

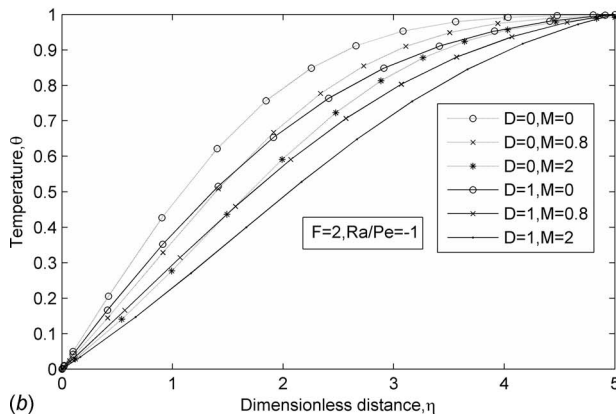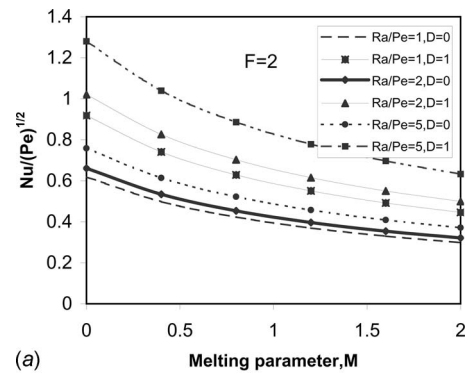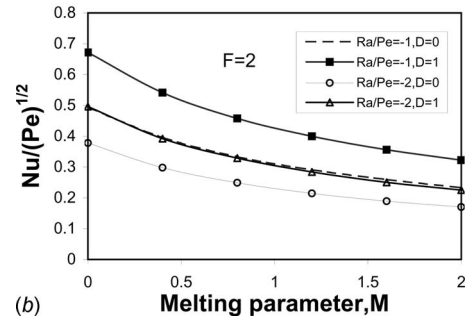technique. The scheme is validated against earlier published results [3,6] that do not include thermal dispersion and inertia effects. The effects of thermal dispersion (D), melting (M), inertia (F), and mixed convection (Ra/Pe) on the flow are graphically illustrated by obtaining the Nusselt number (Nu) and the nondimensionalized velocity and temperature profiles. In non-Darcian framework, comparisons are made in the following cases: (i) mixed convection when both melting and thermal dispersion are absent, and (ii) mixed convection with melting alone, with the present results when melting and thermal dispersion are both present together with mixed convection.

(1) It is observed that thermal dispersion and melting tend to increase/decrease the velocity within the boundary layer in aiding/

opposing flows (Fig. 2). (2) Increase in melting parameter decreases the temperature. Within the boundary layer, temperature decreases with an increase in thermal dispersion (Figs. 3(a) and 3(b)). (3) However, it is found that the rate of heat transfer decreases with the increasing melting parameter while it increases with an increase in thermal dispersion. Melting with thermal dispersion increases the heat transfer more significantly than when melting occurs without thermal dispersion. In aiding flow, as (Ra/

Pe) increases, the Nusselt number increases, but this increase is less in the absence of thermal dispersion than in the presence of thermal dispersion. In an opposing flow, the Nusselt number is found to decrease as $|\text{Ra}/\text{Pe}|$ increases (Figs. 4(*a*) and 4(*b*)). (4) The Nusselt number is decreasing/increasing with the increasing inertia effect in aiding/opposing flow. But, this decrease/increase is less in the absence of thermal dispersion than in the presence of thermal dispersion (Figs. 5(*a*) and 5(*b*)). (5) It is also seen that the velocity increases with an increase in aiding buoyancy, both in the presence and the absence of thermal dispersion while the velocity decreases as the opposing buoyancy becomes larger. (6) Furthermore, the present model shows that in the non-Darcian case, the velocity of the flow with aiding buoyancy is less compared with the velocity in the Darcian case with aiding buoyancy and the effect is seen to be reversed in the opposing buoyancy. Illustrations for 5 and 6 are not shown for want of space.

It is hoped that this paper will be of interest to experimentalists.

Nomenclature

C = inertial coefficient
c_f = specific heat of convective fluid (J/kg K)
c_s = specific heat of solid phase (J/kg K)
d = mean particle diameter
D = thermal dispersion parameter defined in Eq. (17)
f = dimensionless stream function
F = dimensionless inertia parameter defined in Eq. (16)
g = acceleration due to gravity (m/s^2)
h = local heat transfer coefficient
h_{sf} = latent heat of melting of solid (J/kg)
k_d = dispersion thermal conductivity (J/s m K)
k = effective thermal conductivity (J/s m K)
K = permeability of the porous medium (m^2)
M = melting parameter defined in Eq. (20)
Nu = local Nusselt number defined in Eq. (23)
Pe$_x$ = local Peclet number defined in Eq. (15)
q_w = wall heat flux (J/s m^2)
Ra$_x$ = local Rayleigh number defined in Eq. (14)
T = temperature in thermal boundary layer (K)

T_0 = temperature at the solid region (K)
u = velocity in x-direction (m/s)
u_∞ = external flow velocity (m/s)
v = velocity in y-direction (m/s)
x = coordinate along the melting plate (m)
y = coordinates normal to melting plate (m)

Greek Symbols

α = equivalent thermal diffusivity (m^2/s)
β = coefficient of thermal expansion (1/K)
η = dimensionless similarity variable defined in Eq. (10)
θ = dimensionless temperature defined in Eq. (11)
μ = dynamic viscosity of fluid (kg/s m)
ν = kinematic viscosity of fluid (m^2/s)
ρ = density of convective fluid (kg/m^3)
ψ = stream function (m^2/s) defined in Eq. (9)

Subscripts

m = melting point
∞ = condition at infinity

References

[1] Nield, D. A., and Bejan, A., 1992, *Convection in Porous Media*, Springer-Verlag, New York.
[2] Amiri, A., and Vafai, K., 1994, "Analysis of Dispersion Effects and Non-Thermal Equilibrium, Non-Darcian, Variable Porosity Incompressible Flow Through Porous Media," Int. J. Heat Mass Transfer, **37**, pp. 939–954.
[3] Gorla, R. S. R., Mansour, M. A., Hassanien, I. A., and Bakier, A. Y., 1999, "Mixed Convection Effect on Melting From a Vertical Plate in a Porous Medium," Transp. Porous Media, **36**, pp. 245–254.
[4] Tashtoush, B., 2005, "Magnetic and Buoyancy Effects on Melting From a Vertical Plate Embedded in Saturated Porous Media," Energy Convers. Manage., **46**, pp. 2566–2577.
[5] Nield, D. A., 2007, "Impracticality of MHD Convection in a Porous Medium," Transp. Porous Media, **73**, pp. 379–380.
[6] Cheng, W. T., and Lin, C. H., 2007, "Melting Effect on Mixed Convective Heat Transfer With Aiding and Opposing External Flows From the Vertical Plate in a Liquid-Saturated Porous Medium," Int. J. Heat Mass Transfer, **50**, pp. 3026–3034.
[7] Murthy, P. V. S. N., 1998, "Thermal Dispersion and Viscous Dissipation Effects on Non-Darcy Mixed Convection in a Fluid Saturated Porous Medium," Int. J. Heat Mass Transfer, **33**, pp. 295–300.
[8] Plumb, O. A., 1983, "The Effect of Thermal Dispersion on Heat Transfer in Packed Bed Boundary Layers," *Proceedings of the First ASME/JSME Thermal Engineering Joint Conference*, Vol. 2, pp. 17–21.

Initial Buoyancy Reduction in Exhausting Smoke With Solar Chimney Design

C. L. Chow
Department of Architecture,
Wolfson College,
University of Cambridge,
Cambridge, UK

W. K. Chow[1]
Department of Building Services Engineering,
Research Centre for Fire Engineering,
The Hong Kong Polytechnic University,
Hung Hom, Kowloon,
Hong Kong, China
e-mail: bewkchow@polyu.edu.hk

A possible problem in using solar chimney as a natural smoke exhaust system will be identified in this paper. Smoke generated in a fire might not be removed effectively if the glazing walls are heated up due to exposure to solar radiation. It is because the buoyancy of the smoke is reduced initially in the solar chimney. This phenomenon of reducing buoyancy will be discussed. A simple equation of motion on smoke movement was set up. Some of the results of full-scale burning experiments carried out earlier for assessing the fire response of a glass façade system were applied to support the argument. Experiments indicated that smoke would take a longer time to move up when the glazing wall temperature is higher. A better smoke exhaust design accounting the reduction in buoyancy at this early stage of a fire should be worked out. [DOI: 10.1115/1.3211860]

Keywords: full-scale burning tests, glass solar chimney, buoyancy, smoke exhaust

1 Introduction

Conventional chimneys induce natural ventilation by both stack effect and buoyancy [1]. Stack effect is due to the differences between the indoor and outdoor temperatures. The resulting stack pressure also depends on the height. Buoyancy refers to the upward force due to the lighter density of the hot bulk of gases with temperature higher than the ambient.

A solar chimney is a way to introduce natural ventilation through solar energy [2]. It is similar to a conventional chimney but with some walls, normally facing south replaced by glazing. Due to exposure to solar radiation, the chimney interior would absorb solar energy and heat up the air inside. The air temperature inside the solar chimney would increase to give possible stack effect in driving natural ventilation. Usually, the solar chimney is located at the top of the building. Performance of solar chimneys on inducing natural ventilation have been studied extensively and reported in the literature.

Solar chimneys are proposed to be used as natural smoke exhaust systems in some new projects because of space limitation, cost reduction, or saving energy in operating mechanical smoke

exhaust systems [3] to satisfy the design criteria on green or sustainable buildings [4]. Thermal radiation on the glass panels would give higher temperatures. This would induce air flow from other parts of the building. Solar chimneys of sufficient height would give stack effect in driving smoke movement. Solar heating will give higher wall temperature, leading to a lower temperature difference between hot smoke and wall surfaces. Reducing buoyancy of smoke may thus give problems in exhausting smoke through solar chimneys at the early stage of the fire.

The reduction in buoyancy will be discussed in this paper. Experimental studies reported earlier [5] on a glass facade system model box will be applied to support the argument. It is better to consider this identified problem carefully in designing smoke exhaust system for the early stage of a fire.

2 Reduction in Buoyancy

A normal chimney with smoke at temperature T_s and density ρ_s moving up, as shown in Fig. 1(a), is taken as an example. Temperature of the wall is T_o and air density at that temperature is ρ_o. The buoyancy of smoke for the normal chimney B_{NC} is

$$B_{\mathrm{NC}} = (\rho_o - \rho_s)g \qquad (1)$$

The pressure difference induced by smoke with low temperature rise for a normal chimney is less than 10^3 Pa. This is much smaller than the atmospheric pressure ρ_0 (about 10^5 Pa). Applying the ideal gas law gives

$$\rho_o T_o = \rho_s T_s \qquad (2)$$

Putting in Eq. (1) gives

$$B_{\mathrm{NC}} = \rho_o T_o \left\{ \frac{T_s - T_o}{T_s T_o} \right\} g \qquad (3)$$

For a solar chimney, the hotter glazing wall is heated up by thermal radiation to temperature T_{hw}. The buoyancy of smoke for the solar chimney B_{SC} is

$$B_{\mathrm{SC}} = \rho_o T_o \left\{ \frac{T_s - T_{\mathrm{hw}}}{T_s T_{\mathrm{hw}}} \right\} g \qquad (4)$$

The ratio γ of the smoke buoyancy in a solar chimney to that in a normal chimney is

$$\gamma = \frac{B_{\mathrm{SC}}}{B_{\mathrm{NC}}} \qquad (5)$$

or

$$\gamma = \left(\frac{T_s - T_{\mathrm{hw}}}{T_s - T_o} \right) \left(\frac{T_o}{T_{\mathrm{hw}}} \right) \qquad (6)$$

Note that $T_{\mathrm{hw}} > T_o$ and so $\gamma < 1$. Before hot smoke at T_s moves out of the chimney to meet the cool air outside at T_o, the buoyancy would be reduced. It takes some time for warming up the cool glass chimney so that the value of γ would increase back to 1.

3 Experimental Studies

Experimental studies on different glass facade systems were reported [5] in the literature. Some of the results assessing the fire response of a model box with a double skin facade are useful for supporting the argument in this paper. Such experiments were carried out [5] in a full-scale burning site in Northeastern China. Tests on the glass model box similar to part of a solar chimney, as shown in Fig. 1(b), were considered. The glass model has a height of 3.5 m, and cross-section of 1×0.2 m², as shown in Fig. 1(b).

A fire room with a length of 1.5 m, width of 2 m, and height of 2.1 m, as shown in Fig. 1(b), was put adjacent to the glass box. A 22 kW pool fire with a diameter of 0.2 m with 150 ml gasoline was set up inside the room. An opening with a width of 0.1 m and height of 0.75 m was designed to direct smoke and heat from the fire room into the solar chimney model.
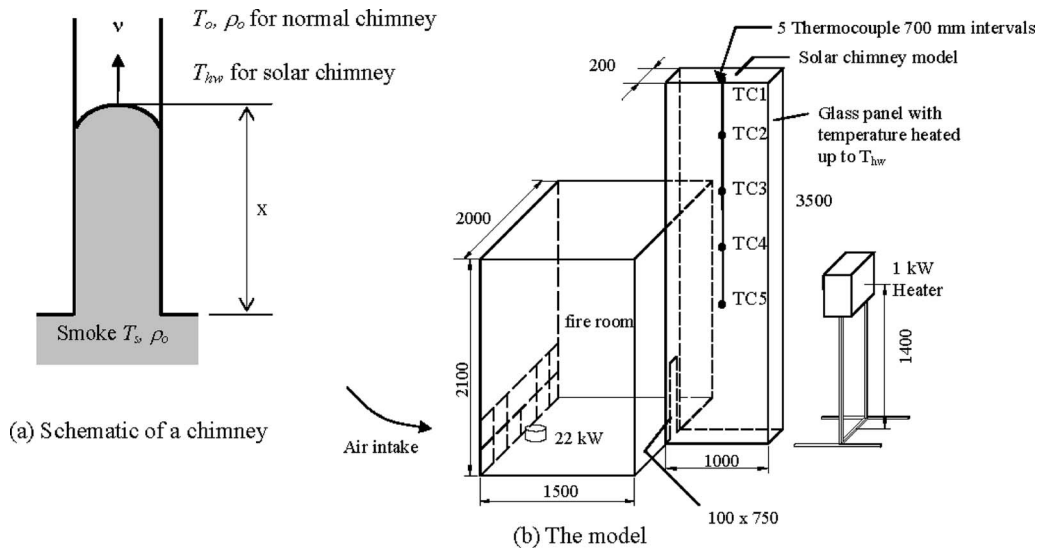
Fig. 1 The experimental setup

The glass panel was kept at different initial surface temperatures T_{hw} heated up by thermal radiation from an electrical heater, as shown in Fig. 1(b). Results on two sets of tests with surface temperatures of the glasses at 19°C (Test SC1) and 45°C (Test SC2) were used. The ambient temperature T_o was about 16°C.

In the tests, five thermocouples labeled TC1 (at the highest point) to TC5 were placed at the center of the solar chimney model to measure the vertical temperature profile (Fig. 1(b)). Two trials were carried out for each test with results on the transient temperatures for tests SC1 and SC2 [5].

4 Discussion

In view of the temperature distributions for the tests SC1 and SC2, as reported in Ref. [5], T_s was about 50°C or 323 K. It took about 45 s after starting the fire for smoke with higher temperature to move out of the chamber.

As observed from the temperature curve at the highest location TC1, as shown in Fig. 2, the time for the smoke front to reach

TC1 would be faster (at about 60 s) in test SC1 than in test SC2 (at about 80 s). This shows that smoke has lower buoyancy in chimney walls with higher temperature T_{hw}.

Putting in numerical values for T_s and T_o for these two tests to γ given by Eq. (6), we have

$$\gamma = 85 \left(\frac{323 - T_{hw}}{T_{hw}} \right) \qquad (7)$$

Variation in γ with T_{hw} would give how smoke buoyancy is reduced with hot wall temperatures.

An equation of motion [6] for smoke volume $\Delta\tau$ of density ρ_s at temperature T_s with travel distance x up the ceiling, as shown in Fig. 1(a), can be set up as

$$(\rho_s \Delta\tau) \frac{d^2x}{dt^2} = (\rho_s - \rho_{hw}) g \Delta\tau \qquad (8)$$

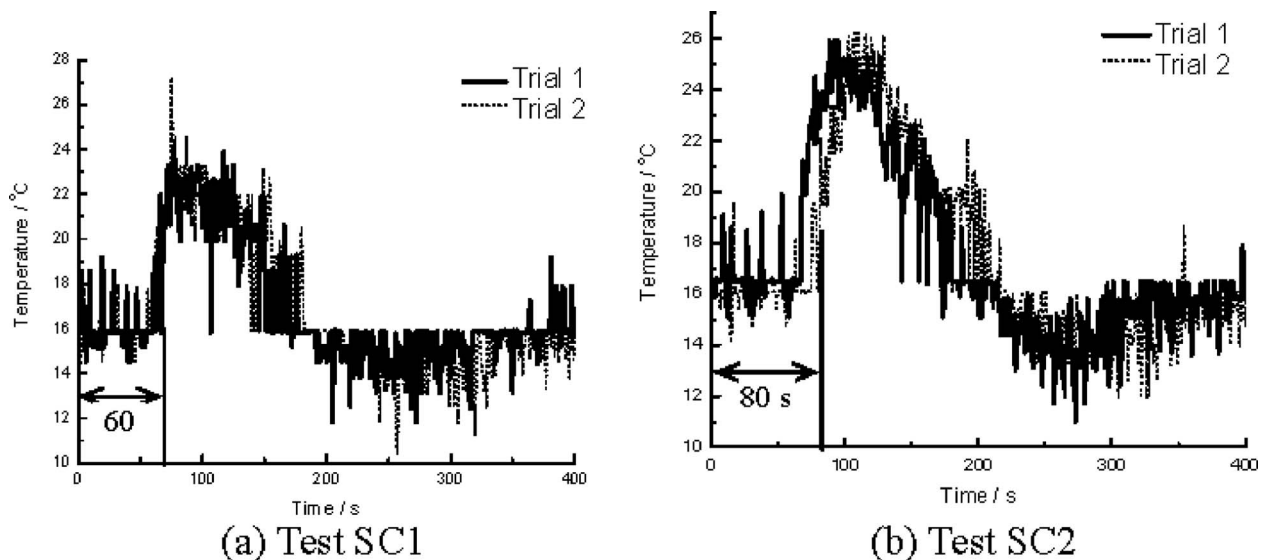Solving it gives x for initial speed ν_o at t with initial conditions $x=0$ when $t=0$

Fig. 2 Smoke temperature at the highest point TC1 of the solar chimney model

$$x = \frac{1}{2}\left(\frac{\rho_s - \rho_{hw}}{\rho_s}\right)gt^2 + \nu_o t \qquad (9)$$

Ideal gas with low pressure variation gives

$$\rho_s T_s = \rho_{hw} T_{hw} \qquad (10)$$

which when combined with Eq. (9) gives

$$x = \frac{g}{2}\left(\frac{T_{hw} - T_s}{T_{hw}}\right)t^2 + \nu_o t \qquad (11)$$

In traveling the same distance x up to the highest thermocouple location at TC1, the times were t_1 and t_2 for two different hot wall temperatures T_{hw1} and T_{hw2}, respectively. For low initial velocity $\nu_o \rightarrow 0$ ms^{-1}

$$\frac{g}{2}\left(\frac{T_{hw1} - T_s}{T_s}\right)t_1{}^2 = \frac{g}{2}\left(\frac{T_{hw2} - T_s}{T_s}\right)t_2{}^2$$

This gives

$$\frac{t_1}{t_2} = \left(\frac{T_{hw2} - T_s}{T_{hw1} - T_s}\right)^{1/2} \qquad (12)$$

For $T_{hw1} = 19\,^{\circ}$C or 292 K, $T_{hw2} = 45\,^{\circ}$C or 318 K

$$\frac{t_1}{t_2} = \left(\frac{318 - 323}{292 - 323}\right)^{1/2} \sim 0.402$$

This agreed fairly well with the observed temperature pattern on t_1 of (60–45) s or 15 s and t_2 of (80–45) s or 35 s as shown in Eq. (7), giving t_1/t_2 of 0.428 if the smoke temperature T_s was 50 °C. Slight deviation is expected in the above tests with a short solar chimney. Further, heat transfer in the smoke volume is not included. Smoke would be cooled down while moving up.

5 Conclusion

A possible problem on the initial flow of smoke through the solar chimney [2] as a static smoke exhaust system is discussed in this paper. The higher surface temperature of the solar chimney wall might reduce the buoyancy of smoke as demonstrated in the above analysis. This was supported by some experimental results reported earlier [5] on a glass facade model. Therefore, the vent area of the exhaust system should be determined carefully at the early stage of a fire. Once a steady flow is achieved, the smoke flow through the chimney would be improved, or at least resumed to normal, as a result of the heated chimney to reduce heat lost of smoke in maintaining the buoyancy.

The height of the experimental solar chimney model, which is only 3.5 m, may not be tall enough in the reported experimental studies [5] to understand the effect of buoyancy in actual construction. Further experiments with a longer solar chimney are suggested to give a better demonstration on the possible reduction

in buoyancy at the early stage, and possibility of improving the efficiency at the later stage. Full-scale tests in models of actual design are recommended.

Several important issues should be considered. First, a lower smoke temperature increasing rate would result from a slow growing fire. Therefore, buoyancy might not be reduced as much if heating rate of smoke is slow. Second, reduction in smoke buoyancy due to high wall temperature might be found not only in solar chimneys, but also in all buildings with glass facades. Finally, smoke exhaust efficiency might be better when outside temperature is warmer than inside. The smoke extract used in the above experiments was only one of the possible fire scenarios. This is a proposition of uncertain performance on the natural ventilation of the main parts of the building with a complex design of vertical shafts for releasing of smoke [7].

Nomenclature

B_{NC} = buoyancy of smoke for normal chimney
B_{SC} = buoyancy of smoke for solar chimney
g = acceleration due to gravity
P_o = atmospheric pressure
T_o, T_s = temperatures of outside air and smoke
T_{hw} = temperature of hot wall of chimney
t = time
t_1, t_2 = times traveled up for chimney with hot wall temperatures T_{hw1} or T_{hw2}
υ = velocity of smoke
x = distance traveled up

Greek Symbols

γ = ratio of buoyancy of solar chimney to normal chimney
ρ_o, ρ_s = densities of outside air and smoke
$\Delta\tau$ = smoke volume element

References

[1] Mowrer, F. W., Milke, J. A., and Torero, J. L., 2004, "A Comparison of Driving Forces for Smoke Movement in Buildings," J. Fire Protect. Eng., **14**(4), pp. 237–264.
[2] Afonso, C., and Oliveria, A., 2000, "Solar Chimneys: Simulation and Experiment," Energy Build., **32**, pp. 71–79.
[3] Ding, W., Minegishi, Y., Hasemi, Y., and Yamada, T., 2004, "Smoke Control Based on a Solar-Assisted Natural Ventilation System," Build. Environ., **39**(7), pp. 775–782.
[4] Chow, W. K., and Chow, C. L., 2003, "Green Influences," Fire Prevention & Fire Engineers Journal, September, pp. 34–35.
[5] Chow, W. K., Gao, Y., Dong, H., Zou, G. W., Han, S. S., and Chow, C. L., 2006, "Experimental Studies on Fire Response of Glass Facade Systems," Int. J. Eng. Perform.-Based Fire Codes, **8**(2), pp. 74–88.
[6] Tanaka, T., Fujita, T., and Yamaguchi, J., 2000, "Investigation Into Rise Time of Buoyant Fire Plume Fronts," Int. J. Eng. Perform.-Based Fire Codes, **2**(1), pp. 14–25.
[7] Shahin, G. A., and Floryan, J. M., 1999, "Heat Transfer Enhancement Generated by the Chimney Effect in Systems of Vertical Channels," ASME J. Heat Transfer, **121**, pp. 230–232.

Buoyant Convection in Superposed Metal Foam and Water Layers[1]

V. Kathare[2]

F. A. Kulacki[3]
Fellow ASME
e-mail: kulacki@me.umn.edu

Jane H. Davidson
Fellow ASME
e-mail: jhd@me.umn.edu

Department of Mechanical Engineering,
111 Church Street Southeast,
University of Minnesota,
Minneapolis, MN 55455

Heat transfer measurements for natural convection in superposed metal foam and water layers are reported. Two systems heated at the lower boundary are considered: a water-filled cavity with a foam layer on the heated surface and a water-filled cavity with foam layers on the upper and lower surfaces. The present experiments use open cell copper foams with a nominal porosity of 92%, and the relative thicknesses of the water and foam layers are varied. Steady state Nusselt numbers show that the presence of foam on the boundaries enhances overall heat transfer coefficients over that for the water-only layer. Enhancement of overall Nusselt numbers varies from 12% to 60% depending on Rayleigh number. Sublayer configurations with foam on both heat transfer surfaces are more effective for enhancement than a configuration with foam only on the heated surface. [DOI: 10.1115/1.3194767]

Keywords: natural convection, metal foam, heat transfer enhancement

1 Introduction

Recently Kathare et al. [1] published data for natural convection heat transfer in a water-saturated layer of 10 PPI and 20 PPI (PPI denotes pores per inch) copper foams enclosed in an insulated cavity and heated from below. The porous medium Nusselt number was correlated with the porous medium Rayleigh and modified Prandtl numbers. Conduction and buoyant advection were the dominant modes of heat transfer. Enhancement of the heat transfer rate compared with that in a water layer was found for $Ra_f \sim 10^8$ and $1.2 \times 10^{-5} \leq Da \leq 2.4 \times 10^{-5}$. The prior study leaves open the question of whether the observed heat transfer enhancement is governed by the boundary layer mechanism or the bulk characteristics of the foam-water combination. The present work answers this question in part via heat transfer measurements in natural convection for foam layers superposed by a fluid layer of varying heights. To our knowledge, no previous work has ap-

peared on such a system, but measurements and numerical studies of flow and natural convection exist for packed beds superposed by a fluid layer for a wide range of k_s / k_f [2–10]. Though not exhaustive, these studies suggest that metal foams, with their large values of permeability, Darcy number, and k_s / k_f, might offer heat transfer enhancement in natural convection for bottom-heated superposed fluid and porous layers. However, experiments to validate this inference are required.

Based on our prior experiments [1], a water-metal foam system presents a significantly different wall boundary condition than a packed bed owing to the more uniform porosity and permeability at the heated wall. The present study therefore focuses on heat transfer enhancement due to copper metal foam over that in a layer of water and extends the database of the above referenced literature on packed beds with a superposed fluid layer. Further, the motivation for the present study is to expand upon the results of our previous study as well as to enlarge the design database for possible use of metal foams in sensible heat water storage systems.

2 Apparatus and Procedure

The experimental apparatus and procedure are the same as described by Kathare et al. [1,11], and the following is a brief description of their primary features. The test chamber is a well insulated vertical acrylic cylinder of 12.7 cm inside diameter ×0.0635 cm wall, a heated lower boundary, and a vertically adjustable constant temperature upper boundary. The working fluid is degassed water. Superposed water and metal foam layers are created either with a water layer over laying a metal foam layer on the lower boundary (Type A, Fig. 1(*a*)) or with a foam layer on both the upper and lower surfaces (Type B, Fig. 1(*b*)). Heating from the bottom is provided by a resistance element located beneath a 9.53 mm thick copper bottom plate. A similar guard heater and a separator plate assembly at the bottom minimize heat loss to 3% of the applied flux. Net heat flow through the foam-water layers is held at ~63 W. The top plate is held at ~292±0.5 K with a spiral wound brazed copper tube through which cooling water is circulated.

Individually calibrated 36 Ga Type E thermocouples referenced to an ice bath are used for temperature measurements. For the top and bottom copper plates, six thermocouple junctions are located 0.53 mm beneath the surface in contact with the metal foam-water medium. Similarly positioned thermocouples are located on the bottom plate beneath the surface and in the copper plate below the acrylic separator plate. Temperatures of the bounding surfaces are recorded at steady state ~2 h after the initiation of heating.

Disks (2.54 cm×12.7 cm diameter) of open cell copper alloy (C10100) foam of 10 PPI and 20 PPI with cells generally comprising either 12 or 14 sided polyhedrons with either pentagonal or hexagonal faces and measured porosity of 0.92±0.02 were obtained from ERG Aerospace. The stagnant thermal conductivity of the 10 PPI and 20 PPI water-saturated foams ($k_m = 9.5 \pm 0.4$ W/m K) is obtained via measurements under a stable temperature gradient for a layer completely filled with foam. Values of K and C_f are obtained from a regression analysis in the form of a quadratic expression for measured pressure drop per unit depth of foam [11]. A summary of the transport parameters is shown in Table 1.

In the reduction in data, all thermophysical properties are evaluated at the mean of the lower and upper surface temperatures. The overall heat transfer coefficient is determined with the difference between the average temperatures of the upper and lower surfaces and the net heat flux through the foam-water layer. Maximum experimental uncertainties in the Darcy, Rayleigh, and Nusselt numbers are 8%, 11%, and 12%, respectively.
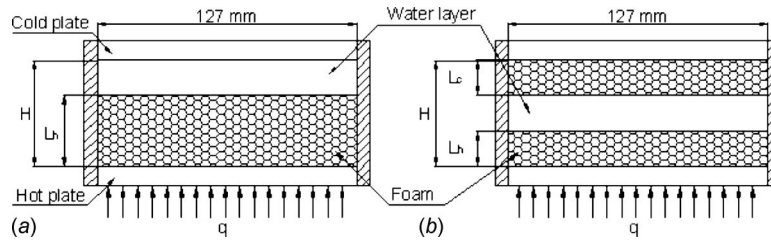
Fig. 1 Sublayer configurations. (a) Type A: Overlying water sublayer. (b) Type B: Interposed water sublayer.

3 Results

Table 2 lists the cases included in the experiments. Baseline data are presented for Rayleigh–Bénard convention in water layers of 0.0762 m (Case i) and 0.1016 m (Case ii). The measured Nu_f follows the correlation of Garon and Goldstein [12]. Superposed foam and water layers are represented by Cases ii–iv for $H = 0.0762$ m and Case vii for $H = 0.1016$ m. The limiting Cases v ($H = 0.0762$ m) and viii ($H = 0.1016$ m) are layers completely filled with foam. Results of the present heat transfer measurements are summarized in Table 3.

The effective conductivity of the water-foam combination is determined using a series resistance formula

$$\frac{H}{\tilde{k}} = \frac{H - L_h - L_c}{k_f} + \frac{L_h + L_c}{k_m} \qquad (1)$$

In the limiting Cases v and viii, $\tilde{k} = k_m$.

The primary effect of the foam on heat transfer rate is the change in Nu_f for $1.02 \times 10^8 \leq Ra_f \leq 3.11 \times 10^8$. Note that the fluid Rayleigh numbers are of the same order of magnitude because the experiments were run with the same applied heat flux. For the present experiments, the availability of a limited number

of copper foam sublayers and two PPI values does not permit an analysis of a wider range of dimensionless groups for characterizing the effects of pore size and sublayer depth.

For determining enhancement of heat transfer in the presence of the metal foam, we employ two enhancement ratios. The ratio E signifies the overall enhancement in heat transfer rate due to the presence of foam as compared with the water layer without foam for the same Ra_f.

$$E = \left. \frac{q_{\text{foam}}}{q_f} \right|_{Ra_f} \qquad (2)$$

Within this ratio is embedded all the hydrodynamic and the thermal effects of the foam on heat transfer. In terms of the relevant dimensionless groups, Eq. (2) reduces to

$$E = \left. \frac{Nu_{f,\text{foam}}}{0.10 \ Ra_f^{0.31}} \right|_{Ra_f} \qquad (3)$$

A second enhancement ratio $\tilde{E}$ is defined to emphasize the role of advection with the foam present,

Table 1 Foam layers with key transport parameters. Layers with multiple PPIs are obtained by stacking (PPI from bottom to top). A range of mean Prandtl numbers is given owing to the variation in fluid viscosity.

Foam layer PPI (L (m))	H/D	d_p ($\times 10^3$ m)	$K (\times 10^7$ m) (± 0.1)	C_f (± 0.0005)	Da($\times 10^5$)	Pr_m
10 (L=0.0254 m)	5	2.54	1.6	0.068	25.4	0.49–0.54
20 (L=0.0254 m)	5	1.25	1.1	0.083	16.5	0.40–0.44
10 (L=0.0508 m)	2.5	2.54	1.6	0.068	6.3	0.44–0.54
20 PPI (L=0.0508 m)	2.5	1.25	1.1	0.083	4.1	0.41–0.45
10–20–10 PPI (each 0.0254 m thick; L=0.0762 m)	1.67	2.54	1.4	0.074	2.4	0.40–0.49
20–10–20 PPI (each 0.0254 m thick, L=0.0762 m)	1.25	2.54	1.3	0.076	1.2	0.45–0.49

Table 2 Water and foam sublayer configurations with Rayleigh number based on fluid properties

Case	H (m)	L_h (m)	L_c (m)	Foam (PPI)	Type (Fig. 1)	Ra_f ($\times 10^{-8}$)
i	0.0762	No foam		NA	NA	1.09
ii		0.0254	0	10	A	1.62
iii		0.0508	0	10	A	1.57
iv		0.0254	0.0254	10	B	1.21
v		Foam filled		10–20–10	NA	1.02
vi	0.1016	No foam		NA	NA	2.69
vii		0.0254	0.0254	10	B	3.11
viii		Foam filled		10–20–20–10	NA	2.54

Table 3 Nusselt numbers with foam sublayers in comparison to water-only values

Case	$\widetilde{k}$ (W/m K)	Ra_f ($\times 10^{-8}$)	Nu_f	E	$\widetilde{E}$
i	0.59	1.09	31.5	NA	NA
ii	0.87	1.62	39.2	1.12	1.11
iii	1.59	1.57	40.1	1.15	1.11
iv	1.59	1.21	47.0	1.47	1.53
v	8.84	1.02	48.0	1.58	1.09
vi	0.58	2.69	42.4	NA	NA
vii	1.12	3.11	58.0	1.35	1.34
viii	8.84	2.54	59.6	1.48	1.11

$$\widetilde{E} = \left. \frac{(q - q_{\text{cond}})_{\text{foam}}}{(q - q_{\text{cond}})_{\text{water}}} \right|_{Ra_f} = \left. \frac{q\widetilde{k}}{(0.10 \ Ra_f^{0.31} - 1)k_f} \right|_{Ra_f} \quad (4)$$

In Eqs. (3) and (4), heat transfer rates are net quantities (total minus losses) delivered through the bottom surface to the water/foam system.

We now consider the several cases and the evidence of enhancement of the heat transfer rate due to the presence of the foam. First, consider the results when the height of the enclosure is 0.0762 m. The addition of 0.0254 m thick 10 PPI copper foam adjacent to the hot plate (Type A, Case ii) increases Nu_f compared with that in the water layer (Case i) and provides 12% enhancement of the heat transfer coefficient. The addition of a second layer of 0.0254 m thick 10 PPI foam adjacent to the hot plate (Type A, Case iii) increases Nu_f by an additional 2.3% (from 39.2 to 40.1) over the increase seen in Case ii for approximately the same Ra_f.

Comparison of Cases iii and iv, which have the same stagnant thermal conductivity but foam at different locations, indicates that when the foam is adjacent to both boundaries (Type B, Case iv), it provides much greater enhancement of heat transfer compared with enhancement in the Type A configuration. Case iv, which has a 0.0254 m thick 10 PPI foam positioned adjacent to both the hot and the cold plates with a 2.54 cm thick water layer in between, provides a value of Nu_f that is 17.2% larger than that in Case iii, even though Ra_f is $\sim 22\%$ less than that in Case iii. It also provides 47% enhancement of the heat transfer coefficient when compared with the heat transfer coefficient for a water layer of the same height without foam (Case i).

In Case v, the enclosure is completely filled with foam. The stagnant thermal conductivity is 5.9 times larger than that for Case iv. Case v provides the greatest enhancement of heat transfer, 58% greater than the water layer of the same height. However, this case provides only a marginal increase over Case iii, which uses less foam (5.08 cm versus 7.62 cm).

In a second series of experiments, a layer thickness of 0.1016 m is used. The base case, Case vi, has no foam. Case vii has two 10 PPI foam layers, each 0.0254 m thick adjacent to the isothermal plates and the water layer in between the foam is 0.0508 m thick. Case viii has a foam throughout the enclosure. Case viii, with the highest stagnant thermal conductivity, provides the maximum heat transfer enhancement, 48%, compared with a water layer of the same thickness. However, once again, placing the foam adjacent to both boundaries (Case vii) provides substantial heat transfer enhancement with less foam. Enhancement for Case vii is 35% in spite of having a stagnant thermal conductivity $\sim 12\%$ of that in Case viii.

We now consider advective enhancement $\widetilde{k}$ for a height of 0.0762 m. Cases ii and iii provide 11% enhancement in the advective heat transfer, whereas Case iv has the highest advective enhancement, 53%. Case v, with the cavity completely filled with the saturated foam, has the lowest enhancement of advective heat transfer, which is just 9%, even though the net enhancement of

heat transfer is highest at 58%. For $H = 10.16$ cm, Case vii with foam on both the boundaries provides 34% enhancement in advective heat transfer, whereas Case viii with foam throughout the cavity provides 11% enhancement in advective heat transfer.

Comparison of Cases ii and iii shows that there is no additional enhancement in advective heat transfer by adding the second layer of foam near the hot boundary, even though there is a very small increase in the overall heat transfer due to the rise in stagnant conductivity of the combination from 0.87 W/m K to 1.59 W/m K. Case iv with foam on both the boundaries increases the advective heat transfer enhancement considerably compared with Case iii. The addition of another layer of foam, i.e., filling the cavity completely with the foam, decreases the enhancement of advective heat transfer. This conclusion is supported by comparing $\widetilde{E}$ for Cases vii and viii.

4 Conclusion

The present study suggests that heat transfer enhancement in natural convection can be obtained for specific combinations of the sublayer thickness of the foam for the bottom-heated layer configuration. Comparison of Cases iv and v indicates that a substantial enhancement of overall heat transfer rate can be obtained by providing foam only on the boundaries. When the foam occupies the entire layer, heat transfer enhancement is primarily the result of the high stagnant conductivity of the foam-water combination, and advective enhancement is minimal. In this case, the foam away from the boundaries suppresses buoyancy.

With foam on the boundaries, heat transfer is influenced more by boundary phenomena than by bulk phenomena. The thickness and placement of the foam, foam morphology (PPI and ligament structure), and thermal conductivity ratio thus are the primary quantities determining the overall Nusselt number and enhancement factors. Development of the functional relation requires an extensive series of controlled experiments in concert with modeling and numerical analysis. To some extent, the literature reviewed in this paper and our earlier paper [1] suggests that a good start has been made toward a general heat transfer law, albeit for superposed layers of fluid and a packed bed of particles.

Our results and those of the prior literature also suggest that for practical applications, there exists an optimal thickness of foam adjacent to the thermal boundaries, and there would be a diminishing advantage and cost penalty for adding foam beyond it.

Nomenclature

C = specific heat (J/kg K)
C_f = form drag coefficient
d_p = pore diameter (m)
D = diameter of enclosure (m)
Da = Darcy number, K/d^2
E = heat transfer enhancement factor, Eq. (3)
$\widetilde{E}$ = convective enhancement factor, Eq. (4)
g = constant of gravitational acceleration (m/s^2)
h = heat transfer coefficient, $q/Ak_f(T_h - T_c)$ (W/m^2 K)
H = thickness saturated foam and water sublayers (m)
K = thermal conductivity (W/m K)
k_m = stagnant thermal conductivity of the porous medium (W/m K)
$\widetilde{k}$ = effective stagnant thermal conductivity of the foam-water system (W/m K), Eq. (1)

K = permeability (m^2)
L = thickness of the foam sublayer (m)
Nu$_f$ = Nusselt number for the fluid layer, hH/k_f
Pr$_m$ = Prandtl number for the saturated foam, $\mu C/k_m$
q = heat transfer rate (W)
Ra$_f$ = fluid Rayleigh number, $g\beta(T_h-T_c)H^3/(\alpha\nu)_f$
T = temperature (K)

Greek Symbols

α = thermal diffusivity (m^2/s)
β = isobaric coefficient of thermal expansion (K^{-1})
ν = kinematic viscosity of the fluid (m^2/s)
μ = dynamic viscosity of the fluid (kg/m s)

Subscripts

c = cold surface
cond = conduction
f = fluid
foam = with foam present
h = hot surface
m = porous medium
s = solid
water = value for water without foam present

References

[1] Kathare, V., Davidson, J. H., and Kulacki, F. A., 2008, "Natural Convection in Water-Saturated Metal Foam," Int. J. Heat Mass Transfer, **51**(15–16), pp. 3794–3802.
[2] Prasad, V., Brown, K., and Tina, Q., 1991, "Flow Visualization and Heat Transfer Experiments in Fluid Superposed Porous Layers Heated From Below," Exp. Therm. Fluid Sci., **4**, pp. 12–24.
[3] Prasad, V., and Tian, Q., 1990, "An Experimental Study of Thermal Convection in Fluid Superposed Porous Layers Heated From Below," *Heat Transfer 1990, Proceedings of the Ninth International Heat Transfer Conference*, Hemisphere, New York, Vol. 5, pp. 207–212.
[4] Prasad, V., 1993, "Flow Instabilities and Heat Transfer in Fluid Overlying Horizontal Porous Layers," Exp. Therm. Fluid Sci., **6**, pp. 135–146.
[5] Chen, F., and Chen, C. F., 1989, "Experimental Investigation of Convective Stability in a Superposed Fluid and Porous Layer When Heat From Below," J. Fluid Mech., **207**, pp. 311–321.
[6] Poulikakos, D., Bejan, A., Selimos, B., and Blake, K. R., 1986, "High Rayleigh Number Convection in a Fluid Overlaying a Porous Bed," Int. J. Heat Fluid Flow, **7**, pp. 109–116.
[7] Poulikakos, D., 1986, "Buoyancy-Driven Convection in a Horizontal Fluid Layer Extending Over a Porous Substrate," Phys. Fluids, **29**, pp. 3949–3957.
[8] Kladias, N., and Prasad, V., 1989, "Natural Convection in Horizontal Porous Layers: Effects of Darcy and Prandtl Numbers," ASME J. Heat Transfer, **111**, pp. 926–935.
[9] Jou, J. J., Kung, K. U., and Hsu, C. H., 1996, "Thermal Instability of Horizontally Superposed Porous and Fluid Layers in a Rotating System," Int. J. Heat Mass Transfer, **39**, pp. 1847–1857.
[10] Kim, S. J., and Choi, C. Y., 1996, "Convective Heat Transfer in Porous and Overlying Fluid Layers Heated From Below," Int. J. Heat Mass Transfer, **39**, pp. 319–329.
[11] Kathare, V., 2007, "Natural Convection in Water-Saturated Metal Foam," MS thesis, University of Minnesota, Minneapolis, MN.
[12] Garon, A. M., and Goldstein, R. J., 1973, "Velocity and Heat Transfer Measurements in Thermal Convection," Phys. Fluids, **16**, pp. 1818–1825.

Contributions of Inter- and Intraband Excitations to Electron Heat Capacity and Electron-Phonon Coupling in Noble Metals

Patrick E. Hopkins

Engineering Sciences Center,
Sandia National Laboratories,
P.O. Box 5800,
Albuquerque, NM 87185-0346
e-mail: pehopki@sandia.gov

This work examines the effects of photonically induced interband excitations from the d-band to states at the Fermi energy on thermophysical properties in noble metals. The change in the electron population in the d-band and the conduction band causes a change in electron heat capacity and electron-phonon coupling factor, which in turn impacts the evolution of the temperature after pulse absorption and electron thermalization. Expressions for heat capacity and electron-phonon coupling factor are derived for electrons undergoing both inter- and intraband transitions. In noble metals, due to the large d-band to Fermi energy separation, the contributions to electron heat capacity and electron-phonon coupling factor of intra- and interband transitions can be separated. At high absorbed laser fluences and pulse energies greater than the interband transition threshold, the interband and intraband contributions to thermophysical properties differ. [DOI: 10.1115/1.3192133]

Keywords: intraband transition, interband transition, electron-phonon coupling factor, short pulsed laser heating, electronic band structure

1 Introduction

The well known two temperature model (TTM) [1], which describes the rate of energy transfer from a hot thermalized electron system to a cooler phonon system, has been used to predict temperature changes and to deduce thermophysical properties in a wide array of studies, including ablation of metal targets [2–4], electron-phonon heat transfer in thin films [5–7], effects of microstructural disorder on electron-phonon scattering [8,9], excitations in nanoparticles [10–12], and electron-interface heat transfer [13–17]. In all of these aforementioned studies, including original derivation of the TTM by Anisimov et al. [1], a source term from an optical excitation is considered. However, this source term is only considered as a thermal excitation in heat transfer analyses. In the case of an incident optical excitation, such as that delivered by an ultrashort laser pulse, the incident photon energy will cause the electrons in the metal to undergo various inter- and intraband transitions. In the case of interband transitions, the population in the electronic bands participating in thermal processes will change, which will affect the electron heat capacity and electron-phonon coupling factor [18,19], subsequently affecting the predicted temperature change after the optical excitation [20].

In this technical brief, the effects of optically and thermally excited interband transitions from the d-band (below the Fermi surface) to the Fermi surface on the electron heat capacity and

electron-phonon coupling factor responses are considered and compared with the effects of intraband excitations. Both thermal transitions from Fermi smearing [18,19] and optical excitations from incident photon energies [20] cause a change in the electronic density of states, which in turn affects the thermal properties and temperature changes after the excitation. Based on changes in the electronic population in the conduction band and lower d-band, expressions are derived for heat capacity and electron-phonon coupling factors in the case of inter- and intraband transitions. Specific calculations of electronic heat capacity and electron-phonon coupling factor are presented for Au. Also, the intra- and interband contributions to the thermal properties are separated.

2 Separating Intra- and Interband Transitions

The electronic heat capacity, $C_e(T_e)$, and the electron-phonon coupling factor, $G(T_e)$, are dependent on the population of the electron bands within a few $k_B T_e$ of the Fermi surface [9], where k_B is Boltzmann's constant and T_e is the temperature of the electron system. Therefore, the density of states and the electronic distribution around the Fermi surface will dictate $C_e(T_e)$ and $G(T_e)$ [9]. In the case of intraband transitions, the population in the electron bands does not change, so $C_e(T_e)$ and $G(T_e)$ are governed by classical low temperature solid state theory. However, interband transitions increase/decrease the electron populations at various energies depending on the nature of the excitation, and therefore the density of states of the various bands below the Fermi surface must be taken into account.

In this development, an isotropic dispersion is assumed for the electron bands. Implications of this assumption are discussed and some calculations are compared with previous results using ab initio calculations for the density of states [19]. For the specific Au calculations involving interband excitations, only the outermost d-bands ($5d^{10}$) are considered, since for electron temperatures and photon energies of interest (0–10,000 K and 0–2.4 eV), this is the only band that will contribute excited electrons to the Fermi level. Excitations from the Fermi level to higher energy bands will not be considered since those higher energy bands are initially empty and, therefore, there is no net change in electron population above the Fermi level from excitations originating at the Fermi level. In addition, the $5d^{10}$ band to Fermi surface transitions is the dominant population changing transition in Au, as shown in its thermomodulation spectra [21]. This transition, often called the interband transition threshold (*ITT*) [7], is 2.4 eV in Au [22] and assumed constant with wavevector in this work due to the assumption of an isotropic dispersion.

An intraband transition occurs from an excitation with energy less than the interband transition threshold energy, ε_{ITT}. If the thermal excitation of energy $k_B T_e$ or optical excitation of energy $h\nu$, where h is Planck's constant and ν is the photon frequency, is less than ε_{ITT}, then the thermal properties are only subject to intraband effects. Intraband transitions would occur within the conduction band only as electrons are thermally or optically excited. At these low energies (i.e., excitation energies less than ε_{ITT}), a thermal or optical excitation does not excite any electrons from the d-bands. Therefore, the electron heat capacity is calculated by

$$C_e(T_e) = \int_{-\infty}^{\infty} \varepsilon D_C(\varepsilon) \frac{\partial f(\varepsilon, \mu(T_e), T_e)}{\partial T_e} d\varepsilon \qquad (1)$$

where ε is the electron energy, $D_C(\varepsilon)$ is the conduction band density of states (in the case of Au, the $6s^1$ band), and f is the Fermi–Dirac distribution function with $\mu(T_e)$ being the chemical potential, which is a function of electron temperature. In the low temperature limit, $\mu(T_e)$ is approximately equal to the Fermi energy, ε_F, and Eq. (1) can be expressed as $C_e(T_e) = \gamma T_e$, where γ is commonly called the Sommerfeld coefficient, which is theoreti-

cally 62.9 J m^{-3} K^{-2} [23]. The reduction of Eq. (1) to $C_e(T_e) = \gamma T_e$ also assumes that only electrons at the Fermi energy participate in energy storage, that is, $C_e(T_e) \propto D_C(\varepsilon_F)$.

The general form for the electron–phonon coupling factor is given by [24]

$$G(T_e) = \pi\hbar k_B \lambda \langle \omega^2 \rangle \int_{-\infty}^{\infty} \frac{(D_T(\varepsilon))^2}{D_T(\varepsilon_F)} \left(-\frac{\partial f(\varepsilon, \mu(T_e), T_e)}{\partial \varepsilon} \right) d\varepsilon \quad (2)$$

where $\hbar$ is the reduced Planck's constant, λ is the dimensionless electron-phonon mass enhancement parameter [25], $\langle \omega^2 \rangle$ is the second moment of the phonon spectrum [26], and $D_T(\varepsilon)$ is density of states of all the electron bands modified by the excitation. For Au, $\lambda\langle \omega^2 \rangle = 23$ meV$^2/\hbar^2$ [27]. In the case of only intraband transitions in the conduction band, Eq. (2) is given by

$$G(T_e) = \pi\hbar k_B \lambda \langle \omega^2 \rangle \int_{-\infty}^{\infty} \frac{(D_C(\varepsilon))^2}{D_C(\varepsilon_F)} \left(-\frac{\partial f(\varepsilon, \mu(T_e), T_e)}{\partial \varepsilon} \right) d\varepsilon \quad (3)$$

At relatively low temperatures, $\partial f(\varepsilon, \mu(T_e), T_e)\partial\varepsilon \approx \delta(\varepsilon - \mu(T_e)) \approx \delta(\varepsilon)$ and Eq. (3) reduces to $G_0 = \pi\hbar k_B \lambda \langle \omega^2 \rangle D_C(\varepsilon_F)$, which is the original expression derived by Allen [28].

An interband transition occurs from an excitation with energy greater than ε_{ITT}. In this case, electrons in the d-band are excited to empty states around the Fermi energy and must be considered in thermal processes. Therefore, the total electron heat capacity taking into account the conduction band and d-band is given by

$$C_e(T_e) = \int_{-\infty}^{\infty} \varepsilon D_T(\varepsilon) \frac{\partial f(\varepsilon, \mu(T_e), T_e)}{\partial T_e} d\varepsilon \quad (4)$$

and the electron-phonon coupling factor is given by Eq. (2). However, in the event that an electron moves from a filled state in a d-band to an empty state near the Fermi level through an optical excitation, the density of states of the conduction band and the d-band will be changed without a change in Fermi smearing and, therefore, calculations of $C_e(T_e)$ and $G(T_e)$ will be altered. In this case, the number density of the electrons in each band will change. The number of empty states in the conduction band for which there is sufficient photon energy to excite an electron is given by [20]

$$n_{\text{available}} = \int_{-\infty}^{\infty} D_C(\varepsilon)(1 - f(\varepsilon, \mu(T_e), T_e))(1 - H[\varepsilon - (\mu(T_e) - (\varepsilon_{ITT} - h\nu))]) d\varepsilon \quad (5)$$

where $H[\cdots]$ is the Heaviside function. Equation (5) will affect the density of states calculations. Note that this expression for available states is more physical than the expression used previously [20] since Eq. (5) does not put any stipulation on the width of the Fermi surface that is available for electronic excitation, in addition to accounting for the maximum number of electrons that can fill the bands, as opposed to arbitrarily increasing the number density.

Separation of the interband contribution to electron heat capacity is straightforward recognizing that any excitation involving the d-band electrons is an interband contribution to electron heat capacity. Therefore, since heat capacity is an additive property, the interband contribution to electron heat capacity is given by

$$C_{e,\text{inter}}(T_e) = \int_{-\infty}^{\infty} \varepsilon D_D(\varepsilon) \frac{\partial f(\varepsilon, \mu(T_e), T_e)}{\partial T_e} d\varepsilon \quad (6)$$

where $D_D(\varepsilon)$ is density of states of the d-band and $D_T(\varepsilon) = D_C(\varepsilon) + D_D(\varepsilon)$ and, therefore, $C_{e,\text{intra}}(T_e)$ is defined by Eq. (1), which can be rewritten as

$$C_{e,\text{intra}}(T_e) = \int_{-\infty}^{\infty} \varepsilon D_c(\varepsilon) \frac{\partial f(\varepsilon, \mu(T_e), T_e)}{\partial T_e} d\varepsilon \quad (7)$$

The separation of the transitions on electron-phonon coupling factor is dependent on the band structure, however. Equation (2) can be rewritten as

$$G(T_e) = \pi\hbar k_B \lambda \langle \omega^2 \rangle \int_{-\infty}^{\infty} \frac{(D_C(\varepsilon) + D_D(\varepsilon))^2}{D_C(\varepsilon_F) + D_D(\varepsilon_F)} \left(-\frac{\partial f(\varepsilon, \mu(T_e), T_e)}{\partial \varepsilon} \right) d\varepsilon \quad (8)$$

In noble metals (Au, Ag, and Cu), the density of states of the d-band at the Fermi level is zero, that is, $D_D(\varepsilon_F) = 0$. Therefore, Eq. (8) reduces to

$$G(T_e) = \pi\hbar k_B \lambda \langle \omega^2 \rangle \int_{-\infty}^{\infty} \frac{(D_C(\varepsilon) + D_D(\varepsilon))^2}{D_C(\varepsilon_F)} \left(-\frac{\partial f(\varepsilon, \mu(T_e), T_e)}{\partial \varepsilon} \right) d\varepsilon \quad (9)$$

Now considering only intraband transitions, Eq. (9) reduces to Eq. (3). In noble metals, the density of states of the d-band is so much greater than that of the conduction band that the conduction band density of states is relatively constant with energy (this is especially true in Au as evident from ab initio electronic structure calculations [19,29]) and, therefore, Eq. (3) reduces to the expression for G_0 derived by Allen, even at high temperature. Thus, the interband contribution is given by

$$G_{\text{inter}}(T_e) = \pi\hbar k_B \lambda \langle \omega^2 \rangle \int_{-\infty}^{\infty} \frac{(D_D(\varepsilon))^2}{D_C(\varepsilon_F)} \left(-\frac{\partial f(\varepsilon, \mu(T_e), T_e)}{\partial \varepsilon} \right) d\varepsilon \quad (10)$$

The reader is cautioned that Eq. (10) is only valid for noble metals due to the large d-band separation from the Fermi energy. Since the intraband contribution to G reduces to G_0 for noble metals

$$G_{\text{total}}(T_e) = G_0 + G_{\text{inter}}(T_e) \quad (11)$$

showing that, for noble metals, the inter- and intraband contributions to the electron-phonon coupling factor are additive, similar to heat capacity.

3 Effects of Optical Excitations

The key to evaluating $C_e(T_e)$ and $G(T_e)$ lies in determining $\mu(T_e)$, which, when only considering intraband transitions, can be approximated by the Sommerfeld expansion [30], but when taking into account d-band excitations must be calculated by conservation of electron number density by evaluating

$$n_C + n_D = \int_{-\infty}^{\infty} (D_C(\varepsilon) + D_D(\varepsilon)) f(\varepsilon, \mu(T_e), T_e) d\varepsilon \quad (12)$$

where $n_C + n_D$ is a constant and $\mu(T_e)$ is iterated for each temperature. For Au, n_C is 5.9×10^{28} m^{-3} and n_D is 5.9×10^{29} m^{-3}, which is estimated by the atomic density [23] and the number of electrons in the $6s^1$ and $5d^{10}$ bands, respectively [31]. The conduction band density of states is estimated by $D_C = 3n_{C,\text{total}}\varepsilon^{1/2}/(2\varepsilon_F^{3/2})$, where the Fermi energy of Au is 5.53 eV [23], and $n_{C,\text{total}}$ is the total number of electrons in the conduction band after the excitation, which is given by $n_{C,\text{total}} = n_C + n_{\text{excited}}$. Here, n_{excited} is the number of electrons excited from the d-band to the conduction band from incident photons, which is a function of the number of photons absorbed by the material. If there are enough photons absorbed by the metal to excite all the electrons in the d-band up to available states in the conduction band, then $n_{\text{excited}} = n_{\text{available}}$, where $n_{\text{available}}$ is defined by Eq. (5), and therefore $n_{C,\text{total}} = n_C + n_{\text{available}}$. For this condition to be true, then $n_{\text{available}} \leq n_{\text{photons}}$, where n_{photons} is the number of photons per unit
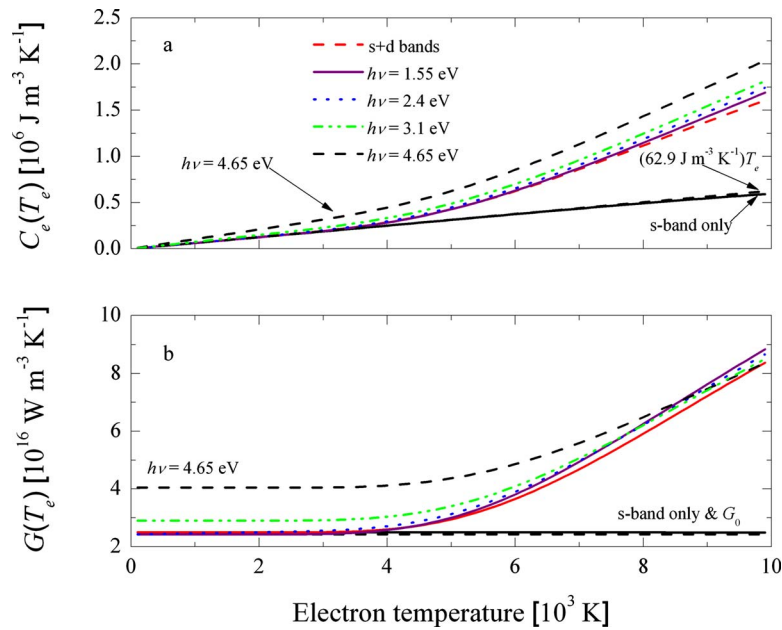
Fig. 1 Predictions of (*a*) electron heat capacity and (*b*) electron-phonon coupling factor in Au. The numerical calculations are performed using only the s-band density of states (s-band only), the s- and d-band density of states with no photonic excitation (*s*+*d* bands), and the s- and d-band density of states with a photonic excitation, *hν* (*hν*=1.55 eV, *hν*=2.4 eV, *hν* =3.1 eV, and *hν*=4.65 eV). The s-band density of states calculations show close agreement to low temperature theory throughout the temperature range T_e=0–10,000 K.

volume in the absorbed laser pulse. The number of photons per volume can be estimated as $n_{photons}=A/(h\nu\delta)$, where A is the absorbed fluence and δ is the optical penetration depth at $h\nu$. In the case $n_{photons}$ is less than $n_{available}$, then only $n_{photons}/n_{available}$ of the empty states in the conduction band will be filled by electrons undergoing interband transitions.

Assuming that all empty states in the conduction band below the Fermi level are filled by interband excited electrons, that is $n_{available} \leq n_{photons}$ and $n_{C,total}=n_C+n_{available}$, the number of states in the d-band after photonically induced interband transitions is given by $n_{D,total}=n_D-n_{available}$. The density of states of the $5d^{10}$ band in Au can be approximated by a square function with a width of 5.28 eV [32,33] and the high energy edge of the square function 2.4 eV below the Fermi energy, giving rise to the *ITT* energy in Au, so that $D_D(\varepsilon)=n_{D,total}/5.28(-H[\varepsilon-3.13]+H[\varepsilon+2.15])$. Note the calculation of temperature dependent thermophysical properties using this approximate band structure has shown close agreement with calculations of thermophysical properties using exact ab initio calculations for electronic band structure [29].

Figure 1 shows the calculations for (a) the electronic heat capacity, $C_e(T_e)$, and (b) electron-phonon coupling factor, $G(T_e)$, as a function of temperature in Au for photonic excitations of various energies, $h\nu$=1.55, 2.40, 3.10, and 4.65 eV. 1.55 eV is the fundamental output of Ti:Al$_2$O$_3$ oscillators, which are typically used to examine electron-phonon coupling; 3.10 eV and 4.65 eV are the frequency doubled and tripled components of the fundamental Ti:Al$_2$O$_3$ frequency; 2.40 eV is the interband transition threshold of Au. Figure 1(a) shows predictions for the electron heat capacity for the different band excitation cases presented in Fig. 1(a). When only considering the 6s band in the numerical calculation, the results are almost identical to the theoretical value for heat capacity predicted by $C_e(T_e)=\gamma T_e$, where γ=62.9 J m^{-3} K^{-2}. When considering the 5d band, $C_e(T_e)$ increases due to Fermi smearing and thermal excitation of the d-band electrons. This is intuitive since, when considering d-band electrons at elevated

temperatures, there are more electrons available to "store" heat. Photonic excitations that completely fill empty states in the conduction band increase the electron heat capacity; the increasing trend in heat capacity increases as more empty states in the conduction band are filled.

Figure 1(b) shows the calculations for the electron-phonon coupling factor for the different excitation cases discussed. The s-band only calculations show a constant trend in G with temperature and are very close to the predictions of G_0. This further supports Eq. (12) where the constant G is the intraband contribution. The difference between the two values most likely lies in the assumption in the numerical calculation of a parabolic density of states with energy and error in the numerical integration method. However, the difference between the predicted G_0 from theory $(2.43\times10^{16}$ W m^{-3} K$^{-1})$ and the constant G predicted from the numerical calculations $(2.49\times10^{16}$ W m^{-3} K$^{-1})$ is negligible when comparing to G with d-band excitations. Including d-band excitations to empty states above the Fermi surface noticeably increases the electron-phonon coupling factor at low temperatures. In both Figs. 1(a) and 1(b), when the photon energy is greater than ε_{ITT}, the values and trends of the thermophysical properties change due to a change in number density in the electron bands around the Fermi energy which affects the electron density of states.

Figures 1(a) and 1(b) show the total $C_e(T_e)$ and $G(T_e)$, which include both intra- and interband contributions. The intraband contribution in each figure is depicted by the "s-band only" data. Therefore, the interband contribution is determined by subtracting the s-band only data from the total $C_e(T_e)$ and $G(T_e)$ predictions. The intraband contribution to the heat capacity is given by $C_{e,intra}(T_e)=62.9T_e$ over the entire temperature range. The intraband contribution to electron-phonon coupling is simply an offset of $G_{intra}=G_0\approx2.49\times10^{16}$ W m^{-3} K^{-1}.

4 Conclusions

This work examines the effects of photonically induced interband excitations from the d-band to states at the Fermi energy on thermophysical properties in noble metals. The change in the electron population in the d-band and the conduction band causes a change in electron heat capacity and electron-phonon coupling factor, which in turn impacts the evolution of the temperature after pulse absorption and electron thermalization. Expressions for heat capacity, electron-phonon coupling factor, and transient temperature change are derived for electrons undergoing both inter- and intraband transitions. In noble metals, due to the large d-band to Fermi energy separation, the contributions to electron heat capacity and electron-phonon coupling factor of intra- and interband transitions can be separated. At high absorbed laser fluences and pulse energies greater than the interband transition threshold, the interband and intraband contributions to thermophysical properties differ.

Acknowledgment

Nomenclature

C_e = electron heat capacity, J m^{-3} K^{-1}
D = electron spectral density of states per unit volume, m^{-3} eV^{-1}
f = Fermi–Dirac distribution function
G = electron-phonon coupling factor, W m^{-3} K^{-1}
H = Heaviside function
h = Planck's constant, J s
$\hbar$ = Planck's constant divided by 2π, J s
k_B = Boltzmann constant, J K^{-1}
n = number density, m^{-3}
T_e = electron temperature, K

Greek Symbols

ε = electron energy, eV
γ = Sommerfeld coefficient (linear coefficient to heat capacity), J m^{-3} K^{-2}
λ = electron-phonon mass enhancement parameter
$\langle \omega^2 \rangle$ = second moment of the phonon spectrum
μ = chemical potential, eV
ν = photon frequency, Hz

Subscripts

C = conduction band
D = d-band
F = Fermi
inter = interband transition
intra = intraband transition
T = total

References

[1] Anisimov, S. I., Kapeliovich, B. L., and Perel'man, T. L., 1974, "Electron Emission From Metal Surfaces Exposed to Ultrashort Laser Pulses," Sov. Phys. JETP, **39**, pp. 375–377.

[2] Ivanov, D. S., and Zhigilei, L. V., 2003, "Combined Atomistic-Continuum Modeling of Short-Pulse Laser Melting and Disintegration of Metal Films," Phys. Rev. B, **68**, p. 064114.

[3] Zhigilei, L. V., and Ivanov, D. S., 2005, "Channels of Energy Redistribution in Short-Pulse Laser Interactions With Metal Targets," Appl. Surf. Sci., **248**, pp. 433–439.

[4] Jiang, L., and Tsai, H.-L., 2005, "Improved Two-Temperature Model and Its Application in Ultrashort Laser Heating of Metal Films," ASME J. Heat Transfer, **127**, pp. 1167–1173.

[5] Qiu, T. Q., and Tien, C. L., 1993, "Heat Transfer Mechanisms During Short-Pulse Laser Heating of Metals," ASME J. Heat Transfer, **115**, pp. 835–841.

[6] Eesley, G. L., 1986, "Generation of Nonequilibrium Electron and Lattice Temperatures in Copper by Picosecond Laser Pulses," Phys. Rev. B, **33**, pp. 2144–2151.

[7] Hohlfeld, J., Wellershoff, S. S., Gudde, J., Conrad, U., Jahnke, V., and Matthias, E., 2000, "Electron and Lattice Dynamics Following Optical Excitation of Metals," Chem. Phys., **251**, pp. 237–258.

[8] Hostetler, J. L., Smith, A. N., Czajkowsky, D. M., and Norris, P. M., 1999, "Measurement of the Electron-Phonon Coupling Factor Dependence on Film Thickness and Grain Size in Au, Cr, and Al," Appl. Opt., **38**, pp. 3614–3620.

[9] Qiu, T. Q., and Tien, C. L., 1993, "Size Effects on Nonequilibrium Laser Heating of Metal Films," ASME J. Heat Transfer, **115**, pp. 842–847.

[10] Arbouet, A., Voisin, C., Christofilos, D., Langot, P., Del Fatti, N., Vallee, F., Lerme, J., Celep, G., Cottancin, E., Gaudry, M., Pellarin, M., Broyer, M., Maillard, M., Pileni, M. P., and Treguer, M., 2003, "Electron-Phonon Scattering in Metal Clusters," Phys. Rev. Lett., **90**, p. 177401.

[11] Hartland, G. V., 2004, "Electron-Phonon Coupling and Heat Dissipation in Metal Nanoparticles," Int. J. Nanotechnol., **1**, pp. 307–327.

[12] Hodak, J. H., Henglein, A., and Hartland, G. V., 2000, "Electron-Phonon Coupling Dynamics in Very Small (Between 2 and 8 nm) Diameter Au Nanoparticles," J. Chem. Phys., **112**, pp. 5942–5947.

[13] Hopkins, P. E., 2009, "Effects of Electron-Boundary Scattering on Changes in Thermoreflectance in Thin Metal Films Undergoing Intraband Transitions," J. Appl. Phys., **105**, p. 093517.

[14] Hopkins, P. E., Kassebaum, J. L., and Norris, P. M., 2009, "Effects of Electron Scattering at Metal-Nonmetal Interfaces on Electron-Phonon Equilibration in Gold Films," J. Appl. Phys., **105**, p. 023710.

[15] Hopkins, P. E., and Norris, P. M., 2009, "Contribution of Ballistic Electron Transport to Energy Transfer During Electron-Phonon Nonequilibrium in Thin Films," ASME J. Heat Transfer, **131**, p. 043208.

[16] Hopkins, P. E., Norris, P. M., Stevens, R. J., Beechem, T., and Graham, S., 2008, "Influence of Interfacial Mixing on Thermal Boundary Conductance Across a Chromium/Silicon Interface," ASME J. Heat Transfer, **130**, p. 062402.

[17] Norris, P. M., and Hopkins, P. E., 2009, "Examining Interfacial Diffuse Phonon Scattering Through Transient Thermoreflectance Measurements of Thermal Boundary Conductance," ASME J. Heat Transfer, **131**, p. 043207.

[18] Lin, Z., and Zhigilei, L. V., 2007, "Temperature Dependences of the Electron-Phonon Coupling, Electron Heat Capacity and Thermal Conductivity in Ni Under Femtosecond Irradiation," Appl. Surf. Sci., **253**, pp. 6295–6300.

[19] Lin, Z., Zhigilei, L. V., and Celli, V., 2008, "Electron-Phonon Coupling and Electron Heat Capacity of Metals Under Conditions of Strong Electron-Phonon Nonequilibrium," Phys. Rev. B, **77**, p. 075133.

[20] Hopkins, P. E., Duda, J. C., Salaway, R. N., Smoyer, J. L., and Norris, P. M., 2008, "Effects of Intra- and Interband Transitions on Electron-Phonon Coupling and Electron Heat Capacity After Short Pulsed Laser Heating," Nanoscale Microscale Thermophys. Eng., **12**, pp. 320–333.

[21] Scouler, W. J., 1967, "Temperature-Modulated Reflectance of Gold From 2 to 10 eV," Phys. Rev. Lett., **18**, pp. 445–448.

[22] Schoenlein, R. W., Lin, W. Z., Fujimoto, J. G., and Eesley, G. L., 1987, "Femtosecond Studies of Nonequilibrium Electronic Processes in Metals," Phys. Rev. Lett., **58**, pp. 1680–1683.

[23] Kittel, C., 1996, *Introduction to Solid State Physics*, Wiley, New York.

[24] Wang, X. Y., Riffe, D. M., Lee, Y.-S., and Downer, M. C., 1994, "Time-Resolved Electron-Temperature Measurement in a Highly Excited Gold Target Using Femtosecond Thermionic Emission," Phys. Rev. B, **50**, pp. 8016–8019.

[25] Grimvall, G., 1981, *The Electron-Phonon Interactions in Metals* (Selected Topics in Solid State Physics), North-Holland, New York.

[26] Mcmillan, W. L., 1968, "Transition Temperature of Strong-Coupled Superconductors," Phys. Rev., **167**, pp. 331–344.

[27] Brorson, S. D., Kazeroonian, A., Moodera, J. S., Face, D. W., Cheng, T. K., Ippen, E. P., Dresselhaus, M. S., and Dresselhaus, G., 1990, "Femtosecond Room-Temperature Measurement of the Electron-Phonon Coupling Constant λ in Metallic Superconductors," Phys. Rev. Lett., **64**, pp. 2172–2175.

[28] Allen, P. B., 1987, "Theory of Thermal Relaxation of Electrons in Metals," Phys. Rev. Lett., **59**, pp. 1460–1463.

[29] Lin, Z., and Zhigilei, L. V., 2006, "Thermal Excitation of D Band Electrons in Au: Implications for Laser-Induced Phase Transformations," Proc. SPIE, **6261**, p. 62610U.

[30] Pathria, R. K., 2006, *Statistical Mechanics*, Elsevier Butterworth-Heinemann, Burlington, MA.

[31] Gray, D. E., 1972, *American Institute of Physics Handbook*, McGraw-Hill, New York.

[32] Harrison, W. A., 1980, *Electronic Structure and the Properties of Solids: The Physics of the Chemical Bond*, W. H. Freeman and Company, San Francisco, CA.

[33] Heiner, E., 1988, "Nonequilibrium Thermalized Stage of Noble Metals," Phys. Status Solidi B, **148**, pp. 599–609.